CYLINDRICAL LIQUID-LIQUID JET INSTABILITY

A DISSERTATION SUBMITTED TO THE GRADUATE DIVISION OF THE UNIVERSITY OF HAWAI‘I IN PARTIAL FULFILLMENT OF THE REQUIREMENTS FOR THE DEGREE OF

DOCTOR OF PHILOSOPHY

IN

OCEAN ENGINEERING

AUGUST 2004

By
Liujuan Tang

Dissertation Committee:

Stephen M. Masutani, Chairperson
Gérard C. Nihous
Hans-Jürgen Krock
Kwok Fai Cheung
Ronald H. Knapp
Charles M. Kinoshita

To my parents Daihua and Hualin

ACKNOWLEDGMENTS

This dissertation could not have been written without Dr. Stephen Masutani who not only served as my supervisor but also gave me full support throughout my academic and research programs, and maximum degrees of freedom to do what I was interested in. He has taught me more than I could ever give him credit for here.

I would like to thank all the committee members for serving on the committee and providing thoughtful guidance to the dissertation. Special thanks to Dr. Gérard Nihous for introducing me to the subject of numerical simulation of CO_2 plume besides my dissertation, and for those long meetings we had. And thanks to Dr. Eric Adams for his useful opinions.

For all the help at Look lab and the discussions on any imaginable subjects, my sincere thanks to Roland Kanno. I am also grateful to my colleagues, Dr. Thomas Gorgas, the best videographer I've worked with, Drs. Traci Sylva and Brandon Yoza, Ryan Kurasaki, Shu Ki Tsang, Tersha Enriques and Aparna Krishnamurthy for their help and friendship. Thanks to Mr. Charles Nelson for machining the experimental components. Thanks also to Ms. Edith Katada, the best secretary I ever knew, for her care and assistance with the countless forms I needed to fill out in order to graduate.

My deepest gratitude to the members of my family: my parents, whose love and guidance are with me in whatever I pursue; my sisters Liuyan and Liuling, and my niece Xinru, who always believe in me; most importantly, my husband, Yong, whenever, wherever and whatever I am short of hands, he is always the No. 1 backup. Thanks to

Grandma Kuo and all of my friends in Hawaii and China for all the support they gave me during such a long journey.

Support for this work was provided in part by the Research Institute of Innovative Technology for the Earth (RITE) via a grant from the Pacific International Center for High Technology Research (PICHTR). Additional funding was provided by National Energy Technology Laboratory of the U.S. Department of Energy, U.S. Department of the Interior, Mineral Management Service, and the State of Hawaii, Department of Business, Economic Development and Tourism.

ABSTRACT

Experiments were conducted to investigate the breakup of liquid jets discharging into another liquid over the full range of instabilities extending from disintegration of laminar jets to turbulent atomization. The present study focused upon elucidating the fundamental mechanisms and parameters that control jet breakup; identifying liquid-liquid jet instability regimes and determining the boundaries of these regimes; and securing quantitative data on droplet size spectra that could provide insight into the breakup phenomena and which could be applied to the development and testing of models. A secondary objective was to explore the effects of solid hydrate formation on CO_2 jets in the deep ocean environment. This topic is relevant to CO_2 ocean sequestration.

The experiments were conducted in several facilities. Jet fluids including four deepwater crude oils, two silicone fluids, and liquid CO_2 with very different properties were injected into tap water, natural seawater or synthetic seawater over a range of flow rates, temperatures, and pressures from a variety of injection nozzles. The independent parameters of the tests were: (1) jet velocity; (2) jet and ambient fluid properties; and (3) injector diameter and geometry. Flow visualization and Phase Doppler particle analysis were the primary measurement techniques.

The major results and conclusions of this study are summarized below:

1. Five instability regimes were identified by a comprehensive review of the digital video records of the 294 test runs. The five regimes which occur in sequence as

liquid-liquid jet disintegration progresses from laminar instability to turbulent atomization are: (1) varicose breakup, where Rayleigh instability dominates and a symmetric surface wave forms and grows, eventually pinching off the jet; (2) sinuous wave breakup, where an asymmetric instability emerges that causes the jet to wave sinuously and generate a polydispersion of droplets; (3) filament core breakup, where the surface of the jet becomes unstable to short wavelength disturbances and disintegrates close to the orifice into fine droplets, while the core of the jet persists as a continuum fluid filament that breaks up further downstream into large droplets; (4) wave atomization, where the breakup location of the jet core filament moves closer to the orifice and the fraction of fine droplets increases; and (5) full atomization.

2. A linear regression to the data yielded relationships for the boundaries between the five instability regimes in dimensionless Ohnesorge Number, *Oh*, and jet Reynolds Number, *Re*, space. The relationships are:

   Boundary 1 between instability regions **1** and **2**:

   $$Oh = 4.9196 \; Re^{-1.0459}$$

   Boundary 2 between instability regions **2** and **3**:

   $$Oh = 9.5979 \; Re^{-1.0255}$$

   Boundary 3 between instability regions **3** and **4**:

   $$Oh = 15.4108 \; Re^{-0.9989}$$

   Boundary 4 between instability regions **4** and **5**:

   $$Oh = 24.9548 \; Re^{-1.0027}$$

3. The exponent for *Re* in the relationships for the instability regime boundaries are all very close to –1. Referring to the definitions of *Re* and *Oh*, this means that the

transition between regimes is independent of jet viscosity, and the relationships for the boundaries can be rewritten as *We* ~ constant, where *We* is the Weber number. The critical transitional Weber numbers are the square of the coefficient of *Re* in the relationships for the boundaries, i.e.,

Boundary 1 between instability regions **1** and **2**:

$We \sim 24$

Boundary 2 between instability regions **2** and **3**:

$We \sim 92$

Boundary 3 between instability regions **3** and **4**:

$We \sim 237$

Boundary 4 between instability regions **4** and **5**:

$We \sim 623$

4. Although the present results suggest that the transition between instability regimes may be independent of jet viscosity, the average jet breakup length in instability regime 1 appears to be affected significantly by jet viscosity. Jet breakup length was greater for high viscosity fluids. The effect of viscosity on breakup length diminished in regime 2 as velocity increases and essentially disappears as the transition to regime 3 is approached. The results also suggest that the properties of the ambient fluid can impact breakup length, probably through surface tension.
5. Tube nozzles produced longer breakup lengths than sharp edge orifices of the same inside diameter at instability regime 2. This indicates the influence of jet velocity profiles at separation on the development of the instability. As in the case of jet

viscosity, the difference in breakup length decreased in regime 2 as velocity increases and essentially disappears as the transition to regime 3 is approached.

6. While breakup length appears to scale roughly with orifice diameter, D, the results suggest that may not be the appropriate length scale to non-dimensionalize breakup length data.
7. A method was developed to obtain a complete, composite droplet size spectra by combining size data from the PDPA and image analysis. The PDPA was not able to measure droplets larger than about 4 mm. The digital video image analysis could not measure droplets smaller than about 3 mm. The method exploits the overlap between the two incomplete size spectra and can be applied to similar situations involving different particle size diagnostics.
8. Droplet size spectra was measured for liquid-liquid jet breakup over the full range of instabilities from regime 1 through regime 5. Characteristic average diameters and other statistics were calculated from these spectra. Over the range of conditions examined in this study, jet velocity, orifice size and geometry, and jet fluid viscosity affected droplet size. There appeared to be limited or no difference in spectra obtained for injection into tap water and sea water or for liquid CO_2 tests conducted at 52 and 62 bar.
9. Characteristic diameters decrease steadily with increasing jet velocity (and increasing *We*) in instability regimes 1 through 4, attaining an asymptotic value in regime 5. Orifice diameter appears to influence average droplet size at low *We* in regimes 1 and 2. This effect diminishes as regime 3 is approached and essentially disappears in regimes 4 and 5; the characteristic droplet diameters appeared to be the same for 2

mm, 5 mm, and 10 mm orifices, at the same value of *We*, in these regimes. This may reflect the lack of sensitivity to the transverse length scale (i.e., jet or orifice diameter) of higher order surface instabilities that have been postulated to generate small droplets. Orifice geometry (sharp edge or tube) did not seem to have a significant effect for the very low viscosity liquid CO_2, but did impact droplet size for higher viscosity jet fluids. Larger droplets and a more uniform distribution were produced when silicone fluid was injected from the tube nozzle. Finally, at low *We* in regime 1, jet viscosity seemed to have little effect on mean droplet size. In the transitional breakup regimes, droplet diameters appeared to increase slightly with viscosity.

10. A novel weighted multimodal distribution concept was developed to obtain functional representations of the experimental size distributions (both PDFs and CDFs) that can be applied for model development and testing. The appropriate multimodal distributions for the different instability regimes were selected based on K-S tests and goodness of fit statistics and these functions were fitted to the data.
11. Weighted bimodal functions were found best to describe the droplet size spectra in instability regimes 1, 2, and 5. In instability regimes 3 and 4, both the video records and the size distribution data indicate that multiple instabilities can operate in parallel and manifest themselves in complex, multimodal spectra. In these regimes, trimodal or four-modal functions may be necessary to adequately represent the data.
12. For liquid CO_2 injection under deep ocean conditions, a variety of solid hydrates were observed to form, depending mainly on jet velocity, provided that temperatures and pressures were within the hydrate stability regime. At low CO_2 flow rates, in

instability regime 1, thin film hydrate tubes are likely to form on the jet surface. Hydrate tubes were not evident in the transitional breakup regimes 3 and 4, but thick hydrate tubes did form for some cases (with sub-zero CO_2 temperatures) in the atomization regime 5. The streamwise growth rate of the thick hydrate tube appears to scale with CO_2 flow rate.

13. Pre-breakup hydrate formation appears to affect the size distribution of the droplet phase primary by changing the effective geometry of the jet. When a hydrate tube forms, the interface between the CO_2 and water begins at the end of the tube, which may have a different size and shape opening than the original orifice. Furthermore, flow through the tube will alter the jet inlet velocity distribution, producing more time for boundary layer growth. In the case of thick tubes, hydrate branches will divert some of the CO_2 out of the main jet flow and could produce larger droplets.
14. CO_2 droplet concentration was determined to be a critical factor which influences agglomeration. High flow rates corresponding to transitional or atomization breakup generate large numbers of droplet in close proximity near the orifice. This enhances the probability of contact and agglomeration. Aggregate droplet clusters were not observed frequently in the varicose or transitional breakup regimes where droplet concentration is relatively low. Droplets aggregated readily on contact, but the hydrate films on their surfaces prevented coalescence.

TABLE OF CONTENTS

LIST OF TABLES

LIST OF FIGURES

CHAPTER 1 INTRODUCTION

1.1 Chapter Overview

This chapter provides a background on the problem of liquid-liquid jet instability and defines the scope of the present investigation. Section 1.2 introduces the practical applications and motivation for this study. A literature review of the experimental, theoretical and numerical aspects of jet instability is provided in section 1.3. Section 1.4 defines the scope of the present study and the organization of the dissertation is outlined in section 1.5.

1.2 Practical Applications

Liquid-liquid jet instability and breakup into a dispersed phase are important phenomena that have direct relevance to a host of ocean resource engineering applications. For example, during the past decade, two scenarios involving liquid droplet contaminant plumes in the ocean emerged-sequestration of anthropogenic CO_2 in the ocean and deep offshore oil spills – which provide the motivation for new experimental and modeling studies (Masutani & Adams, 2004).

The breakup of cylindrical liquid jets due to hydrodynamic instability is also important in many phase-contact situations, such as the combustion of liquid fuel jets in engines, liquid-liquid extraction and emulsification, and other applications in chemical and environmental engineering, agriculture, meteorology and medicine (Lefebvre, 1989; Kuo, 1996).

1.2.1 Ocean Sequestration of Anthropogenic Carbon Dioxide

Conventional means to reduce greenhouse gas emissions include expansion of nuclear power, energy conservation, switching from coal and oil to a lower-carbon fuel such as natural gas, upgrading the efficiencies of fossil fuel energy systems and displacement of fossil fuel by renewable energy sources. Another approach is ocean sequestration of anthropogenic carbon dioxide. CO_2 captured from fossil fuel power systems may be discharged into the deep ocean as a liquid or solid as depicted in Figure 1.1 (Auerbach, 1996), where it can remain isolated from the atmosphere for centuries. The figure shows several methods that have been proposed to implement ocean sequestration including the generation of a sinking plume of CO_2 dissolved in sea water; discharge through stationary or moving conduits at intermediate depths (around 1,000 m) where the liquid CO_2 is buoyant; discharge below around 3,000 m where the CO_2 will sink and accumulate on the seafloor; and disposal as blocks of dry ice. In the near term, direct injection of liquid CO_2 at intermediate depths appears to be the most practicable alternative.

Liquid CO_2 jets discharged into the deep ocean through injectors at the end of a submerged conduit are hydrodynamically unstable and will break up into a dispersed droplet phase. Dissolution of CO_2 increases the density of the seawater in the resulting droplet plume and decreases its pH. This CO_2-enriched and acidified seawater subsequently is diluted and dispersed by ocean turbulence and currents.

The viability of deep ocean CO_2 sequestration as a mean to mitigate climate change depends on two primary issues: (1) the effectiveness of this strategy in reducing atmospheric CO_2 levels over time and (2) impacts on the marine environment. The

magnitude and extent of seawater acidification depend on the initial size spectra of the dissolving dispersed phase and its transport by buoyancy and advection.

1.2.2 Deep Oil Spills

Offshore oil and gas exploration and recovery activities have been moving into increasingly deeper water. During these operations, undersea well blowout or oil leakage may occur. One such scenario is shown in Figure 1.2 (Rygg & Emilsen, 1998). Accurate predictive models of deep ocean spills must be developed to address safety and environmental concerns. The fraction, location and distribution of the contaminants that reach the surface are critical factors in devising effective clean-up procedures. Modeling efforts need to be complemented by well-designed laboratory and field experiments to elucidate the physical processes upon which the models are based, and to provide data for model calibration and validation.

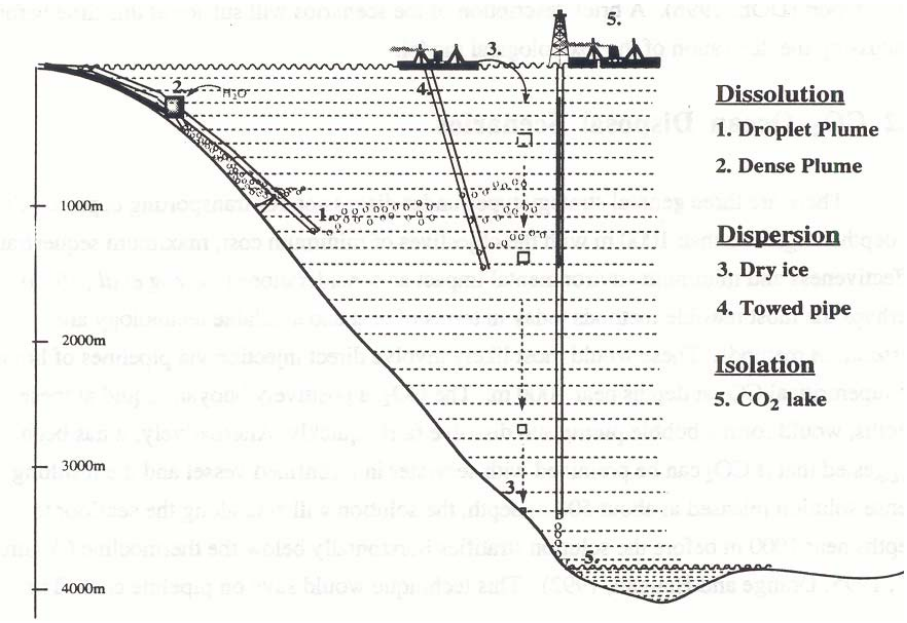

Figure 1.1 Schematic illustration of CO_2 ocean disposal scenarios (from Auerbach, 1996).

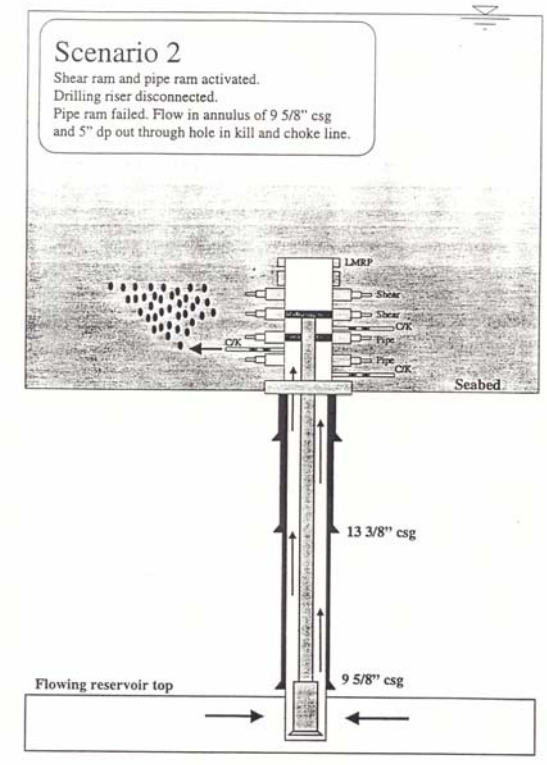

Figure 1.2 Diagram of possible oil well blowout incident (from Rygg and Emilsen, 1998).

1.3 Literature Review

The instability of cylindrical jets has been studied for more than 165 years via experimental, theoretical and numerical approaches. Major investigations of jet instability conducted previously are summarized in Table 1.1. The majority of investigations have focused on liquid-gas systems (e.g., liquid jets discharging into air). Liquid-liquid jet instability has not been investigated as extensively as liquid-gas systems. While there are similarities between liquid-liquid and liquid-gas phenomena, there are some very important differences. For example, in liquid-gas systems, the gas can usually be treated as an inviscid fluid and pressure may be assumed to be constant on the liquid-gas interface, while in liquid-liquid systems, viscosity of both fluids are important and dynamic pressure variations exist on the interface. "*On the whole, one may conclude the journey from gas-liquid systems to liquid-liquid systems is indeed a difficult one*!" – Hewitt (1997).

The breakup of liquid jets into droplets is driven by a competition between cohesive and disruptive forces. Instabilities that can lead to deformation of the jet surface may be amplified or damped. The dominant mode of instability depends on a number of factors, including jet velocity and fluid properties, and manifests itself in the appearance of the disintegrating jet. Studies have identified a number of distinct flow regimes wherein breakup apparently proceeds by different mechanisms that change the characteristics of the generated droplet ensemble. An understanding of the boundaries of these regimes is important in order to be able to anticipate the type (i.e., size; mono- or polydispersion) of droplets produced by different jet breakup scenarios.

Table 1.1 Previous studies of cylindrical liquid jet instability.

		Laminar								Transitional and Turbulent	
		Linear				Nonlinear					
		Temporal		Spatial		Temporal		Spatial			
		Liquid-Air	Liquid-Liquid	Liquid-Air	L-L	Liquid-Air	L-L	Liquid-Air	L-L		
Theory	Inviscid	Rayleigh (1878)	Tomotika (1935)	Keller (1973) Lieb(1986) Pimbely(1976) Bogy(1978)		Yuen (1968) Lafrance (1975) Chaudhary (1980)	Pimbley(977) Bogy (1978)	Pimbley&Lee (1977) Bogy(1978) Torpey (1989)			
	Viscous	Weber (1931) Ohnesorge(1936) Teng (1994)	Tyler (1934) Tomotika (1935) Meister&Scheele (1969) Kitamura (1986) Teng (1994)	Lieb (1986) Bogy (1978)		Green (1976)					
Numerical studies	Inviscid	Mansour & Lundgren(1990) Papageorgiou & Orellana (1998) Egger & Dupont (1994)			Richards (1994,1995)	Shokoohi & Elrod, 1987		Mansour & Lundgren (1990)	Homma *et al.* (2000)		
	Viscous	Ashgriz & Mashayek (1995)				Papageorgiou (1993)					
Experimental studies		Liquid-Air				Liquid-Liquid				L-A	L-L
		Halenlein (1932) Goedde & Yuen (1970) Arai & Amagai (1999)		Donnelly & Glaberson (1966) Kowalewski (1996) Lin (2003)		Hayworth & Treybal (1950) Kumar & Hartland (1984,1996) Skelland & Walker (1989) Longmire *et al.* (2001)		Kitamura *et al.* (1986) Das (1997) Milosevic & Longmire (2002)			Masutani & Adams (2000) Tang *et al* (2002, 2003)

1.3.1 Experimental Studies

Figure 1.3 from Grant and Middleman (1966) shows the typical evolution of jet breakup length observed as jet discharge velocity is increased. Breakup length is the distance from the discharge orifice to the point where discrete droplets are formed. Upstream of this point, the jet remains continuous and intact.

At very low velocities, large droplets are produced at the orifice (sometimes called drip flow). As velocity is increased, a laminar jet forms (point C) and breakup length increases linearly until it reaches a maximum. In this Rayleigh instability regime, axisymmetric disturbances grow in amplitude on the jet surface, eventually pinching off the jet column to generate a stream of essentially monodispersed droplets about 2 times of the initial jet diameter. Surface tension force is dominant over this range. The Rayleigh instability regime has been the subject of extensive theoretical analyses (Tomotika, 1935 and 1936; Weber, 1931; Teng *et al.*, 1994).

After attaining a maximum value, breakup length decreases. Droplet size remains nearly uniform and larger than the jet diameter (for liquid jets discharging into a gas). This flow regime is referred to as the "first wind-induced breakup." Hydrodynamic forces arising from the relative velocities of the jet and ambient fluid accelerate breakup. Beyond point F on the curve, the relative influence of surface tension decreases and breakup is determined by hydrodynamic forces. The term "sinuous instability" is often used to describe the process in this "second wind-induced breakup regime" and droplet size decreases and becomes irregular (polydispersed). Breakup length can increase slightly or decrease steadily before falling to zero. At higher velocities, instability begins

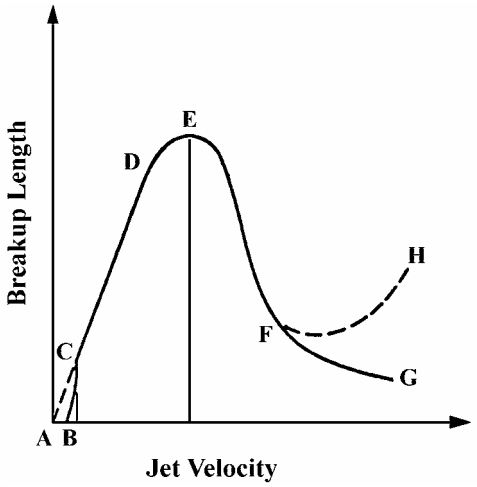

Figure 1.3 Variation of jet breakup length with velocity (from Grant & Middleman, 1966).

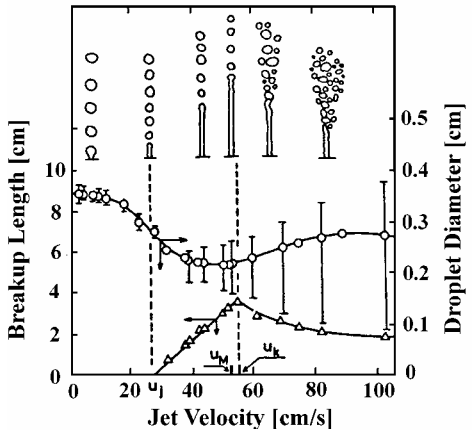

Figure 1.4 Jet breakup length and droplet size as functions of velocity for a liquid (water) jet discharging into liquid carbon tetrachloride (from Kitamura & Takahashi, 1986). Orifice diameter was 0.118 cm. The figure also shows sketches of the appearance of the jet.

on the jet surface and produces a polydispersed spray of fine droplets immediately downstream of the orifice; however, the core of the jet may remain intact and this

filament can persist for some distance before disintegrating (Masutani & Adams, 2000 and 2004). A single breakup length may not be adequate to describe the jet in this atomization regime and also during the latter stages of the second wind-induced breakup. Reitz & Bracco (1986) propose that both intact-surface and intact-core lengths be used to describe the jet.

The preceding regimes have been identified based on observations of liquid jets discharging into a gas. Figure 1.4 from Kitamura & Takahashi (1986) presents measured breakup lengths and droplet sizes for a liquid-liquid system (i.e., water injected into carbon tetrachloride). The figure also contains sketches of the jet appearance at different velocities. The general shape of the breakup curve resembles Figure 1.3; however, droplet size non-uniformities (indicated by the height of the bars around the droplet diameter data points) appear earlier and can be much more pronounced than in most liquid-gas systems. Based on the rather disorderly mode of breakup, Kitamura and Takahashi (1986) proposed that the process be designated as turbulent once jet velocity exceeds the value corresponding to the maximum jet length.

In order to extend the application of case-specific data and to develop general relationships, attempts have been made to correlate experimental observations against the non-dimensional Reynolds (Re_D) and Ohnesorge (Z) numbers (Ohnesorge, 1936). Figure 1.5a provides an example of the experimentally determined boundaries of the primary instability regimes determined from liquid-gas experiments. The figure also indicates that breakup can be influenced by additional factors, such as ambient fluid density (and other properties) and the initial state of the jet, which are not accounted for by Re_D and Z. A complete characterization of the breakup process probably requires that regime

boundaries be presented as surfaces rather than lines, such as in the conceptual sketch prepared by Reitz (1978) shown in Figure 1.5b.

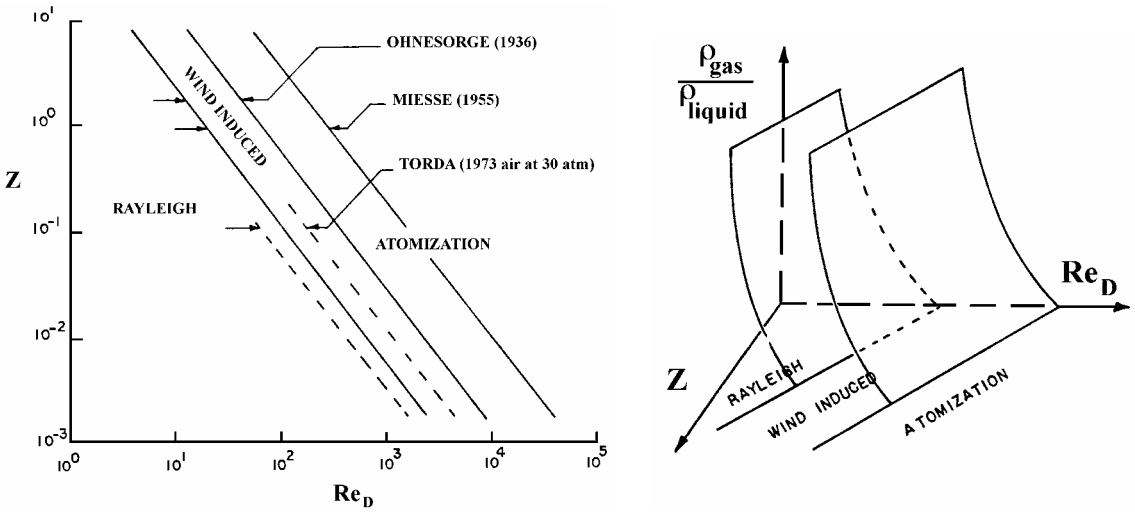

(a) (b)

Figure 1.5 (a) Instability regimes as a function of Ohnesorge (Z) and Reynolds (Re_D) numbers; the dotted lines show a shift in the boundaries due to ambient fluid density (from Reitz & Bracco, 1986); (b) conceptual sketch by Reitz (1978) showing regime boundaries as surfaces to account for the relative densities of the jet and ambient fluids.

1.3.2 Theoretical Studies

Theoretical investigations have primarily considered either perturbation-type or one-dimensional models (Mashayekhi, 1994) and have been generally restricted to the laminar flow regime. The approach taken falls into one of two categories, namely, temporal (or Lagrangian) or spatial (or Eulerian) analysis. In temporal analysis, an infinite jet, stationary relative to a moving observer, is considered and the growth rate of the disturbance amplitude is determined. In spatial analysis, the growth of a disturbance propagating along a semi-infinite jet is considered with the nozzle (i.e., inlet boundary)

conditions fixed. Linear or nonlinear perturbation techniques or direct numerical methods are employed in both temporal and spatial analyses.

Perturbation analyses were applied in early investigations where a surface disturbance to the jet was imposed to produce unstable waves on the jet surface. These studies focused on deriving a viable dispersion equation (i.e., the relationship between the amplitude growth rate and the wave number) and identifying the most unstable wave that causes the jet to disintegrate.

Rayleigh (1879) used linear perturbation to derive the first analytical description of the temporal instability of both an inviscid and a viscous incompressible jet in gas (the effects of the ambient fluid on jet instability were assumed to be negligible in Rayleigh's analysis). He showed that an axisymmetric harmonic disturbance of the form

$$r = 1 + \varepsilon_0 \exp(\omega t - ikz) \tag{1.1}$$

grows in time according to

$$\omega = \left[\frac{I_1(k)}{I_2(k)} (1 - k^2) k \right]^{1/2} \tag{1.2}$$

where ω is the growth rate, ε_0 is the initial disturbance amplitude, k is the disturbance wave number, and I_0 and I_1 are the modified Bessel function of the first kind. Rayleigh 's result is valid only for low-velocity jets. His maximum-instability theory formed the basis for subsequent studies of instability of viscous, cylindrical liquid jets.

Weber (1931) derived a dispersion equation for liquid-gas systems that included both the influence of viscosity and hydrodynamic effects. The motion of both the jet and the ambient fluid were modeled as Stokes flows by Tomotika (1935), who extended Rayleigh's analyses for a single jet fluid phase to two phases comprising both the jet and

the ambient fluid. Tomotika's dispersion equation is relatively complicated and he was only able to obtain a numerical solution to his general dispersion equation for the limiting case of a highly viscous liquid jet discharging into another highly viscous liquid with inertial effects neglected. Teng (1994) derived a general, explicit dispersion equation for the laminar instability of cylindrical liquid jets in both liquid-gas and liquid-liquid systems. Under equivalent conditions, Teng's dispersion equation reduces to the results of Rayleigh, Weber, and Bogy, and agrees with Tomotika's relationship.

The instability models described above are based on linear relationships. According to these linearized theories, surface deformation of the jet is harmonic and jet breakup produces uniformly sized droplets. Linear theory predicts well the disturbance growth rate measured by Donnelly and Glaberson (1966) and Goedde and Yuen (1970). however, linear analyses cannot explain the formation of satellite droplets (i.e., small droplets that accompany the primary train of larger droplets) that are observed in both liquid-liquid and liquid-gas systems.

Yuen (1968) was the first to analyze the formation of non-uniform-size droplets. He developed a third-order perturbation solution for a cylindrical, inviscid, liquid jet in gas, and showed that non-uniform-size droplets form as results of nonlinear effects which were neglected in Rayleigh's analysis. It is believed, however, that Yuen's analysis is flawed: errors occur at the second order solutions for both the disturbance function and the velocity potential. Lafrance (1975) and Chaudhary (1977, 1980) performed similar nonlinear analyses; however, the undisturbed surface tension pressure term is missing in Lafrance's equation and Chaudhary derived boundary conditions using Bernoulli's equation. In the analyses of Yuen, Lafrance, and Chaudhary, the original nonlinear

problem was posed by directly applying Rayleigh's linearized initial condition, which is inconsistent with the assumption of finite initial disturbance. As a result, the disturbance function in the problem for each order has to be assumed arbitrarily, without regard to the constraint of the original nonlinear problem. This would likely influence the accuracy of the nonlinear analyses.

Both the linear and nonlinear methods mentioned above entail normal-mode type analyses. Berger (1988) noted that normal-mode analysis ignores the initial growth phase of the disturbances and perturbations to the ambient flow. He treated the jet instability as an initial-value problem and after linearization showed that the initial instability does not grow exponentially, as normal-mode linear analysis predicts. Teng *et al*. (1995) conducted a third order perturbation analysis to examine liquid-core instability in inverted annular flow. The shape of the liquid/vapor interface and the breakup pattern of the liquid core are found to be influenced strongly by the disturbance mode and initial disturbance amplitude. Either uniform or non-uniform surface distortions can form.

1.3.3 Numerical Studies

Schulkes (1993) and Papageorgiou & Orellana (1998) derived the complete one-dimension equations governing the motion of an axisymmetric inviscid liquid jet. Schulkes solved his newly derived equations with proper boundary conditions numerically and observed that, as disturbances grow, the characteristic axial length scales typically became of the order of the radius of the jet. This result brings into question the validity of the one-dimension approximation of the nonlinear liquid jet.

Shokoohi & Elrod (1987) used a vorticity-stream function formulation to simulate the dynamics of a liquid jet. Mansour and Lundgren (1990) used a boundary-integral method to study the instability of an inviscid jet in air. They calculated the main and satellite drop sizes as functions of the disturbance wave number. Tjahjadi *et al.* (1992) investigated the breakup of a long liquid filament in a quiescent viscous fluid by a boundary-integral calculation to study the evolution of the filament as a function of the viscosity ratio of the fluids and the initial wave numbers of the interface perturbation. Ashgriz and Mashayek (1995) studied an axisymmetric incompressible Newtonian liquid jet in vacuum and zero gravity using the volume of fluid (VOF) method. Richard (1993, 1994, 1995) used the VOF method in liquid-liquid jet breakup for the interface reconstruction and a finite difference method to solve the Navier-Stokes equations. Instead of a boundary condition, the interfacial tension was coupled in the moment equations by a continuum surface force (CFS) model, which was first introduced by Brackbill *et al.* (1992). Homma *et al*. (2000) numerically investigate a laminar jet breakup into drops in liquid-liquid systems by a front tracking / finite difference method with cylindrical axisymmetric coordinate. For moderate Weber numbers, two sizes of the drops are observed as a result of end-pinching and capillary wave instability that both influence the drop size. The numerical method has been extended to cases where mass and/or heat transfer occurs.

1.4 Scope of Present Study

While theoretical and numerical studies performed to date provide significant insight into liquid jet instability, results have generally been limited to capillary and laminar flow situations. The aforementioned perturbation analyses and one-dimensional models apply

to laminar jet flows at low velocities. Many important applications, however, involve the breakup of transitional and turbulent jets. Jet instability theory is deficient in these flow regimes and numerical solution of the governing equations are difficult or intractable. Hence, experiments continue to remain the only way to provide information on liquid-liquid jet disintegration over the entire range spanning the laminar to turbulent flow regimes.

It is proposed that liquid-liquid jet breakup into a dispersed phase is a subject of considerable scientific and practical value for a number of disciplines, including ocean resource engineering. The deficiency in our understanding of the instability and disintegration of transitional and turbulent liquid jets warrants further investigation. Toward this end, a experimental study of jet breakup phenomena has been undertaken.

Laboratory experiments were conducted to obtain a relatively comprehensive data set on the size spectra of droplets generated by the breakup of jets of liquids with different properties (e.g., viscosity and surface tension) discharging into water; and to secure qualitative insight via flow visualization of the breakup phenomena. Jet fluids included crude oils, silicone fluids, and liquid CO_2; viscosities of these fluids ranged over more than three orders of magnitudes. Emphasis has been placed on transitional and turbulent jets and measurements were conducted at different jet velocities and with various size jet discharge orifices.

1.5 Organization of the Dissertation

Chapter 2 provides a detailed description of the experimental facilities and the diagnostic techniques that were employed. Experimental results are presented and discussed in Chapters 3, 4, 5 and 6. Information on liquid-liquid jet breakup regimes is included in Chapter 3 and jet breakup length study is presented in Chapter 4. Droplet size spectra data are investigated in Chapter 5. Since Deep Ocean CO_2 sequestration was a primary focus area of this study, hydrate formation during liquid CO_2 jet breakup is discussed in Chapter 6. Finally, a summary of the experimental results and the conclusions of this study are given in Chapter 7.

CHAPTER 2 EXPERIMENTAL SETUP

2.1 Chapter Overview

Descriptions of the experimental facilities, instrumentation, conditions, and procedures employed in this investigation are provided in this chapter. Section 2.2 discusses the two optical techniques used to measure droplet size and the algorithm employed to integrate these two data sets to obtain comprehensive size spectra. Details of the injection facilities and the jet fluids are provided in section 2.3.

2.2 Droplet Size Measurement Techniques

For liquid droplet measurements, optical particle size methods are the general choice. Optical methods can be conveniently grouped into two categories: imaging and non-imaging techniques.

Imaging techniques include photography, holography and automatic image analysis, and high-resolution imaging and digital processing techniques. Rapid strides have been made in the use of digital image processing techniques for data acquisition in the last two decades. Technique such as fringe thinning, fringe clustering, fringe tracing, phase shifting, polarization stepping and Fourier transform methods have significantly contributed to the automation of data acquisition. A variety of electronic image sensors are available today, such as charge-coupled devices (CCD), charge injection devices (CID) and metal oxide silicon capacitors (CMOS). Of these, CCDs are probably the most widely used.

Boyle and Smith invented the CCD in 1970. The heart of a solid state camera is a CCD array. It performs a conversion of light intensity to a measurable voltage signal at a matrix of discrete locations. When the array is fed directly into an image processor, digital output is possible, which ensures the maximum image fidelity (Ramesh, 2000).

Non-imaging techniques include laser-based techniques such as single particle counter systems and Fraunhofer diffraction methods, x-ray radiography, phase Doppler particle analysis, and planar laser-included fluorescence. Like imaging techniques, significant technical advancements have been made over the past decade.

In the current study, image analysis of digital video data and a non-imaging Phase Doppler Particle Analyzer (PDPA) were employed to measure droplet size. The PDPA also has the capability to perform simultaneous measurements of droplet velocity. The two different measurement techniques were needed to accommodate the full range of droplet sizes from submillimeter to more than 20 mm that were encountered in the experiments.

The PDPA optics were optimized to provide a broad measurement range extending from 0.082 to 4.056 mm. Larger droplets formed during laminar and transitional breakup were measured using digital video data collected with three 3-CCD digital camcorders, two SONY PD100s and one PD150. Results indicate that droplets with diameters greater than approximately 3 mm can be reliably sized by digital video image analysis.

2.2.1 Phase Doppler Particle Analyzer

2.2.1.1 Major Components of the PDPA

The PDPA comprises the following major components (Figure 2.1):

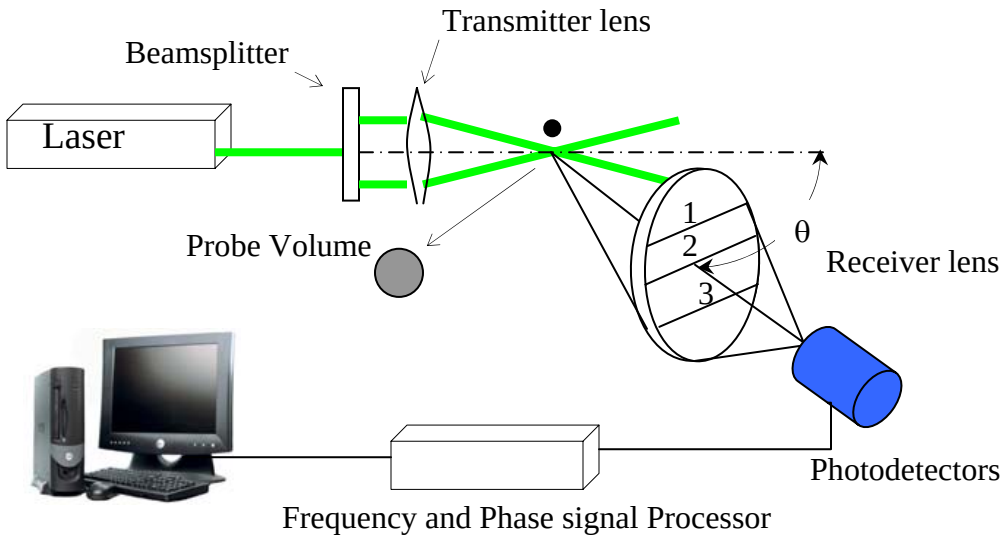

Figure 2.1 Major components of the PDPA (Replotted from http://www.tsi.com/).

(1) Air-cooled Argon-Ion laser; maximum 150mW power output (all lines).

(2) Transmitting optics including a beamsplitter, fiberoptic link, and focusing lens.

(3) Receiver Module (RCM) comprising photomultiplier tubes (PMT), tube preamplifiers and the optomechanical hardware. The RCM collects laser light scattered by droplets passing through the optical probe volume and converts it into electronic signals.

(4) Real-time Signal Analyzer (RSA) and PC that processes the phase Doppler signals using a discrete Fourier transform method to obtain size and velocity data that is stored in the PC.

2.2.1.2 PDPA Measurement Principles

Bachalo (1980) derived the basic theory for dual beam light scattering and interference that constitutes the basis of operation of the PDPA. He determined that the phase shift of light scattered by refraction or reflection from two intersecting laser beams could be used to size spherical particles. PDPA measurements are performed utilizing a small, non-intrusive optical probe volume defined by the intersection of two laser beams. The intersection of the two beams creates a fringe pattern (i.e., alternating light and dark bands) within the probe volume. As a particle passes through the standing fringe, it scatters light that is collected by a receiving lens located at an off-axis collection angle. The lens projects a portion of the scattered light onto 3 photodetectors located at slightly different angles from the probe volume. Each detector produces a Doppler burst signal with a frequency proportional to the particle velocity (Figure 2.2). The phase shift between the Doppler burst signals from two different detectors is proportional to the size of the spherical particles. Figure 2.3 provides theoretical predictions showing that the phase shift is linearly related to the diameter of the scattering particle. The figure shows the calculated phase shift between signals from three detectors (i.e., between detectors 1 and 2 ($\phi_{1\text{-}2}$) and 1 and 3 ($\phi_{1\text{-}3}$)) as a function of non-dimensional particle diameter. Two pairs of detectors are employed to eliminate ambiguities that might occur when the droplet size range is large.

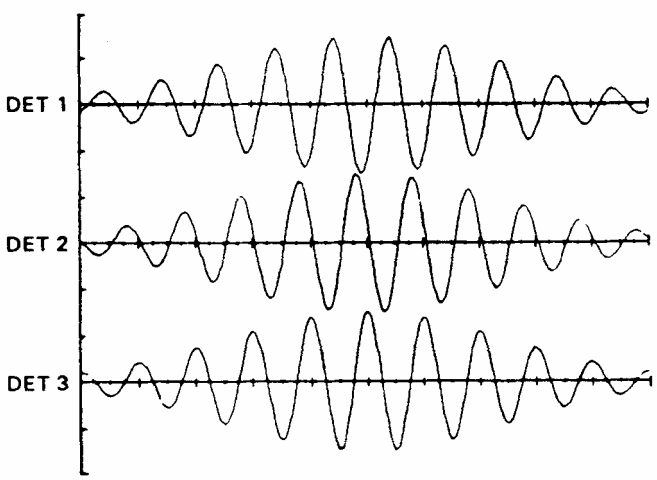

Figure 2.2 Phase shift of signals from three separate photodetectors monitoring light scattered by the same particle traversing the interference fringes at the intersection of two laser beams. The signals have been high-pass filtered to remove the Gaussian pedestal. Figure from Bachalo & Houser (1984).

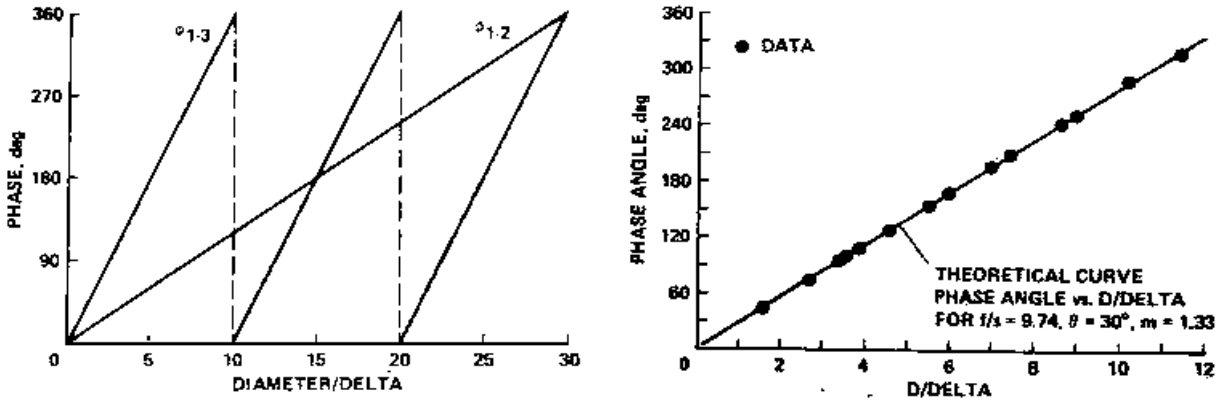

(a) (b)

Figure 2.3 Theoretical prediction showing the dependence of phase shift on dimensionless droplet size: (a) relationship for signals from three photodetectors and (b) comparison with experiment. Figures from Bachalo & Houser (1984).

2.2.1.3 PDPA Measurement Error

The theory of operation for the PDPA is based on a Mie scattering analysis that assumes the particle is spherical and its surface is smooth. Departures from this condition can result in errors. Figure 2.4 provides examples of the types of measurement errors that may occur when a non-spherical particle crosses the optical probe volume.

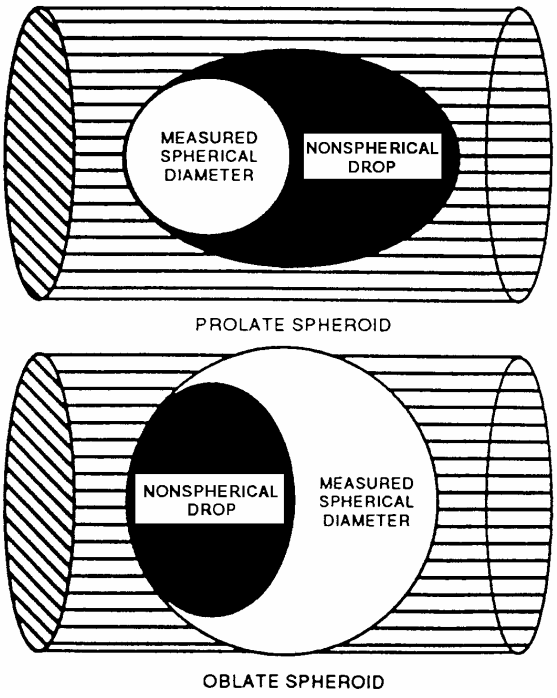

Figure 2.4 Examples of the response of the PDPA to non-spherical droplets (Bachalo, 1994).

2.2.2 Image Analysis

Digital video image analysis is employed to estimate the size of liquid droplets that fall outside the measurement range of the PDPA (i.e., are larger than about 4 mm). Our tests suggest that, for the camera optics employed in the study, video image analysis can reliably size droplets greater than approximately 3 mm in diameter. The overlap between the measurement size ranges of the PDPA and video image analysis (i.e., 3 mm to 4 mm) is exploited to prepare composite size spectra and to provide a check of the accuracy of the data sets measured by the two techniques.

Video frames from the digital camcorder records are sampled at selected time intervals over the course of an experiment (for example, to provide enough time between frames for droplets to move out of the field of view to avoid being counted more than once). These frames are analyzed using Matlab programs including functions that we developed from the Matlab Image Processing Toolbox. Droplet size is estimated by comparing the projected area (in pixels) of a droplet with a size reference standard installed in the flow field and recorded with the video system.

2.2.2.1 Image Analysis Algorithms

Algorithms have been developed to estimate droplet size depending on image quality. For droplet images with good contrast, such as the one of a liquid CO_2 drop shown in Figure 2.5a, the Matlab Image Processing Toolbox provides standard functions to find object edges and to determine the number of pixels within these edges (Figures 2.5c and 2.5b, respectively). When image quality is poor, as in Figure 2.6a where a portion of the

droplet overlaps with the viewport wall in the background, or when two or more droplets overlap in the image, the standard Matlab functions may fail to calculate the pixel count (projected area) correctly (Figure 2.6 b). An alternative algorithm was therefore developed for this situation that requires manually identifying about 8 points nearly evenly distributed around the edge of the droplet. The Matlab cubic spline interpolation function is then employed to perform a curve fit the between those points. The projected area is calculated by integration and the result is shown in Figure 2.6c. This algorithm requires significant user input and is therefore quite time-consuming.

An equivalent diameter is estimated by comparison of the calculated droplet projected area (number of pixels within the droplet edges) with the projected area of known standards such as solid spherical beads of known diameters installed in the field of view of the camcorders. The camcorder optics (i.e., depth of field and magnification) limit sizing ambiguities associated with differences in the position of imaged droplets and the reference size standards along the line of sight of the camcorder.

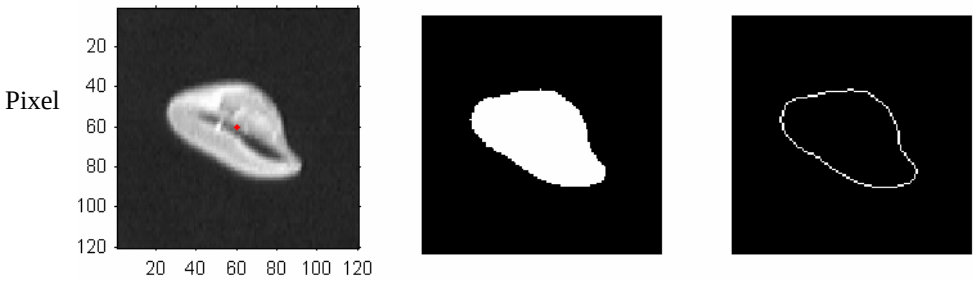

Figure 2.5 Algorithm to estimate droplet size by image analysis for high quality images. Figure (a) shows the video image of a liquid CO_2 droplet (units shown are in pixels). Figures (b) & (c) show, respectively, the projected area and the edges determined using standard Matlab functions.

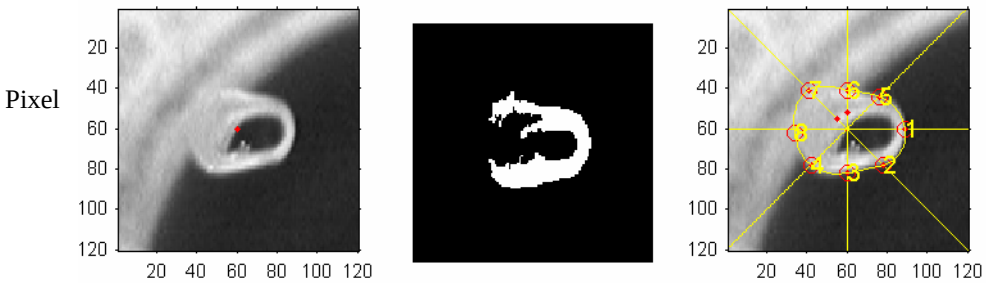

(a) (b) (c)

Figure 2.6 Algorithm to estimate droplet size by image analysis for lower quality images. Figure (a) shows the image of a liquid CO_2 droplet that overlaps with the background viewport wall. Figure (b) indicates that the standard Matlab function fails to calculate correctly the projected area (shown in white). Figure (c) shows the result obtained using the alternative algorithm.

2.2.3 Composite Size Distribution from PDPA and Video Image Analysis

The size ranges of the droplets produced in some of the experiments are relatively broad and exceed the individual measurement ranges of either the PDPA or the digital video image analysis technique. A complete droplet size spectra for such cases required combining the data from these two measurement techniques. A method to do this was developed and is described below.

As noted previously, the PDPA is capable of measuring droplets with diameters between 0.08 to 4.056 mm using the optics we have selected. Image analysis, on the other hand, can reliably size droplets greater than about 3 mm. Our experience indicates that the level of required effort and relative uncertainty associated with sizing droplets smaller than 3 mm is excessive. The effective minimum image analysis measurement size was therefore taken to be 3 mm. The overlap in the measurement size ranges of the PDPA and

the image analysis technique (between 3 mm and 4 mm) can be exploited to estimate a composite droplet size spectrum from the two incomplete data sets.

We assume that a complete size spectrum can be assembled from two partial spectra extending from approximately 0 to 4 mm and for ≥ 3 mm and expressed in Figure 2.7.

If n is the total number of samples used to calculate the size distribution histogram, then

$$n = a + b + c \tag{2.1}$$

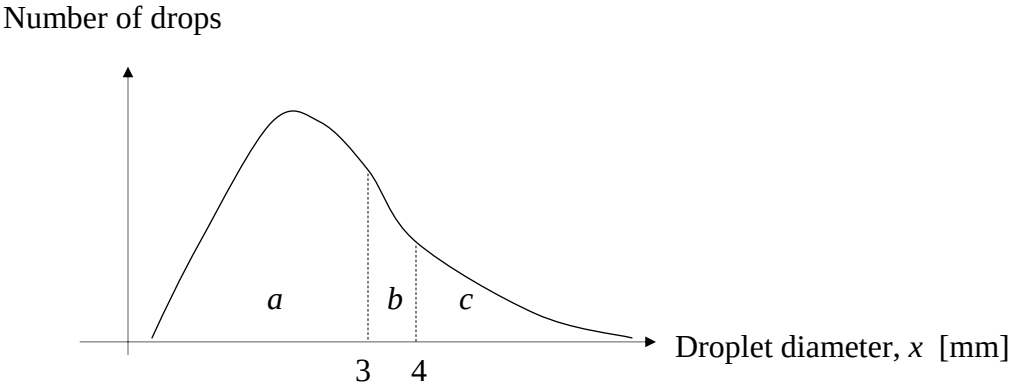

Figure 2.7 Composite droplet size distribution. *a* is the total number of drops with *x* <3 mm; *b* is the total number of drops with $3 \le x \le 4$; *c* is the total number of drops with *x* >4 mm.

Consider the hypothetical case where the measurement size ranges of the PDPA and image analysis are not limited and the two techniques are used to determine the size distribution for the same test independently. For the PDPA, the relationship between the number of samples that are used to determine the probability histogram is

$$n_1 = a_1 + b_1 + c_1 \tag{2.2}$$

where, for the actual PDPA which yields an incomplete data set, a_1 and b_1 are measured and known and c_1 and n_1 are unknown (since c_1 lies outside the measurement range of the actual instrument).

For the image analysis data, we have

$$n_2 = a_2 + b_2 + c_2 \tag{2.3}$$

where, once again for the actual situation, b_1 and c_1 can be measured and a_2 and n_2 are unknown.

Since the PDPA and image analysis data are describing the same test, they must have the same Probability Density Function (PDF), $f(d)$, and Cumulative Distribution Function (CDF), $F(d)$. Hence,

$$\int_{0.08}^{3} f(x)dx = F(3) - F(0.08) \cong F(3)$$

same for both sets $$\Rightarrow \frac{a_1}{n_1} = \frac{a_2}{n_2} \tag{2.4}$$

$$\int_{3}^{4} f(x)dx = F(4) - F(3)$$

same for both sets $$\Rightarrow \frac{b_1}{n_1} = \frac{b_2}{n_2} \tag{2.5}$$

$$\int_{4}^{+\infty} f(x)dx = 1 - F(4)$$

same for both sets $$\Rightarrow \frac{c_1}{n_1} = \frac{c_2}{n_2} \tag{2.6}$$

From Equations (2.4), (2.5), and (2.6), we obtain

$$\frac{a_1}{a_2} = \frac{b_1}{b_2} = \frac{c_1}{c_2} \tag{2.7}$$

$$\Rightarrow \begin{cases} c_1 = c_2 \cdot b_1 / b_2 \\ a_2 = a_1 \cdot b_2 / b_1 \end{cases} \tag{2.8}$$

Substitution of (2.8) into (2.2) and (2.3) provides relationships for n_1 and n_2 that only employ data that can be measured (i.e., a_1, b_1, b_2, and c_2). A composite probability distribution function (PDF), $f(x)$, can then be estimated from the incomplete PDPA and image analysis data sets by

$$F(x \le x_j) = \begin{cases} \dfrac{N_{j \text{ from pdpa}}}{n_1} \dfrac{1}{\Delta D} \text{ for } x_j < 3 \\ \dfrac{N_{j \text{ from pdpa/image}}}{n_1} \dfrac{1}{\Delta D} \text{ for } 3 \le x_j \le 4 \\ \dfrac{N_{j \text{ from image}}}{n_2} \dfrac{1}{\Delta D} \text{ for } x_j > 4 \end{cases} \tag{2.9}$$

where N_j is the number of droplets in the diameter class j and ΔD is the diameter class range.

The following constraint also applies

$$\frac{a_1}{n_1} + \frac{b_1}{n_1} + \frac{c_2}{n_2} = \frac{a_1}{n_1} + \frac{b_2}{n_2} + \frac{c_2}{n_2} = 1 \tag{2.10}$$

Codes to calculate composite distributions based on the above approach have been tested using Normal and Weibull distributions. For example, as shown in Figure 2.8, two groups of normal random numbers with the same mean and variance were generated, with 2000 samples in group 1 and 200 samples in group 2. For this example, n_1 = 2000 and n_2 = 200. Samples in group 1 with values greater than 4 and samples in group 2 with values smaller than 3 were then discarded (Figure 2.8 (3) and (4)). The code was used to

generate a composite distribution from these two incomplete data sets. The composite distribution should have the same statistics as the original distributions. The corresponding n_1 and n_2 of the composite distribution are 2034 and 204 for this test, which differ by 1.7% and 2.0% from the real values of n_1 = 2000 and n_2 = 200. Results are shown in the Figure 2.8 (5) and (6). For the values smaller than 3, $f(x)*\Delta D$ was calculated with numbers from group 1. Data from group 2 were used to calculate the $f(x)*\Delta D$ when $x>4$. For $3 \leq x \leq 4$, the numbers from either group 1 (Figure 2.8 (5)) or group 2 (Figure 2.8 (6)) fall in this range can be used to calculate $f(x)*\Delta D$. The application of the code to produce a composite Weibull distribution is shown in Figure 2.9. The PDF and CDF definitions of the Normal and Weibull distributions are given in section 5.3.

Tests of the above method to estimate a composite probability distribution from incomplete PDPA and image analysis size data sets suggest that the results are reasonably accurate, provided that there is no measurement bias in these incomplete data sets; i.e., that all droplets (regardless of their size) within their respective measurement size ranges are sampled equally by the PDPA and by the image analysis technique.

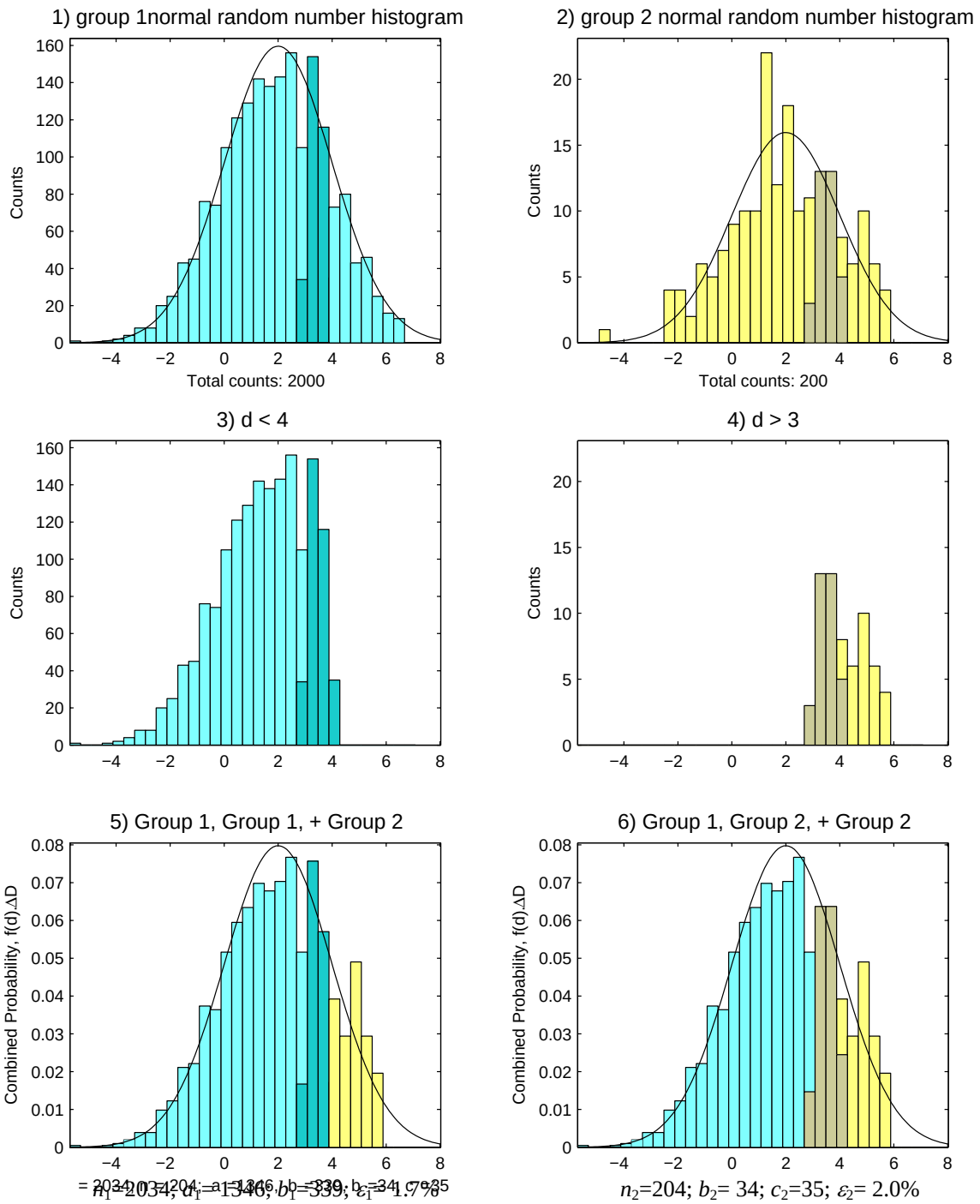

Figure 2.8 Composite Normal distribution. A total of (1) 2000 and (2) 200 random numbers were generated from the Normal distribution with the same parameters. Samples in group 1 with values greater than 4 and samples with values smaller than 3 in group 2 were discarded. New composite distributions obtained from samples shown in (3) and (4) have the same statistics as the original distributions in (1) and (2). The solid line is the Normal probability density function with the same parameters as histograms (1) & (2).

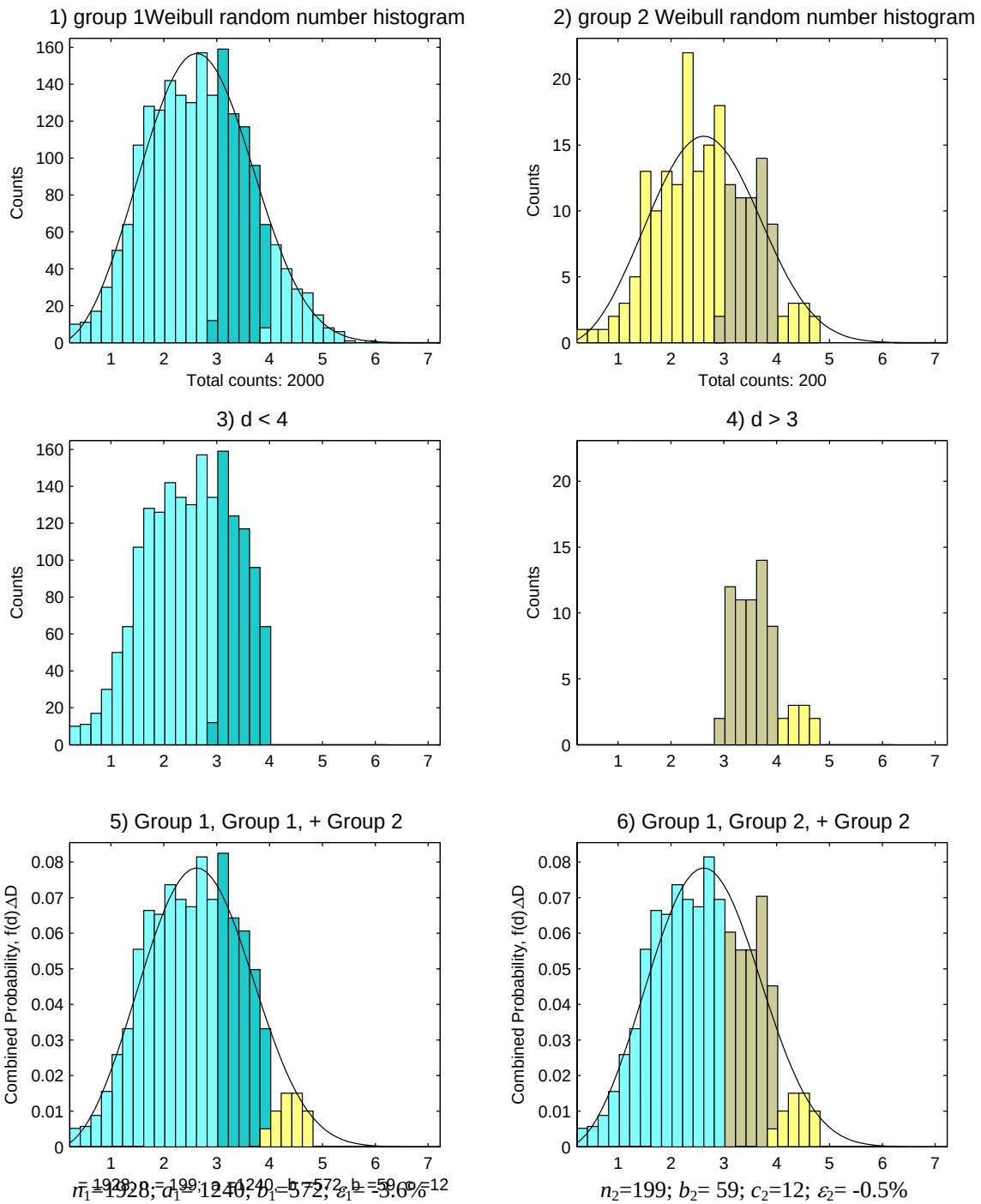

Figure 2.9 Composite Weibull distribution. A total of (1) 2000 and (2) 200 random numbers were generated from the Weibull distribution with the same parameters. Samples in group 1 with values greater than 4 and samples with values smaller than 3 in group 2 were discarded. New composite distributions obtained from samples shown in (3) and (4) have the same statistics as the original distributions in (1) and (2). The solid line is the Weibull probability density function with the same parameters as histograms (1) & (2).

2.3 Experimental Details

Experiments were conducted to examine the instability and breakup of jets of various fluids issuing from a number of different orifices into tap water (WT), natural surface sea water (WN) or synthetic sea water (WS). Injection conditions were selected to span the entire range extending from laminar to turbulent jet flow. Jet fluids were chosen to: (1) accommodate specific research project objectives to simulate CO_2 ocean sequestration and undersea oil spills; and (2) to provide a relatively wide range of jet fluid properties that would provide insight into how these properties affect breakup.

Three experimental facilities were employed to conduct the experiments. Since liquid CO_2 will boil if it is not maintained at high pressures and relatively low temperatures, injection was performed in a pressure vessel that was designed and fabricated to simulate the deep ocean environment. Two atmospheric pressure water tanks were used to conduct tests where the jet fluid does not need to be pressurized to avoid flash evaporation (e.g., crude oils and silicone fluids). This section provides details of the experiments.

2.3.1 Liquid CO_2 Injection Tests

A photograph of the Deep Ocean Simulator (DOS) is provided in Figure 2.10. Figure 2.11 shows the general experimental set up employed in the liquid CO_2 injection tests. Optical access for the PDPA and video camcorders was provided by 18 viewpoints (9.8 cm diameter clear aperture) fitted with annealed acrylic windows. To provide illumination for the digital video camcorders, three underwater lamps were installed inside the DOS. One lamp is positioned at the top and two on the bottom of the tank submerged in water. External video lamps were employed as necessary (Figure 2.12).

Calibrated spherical beads were installed in the field of view of the video cameras to serve as size reference standards for the digital video image analysis (see Section 2.2.2).

During operation, the DOS is partially filled with tap or seawater chilled to a selected temperature. The water is pressurized by charging the space above the water column with an inert gas such as N_2. A single-action, positive displacement pump (CS&P Cryogenics model ICP-75) coupled with the Toshiba Tosvert VF-S9 control system is used to pressurize and transfer liquid CO_2 from a 3-ton refrigerated storage tank and inject it upward through various orifices mounted on a removable nozzle into chilled and pressurized water or seawater contained in the DOS. The variable frequency drive pump is capable of providing CO_2 at flow rates up to about 12 ~18 kg/min (approximately 200 to 300 cc/s) at pressure up to about 102 bar (1500 psi). To control the CO_2 temperature, an array of counter flow, coaxial heat exchanger tubes are plumbed into the CO_2 flow system immediately downstream of a large bladder accumulator that is employed to dampen pump pressure pulses.

Electrical heating tape was wrapped around the line feeding into the heat exchanger (HX) to supplement the heat addition from the warm water flowing through the HX. The heat gained through the HX is monitored by means of thermistors inserted into the CO_2 line before and after the HX (T1 and T2 in Figure 2.11). The temperature of the CO_2 being injected is measured by a thermistor T3 located about 20 cm from the inlet into the DOS.

A differential pressure transducer (D1) monitors the water level in the DOS. Temperature of the gas above the water in the DOS is measured by thermocouple T4. A pressure transducer (P1) is coupled to an electronic feedback/control device that actuates

an electronic valve to vent the gas and maintain constant pressure in the DOS (< ±1%) as liquid CO_2 is injected and compresses the gas volume. To address the problem of increasing water temperature in the vessel due to heat addition from the surroundings, a water circulation loop was installed. A high pressure gear pump draws water from the vessel and passes it through chiller before returning to the pressure vessel. Water temperature in the tank is measured by thermistor T5. A Sea Bird SBE18 pH probe monitors the pH of the water upstream of the gear pump. Two flowmeters are available to measure CO_2 flow rate: a totalizer and Omega FTB9512 Precision Turbine flowmeter coupled with a FC-22 flow computer (F2).

The PDPA was positioned as shown in Figure 2.13. The CO_2 injector was aligned with the vessel centerline and the top of the injection orifice was set at the level of the lowest row of viewports. The PDPA optics were located at the second row of viewports, approximately 70 cm above the injection orifice. As indicated in Figures 2.13 and 2.14, the two 514.5 nm laser beams emerging from the transmitter are steered with a pair of dielectric mirrors in side the vessel and cross and form an interference fringe pattern directly above the injection orifice on the vessel centerline. The angle between the transmitted laser beams and the receiver optics was selected to optimize the PDPA measurements of reflective CO_2 droplets. CO_2 droplets that traverse through the PDPA optical probe volume scatter light that is collected off-axis by the receiver. Two or three digital video cameras monitor the flow through the viewports at the level of the PDPA and the injector.

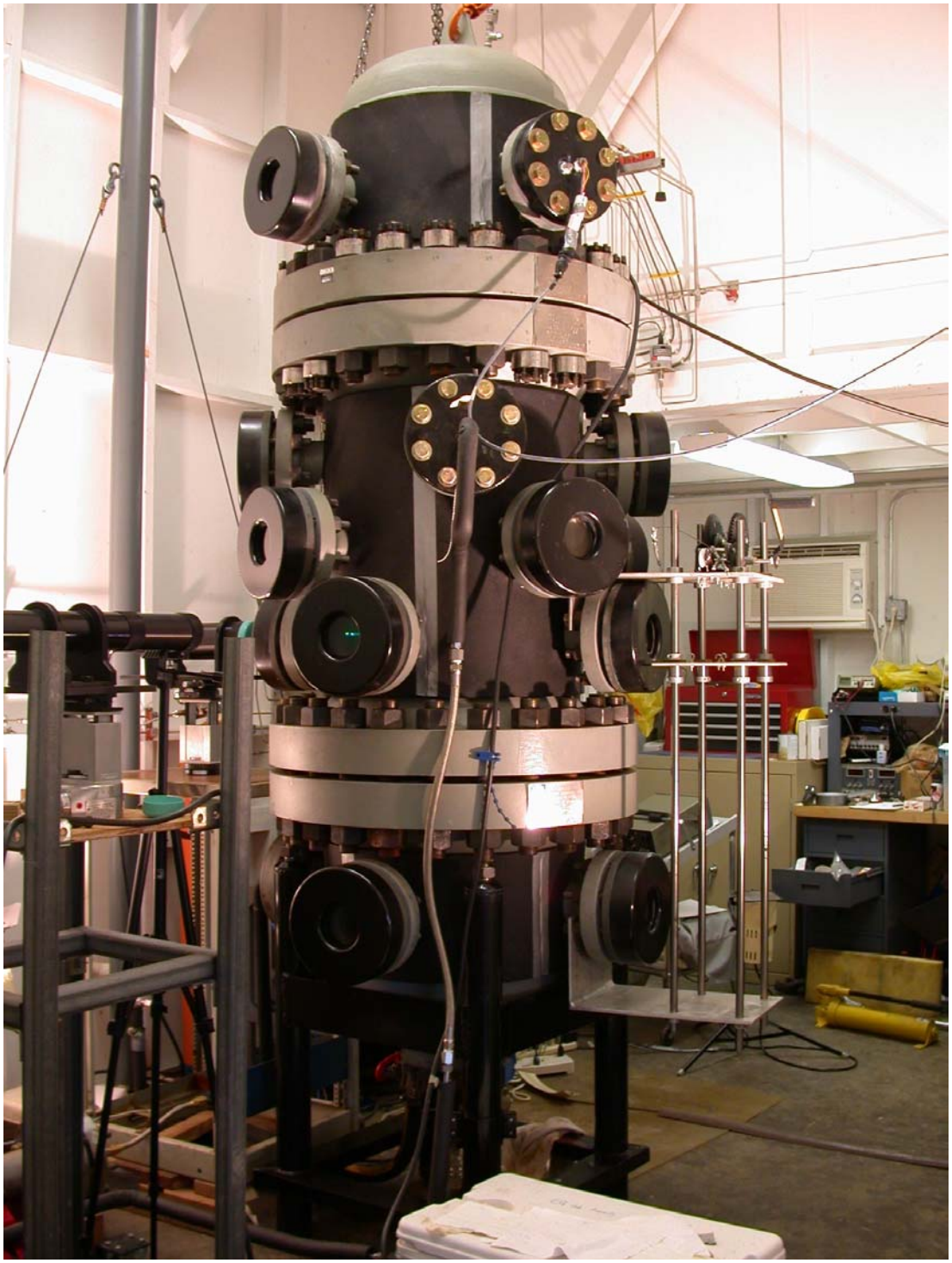

Figure 2.10 Deep Ocean Simulator

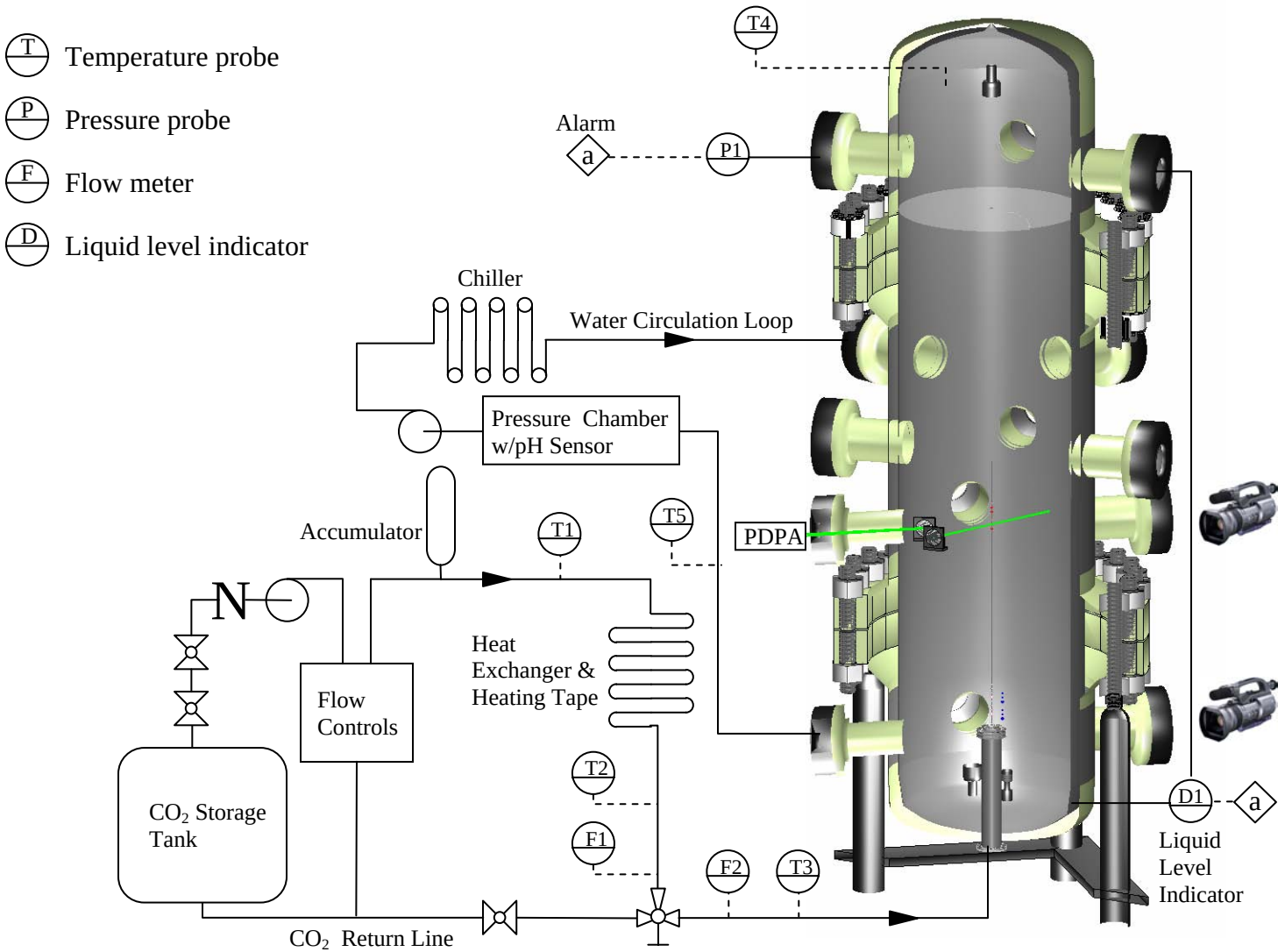

Figure 2.11 Experimental layout for the liquid CO_2 injection tests.

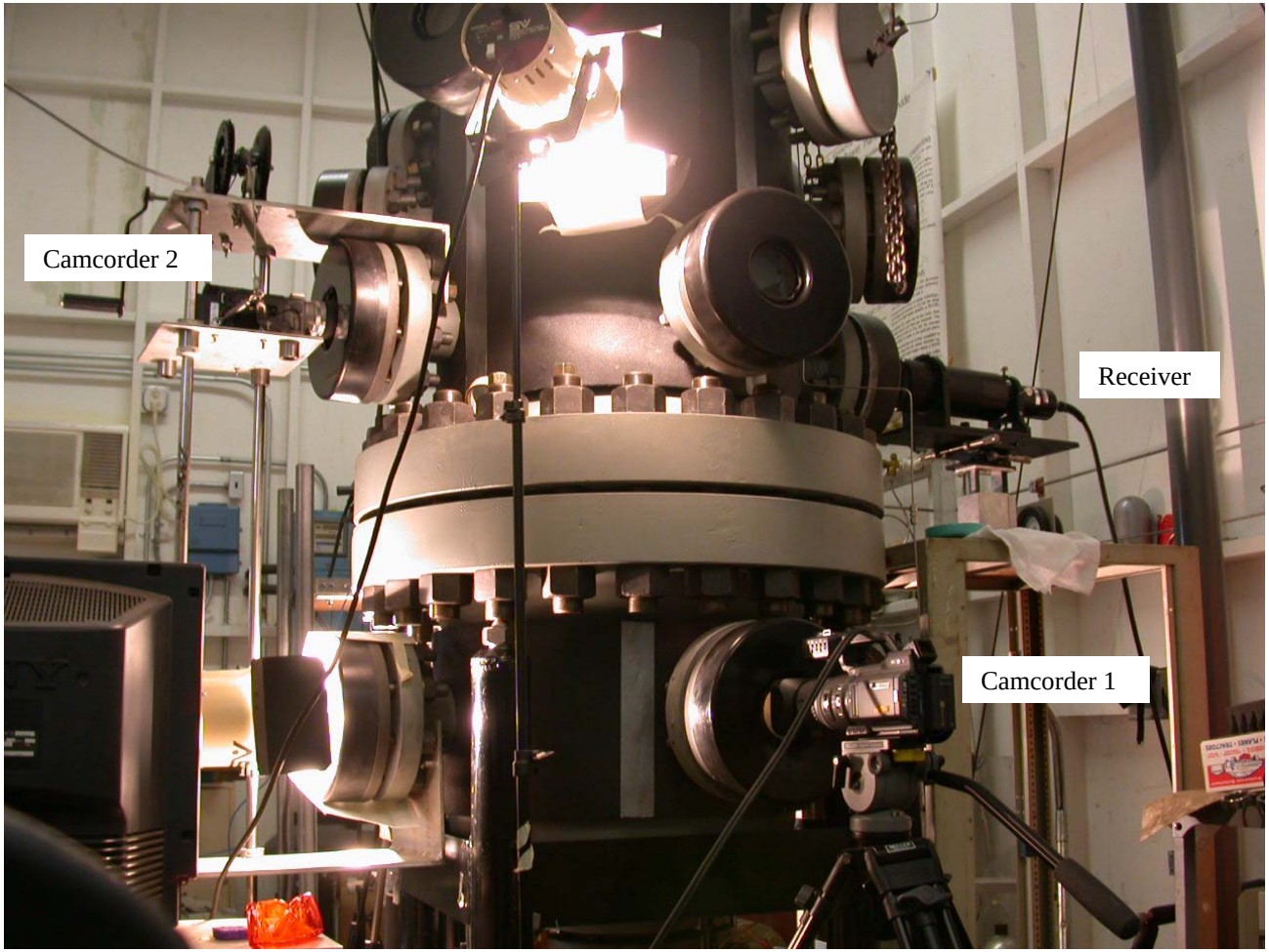

Figure 2.12 A photo taken during CO_2 injection test.

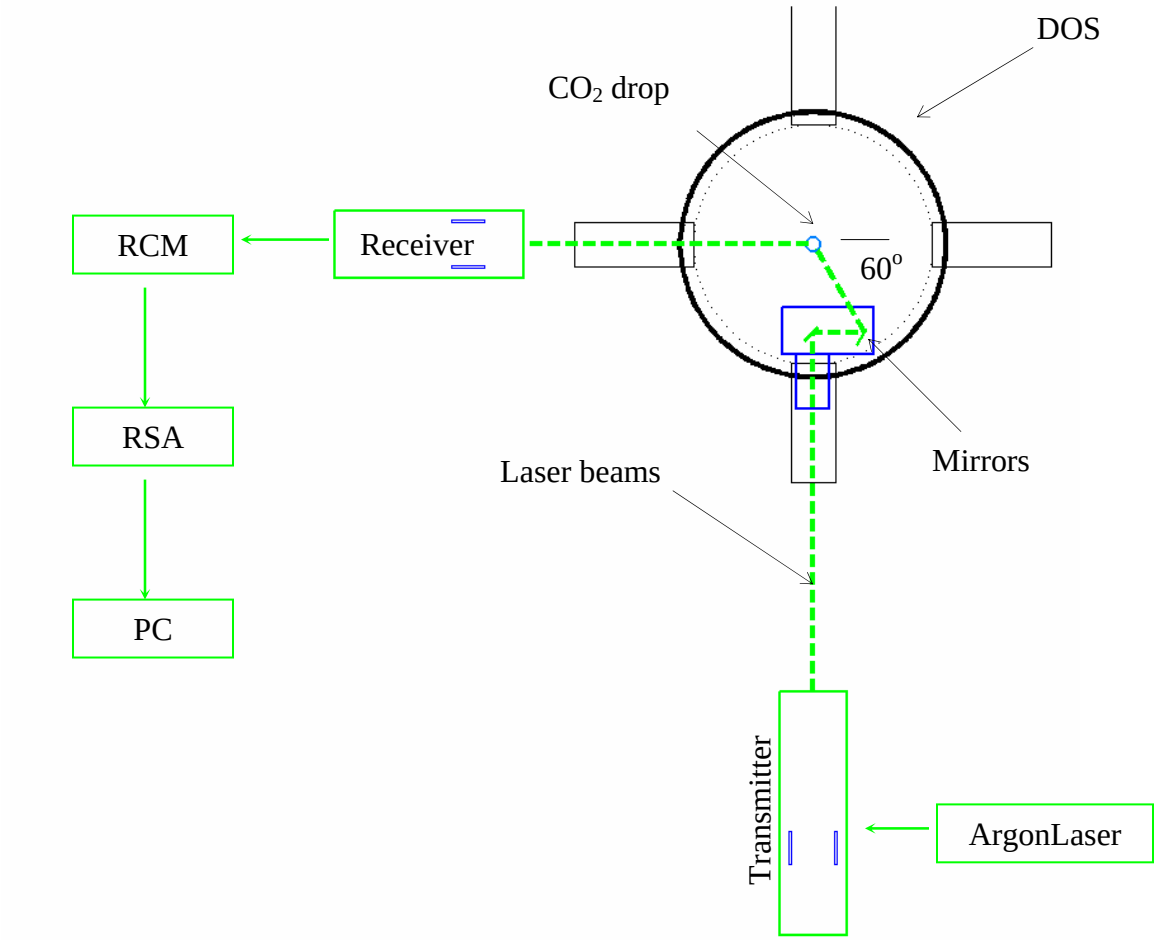

Figure 2.13 PDPA setup for liquid CO_2 injection tests.

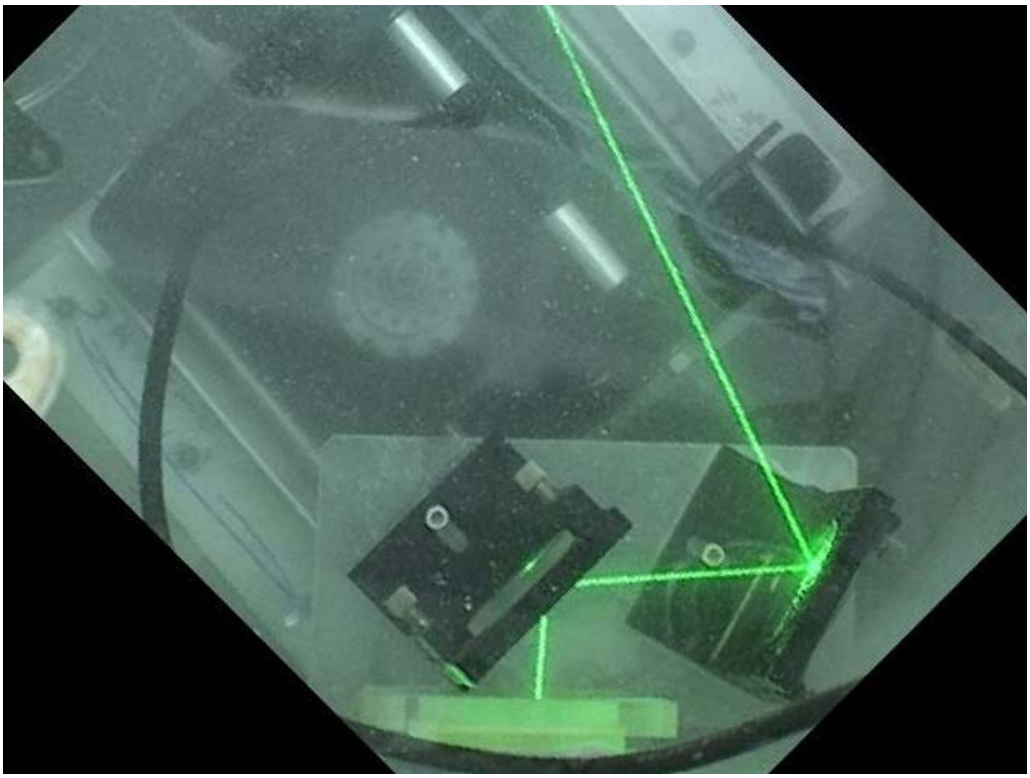

Figure 2.14 A pair of dielectric mirrors installed inside the DOS steers the laser beams.

2.3.2 Oil Injection Tests

A photograph of the atmospheric pressure Plexiglas tank used for the crude oil and some silicone fluid injection experiments is provided in Figure 2.15 and a schematic drawing is shown in Figure 2.16. The tank was constructed to test optical systems used in the DOS and was therefore designed with similar dimensions. The square tank measures approximately 55 cm (21.5 in.) between the interior surfaces of the walls, and is about 1.3 m (51 in.) tall. It has a capacity of 400 liters (106 gallons) of water. The tank is constructed from structural aluminum angle and plate, and clear cast acrylic Plexiglas. A thermistor probe is threaded through one of the lower circular windows and a second probe can be suspended from the top to monitor water temperature. Oil injection nozzles

were mounted on a horizontal traversing mechanism installed diagonally across the tank on two vertical shafts. The manual traverse was driven by an acetal chain and a gear-crank mechanism and was used to position the nozzle at an appropriate location relative to the PDPA optical sample volume. Oil was injected vertically upward. The height of the nozzle could be changed before a test by moving and locking the traverse assembly along the vertical shafts.

Figure 2.17 presents a schematic of the experimental set up that was employed for the oil and a number of silicone fluid injection tests. A pulseless, magnetic drive, cavity-style gear pump (Micropump Series 2200) coupled to a Leeson variable speed 1 hp motor draws the jet fluid from a small (about 8 liter) reservoir. The reservoir is closed and immersed in the constant temperature water bath to minimize devolatilization of the crude oils. Devolatilization produces undesirable changes in oil properties (i.e., composition, viscosity, and density). Silicone fluid, on the other hand, is a pure substance whose properties are not affected by evaporation.

Flow rate (and jet velocity) is set by adjusting the pump motor speed and two needle valves dividing the flow between the injector and a bypass line back to the reservoir. A positive displacement flowmeter (Omega Engineering FTB-1002) is installed inline with the injector to measure the flow rate of oil into the tank. Oil temperature and pressure are monitored with an inline thermistor and precision pressure gauge, respectively. All wetted parts are compatible with, and insoluble in, the oils. Oil enters the tank through a pipe fitting in its base and flows through a short service loop of 9.5 mm (0.375 in.) i.d. flexible tubing before entering the injection nozzle mounted on the horizontal traverse.

Three nozzles were used in the experiments with circular orifice diameters of 1, 2, and 5 mm.

As in the CO_2 injection experiments, jet instability was monitored with several video cameras positioned at different heights above the injector. These video records also were employed to obtain data on the size distribution of the oil droplets that are generated by the disintegration of the jet.

Four deepwater crude oils, Genesis (GE), Mars TLP (MA), Neptune SPAR (NS), and Platform Gail (PG), were obtained from Chevron and were tested in the oil breakup experiments. These oils have been analyzed by the Environmental Technology Centre of Environment Canada (Masutani & Adams, 2000). Results of those analyses can be found in the Oil Properties Database at www.etcentre.org.

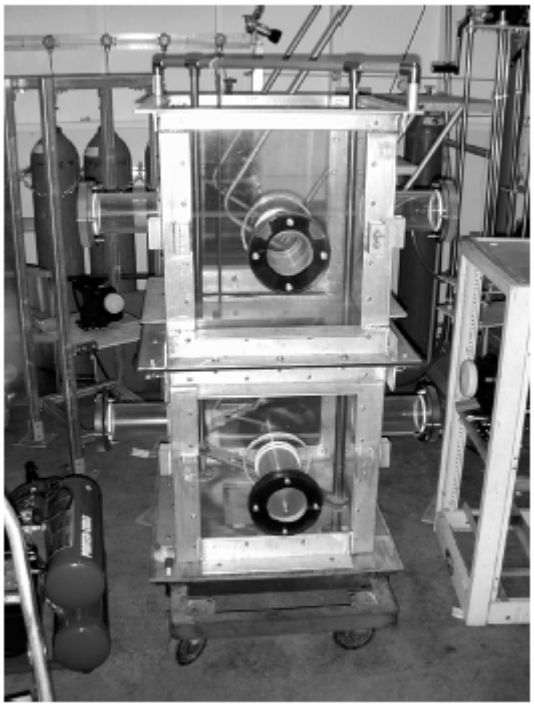

Figure 2.15 Photograph of the Plexiglas water tank (Masutani & Adams, 2000).

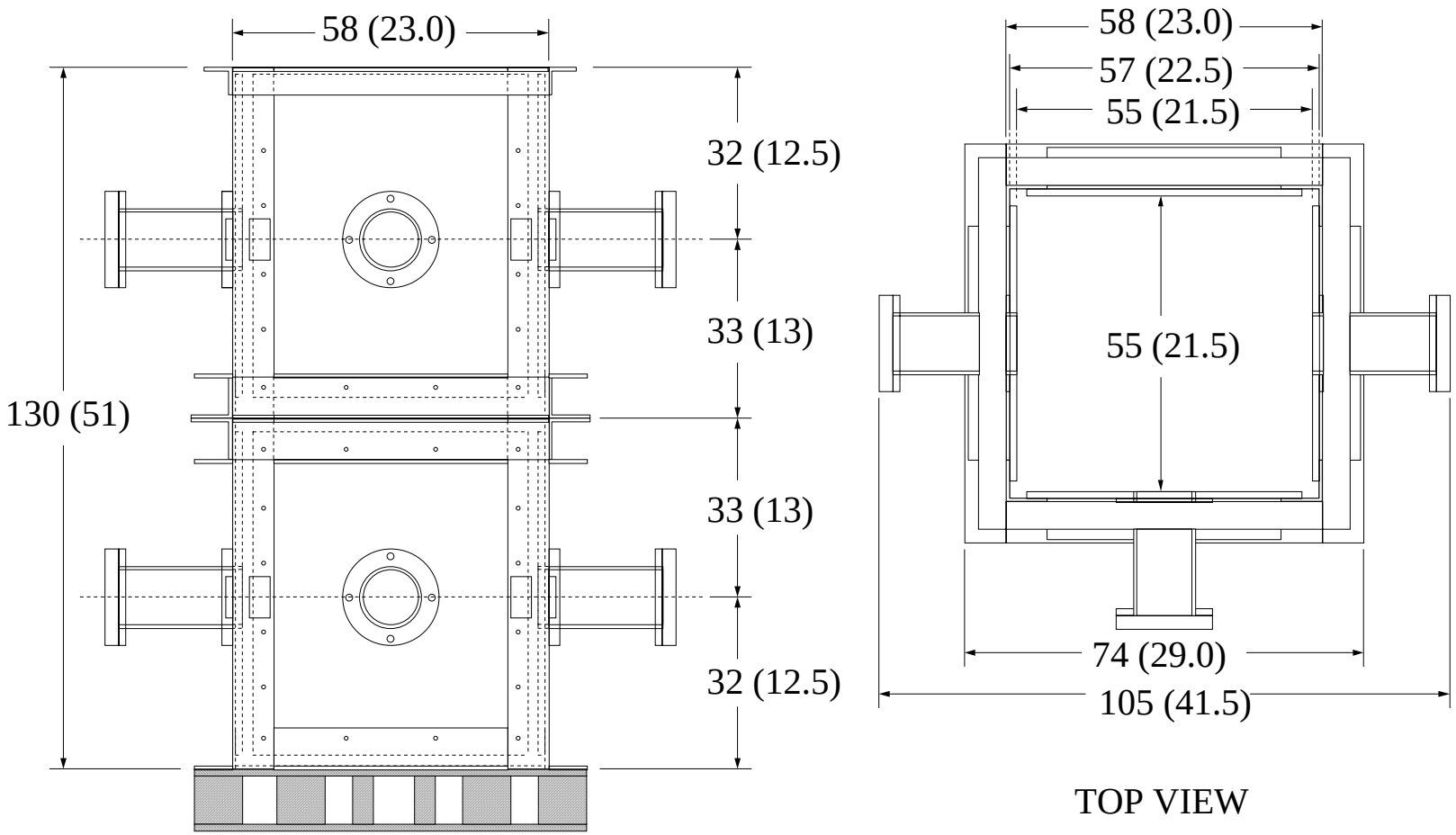

Figure 2.16 Schematic drawing of the Plexiglas tank. Dimensions are given in centimeters and (inches) (Masutani & Adams, 2000).

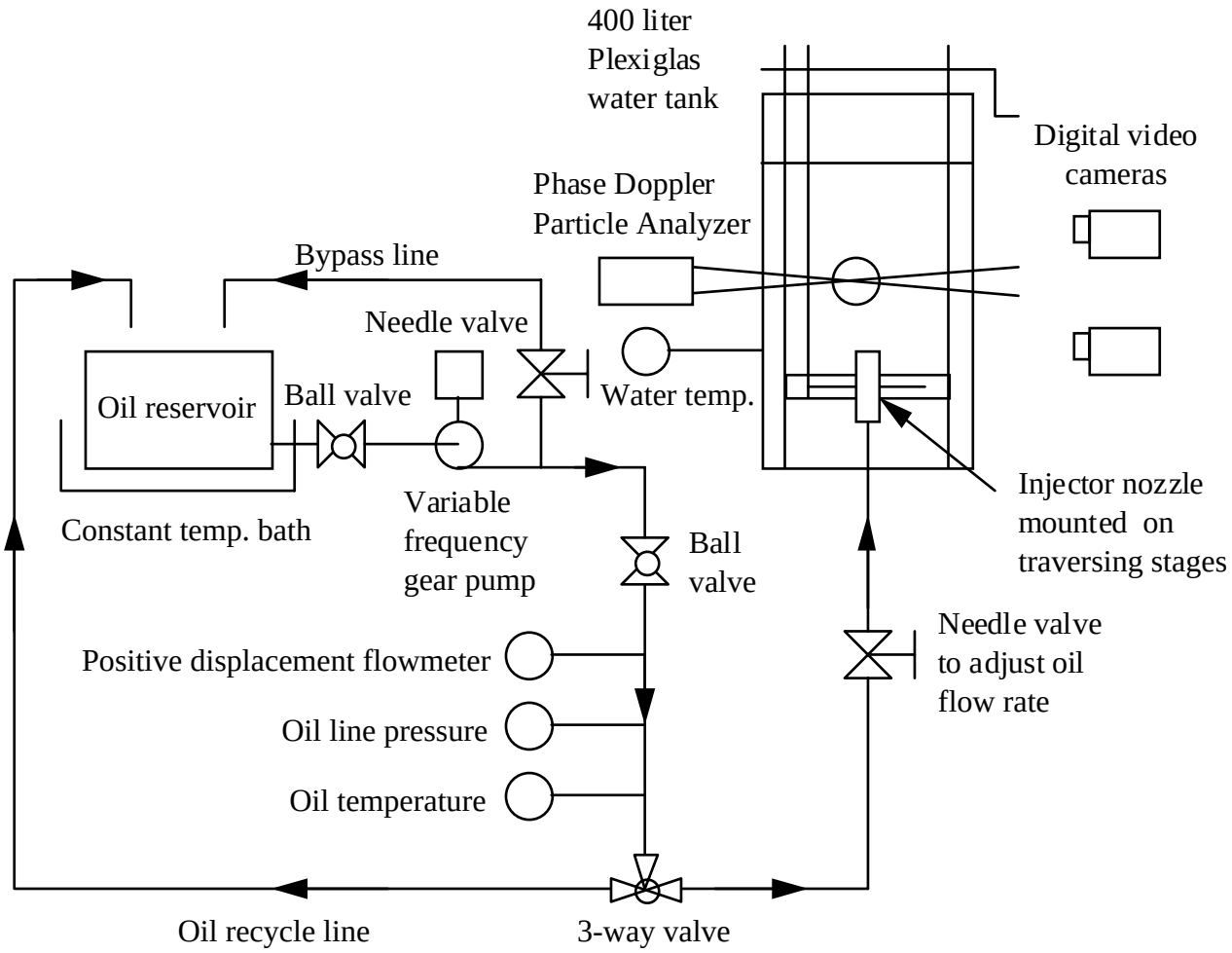

Figure 2.17 Experimental layout for the oil injection tests.

2.3.3 Silicone Fluid Injection Tests

While the breakup of jets of crude oil in water is directly relevant to the practical problem of undersea well blowout and pipeline breakage, crude oils present a number of difficulties as a result of their toxicity, opacity, and high vapor pressures. Since crude oils evaporate (i.e., devolatilize) readily, significant changes in fluid properties can occur over the course of an experiment or between tests. Uncertainties in the values of critical properties such as density, ρ, viscosity, μ, and surface tension, σ, used to calculate dimensionless flow parameters including jet Reynolds number, Weber number, Ohnesorge number, and Bond number can complicate the interpretation of breakup data. It was decided, therefore, to supplement the proposed crude oil experiments by conducting a series of tests using a stable (i.e., properties do not vary over time due to devolatilization) analog fluid that has comparable values of ρ, μ, and σ. After evaluating a large number of candidates, pure polydimethylsiloxane (silicone) fluids were selected. Silicone fluids are non-toxic, have very low vapor pressures at room conditions, and are insoluble in water. Furthermore, unlike the very opaque crude oils, polydimethylsiloxane is transparent (and reflective), which facilitates optical PDPA measurements.

Silicone fluids with different viscosities were procured for the planned experiments. An additional Plexiglas water tank was subsequently constructed for a number of the silicon fluid injection tests. This tank was designed to have wall geometries (Figure 2.18) that are optimized for the PDPA (i.e., the wall surfaces are perpendicular to the PDPA transmitter and receiver optics to minimize losses and refractive effects). Figure 2.19 shows the cross section of this Plexiglas tank.

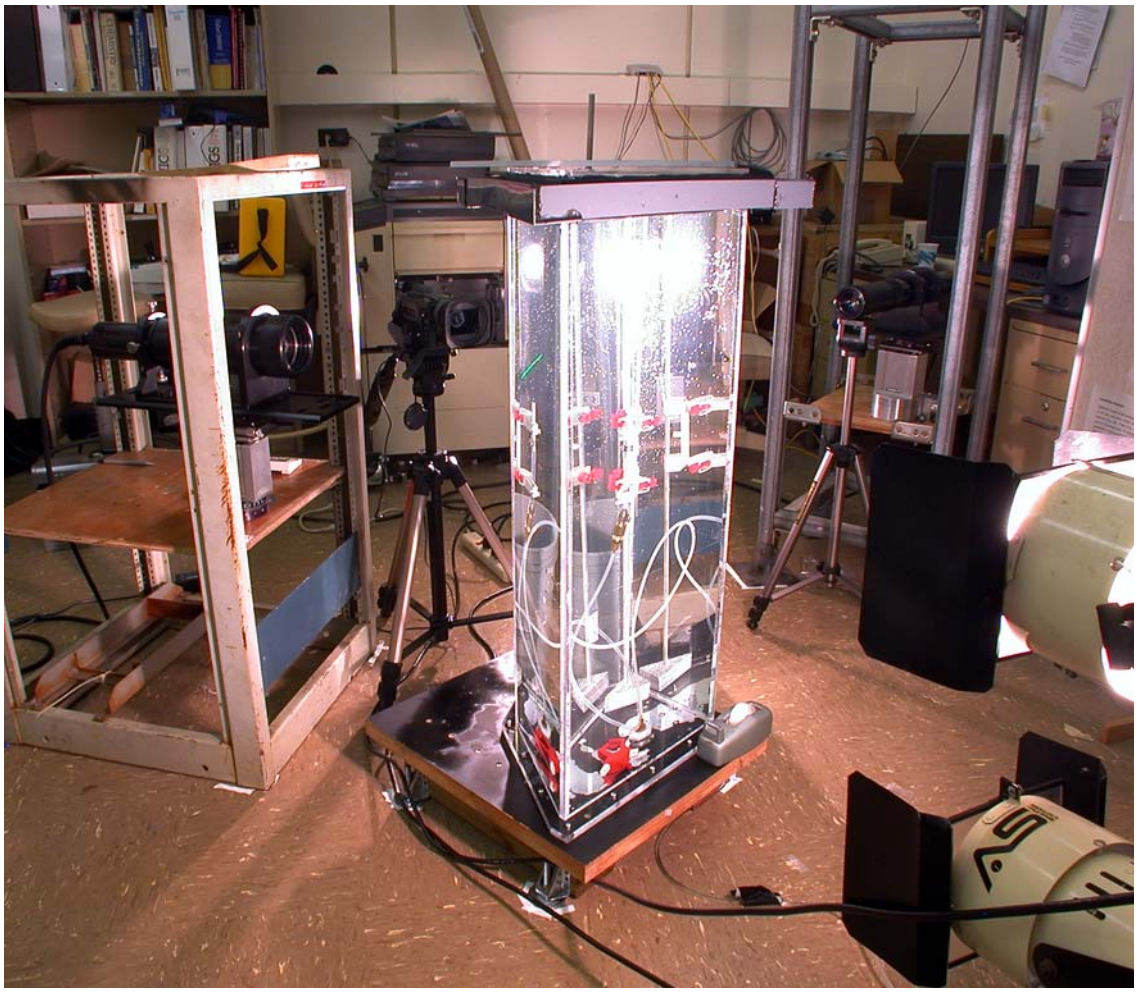

Figure 2.18 Photograph of the Plexiglas tank used for silicone fluid injection tests.

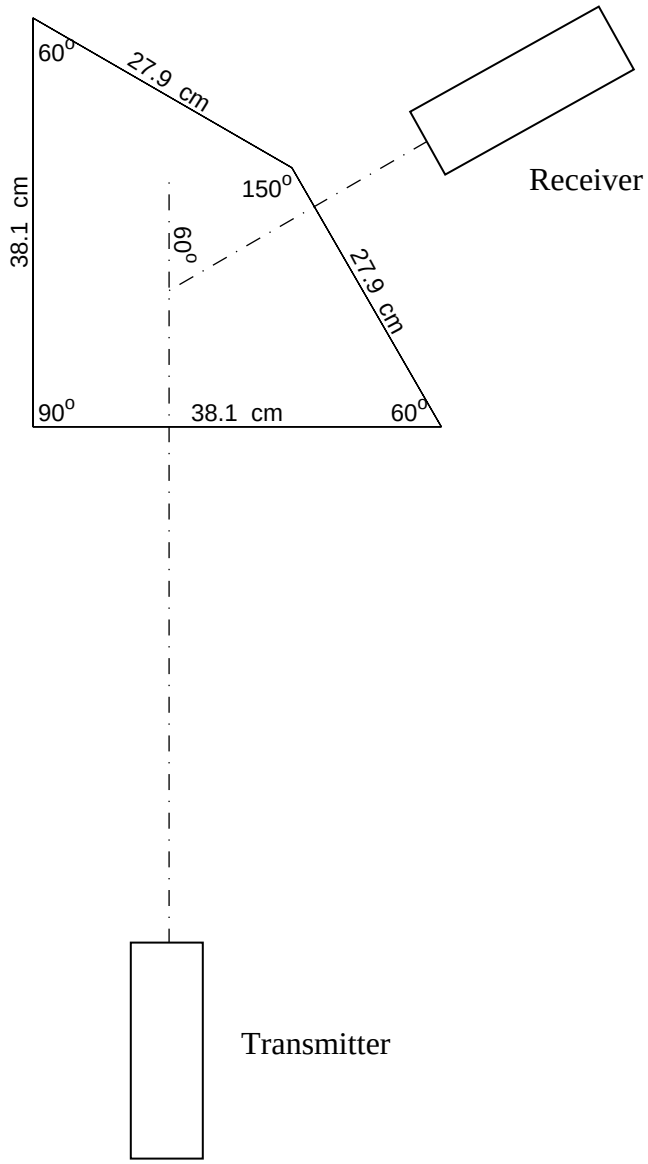

Figure 2.19 Cross section of the Plexiglas tank for silicone fluid injection tests.

2.3.4 Fluid Properties

Comparisons of properties of the crude oils, silicone fluids, and liquid CO_2 that were employed in the jet instability and breakup experiments are provided in Table 2.1 and Figure 2.20. It should be noted that the kinematic viscosities of the selected fluids range over three orders of magnitude.

Table 2.1 Comparison of properties of silicone fluid and four deepwater crude oils at 25°C (0% evaporation); surface tension, σ, of the oils were not measured; values shown were estimated from data on σ for similar crude oils given in the Environmental Technology Centre online database.

Liquid Name	Symbol	Density [kg/m^3]	Kinematic Viscositiy [centistrokes]	Surface Tension [dyne/cm]
Genesis	GE	877	20.5	~25 (estimated)
Mars TLP	MA	882	27.2	~25 (estimated)
Neptune Spar	NS	861	15.1	~25 (estimated)
Platform Gail	PG	922	211	~25 (estimated)
Silicon fluid 0.65	LS	761	0.65	15.9
Silicon fluid 20	SF	977	20	21
Liquid CO_2	CD	838~986[1]	Fig 2.20	27

[1] Liquid CO_2 density range for planned CO_2 injection experiments.

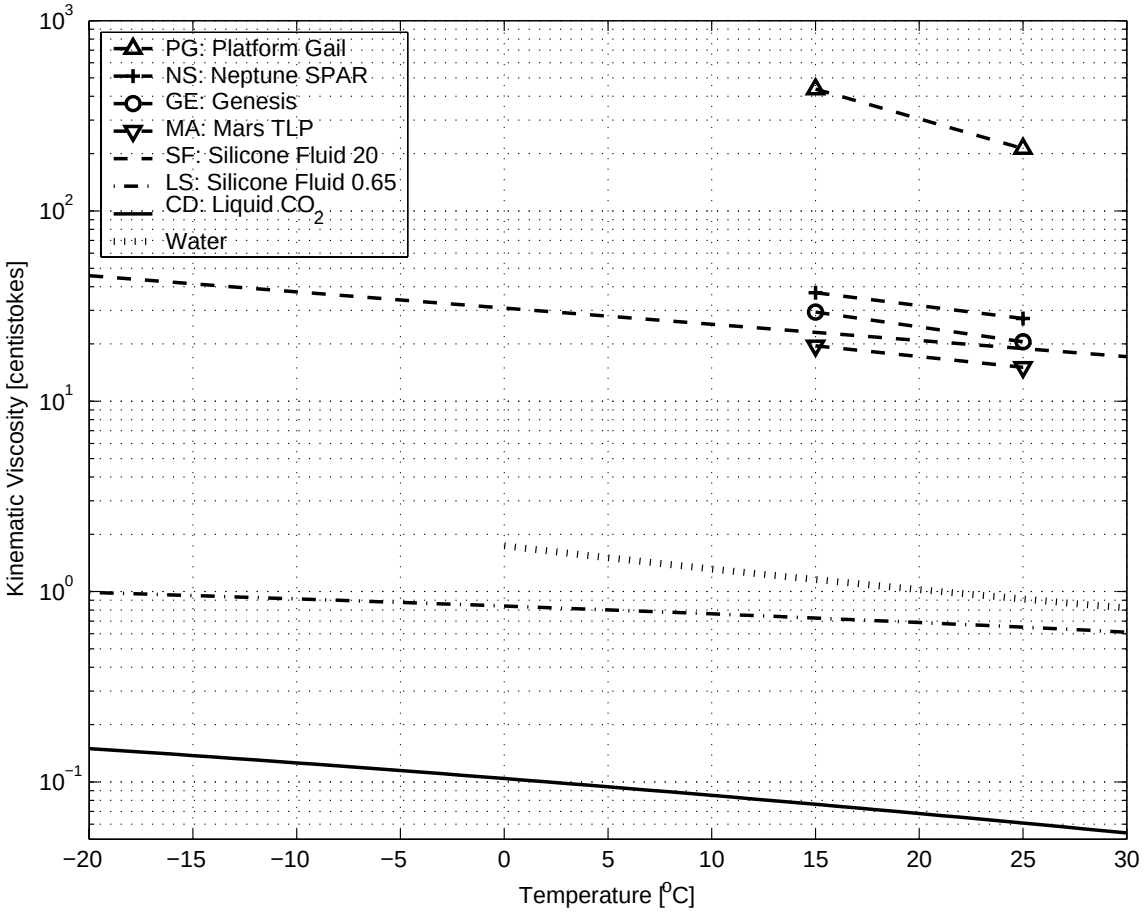

Figure 2.20 Kinematic viscosities (in centistokes) of silicone fluids, four deepwater crude oils, liquid CO_2, and water. The viscosities of silicone fluids are obtained from the manufacturer. Crude oils viscosities are from Masutani and Adams (2000) at 15^{o} C and 25^{o} C for 0% evaporation.

2.3.5 Nozzle Characteristics

The influence of injection nozzle geometry was investigated in these experiments. To determine if boundary layer effects are significant, ASME sharp edge orifices and round tube nozzles were tested under identical flow conditions. The jet issuing from a sharp edge orifice has no separation boundary layer and typically exhibits a *vena contracta*. A boundary layer develops in a tube nozzle that may influence the jet instability and breakup. Comparisons of results for the two types of nozzles were performed.

Properties of the nozzles are summarized in Table 2.2. Examples of sharp edge and tube orifices that were fabricated for the liquid CO_2 injection tests are shown in Figures 2.21, 2.22 and 2.23. These nozzles bolt to the removable injector in the DOS and are positioned above a plenum and a check valve to prevent ingress of water into the liquid CO_2 line. Tube nozzles for CO_2 injection comprise lengths of plastic tubing of different inside diameter. Figure 2.22 shows multiple orifices (7 sharp edged orifice per nozzle) that were employed to investigate jet interactions

Three nozzles with circular ASME sharp edge orifice diameters of 1 mm, 2 mm, and 5 mm were employed in the crude oil and silicone fluid experiments (Figure 2.24). The nozzles were machined from thick wall 25.4 mm (1.0 in.) diameter stainless steel tubing and marine bronze.

Figure 2.25 presents photographs of the CO_2 injector with the 5 mm tube orifice. The injector assembly is mounted on a flange that is bolted to an opening in the bottom of the DOS.

Figure 2.21 Photograph of 2 mm (C02), 5 mm (C05) and 10 mm (C10) sharp edged, single orifice nozzles fabricated for the liquid CO_2 injection tests.

Figure 2.22 Photograph of 2 mm (C72) sharp edged, 7-orifice nozzle fabricated for the liquid CO_2 injection tests.

Figure 2.23 Photograph of the 2 mm (T02) and 5 mm (T05) Delrin tube orifice nozzles.

Figure 2.24 Photograph of the 1 mm (S01), 2 mm (S02) and 5 mm (S05) sharp edged orifice nozzles.

Figure 2.25 Photographs of the CO_2 injector with the 5 (T05) mm Delrin tube orifice mounted on a flange that is bolted to an opening in the bottom of the DOS.

Table 2.2 Nozzle properties

Nozzle Symbol	Orifice Diameter D [mm]	Orifice Number	Orifice Shape	Nozzle Material	Test Jet Fluid
C02	2	1	ASME sharp edged	Stainless Steel	CO_2
C05	5	1	ASME sharp edged	Stainless Steel	CO_2
C10	10	1	ASME sharp edged	Stainless Steel	CO_2
S01	1	1	ASME sharp edged	Bronze	Oils
S02	2	1	ASME sharp edged	Bronze	Oils/ Silicone fluids
S05	5	1	ASME sharp edged	Bronze	Oils
C72	2	7	ASME sharp edged	Aluminum	CO_2
T02	2	1	Tube	Delrin	CO_2/LS
T05	5	1	Tube	Delrin	CO_2

CHAPTER 3 EXPERIMENTAL RESULTS: LIQUID-LIQUID JET INSTABILITY REGIMES

3.1 Chapter Overview

Jets disintegrate into a dispersed phase as the result of the competition between cohesive forces (interfacial tension and viscous force) and disruptive forces (gravitational and hydrodynamic or aerodynamic forces). Instability regimes are used to indicate the dominant mode(s) of instability and provide general, qualitative information about droplet size spectra, jet breakup length and other flow characteristics. They are useful devices to classify disintegrating jets.

For liquid-liquid system, information pertaining to breakup and droplet formation is largely based on experimental observations. Experiments were conducted by Hayworth and Treybal (1950), Meister and Scheele (1969), Kitamura *et al*. (1982), Kumar and Hartland (1984), Skelland and Walker (1989), Kato *et al*. (2000), Longmire *et al*. (2001) and others to study liquid-liquid jet breakup. These studies have provided useful data on droplet size and breakup length but were limited to laminar jet flow. In many practical applications involving liquid-liquid jet breakup, such deep oil spills or CO_2 sequestration, transitional and turbulent breakup events may occur. Neither breakup modes nor instability regimes have been clearly defined for liquid-liquid systems over the entire breakup range extended from dripping to full atomization. To address this deficiency, the extensive experimental database from this investigation was analyzed to identify the primary liquid-liquid instability modes and to define associated breakup regimes. The

boundaries of these regimes were determined on the basis of certain dimensionless parameters that are discussed in section 3.2.

3.2 Dimensionless Parameters

Following standard practice to develop scale-independent results, the present data were analyzed and, wherever possible, presented in non-dimensional space. It is generally agreed that the following dimensionless parameters characterize jet instability (Reitz & Bracco, 1986; Kitamura & Takahashi, 1986; Lefebvre, 1989; Teng, 1994; Masutani & Adams, 2000):

Reynolds Number, *Re*

$$Re \equiv \frac{U_j D}{\nu_j} \tag{3.1}$$

Weber Number, *We*

$$We \equiv \frac{\rho_j U_j^2 D}{\sigma} \tag{3.2}$$

Ohnesorge Number, *Oh*, and Modified Ohnesorge Number, *Oh**

$$Oh \equiv \frac{\mu_j}{\sqrt{\rho_j \sigma D}} = \frac{\sqrt{We}}{\mathrm{Re}_D} \tag{3.3a}$$

$$Oh^* \equiv \frac{3\mu_j + \mu}{\sqrt{\rho_j \sigma D}} \tag{3.3b}$$

Bond Number, *Bo*

$$Bo \equiv \frac{g\Delta\rho D^2}{\sigma} \tag{3.4}$$

The subscript *j* denotes properties of the jet fluid; ambient fluid properties are not subscripted. U_j is taken to be the bulk-mean inlet velocity of the jet (calculated as the volumetric flow rate of jet fluid divided by the cross sectional area of the injection orifice); *D* is the injection orifice diameter; *g* is the gravitational constant; ρ, μ, ν, and σ are, respectively, fluid density, dynamic viscosity, kinematic viscosity, and interfacial tension; and $\Delta\rho$ is the difference in the densities of the jet and ambient fluids.

Re is the ratio of inertial to viscous forces; *We* is the ratio of disruptive momentum (hydrodynamic) forces to restoring surface tension; and *Oh*, a stability index given as the ratio of viscous forces to surface tension. The modified Ohnesorge number (Teng *et al.*, 1995), *Oh**, accounts for the influence of ambient fluid viscosity on jet instability and breakup. Ambient density effects appear in the Bond number, *Bo* (sometimes called the Eötvös number; *vide* Kumar & Hartland, 1984); ambient density also is employed occasionally to calculate the Weber number. *Bo* is important for buoyancy-driven flows (e.g., gases leaking upward into a liquid; liquids falling through a gas) and is less relevant for high Weber number jets.

As mentioned previously, other factors not included in the above dimensionless groups are believed to influence jet breakup and, hence, the size distribution of the dispersed phase. The development of free shear flows, such as a contaminant oil or liquid CO_2 jet, is known to depend strongly on the condition of the wall boundary layer at the point of separation and on upstream and downstream pressure fluctuations. To date, a viable approach to account for these factors in the analysis of breakup data has not been identified (furthermore, precise measurements of the jet initial and boundary conditions

are not trivial) – which could explain some of the scatter encountered when data is correlated.

3.3 Liquid-liquid Jet Instability Regimes

3.3.1 Definition of the Breakup regimes

The delineation of breakup regimes has been an important focus of recent work on liquid-liquid jet instability. When a liquid jet emerges from a nozzle as a continuous body of cylindrical form, the competition between cohesive and disruptive forces gives rise to oscillations and distortions of the interface. These disturbances can grow until the liquid body disintegrates into a dispersed droplet phase. In our experiments involving different fluids, injectors, and facilities we consistently observed a progression of five breakup modes as jet velocity increased. Figure 3.1 shows a sketch of the breakup modes that define the five instability regimes. Video data frames from the numerous experiments, on which the sketch was based, are provided in Figures 3.2 to 3.12.

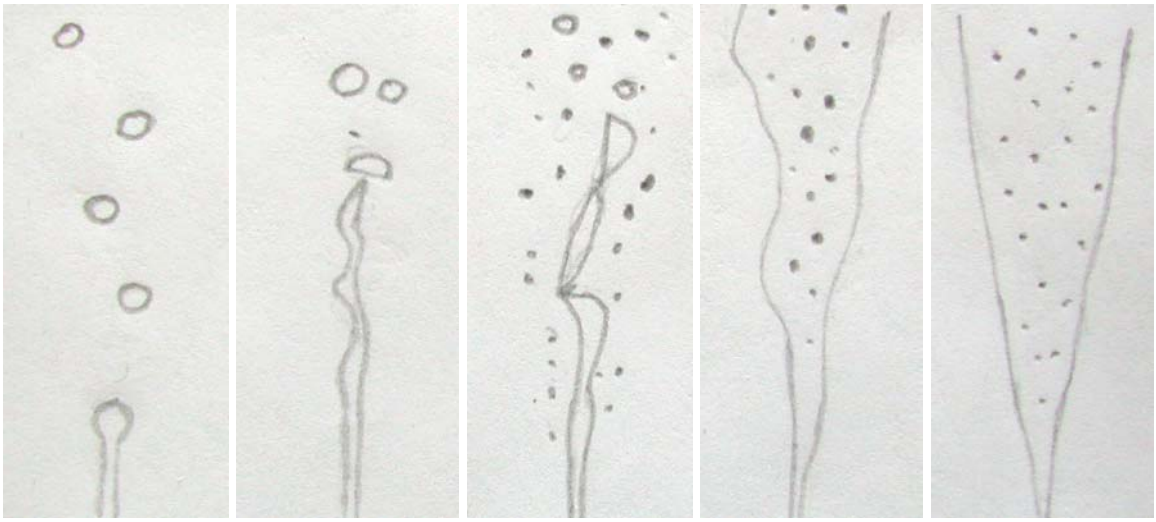

(a) (b) (c) (d) (e)

Figure 3.1 Sketch showing the general characteristics of the 5 jet breakup modes observed consistently in the liquid-liquid injection tests. Jet velocity increases from left to right. (a) Varicose breakup at instability regime 1. (b) Sinuous wave breakup at instability regime 2. (c) Filament core breakup at instability regime 3. (d) Wave shape atomization at instability regime 4. (e) Full atomization at instability regime 5.

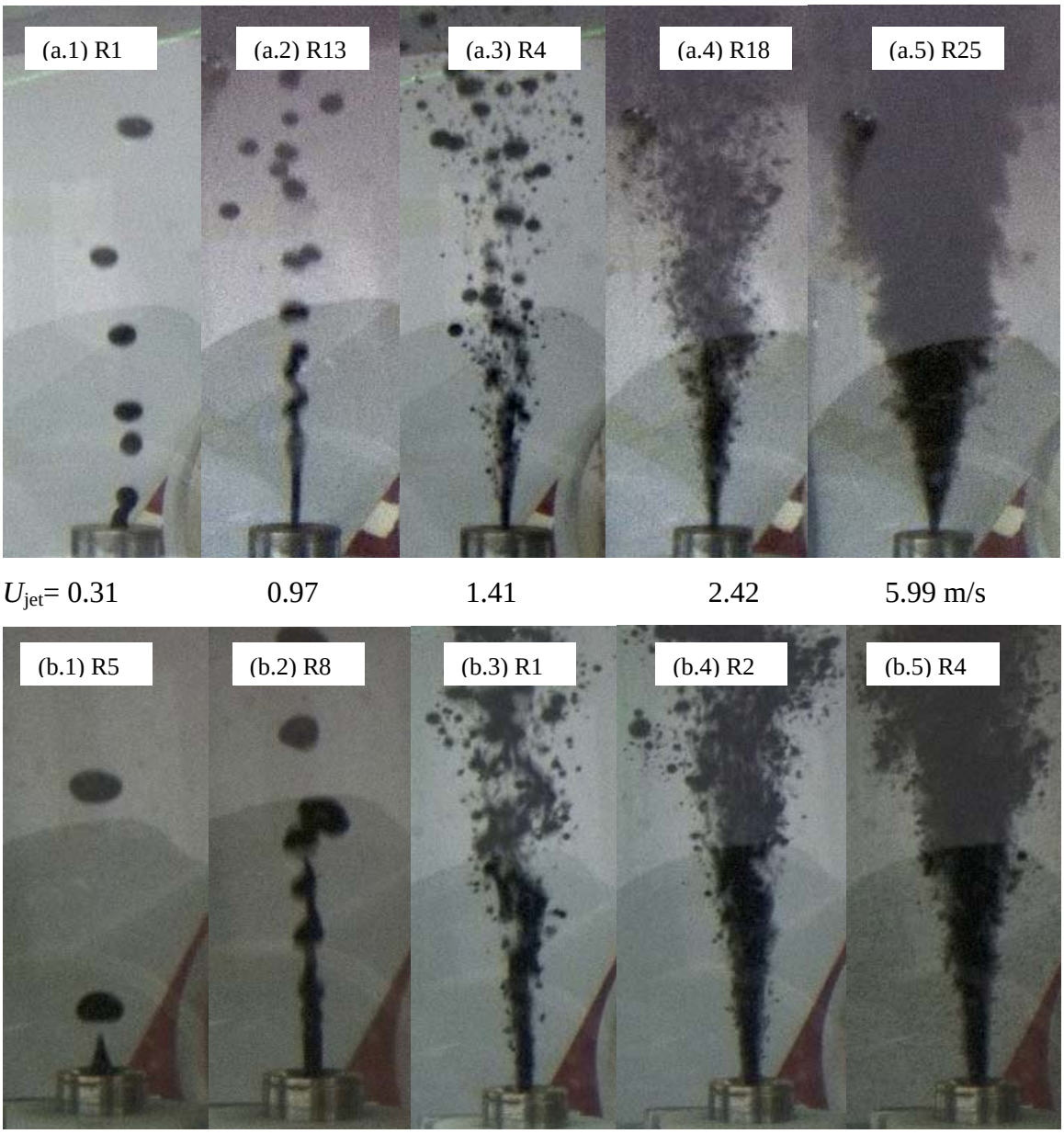

Figure 3.2 Five breakup modes of Genesis crude oil; injection into tap water. Frames a.1 to a.5 use 2 mm sharp edge nozzle; conditions given in Table 3.2 for Case GES02WTR. Frames b.1 to b.5 use 5 mm sharp edge orifice; Case GES05WTR. The outside diameter of the injection nozzles is 2.54 cm.

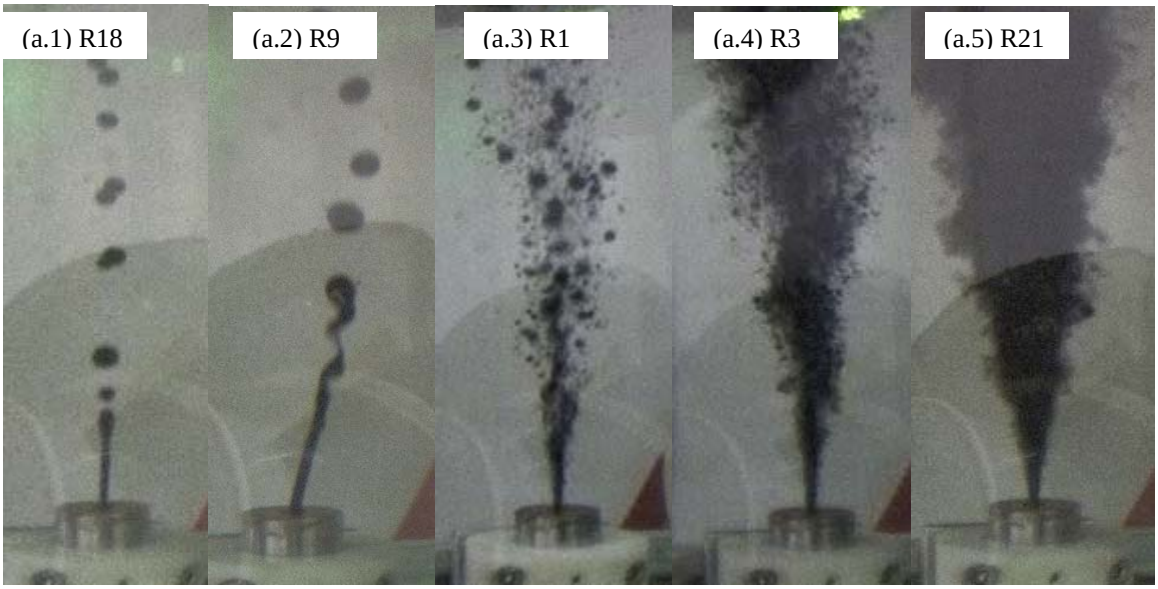

U_{jet} = 0.33 0.84 1.68 2.92 6.84 m/s

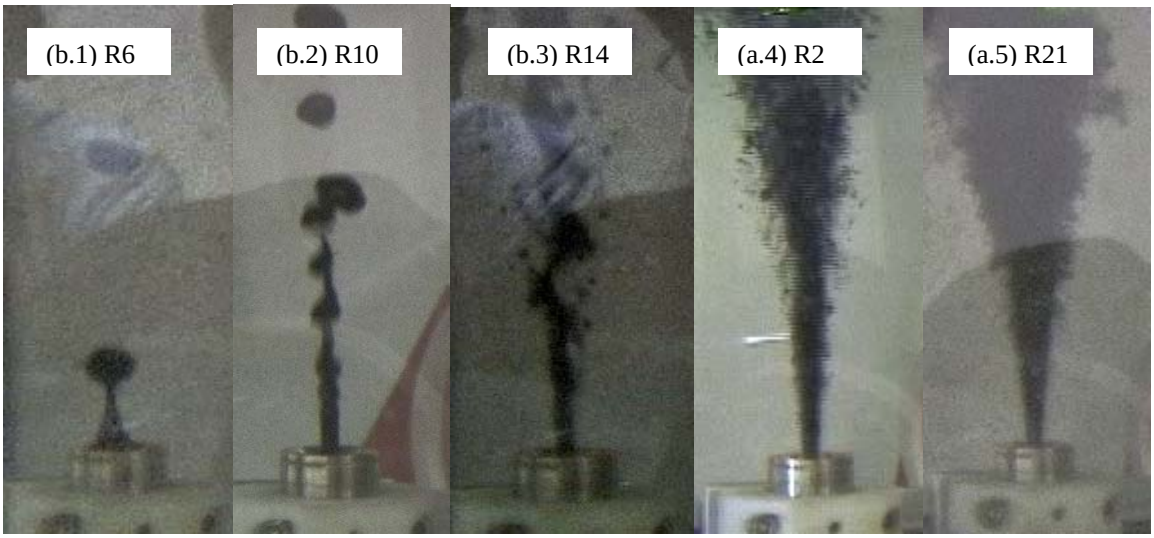

U_{jet}= 0.09 0.35 0.72 1.34 2.45 m/s

Figure 3.3 Five breakup modes of Mars TLP crude oil; injection into tap water at room temperature from 2 mm and 5 mm sharp edge orifices. Frames a.1 to a.5 correspond to Case MAS02WTR. Frames b.1 to b.5 correspond to Case MAS05WTR .

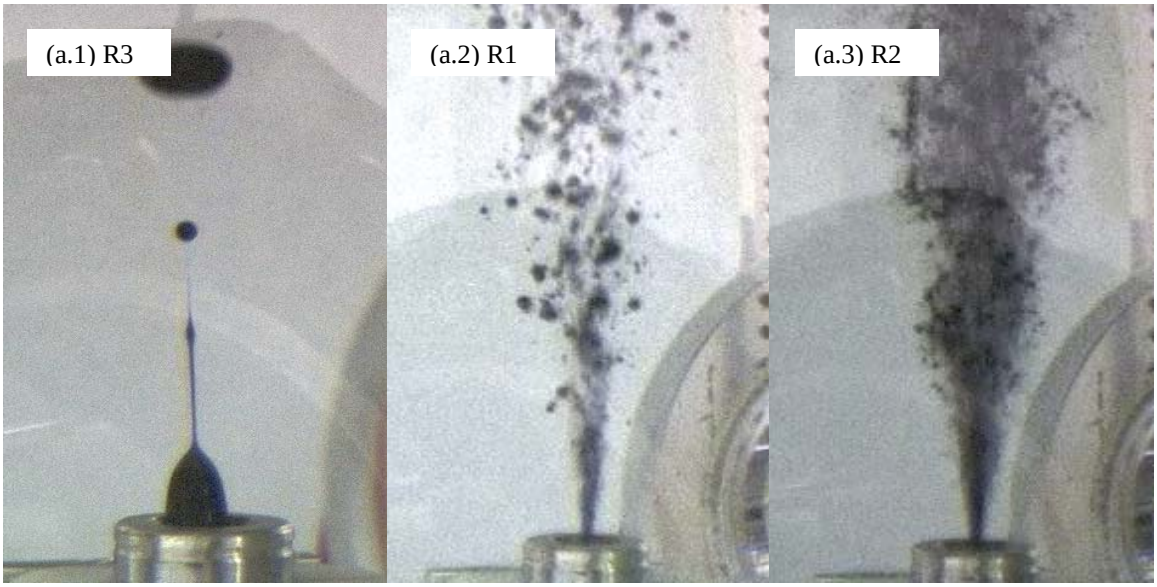

U_{jet} = 1.2 3.73 5.41 m/s

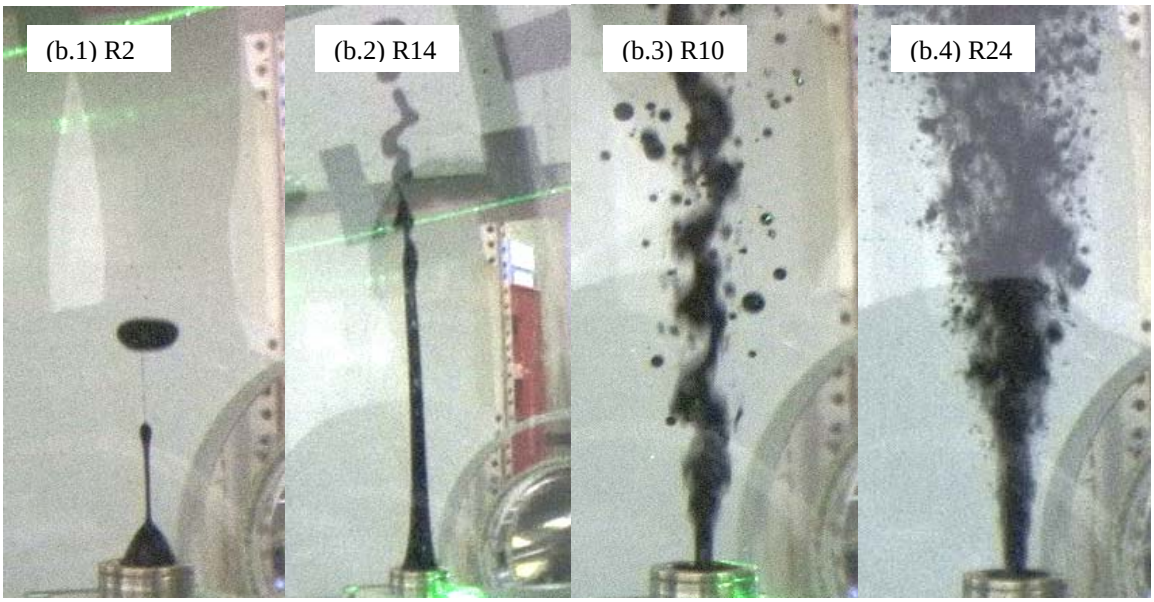

U_{jet}= 0.04 0.34 0.89 1.72 m/s

Figure 3.4 Breakup of very high viscosity Platform Gail crude oil; injection into tap water at room temperature from 1 mm and 5 mm sharp edge orifices. Frames a.1 to a.3 represent breakup modes 1, 3 and 4 for Case PGS01WTR. Frames b.1 to b.4 show breakup modes 1, 2, 3 and 4 for Case PGS05WTR.

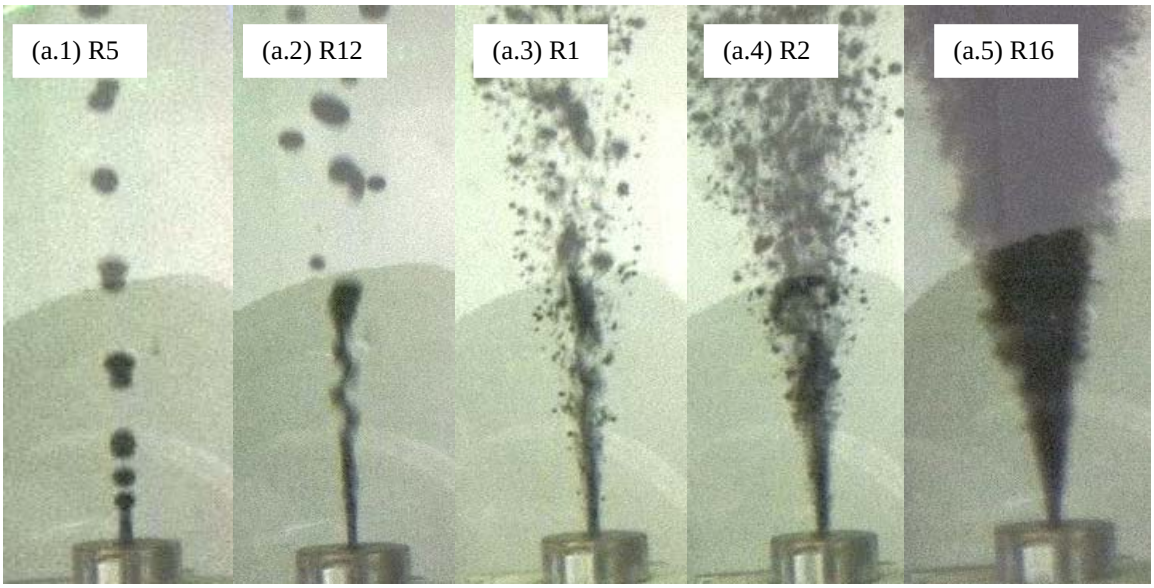

U_{jet}= 0.36 0.87 1.65 2.17 5.13 m/s

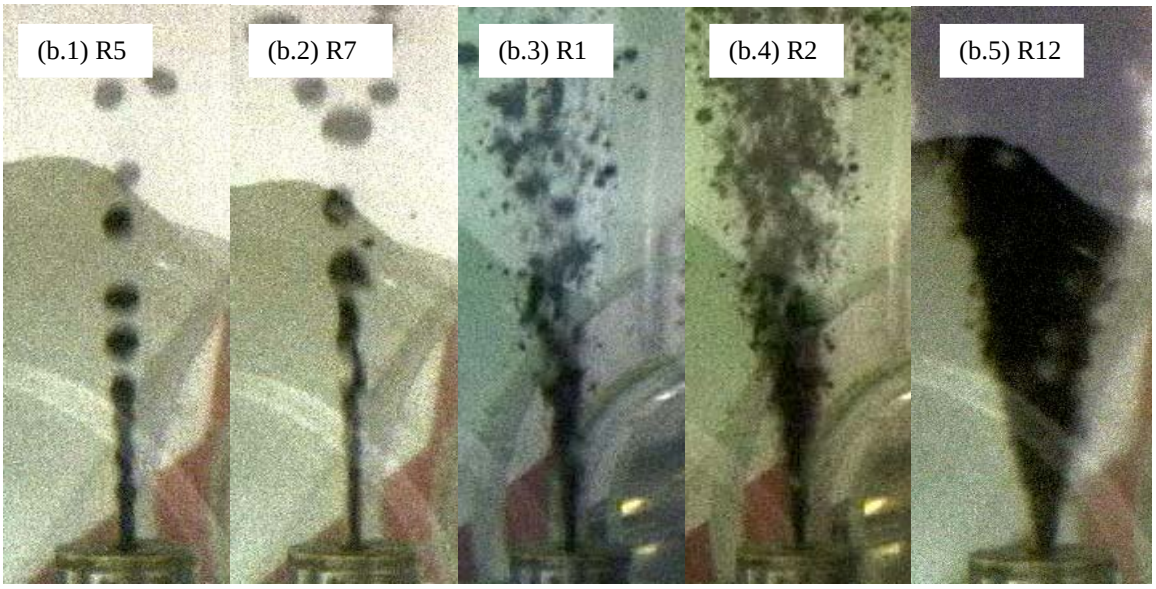

U_{jet}= 0.32 0.86 1.65 2.08 6.84 m/s

Figure 3.5 Five break-up modes of Neptune Spar crude oil; injection tests in tap water and natural surface sea water from 2 mm sharp edge orifice. Frames a.1 to a.5 correspond to Case NSS02WTR using tap water. Frames b.1 to b.5 correspond to Case NSS02WNR using sea water.

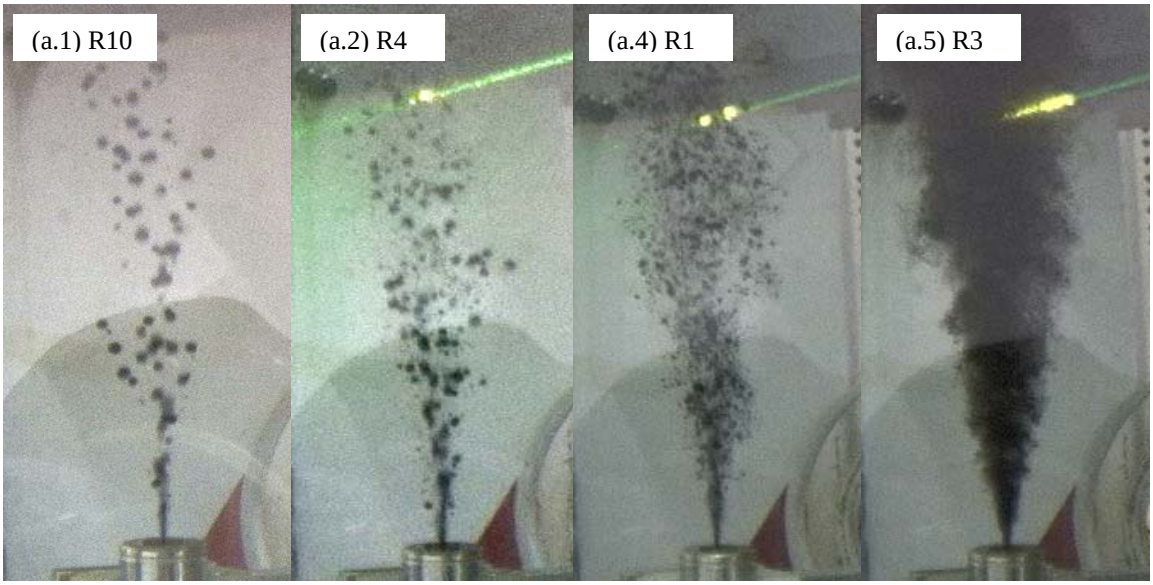

U_{jet}= 1.03 1.63 2.4 5.62 m/s

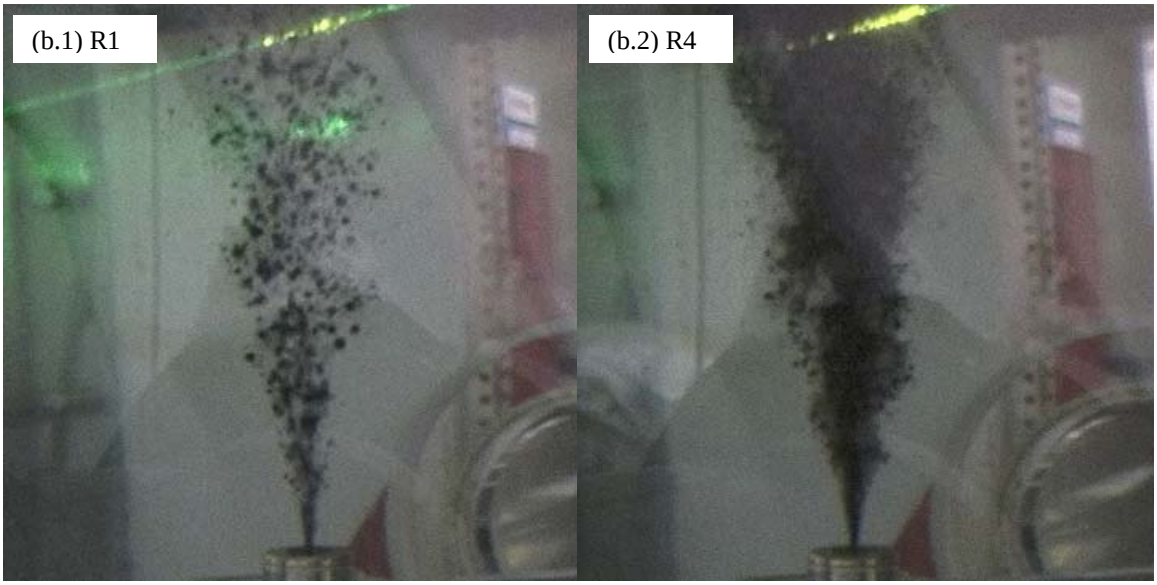

U_{jet} = 1.61 4.59 m/s

Figure 3.6 Neptune SPAR crude oil injections into tap water at different water temperatures from 1 mm sharp edge orifice (S01). Frames a.1 to a.4 represent breakup modes 2, 3 4 and 5 at water temperature of 18.8°C for Case NSS01WTR. Frames b.1 and b.2 represent breakup modes 3 and 4 at water temperature of 8.5°C for Case NSS01WTC.

(a.1) (a.2) R2 (a.3) R3 (a.4) R7 (a.5) R9

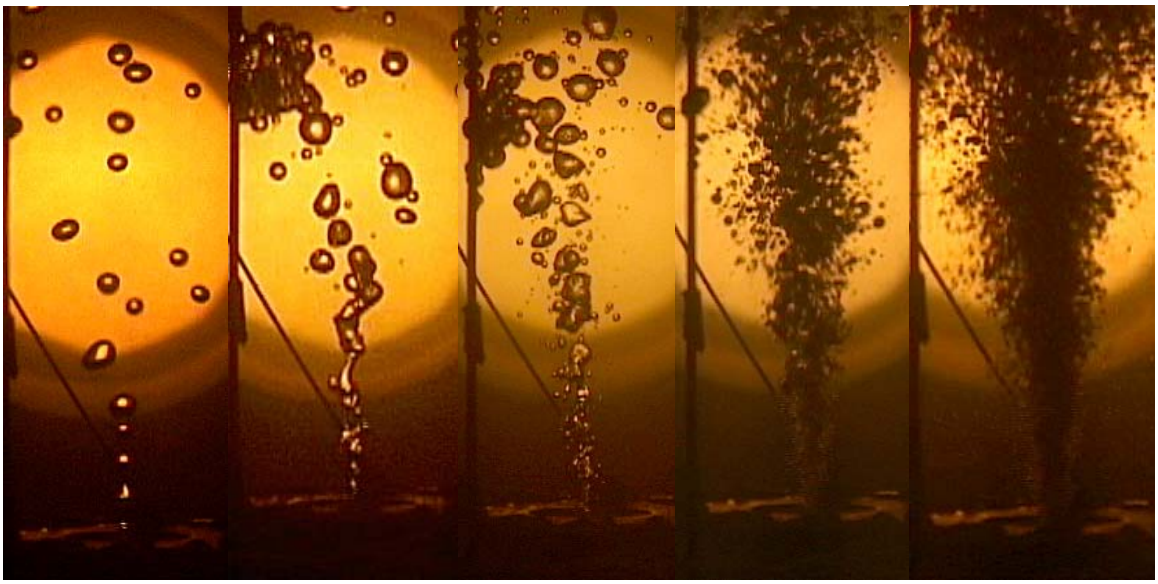

U_{jet}= <0.67 0.77 1.13 2.58 4.01 m/s

(b.1) R4 (b.2) R11 (b.3) R15 (b.4) R25 (b.5) R19

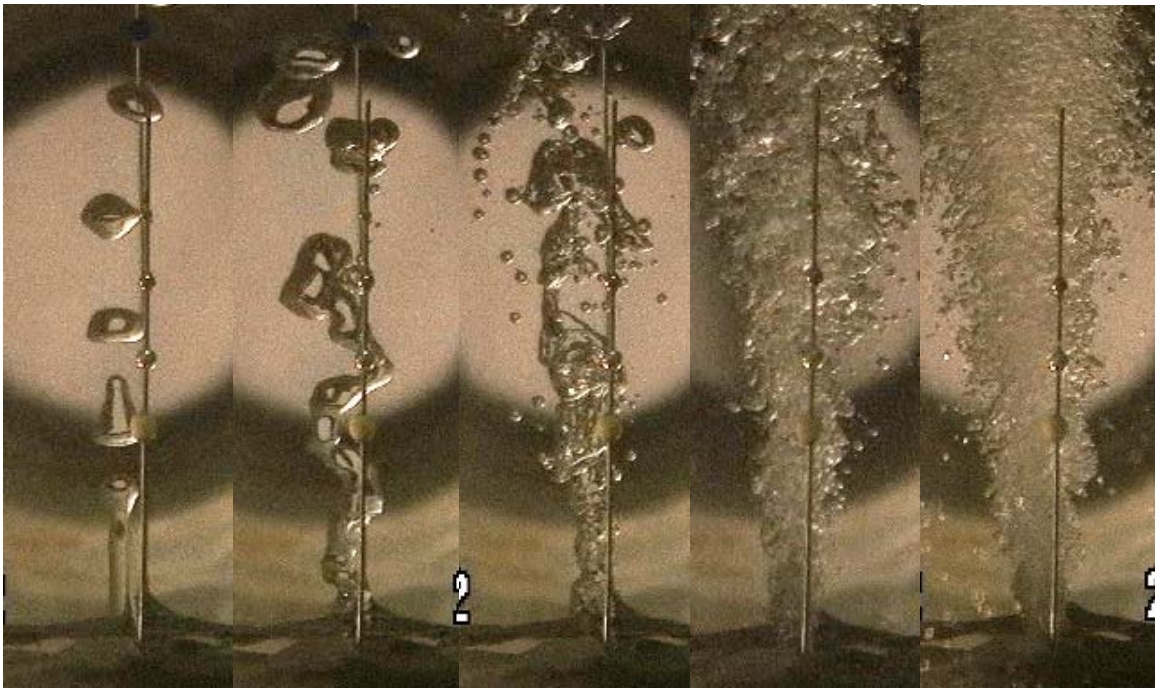

U_{jet}= 0.1 0.44 1.13 0.87 2.48 m/s

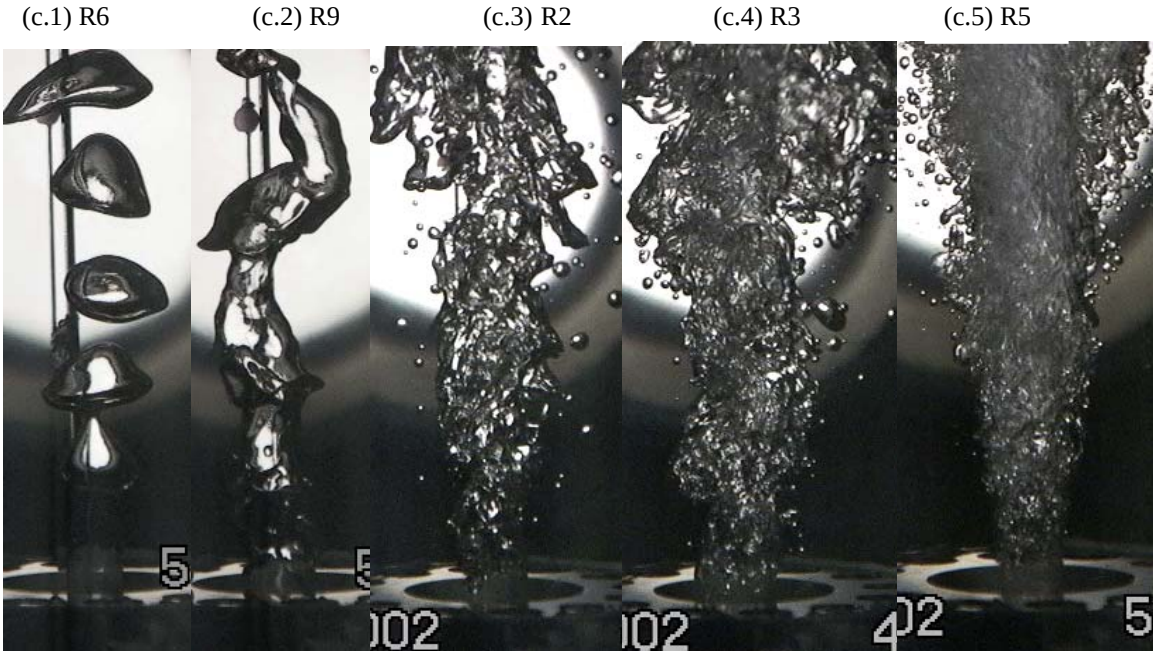

Figure 3.7 Five breakup modes observed during liquid CO_2 injection tests in tap water with the ASME sharp edge orifices of different diameters at pressure of 52 bars. Frames a.1 to a.5 show 2 mm sharp edge orifice for Case CDC02WTP52. Frames b.1 to b.5 show 5 test runs with 5 mm sharp edge orifice for Case CDC05WTP52. Frame c.1 to c.5 show 5 test runs with 10 mm sharp edge orifice for Case CDC10WTP52.

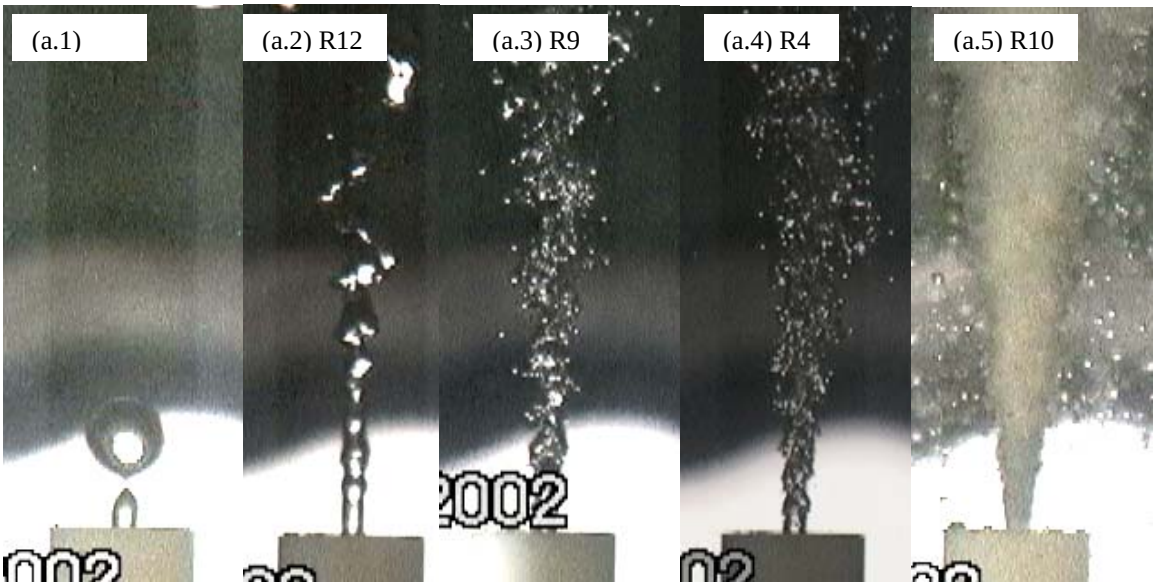

U_{jet} = <0.67 0.77 2.09 2.58 17.81 m/s

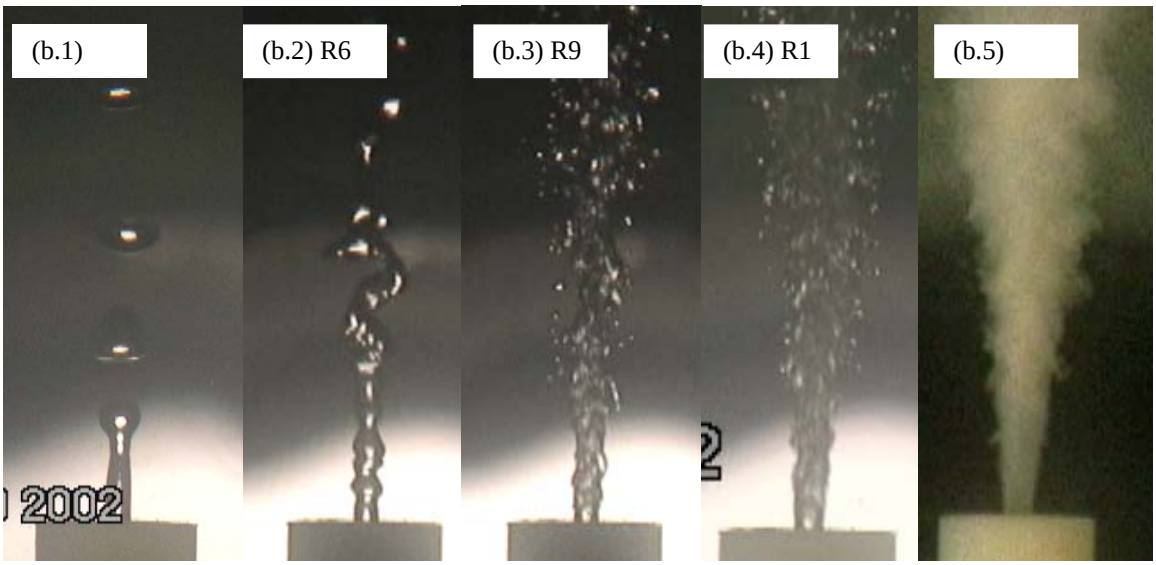

U_{jet}= <0.67 0.78 1.95 2.56 >3.89 m/s

Figure 3.8 Five breakup modes observed during liquid CO_2 injection tests from a 2 mm tube orifice. Frames a.1 to a.5 employ tap water for Case CDT02WTP52. Frames b.1 to b.5 employ natural seawater for Case CDT02WNP52. Flow rates of (a.1) and (b.1) are lower than the flow meter measurement range. The outside diameter of the tube orifice is 1.27 cm (0.5 inch).

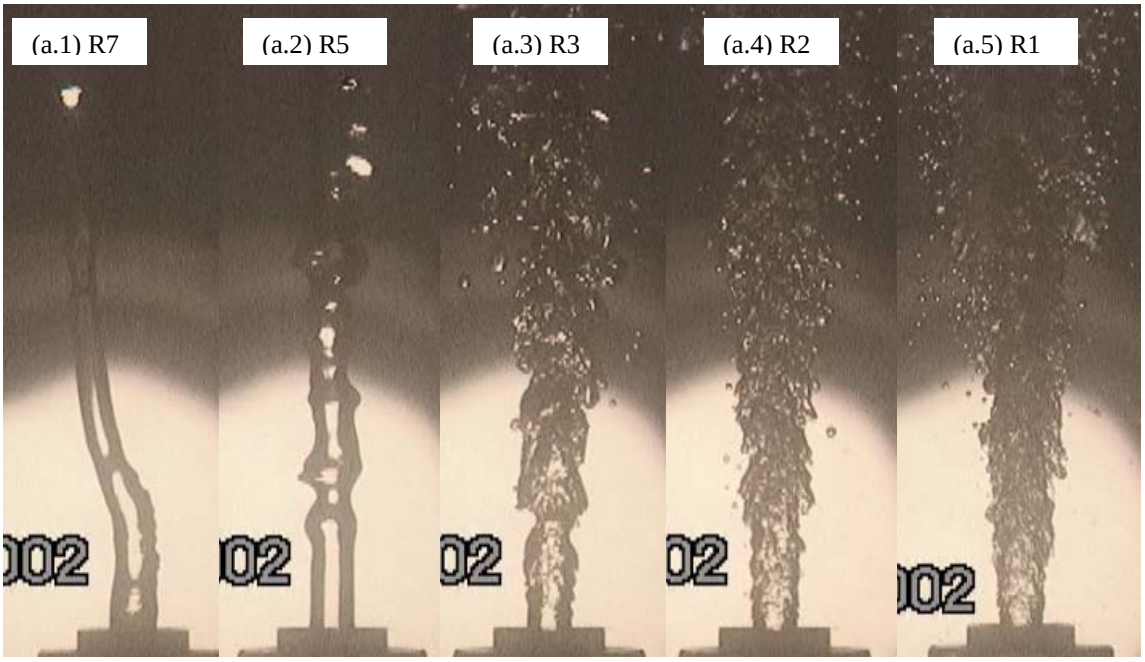

U_{jet}= 0.09 0.36 1.21 1.80 2.35 m/s

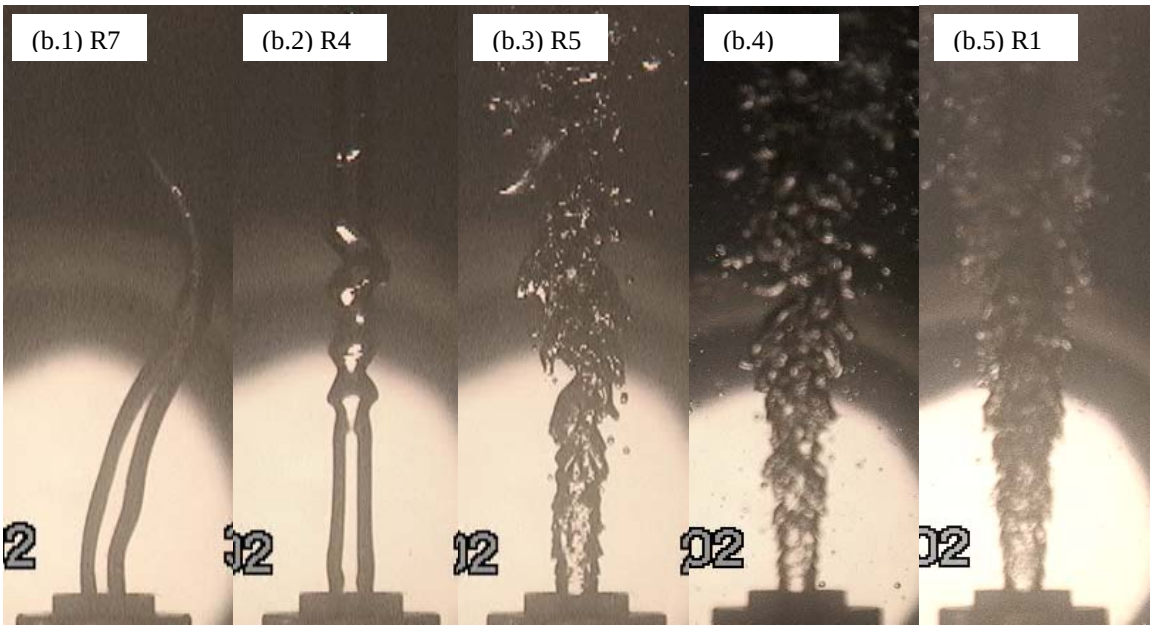

U_{jet}= 0.09 0.37 1.21 1.88 2.34 m/s

Figure 3.9 Five breakup modes observed during liquid CO_2 injection into tap water from 5 mm tube orifice at different pressures. Frames a.1 to a.5 correspond to Case CDT05WTP52 at 52 bar. Frames b.1 to b.5 correspond to Case CDT05WNP61 at 61 bar.

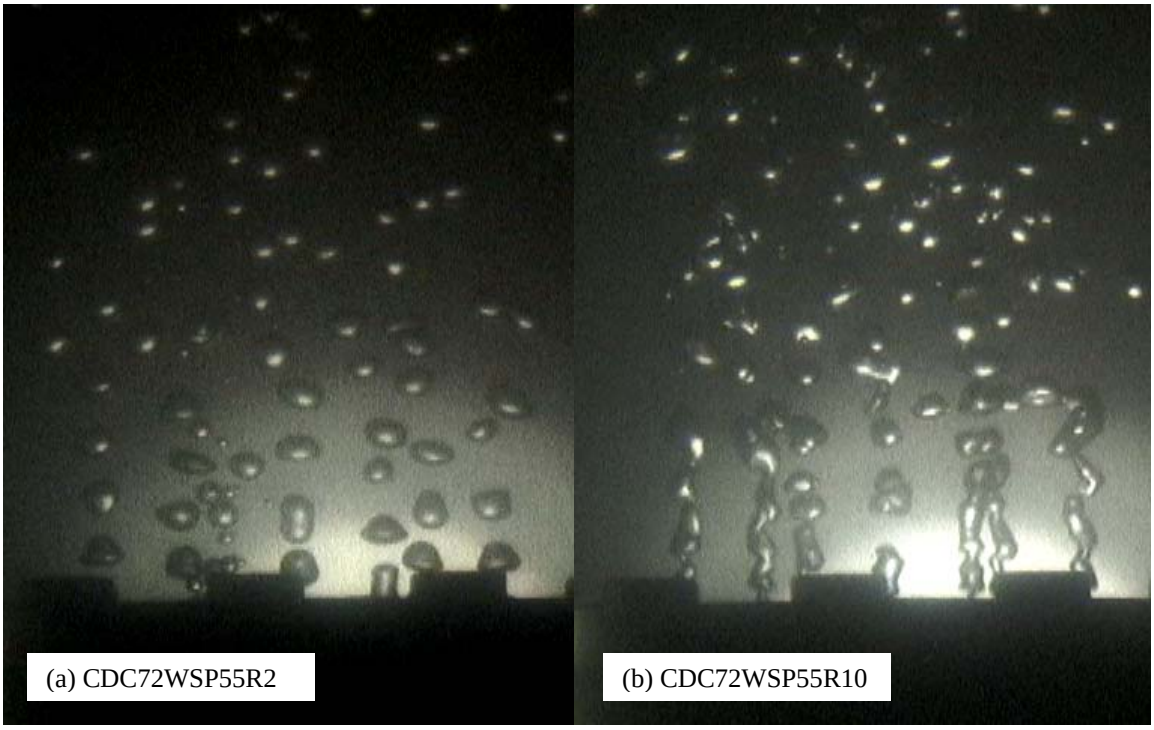

U_{jet} = 0.27 U_{jet} = 0.41

U_{jet} = 1.2 U_{jet} = 2.75

U_{jet} = 4.69 m/s

Figure 3.10 CO_2 injection into synthetic seawater from multi-orifice injector. Frames a, b, c, d and e show breakup modes 1, 2, 3, 4, and 5 respectively. The allen screw heads visible in silhouette in the frames are 9.5 mm (3/8 inch) in diameter.

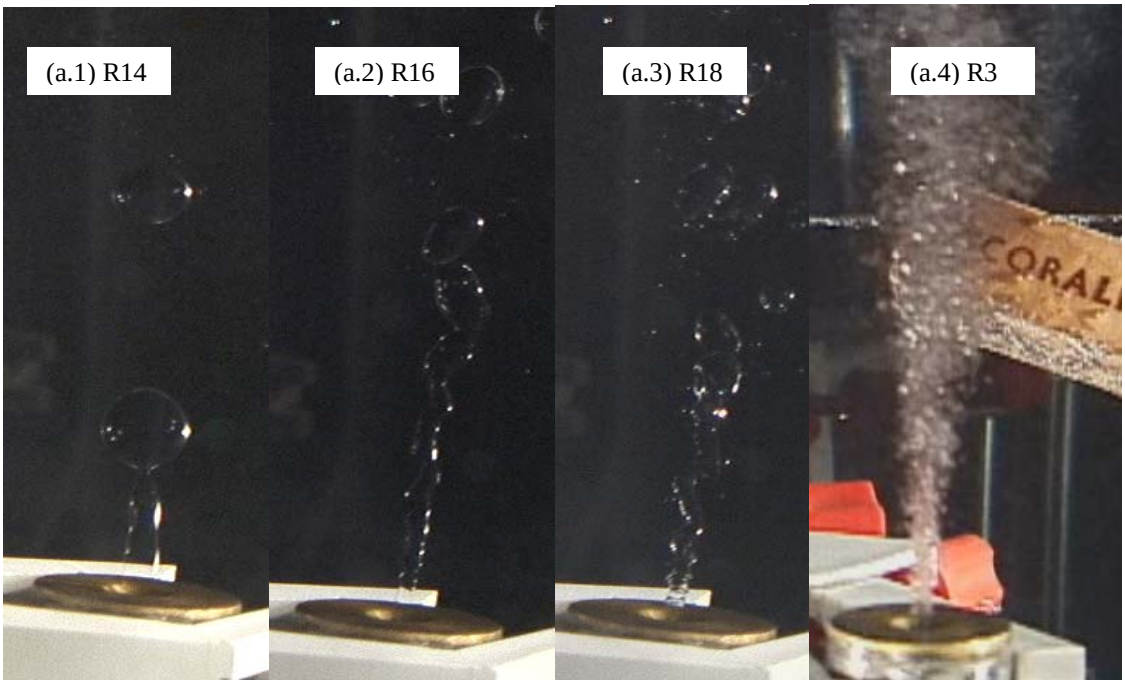

U_{jet}= 0.14 0.74 1.12 2.61 m/s

Figure 3.11 Breakup modes observed during silicone fluid injection into tap water from a 2 mm ASME sharp edge orifice. Case SFS02WTR.

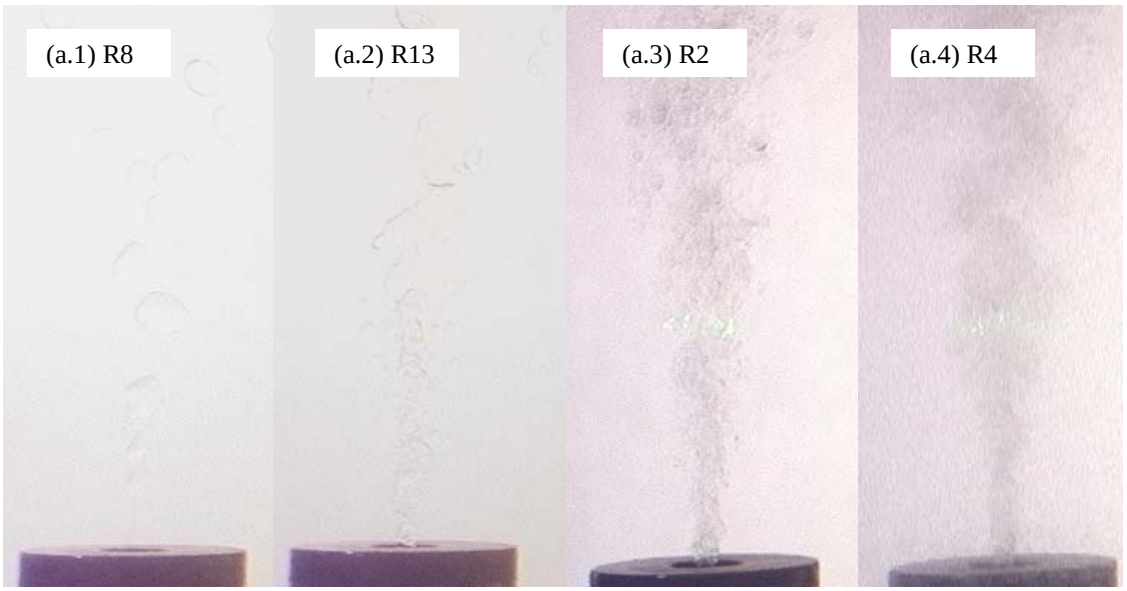

U_{jet}= 0.28 1.24 2.77 3.47 m/s

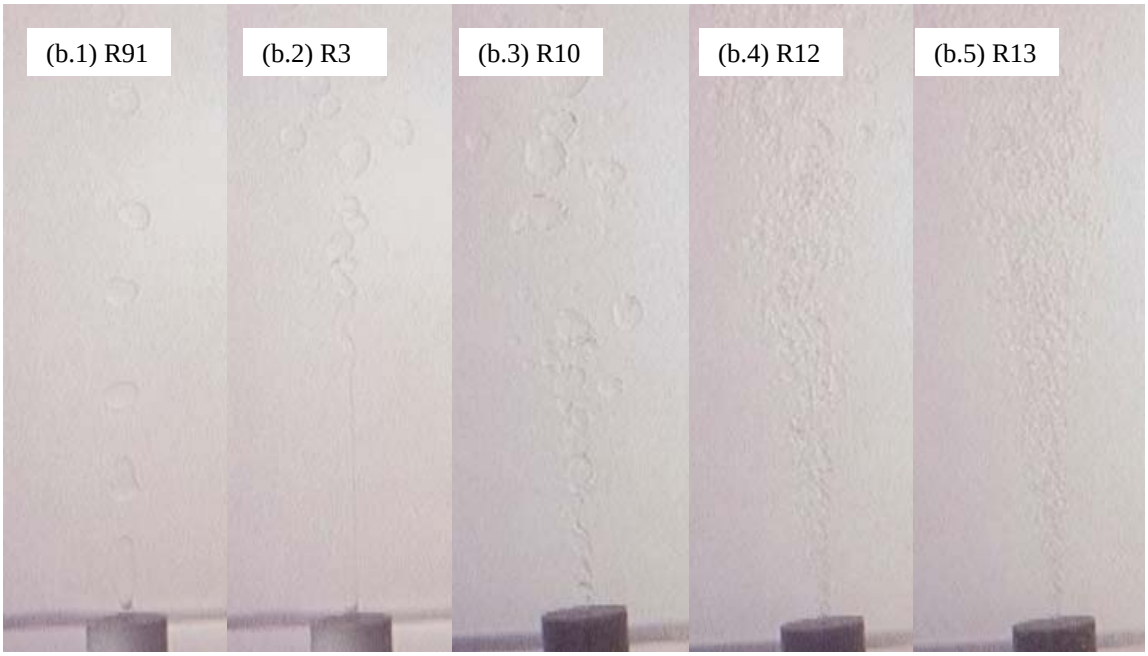

U_{jet}= <0.17 0.31 1.22 2.69 3.56 m/s

Figure 3.12 Low viscosity silicone fluid injection into tap water. Frames a.1 to a.4 show breakup modes 1, 2, 3 and 4 for Case LSS02WTR. Frames b.1 to b.5 show the 5 breakup modes for Case LST02WTR.

3.3.1.1 Instability Regime 1: Varicose Breakup

Varicose breakup has been studied extensively. At very low velocities, a symmetric surface wave forms and grows, eventually pinching off the jet and producing a train of droplets. The droplets are almost uniformly sized and their diameters exceed that of the jet.

In some situations, satellite droplets much smaller than the primary droplets, may pinch off between two primary droplets. Satellite droplet formation has been analyzed by Goedde and Yuen (1970), who calculated the pressure distribution in the liquid from experimentally derived wave profiles. They noted that the pressure gradient near the separation point increases as the surface contracts, and accelerates the detachment process. This results in a sharply pointed ligament whose internal pressure distribution increases to an extreme value at its point, and a droplet whose internal pressure is essentially constant. The ligament subsequently rolls up into a satellite droplet.

In our experiments, satellite droplets were observed only during injection of high viscosity Platform Gail crude oil into water from both 1 and 5 mm sharp edge orifices (Figures 3.13 and 3.14). The kinematic viscosity of Platform Gail crude oil is 211 centistrokes which was an order of magnitude higher than the next most viscous jet fluid. Viscosity apparently plays a critical role in the formation of satellite droplets. This supports the explanation why Rayleigh instability theory is unable to predict satellite droplets since viscous force is not considered. This deficiency is one reason why we chose to identify this instability regime as varicose breakup rather than Rayleigh instability. The principal characteristic of instability regime 1 is that the jet break-up instability is axisymmetric.

3.3.1.2 Instability Regime 2: Sinuous Wave Breakup

As jet velocity increases, the breakup length of the laminar jet increases. An asymmetric instability emerges and causes the jet to wave sinuously and generates non-uniform size droplets. This is called the first-wind induced breakup regime in liquid-gas systems. The inertial effects of the surrounding fluids can no longer be neglected.

Examples of sinuous wave breakup for various jet fluids and injection nozzles are provided in Figures 3.15 through 3.19. The data indicate that the tube nozzle (Figures 3.18 and 3.19) produced jets that were remarkably more stable than jets from a sharp edge orifice. A well-developed boundary layer that forms in the tube orifice results in a velocity profile at the orifice exit that is different from the jet exit velocity profile for a sharp edge orifice. This suggests a coupling between the initial velocity profile of the jet and the instability mechanism.

3.3.1.3 Instability Regime 3: Filament Core Breakup

At higher velocities, two instabilities mechanisms appear to operate in parallel: the surface of the jet becomes unstable to short wavelength disturbances and disintegrates close to the orifice into fine droplets, while the core of the jet persists as a continuum fluid filament that breaks up further downstream into large droplets (e.g., Figure 3.2 a.3). These two distinct instability mechanisms result in a polydispersion of droplets, initially comprising two different size groups.

3.3.1.4 Instability Regime 4: Wave atomization

Raising the velocities moves the breakup location of the jet core filament closer to the orifice and also increases the fraction of fine droplets (e.g., frames a.4 and b.4 in Figures 3.2 to 3.9). The two edges of the jet wave sinuously. In our experiments, the dense cloud of fine droplets on the perimeter of the jet obscures its interior and it could not be determined clearly whether breakup of the core filament persists and continues to produce relatively large droplets.

3.3.1.5 Instability Regime 5: Full Atomization

Finally, at high flow rates, atomization is attained. The jet breaks up into fine droplets very close to the injection orifice. As will be shown in Chapter 5, droplet sizes in this breakup regime are relative uniform compared with those in instability regimes 3 and 4. The large droplet peaks of the multimodal distributions characteristic of regimes 3 and 4 disappear as atomization is achieved.

3.3.2 Injection Test Matrix

Tables 3.1, 3.2 and 3.3 summarize the injection tests: 97 runs with liquid CO_2; 154 runs with 4 crude oils; and 43 runs with two silicone fluids. Each run is identified by a unique alphanumeric name assigned according to following convention:

1. First two letters indicate the jet fluid. CD stands for liquid Carbon Dioxide; GE for Genesis crude oil; MA for Mars TLP crude oil; NS for Neptune SPAR crude oil; PG for Platform Gail crude oil; SF for the Silicone Fluid with 20 cs viscosity and LS for the low viscosity silicone fluid.

2. The next letter and two digits describe the orifice. C stands for sharp edge orifice for liquid CO_2 tests; S for sharp edge orifice for tests of crude oils and silicone fluids; T for tube orifice. The digits provide the diameter of the orifice in mm; either 01, 02, 05 or 10. Multiple orifice nozzles are indicated by C72. C stands for sharp edge orifice; 7 for the number of the orifices and 2 for the diameter of the each orifice.

3. The following two letters indicate the ambient fluid: WT = tap water; WN = natural surface seawater; WS = synthetic seawater.

4. For liquid CO_2 injection tests, the next letter "P" means pressure. The two digits following "P" is the pressure of the run in bar.

   For the crude oil and silicone fluid injection tests, the letters "R" or "C" are used instead of "P". "R" indicates that the water is at room temperature (around 18°C) and "C" indicates that the water was chilled.

5. Finally, "R"+ digits indicates the run number for a general set of conditions. Typically, flow rate varies for different run numbers.

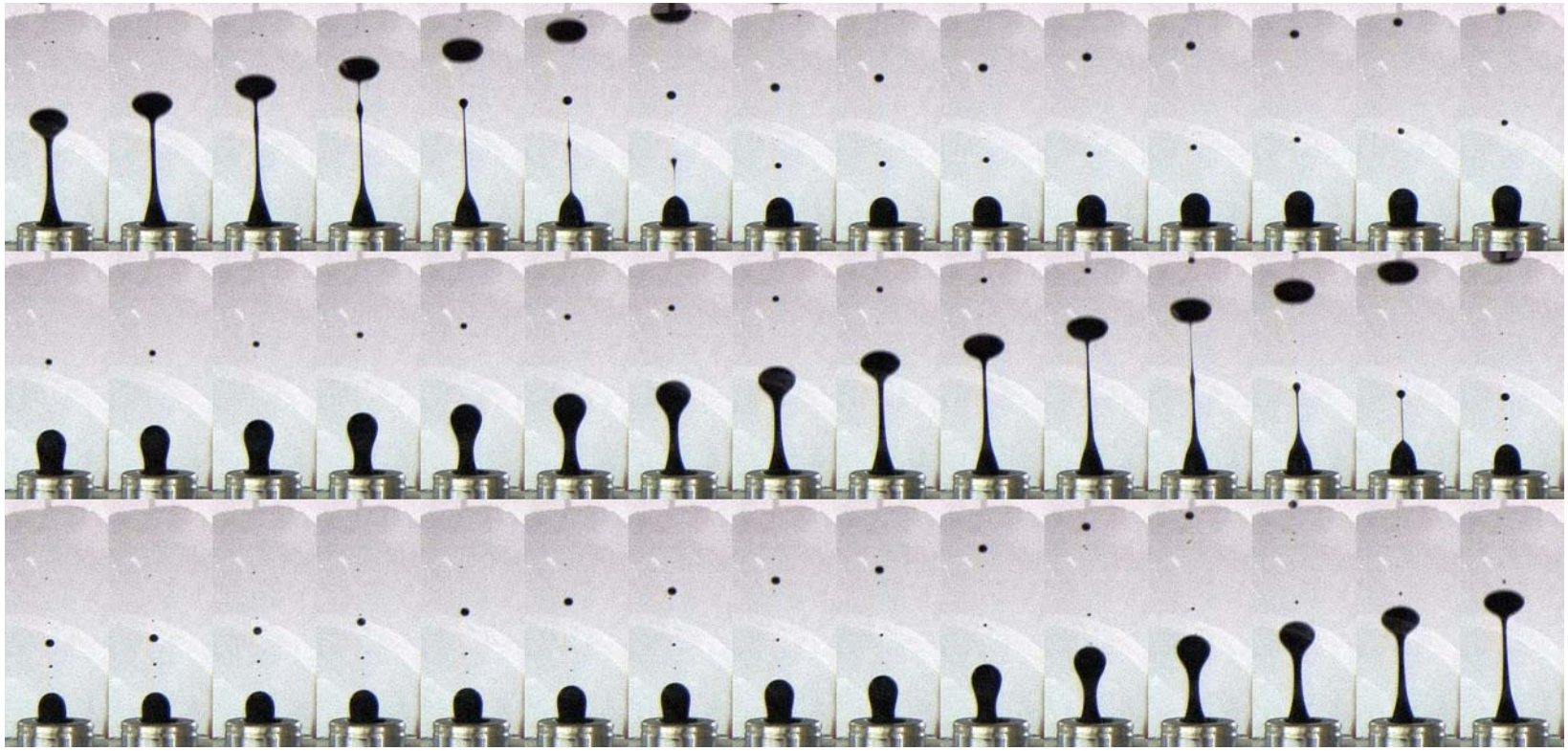

Figure 3.13 Satellite droplets observed when high viscosity Platform Gail crude oil is injected into tap water from a 1 mm sharp edge orifice at varicose breakup mode, run PGS01WTRR5. Time interval between any two adjacent frames is 1/15 second.

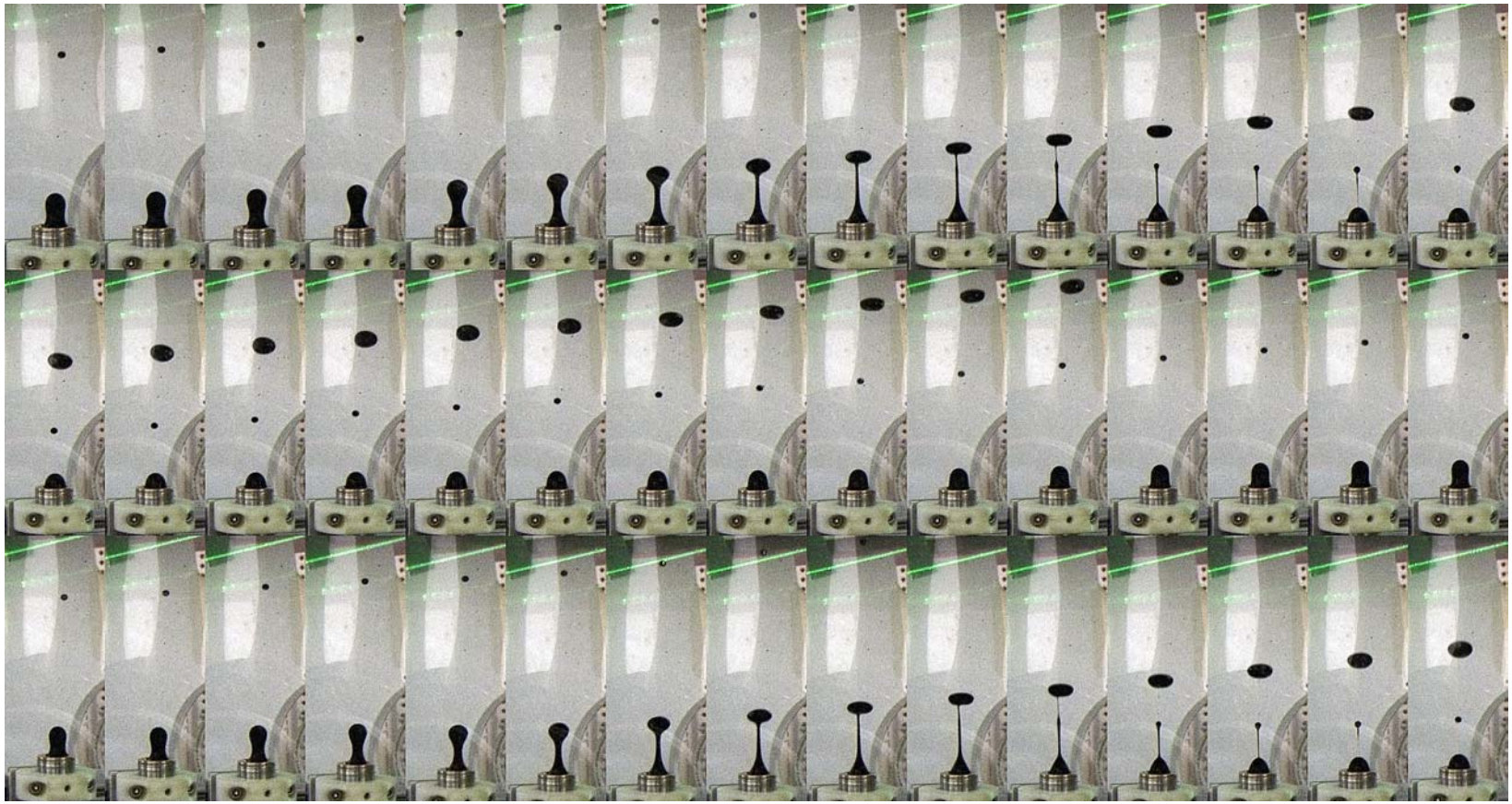

Figure 3.14 Satellite droplets observed when high viscosity Platform Gail crude oil is injected into tap water from 5 mm sharp edge orifice, run PGS05WTRR2. Time interval between any two adjacent frames is 1/15 second. U_{jet} = 0.04 m/s.

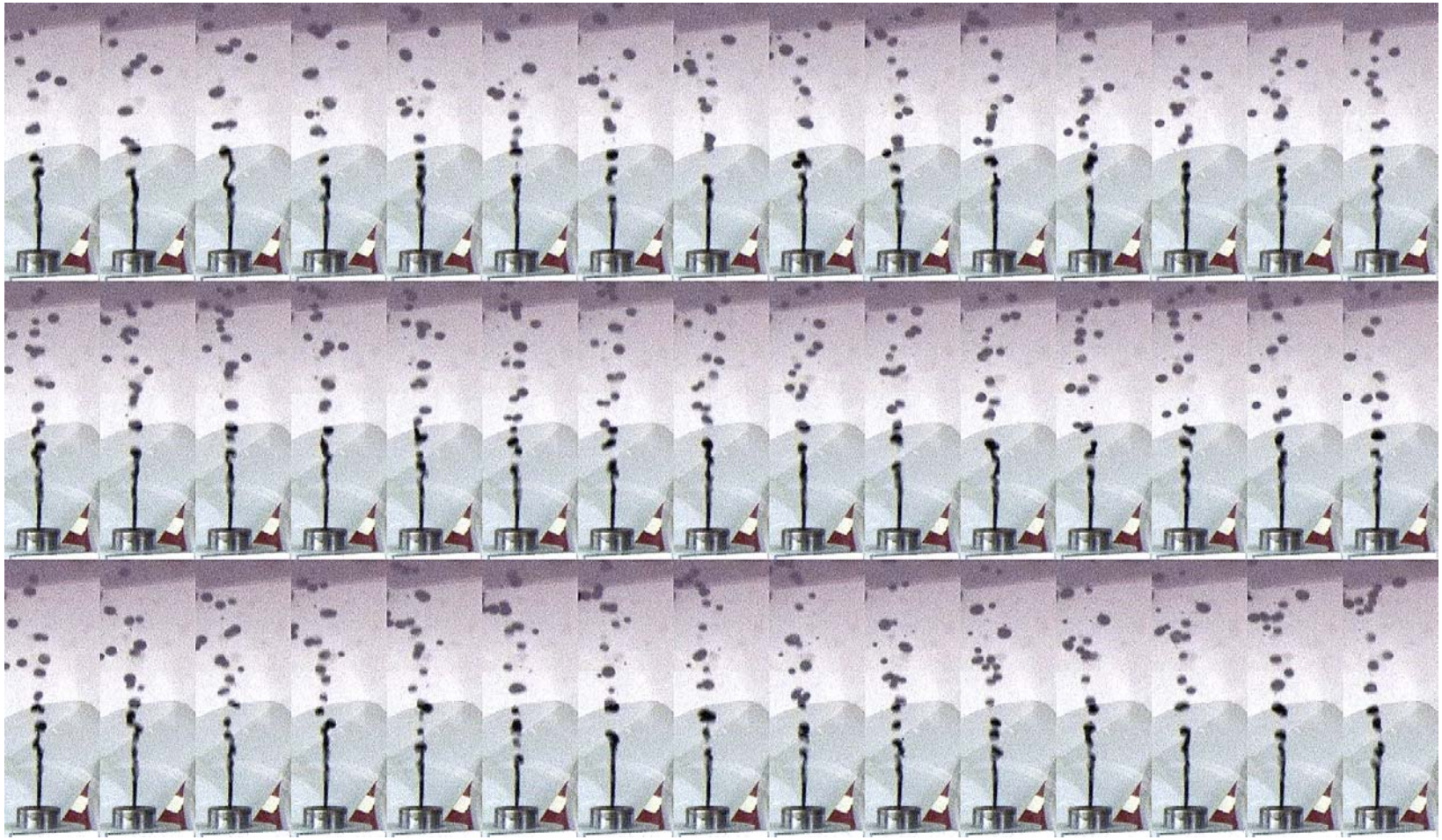

Figure 3.15 Sinuous wave breakup; instability regime 2. Frames are from test run GES02WTRR13. Genesis crude oil injected into tap water from a 2 mm sharp edge orifice. Time interval between any two adjacent frames is 1/15 second.

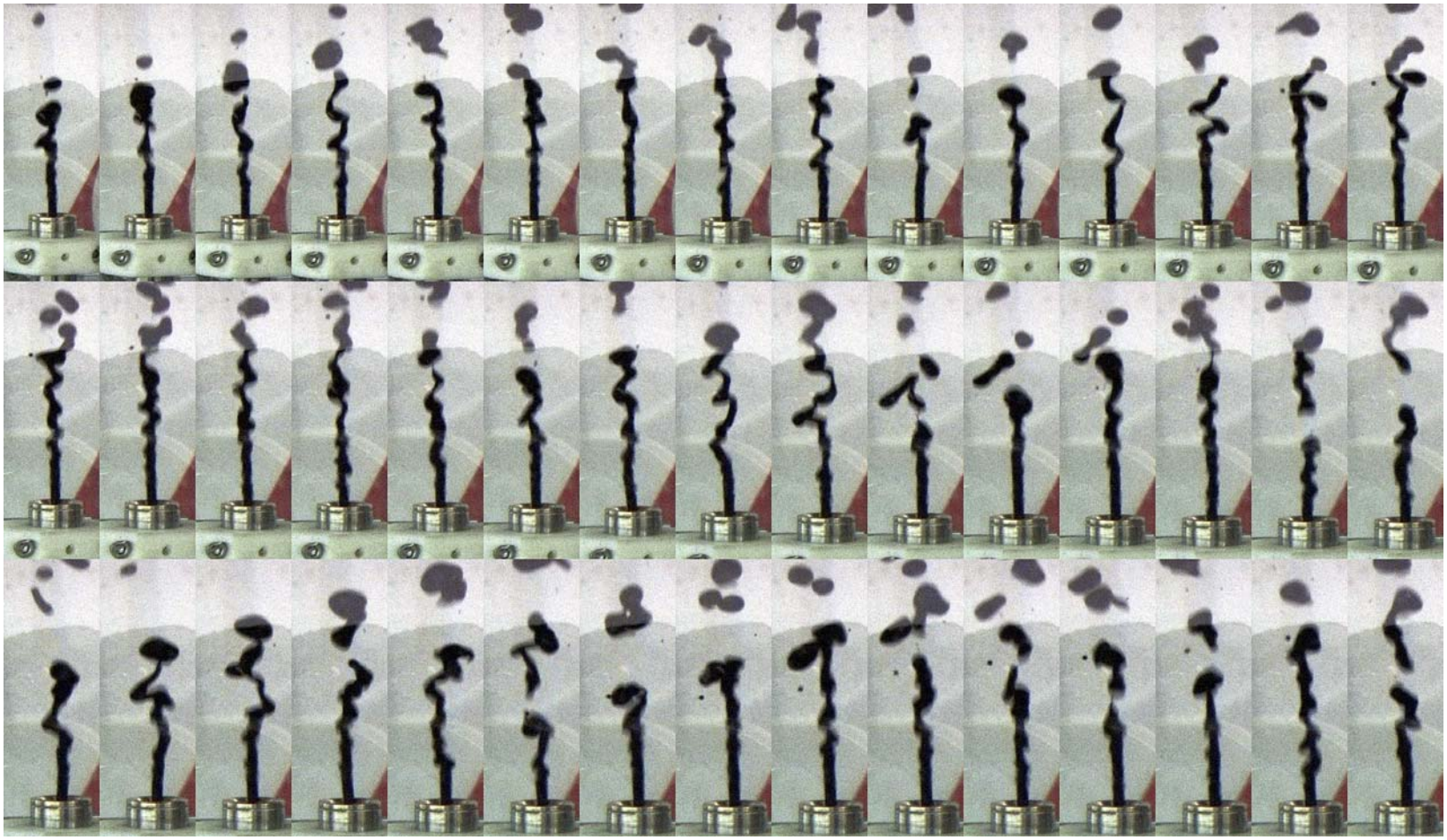

Figure 3.16 Sinuous wave breakup; instability regime 2. Frames are from test run GES05WTRR9. Genesis crude oil injected into tap water from 5 mm sharp edge orifice. Time interval between any two adjacent frames is 1/15 second.

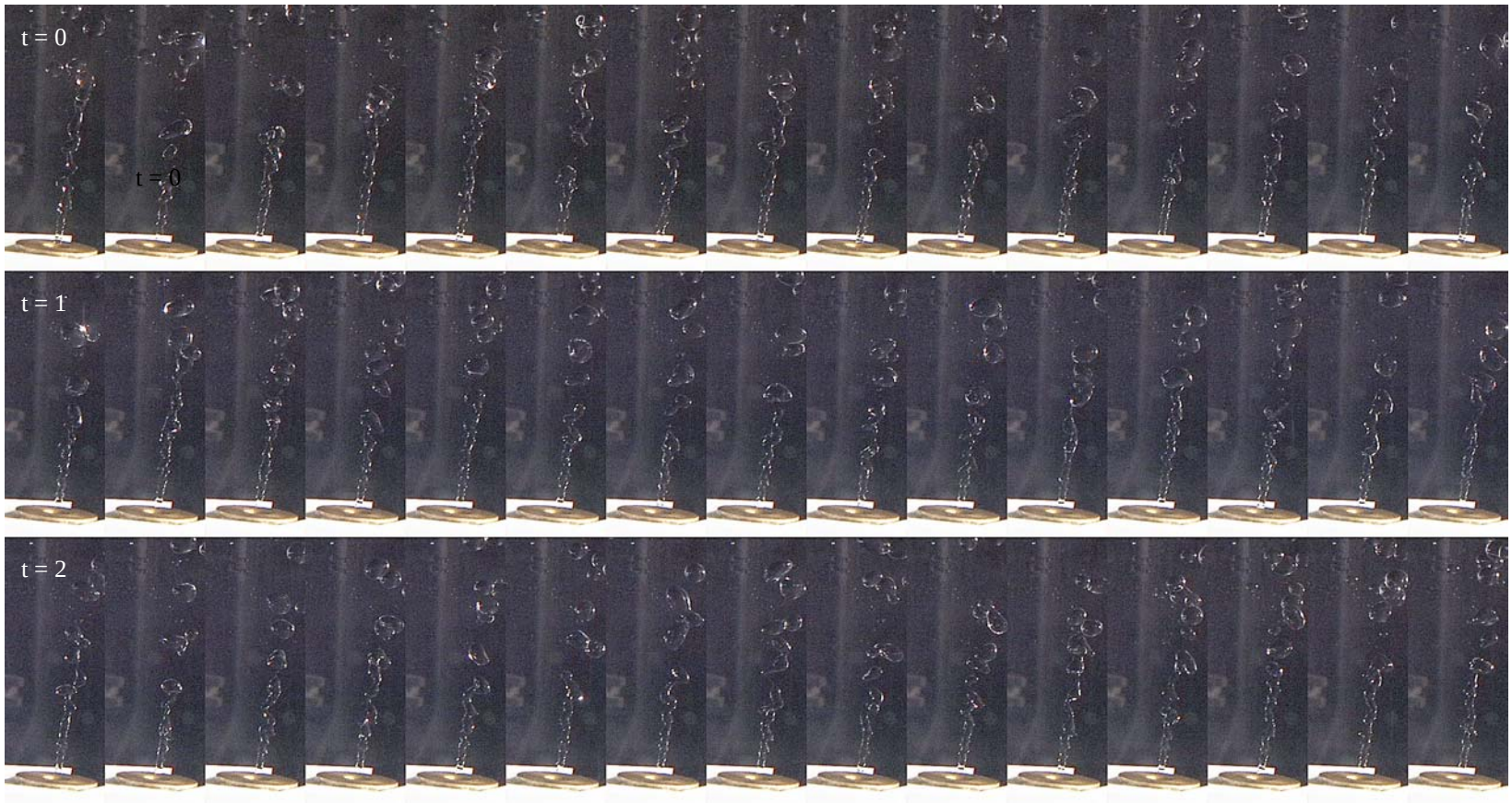

Figure 3.17 Sinuous wave breakup; instability regime 2. Frames are from test run SFS02WTRR17. Silicone fluid injected into tap water from 2 mm sharp edge orifice. Time interval between any two adjacent frames is 1/15 second.

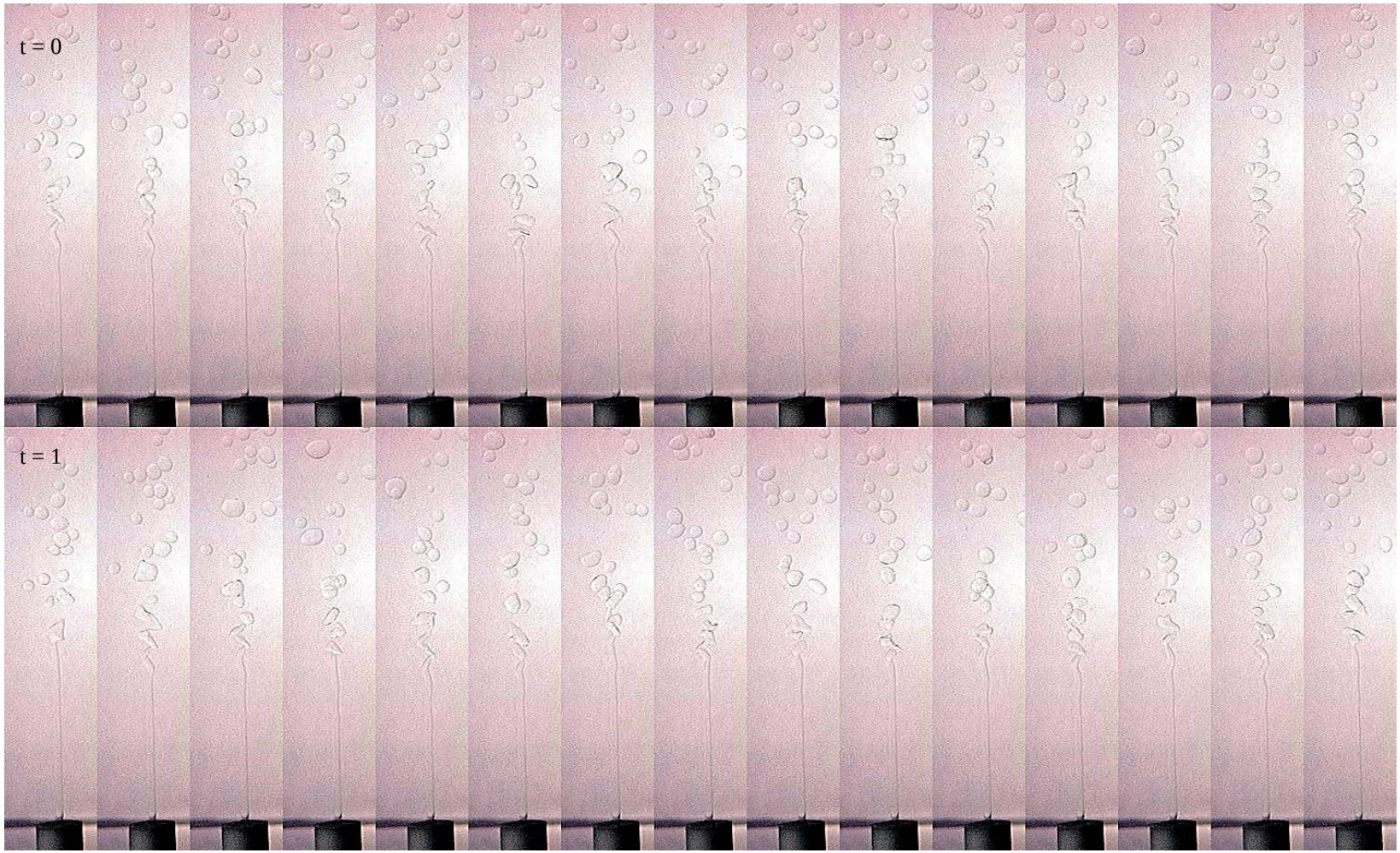

Figure 3.18 Sinuous wave breakup; instability regime 2. Test run LST02WTRR3. Low viscosity silicone fluid injected into tap water from a 2 mm i.d. tube orifice. Time interval between any two adjacent frames is 1/15 second.

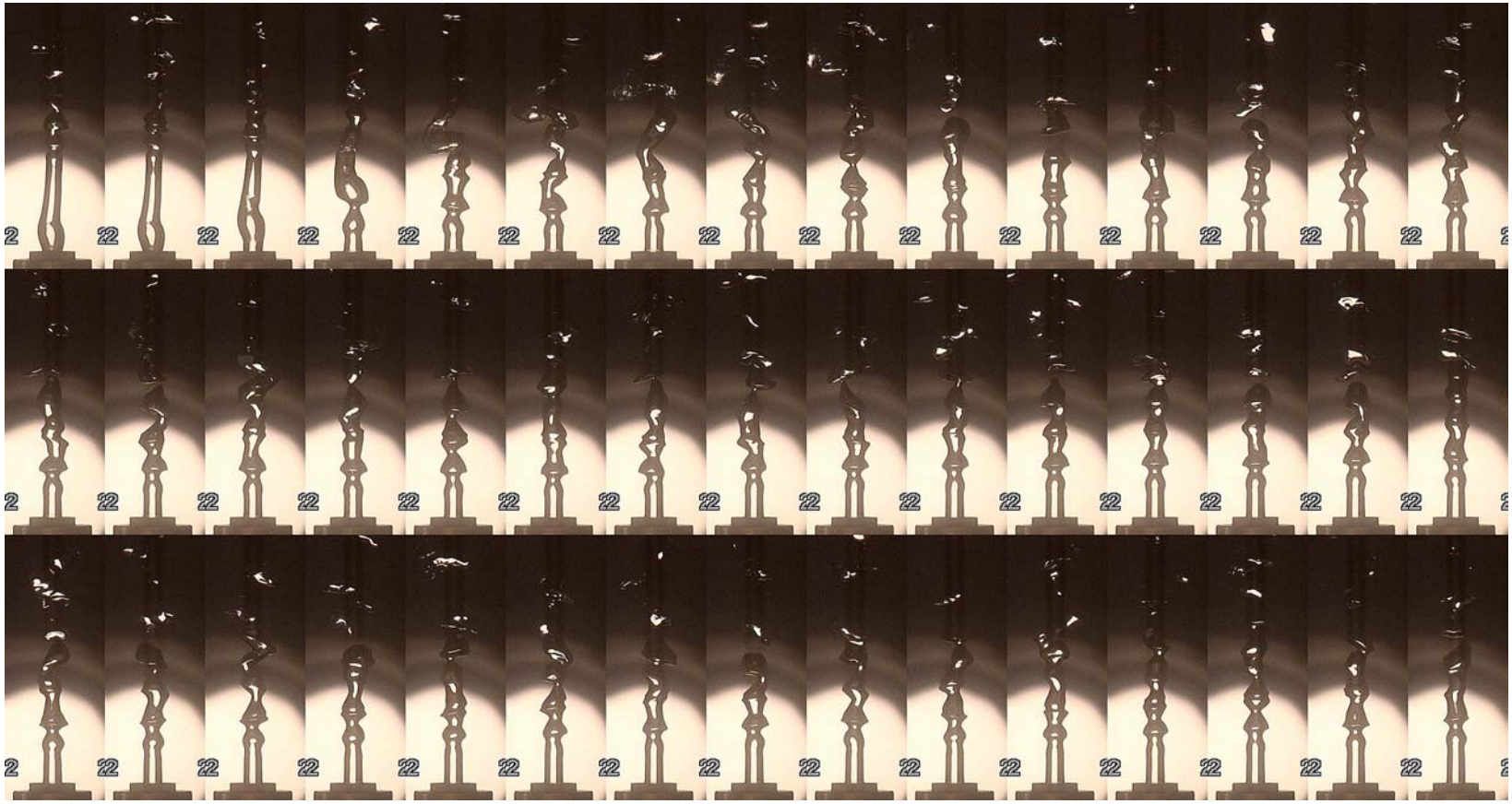

Figure 3.19 Sinuous wave breakup; instability regime 2. Test run CDT05WTP61R4. Liquid CO_2 injected into tap water from 5 mm i.d. tube orifice. Time interval between any two adjacent frames is 1/15 second.

Table 3.1 Liquid CO_2 Injection Test Matrix

CO_2 Test No.	Test Name	Orifice	Water Type	Press. *P* [bar]	Run No.	Run Time [min]	Water Temp. [°C]	CO_2 Temp. [°C]	CO_2 Mass Flowrate [kg/h]	Jet Vel. [m/s]	CO_2 Density [kg/m^3]	CO_2 Kine. Visc. [Pa s]	*IR*	*We*	*Re*	*Oh*
1	CDC02WTP52R1	C02	WT	52	1	2.92	6.88	-3.59	7.35	0.67	965.4	1.12E-04	2	3.24E+01	1.16E+04	4.89E-04
2	CDC02WTP52R2	C02	WT	52	2	2.42	6.9	0.63	8.17	0.77	940.5	1.03E-04	2	4.11E+01	1.40E+04	4.57E-04
3	CDC02WTP52R3	C02	WT	52	3	2.43	7.09	7.05	11.44	1.13	897.1	9.04E-05	2	8.45E+01	2.24E+04	4.11E-04
4	CDC02WTP52R4	C02	WT	52	4	5.73	7.31	10.74	16.62	1.69	867.5	8.36E-05	3	1.84E+02	3.51E+04	3.86E-04
5	CDC02WTP52R5	C02	WT	52	5	7.47	8.23	3.33	15.8	1.51	923.2	9.75E-05	3	1.57E+02	2.87E+04	4.37E-04
6	CDC02WTP52R6	C02	WT	52	6	6.32	8.58	9.45	19.89	2	878.4	8.59E-05	3	2.61E+02	4.09E+04	3.95E-04
7	CDC02WTP52R7	C02	WT	52	7	6.53	8.84	9.61	25.61	2.58	877.0	8.57E-05	4	4.33E+02	5.29E+04	3.94E-04
8	CDC02WTP52R8	C02	WT	52	8	7.65	9.14	9.39	31.87	3.21	878.8	8.61E-05	4	6.69E+02	6.55E+04	3.95E-04
9	CDC02WTP52R9	C02	WT	52	9	11.7	9.49	8.97	40.04	4.01	882.2	8.68E-05	5	1.05E+03	8.16E+04	3.98E-04
10	CDC02WTP52R10	C02	WT	52	10	8.42	10.12	7.82	15.8	1.57	891.3	8.89E-05	3	1.62E+02	3.14E+04	4.05E-04
11	CDC05WTP52R1	C05	WT	52	1	0.7	6.04	-5.27	2.72	0.04	974.7	1.15E-04	1	2.82E-01	1.67E+03	3.18E-04
12	CDC05WTP52R2	C05	WT	52	2	0.73	5.95	0	14.98	0.22	944.3	1.04E-04	1	8.81E-00	1.02E+04	2.92E-04
13	CDC05WTP52R3	C05	WT	52	3	1.25	6.07	-0.26	5.45	0.08	945.9	1.05E-04	1	1.16E-00	3.68E+03	2.93E-04
14	CDC05WTP52R4	C05	WT	52	4	1.15	6.4	1.42	6.81	0.1	935.5	1.01E-04	1	1.84E-00	4.75E+03	2.85E-04
15	CDC05WTP52R5	C05	WT	52	5	1	7.36	8.95	7.9	0.13	882.4	8.69E-05	1	2.62E-00	6.43E+03	2.52E-04
16	CDC05WTP52R6	C05	WT	52	6	1.02	7.55	9.39	11.17	0.18	878.8	8.61E-05	1	5.26E-00	9.18E+03	2.50E-04
17	CDC05WTP52R7	C05	WT	52	7	0.72	7.64	9.76	14.16	0.23	875.8	8.54E-05	1	8.49E-00	1.17E+04	2.48E-04
18	CDC05WTP52R8	C05	WT	52	8	0.75	7.74	10.18	17.16	0.28	872.3	8.46E-05	2	1.25E+01	1.43E+04	2.47E-04
19	CDC05WTP52R9	C05	WT	52	9	0.67	7.81	10.34	20.16	0.33	870.9	8.43E-05	2	1.73E+01	1.69E+04	2.46E-04
20	CDC05WTP52R10	C05	WT	52	10	0.65	7.91	9.96	24.24	0.39	874.1	8.50E-05	2	2.49E+01	2.02E+04	2.48E-04
21	CDC05WTP52R11	C05	WT	52	11	0.67	7.96	9.64	26.97	0.44	876.8	8.56E-05	2	3.07E+01	2.23E+04	2.49E-04
22	CDC05WTP52R12	C05	WT	52	12	0.57	8.01	9.19	34.05	0.55	880.5	8.64E-05	2	4.88E+01	2.79E+04	2.51E-04
23	CDC05WTP52R13	C05	WT	52	13	0.6	8.11	8.68	39.5	0.63	884.5	8.73E-05	3	6.54E+01	3.20E+04	2.53E-04
24	CDC05WTP52R14	C05	WT	52	14	0.58	8.12	7.48	47.13	0.75	893.8	8.96E-05	3	9.21E+01	3.72E+04	2.58E-04
25	CDC05WTP52R15	C05	WT	52	15	0.63	8.2	6.12	55.84	0.87	903.9	9.21E-05	3	1.28E+02	4.29E+04	2.64E-04

Table 3.1 (continued)

CO_2 Test No.	Test Name	Orifice	Water Type	Press. *P* [bar]	Run No.	Run Time [min]	Water Temp. [°C]	CO_2 Temp. [°C]	CO_2 Mass Flowrate [kg/h]	Jet Vel. [m/s]	CO_2 Density [kg/m^3]	CO_2 Kine. Visc. [Pa s]	*IR*	*We*	*Re*	*Oh*
26	CDC05WTP52R16	C05	WT	52	16	0.57	8.23	4.86	68.64	1.06	912.8	9.45E-05	3	1.91E+02	5.14E+04	2.69E-04
27	CDC05WTP52R17	C05	WT	52	17	0.52	8.38	3.25	83.9	1.28	923.7	9.77E-05	4	2.82E+02	6.08E+04	2.77E-04
28	CDC05WTP52R18	C05	WT	52	18	0.43	8.51	1.02	137.56	2.07	938.0	1.02E-04	5	7.48E+02	9.53E+04	2.87E-04
29	CDC05WTP52R19	C05	WT	52	19	0.48	8.6	-1.27	166.71	2.48	952.0	1.07E-04	5	1.08E+03	1.10E+05	2.98E-04
30	CDC05WTP52R20	C05	WT	52	20	10.2	9	4.84	38.14	0.59	913.0	9.46E-05	3	5.90E+01	2.85E+04	2.69E-04
31	CDC05WTP52R21	C05	WT	52	21	13.45	9.8	3.63	47.4	0.73	921.2	9.69E-05	3	9.04E+01	3.46E+04	2.75E-04
32	CDC05WTP52R22	C05	WT	52	22	8.65	9.88	2.23	56.39	0.86	930.4	9.97E-05	3	1.27E+02	4.00E+04	2.81E-04
33	CDC05WTP52R23	C05	WT	52	23	5.63	9.97	1.05	68.1	1.03	937.9	1.02E-04	4	1.83E+02	4.72E+04	2.87E-04
34	CDC05WTP52R24	C05	WT	52	24	4.67	10.05	0.59	82.81	1.25	940.7	1.03E-04	4	2.70E+02	5.69E+04	2.89E-04
35	CDC05WTP52R25	C05	WT	52	25	4.5	10.24	-2.45	127.21	1.88	958.9	1.09E-04	4	6.26E+02	8.23E+04	3.04E-04
36	CDC05WTP52R26	C05	WT	52	26	4.35	10.18	-4.63	165.07	2.4	971.2	1.14E-04	5	1.04E+03	1.02E+05	3.15E-04
37	CDC10WTP52R1	C10	WT	52	1	10.47	11.2	-2.82	112.5	0.41	961.0	1.10E-04	3	6.10E+01	3.62E+04	2.16E-04
38	CDC10WTP52R2	C10	WT	52	2	1.05	11.8	-4.34	179.78	0.66	969.6	1.13E-04	3	1.54E+02	5.61E+04	2.21E-04
39	CDC10WTP52R3	C10	WT	52	3	6.92	11.9	-7.18	245.7	0.88	985.0	1.20E-04	4	2.84E+02	7.27E+04	2.32E-04
40	CDC10WTP52R4	C10	WT	52	4	2.72	12.2	-9.01	330.69	1.18	994.6	1.24E-04	5	5.09E+02	9.46E+04	2.39E-04
41	CDC10WTP52R5	C10	WT	52	5	5.13	12.5	-9.75	409.69	1.45	998.4	1.25E-04	5	7.79E+02	1.16E+05	2.41E-04
42	CDC10WTP52R6	C10	WT	52	6	1.05	12.8	-2.39	34.87	0.13	958.5	1.09E-04	1	5.88E-00	1.13E+04	2.15E-04
43	CDC10WTP52R7	C10	WT	52	7	2.1	12.9	-1.63	60.75	0.23	954.1	1.08E-04	2	1.79E+01	2.00E+04	2.12E-04
44	CDC10WTP52R8	C10	WT	52	8	1.88	13	0	73.55	0.28	944.3	1.04E-04	2	2.65E+01	2.50E+04	2.06E-04
45	CDC10WTP52R9	C10	WT	52	9	1.93	13.1	-4	83.9	0.31	967.7	1.13E-04	2	3.37E+01	2.64E+04	2.20E-04
46	CDC10WTP52R10	C10	WT	52	10	1.08	13.2	-2.7	26.42	0.1	960.3	1.10E-04	1	3.37E-00	8.51E+03	2.16E-04
47	CDC10WTP52R11	C10	WT	52	11	1.15	13.2	-2	17.71	0.07	956.3	1.08E-04	1	1.52E-00	5.78E+03	2.13E-04
48	CDC10WTP52R12	C10	WT	52	12	2.98	13.3	-0.8	10.08	0.04	949.2	1.06E-04	1	4.96E-01	3.37E+03	2.09E-04
49	CDC10WTP52R13	C10	WT	52	13	1.28	13.5	2.7	5.99	0.02	927.3	9.88E-05	1	1.79E-01	2.15E+03	1.97E-04
50	CDT02WTP52R1	T02	WT	52	1	9.55	7.44	13.86	16.07	1.7	838.0	7.82E-05	3	1.79E+02	3.63E+04	3.68E-04
51	CDT02WTP52R2	T02	WT	52	2	10.23	7.91	12.85	17.16	1.79	848.1	7.99E-05	3	2.01E+02	3.80E+04	3.73E-04

Table 3.1 (continued)

CO_2 Test No.	Test Name	Orifice	Water Type	Press. *P* [bar]	Run No.	Run Time [min]	Water Temp. [°C]	CO_2 Temp. [°C]	CO_2 Mass Flowrate [kg/h]	Jet Vel. [m/s]	CO_2 Density [kg/m^3]	CO_2 Kine. Visc. [Pa s]	*IR*	*We*	*Re*	*Oh*
52	CDT02WTP52R3	T02	WT	52	3	8.82	8.32	12.2	20.16	2.09	854.3	8.11E-05	3	2.75E+02	4.40E+04	3.77E-04
53	CDT02WTP52R4	T02	WT	52	4	8.38	8.67	11.6	25.06	2.58	859.8	8.21E-05	4	4.23E+02	5.40E+04	3.81E-04
54	CDT02WTP52R5	T02	WT	52	5	7.98	8.99	10.3	31.33	3.18	871.3	8.44E-05	4	6.52E+02	6.56E+04	3.89E-04
55	CDT02WTP52R6	T02	WT	52	6	7.95	9.33	9.49	38.95	3.92	878.0	8.59E-05	5	1.00E+03	8.02E+04	3.94E-04
56	CDT02WTP52R7	T02	WT	52	7	5.63	9.61	6.59	56.39	5.54	900.5	9.12E-05	5	2.04E+03	1.09E+05	4.14E-04
57	CDT02WTP52R8	T02	WT	52	8	8.27	9.94	2.95	82.54	7.88	925.7	9.83E-05	5	4.26E+03	1.49E+05	4.39E-04
58	CDT02WTP52R9	T02	WT	52	9	4.98	10.26	1.07	136.74	12.89	937.7	1.02E-04	5	1.15E+04	2.37E+05	4.53E-04
59	CDT02WTP52R10	T02	WT	52	10	3.95	10.48	-3.11	193.95	17.81	962.7	1.11E-04	5	2.26E+04	3.10E+05	4.85E-04
60	CDT02WTP52R11	T02	WT	52	11	3	10.59	-2.55	11.17	1.03	959.5	1.09E-04	2	7.53E+01	1.80E+04	4.81E-04
61	CDT02WTP52R12	T02	WT	52	12	2.78	10.64	0.42	8.17	0.77	941.8	1.03E-04	2	4.11E+01	1.40E+04	4.58E-04
62	CDT02WTP52R13	T02	WT	52	13	1.95	10.7	2.8	7.08	0.68	926.7	9.86E-05	2	3.13E+01	1.27E+04	4.41E-04
63	CDT02WTP52R14	T02	WT	52	14	1.77	10.73	4.39	5.45	0.53	916.0	9.54E-05	2	1.88E+01	1.01E+04	4.29E-04
64	CDT02WNP52R1	T02	WN	52	1	14.12	11.89	5	26.42	2.56	911.8	9.43E-05	4	4.43E+02	4.96E+04	4.25E-04
65	CDT02WNP52R2	T02	WN	52	2	17.25	12.44	4.31	40.32	3.89	916.6	9.56E-05	5	1.03E+03	7.46E+04	4.30E-04
66	CDT02WNP52R4	T02	WN	52	4	0.1	13.43	0.83	5.45	0.51	939.2	1.03E-04	2	1.83E+01	9.40E+03	4.55E-04
67	CDT02WNP52R5	T02	WN	52	5	1.58	13.46	1.44	7.35	0.7	935.4	1.01E-04	2	3.35E+01	1.28E+04	4.51E-04
68	CDT02WNP52R6	T02	WN	52	6	0.18	13.47	2.81	8.17	0.78	926.6	9.85E-05	2	4.17E+01	1.47E+04	4.41E-04
69	CDT02WNP52R7	T02	WN	52	7	0.68	13.51	3.12	11.44	1.09	924.6	9.79E-05	3	8.20E+01	2.07E+04	4.38E-04
70	CDT02WNP52R8	T02	WN	52	8	9.22	13.54	3.92	15.53	1.49	919.2	9.64E-05	3	1.52E+02	2.85E+04	4.32E-04
71	CDT02WNP52R9	T02	WN	52	9	10.83	13.6	6.67	19.89	1.95	899.9	9.11E-05	3	2.54E+02	3.86E+04	4.13E-04
72	CDT05WTP61R1	T05	WT	61	1	8.58	7.98	-0.39	84.72	1.26	954.2	1.05E-04	3	2.79E+02	5.71E+04	2.93E-04
73	CDT05WTP61R2	T05	WT	61	2	7.62	8.36	-3.25	160.44	2.34	970.1	1.11E-04	5	9.83E+02	1.02E+05	3.07E-04
74	CDT05WTP61R3	T05	WT	61	3	2.5	8.78	0.09	46.85	0.7	951.4	1.04E-04	3	8.55E+01	3.19E+04	2.90E-04
75	CDT05WTP61R4	T05	WT	61	4	3.27	8.96	1.31	24.79	0.37	944.2	1.02E-04	2	2.41E+01	1.73E+04	2.84E-04
76	CDT05WTP61R5	T05	WT	61	5	1.83	9.1	-1.8	82.54	1.21	962.1	1.08E-04	3	2.62E+02	5.41E+04	2.99E-04
77	CDT05WTP61R6	T05	WT	61	6	2.63	9.16	-0.31	14.16	0.21	953.7	1.05E-04	1	7.80E-00	9.56E+03	2.92E-04

Table 3.1 (continued)

CO_2 Test No.	Test Name	Orifice	Water Type	Press. *P* [bar]	Run No.	Run Time [min]	Water Temp. [°C]	CO_2 Temp. [°C]	CO_2 Mass Flowrate [kg/h]	Jet Vel. [m/s]	CO_2 Density [kg/m^3]	CO_2 Kine. Visc. [Pa s]	*IR*	*We*	*Re*	*Oh*
78	CDT05WTP61R7	T05	WT	61	7	3.1	9.26	2.11	5.99	0.09	939.5	9.99E-05	1	1.42E-00	4.24E+03	2.81E-04
79	CDT05WTP52R1	T05	WT	52	1	3.85	9.45	-2.18	158.81	2.35	957.3	1.09E-04	5	9.76E+02	1.03E+05	3.02E-04
80	CDT05WTP52R2	T05	WT	52	2	6.4	9.53	-3.53	123.12	1.8	965.0	1.12E-04	4	5.82E+02	7.81E+04	3.09E-04
81	CDT05WTP52R3	T05	WT	52	3	7.6	9.62	-1.16	82.54	1.23	951.3	1.07E-04	3	2.65E+02	5.48E+04	2.97E-04
82	CDT05WTP52R4	T05	WT	52	4	2.92	9.72	0.67	47.13	0.71	940.2	1.03E-04	3	8.75E+01	3.24E+04	2.89E-04
83	CDT05WTP52R5	T05	WT	52	5	2.55	9.8	-0.89	23.97	0.36	949.7	1.06E-04	2	2.24E+01	1.60E+04	2.96E-04
84	CDT05WTP52R6	T05	WT	52	6	2.97	9.91	0.14	13.89	0.21	943.5	1.04E-04	1	7.58E-00	9.46E+03	2.91E-04
85	CDT05WTP52R7	T05	WT	52	7	2.97	10.02	0.88	5.72	0.09	938.9	1.02E-04	1	1.29E-00	3.95E+03	2.88E-04
86	CDC72WSP55R1	C72	WS	55	1	8	2	-10	1.95	0.17	1001.6	1.26E-04	1	2.19E-00	2.73E+03	5.41E-04
87	CDC72WSP55R2	C72	WS	55	2	33	2	-10	3.11	0.27	1001.6	1.26E-04	1	5.60E-00	4.37E+03	5.41E-04
88	CDC72WSP55R3	C72	WS	55	3	18	2	-10	3.89	0.34	1001.6	1.26E-04	2	8.76E-00	5.47E+03	5.41E-04
89	CDC72WSP55R4	C72	WS	55	4	27	2	-10	5.84	0.52	1001.6	1.26E-04	2	1.97E+01	8.20E+03	5.41E-04
90	CDC72WSP55R5	C72	WS	55	5	18	2	-10	7.78	0.69	1001.6	1.26E-04	3	3.50E+01	1.09E+04	5.41E-04
91	CDC72WSP55R6	C72	WS	55	6	12	2	-10	13.62	1.2	1001.6	1.26E-04	3	1.07E+02	1.91E+04	5.41E-04
92	CDC72WSP55R7	C72	WS	55	7	8	2	-10	19.46	1.72	1001.6	1.26E-04	4	2.19E+02	2.73E+04	5.41E-04
93	CDC72WSP55R8	C72	WS	55	8	8	2	-10	38.91	3.44	1001.6	1.26E-04	5	8.76E+02	5.47E+04	5.41E-04
94	CDC72WSP55R9	C72	WS	55	9	1	2	-10	53.08	4.69	1001.6	1.26E-04	5	1.63E+03	7.46E+04	5.41E-04
95	CDC72WSP55R10	C72	WS	55	10	24	2	-10	4.67	0.41	1001.6	1.26E-04	2	1.26E+01	6.56E+03	5.41E-04
96	CDC72WSP55R11	C72	WS	55	11	28	2	-10	7	0.62	1001.6	1.26E-04	3	2.84E+01	9.84E+03	5.41E-04
97	CDC72WSP55R12	C72	WS	55	12	4	2	-10	31.13	2.75	1001.6	1.26E-04	4	5.60E+02	4.37E+04	5.41E-04

Table 3.2 Crude Oil Injection Test Matrix

Oil Test No.	Test Name	Oil Type	Orifice	Water Type	Run No.	Run Time [min]	Water Temp. [°C]	Oil Temp. [°C]	Oil Flow Rate [l/h]	Jet Vel. [m/s]	Oil Density [kg/m^3]	Oil Kine. Visc. [cs]	*IR*	*We*	*Re*	*Oh*
1	GES02WTRR1	GE	S02	WT	1	0.18	18.07	27.19	3.48	0.31	884.09	16.25	1	6.70E-00	3.35E+01	7.73E-02
2	GES02WTRR2	GE	S02	WT	2	0.45	18.08	27.26	4.55	0.40	884.09	16.19	1	1.15E+01	4.40E+01	7.70E-02
3	GES02WTRR3	GE	S02	WT	3	0.53	18.11	27.28	8.52	0.75	884.09	16.18	2	4.01E+01	8.23E+01	7.69E-02
4	GES02WTRR4	GE	S02	WT	4	3.32	18.11	27.32	15.96	1.41	884.09	16.14	3	1.41E+02	1.55E+02	7.68E-02
5	GES02WTRR5	GE	S02	WT	5	0.97	18.24	27.63	24.48	2.16	884.09	15.90	3	3.31E+02	2.41E+02	7.56E-02
6	GES02WTRR6	GE	S02	WT	6	1.05	18.26	27.62	32.76	2.90	884.09	15.90	4	5.93E+02	3.22E+02	7.56E-02
7	GES02WTRR7	GE	S02	WT	7	1.83	18.21	27.72	37.89	3.35	884.09	15.82	5	7.94E+02	3.74E+02	7.53E-02
8	GES02WTRR8	GE	S02	WT	8	3.70	18.41	27.72	42.69	3.77	884.09	15.83	5	1.01E+03	4.22E+02	7.53E-02
9	GES02WTRR9	GE	S02	WT	9	0.18	18.71	27.56	3.09	0.27	884.09	15.95	1	5.28E-00	3.03E+01	7.59E-02
10	GES02WTRR10	GE	S02	WT	10	0.10	18.71	27.56	3.84	0.34	884.09	15.95	1	8.15E-00	3.76E+01	7.59E-02
11	GES02WTRR11	GE	S02	WT	11	0.27	18.71	27.56	5.00	0.44	884.09	15.95	1	1.38E+01	4.90E+01	7.59E-02
12	GES02WTRR12	GE	S02	WT	12	0.15	18.71	27.56	8.10	0.72	884.09	15.95	2	3.63E+01	7.94E+01	7.59E-02
13	GES02WTRR13	GE	S02	WT	13	0.15	18.71	27.56	10.92	0.97	884.09	15.95	2	6.59E+01	1.07E+02	7.59E-02
14	GES02WTRR14	GE	S02	WT	14	0.20	18.71	27.56	13.86	1.23	884.09	15.95	3	1.06E+02	1.36E+02	7.59E-02
15	GES02WTRR15	GE	S02	WT	15	0.07	18.71	27.56	15.24	1.35	884.09	15.95	3	1.28E+02	1.49E+02	7.59E-02
16	GES02WTRR16	GE	S02	WT	16	0.12	18.71	27.56	18.12	1.60	884.09	15.95	3	1.82E+02	1.78E+02	7.59E-02
17	GES02WTRR17	GE	S02	WT	17	0.12	18.71	27.56	21.06	1.86	884.09	15.95	3	2.45E+02	2.06E+02	7.59E-02
18	GES02WTRR18	GE	S02	WT	18	0.12	18.71	27.56	27.42	2.42	884.09	15.95	4	4.16E+02	2.69E+02	7.59E-02
19	GES02WTRR19	GE	S02	WT	19	0.22	18.71	27.56	34.32	3.03	884.09	15.95	5	6.51E+02	3.36E+02	7.59E-02
20	GES02WTRR20	GE	S02	WT	20	0.08	18.71	27.56	41.10	3.63	884.09	15.95	5	9.34E+02	4.03E+02	7.59E-02
21	GES02WTRR21	GE	S02	WT	21	0.07	18.71	27.56	42.60	3.77	884.09	15.95	5	1.00E+03	4.18E+02	7.59E-02
22	GES02WTRR22	GE	S02	WT	22	0.07	18.71	27.56	55.20	4.88	884.09	15.95	5	1.68E+03	5.41E+02	7.59E-02
23	GES02WTRR23	GE	S02	WT	23	0.12	18.71	27.56	60.30	5.33	884.09	15.95	5	2.01E+03	5.91E+02	7.59E-02
24	GES02WTRR24	GE	S02	WT	24	0.10	18.71	27.56	67.80	5.99	884.09	15.95	5	2.54E+03	6.64E+02	7.59E-02
25	GES05WTRR1	GE	S05	WT	1	1.92	18.74	27.36	69.60	0.98	884.09	16.11	4	1.71E+02	2.70E+02	4.85E-02

Table 3.2 (continued)

Oil Test No.	Test Name	Oil Type	Orifice	Water Type	Run No.	Run Time [min]	Water Temp. [°C]	Oil Temp. [°C]	Oil Flow Rate [l/h]	Jet Vel. [m/s]	Oil Density [kg/m^3]	Oil Kine. Visc. [cs]	*IR*	*We*	*Re*	*Oh*
26	GES05WTRR2	GE	S05	WT	2	1.60	18.79	27.00	90.00	1.27	884.09	16.40	4	2.87E+02	3.43E+02	4.93E-02
27	GES05WTRR3	GE	S05	WT	3	2.45	19.01	27.14	117.00	1.66	884.09	16.29	4	4.84E+02	4.49E+02	4.90E-02
28	GES05WTRR4	GE	S05	WT	4	1.92	19.09	27.30	134.40	1.90	884.09	16.16	5	6.39E+02	5.20E+02	4.86E-02
29	GES05WTRR5	GE	S05	WT	5	0.17	19.30	26.69	6.00	0.08	884.09	16.65	1	1.27E-00	2.25E+01	5.01E-02
30	GES05WTRR6	GE	S05	WT	6	0.27	19.30	26.69	11.40	0.16	884.09	16.65	1	4.60E-00	4.28E+01	5.01E-02
31	GES05WTRR7	GE	S05	WT	7	0.27	19.30	26.69	17.82	0.25	884.09	16.65	1	1.12E+01	6.69E+01	5.01E-02
32	GES05WTRR8	GE	S05	WT	8	0.13	19.30	26.69	25.20	0.36	884.09	16.65	2	2.25E+01	9.47E+01	5.01E-02
33	GES05WTRR9	GE	S05	WT	9	0.20	19.30	26.69	31.20	0.44	884.09	16.65	2	3.44E+01	1.17E+02	5.01E-02
34	GES05WTRR10	GE	S05	WT	10	0.27	19.30	26.69	45.00	0.64	884.09	16.65	2	7.17E+01	1.69E+02	5.01E-02
35	GES05WTRR11	GE	S05	WT	11	0.27	19.30	26.69	51.72	0.73	884.09	16.65	3	9.47E+01	1.94E+02	5.01E-02
36	GES05WTRR12	GE	S05	WT	12	0.40	19.30	26.69	59.82	0.85	884.09	16.65	3	1.27E+02	2.25E+02	5.01E-02
37	GES05WTRR13	GE	S05	WT	13	0.13	19.30	26.69	69.60	0.98	884.09	16.65	3	1.71E+02	2.61E+02	5.01E-02
38	GES05WTRR14	GE	S05	WT	14	0.13	19.30	26.69	75.00	1.06	884.09	16.65	4	1.99E+02	2.82E+02	5.01E-02
39	GES05WTRR15	GE	S05	WT	15	0.15	19.30	26.69	91.20	1.29	884.09	16.65	4	2.94E+02	3.43E+02	5.01E-02
40	GES05WTRR16	GE	S05	WT	16	0.30	19.30	26.69	104.10	1.47	884.09	16.65	4	3.84E+02	3.91E+02	5.01E-02
41	GES05WTRR17	GE	S05	WT	17	0.17	19.30	26.69	108.00	1.53	884.09	16.65	5	4.13E+02	4.06E+02	5.01E-02
42	MAS05WTRR1	MA	S05	WT	1	1.33	16.74	27.98	69.27	0.98	869.69	11.81	4	1.67E+02	3.61E+02	3.58E-02
43	MAS05WTRR2	MA	S05	WT	2	1.87	16.66	28.12	95.07	1.35	869.69	11.75	4	3.15E+02	4.98E+02	3.56E-02
44	MAS05WTRR3	MA	S05	WT	3	1.78	16.81	28.11	120.75	1.71	869.69	11.76	4	5.08E+02	6.32E+02	3.57E-02
45	MAS05WTRR4	MA	S05	WT	4	2.13	16.92	28.05	168.00	2.38	869.69	11.78	5	9.83E+02	8.77E+02	3.57E-02
46	MAS05WTRR5	MA	S05	WT	5	0.15	17.07	28.17	4.50	0.06	869.69	11.73	1	7.05E-01	2.36E+01	3.56E-02
47	MAS05WTRR6	MA	S05	WT	6	0.10	17.08	28.22	6.60	0.09	869.69	11.71	1	1.52E-00	3.47E+01	3.55E-02
48	MAS05WTRR7	MA	S05	WT	7	0.23	17.08	28.10	10.26	0.15	869.69	11.76	1	3.66E-00	5.37E+01	3.57E-02
49	MAS05WTRR8	MA	S05	WT	8	0.10	17.09	28.12	11.94	0.17	869.69	11.75	1	4.96E-00	6.25E+01	3.56E-02
50	MAS05WTRR9	MA	S05	WT	9	0.07	17.09	28.13	16.62	0.24	869.69	11.75	1	9.62E-00	8.70E+01	3.56E-02
51	MAS05WTRR10	MA	S05	WT	10	0.12	17.10	28.15	24.60	0.35	869.69	11.74	2	2.11E+01	1.29E+02	3.56E-02

Table 3.2 (continued)

Oil Test No.	Test Name	Oil Type	Orifice	Water Type	Run No.	Run Time [min]	Water Temp. [°C]	Oil Temp. [°C]	Oil Flow Rate [l/h]	Jet Vel. [m/s]	Oil Density [kg/m^3]	Oil Kine. Visc. [cs]	*IR*	*We*	*Re*	*Oh*
52	MAS05WTRR11	MA	S05	WT	11	0.10	17.10	28.16	31.80	0.45	869.69	11.74	2	3.52E+01	1.67E+02	3.56E-02
53	MAS05WTRR12	MA	S05	WT	12	0.18	17.11	28.18	40.80	0.58	869.69	11.73	3	5.79E+01	2.14E+02	3.56E-02
54	MAS05WTRR13	MA	S05	WT	13	0.23	17.12	28.19	45.60	0.65	869.69	11.72	3	7.24E+01	2.39E+02	3.56E-02
55	MAS05WTRR14	MA	S05	WT	14	0.17	17.12	28.20	50.76	0.72	869.69	11.72	3	8.97E+01	2.66E+02	3.55E-02
56	MAS05WTRR15	MA	S05	WT	15	0.20	17.12	28.22	61.80	0.87	869.69	11.71	3	1.33E+02	3.25E+02	3.55E-02
57	MAS05WTRR16	MA	S05	WT	16	0.35	17.12	28.23	68.40	0.97	869.69	11.71	4	1.63E+02	3.59E+02	3.55E-02
58	MAS05WTRR17	MA	S05	WT	17	0.15	17.12	28.30	97.32	1.38	869.69	11.68	4	3.30E+02	5.13E+02	3.54E-02
59	MAS05WTRR18	MA	S05	WT	18	0.30	17.13	28.37	42.60	0.60	869.69	11.65	3	6.32E+01	2.25E+02	3.53E-02
60	MAS05WTRR19	MA	S05	WT	19	0.17	17.13	28.43	30.00	0.42	869.69	11.63	2	3.13E+01	1.59E+02	3.53E-02
61	MAS05WTRR20	MA	S05	WT	20	0.23	17.14	28.50	18.00	0.25	869.69	11.60	1	1.13E+01	9.55E+01	3.52E-02
62	MAS05WTRR21	MA	S05	WT	21	2.00	17.34	28.41	173.40	2.45	869.69	11.64	5	1.05E+03	9.17E+02	3.53E-02
63	MAS02WTRR1	MA	S02	WT	1	0.95	18.27	26.76	19.02	1.68	869.69	12.30	3	1.97E+02	2.38E+02	5.90E-02
64	MAS02WTRR2	MA	S02	WT	2	0.47	18.24	26.79	24.60	2.18	869.69	12.28	4	3.29E+02	3.08E+02	5.89E-02
65	MAS02WTRR3	MA	S02	WT	3	0.63	18.25	26.82	33.00	2.92	869.69	12.27	4	5.92E+02	4.14E+02	5.89E-02
66	MAS02WTRR4	MA	S02	WT	4	1.10	18.22	26.87	38.73	3.42	869.69	12.25	5	8.16E+02	4.86E+02	5.88E-02
67	MAS02WTRR5	MA	S02	WT	5	2.10	18.23	26.93	44.94	3.97	869.69	12.23	5	1.10E+03	5.65E+02	5.86E-02
68	MAS02WTRR6	MA	S02	WT	6	0.05	18.30	26.80	3.24	0.29	869.69	12.28	1	5.71E-00	4.06E+01	5.89E-02
69	MAS02WTRR7	MA	S02	WT	7	0.10	18.32	26.88	3.76	0.33	869.69	12.25	1	7.67E-00	4.72E+01	5.87E-02
70	MAS02WTRR8	MA	S02	WT	8	0.13	18.33	26.96	7.29	0.64	869.69	12.22	1	2.89E+01	9.18E+01	5.86E-02
71	MAS02WTRR9	MA	S02	WT	9	0.18	18.35	26.98	9.48	0.84	869.69	12.21	2	4.89E+01	1.19E+02	5.85E-02
72	MAS02WTRR10	MA	S02	WT	10	0.17	18.37	26.99	12.06	1.07	869.69	12.20	3	7.91E+01	1.52E+02	5.85E-02
73	MAS02WTRR11	MA	S02	WT	11	0.18	18.39	27.01	14.46	1.28	869.69	12.20	3	1.14E+02	1.82E+02	5.85E-02
74	MAS02WTRR12	MA	S02	WT	12	0.18	18.40	27.02	17.46	1.54	869.69	12.19	3	1.66E+02	2.20E+02	5.85E-02
75	MAS02WTRR13	MA	S02	WT	13	0.12	18.42	27.02	4.11	0.36	869.69	12.19	1	9.19E-00	5.18E+01	5.85E-02
76	MAS02WTRR14	MA	S02	WT	14	0.10	18.44	27.02	4.62	0.41	869.69	12.19	1	1.16E+01	5.83E+01	5.85E-02
77	MAS02WTRR15	MA	S02	WT	15	0.17	18.46	27.02	5.91	0.52	869.69	12.19	1	1.90E+01	7.46E+01	5.85E-02

Table 3.2 (continued)

Oil Test No.	Test Name	Oil Type	Orifice	Water Type	Run No.	Run Time [min]	Water Temp. [°C]	Oil Temp. [°C]	Oil Flow Rate [l/h]	Jet Vel. [m/s]	Oil Density [kg/m^3]	Oil Kine. Visc. [cs]	*IR*	*We*	*Re*	*Oh*
78	MAS02WTRR16	MA	S02	WT	16	0.28	18.46	27.02	7.11	0.63	869.69	12.19	1	2.75E+01	8.97E+01	5.85E-02
79	MAS02WTRR17	MA	S02	WT	17	0.15	18.46	27.02	4.38	0.39	869.69	12.19	1	1.04E+01	5.53E+01	5.85E-02
80	MAS02WTRR18	MA	S02	WT	18	0.12	18.46	27.02	3.75	0.33	869.69	12.19	1	7.65E-00	4.73E+01	5.85E-02
81	MAS02WTRR19	MA	S02	WT	19	0.05	18.46	27.02	6.96	0.62	869.69	12.19	1	2.63E+01	8.78E+01	5.85E-02
82	MAS02WTRR20	MA	S02	WT	20	1.00	18.45	27.10	18.30	1.62	869.69	12.16	3	1.82E+02	2.31E+02	5.83E-02
83	MAS02WTRR21	MA	S02	WT	21	0.52	18.49	27.17	77.40	6.84	869.69	12.13	5	3.26E+03	9.81E+02	5.82E-02
84	MAS02WTRR22	MA	S02	WT	22	0.67	18.45	27.24	51.30	4.54	869.69	12.10	5	1.43E+03	6.52E+02	5.80E-02
85	PGS01WTRR1	PG	S01	WT	1	1.92	17.67	27.25	10.54	3.73	929.69	148.75	3	5.16E+02	2.33E+01	9.76E-01
86	PGS01WTRR2	PG	S01	WT	2	2.43	17.66	27.47	15.30	5.41	929.69	144.13	4	1.09E+03	3.49E+01	9.45E-01
87	PGS01WTRR3	PG	S01	WT	3	0.28	17.81	27.39	3.39	1.20	929.69	145.81	1	5.33E+01	7.63E-00	9.56E-01
88	PGS05WTRR1	PG	S05	WT	1	1.10	17.63	27.33	8.16	0.12	929.69	147.07	1	2.48E-00	3.65E-00	4.31E-01
89	PGS05WTRR2	PG	S05	WT	2	0.17	17.67	27.38	3.00	0.04	929.69	146.02	1	3.35E-01	1.35E-00	4.28E-01
90	PGS05WTRR3	PG	S05	WT	3	0.72	17.70	27.42	5.27	0.07	929.69	145.18	1	1.03E-00	2.39E-00	4.26E-01
91	PGS05WTRR4	PG	S05	WT	4	0.45	17.82	27.47	8.94	0.13	929.69	144.13	1	2.97E-00	4.08E-00	4.23E-01
92	PGS05WTRR5	PG	S05	WT	5	0.42	17.95	27.51	13.68	0.19	929.69	143.29	1	6.96E-00	6.28E-00	4.20E-01
93	PGS05WTRR6	PG	S05	WT	6	0.23	17.95	27.54	20.22	0.29	929.69	142.66	2	1.52E+01	9.32E-00	4.18E-01
94	PGS05WTRR7	PG	S05	WT	7	0.17	17.95	27.56	28.14	0.40	929.69	142.24	2	2.95E+01	1.30E+01	4.17E-01
95	PGS05WTRR8	PG	S05	WT	8	0.17	17.95	27.59	37.50	0.53	929.69	141.61	2	5.23E+01	1.74E+01	4.15E-01
96	PGS05WTRR9	PG	S05	WT	9	0.17	17.95	27.62	43.74	0.62	929.69	140.98	2	7.12E+01	2.04E+01	4.14E-01
97	PGS05WTRR10	PG	S05	WT	10	0.13	17.96	27.65	63.12	0.89	929.69	140.35	3	1.48E+02	2.96E+01	4.12E-01
98	PGS05WTRR11	PG	S05	WT	11	0.12	17.96	27.67	54.00	0.76	929.69	139.93	3	1.09E+02	2.54E+01	4.10E-01
99	PGS05WTRR12	PG	S05	WT	12	0.08	17.96	27.70	51.00	0.72	929.69	139.30	3	9.68E+01	2.41E+01	4.09E-01
100	PGS05WTRR13	PG	S05	WT	13	0.15	17.96	27.73	43.20	0.61	929.69	138.67	2	6.95E+01	2.05E+01	4.07E-01
101	PGS05WTRR14	PG	S05	WT	14	0.07	17.97	27.76	24.00	0.34	929.69	138.04	2	2.14E+01	1.14E+01	4.05E-01
102	PGS05WTRR15	PG	S05	WT	15	0.13	17.97	27.78	48.00	0.68	929.69	137.62	3	8.57E+01	2.29E+01	4.04E-01
103	PGS05WTRR16	PG	S05	WT	16	0.02	17.97	27.81	101.40	1.43	929.69	136.99	4	3.83E+02	4.87E+01	4.02E-01

Table 3.2 (continued)

Oil Test No.	Test Name	Oil Type	Orifice	Water Type	Run No.	Run Time [min]	Water Temp. [°C]	Oil Temp. [°C]	Oil Flow Rate [l/h]	Jet Vel. [m/s]	Oil Density [kg/m^3]	Oil Kine. Visc. [cs]	*IR*	*We*	*Re*	*Oh*
104	PGS05WTRR17	PG	S05	WT	17	0.02	17.97	27.84	54.00	0.76	929.69	136.36	3	1.09E+02	2.60E+01	4.00E-01
105	PGS05WTRR18	PG	S05	WT	18	0.02	17.98	27.87	88.20	1.25	929.69	135.73	4	2.89E+02	4.27E+01	3.98E-01
106	PGS05WTRR19	PG	S05	WT	19	0.05	17.98	27.89	55.80	0.79	929.69	135.31	3	1.16E+02	2.71E+01	3.97E-01
107	PGS05WTRR20	PG	S05	WT	20	0.07	17.98	27.92	49.80	0.70	929.69	134.68	3	9.23E+01	2.43E+01	3.95E-01
108	PGS05WTRR21	PG	S05	WT	21	0.07	17.98	27.95	42.00	0.59	929.69	134.05	2	6.56E+01	2.06E+01	3.93E-01
109	PGS05WTRR22	PG	S05	WT	22	0.12	17.99	27.98	31.20	0.44	929.69	133.42	2	3.62E+01	1.54E+01	3.91E-01
110	PGS05WTRR23	PG	S05	WT	23	1.08	17.99	28.00	83.16	1.18	929.69	133.00	3	2.57E+02	4.11E+01	3.90E-01
111	PGS05WTRR24	PG	S05	WT	24	2.53	17.99	28.03	121.80	1.72	929.69	132.37	4	5.52E+02	6.05E+01	3.88E-01
112	PGS05WTRR25	PG	S05	WT	25	3.00	18.17	27.82	103.77	1.47	929.69	136.78	4	4.01E+02	4.99E+01	4.01E-01
113	NSS02WTRR1	NS	S02	WT	1	1.58	17.50	28.37	18.63	1.65	888.29	20.97	3	1.93E+02	1.40E+02	9.95E-02
114	NSS02WTRR2	NS	S02	WT	2	1.18	17.50	28.65	24.54	2.17	888.29	20.72	4	3.35E+02	1.86E+02	9.83E-02
115	NSS02WTRR3	NS	S02	WT	3	1.85	17.52	28.74	32.40	2.86	888.29	20.64	4	5.83E+02	2.47E+02	9.79E-02
116	NSS02WTRR4	NS	S02	WT	4	2.30	17.53	28.87	39.81	3.52	888.29	20.52	5	8.80E+02	3.05E+02	9.74E-02
117	NSS02WTRR5	NS	S02	WT	5	0.27	17.63	28.78	4.08	0.36	888.29	20.60	1	9.25E-00	3.11E+01	9.77E-02
118	NSS02WTRR6	NS	S02	WT	6	0.23	17.66	28.69	7.26	0.64	888.29	20.68	2	2.93E+01	5.51E+01	9.81E-02
119	NSS02WTRR7	NS	S02	WT	7	0.22	17.68	28.40	8.79	0.78	888.29	20.94	2	4.29E+01	6.59E+01	9.94E-02
120	NSS02WTRR8	NS	S02	WT	8	0.23	17.69	28.10	12.30	1.09	888.29	21.21	3	8.41E+01	9.11E+01	1.01E-01
121	NSS02WTRR9	NS	S02	WT	9	0.23	17.70	28.37	15.00	1.33	888.29	20.97	3	1.25E+02	1.12E+02	9.95E-02
122	NSS02WTRR10	NS	S02	WT	10	0.08	17.70	28.64	17.10	1.51	888.29	20.72	3	1.62E+02	1.30E+02	9.83E-02
123	NSS02WTRR11	NS	S02	WT	11	0.25	17.71	28.91	11.46	1.01	888.29	20.48	2	7.30E+01	8.79E+01	9.72E-02
124	NSS02WTRR12	NS	S02	WT	12	0.25	17.71	28.93	9.84	0.87	888.29	20.46	2	5.38E+01	7.55E+01	9.71E-02
125	NSS02WTRR13	NS	S02	WT	13	0.18	17.71	28.95	6.60	0.58	888.29	20.45	2	2.42E+01	5.07E+01	9.70E-02
126	NSS02WTRR14	NS	S02	WT	14	0.23	17.72	28.96	3.90	0.34	888.29	20.44	1	8.45E-00	3.00E+01	9.70E-02
127	NSS02WTRR15	NS	S02	WT	15	0.90	17.72	28.98	45.30	4.01	888.29	20.42	5	1.14E+03	3.49E+02	9.69E-02
128	NSS02WTRR16	NS	S02	WT	16	1.57	17.73	28.88	60.00	5.31	888.29	20.51	5	2.00E+03	4.60E+02	9.73E-02
129	NSS01WTRR1	NS	S01	WT	1	0.72	18.69	26.73	6.78	2.40	888.29	22.44	4	2.04E+02	9.48E+01	1.51E-01

Table 3.2 (continued)

Oil Test No.	Test Name	Oil Type	Orifice	Water Type	Run No.	Run Time [min]	Water Temp. [°C]	Oil Temp. [°C]	Oil Flow Rate [l/h]	Jet Vel. [m/s]	Oil Density [kg/m^3]	Oil Kine. Visc. [cs]	*IR*	*We*	*Re*	*Oh*
130	NSS01WTRR2	NS	S01	WT	2	1.10	18.75	26.71	12.60	4.46	888.29	22.46	4	7.06E+02	1.76E+02	1.51E-01
131	NSS01WTRR3	NS	S01	WT	3	3.13	18.65	26.73	15.90	5.62	888.29	22.44	5	1.12E+03	2.23E+02	1.51E-01
132	NSS01WTRR4	NS	S01	WT	4	2.37	18.67	26.82	4.60	1.63	888.29	22.36	3	9.38E+01	6.46E+01	1.50E-01
133	NSS01WTRR5	NS	S01	WT	5	2.48	18.71	26.89	9.53	3.37	888.29	22.30	4	4.03E+02	1.34E+02	1.50E-01
134	NSS01WTRR6	NS	S01	WT	6	0.45	18.95	27.10	3.14	1.11	888.29	22.11	3	4.38E+01	4.46E+01	1.48E-01
135	NSS01WTRR7	NS	S01	WT	7	0.25	18.94	27.18	5.66	2.00	888.29	22.04	4	1.42E+02	8.06E+01	1.48E-01
136	NSS01WTRR8	NS	S01	WT	8	0.08	18.93	27.26	4.88	1.73	888.29	21.97	3	1.06E+02	6.98E+01	1.47E-01
137	NSS01WTRR9	NS	S01	WT	9	0.20	18.92	27.34	3.54	1.25	888.29	21.89	3	5.56E+01	5.07E+01	1.47E-01
138	NSS01WTRR10	NS	S01	WT	10	0.18	18.92	27.18	2.92	1.03	888.29	22.04	2	3.79E+01	4.16E+01	1.48E-01
139	NSS01WTCR1	NS	S01	WT	1	1.20	8.37	27.53	4.57	1.61	888.29	21.72	3	9.26E+01	6.60E+01	1.46E-01
140	NSS01WTCR2	NS	S01	WT	2	0.52	8.39	27.59	6.83	2.42	888.29	21.67	4	2.07E+02	9.90E+01	1.45E-01
141	NSS01WTCR3	NS	S01	WT	3	1.97	8.51	27.64	9.79	3.46	888.29	21.62	4	4.26E+02	1.42E+02	1.45E-01
142	NSS01WTCR4	NS	S01	WT	4	6.62	8.82	27.78	12.99	4.59	888.29	21.50	4	7.49E+02	1.90E+02	1.44E-01
143	NSS02WNRR1	NS	S02	WN	1	2.92	18.27	26.98	18.63	1.65	888.29	22.22	3	1.93E+02	1.32E+02	1.05E-01
144	NSS02WNRR2	NS	S02	WN	2	2.42	18.38	22.12	23.49	2.08	888.30	26.60	4	3.07E+02	1.39E+02	1.26E-01
145	NSS02WNRR3	NS	S02	WN	3	3.43	18.41	27.27	30.90	2.73	888.29	21.96	5	5.30E+02	2.21E+02	1.04E-01
146	NSS02WNRR4	NS	S02	WN	4	4.45	18.46	27.44	42.63	3.77	888.29	21.81	5	1.01E+03	3.07E+02	1.03E-01
147	NSS02WNRR5	NS	S02	WN	5	0.43	18.55	27.42	3.60	0.32	888.29	21.82	1	7.20E-00	2.59E+01	1.04E-01
148	NSS02WNRR6	NS	S02	WN	6	0.30	18.55	27.47	5.10	0.45	888.29	21.78	1	1.45E+01	3.68E+01	1.03E-01
149	NSS02WNRR7	NS	S02	WN	7	0.28	18.55	27.52	9.72	0.86	888.29	21.73	2	5.25E+01	7.03E+01	1.03E-01
150	NSS02WNRR8	NS	S02	WN	8	0.40	18.55	27.57	14.43	1.28	888.29	21.69	3	1.16E+02	1.05E+02	1.03E-01
151	NSS02WNRR9	NS	S02	WN	9	0.67	18.55	27.61	18.60	1.64	888.29	21.65	3	1.92E+02	1.35E+02	1.03E-01
152	NSS02WNRR10	NS	S02	WN	10	0.33	18.51	27.64	12.00	1.06	888.29	21.62	2	8.00E+01	8.72E+01	1.03E-01
153	NSS02WNRR11	NS	S02	WN	11	0.25	18.57	27.72	8.46	0.75	888.29	21.55	2	3.98E+01	6.17E+01	1.02E-01
154	NSS02WNRR12	NS	S02	WN	12	0.17	18.57	27.72	77.40	6.84	888.29	21.55	5	3.33E+03	5.64E+02	1.02E-01

Table 3.3 Silicone Fluid Injection Test Matrix

Fluid Test No.	Test Name	Fluid Type	Orifice	Water Type	Run No.	Run Time [min]	Water Temp. [°C]	Fluid Temp. [°C]	Fluid Flow Rate [l/h]	Jet Vel. [m/s]	Fluid Dens. [kg/m^3]	Fluid Kine. Visc. [cs]	*IR*	*We*	*Re*	*Oh*
1	SFS02WTRR1	SF	S02	WT	1	0.87	24.01	21.59	19.22	1.70	953	21.95	4	2.65E+02	1.55E+02	1.05E-01
2	SFS02WTRR3	SF	S02	WT	3	0.53	23.40	21.66	29.49	2.61	953	21.91	4	6.23E+02	2.38E+02	1.05E-01
3	SFS02WTRR4	SF	S02	WT	4	0.68	24.19	21.70	14.99	1.33	953	21.89	3	1.61E+02	1.21E+02	1.05E-01
4	SFS02WTRR5	SF	S02	WT	5	0.37	24.12	21.74	23.55	2.08	953	21.86	4	3.97E+02	1.90E+02	1.05E-01
5	SFS02WTRR6	SF	S02	WT	6	1.77	24.15	21.77	12.61	1.11	953	21.85	2	1.14E+02	1.02E+02	1.05E-01
6	SFS02WTRR7	SF	S02	WT	7	0.77	24.31	21.81	5.66	0.50	953	21.82	2	2.30E+01	4.59E+01	1.04E-01
7	SFS02WTRR8	SF	S02	WT	8	0.65	24.27	21.85	2.79	0.25	953	21.80	1	5.57E-00	2.26E+01	1.04E-01
8	SFS02WTRR9	SF	S02	WT	9	0.62	24.36	21.88	7.03	0.62	953	21.78	2	3.54E+01	5.71E+01	1.04E-01
9	SFS02WTRR10	SF	S02	WT	10	1.05	24.40	21.92	8.08	0.71	953	21.76	2	4.68E+01	6.57E+01	1.04E-01
10	SFS02WTRR11	SF	S02	WT	11	0.83	24.51	21.96	9.18	0.81	953	21.74	2	6.03E+01	7.47E+01	1.04E-01
11	SFS02WTRR12	SF	S02	WT	12	1.55	24.55	21.99	10.01	0.89	953	21.72	2	7.18E+01	8.15E+01	1.04E-01
12	SFS02WTRR13	SF	S02	WT	13	0.78	24.68	22.03	12.13	1.07	953	21.70	3	1.05E+02	9.89E+01	1.04E-01
13	SFS02WTRR14	SF	S02	WT	14	0.27	25.55	22.03	1.62	0.14	953	21.70	1	1.89E-00	1.32E+01	1.04E-01
14	SFS02WTRR15	SF	S02	WT	15	0.78	25.93	22.07	5.57	0.49	953	21.67	1	2.23E+01	4.55E+01	1.04E-01
15	SFS02WTRR16	SF	S02	WT	16	0.67	25.99	22.10	8.41	0.74	953	21.66	2	5.07E+01	6.87E+01	1.04E-01
16	SFS02WTRR17	SF	S02	WT	17	0.67	26.03	22.14	10.32	0.91	953	21.63	2	7.63E+01	8.44E+01	1.04E-01
17	SFS02WTRR18	SF	S02	WT	18	0.60	26.05	22.18	12.67	1.12	953	21.61	2	1.15E+02	1.04E+02	1.03E-01
18	LSS02WTRR1	LS	S02	WT	1	0.30	23.47	23.99	19.11	1.69	760	0.66	3	2.73E+02	5.14E+03	3.22E-03
19	LSS02WTRR2	LS	S02	WT	2	0.30	23.52	23.99	31.38	2.77	760	0.66	4	7.36E+02	8.44E+03	3.22E-03
20	LSS02WTRR3	LS	S02	WT	3	0.47	23.54	23.99	36.75	3.25	760	0.66	4	1.01E+03	9.88E+03	3.22E-03
21	LSS02WTRR4	LS	S02	WT	4	0.77	23.56	23.99	39.27	3.47	760	0.66	4	1.15E+03	1.06E+04	3.22E-03
22	LSS02WTRR5	LS	S02	WT	5	0.38	23.68	23.99	24.18	2.14	760	0.66	3	4.37E+02	6.50E+03	3.22E-03
23	LSS02WTRR6	LS	S02	WT	6	0.90	23.70	23.99	14.83	1.31	760	0.66	3	1.64E+02	3.99E+03	3.22E-03

Table 3.3 (continued)

Fluid Test No.	Test Name	Fluid Type	Orifice	Water Type	Run No.	Run Time [min]	Water Temp. [°C]	Fluid Temp. [°C]	Fluid Flow Rate [l/h]	Jet Vel. [m/s]	Fluid Dens. [kg/m^3]	Fluid Kine. Visc. [cs]	*IR*	*We*	*Re*	*Oh*
24	LSS02WTRR7	LS	S02	WT	7	1.60	23.77	23.99	13.22	1.17	760	0.66	3	1.31E+02	3.55E+03	3.22E-03
25	LSS02WTRR8	LS	S02	WT	8	0.67	23.17	23.99	3.12	0.28	760	0.66	1	7.27E-00	8.39E+02	3.22E-03
26	LSS02WTRR9	LS	S02	WT	9	0.52	23.48	23.99	7.34	0.65	760	0.66	2	4.02E+01	1.97E+03	3.22E-03
27	LSS02WTRR10	LS	S02	WT	10	0.58	23.59	23.99	5.97	0.53	760	0.66	2	2.66E+01	1.61E+03	3.22E-03
28	LSS02WTRR11	LS	S02	WT	11	0.58	23.63	23.99	10.32	0.91	760	0.66	2	7.95E+01	2.77E+03	3.22E-03
29	LSS02WTRR12	LS	S02	WT	12	0.58	23.60	23.99	11.76	1.04	760	0.66	3	1.03E+02	3.16E+03	3.22E-03
30	LSS02WTRR13	LS	S02	WT	13	0.60	23.61	23.99	14.03	1.24	760	0.66	3	1.47E+02	3.77E+03	3.22E-03
31	LST02WTRR1	LS	T02	WT	1	1.03	24.14	24.48	3.78	0.33	760	0.65	2	1.07E+01	1.02E+03	3.20E-03
32	LST02WTRR2	LS	T02	WT	2	0.53	24.25	24.48	1.88	0.17	760	0.65	2	2.63E-00	5.07E+02	3.20E-03
33	LST02WTRR3	LS	T02	WT	3	0.62	24.25	24.48	3.49	0.31	760	0.65	2	9.10E-00	9.44E+02	3.20E-03
34	LST02WTRR4	LS	T02	WT	4	0.60	24.32	24.48	5.88	0.52	760	0.65	2	2.58E+01	1.59E+03	3.20E-03
35	LST02WTRR5	LS	T02	WT	5	0.58	24.39	24.48	7.93	0.70	760	0.65	2	4.70E+01	2.15E+03	3.20E-03
36	LST02WTRR6	LS	T02	WT	6	0.57	24.33	24.48	9.01	0.80	760	0.65	2	6.07E+01	2.44E+03	3.20E-03
37	LST02WTRR7	LS	T02	WT	7	0.55	24.47	24.48	11.67	1.03	760	0.65	2	1.02E+02	3.16E+03	3.20E-03
38	LST02WTRR8	LS	T02	WT	8	0.58	24.44	24.48	13.77	1.22	760	0.65	3	1.42E+02	3.73E+03	3.20E-03
39	LST02WTRR9	LS	T02	WT	9	0.57	24.52	24.48	1.88	0.17	760	0.65	2	2.64E-00	5.08E+02	3.20E-03
40	LST02WTRR10	LS	T02	WT	10	4.48	24.80	24.48	16.10	1.42	760	0.65	3	1.94E+02	4.35E+03	3.20E-03
41	LST02WTRR11	LS	T02	WT	11	3.38	24.86	24.48	20.85	1.84	760	0.65	3	3.25E+02	5.64E+03	3.20E-03
42	LST02WTRR12	LS	T02	WT	12	2.20	24.92	24.48	30.44	2.69	760	0.65	4	6.92E+02	8.23E+03	3.20E-03
43	LST02WTRR13	LS	T02	WT	13	2.82	24.93	24.48	40.29	3.56	760	0.65	5	1.21E+03	1.09E+04	3.20E-03

3.3.3 Boundaries of the Liquid-liquid Jet Instability Regimes

Digital video records of each of the 294 tests using liquid CO_2, 4 crude oils or two silicone fluids were reviewed and classified as one of the five breakup modes shown in Figure 3.1. Following convention used in previous studies of jet breakup, these data were plotted against the corresponding dimensionless Ohnesorge Number, *Oh*, and jet Reynolds Number, *Re*, to establish the boundaries of the different instability regimes. This has significant practical importance since the instability regime determines the characteristics of the droplet size distribution (i.e., monodisperse; polydisperse; coarse or fine droplets). *Re* and *Oh* can be calculated from fluid properties and known or estimated jet flow rate and orifice diameter, and can be compared with the instability diagram to predict the mode of breakup and the general characteristics of droplet size. The five instability regimes are separated by 4 boundaries, which are referred to as boundaries 1, 2, 3, and 4 in the following text.

A linear least square regression was applied to find the four best-fit boundaries between the 5 breakup regimes. Values of *Re* and *Oh* corresponding to points adjacent to the regime boundaries can be identified by examining the video records. A linear fit to these data points was performed for each boundary.

As an example, for Case GES05WTR, where Genesis crude oil was injected into tap water from a 5 mm sharp edge orifice, 17 runs were performed in which flow rate (jet velocity) was varied. The original sequences of the tests are shown on the left of Table 3.4. These entries were re-sorted in increasing value of *Re* as shown on the right of Table 3.2. Points (runs) that straddled the boundaries between regimes were selected to be

included in the data set used to identify those boundaries. For example, the transition between instability regimes 1 and 2 occurred between runs 7 and 8. We selected both runs 7 and 8, the highest and lowest values of *Re* collected for regimes 1 and 2, respectively, for inclusion in the data set used to locate the boundary between regimes 1 and 2. Similarly, values of *Re* and *Oh* for runs 10 and 11, runs 1 and 14 and runs 16 and 17 were included in the data sets for the curve fits for the boundaries of regimes 2, 3, and 4, respectively.

Table 3.4 Determination of regime boundary points for case GES05WTR.

Original Order				New Order			
Run No.	Instability Regime *IR*	*Re*	*Oh*	Run No.	Instability Regime *IR*	*Re*	*Oh*
1	3	2.70E+02	4.85E-02	5	1	2.25E+01	5.01E-02
2	4	3.43E+02	4.93E-02	6	1	4.28E+01	5.01E-02
3	5	4.49E+02	4.90E-02	7	1	6.69E+01	5.01E-02
4	5	5.20E+02	4.86E-02	8	2	9.47E+01	5.01E-02
5	1	2.25E+01	5.01E-02	9	2	1.17E+02	5.01E-02
6	1	4.28E+01	5.01E-02	10	2	1.69E+02	5.01E-02
7	1	6.69E+01	5.01E-02	11	3	1.94E+02	5.01E-02
8	2	9.47E+01	5.01E-02	12	3	2.25E+02	5.01E-02
9	2	1.17E+02	5.01E-02	13	3	2.61E+02	5.01E-02
10	2	1.69E+02	5.01E-02	1	3	2.70E+02	4.85E-02
11	3	1.94E+02	5.01E-02	14	4	2.82E+02	5.01E-02
12	3	2.25E+02	5.01E-02	2	4	3.43E+02	4.93E-02
13	3	2.61E+02	5.01E-02	15	4	3.43E+02	5.01E-02
14	4	2.82E+02	5.01E-02	16	4	3.91E+02	5.01E-02
15	4	3.43E+02	5.01E-02	17	5	4.06E+02	5.01E-02
16	4	3.91E+02	5.01E-02	3	5	4.49E+02	4.90E-02
17	5	4.06E+02	5.01E-02	4	5	5.20E+02	4.86E-02

This process was repeated for each of the other 21 cases, yielding 4 sets of data points straddling the 4 regime boundaries (i.e., the boundaries between regimes 1 & 2,

2& 3, 3& 4 and 4 &5). Each data point comprises a value of *Re* and *Oh*. Linear relations for the four boundaries (i =1, 2, 3, and 4), are postulated:

$$\log Oh = \log a_i + b_i \log Re \qquad i = 1,2,3,4 \tag{3.5}$$

where a_i and b_i are constants to be determined by regression analysis. This least squares analysis yields:

Boundary 1 between instability regions **1** and **2**:

$$Oh = 4.9196 \; Re^{-1.0459} \tag{3.6}$$

Boundary 2 between instability regions **2** and **3**:

$$Oh = 9.5979 \; Re^{-1.0255} \tag{3.7}$$

Boundary 3 between instability regions **3** and **4**:

$$Oh = 15.4108 \; Re^{-0.9989} \tag{3.8}$$

Boundary 4 between instability regions **4** and **5**:

$$Oh = 24.9548 \; Re^{-1.0027} \tag{3.9}$$

These boundaries, identified as the four dashed lines are plotted as in Figure 3.20, along with the complete data set of 294 points. The individual data sets used to identify the four individual boundaries are plotted in Figures 3.21 to 3.24 along with the least-squares curve fit of those regime boundaries.

An important observation is that all the relationships for the boundaries have similar form:

$$Oh = a \; Re^{b}$$

where $b \cong -1$. Comparing this with equations (3.1), (3.2) and (3.3) yields the result that the transitions between regimes will occur when we attain certain critical values of *We* equal to a_i^2. Furthermore, viscosity does not appear in *We* and is not relevant with respect to transition; only the parameters ρ_j, U_j, D and σ are important.

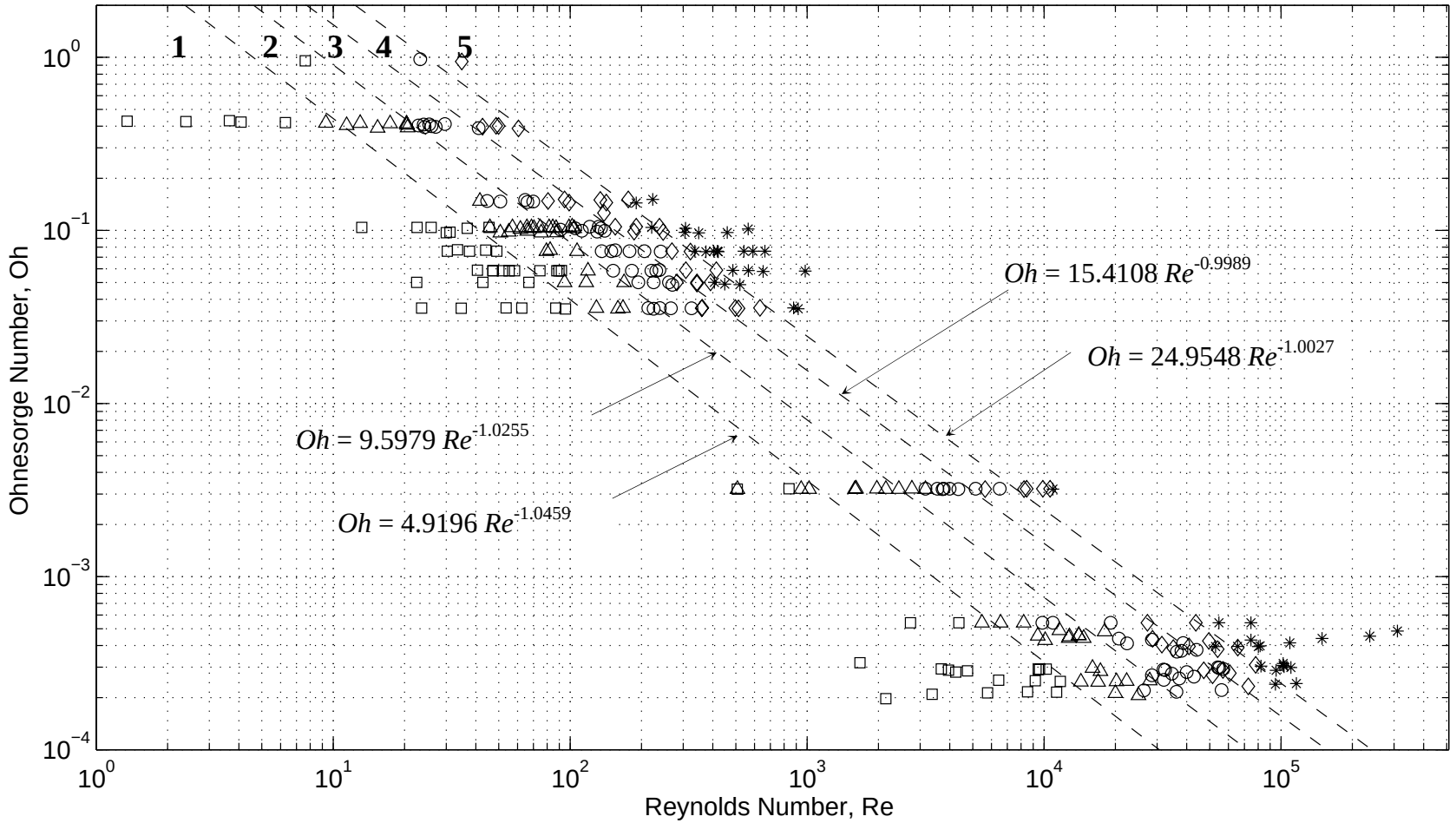

Figure 3.20 Liquid-liquid jet break-up regimes. Data points correspond to 154 oil and 43 silicone fluid injection tests (upper two sets), and 97 liquid CO_2 injection tests (lower right hand corner). □, varicose breakup; Δ, sinuous wave breakup; o, filament breakup; ◊, wave atomization; *, full atomization.

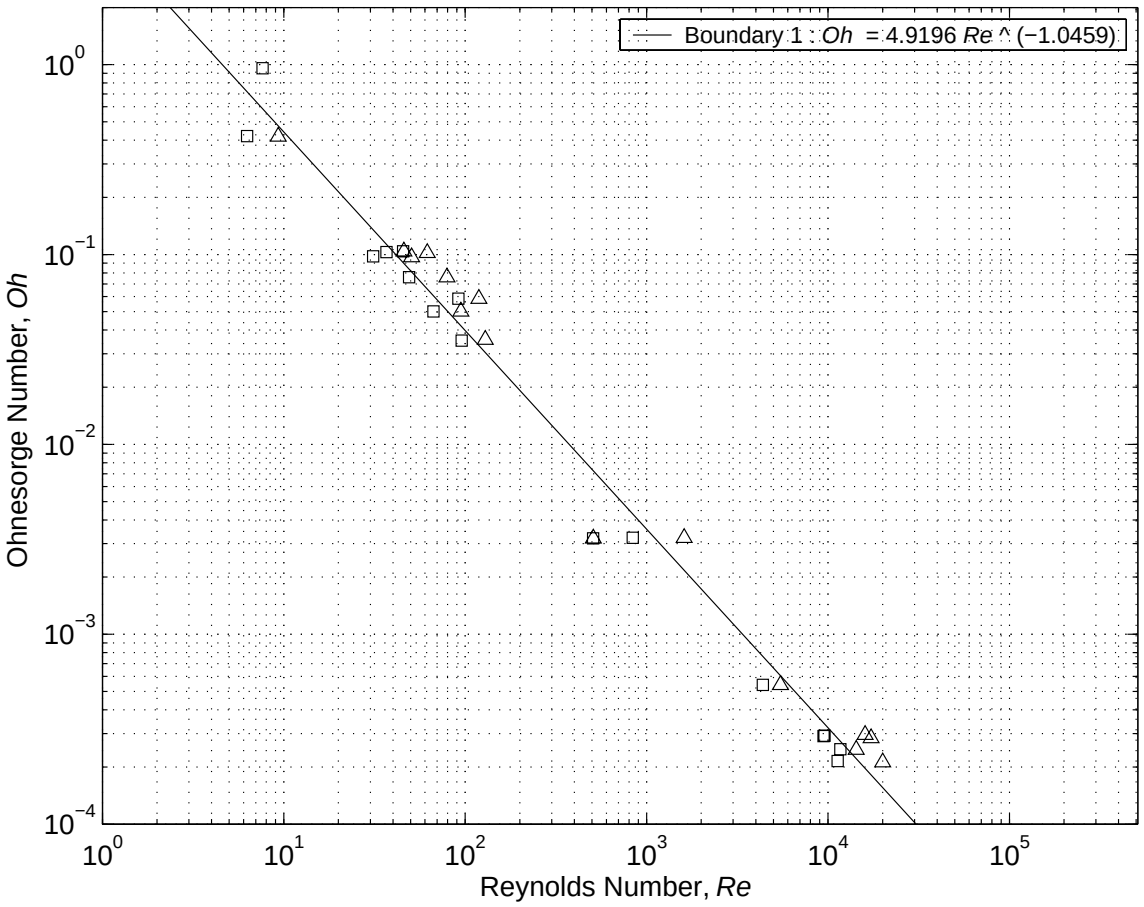

Figure 3.21 Boundary 1 between instability regimes 1 and 2. □, varicose breakup at instability regime 1; Δ, sinuous wave breakup at instability regime 2.

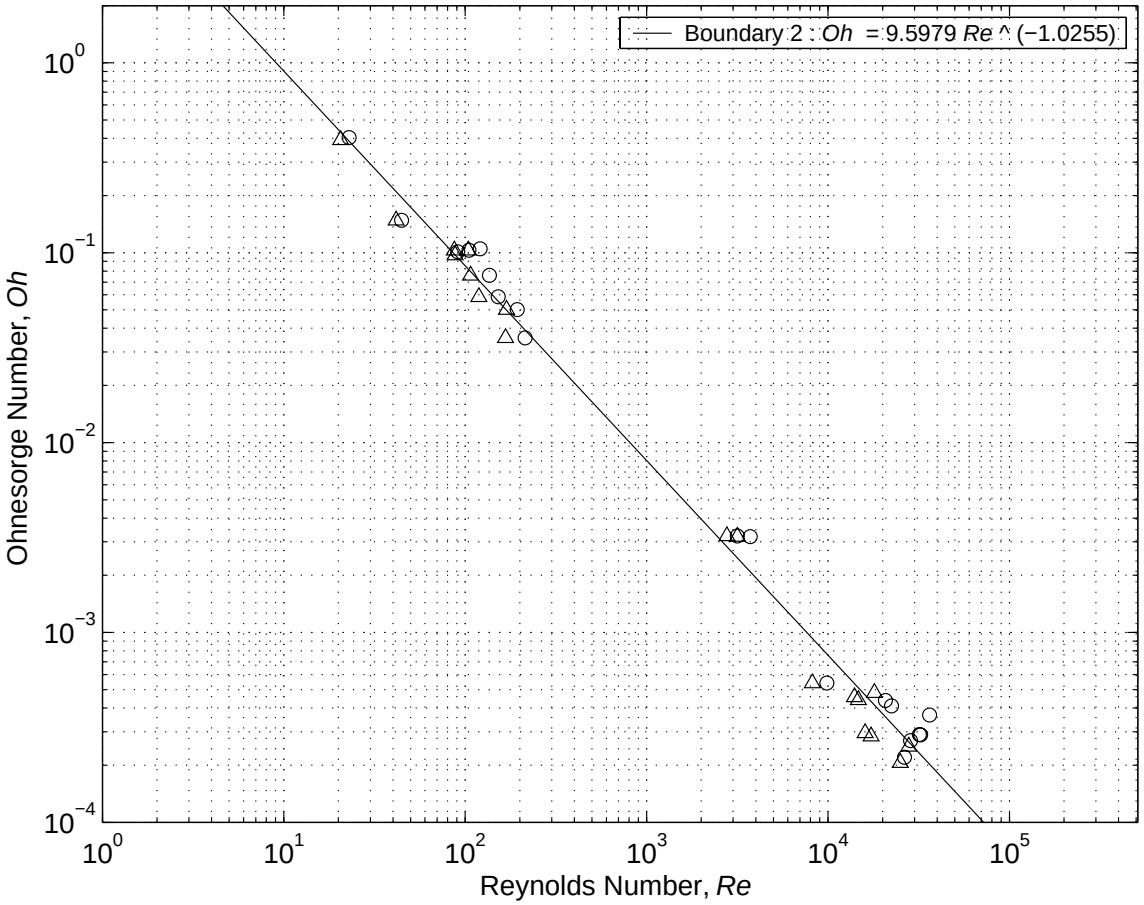

Figure 3.22 Boundary 2 between instability regimes 2 and 3 . Δ, sinuous wave breakup at instability regime 2. o, filament core breakup at instability regime 3.

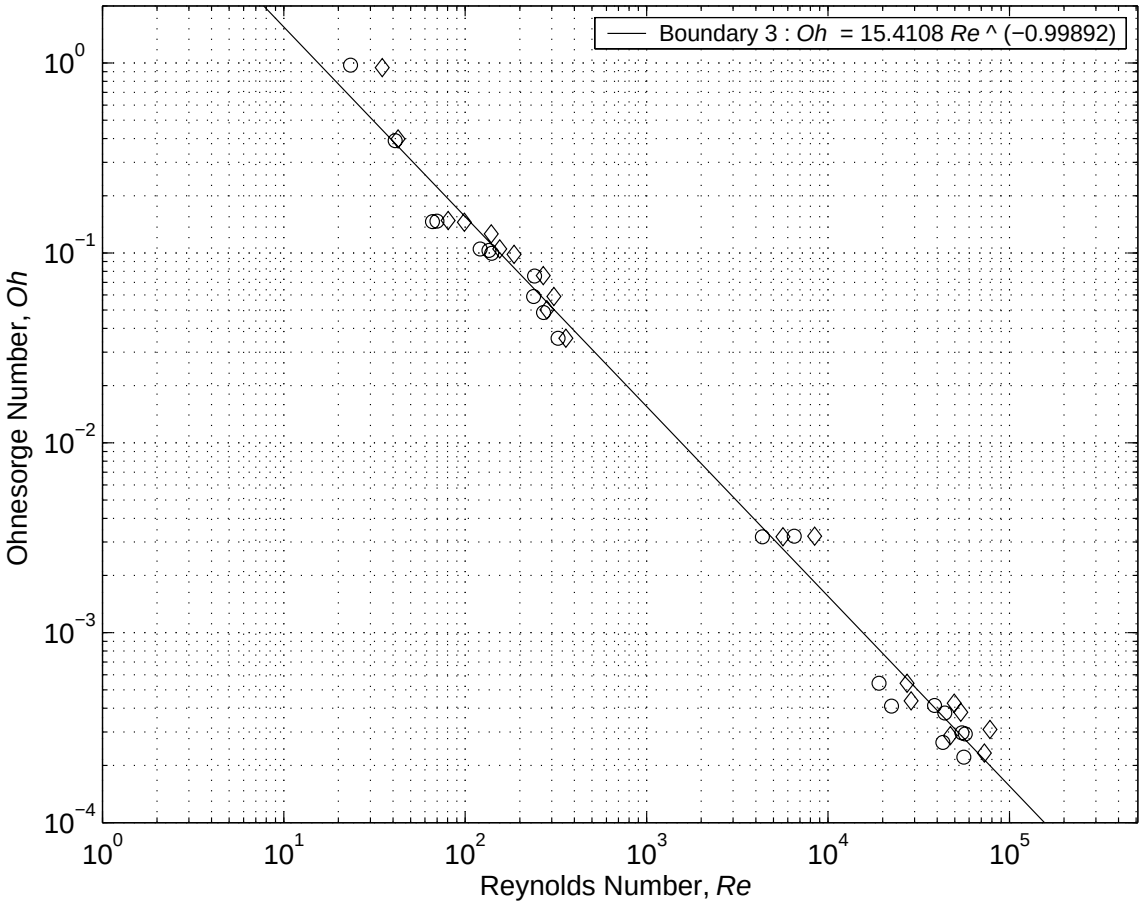

Figure 3.23 Boundary 3 between instability regimes 3 and 4. o, filament core breakup at instability regime 3; ◊, wave atomization at instability regime 4.

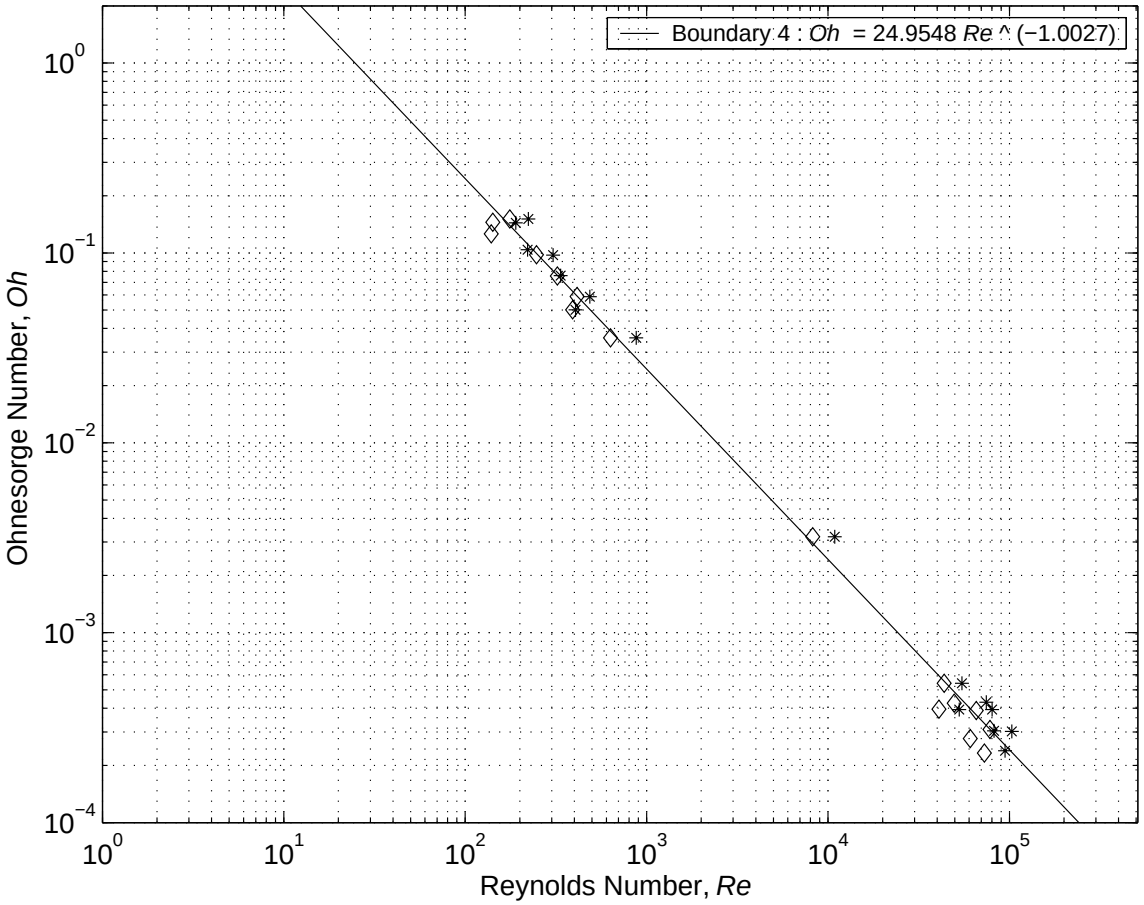

Figure 3.24 Boundary 4 between instability regimes 4 and 5. ◊, wave atomization at instability regime 4. *, full atomization at instability regime 5.

CHAPTER 4 EXPERIMENTAL RESULTS: JET BREAKUP LENGTH

4.1 Chapter Overview

This chapter examines jet breakup length, which is the distance from the discharge orifice to the point where discrete droplets are formed. The effects of viscosity of the dispersed phase, orifice properties and ambient fluids on the variation of jet breakup length with increasing jet velocity or (Weber number) are discussed in section 4.3. A summary of some of the breakup length data for instability regimes 1 to 3 is provided in section 4.4.

4.2 Jet Breakup Length Study

Earlier studies have observed that jet breakup length evolves as jet velocity increases, typically increasing to a maximum, then falling as atomization is approached (Grant & Middleman, 1966; Kitamura & Takahashi, 1986). The present digital video records were employed to estimate jet breakup length, *BL* and to determine how *BL* varies as test conditions change. This analysis was complicated by the fact that small variations in flow rate were observed to result in breakup occurring over a range of distances from the orifice. This introduces uncertainty into the measured values of *BL*. An example of the problem is shown in Figure 4.1 where *BL* varies about 80% in three video frames taken during the same test. In Figure 4.2, *BL* has two different values depending on whether a primary or satellite droplet is formed. To address this problem, multiple frames of the digital video records were analyzed and the average values of *BL* were calculated from

multiple breakup events. In Figure 4.3 the vertical height of the continuous jet filament is plotted against time for a period of 7.1 seconds corresponding to 107 consecutive video frames. About 4 primary droplets and 3 satellite droplets were formed during this period, each with their own *BL*. These types of *BL* data were used to calculate the average values.

A total of 3298 video frames from 83 test runs for 10 out of the 21 cases were analyzed to determine average values of breakup length, $\overline{BL}$. Figures 4.4 to 4.13 provide representatives of the 10 test cases in order of ascending flow rate. The run number corresponding to that frame, $\overline{BL}$, numbers of values (Counts) of *BL* used to calculate $\overline{BL}$, instability regime (*IR*), and jet velocity (U_{jet}) are given below each frame.

Jet breakup lengths were determined only for instability regime 1, 2 and part of 3 since, in the high velocity portion of regime 3 and instability regimes 4 and 5, dense clouds of fine droplets on the perimeter of the jet obscures its interior and makes it impossible to estimate *BL* from the video data. Breakup length analysis was not performed for the liquid CO_2 injection tests due to complications associated with the formation of the hydrate tube on the jet surface in instability regimes 1 and 2. These tubes essentially constituted a new nozzle on top of the original orifice, with an unknown effective diameter. Moreover, the end of the tube was not always evident and makes it impossible to estimate *BL*.

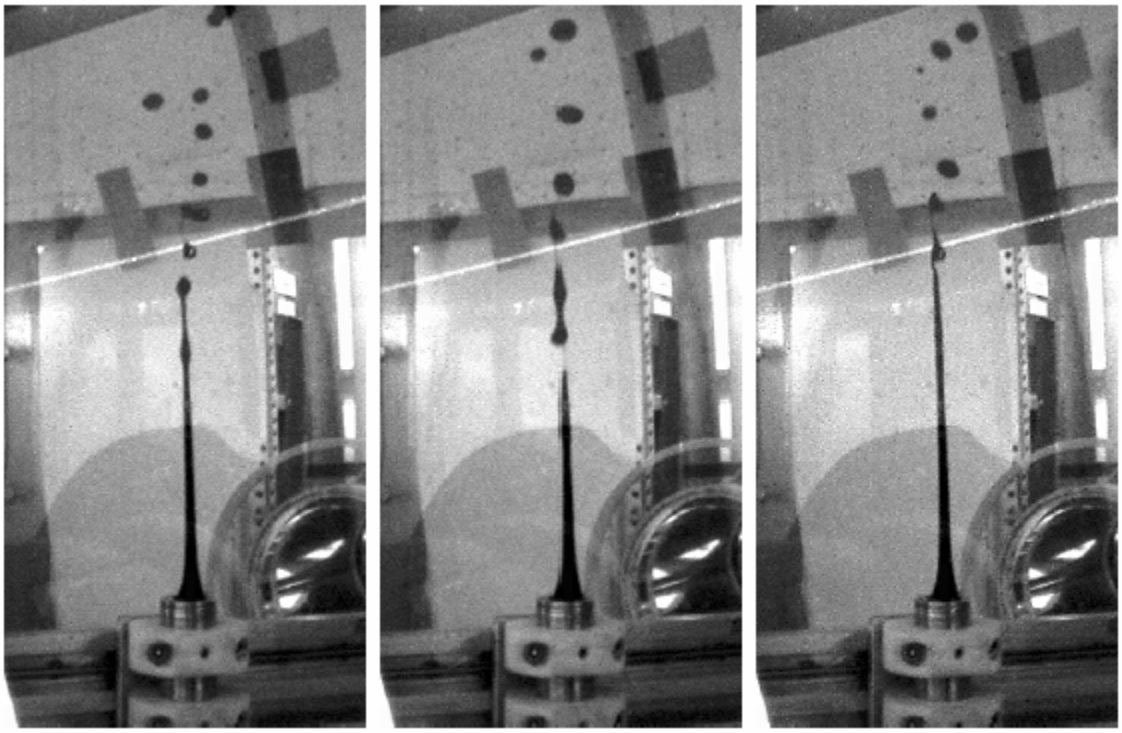

Figure 4.1 Variation in jet breakup length at a fixed test condition. The video frames show Platform Gail oil being injected into water through a 5 mm diameter sharp edge orifice. The bright diagonal line near the top of the pictures is the PDPA laser beam. (Masutani & Adams, 2000).

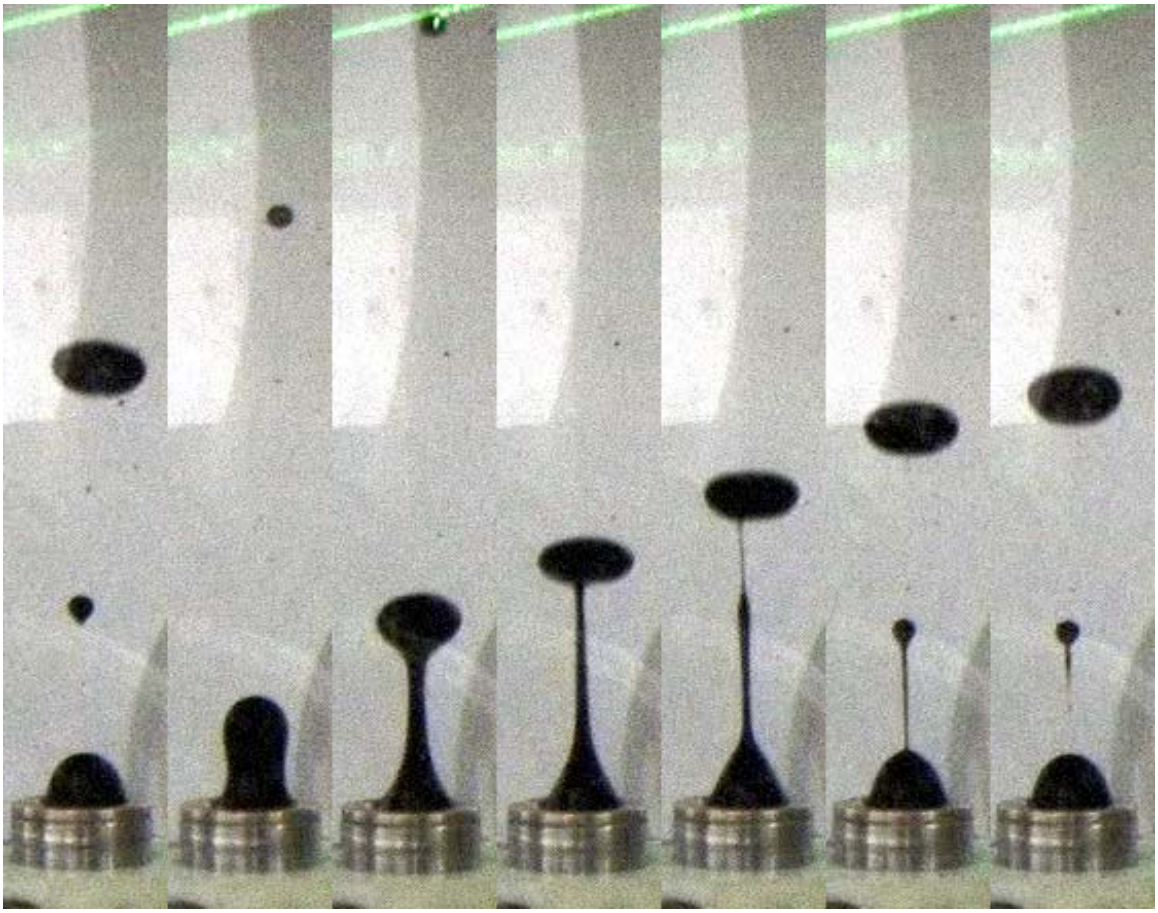

a b c d e f g

Figure 4.2 Variable jet breakup length for primary and satellite droplets. Video frames from test PGS05WTRR2; high viscosity Platform Gail crude oil injection into tap water through a sharp edge 5 mm diameter orifice.

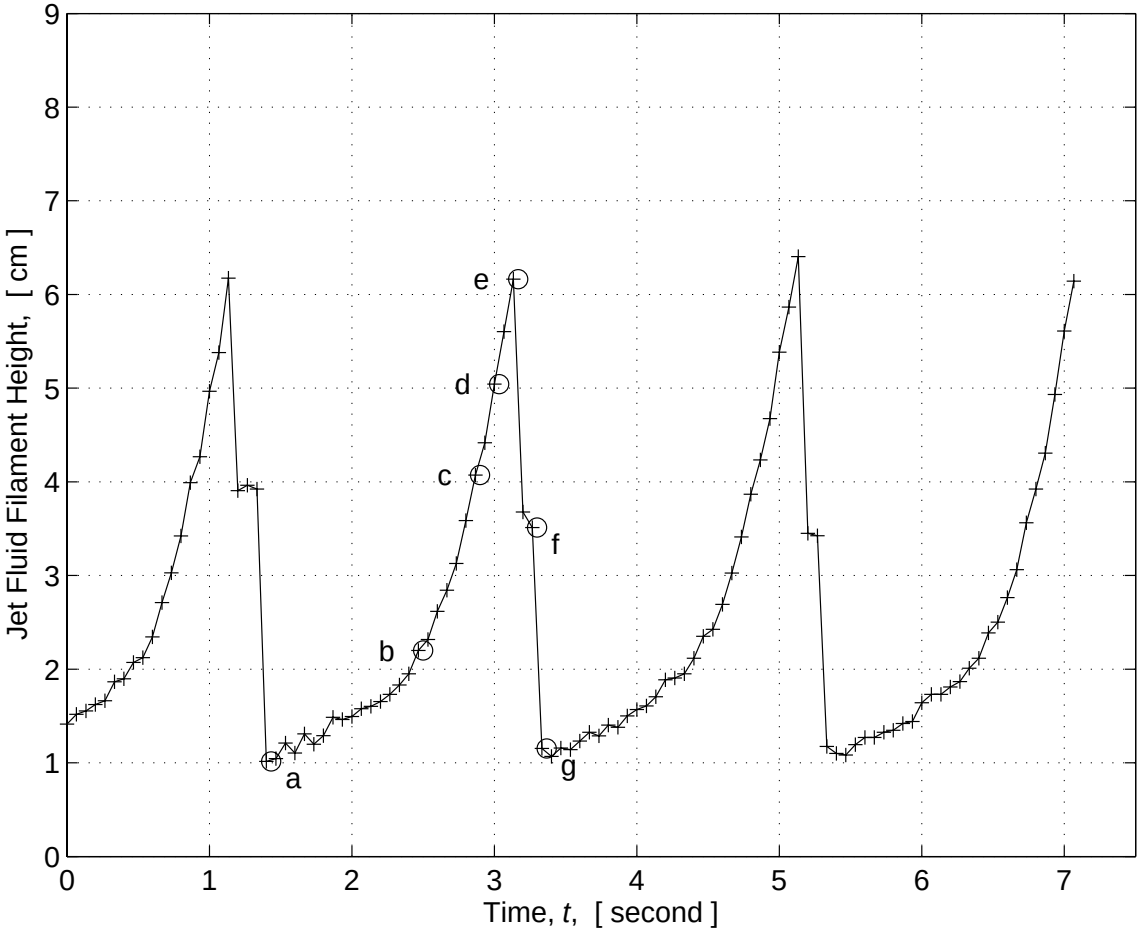

Figure 4.3 Height of jet fluid filament as a function of time corresponding to run shown in Figure 4.2. Circles represent frames a to f shown in Figure 4.2.

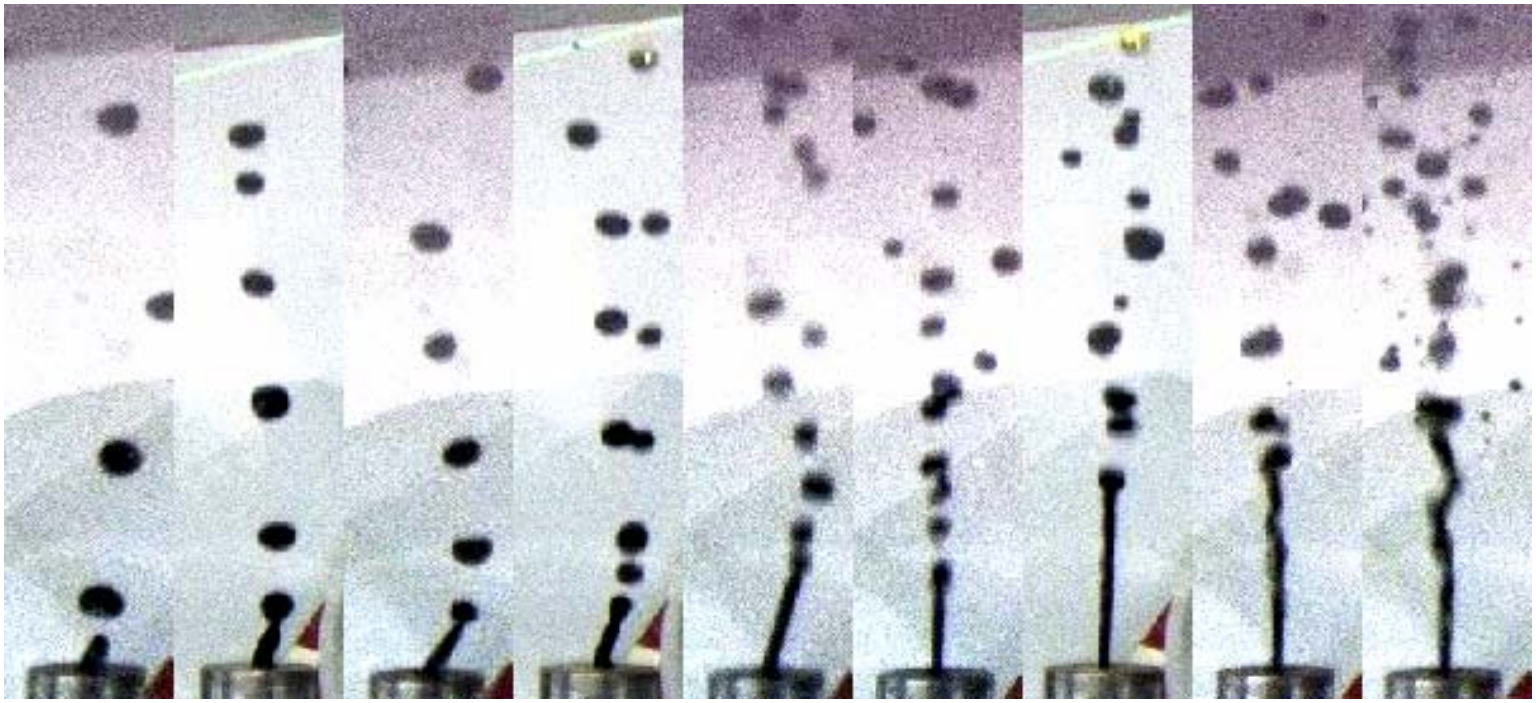

Run No.	9	1	10	2	11	12	3	13	14	
$\overline{BL}$	10.74	17.05	19.54	19.42	28.13	40.97	39.6	46.97	52.4	mm
Counts	52	31	30	40	39	29	45	20	6	
IR	1	1	1	1	1	2	2	2	3	
U_{jet}	0.27	0.31	0.34	0.4	0.44	0.72	0.75	0.97	1.23	m/s

Figure 4.4 Variation of jet breakup length as jet velocity increases. Case GES02WTR. Genesis crude oil injection into water from a 2 mm sharp edge orifice. The outside diameter of the nozzle is 25.4 mm.

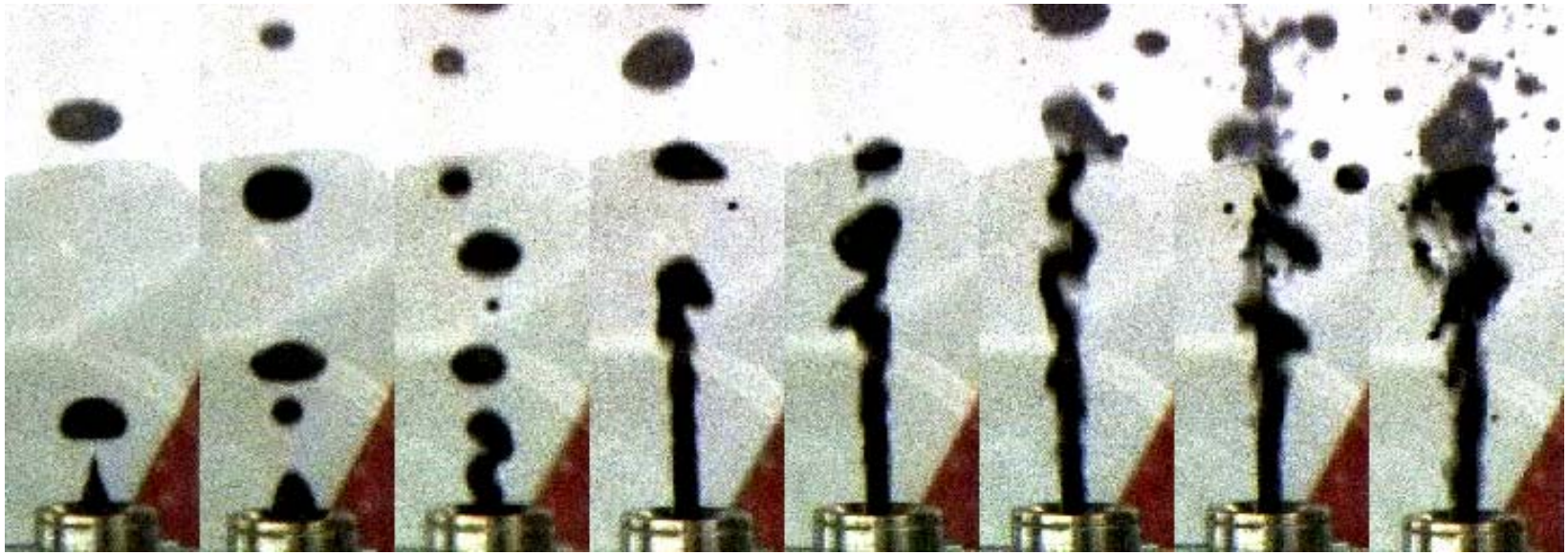

Run #	5	6	7	8	9	10	11	12	
$\overline{BL}$	10.24	16.13	28.54	46.23	67.65	82.88	73.34	78.75	mm
Counts	69	44	30	59	47	28	18	21	
IR	1	1	1	2	2	2	3	3	
U_{jet}	0.08	0.16	0.25	0.36	0.44	0.64	0.73	0.85	m/s

Figure 4.5 Variation of jet breakup length as jet velocity increases. Case GES05WTR. Genesis crude oil injection into water from a 5 mm sharp edge orifice. The outside diameter of the nozzle is 25.4 mm.

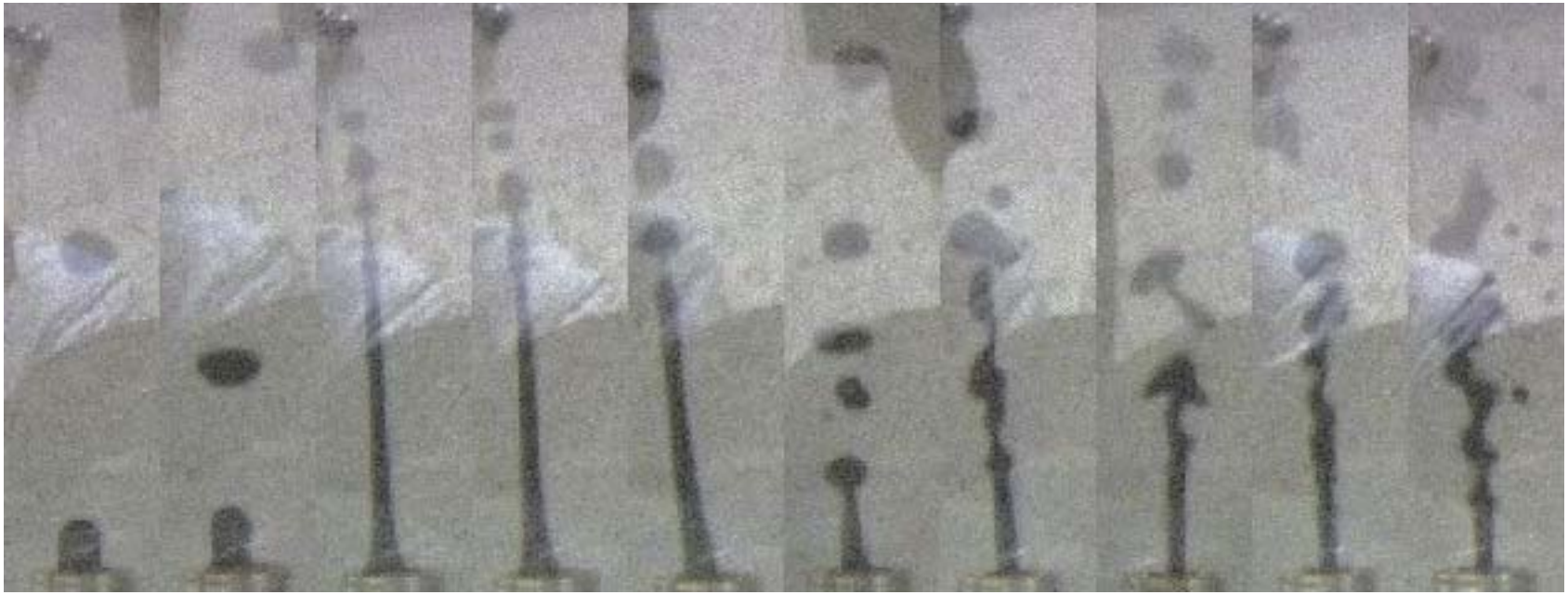

Run #	5	6	7	8	9	20	10	19	11	12	
$\overline{BL}$	14.96	18.46	96.36	88.05	62.6	35.37	61.32	66.13	81.1	71.4	mm
Counts	58	58	17	47	29	24	41	31	38	11	
IR	1	1	1	1	1	1	2	2	2	3	
U_{jet}	0.06	0.09	0.15	0.17	0.24	0.25	0.35	0.42	0.45	0.58	m/s

Figure 4.6 Variation of jet breakup length as jet velocity increases. Case MAS05WTR. Mars TLP crude oil injection into water from a 5 mm sharp edge orifice. The outside diameter of the nozzle is 25.4 mm.

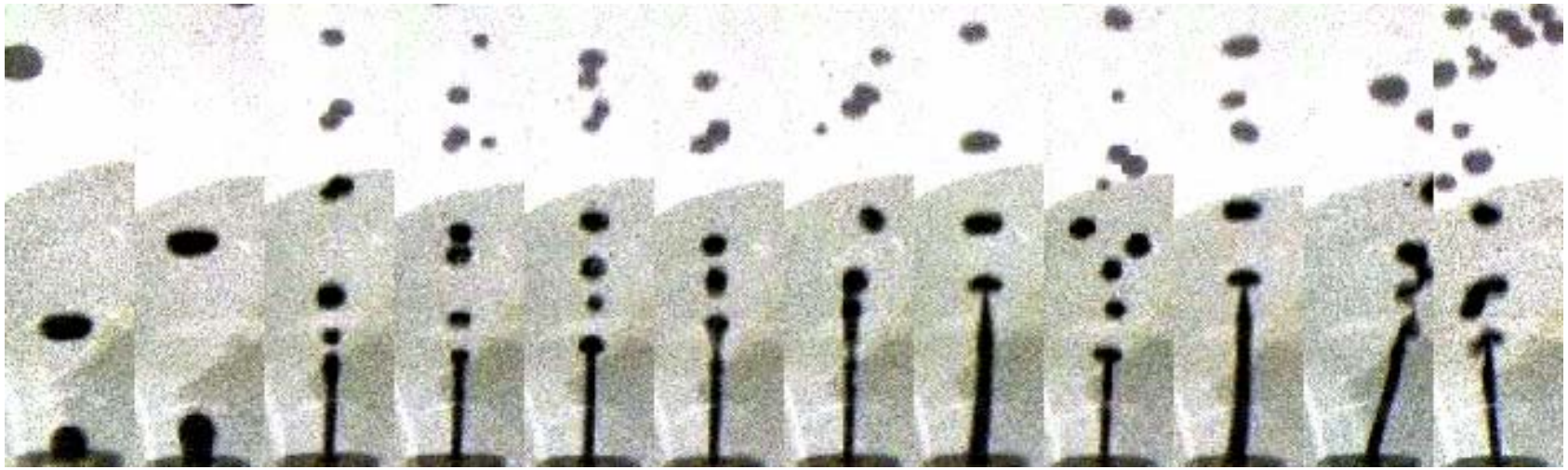

Run #	6	7	18	13	17	14	15	19	16	8	9	10	
$\overline{BL}$	12.83	12.33	24.88	33.65	32.93	32.46	31.88	42.87	35.9	47.81	43.43	32.94	mm
Counts	45	43	26	25	36	35	38	45	28	25	20	27	
IR	1	1	1	1	1	1	1	1	1	1	2	3	
U_{jet}	0.29	0.33	0.33	0.36	0.39	0.41	0.52	0.62	0.63	0.64	0.84	1.07	m/s

Figure 4.7 Variation of jet breakup length as jet velocity increases. Case MAS02WTR. . Mars TLP crude oil injection into water from a 2 mm sharp edge orifice. The outside diameter of the nozzle is 25.4 mm.

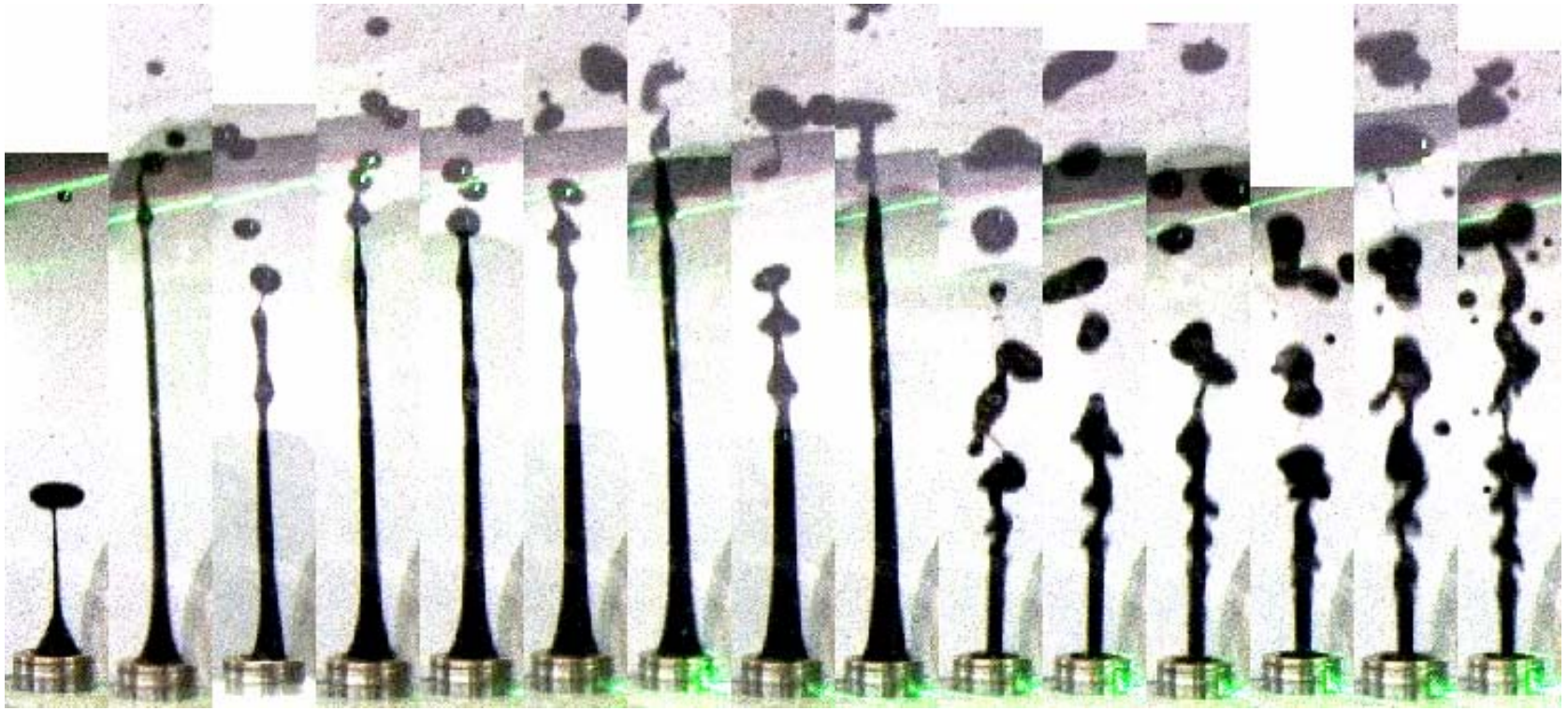

Run #	2	3	1	4	5	6	14	7	22	21	13	9	15	20	12	
$\overline{BL}$	25.91	160.67	120.17	145.3	140.32	147.6	190.23	139.35	191.18	96.36	97.49	88.74	81.95	90.66	86.59	mm
Counts	107	81	138	19	29	4	28	37	43	61	70	27	21	44	67	
IR	1	1	1	1	1	2	2	2	2	2	2	2	3	3	3	
U_{jet}	0.04	0.07	0.12	0.13	0.19	0.29	0.34	0.4	0.44	0.59	0.61	0.62	0.68	0.7	0.72	m/s

Figure 4.8 Variation of jet breakup length as jet velocity increase. Case PGS05WTR. Platform Gail crude oil injection into water from a 5 mm orifice. The outside diameter of the nozzle is 25.4 mm.

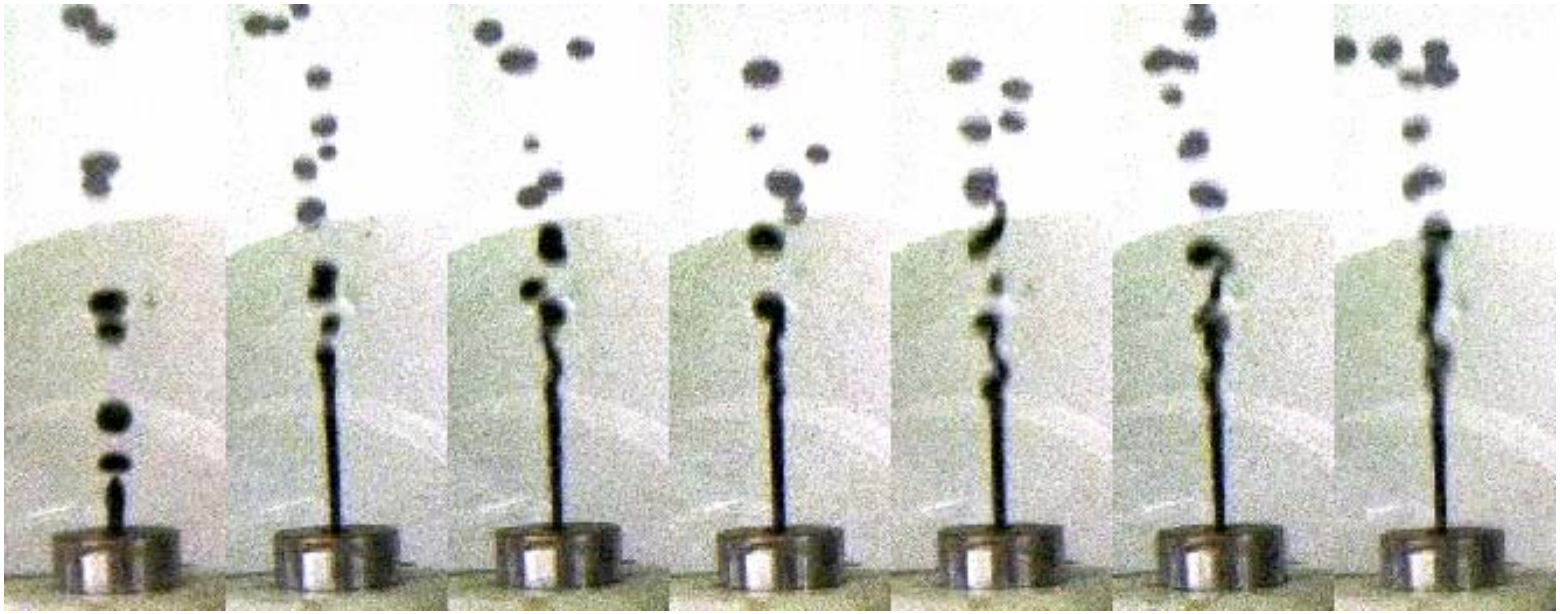

Run #	5	14	13	6	7	12	11	
$\overline{BL}$	16.10	36.48	43.67	46.51	45.78	51.38	56.31	mm
Counts	59	31	32	28	30	37	40	
IR	1	2	2	2	2	2	2	
U_{jet}	0.34	0.35	0.58	0.64	0.78	0.87	1.01	m/s

Figure 4.9 Variation of jet breakup length as jet velocity increases. Case NSS02WTR. Neptune SPAR crude oil injection into water from a 2 mm orifice. The outside diameter of the orifice is 25.4 mm.

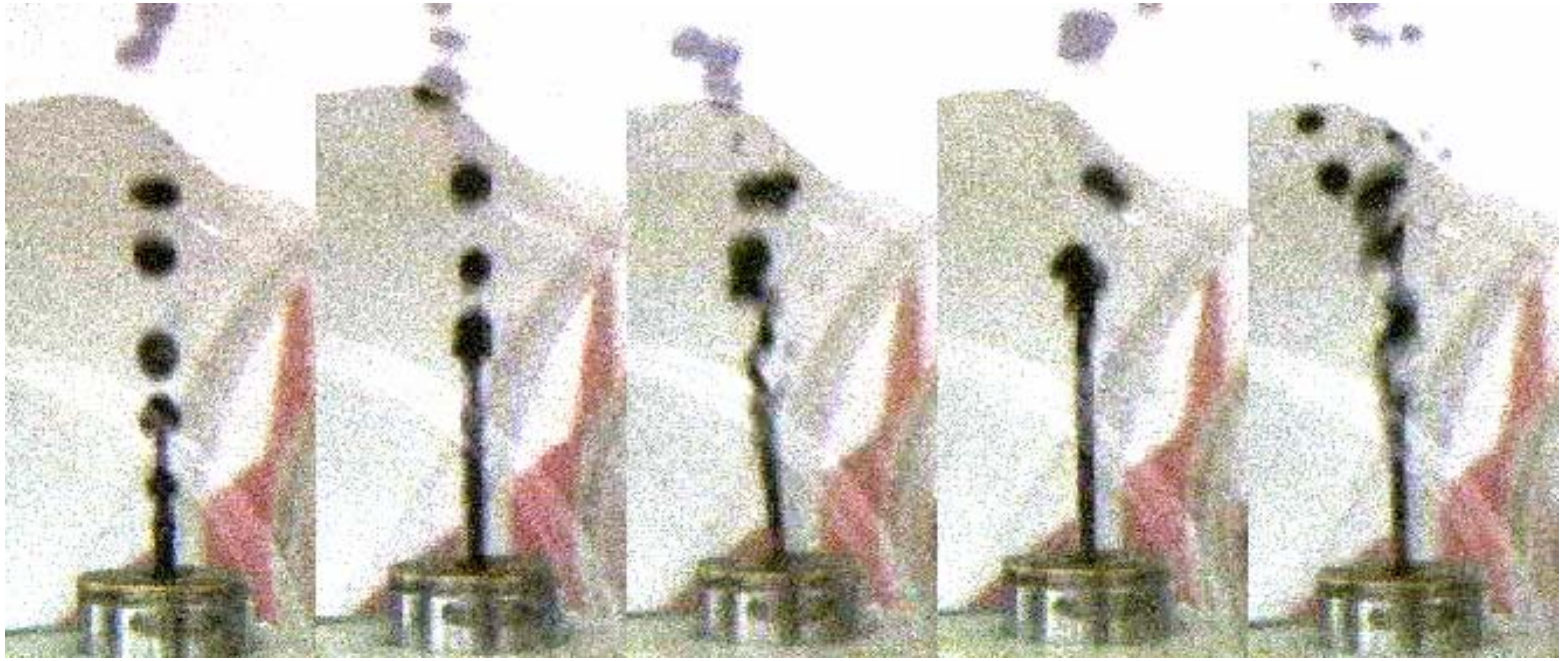

Run #	5	6	11	7	10	
$\overline{BL}$	25.39	34.41	38.79	37.91	39.47	mm
Counts	30	25	13	20	11	
IR	1	1	2	2	2	
U_{jet}	0.32	0.45	0.75	0.86	1.06	m/s

Figure 4.10 Variation of jet breakup length as jet velocity increases. Case NSS02WNR. Neptune SPAR crude oil injection in to sea water from a 2 mm orifice. The outside diameter of the orifice is 25.4 mm.

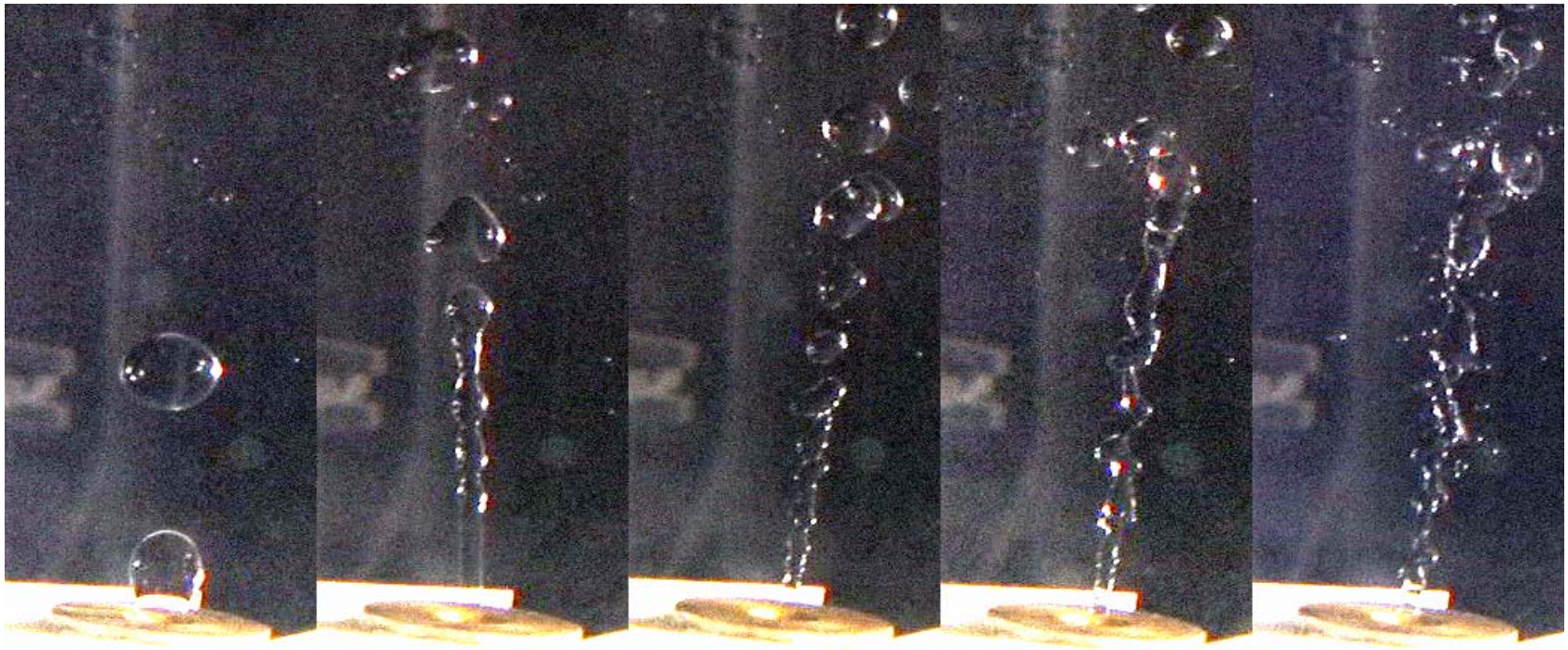

Run #	14	15	16	17	18	
$\overline{BL}$	19.08	38.23	31.21	34.22	35.72	mm
Counts	109	98	100	126	18	
IR	1	1	2	2	2	
U_{jet}	0.14	0.49	0.74	0.91	1.12	m/s

Figure 4.11 Variation of jet breakup length as jet velocity increases. Case SFS02WTRR. Silicone fluid injection into water from a 2 mm orifice. The outside diameter of the nozzle is 25.4 mm.

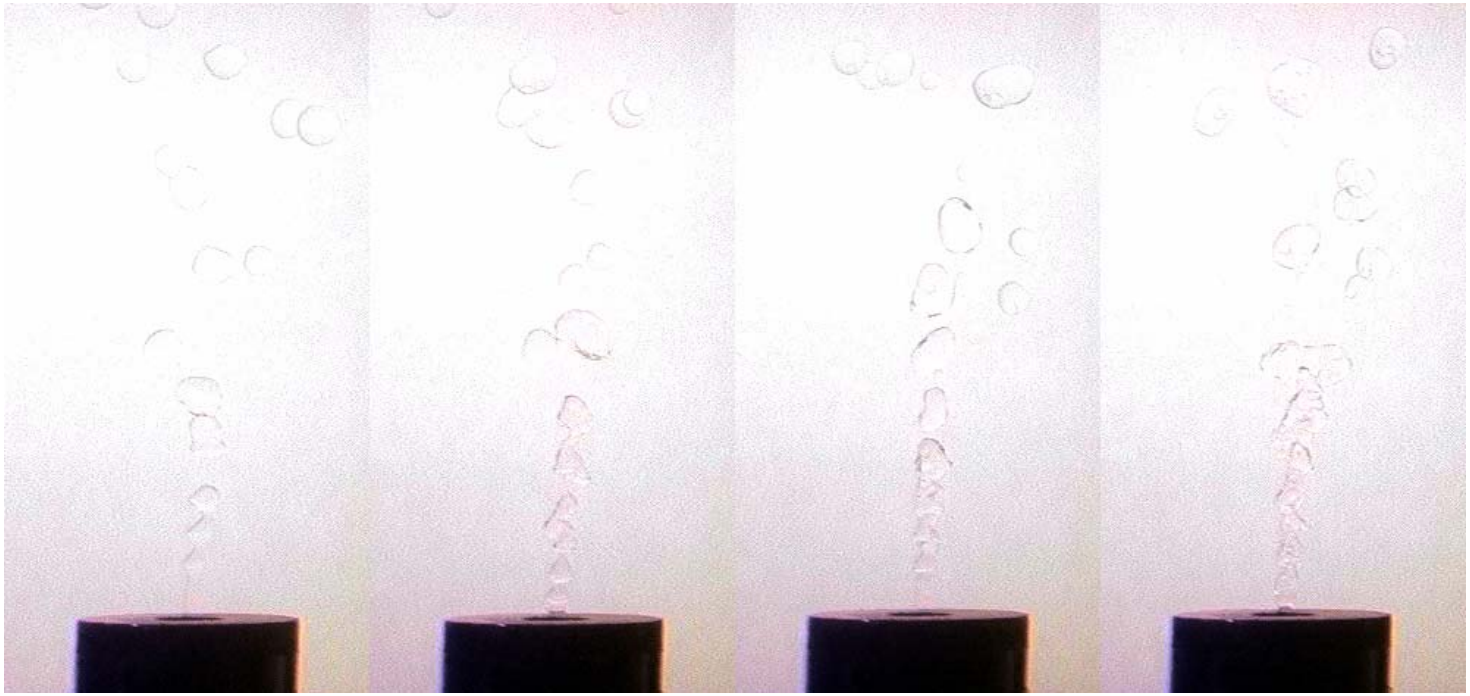

Run #	8	10	9	11	
$\overline{BL}$	15.58	22.24	22.70	30.98	mm
Counts	16	26	18	21	
IR	1	2	2	2	
U_{jet}	0.28	0.53	0.65	0.91	m/s

Figure 4.12 Variation of jet breakup length as jet velocity increases. Case LSS02WTRR. Low viscosity silicone fluid injection into tap water from a 2 mm sharp edge orifice. The outside diameter of the nozzle is 25.4 mm.

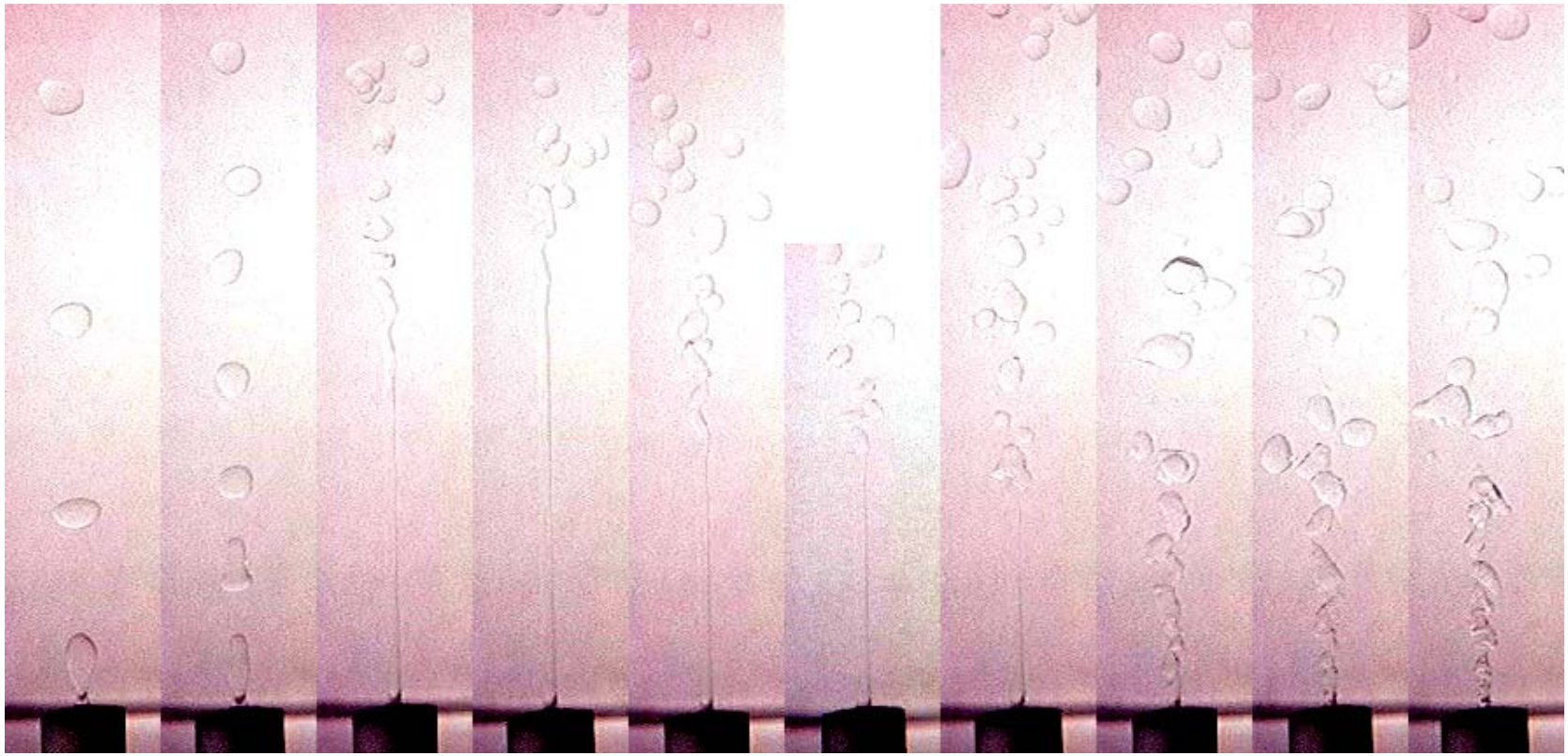

Run #	15	14	2	9	3	1	4	5	6	7	
$\overline{BL}$			72.91	68.08	56.56	54.88	49.91	24.31	27.66	28.20	mm
Counts			41	52	32	52	30	33	20	19	
IR	1	1	1	2	2	2	2	2	2	2	
U_{jet}	<0.28	<0.28	0.1658	0.166	0.31	0.33	0.52	0.70	0.80	1.03	m/s

Figure 4.13 Variation of jet breakup length as jet velocity increases. Case LST02WTRR. Low viscosity silicone fluid injection into water from a 2 mm tube nozzle. The outside diameter of the nozzle is 12.7 mm (0.5 inch).

4.3 Effects of Viscosity, Orifice Properties, and Ambient Fluid on Jet Breakup Length

The previous section discussed the methods used to estimated average jet breakup length from analysis of video data and presented values of $\overline{BL}$ for oil and silicone fluid injection into water, primarily for conditions corresponding to instability regimes 1 and 2. In this section, these results are discussed and analyzed to understand the effects of various parameters on jet breakup length.

4.3.1 Viscosity Effect

As mentioned in Chapter 2, the viscosity of the jet fluids used in the present experiments ranged over three orders of magnitudes. Figures 4.14 and 4.15 plot the dimensionless average breakup length, $\overline{BL}/D$, against Weber number for these different jet fluids. In Figure 4.14, the curves represent three different crude oils with kinematic viscosities of 14, 18 and 158 cs. The oils were injected into tap water from the same 5 mm sharp edge orifice. The oil temperature [°C] differed by ≤ 5%; water temperature [°C] varied by ≤ 9.5%. While there is significant scatter at low *We*, a number of observations can be made. In instability regime 1 and at the lower velocity portion of regime 2, the effect of viscosity can be large (note that, according to the results of Chapter 3, the transition between regimes 1 and 2 occur at $We \cong 25$). High viscosity results in the occurrence of long "threads" of jet fluid stretching upward before breakup with corresponding large values of $\overline{BL}/D$. The scatter reflects the behavior shown in Figure 4.1. As velocity

increases in regime 2, the effect of viscosity is reduced and near the transition to instability regime 3, the three curves approach a common value of $\overline{BL}/D \sim 15$. Similar results were obtained in the silicone fluid injection tests. As seen in Figure 4.15, breakup lengths were longer for the high viscosity silicone fluid (ν = 20 cs) in regime 1. Average breakup lengths for both silicone fluids appear to approach a common value near the transition to instability regime 3, suggesting a reduction in the influence of viscosity. The asymptotic value of $\overline{BL}/D$ is slightly higher than in Figure 4.14, but this may reflect a number of differences in the tests besides jet fluid, for instance, whether the length scale used to nondimensionalize $\overline{BL}$, in this case, *D*, is truly appropriate.

4.3.2 Orifice Properties Effects

Results of the experiments suggest a strong influence of orifice geometry (for the diameter) on jet breakup length. In Figure 4.16, $\overline{BL}/D$ is compared for low viscosity silicone fluid injection from tube and sharp edge orifice nozzles with D = 2 mm. The tube nozzle permits the development of a boundary layer velocity profile at the point of separation of the jet while the sharp edge orifice destroys the boundary layer. The initial velocity profiles of the two jets are therefore different, and this appears to affect the stability of the liquid-liquid jet in regime 1 and part of regime 2. As in the case of viscosity, orifice geometry has a decreasing influence as the transition to regime 3 is approached.

The effect of orifice diameter is examined in Figures 4.17 and 4.18. These data are for crude oil injections from sharp edge orifices with D = 2 mm and 5 mm. $\overline{BL}/D$ is

generally larger for the smaller orifice. Similar results were observed by Meister and Scheele (1969) for heptane injection into water with 5 nozzles with inside diameters ranging from 0.813 to 2.54 mm. This may reflect limitations in employing *D*, the orifice diameter, and initial transverse length scale, to non-dimensionalize $\overline{BL}$.

4.3.3 Ambient Fluid Effect

Figure 4.19 provides information of the effect of ambient fluid on jet breakup length. These data on $\overline{BL}/D$ versus *We* correspond to Neptune SPAR crude oil injection from a 2 mm sharp edge orifice into tap water and natural surface seawater with salinity of $35‰_0$. The average temperatures of the tap and sea water differed by 0.81 °C in these tests; the temperatures of the crude oil varied by 1.3 °C. $\overline{BL}/D$ appears to be smaller for the seawater case by 20% to 30%. Smaller $\overline{BL}/D$ implies faster growth of the jet instability. It is not clear how the modest difference in ambient fluid properties influence breakup to the observed extent.

4.4 Non-dimensional Average Jet Breakup Length for Sharp Edge Orifices

Contours of the non-dimensional jet breakup length, $\overline{BL}/D$, plotted against Weber number, *We*, and Ohnesorge number, *Oh* , are presented in Figure 4.20 for the tests employing 2 mm and 5 mm ASME sharp edge orifices. The data correspond to instability regime 1, 2 and 3.

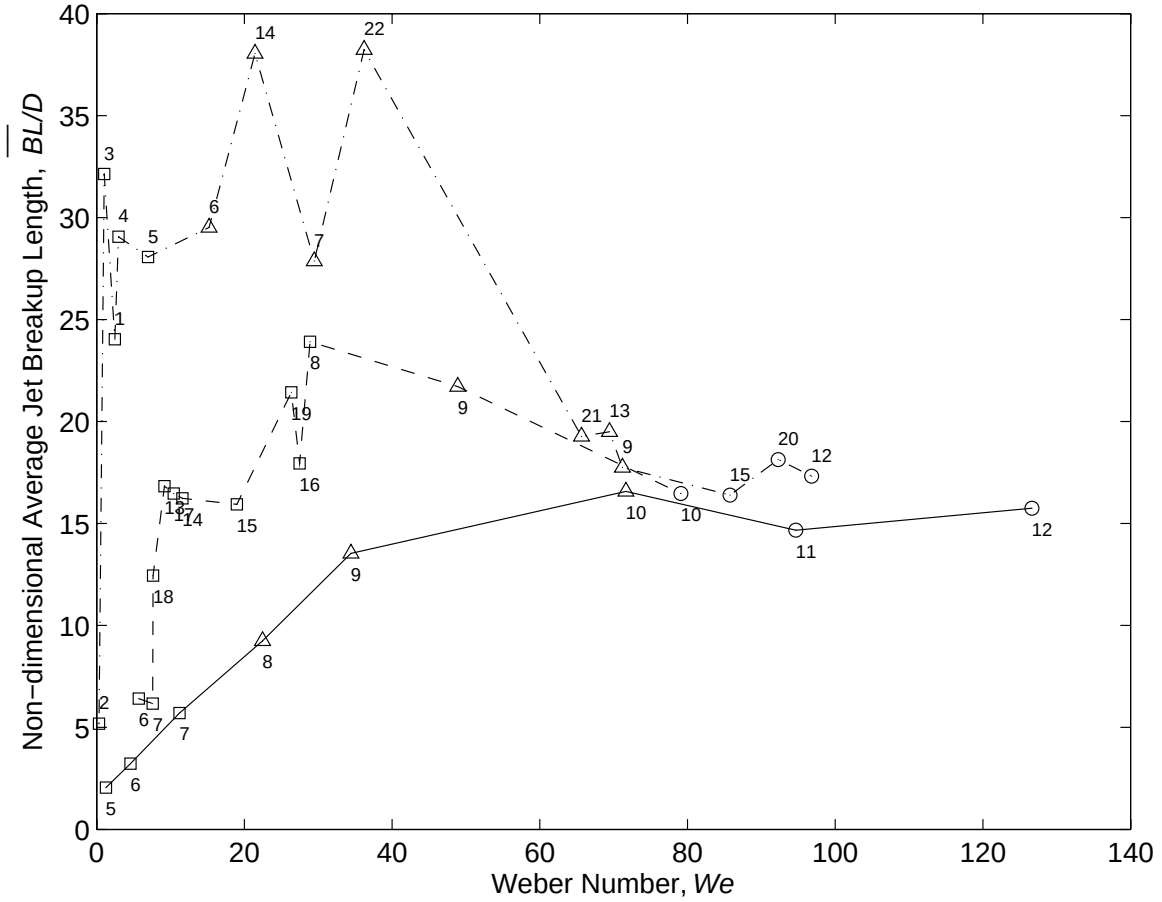

Figure 4.14 Effect of viscosity on the non-dimensional average jet breakup length. - - - - - , Case PGS05WTR, ν = 158 cs; - - - - - - Case MAS05WTR, ν = 18 cs; ——— Case GES05WTR, ν = 14 cs. □ , instability regime 1. Δ, instability regime 2. o, instability regime 3. The number next to the data point indicates the run number. D = 5 mm; injection of crude oil into tap water from a sharp edge orifice.

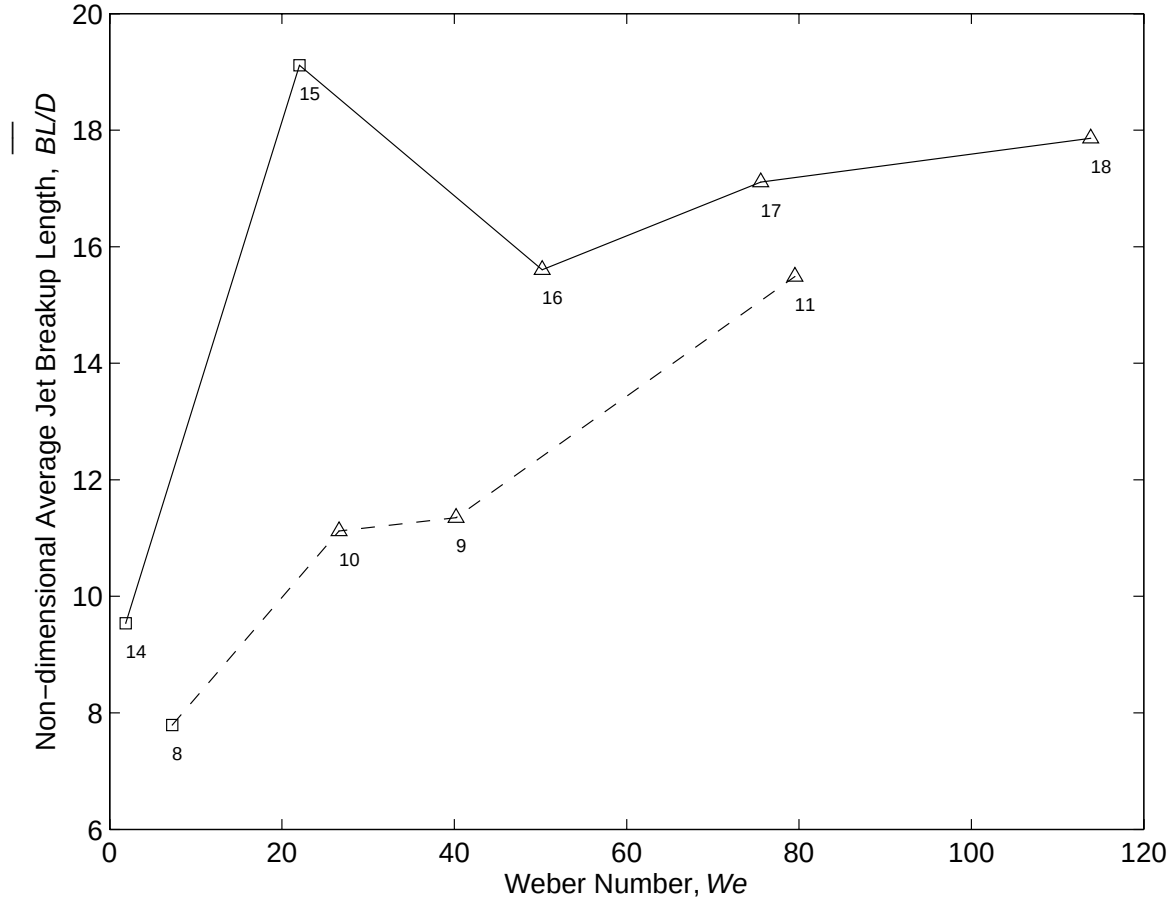

Figure 4.15 Effect of viscosity on the non-dimensional average jet breakup length. ——— Case SFS02WTR ν = 20 cs; - - - - - - Case LSS02WTR, ν = 0.65 cs. □ , instability regime 1. Δ, instability regime 2. The text next to the data point indicates the run number. D = 2 mm; injection of silicone fluid into tap water from a sharp edge orifice.

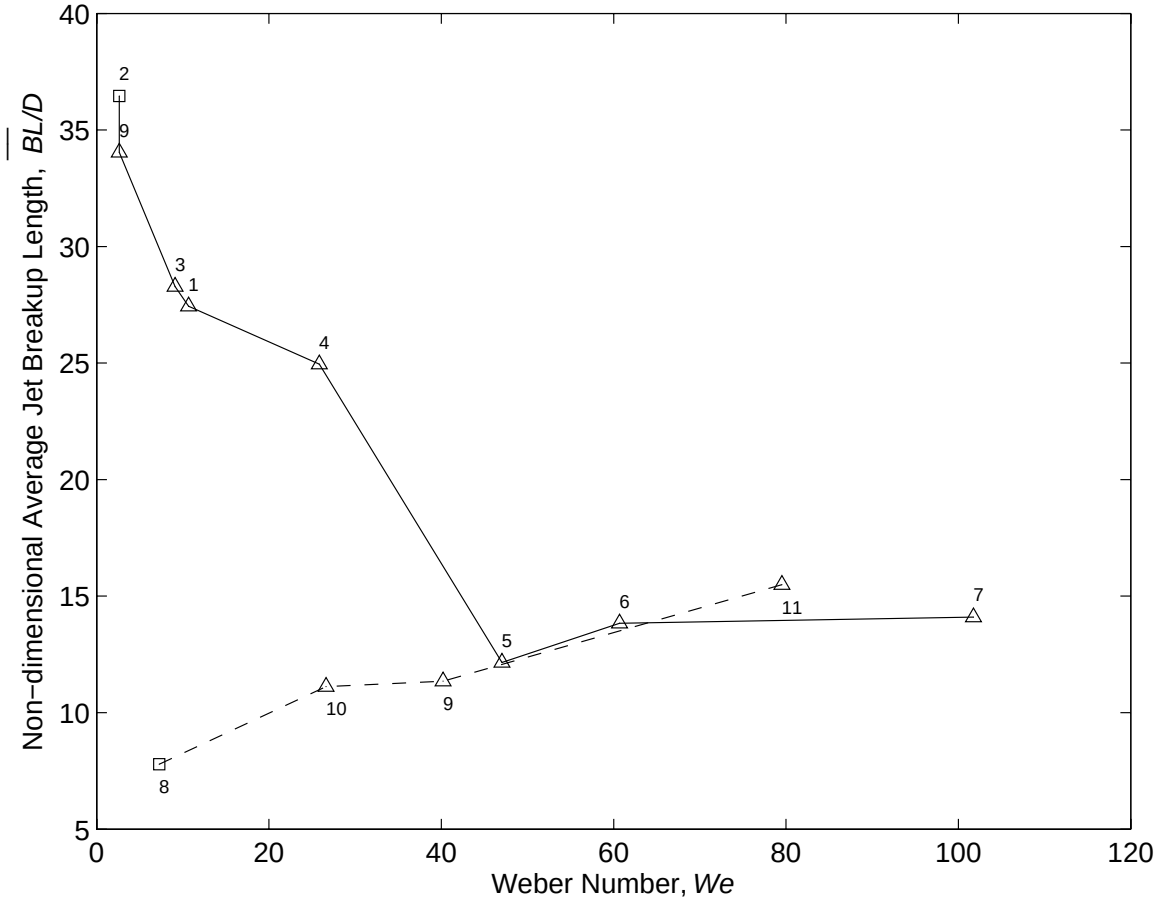

Figure 4.16 Effect of orifice geometry on non-dimensional average jet breakup length observed in low viscosity (ν = 0.65 cs) silicone fluid injection tests using tube and sharp edge orifices. _____ Case LST02WTR, tube nozzle; - - - - - - Case LSS02WTR, sharp edge orifice. □ , instability regime 1. Δ, instability regime 2. The text next to the data point indicates the run number. D = 2 mm.

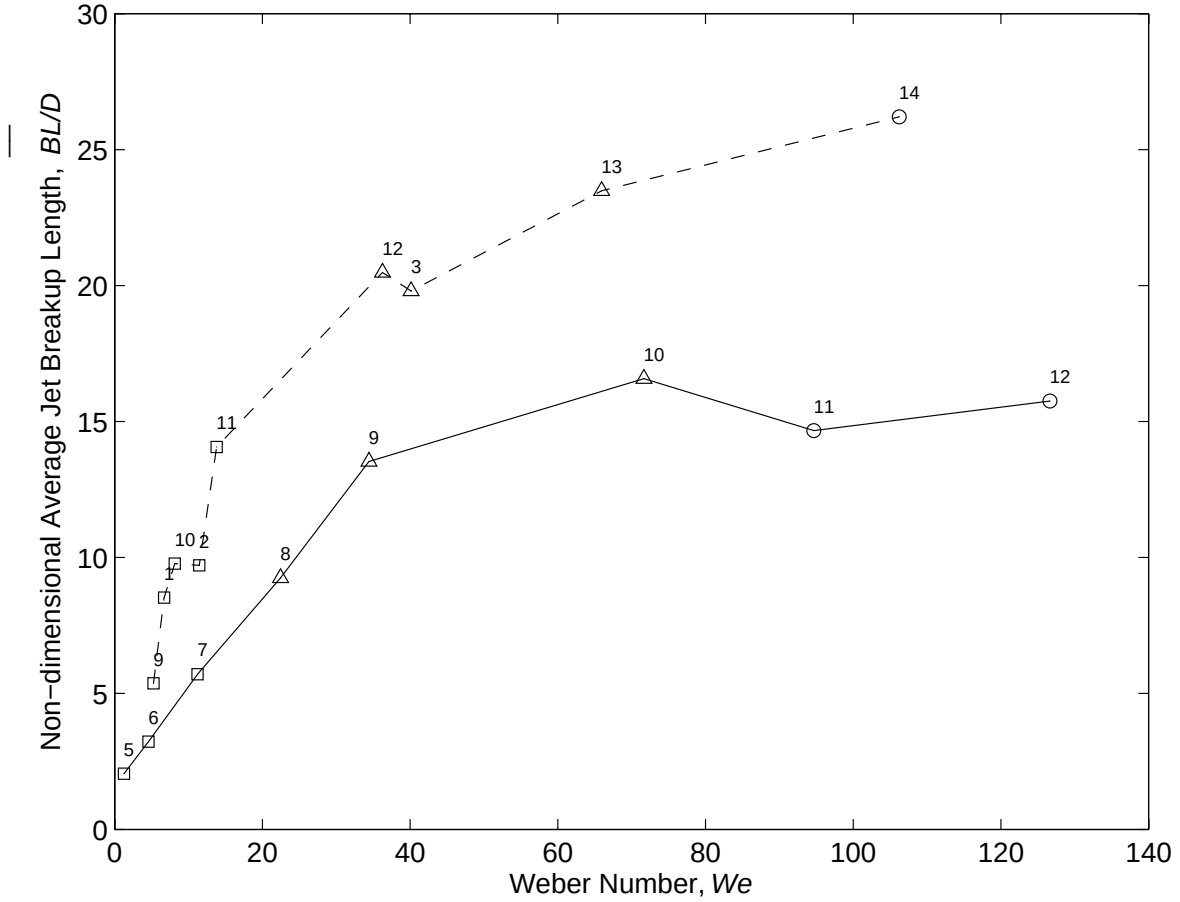

Figure 4.17 Effect of orifice diameter on non-dimensional average jet breakup length. Data are from Genesis crude oil injection into tap water from 2 mm and 5 mm sharp edge nozzle; different orifice diameters. ------Case GES02WTR; D = 2 mm. _____ Case GES05WTR; D = 5 mm. □ , instability regime 1. Δ, instability regime 2. o, instability regime 3. The number next to the data point indicates the run number.

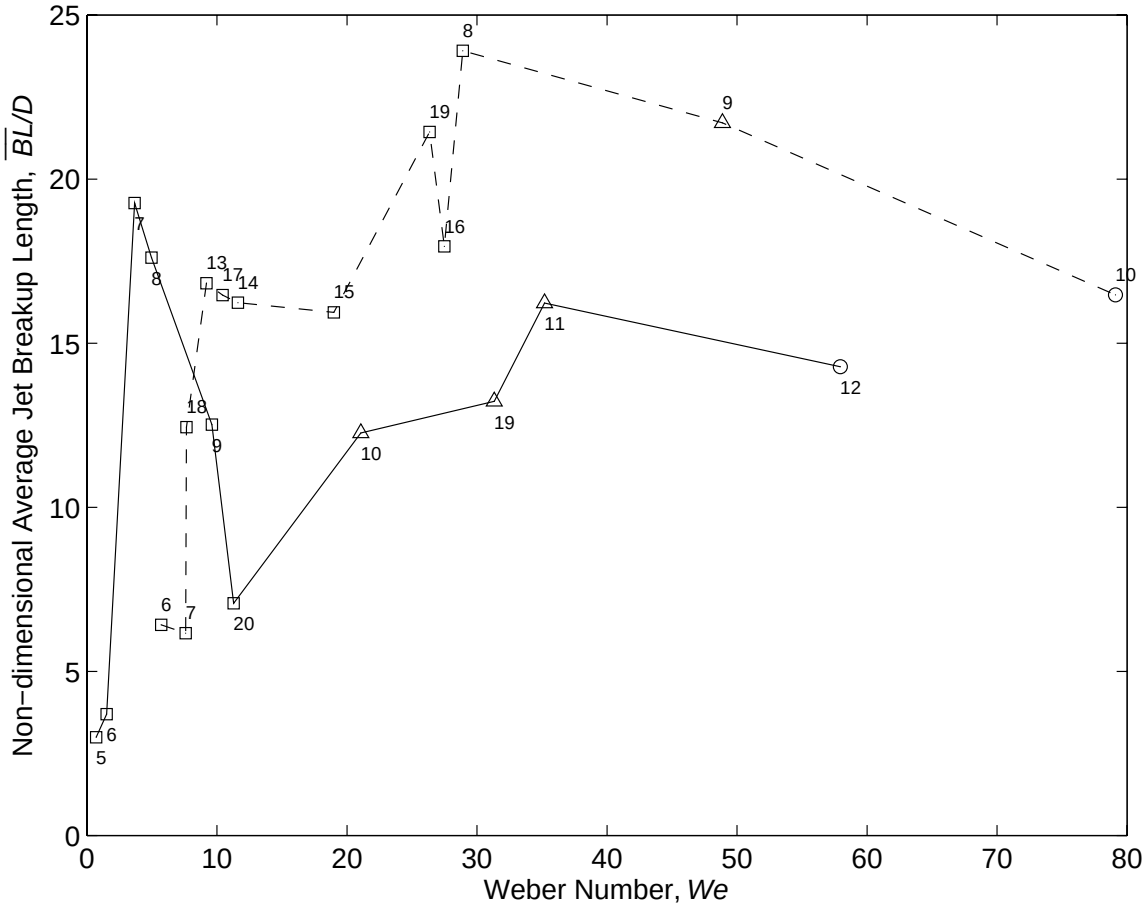

Figure 4.18 Effect of orifice diameter on non-dimensional average jet breakup length. Data are for Mars TLP crude oil injection into tap water from 2 mm and 5 mm sharp edge orifices. - - - - - -Case MAS02WTR; D = 2 mm. ——— Case MAS05WTR; D = 5 mm. □ , instability regime 1. Δ, instability regime 2. o, instability regime 3. The number next to the data point indicates the run number.

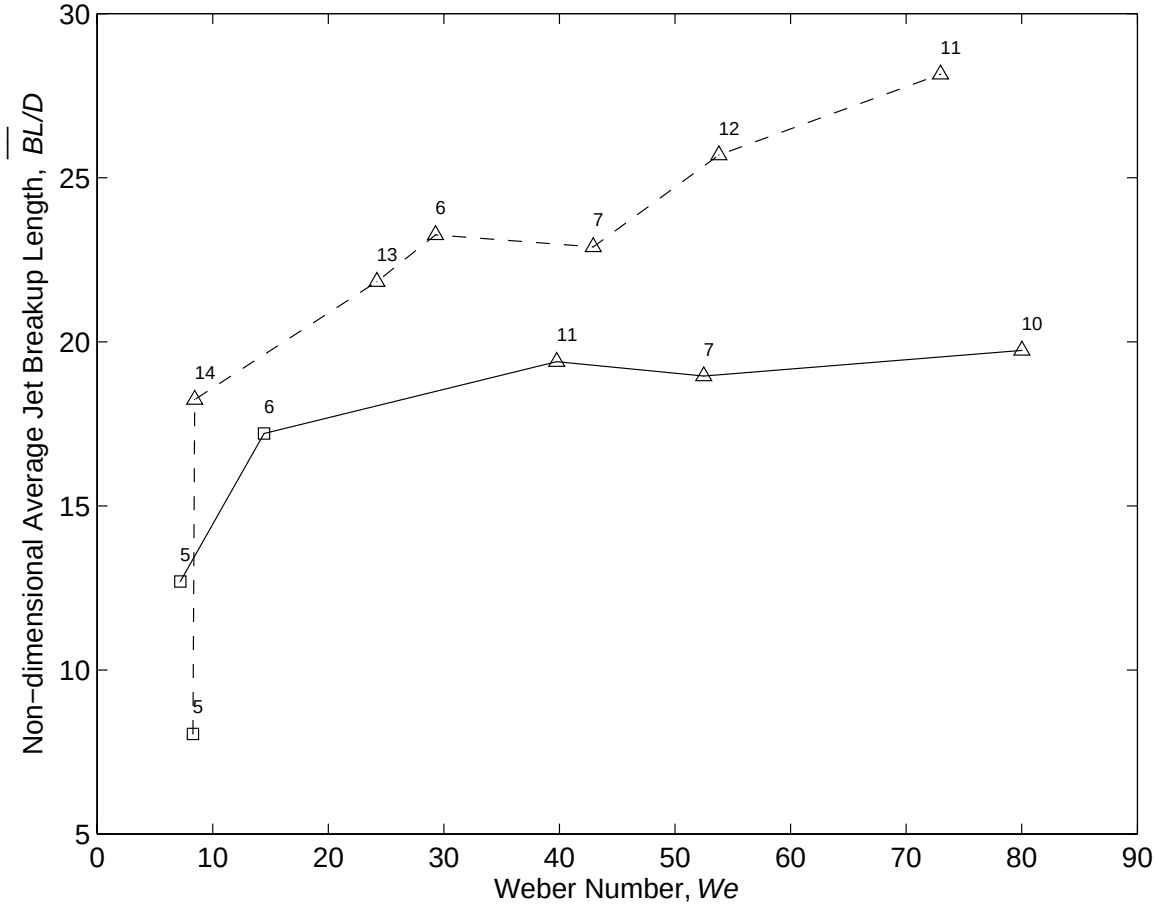

Figure 4.19 Effect of ambient fluid on dimensionless jet breakup length. Neptune Spar crude oil injection from a 2 mm sharp edge orifice. ------ Case NSS02WTR; tap water. _____Case NSS02WNR; natural surface sea water. □ , instability regime 1. Δ, instability regime 2. The text next to the data point indicates the run number.

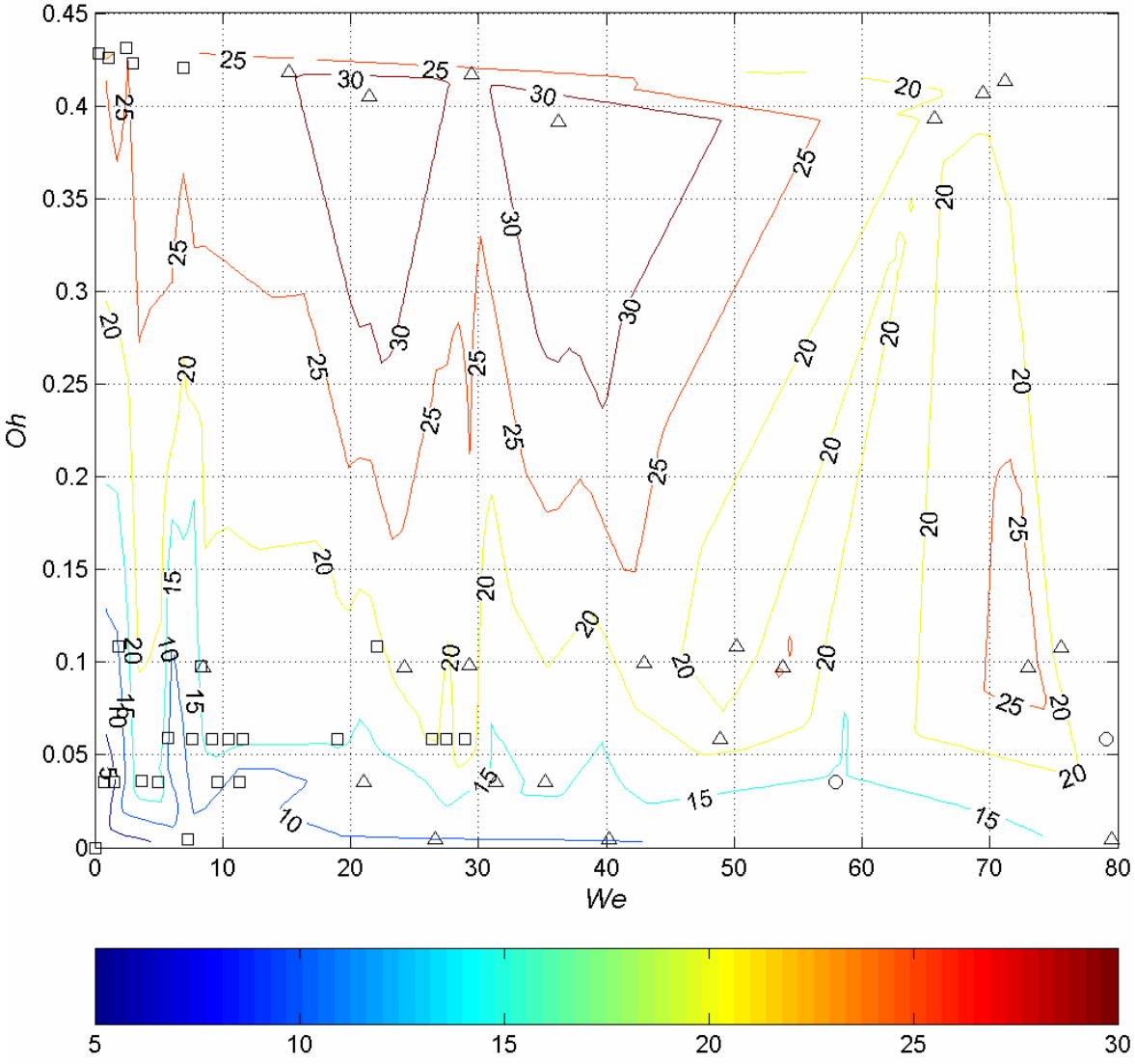

Figure 4.20 Non-dimensional average jet breakup length, $\overline{BL}/D$ for ASME sharp edge orifices vs. *Oh* and *We* numbers. The color bar represents the non-dimensional average jet breakup length. □ , instability regime 1. Δ, instability regime 2. o, instability regime 3.

CHAPTER 5 DROPLET SIZE SPECTRA

5.1 Chapter Overview

This chapter presents the results of the droplet size measurements performed with the PDPA and by digital video analysis. Data from the CO_2 injection experiments comprise the majority of these results, since complete composite size spectra were obtained for a wide range of tests, unlike crude oil which posed problems for the PDPA and the silicone fluid which was difficult to measure by digital video analysis. Section 5.2 presents droplet size histograms and summarizes and compares characteristic diameters and other statistics to understand the effects of injection parameters on droplet size. In section 5.3, functional relationships are obtained that approximate the measured droplet spectra. Section 5.3.1 reviews candidate probability density and cumulative distribution functions. Section 5.3.2 discusses curve fitting procedures and goodness of fit. To approximate the two or more classes of droplets generated in the transitional flow regimes, a weighted multimodal distribution is proposed in section 5.3.3. Application of the weighted multimodal distribution to the CO_2 droplets size distribution in different instability regimes is demonstrated in section 5.3.4 and best fit distributions are presented in section 5.3.5. Finally, experimental uncertainties of the size data are discussed in section 5.4.

5.2 Characteristic Diameters of Measured Droplet Size Data

5.2.1 Definitions of Characteristic Diameters

The diameter of an "average" droplet in an ensemble of polydispersed droplets can be represented by several statistically-determined quantities. Characteristic diameters conventionally employed in multi-phase flow studies that were applied in this investigation are (Masutani & Adams, 2000; Lefebvre, 1989):

Arithmetic Mean Diameter, x_{10}

$$x_{10} \equiv \int_0^{+\infty} x f(x) dx \tag{5.1}$$

For a complete (i.e., non-truncated due to limited instrument measurement range) droplet data set consisting of n droplets, Equation (5.1) can be approximated by the discrete sum:

$$x_{10} = \frac{\sum_{i=1}^{n} x_i}{n} \tag{5.2 a}$$

where x_i is the diameter of ith droplet. For a composite data set obtained from two incomplete data sets by the method described in section 2.2.3, Equation (5.1) can be expressed as:

$$x_{10} = \int_0^{\alpha} x f(x) dx + \int_{\alpha}^{+\infty} x f(x) dx = \frac{\sum_{i=1}^{a_1} x_i}{n_1} + \frac{\sum_{j=1}^{b_2+c_2} x_j}{n_2} \tag{5.2 b}$$

where α is the limiting diameter that divides the two data sets, in this case 3 mm; a_1 is the total number of droplets measured with the PDPA with x_i < 3 mm; b_2+c_2 is the total

number of droplets determined by image analysis with $x_j \geq 3$ mm; and n_1 and n_2 are the size of the composite ensembles defined by Equations (2.2) and (2.3), respectively.

Surface Mean Diameter, x_{20}

$$x_{20} \equiv \left[\int_0^{+\infty} x^2 f(x) dx \right]^{1/2} \tag{5.3}$$

For a complete droplet data set consisting of n droplets, Equation (5.3) can be approximated by the discrete sum:

$$x_{20} = \sqrt{\frac{\sum_{i=1}^{n} x_i^2}{n}} \tag{5.4 a}$$

For a composite data set obtained from two incomplete data sets, Equation (5.3) becomes:

$$x_{20} = \sqrt{\frac{\sum_{i=1}^{a_1} x_i^2}{n_1} + \frac{\sum_{j=1}^{b_2+c_2} x_j^2}{n_2}} \tag{5.4 b}$$

Volume Mean Diameter, x_{30}

$$x_{30} \equiv \left[\int_0^{+\infty} x^3 f(x) dx \right]^{1/3} \tag{5.5}$$

For a complete droplet data set consisting of n droplets, Equation (5.5) can be approximated by the discrete sum:

$$x_{30} = \left[\frac{\sum_{i=1}^{n} x_i^3}{n} \right]^{1/3} \tag{5.6 a}$$

For a composite data set obtained from two incomplete data sets, Equation (5.5) becomes:

$$x_{30} = \left[\frac{\sum_{i=1}^{a_1} x_i^3}{n_1} + \frac{\sum_{j=1}^{b_2+c_2} x_j^3}{n_2} \right]^{1/3} \tag{5.6 b}$$

Sauter Mean Diameter, x_{32}

$$x_{32} \equiv \frac{x_{30}^3}{x_{20}^2} \tag{5.7}$$

In the preceding definitions, x_{10} is the ensemble mean diameter. x_{20} and x_{30} are the diameters that correspond to the calculated average droplet surface area and volume, respectively. The Sauter mean diameter, x_{32}, is the diameter of a droplet that has the same ratio of volume to surface area as the entire ensemble. It is particularly relevant to analyses of droplet mass transfer (e.g., dissolution; evaporation) and chemical reaction (e.g., spray combustion; hydrate formation), while x_{20} applies to studies of surface phenomena, such as hydrodynamic drag and heat transfer, and x_{30} to areas such as momentum transfer and buoyancy. In addition to characteristic diameters, the variance, s^2, also provides information about the droplet size distribution. The definition of the variance is:

$$s^2 \equiv \int_0^{+\infty} f(x)(x-\mu)^2 dx \tag{5.8}$$

where μ is the expectation value, typically the ensemble mean, x_{10}. The variance therefore measures the expected square of the deviation of droplet diameter from its expectation value. For a complete droplet data set consisting of n droplets, Equation (5.8) can be approximated by the discrete sum:

$$s^2 = \frac{1}{n}\sum_{i=1}^{n}\left(x_i - x_{10}\right)^2 \qquad (5.9\text{ a})$$

For a composite data set obtained from two incomplete data sets, Equation (5.8) becomes:

$$s^2 = \frac{\sum_{i=1}^{a_1}\left(x_i - x_{10}\right)^2}{n_1} + \frac{\sum_{j=1}^{b_2+c_2}\left(x_j - x_{10}\right)^2}{n_2} \qquad (5.9\text{ b})$$

The variance is an indicator of the spread of the size distribution, $f(x)$. Large values of s^2 suggest a broad polydispersion, while monodispersions are characterized by small values of s^2.

5.2.2 Summaries of Measured Droplet Size Data

5.2.2.1 Characteristic Diameters and Standard Deviation of CO_2 Droplets

CO_2 droplet size data were collected at 72 different tests conditions. Table 5.1 summarizes the tests results. Test runs are listed in order of increasing jet velocity. The table includes the instability regime (*IR*); Weber (*We*), Reynolds (*Re*), and Ohnesorge (*Oh*) numbers; range of measured droplet diameters; characteristic diameters; and the standard deviation (square root of the variance) for each test condition.

5.2.2.2 Characteristic Diameters and Standard Deviation of Crude Oil Droplets

Characteristic diameters and standard deviations of crude oil droplets formed in instability regimes 1 and 2 are provided in Table 5.2. These size data were obtained by digital video analysis. The opacity of the crude oil droplets mde it impossible to perform

accurate droplet size measurements with the PDPA (Masutani & Adams, 2000); hence, the PDPA data are not reported nor used to calculate droplet size statistics.

5.2.2.3 Size Histograms of Silicone Fluid Droplets from PDPA Measurements

Unlike crude oil, droplets of clear silicone fluid in water could be measured accurately with the PDPA; however, as noted in Chapter 3, silicone fluid is difficult to visualize (unless it is mixed with dye or other colorants–which was not pursued in this study). The refractive indices of silicone fluid and water are nearly the same: 1.40 and 1.33, respectively. The inability to identify clearly the edges of silicone fluid droplets in the digital video images precluded the use of this sizing technique. Since the PDPA measurement range of 0.08 to 4.056 mm excluded large droplets, it was not possible accurately to calculate characteristic diameters and standard deviations. Although incomplete, the PDPA silicone droplet size histograms provide useful insight into the evolution of the spectra at different flow conditions. Representative results corresponding to instability regimes 3, 4 and 5 are presented in Figures 5.1, 5.2 and 5.3. Figure 5.1 corresponds to silicone fluid 20 injection into tap water through a 2 mm sharp edge orifice. Figure 5.2 presents size histograms for low viscosity silicone fluid injected into tap water through a 2 mm sharp edge orifice. In Figure 5.3, the low viscosity silicone fluid was discharged into tap water through a 2 mm tube orifice. Additional information is provided to the right of the histograms: *We* is Weber number; *IR* is instability regime; $x_{10,\mathrm{PDPA}}$ and s_{PDPA} are, respectively, ensemble average droplet diameter and standard deviation calculated using the incomplete PDPA data ensemble; *n* is the size of the ensemble measured with the PDPA.

5.2.3 Effects of Jet Flow Rate, Orifice Properties, Ambient Fluid, Pressure and Viscosity on Droplet Size

This section reviews and analyzes the preceding results to understand the effects of various parameters on droplet size.

5.2.3.1 Flow Rate Effect

The characteristic diameters, x_{10}, x_{20}, x_{30} and x_{32} are plotted against corresponding Weber numbers in Figures 5.4 a to d for the 72 liquid CO_2 injection tests. The characteristic diameters decrease as *We* increases in regimes 1 through 4. In instability regime 5, the characteristic diameters remain essentially constant, exhibiting only a small degree of variation. The standard deviations of the size distributions for the 72 tests are plotted in Figure 5.5 as a function of *We*. In regimes 1 and 5, droplets formed by jet breakup are relatively uniform in size, resulting in small values of the standard deviation. On the other hand, in transitional regimes 2, 3 and 4, breakup generates a wide polydispersion of droplets which is reflected in the large values of *s*. Figures 5.6, 5.7, and 5.8 present the composite droplet size histograms for the 7 different liquid CO_2 injection cases. The data are plotted against non-dimensionalized droplet diameter (x/D; where D is the injection orifice diameter) and *We*.

5.2.3.2 Orifice Effect

The effects of orifice diameter on x_{10}/D and x_{10}, are examined in Figure 5.9. These data are for liquid CO_2 injection into tap water through sharp edge orifices with D = 2 mm, 5

mm, and 10 mm, at a pressure of 52 bars. When the ensemble mean diameter is non-dimensionalized with the orifice diameter, x_{10}/D is larger for smaller D at the same value of *We* (Figure 5.9a). When x_{10} is plotted vs. *We* in Figure 5.9b, however, it becomes clear that a larger orifice produces modestly bigger droplets at low *We* in instability regime 1, but this effect diminishes as the transition to regime 3 is approached. Eventually, in regimes 4 and 5, orifice diameter appears to have little influence on the mean droplet diameter. Similar results were obtained for liquid CO_2 injection into tap water from 2 mm and 5 mm tube orifices at a pressure of 52 bars (Figures 5.10a and b). This behavior is consistent with the postulated evolution of instabilities, wherein higher order surface instabilities begin to dominate in regimes 4 and 5. Provided that the curvature of jet surface is not too great, these surface instabilities may not be sensitive to the initial jet diameter (which is determined by the orifice diameter).

The variation of the standard deviation with *We* observed in the CO_2 injection tests is plotted in Figure 5.11. In instability regimes 2 and 3, the standard deviation of the size distributions increases with orifice diameter, indicating a wider spread of droplets from the expectation value. Similar results were obtained for injection of Genesis (Figure 5.12) and Mars TLP (Figure 5.13) crude oils into tap water from 2 mm and 5 mm sharp edge orifices.

The effects of nozzle geometry on droplet size statistics are presented in Figures 5.14 and 5.15. These data correspond to liquid CO_2 injection into tap water at 52 bar through tube nozzles and sharp edge orifices. As seen in Figure 5.14, there is no obvious difference in the ensemble mean diameter of droplets generated by the tube nozzle and sharp edge orifice (for the same orifice diameter). Figure 5.15 suggests that the size

distribution of droplets produced by the 2 mm tube nozzle may have larger standard deviations than the 2 mm sharp edge orifice at higher values of Weber number, but this effect is not observed for the 5 mm nozzle.

For low viscosity silicone fluid injection (where the kinematic viscosity of the jet fluid is about six times larger than liquid CO_2), nozzle geometry does appear to have an effect on droplet size. Figure 5.16 compares ensemble mean diameters and standard deviations, calculated using the incomplete PDPA size ensemble, for a 2 mm tube nozzle and a 2 mm sharp edge orifice. The tube nozzle produces larger x_{pdpa} and has a more uniform droplet size distribution than the sharp edge orifice. The reason for the difference in behavior from the CO_2 injection results is not clear, but might reflect the influence of jet fluid viscosity on the tube nozzle boundary layer development.

5.2.3.3 Ambient Fluid Effect

The results of this investigation did not provide any clear evidence that the droplet size distribution of the tested jet fluids was significantly different in tap or sea water. Figure 5.17, plots mean diameters and standard deviations for Neptune Spar crude oil injection into tap water and sea water from a 2 mm sharp edge orifice. These data correspond to instability regimes 1 and 2. In Figure 5.18, results from the CO_2 injection tests employing a 2 mm tube orifice and tap water and sea water at P = 52 bar are compared. x_{10} are similar over the entire range of instability regimes. There is some indication that the droplet size distribution has a greater spread (i.e., larger standard deviation) in tap water than sea water at higher values of *We*.

5.2.3.4 Pressure Effect

Figure 5.19 compares the results from liquid CO_2 injection through a 5 mm tube orifice into tap water at 52 and 62 bar. In this range, pressure does not appear to exercise any significant influence on the droplet size statistics.

5.2.3.5 Viscosity Effect

Data corresponding to four jet fluids with kinematic viscosities ranging over three orders of magnitude are plotted in Figure 5.20. These data are for injection through 5 mm sharp edge orifices into tap water. At low *We* in regime 1, jet viscosity seems to have little effect on mean droplet size. As *We* increases, mean droplet size appears to increase slightly with jet fluid viscosity. Additional insight is provided by Figure 5.21 that compares PDPA data from the injection of two silicone fluids and liquid CO_2 into tap water through 2 mm sharp edge orifices. x_{pdpa} is larger for the higher viscosity fluids in the transitional breakup regimes.

Table 5.1 Summary of CO_2 Droplet Size Measurements

No.	Test Name	Table 3.1 No.	*IR*	Jet Vel. [m/s]	*We*	*Re*	*Oh*	Size Range min [mm]	Size Range max [mm]	x_{10} [mm]	x_{20} [mm]	x_{30} [mm]	x_{32} [mm]	Standard Deviation [mm]
1	CDC02WTP52R1	1	2	0.674	3.25E+01	1.16E+04	4.89E-04	1.44	10.95	4.54	4.76	5.01	5.56	1.45
2	CDC02WTP52R2	2	2	0.768	4.11E+01	1.40E+04	4.57E-04	1.13	5.89	3.66	3.84	3.98	4.28	1.17
3	CDC02WTP52R3	3	2	1.128	8.45E+01	2.24E+04	4.11E-04	0.83	6.75	3.00	3.26	3.48	3.97	1.28
4	CDC02WTP52R5	5	3	1.513	1.57E+02	2.87E+04	4.37E-04	0.01	4.86	1.37	1.64	1.88	2.44	0.91
5	CDC02WTP52R10	10	3	1.567	1.62E+02	3.14E+04	4.05E-04	0.01	6.21	1.31	1.46	1.60	1.93	0.63
6	CDC02WTP52R4	4	3	1.694	1.84E+02	3.51E+04	3.86E-04	0.05	3.79	1.25	1.42	1.56	1.88	0.68
7	CDC02WTP52R6	6	3	2.002	2.61E+02	4.09E+04	3.95E-04	0.01	3.96	1.31	1.51	1.67	2.05	0.75
8	CDC02WTP52R7	7	4	2.581	4.33E+02	5.29E+04	3.94E-04	0.02	3.99	1.30	1.43	1.55	1.82	0.60
9	CDC02WTP52R8	8	4	3.207	6.69E+02	6.55E+04	3.95E-04	0.01	3.98	1.22	1.38	1.53	1.88	0.64
10	CDC02WTP52R9	9	5	4.013	1.05E+03	8.16E+04	3.98E-04	0.02	4.03	1.00	1.08	1.16	1.35	0.40
11	CDC05WTP52R1	11	1	0.04	2.82E-01	1.67E+03	3.18E-04	3.29	8.74	5.71	5.86	5.99	6.26	1.28
12	CDC05WTP52R3	13	1	0.081	1.16E+00	3.68E+03	2.93E-04	3.22	10.71	6.71	6.83	6.95	7.21	1.28
13	CDC05WTP52R4	14	1	0.103	1.84E+00	4.76E+03	2.85E-04	4.08	10.14	6.65	6.76	6.87	7.08	1.21
14	CDC05WTP52R5	15	1	0.127	2.62E+00	6.43E+03	2.52E-04	3.80	23.55	6.77	7.23	7.97	9.67	2.55
15	CDC05WTP52R6	16	1	0.18	5.26E+00	9.18E+03	2.50E-04	2.33	10.16	6.74	6.92	7.07	7.38	1.55
16	CDC05WTP52R7	17	1	0.229	8.49E+00	1.17E+04	2.48E-04	1.09	9.97	6.48	6.70	6.88	7.24	1.70
17	CDC05WTP52R8	18	2	0.278	1.25E+01	1.43E+04	2.47E-04	0.78	11.25	6.55	6.79	6.98	7.37	1.79
18	CDC05WTP52R9	19	2	0.327	1.73E+01	1.69E+04	2.46E-04	1.63	10.94	6.20	6.53	6.81	7.40	2.05
19	CDC05WTP52R10	20	2	0.392	2.49E+01	2.02E+04	2.48E-04	1.01	15.71	6.43	6.99	7.50	8.62	2.73
20	CDC05WTP52R11	21	2	0.435	3.07E+01	2.23E+04	2.49E-04	1.80	13.44	6.97	7.49	7.95	8.96	2.75
21	CDC05WTP52R12	22	2	0.547	4.88E+01	2.79E+04	2.51E-04	1.20	14.37	6.32	6.98	7.52	8.74	2.96
22	CDC05WTP52R20	30	3	0.591	5.90E+01	2.85E+04	2.69E-04	0.04	10.80	1.75	2.54	3.34	5.78	1.85
23	CDC05WTP52R21	31	3	0.728	9.04E+01	3.46E+04	2.75E-04	0.01	11.61	4.09	4.85	5.44	6.85	2.61
24	CDC05WTP52R22	32	3	0.857	1.27E+02	4.00E+04	2.81E-04	0.02	12.23	2.73	3.92	4.86	7.48	2.80
25	CDC05WTP52R23	33	4	1.027	1.83E+02	4.72E+04	2.87E-04	0.01	11.13	2.03	2.86	3.62	5.77	2.02
26	CDC05WTP52R24	34	4	1.245	2.70E+02	5.69E+04	2.89E-04	0.01	8.78	2.01	2.74	3.30	4.82	1.85

Table 5.1 (Continued)

No.	Test Name	Table 3.1 No.	*IR*	Jet Vel. [m/s]	*We*	*Re*	*Oh*	Size Range min [mm]	Size Range max [mm]	x_{10} [mm]	x_{20} [mm]	x_{30} [mm]	x_{32} [mm]	Standard Deviation [mm]
27	CDC05WTP52R25	35	4	1.877	6.26E+02	8.23E+04	3.04E-04	0.02	4.05	1.24	1.52	1.78	2.44	0.89
28	CDC05WTP52R26	36	5	2.405	1.04E+03	1.03E+05	3.15E-04	0.02	7.76	1.62	2.39	2.98	4.64	1.76
29	CDC10WTP52R13	49	1	0.023	1.79E-01	2.15E+03	1.97E-04	7.69	10.17	9.10	9.11	9.13	9.17	0.57
30	CDC10WTP52R12	48	1	0.038	4.96E-01	3.37E+03	2.09E-04	2.71	10.78	8.16	8.33	8.47	8.75	1.69
31	CDC10WTP52R10	46	1	0.097	3.37E+00	8.51E+03	2.16E-04	1.89	13.38	8.96	9.46	9.80	10.53	3.05
32	CDC10WTP52R6	42	1	0.129	5.88E+00	1.13E+04	2.15E-04	2.32	16.06	7.75	8.55	9.25	10.81	3.61
33	CDC10WTP52R7	43	2	0.225	1.79E+01	2.00E+04	2.12E-04	0.96	20.53	6.75	7.96	8.96	11.35	4.23
34	CDC10WTP52R8	44	2	0.275	2.65E+01	2.50E+04	2.06E-04	1.36	14.29	5.31	6.29	7.14	9.21	3.36
35	CDC10WTP52R9	45	2	0.307	3.37E+01	2.64E+04	2.20E-04	0.97	18.11	6.98	8.06	8.97	11.11	4.02
36	CDC10WTP52R1	37	3	0.414	6.10E+01	3.62E+04	2.16E-04	0.01	13.73	2.67	3.79	4.73	7.34	2.70
37	CDC10WTP52R2	38	3	0.656	1.54E+02	5.61E+04	2.22E-04	0.02	13.78	1.17	2.16	3.18	6.90	1.82
38	CDC10WTP52R3	39	4	0.882	2.84E+02	7.27E+04	2.32E-04	0.01	11.01	2.23	3.35	4.29	7.02	2.50
39	CDC10WTP52R4	40	5	1.176	5.09E+02	9.46E+04	2.39E-04	0.02	4.04	1.14	1.47	1.75	2.49	0.93
40	CDC10WTP52R5	41	5	1.451	7.79E+02	1.16E+05	2.41E-04	0.01	1.51	0.51	0.54	0.57	0.65	0.18
41	CDT02WTP52R14	63	2	0.526	1.88E+01	1.01E+04	4.29E-04	1.27	6.80	4.15	4.27	4.36	4.55	0.98
42	CDT02WTP52R13	62	2	0.676	3.14E+01	1.27E+04	4.41E-04	1.17	7.01	4.54	4.71	4.83	5.09	1.23
43	CDT02WTP52R12	61	2	0.767	4.11E+01	1.40E+04	4.58E-04	1.00	7.77	3.90	4.24	4.50	5.07	1.67
44	CDT02WTP52R11	60	2	1.029	7.53E+01	1.80E+04	4.81E-04	1.38	8.36	4.35	4.61	4.82	5.28	1.51
45	CDT02WTP52R1	50	3	1.696	1.79E+02	3.64E+04	3.68E-04	0.04	7.53	0.85	1.18	1.70	3.55	0.82
46	CDT02WTP52R2	51	3	1.789	2.01E+02	3.80E+04	3.74E-04	0.03	7.48	1.67	2.42	3.06	4.93	1.75
47	CDT02WTP52R3	52	3	2.086	2.75E+02	4.40E+04	3.77E-04	0.01	6.54	2.58	3.04	3.35	4.06	1.61
48	CDT02WTP52R4	53	4	2.577	4.23E+02	5.40E+04	3.81E-04	0.01	6.84	1.37	1.97	2.49	4.00	1.41
49	CDT02WTP52R5	54	4	3.179	6.52E+02	6.56E+04	3.89E-04	0.01	5.78	1.40	1.87	2.24	3.20	1.25
50	CDT02WTP52R6	55	5	3.923	1.00E+03	8.02E+04	3.94E-04	0.01	4.95	0.94	1.30	1.63	2.54	0.90
51	CDT02WTP52R7	56	5	5.537	2.05E+03	1.09E+05	4.14E-04	0.01	5.58	1.03	1.37	1.65	2.40	0.90
52	CDT02WTP52R8	57	5	7.884	4.26E+03	1.49E+05	4.40E-04	0.01	5.86	1.06	1.50	1.88	2.95	1.06
53	CDT02WTP52R9	58	5	12.894	1.16E+04	2.37E+05	4.53E-04	0.02	5.88	0.89	1.21	1.57	2.64	0.81

Table 5.1 (Continued)

No.	Test Name	Table 3.1 No.	*IR*	Jet Vel. [m/s]	*We*	*Re*	*Oh*	Size Range min [mm]	Size Range max [mm]	x_{10} [mm]	x_{20} [mm]	x_{30} [mm]	x_{32} [mm]	Standard Deviation [mm]
54	CDT02WTP52R10	59	5	17.814	2.26E+04	3.10E+05	4.85E-04	0.01	4.06	1.01	1.32	1.63	2.46	0.85
55	CDT02WNP52R4	66	2	0.513	1.83E+01	9.40E+03	4.55E-04	0.81	5.59	3.56	3.69	3.79	4.01	0.98
56	CDT02WNP52R5	67	2	0.695	3.35E+01	1.28E+04	4.51E-04	0.86	6.44	3.94	4.09	4.22	4.47	1.12
57	CDT02WNP52R6	68	2	0.78	4.17E+01	1.47E+04	4.41E-04	0.83	7.08	3.73	4.01	4.23	4.70	1.47
58	CDT02WNP52R8	70	3	1.493	1.52E+02	2.85E+04	4.33E-04	0.03	6.38	1.53	1.79	2.11	2.93	0.92
59	CDT02WNP52R9	71	3	1.954	2.55E+02	3.86E+04	4.13E-04	0.04	3.76	1.35	1.46	1.56	1.78	0.55
60	CDT02WNP52R1	64	4	2.562	4.43E+02	4.96E+04	4.25E-04	0.03	3.95	1.56	1.67	1.76	1.97	0.59
61	CDT02WNP52R2	65	5	3.889	1.03E+03	7.46E+04	4.30E-04	0.04	3.99	1.57	1.66	1.75	1.92	0.55
62	CDT05WTP61R7	78	1	0.09	1.42E+00	4.24E+03	2.81E-04	1.62	8.09	5.08	5.19	5.28	5.46	1.04
63	CDT05WTP61R6	77	1	0.21	7.80E+00	9.56E+03	2.92E-04	1.37	10.83	6.86	7.19	7.44	7.96	2.15
64	CDT05WTP61R4	75	2	0.371	2.41E+01	1.73E+04	2.84E-04	1.01	12.63	7.01	7.43	7.77	8.50	2.47
65	CDT05WTP61R1	72	3	1.256	2.79E+02	5.71E+04	2.93E-04	0.01	4.03	0.83	1.21	1.57	2.65	0.88
66	CDT05WTP61R2	73	5	2.34	9.84E+02	1.02E+05	3.07E-04	0.01	4.04	0.86	1.10	1.40	2.28	0.68
67	CDT05WTP52R7	85	1	0.086	1.29E+00	3.95E+03	2.88E-04	0.83	7.73	5.68	5.89	6.02	6.30	1.53
68	CDT05WTP52R6	84	1	0.208	7.58E+00	9.46E+03	2.91E-04	0.85	9.98	5.74	6.08	6.31	6.81	2.01
69	CDT05WTP52R5	83	2	0.357	2.24E+01	1.60E+04	2.96E-04	0.82	14.55	6.72	7.35	7.86	9.01	2.98
70	CDT05WTP52R3	81	3	1.227	2.65E+02	5.48E+04	2.97E-04	0.01	12.14	2.72	3.67	4.41	6.37	2.47
71	CDT05WTP52R2	80	4	1.805	5.82E+02	7.81E+04	3.09E-04	0.01	4.05	0.90	1.22	1.56	2.52	0.82
72	CDT05WTP52R1	79	5	2.347	9.76E+02	1.03E+05	3.02E-04	0.01	4.06	0.79	1.05	1.34	2.18	0.70

Table 5.2 Summary of Crude Oil Droplet Size Measurements

No.	Test Name	Table 3.2 No.	*IR*	Jet Velocity [m/s]	*We*	*Re*	*Oh*	Ensemble Size	Size Range min [mm]	Size Range max [mm]	x_{10} [mm]	x_{20} [mm]	x_{30} [mm]	x_{32} [mm]	Standard Deviation [mm]
1	GES02WTRR9	9	1	0.273	5.28E-00	3.03E+01	7.59E-02	28	6.81	9.32	8.24	8.26	8.29	8.34	0.67
2	GES02WTRR1	1	1	0.308	6.70E-00	3.35E+01	7.73E-02	39	5.52	8.66	7.09	7.14	7.20	7.31	0.91
3	GES02WTRR2	2	1	0.403	1.15E+01	4.40E+01	7.70E-02	225	1.17	9.51	5.91	6.00	6.09	6.27	1.06
4	GES02WTRR11	11	1	0.442	1.38E+01	4.90E+01	7.59E-02	134	3.62	8.29	5.44	5.54	5.65	5.86	1.06
5	GES02WTRR12	12	2	0.716	3.63E+01	7.94E+01	7.59E-02	48	3.68	7.29	5.50	5.61	5.70	5.91	1.09
6	GES02WTRR3	3	2	0.753	4.01E+01	8.23E+01	7.69E-02	600	0.92	8.30	4.90	5.06	5.20	5.49	1.24
7	GES02WTRR13	13	2	0.966	6.59E+01	1.07E+02	7.59E-02	68	2.95	8.02	5.83	5.93	6.03	6.23	1.11
8	GES05WTRR6	30	1	0.161	4.60E-00	4.28E+01	5.01E-02	74	5.65	14.31	9.79	9.95	10.11	10.43	1.82
9	GES05WTRR7	31	1	0.252	1.12E+01	6.69E+01	5.01E-02	112	2.82	13.45	8.78	9.12	9.40	9.99	2.49
10	GES05WTRR8	32	2	0.357	2.25E+01	9.47E+01	5.01E-02	37	4.18	13.02	9.24	9.49	9.70	10.15	2.16
11	GES05WTRR9	33	2	0.441	3.44E+01	1.17E+02	5.01E-02	86	3.39	15.18	9.11	9.42	9.69	10.28	2.40
12	GES05WTRR10	34	2	0.637	7.17E+01	1.69E+02	5.01E-02	86	3.88	15.10	7.95	8.36	8.76	9.62	2.59
13	MAS05WTRR7	48	1	0.145	3.66E-00	5.37E+01	3.57E-02	30	5.99	10.78	8.12	8.21	8.29	8.45	1.19
14	MAS05WTRR20	61	1	0.255	1.13E+01	9.55E+01	3.52E-02	59	6.61	12.80	9.74	9.82	9.89	10.05	1.25
15	MAS05WTRR10	51	2	0.348	2.11E+01	1.29E+02	3.56E-02	29	3.34	14.70	10.84	11.15	11.38	11.86	2.65
16	MAS05WTRR19	60	2	0.424	3.13E+01	1.59E+02	3.53E-02	49	7.76	20.29	12.91	13.25	13.59	14.28	3.02
17	MAS05WTRR11	52	2	0.45	3.52E+01	1.67E+02	3.56E-02	25	6.01	16.75	11.95	12.22	12.44	12.91	2.59
18	MAS02WTRR18	80	1	0.332	7.65E-00	4.73E+01	5.85E-02	46	4.23	8.69	5.84	5.93	6.03	6.23	1.04
19	MAS02WTRR13	75	1	0.363	9.19E-00	5.18E+01	5.85E-02	35	3.12	8.47	5.81	5.93	6.04	6.26	1.18
20	MAS02WTRR17	79	1	0.387	1.04E+01	5.53E+01	5.85E-02	45	3.65	8.44	5.68	5.78	5.88	6.09	1.08
21	MAS02WTRR14	76	1	0.408	1.16E+01	5.83E+01	5.85E-02	24	3.62	8.77	6.03	6.11	6.19	6.36	1.04
22	MAS02WTRR15	77	1	0.523	1.90E+01	7.46E+01	5.85E-02	79	3.19	10.99	6.07	6.24	6.40	6.75	1.44
23	MAS02WTRR19	81	1	0.615	2.63E+01	8.78E+01	5.85E-02	21	5.48	9.37	7.37	7.44	7.50	7.63	1.00
24	MAS02WTRR16	78	1	0.629	2.75E+01	8.97E+01	5.85E-02	139	2.57	9.50	5.67	5.88	6.07	6.46	1.57
25	MAS02WTRR8	70	1	0.645	2.89E+01	9.18E+01	5.86E-02	50	5.79	9.73	7.88	7.94	7.99	8.10	0.96

Table 5.2 (Continued)

No.	Test Name	Table 3.2 No.	*IR*	Jet Velocity [m/s]	*We*	*Re*	*Oh*	Ensemble Size	Size Range min [mm]	Size Range max [mm]	x_{10} [mm]	x_{20} [mm]	x_{30} [mm]	x_{32} [mm]	Standard Deviation [mm]
26	MAS02WTRR9	71	2	0.838	4.89E+01	1.19E+02	5.85E-02	67	3.93	10.58	7.21	7.35	7.48	7.75	1.45
27	PGS01WTRR3	87	1	1.197	5.33E+01	7.63E-00	9.56E-01	21	2.66	10.96	6.97	7.93	8.58	10.06	3.87
28	PGS05WTRR3	90	1	0.075	1.03E-00	2.39E-00	4.26E-01	139	3.14	9.89	6.54	6.67	6.81	7.08	1.34
29	PGS05WTRR1	88	1	0.115	2.48E-00	3.65E-00	4.31E-01	227	4.70	13.10	8.17	8.32	8.48	8.79	1.58
30	PGS05WTRR4	91	1	0.126	2.97E-00	4.08E-00	4.23E-01	133	5.03	10.65	7.94	8.02	8.11	8.27	1.15
31	PGS05WTRR5	92	1	0.194	6.96E-00	6.28E-00	4.20E-01	113	6.22	14.61	9.58	9.73	9.87	10.16	1.69
32	PGS05WTRR6	93	2	0.286	1.52E+01	9.32E-00	4.18E-01	51	7.40	16.19	11.29	11.49	11.68	12.08	2.17
33	PGS05WTRR14	101	2	0.34	2.14E+01	1.14E+01	4.05E-01	24	6.82	14.28	10.08	10.27	10.47	10.87	2.03
34	PGS05WTRR7	94	2	0.398	2.95E+01	1.30E+01	4.17E-01	24	8.76	19.29	12.83	13.10	13.35	13.89	2.65
35	PGS05WTRR13	100	2	0.611	6.95E+01	2.05E+01	4.07E-01	47	3.55	17.64	12.01	12.52	12.93	13.80	3.58
36	PGS05WTRR9	96	2	0.619	7.12E+01	2.04E+01	4.14E-01	28	9.13	18.17	13.36	13.54	13.72	14.08	2.23
37	NSS02WTRR14	126	1	0.345	8.45E-00	3.00E+01	9.70E-02	162	2.78	6.57	4.38	4.46	4.54	4.71	0.85
38	NSS02WTRR5	117	1	0.361	9.25E-00	3.11E+01	9.77E-02	78	4.25	9.54	6.75	6.85	6.94	7.13	1.16
39	NSS02WTRR13	125	2	0.584	2.42E+01	5.07E+01	9.70E-02	144	2.67	7.57	4.89	4.99	5.09	5.30	1.02
40	NSS02WTRR6	118	2	0.642	2.93E+01	5.51E+01	9.81E-02	131	2.92	9.49	5.67	5.83	5.98	6.29	1.33
41	NSS02WTRR7	119	2	0.777	4.29E+01	6.59E+01	9.94E-02	144	2.59	8.69	5.56	5.70	5.83	6.11	1.26
42	NSS02WTRR12	124	2	0.87	5.38E+01	7.55E+01	9.71E-02	98	2.68	7.71	5.12	5.27	5.40	5.68	1.25
43	NSS02WTRR11	123	2	1.013	7.30E+01	8.79E+01	9.72E-02	183	1.90	8.91	5.39	5.57	5.73	6.07	1.40
44	NSS01WTRR10	138	2	1.033	3.79E+01	4.16E+01	1.48E-01	78	2.52	5.26	3.47	3.52	3.56	3.65	0.55
45	NSS02WNRR5	147	1	0.318	7.20E-00	2.59E+01	1.04E-01	177	4.08	8.00	5.82	5.86	5.90	5.98	0.67
46	NSS02WNRR6	148	1	0.451	1.45E+01	3.68E+01	1.03E-01	149	2.91	8.49	5.76	5.84	5.92	6.08	0.98
47	NSS02WNRR7	149	2	0.859	5.25E+01	7.03E+01	1.03E-01	186	1.71	10.08	5.98	6.18	6.35	6.70	1.53

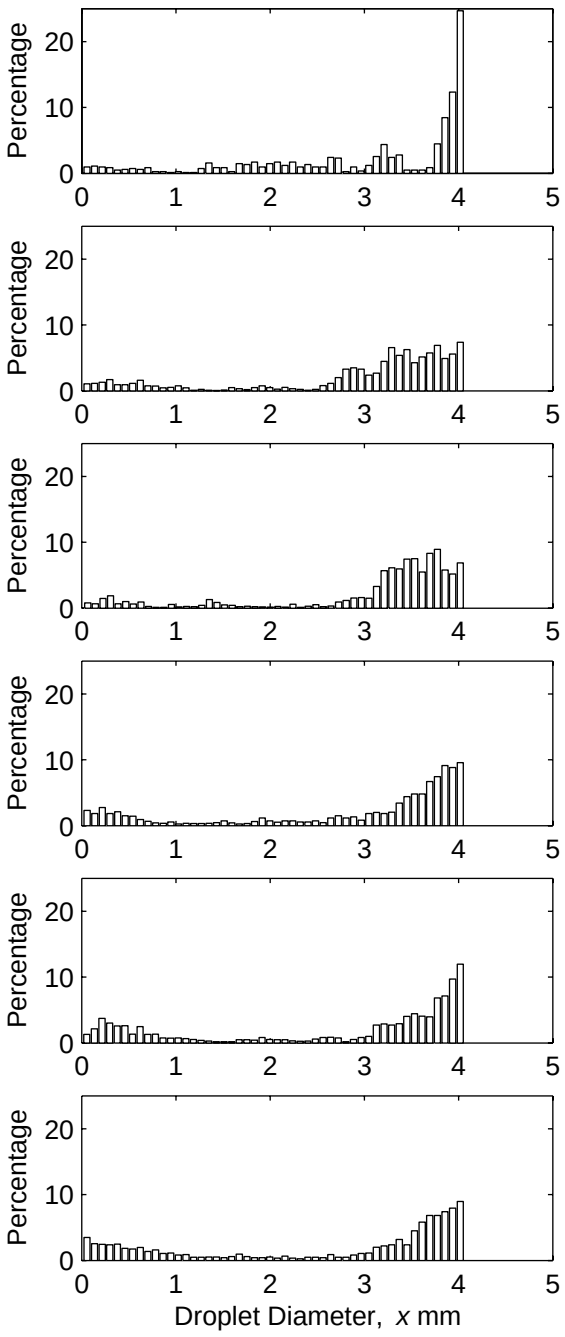

(1) SFS02WTRR6

We = 113.86 *IR* = 2

U_{jet} = 1.11 m/s *n* = 827

x_{pdpa} = 3.08 mm s_{pdpa} = 1.13

(2) SFS02WTRR4

We = 160.97 *IR* = 3

U_{jet} = 1.33 m/s *n* = 2242

x_{pdpa} = 2.98 mm s_{pdpa} = 1.10

(3) SFS02WTRR1

We = 264.64 *IR* = 4

U_{jet} = 1.70 m/s *n* = 2681

x_{pdpa} = 3.12 mm s_{pdpa} = 1.03

(4) SFS02WTRR5

We = 397.32 *IR* = 4

U_{jet} = 2.08 m/s *n* = 1953

x_{pdpa} = 2.90 mm s_{pdpa} = 1.30

(5) SFS02WTRR2

We = 400.36 *IR* = 4

U_{jet} = 2.09 m/s *n* = 2091

x_{pdpa} = 2.73 mm s_{pdpa} = 1.42

(6) SFS02WTRR3

We = 623.02 *IR* = 4

U_{jet} = 2.61 m/s *n* = 1685

x_{pdpa} = 2.66 mm s_{pdpa} = 1.43

Figure 5.1 Silicone fluid droplet size histograms measured with the PDPA. The kinematic viscosity of the silicone fluid was ν = 20 cs; injection into tap water through a 2 mm sharp edge orifice.

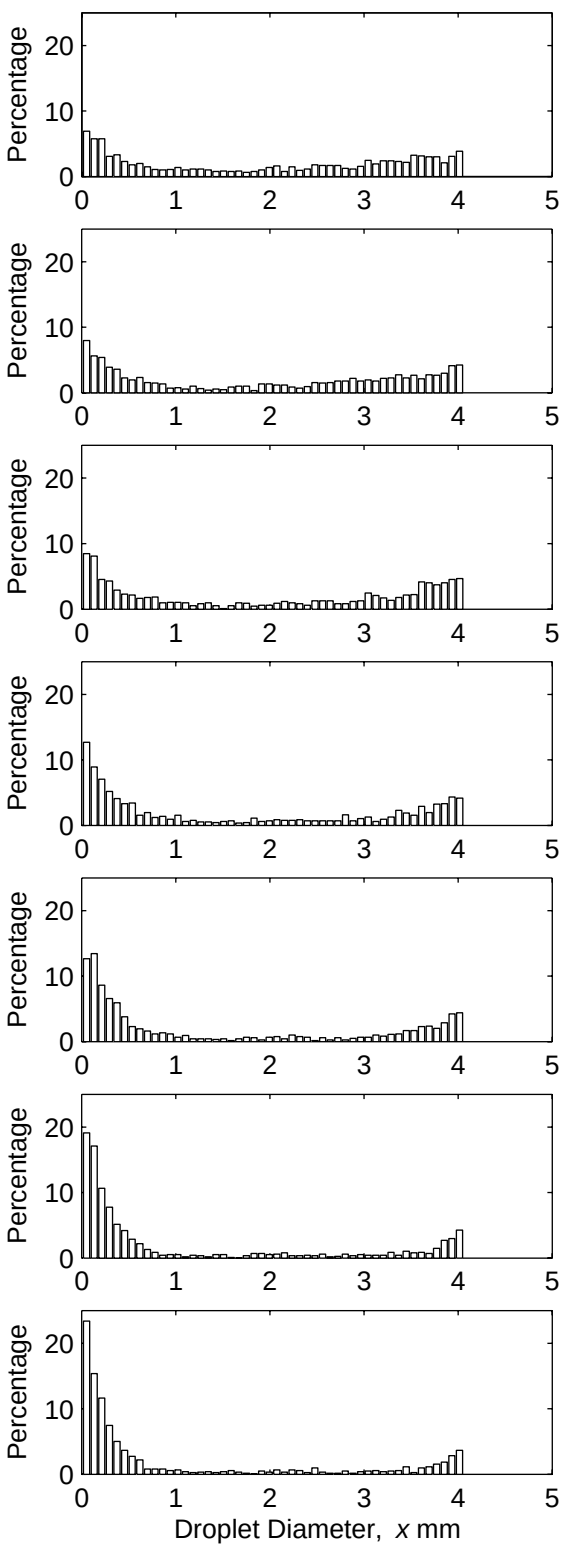

(1) LSS02WTRR7

We = 130.56 *IR* = 3

U_{jet} = 1.17 m/s *n* = 1299

x_{pdpa} = 1.98 mm s_{pdpa} = 1.42

(2) LSS02WTRR6

We = 164.46 *IR* = 3

U_{jet} = 1.31 m/s *n* = 1281

x_{pdpa} = 1.97 mm s_{pdpa} = 1.45

(3) LSS02WTRR1

We = 272.94 *IR* = 3

U_{jet} = 1.69 m/s *n* = 1348

x_{pdpa} = 1.98 mm s_{pdpa} = 1.52

(4) LSS02WTRR5

We = 436.97 *IR* = 3

U_{jet} = 2.14 m/s *n* = 1176

x_{pdpa} = 1.62 mm s_{pdpa} = 1.53

(5) LSS02WTRR2

We = 736.07 *IR* = 4

U_{jet} = 2.77 m/s *n* = 1184

x_{pdpa} = 1.40 mm s_{pdpa} = 1.51

(6) LSS02WTRR3

We = 1009.57 *IR* = 4

U_{jet} = 3.25 m/s *n* = 1147

x_{pdpa} = 1.04 mm s_{pdpa} = 1.39

(7) LSS02WTRR4

We = 1152.84 *IR* = 4

U_{jet} = 3.47 m/s *n* = 1236

x_{pdpa} = 0.95 mm s_{pdpa} = 1.34

Figure 5.2 Silicone fluid droplet size histograms measured with the PDPA. Low viscosity silicone fluid (ν = 0.65 cs) injected into tap water through a 2 mm sharp edge orifice.

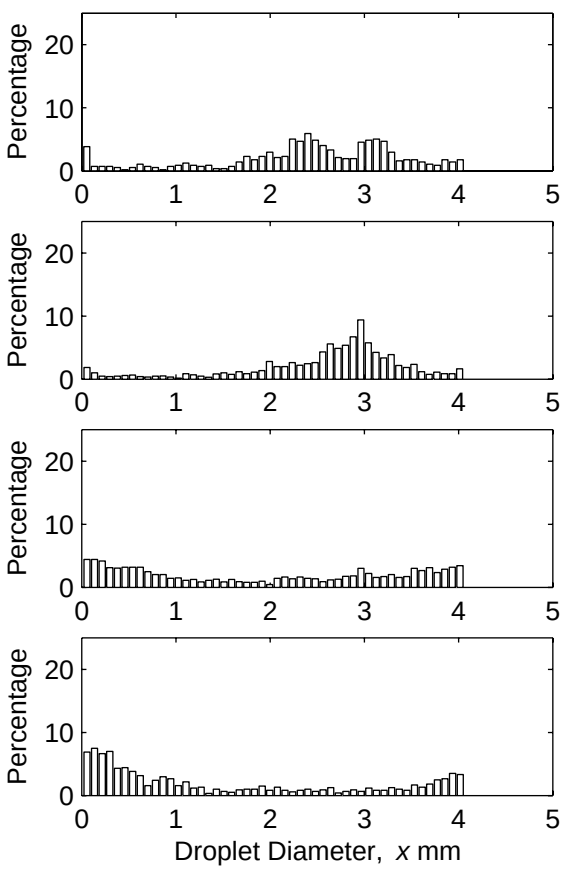

(1) LST02WTRR10

We = 193.78 *IR* = 3

U_{jet} = 1.42 m/s *n* = 576

x_{pdpa} = 2.41 mm s_{pdpa} = 0.96

(2) LST02WTRR11

We = 324.98 *IR* = 3

U_{jet} = 1.84 m/s *n* = 1717

x_{pdpa} = 2.57 mm s_{pdpa} = 0.85

(3) LST02WTRR12

We = 692.34 *IR* = 4

U_{jet} = 2.69 m/s *n* = 1536

x_{pdpa} = 1.96 mm s_{pdpa} = 1.38

(4) LST02WTRR13

We = 1213.27 *IR* = 5

U_{jet} = 3.56 m/s *n* = 1204

x_{pdpa} = 1.49 mm s_{pdpa} = 1.38

Figure 5.3 Silicone fluid droplet size histograms measured with the PDPA. Low viscosity silicone fluid (ν = 0.65 cs) injected into tap water through a 2 mm tube orifice.

(a)

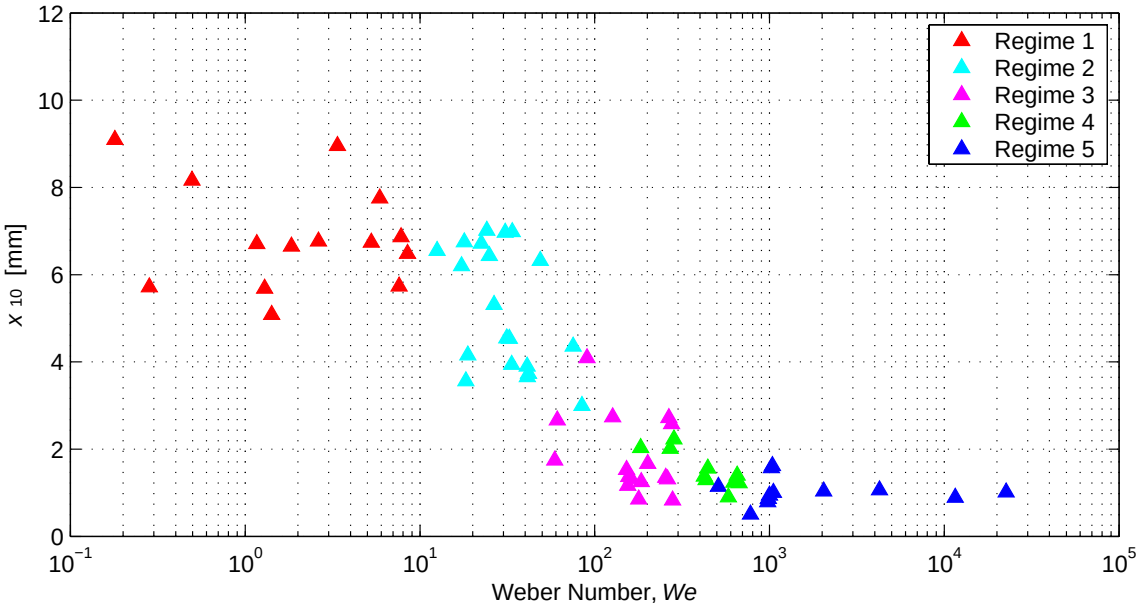
Regime 1
Regime 2
Regime 3
Regime 4
Regime 5
x_{10} [mm]
Weber Number, *We*

(b)

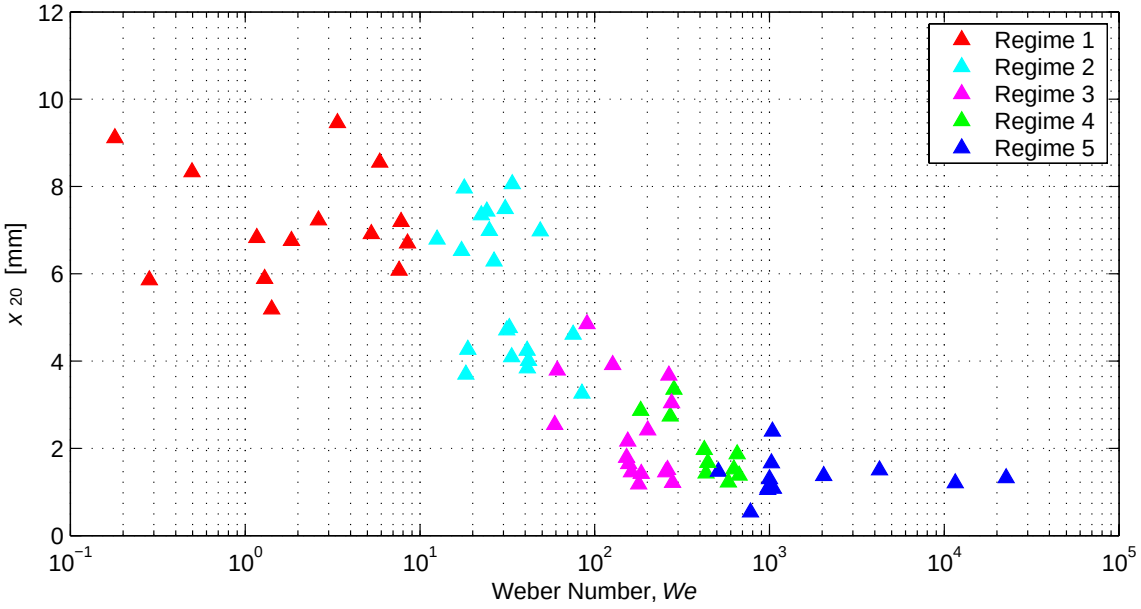
Regime 1
Regime 2
Regime 3
Regime 4
Regime 5
x_{20} [mm]
Weber Number, *We*

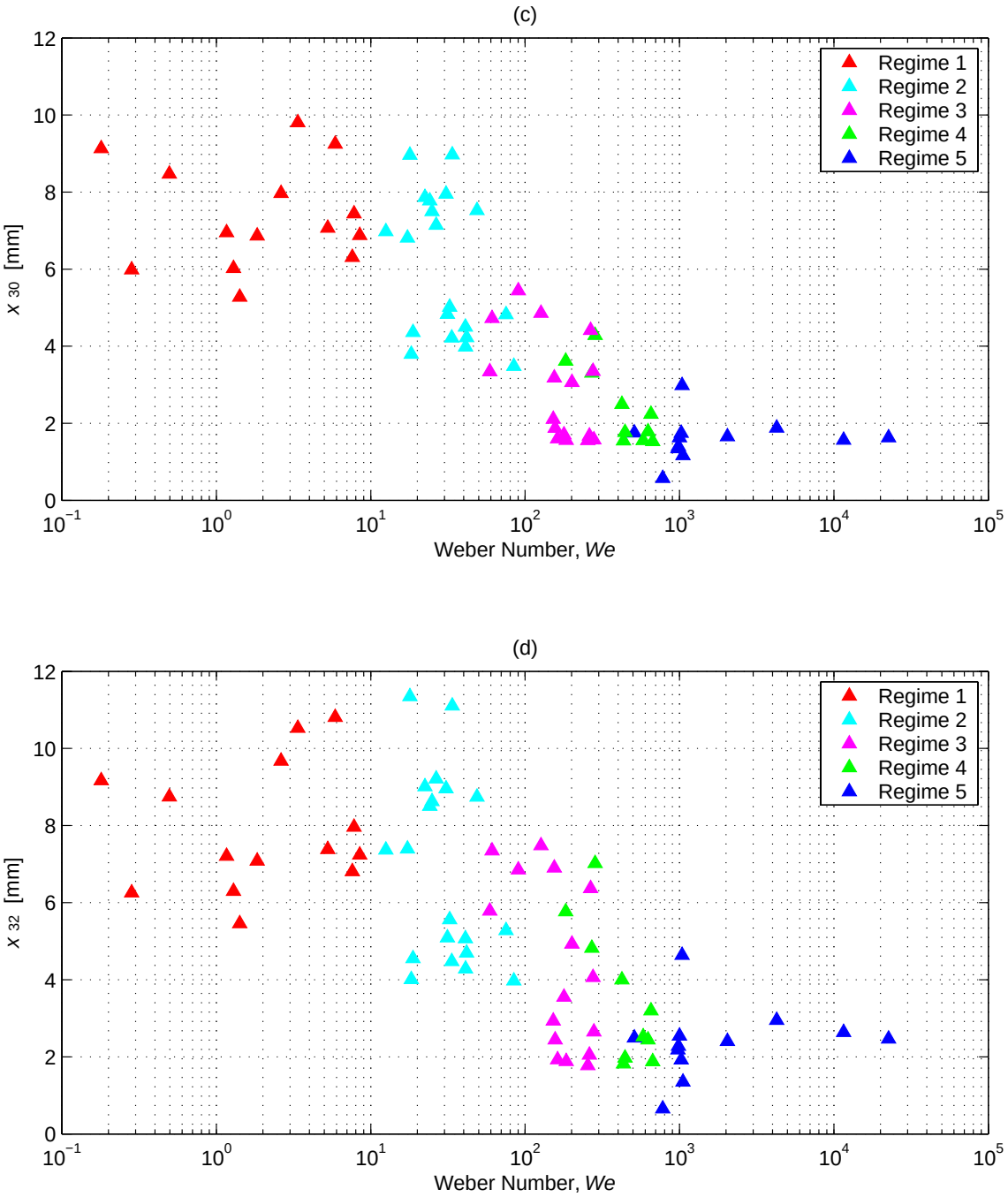

Figure 5.4 Characteristic diameters of CO_2 droplets vs. *We* from 72 tests. (a) x_{10}; (b)x_{20}; (c) x_{30}; (d) x_{32}.

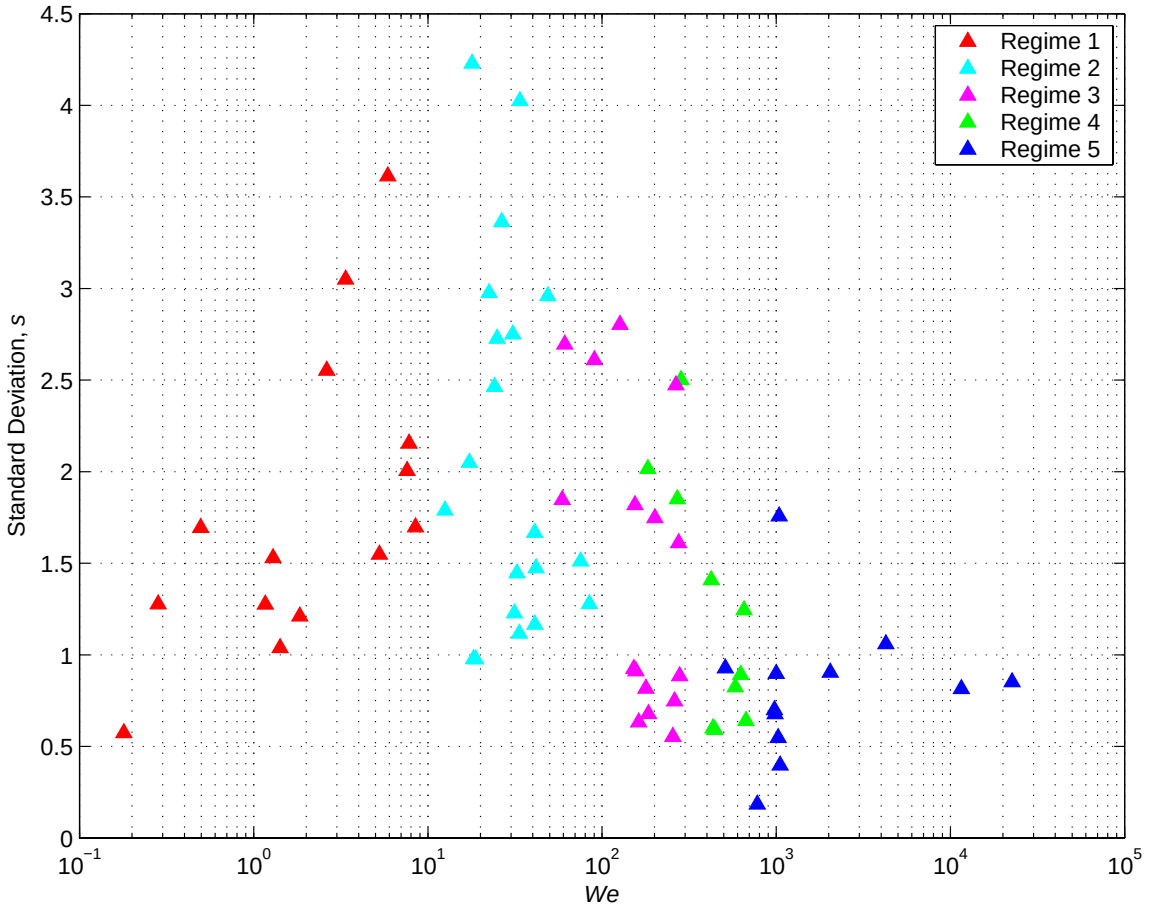

Figure 5.5 Standard deviations of CO_2 droplets vs. *We* from 72 tests.

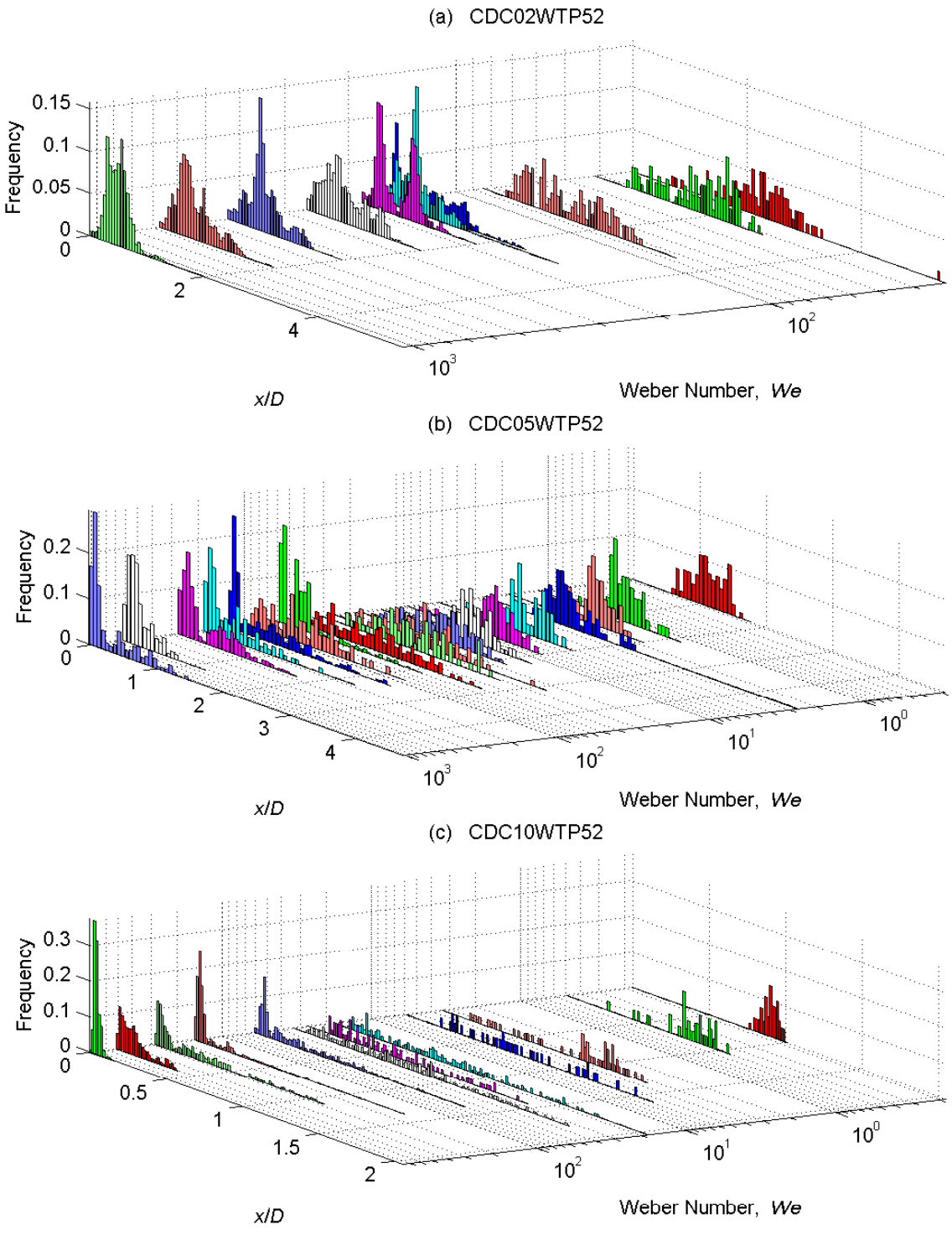

Figure 5.6 CO_2 droplet size histograms. Data are for liquid CO_2 injection into tap water from (a) 2 mm, (b) 5 mm and (c) 10 mm sharp edge orifices. *x*/*D* is droplet diameter non-dimensionalized with the orifice diameter.

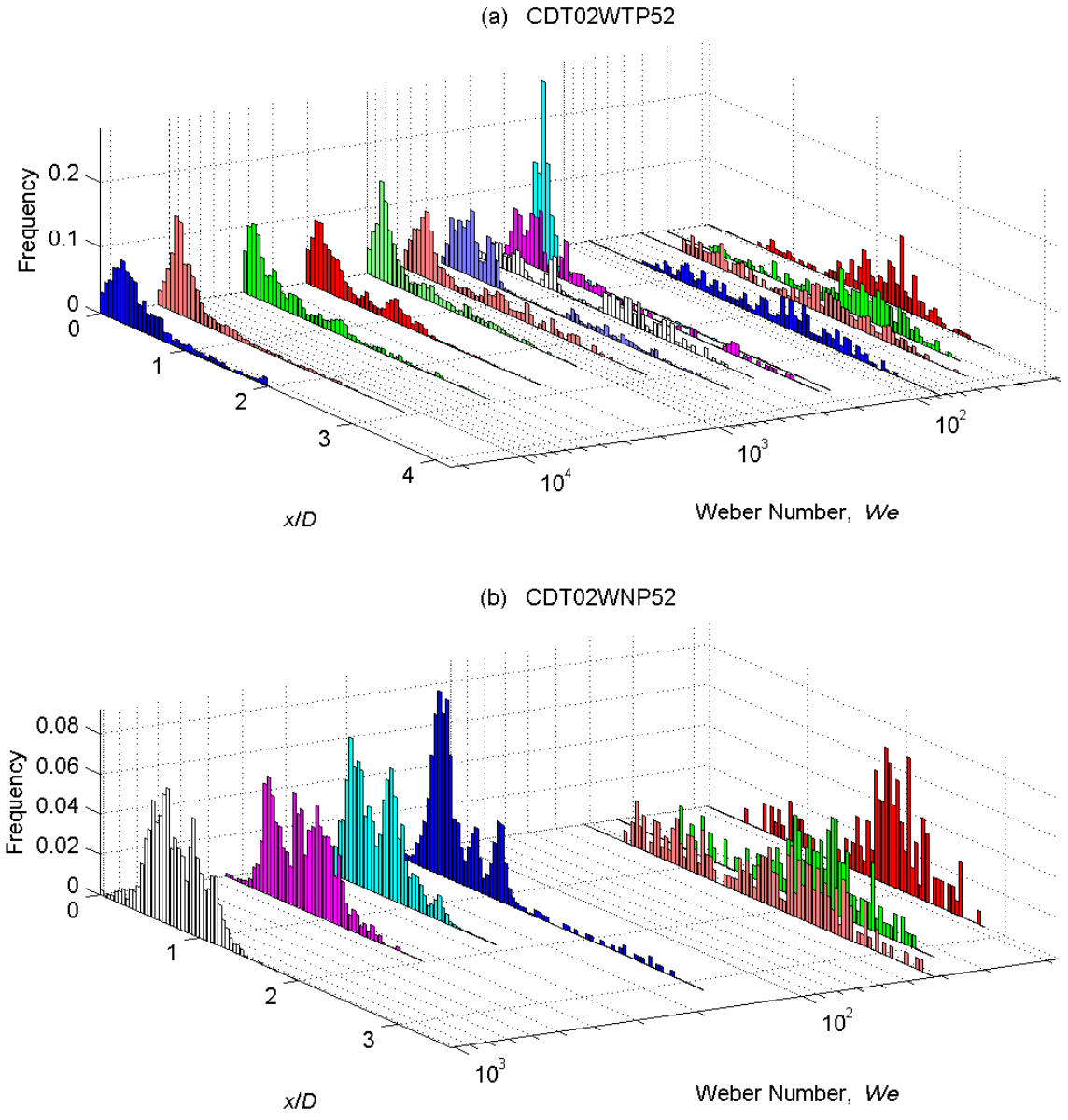

Figure 5.7 CO_2 droplet size histograms. Data are for liquid CO_2 injection through a 2 mm tube orifice into (a) tap water and (b) natural sea water. *x*/*D* is droplet diameter non-dimensionalized with the orifice diameter.

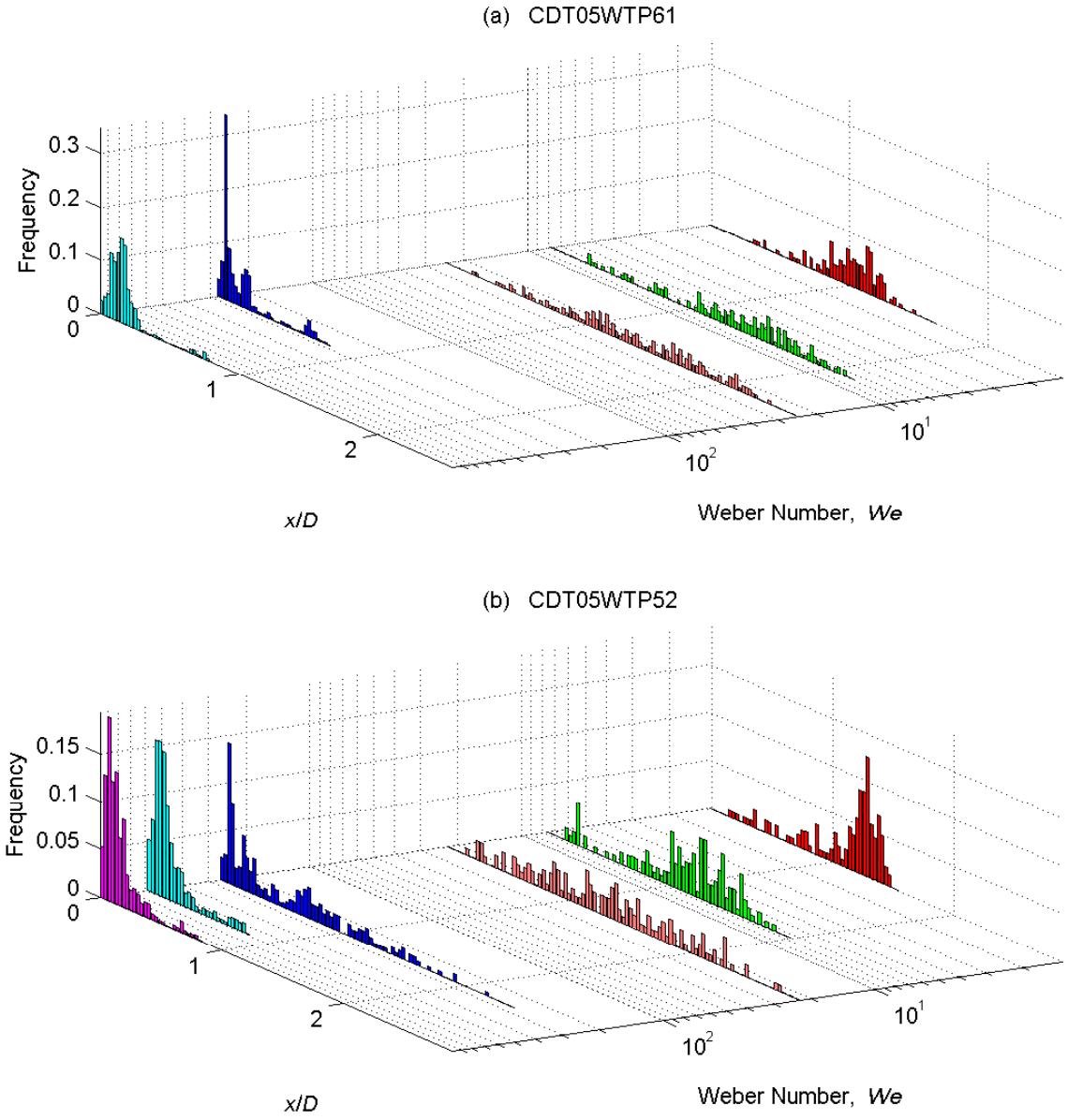

Figure 5.8 CO_2 droplet size histograms. Data are for liquid CO_2 injection through a 5 mm tube orifice into tap water at (a) P = 61 bar and (b) P = 52 bar. x/D is droplet diameter non-dimensionalized with the orifice diameter.

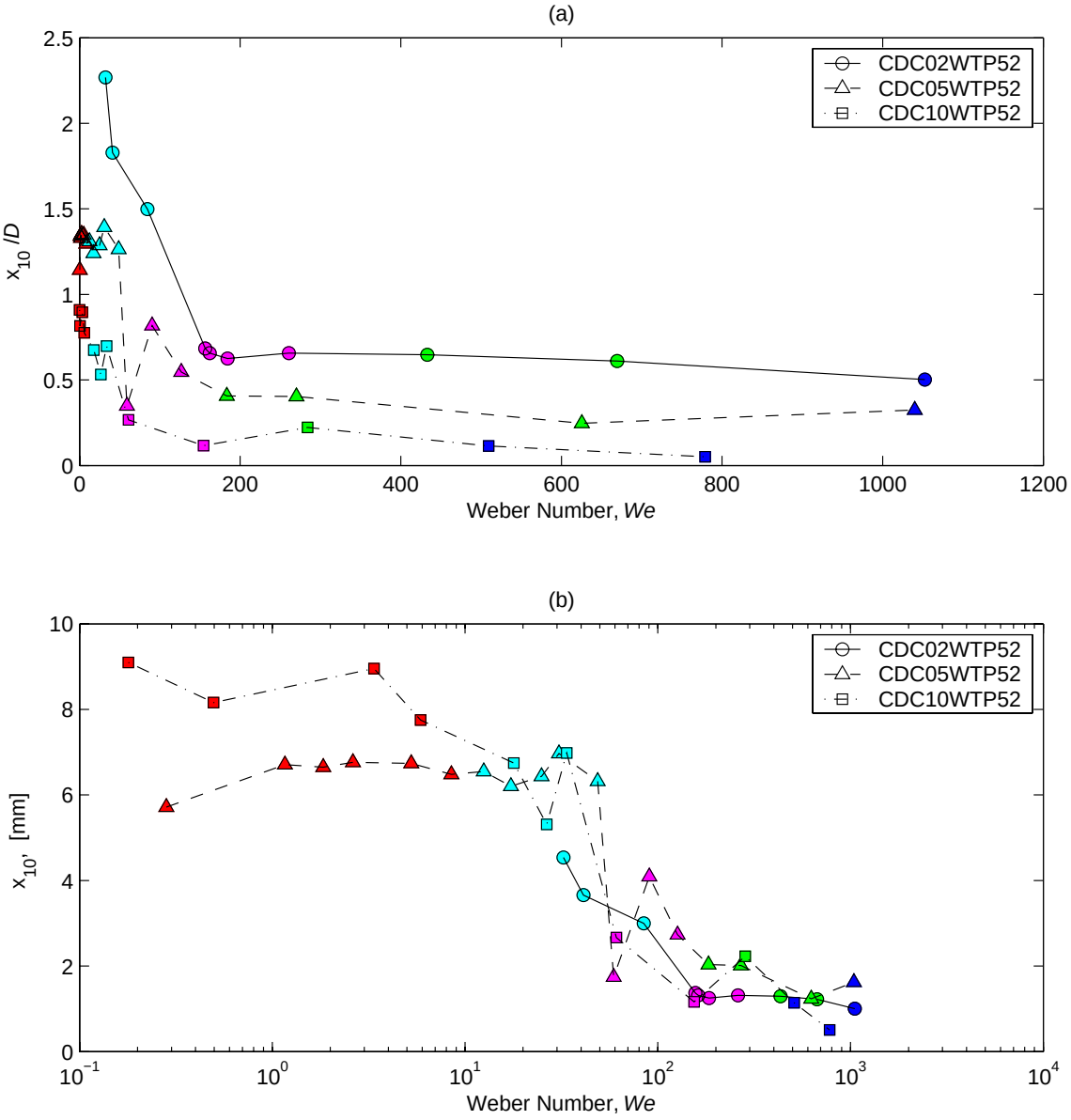

Figure 5.9 Effect of orifice diameter on (a) non-dimensional and (b) dimensional mean droplet diameter. Data are for liquid CO_2 injection into tap water from 2 mm, 5 mm, and 10 mm sharp edge orifices. Red, cyan, magenta, green and blue data points correspond to instability regimes 1, 2, 3, 4, and 5, respectively.

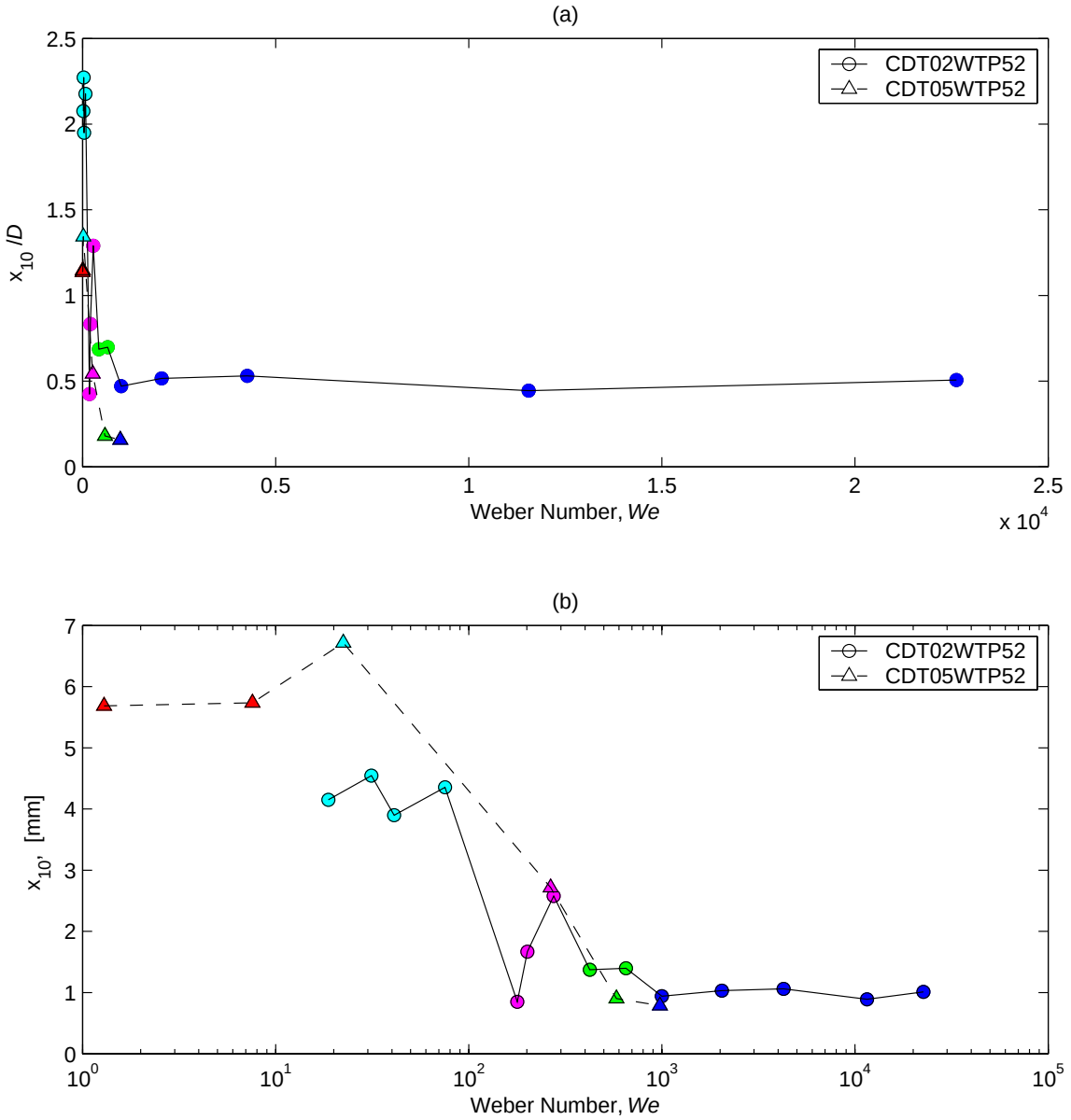

Figure 5.10 Effect of orifice diameter on (a) non-dimensional and (b) dimensional mean droplet diameter. Data are for liquid CO_2 injection into tap water from 2 mm and 5 mm tube orifices at P = 52 bar. Red, cyan, magenta, green and blue data points correspond to instability regimes 1, 2, 3, 4, and 5, respectively.

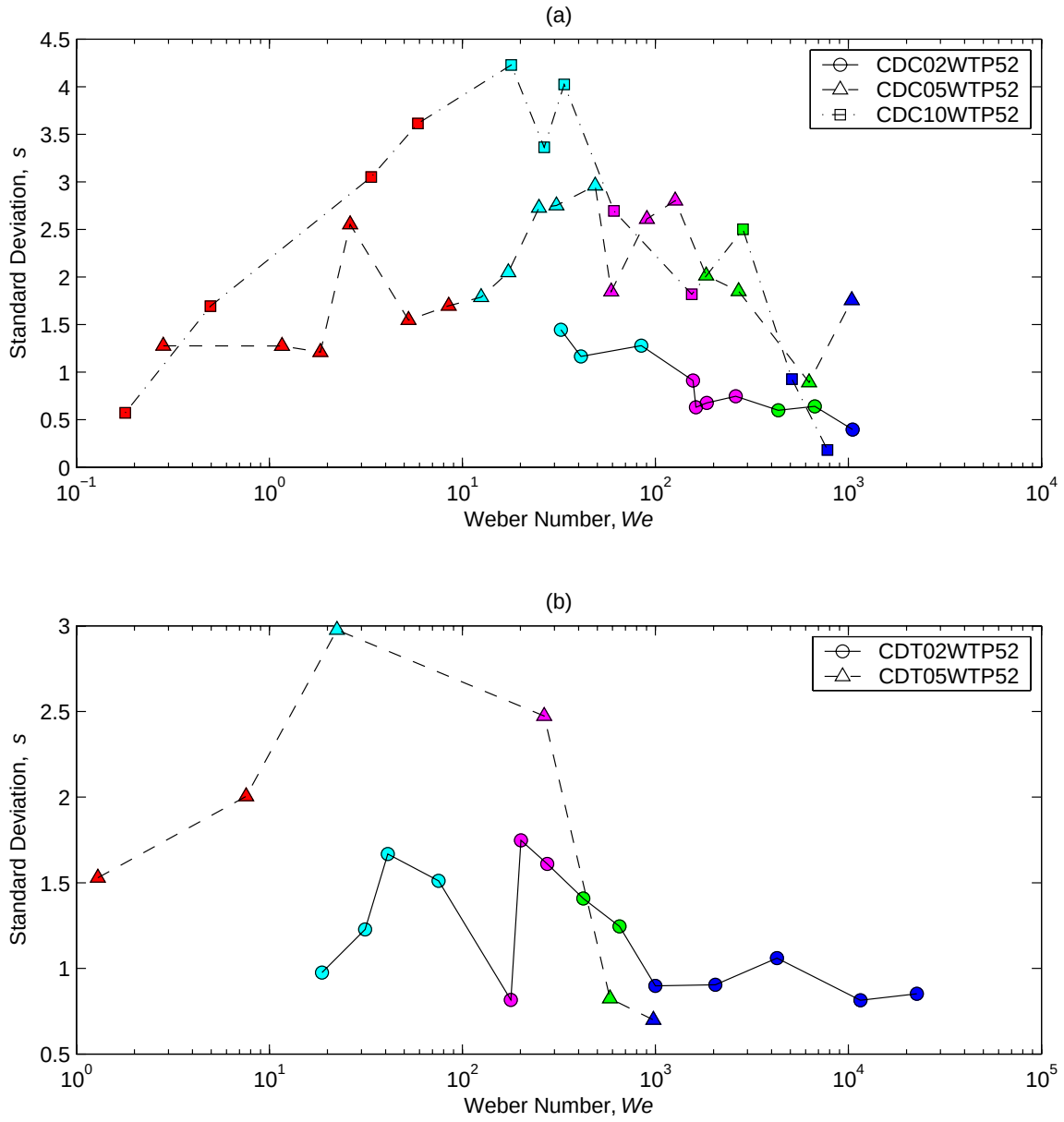

Figure 5.11 Effect of orifice diameter on standard deviation. Data are for liquid CO_2 injection into tap water at 52 bar from (a) sharp edge orifices with 2 mm, 5 mm and 10 mm inside diameters, and (b) tube orifices with 2 mm and 5 mm inside diameters. Red, cyan, magenta, green and blue correspond to instability regimes 1, 2, 3, 4, and 5, respectively.

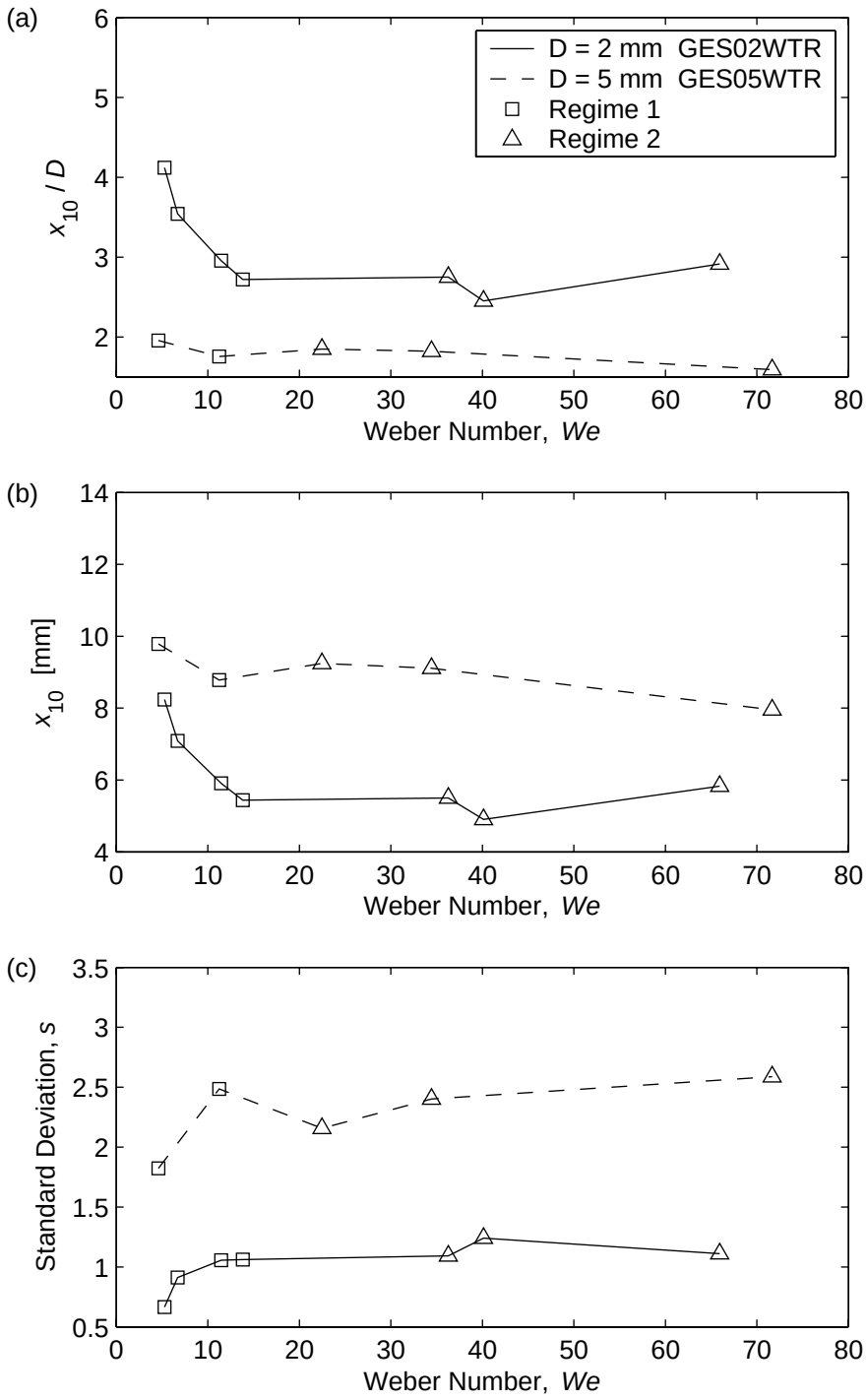

Figure 5.12 Effect of orifice diameter on (a) non-dimensional mean droplet diameter, x_{10}/D, (b) mean diameter x_{10} and (c) standard deviation, s. Data are for Genesis crude oil injection into tap water through sharp edge orifices with 2 mm and 5 mm inside diameters.

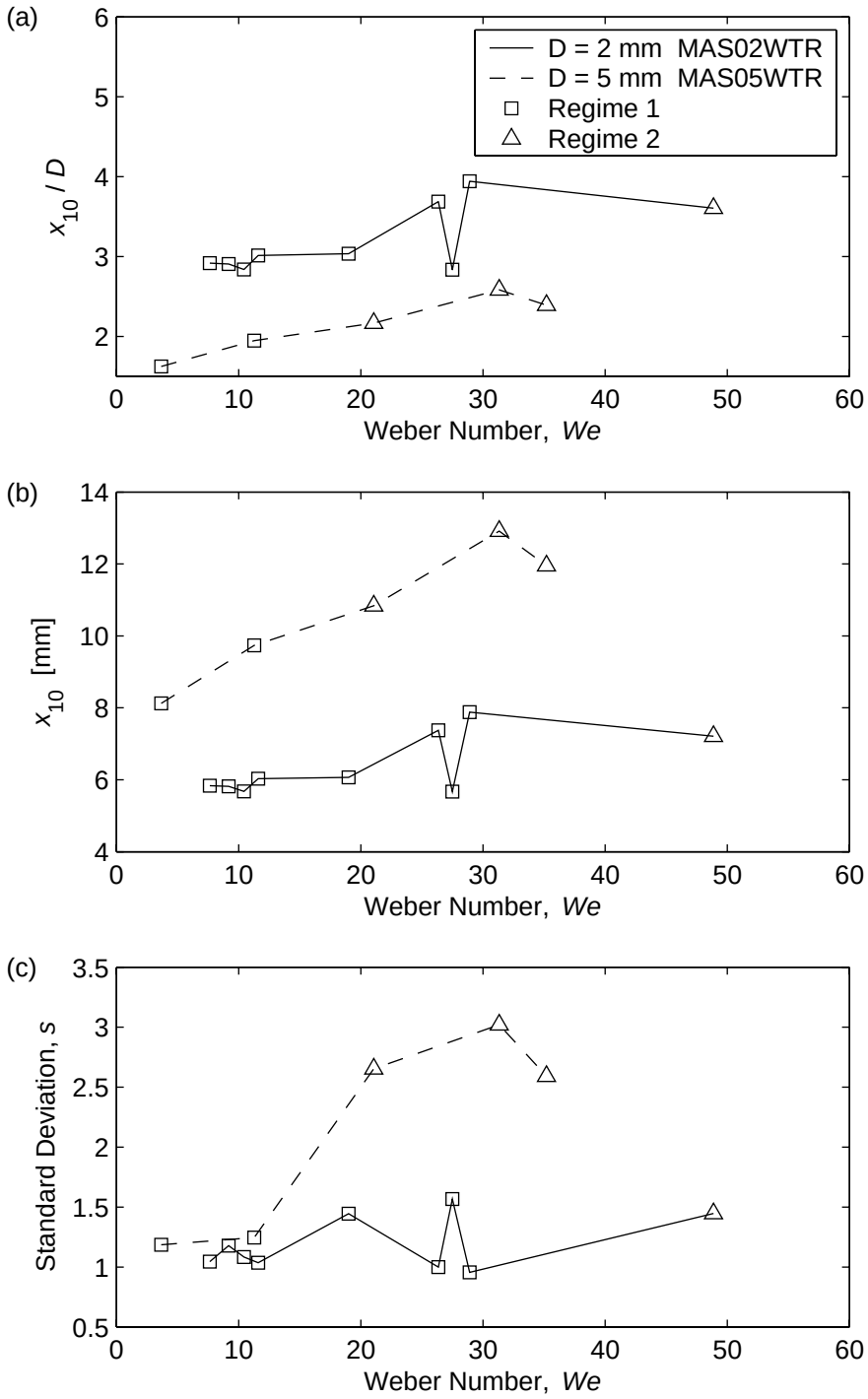

Figure 5.13 Effect of orifice diameter on (a) non-dimensional mean droplet diameter, x_{10}/D, (b) mean diameter x_{10} and (c) standard deviation, s. Data are for Mars TLP crude oil injection into tap water through sharp edge orifices with 2 mm and 5 mm inside diameters.

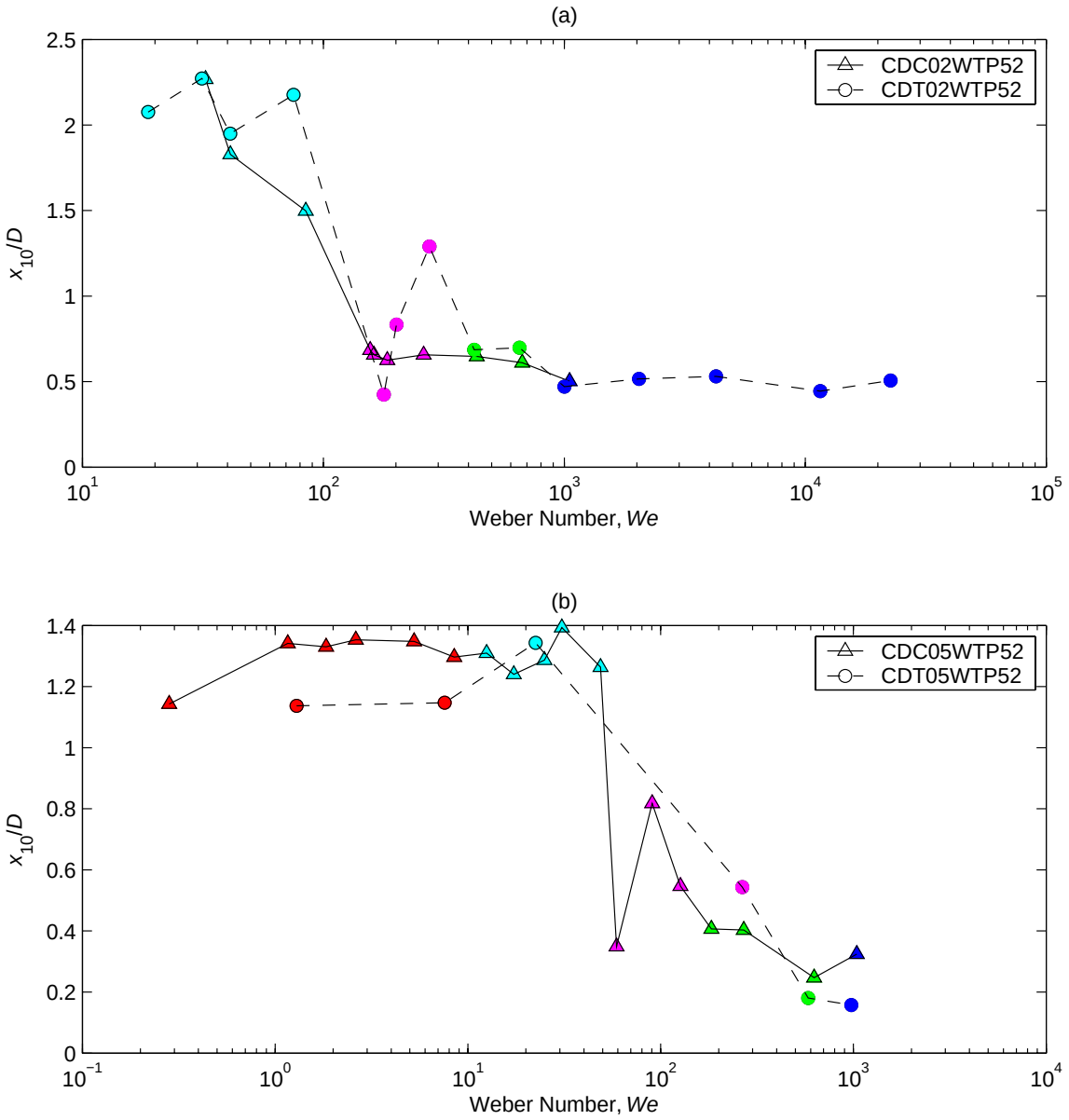

Figure 5.14 Effect of orifice geometry on non-dimensional mean droplet diameter. Data are for liquid CO_2 injection into tap water through sharp edge orifices and tube nozzles with inside diameters of (a) D = 2 mm and (b) D = 5 mm. Red, cyan, magenta, green and blue correspond to instability regimes 1, 2, 3, 4, and 5, respectively.

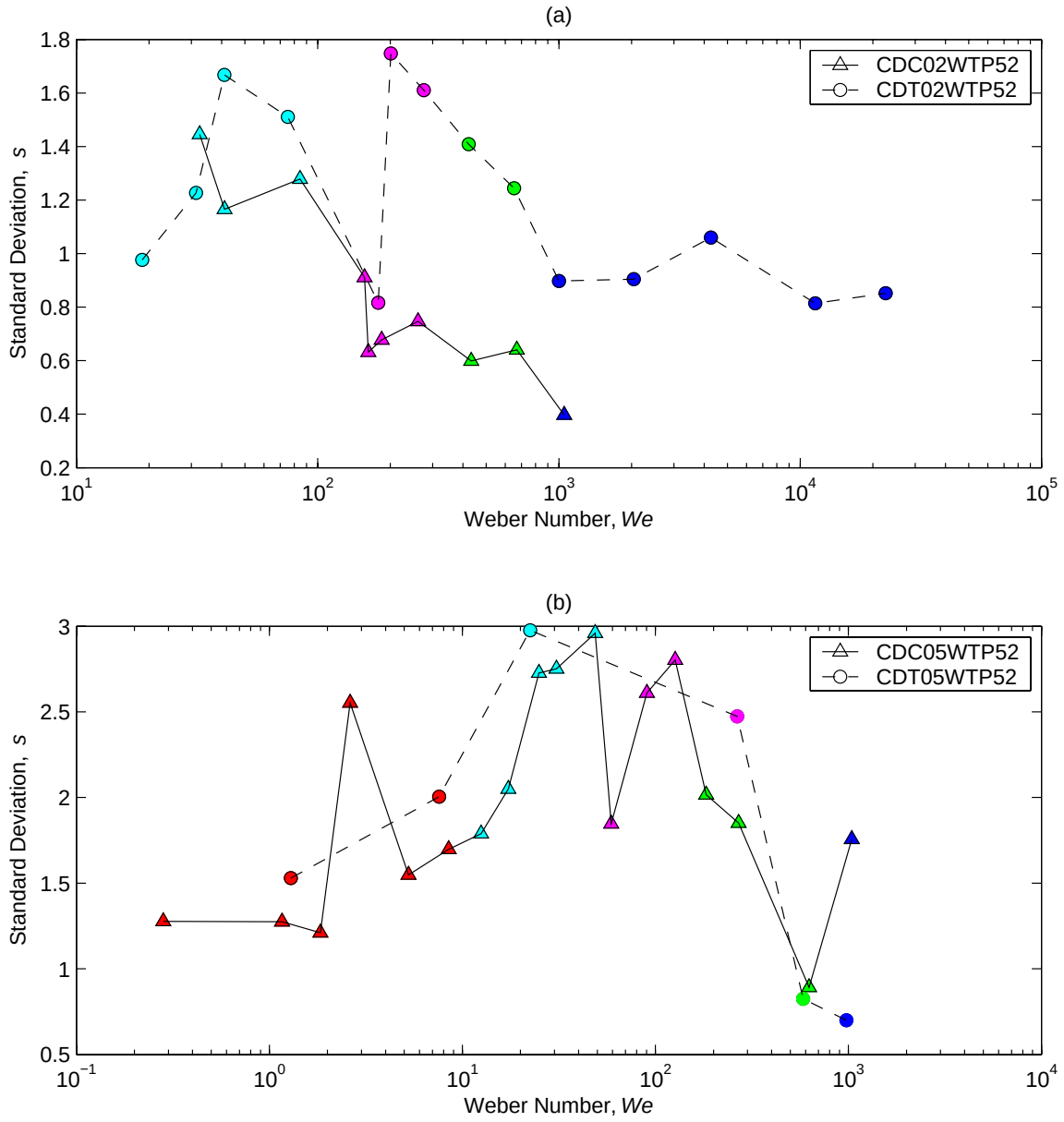

Figure 5.15 Effect of orifice geometry on standard deviation. Data are for liquid CO_2 injection into tap water through sharp edge orifices and tube nozzles with (a) D = 2 mm and (b) D = 5 mm. Red, cyan, magenta, green and blue correspond to instability regimes 1, 2, 3, 4, and 5, respectively.

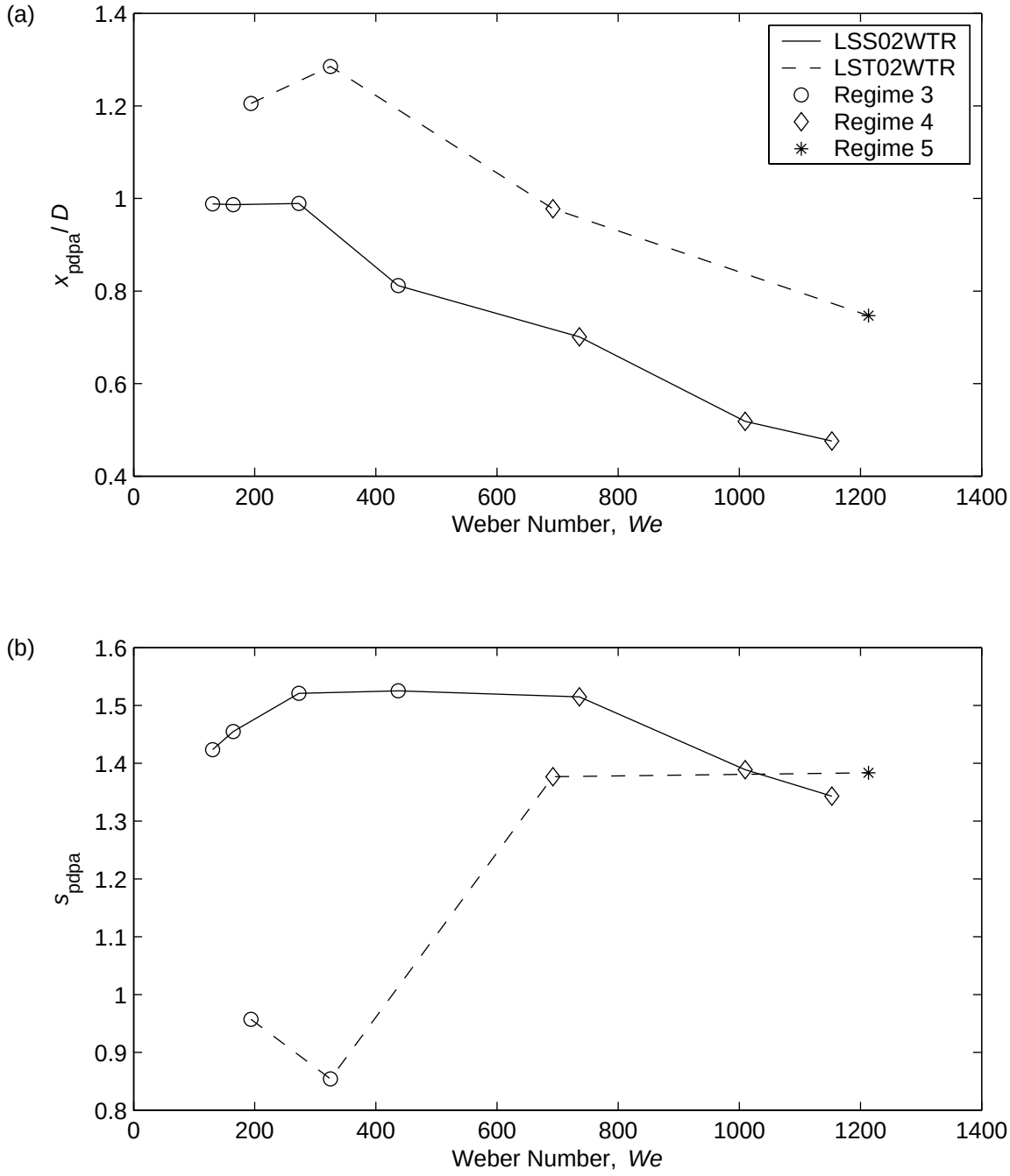

Figure 5.16 Effects of orifice geometry on (a) x_{pdpa} and (b) s_{pdpa}. Data are calculated from incomplete size spectra obtained from PDPA measurements of low viscosity silicone fluid injection into tap water from 2 mm sharp edge orifices and tube nozzles.

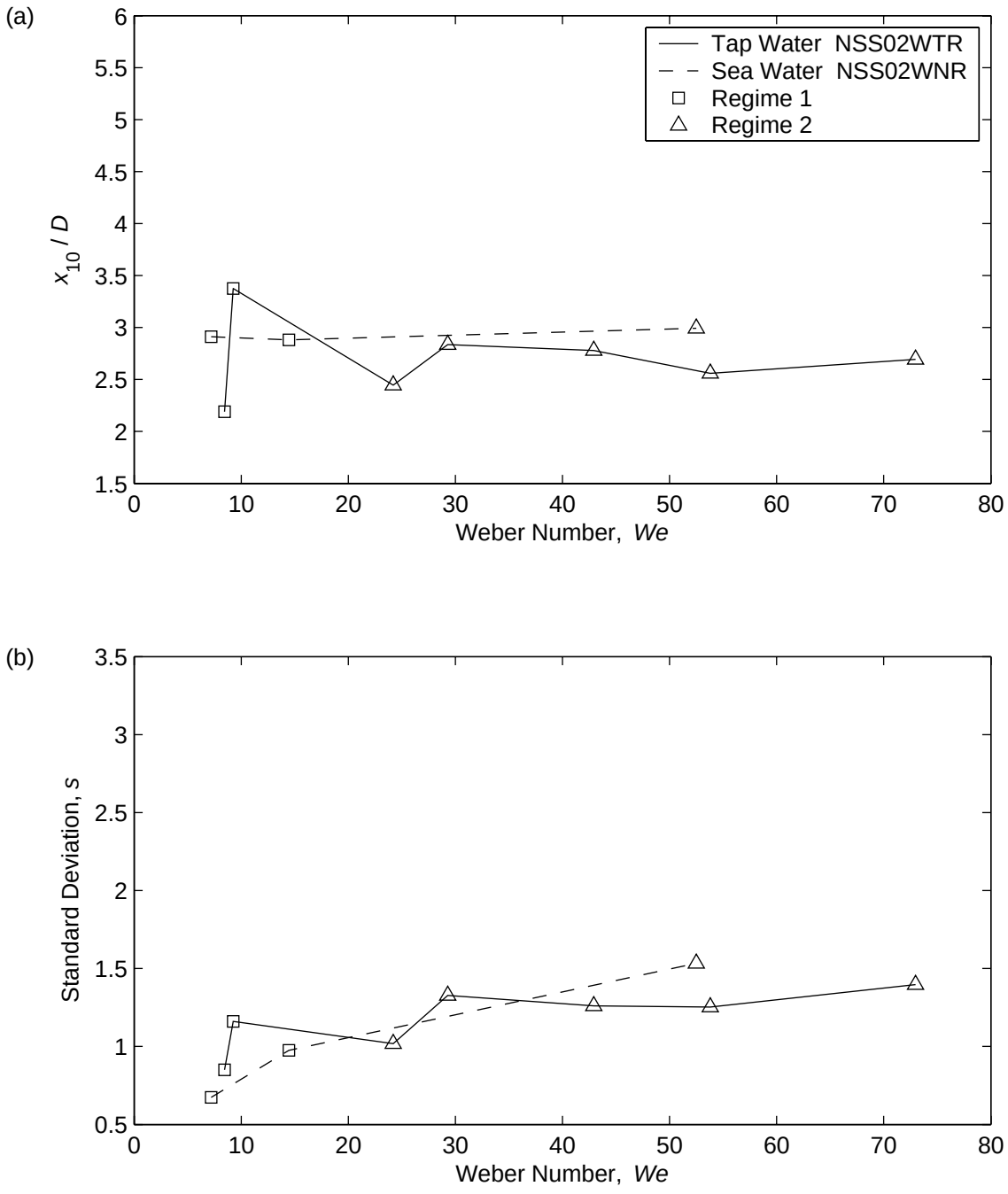

Figure 5.17 Effect of ambient fluid to (a) non-dimensional mean droplet diameter and (b) standard deviation. Data are for Neptune Spar crude oil injection into tap water and natural sea water from a 2 mm sharp edge orifice.

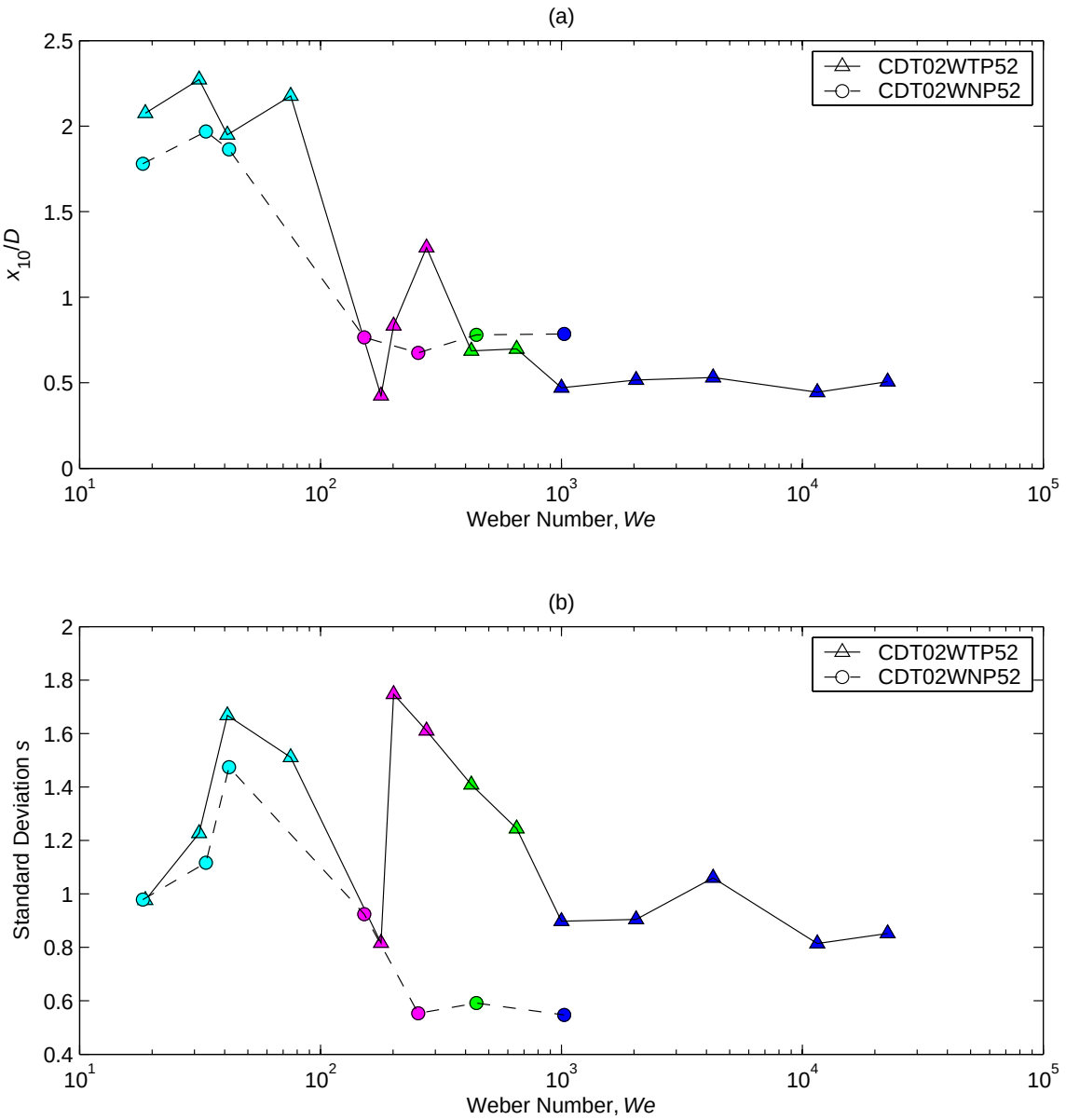

Figure 5.18 Effects of ambient fluid on non-dimensional mean droplet diameter and standard deviation. Data are for liquid CO_2 injection into tap water and natural sea water from a 2 mm tube nozzle. Red, cyan, magenta, green and blue correspond to instability regimes 1, 2, 3, 4, and 5, respectively.

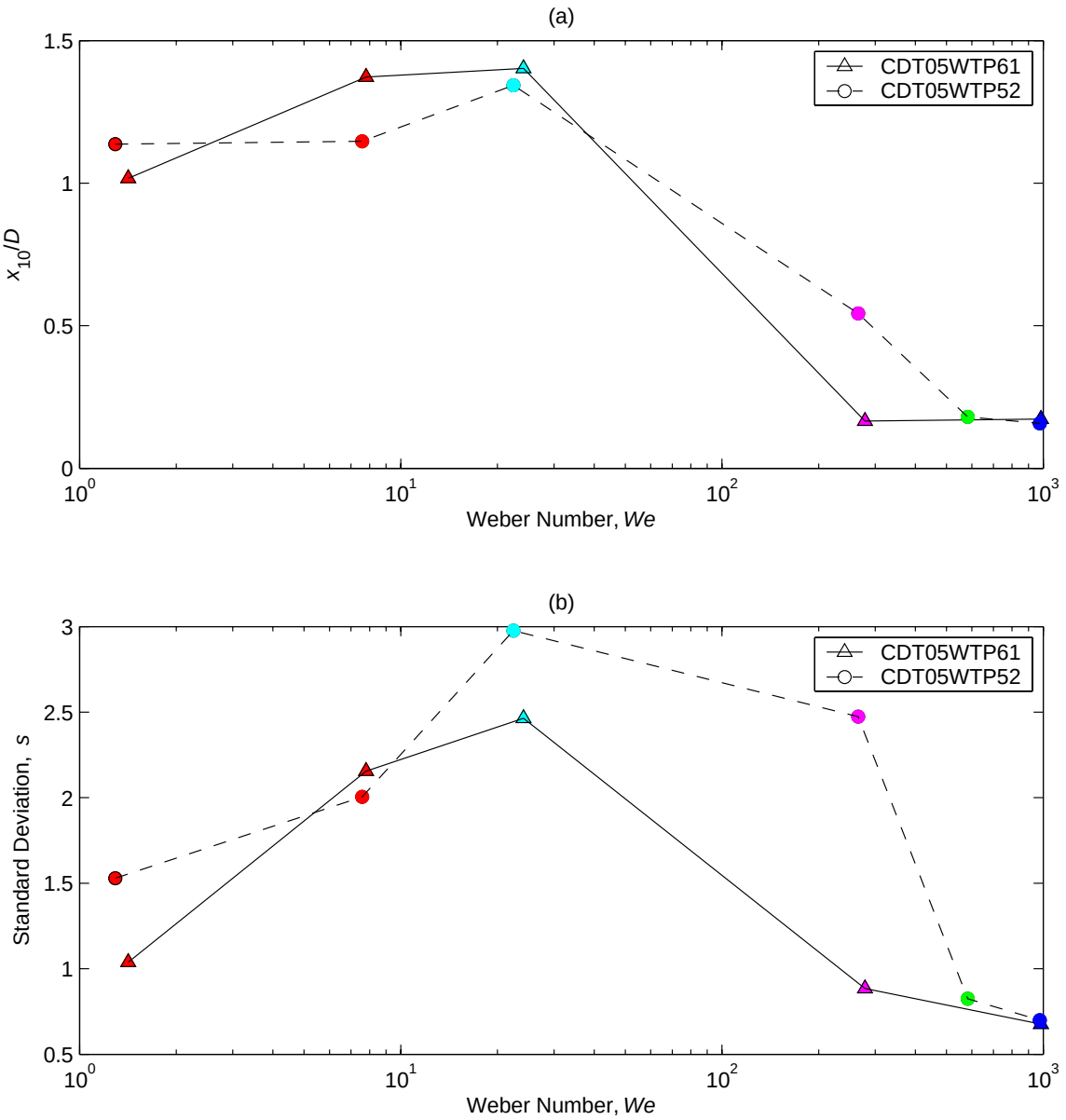

Figure 5.19 Effect of pressure on (a) non-dimensional mean droplet diameter and (b) standard deviation. Data are for liquid CO_2 injection into tap water from a 5 mm tube nozzle at 61 (triangles) and 52 (circles) bar. Red, cyan, magenta, green and blue correspond to instability regimes 1, 2, 3, 4, and 5, respectively.

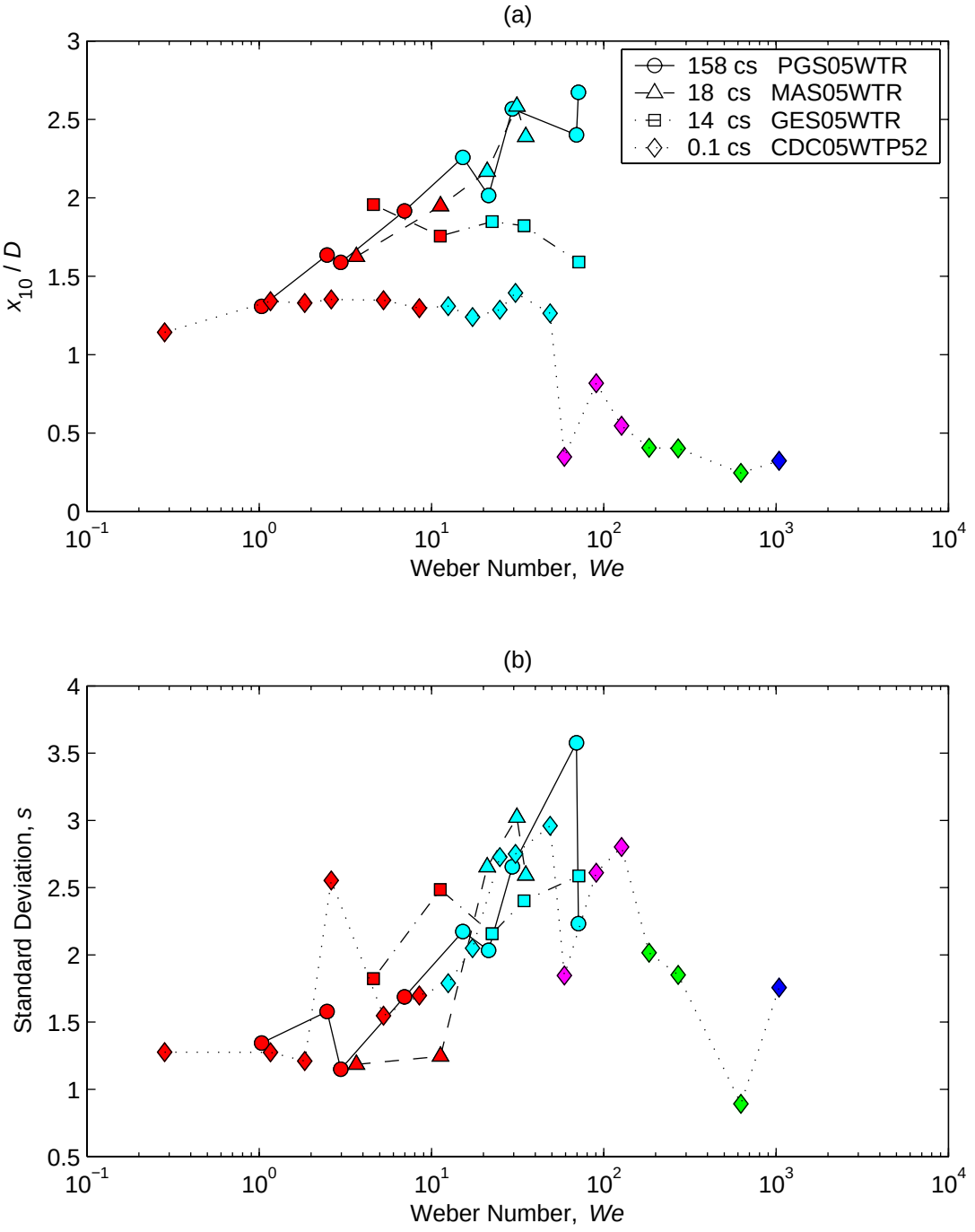

Figure 5.20 Effect of jet fluid viscosity on (a) non-dimensional mean droplet diameter and (b) standard deviation. Data are for injection of 3 crude oils and liquid CO_2 into tap water through 5 mm sharp edge orifices. Red, cyan, magenta, green and blue correspond to instability regimes 1, 2, 3, 4, and 5, respectively.

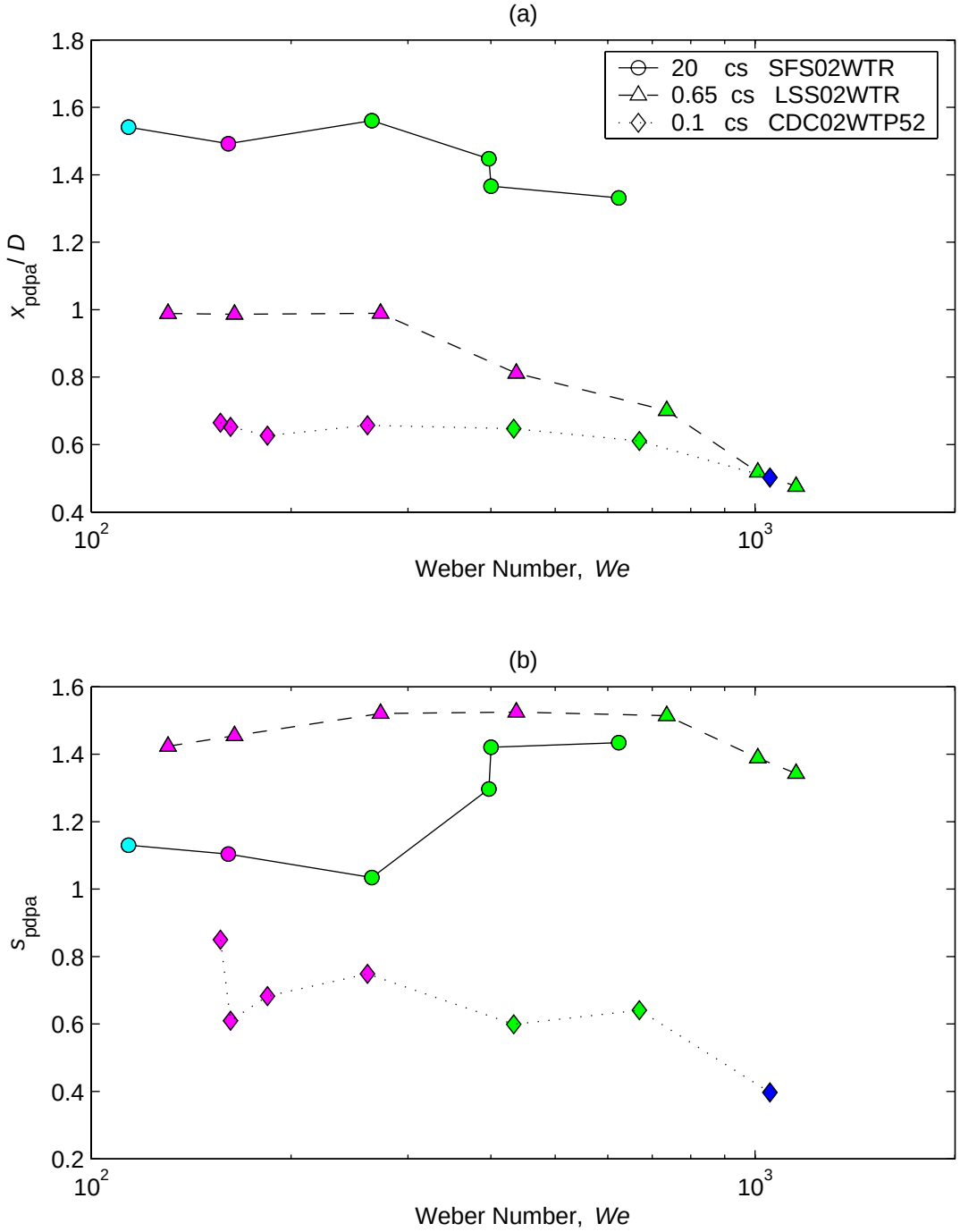

Figure 5.21 Effect of viscosity on (a) x_{pdpa} and (b) s_{pdpa} based on incomplete size spectra obtained from PDPA measurements. Data are for injection of 2 silicone fluids and liquid CO_2 into tap water from 2 mm sharp edge orifices. Cyan, magenta, green and blue correspond to instability regimes 2, 3, 4, and 5, respectively.

5.3 Multimodal Distribution

5.3.1 Distribution Functions

In the absence of a comprehensive fundamental theory of liquid-liquid droplet size distribution, a pragmatic approach is to identify mathematical representations of measured drop size distributions. These functions can then be easily applied to test or calibrate models. Candidate functions include Normal, Log-normal, Weibull, Type I Extreme Value, and Gamma distributions. These functions are described below.

Normal Distribution (norm)

The normal probability density distribution (normpdf) is

$$\text{normpdf}(x,a,b) \equiv f(x|\,a,b) = \frac{1}{\sqrt{2\pi}b}\exp\left[-\frac{(x-a)^2}{2b^2}\right] \tag{5.10}$$

The normal cumulative distribution function (normcdf) is

$$\text{normcdf}(x,a,b) \equiv F(x|\,a,b) = \frac{1}{2}\text{erfc}\left[-\frac{x-a}{b\sqrt{2}}\right] \tag{5.11}$$

Lognormal Distribution (logn)

The lognormal probability density distribution (lognpdf) is

$$\text{lognpdf}(x,a,b) \equiv f(x|a,b) = \frac{1}{xb\sqrt{2\pi}}\exp\left[-\frac{(\ln x-a)^2}{2b^2}\right] \tag{5.12}$$

The lognormal cumulative distribution function (logncdf) is

$$\text{logncdf}(x,a,b) \equiv F(x|\,a,b) = \frac{1}{2}\text{erfc}\left[-\frac{\ln x-a}{b\sqrt{2}}\right] \tag{5.13}$$

Weibull Distribution (wbl)

The Weibull probability density distribution (wblpdf) is

$$\text{wblpdf}(x,a,b) \equiv f(x|a,b) = ba^{-b}x^{b-1}\exp\left[-\left(\frac{x}{a}\right)^{b}\right] \tag{5.14}$$

The Weibull cumulative distribution function (wblcdf) is

$$\text{wblcdf}(x,a,b) \equiv F(x|a,b) = 1-\exp\left[-\left(\frac{x}{a}\right)^{b}\right] \tag{5.15}$$

Type I Extreme Value Distribution (ev)

The type I Extreme Value probability density distribution (evpdf) is

$$\text{evpdf}(x,a,b) \equiv f(x|a,b) = b^{-1}\exp\left[\frac{x-a}{b}-\exp\left(\frac{x-a}{b}\right)\right] \tag{5.16}$$

The type I Extreme Value cumulative distribution function (evcdf) is

$$\text{evcdf}(x,a,b) \equiv F(x|a,b) = 1-\exp\left[-\exp\left(\frac{x-a}{b}\right)\right] \tag{5.17}$$

Gamma Distribution (gam)

The Gamma probability density distribution (gampdf) is

$$\text{gampdf}(x,a,b) \equiv f(x|a,b) = \frac{1}{b^{a}\Gamma(a)}x^{a-1}\exp\left(\frac{x}{b}\right) \tag{5.18}$$

The Gamma cumulative distribution functions (gamcdf) is

$$\text{gamcdf}(x,a,b) \equiv F(x|a,b) = \frac{1}{b^{a}\Gamma(a)}\int_{0}^{x} t^{a-1}e^{\frac{t}{b}}dt \tag{5.19}$$

5.3.2 Cumulative Distribution Function (CDF) Curve Fitting Procedures

In the present study, in order to find the best fit to droplet size cumulative frequency data, the following 3 steps were employed.

Step 1: Parametric fitting

Functions from Matlab Curve Fitting Toolbox were used to fit nonlinear CDFs to data (x_i, P_i), where x_i is droplet size and P_i is the corresponding cumulative frequency, by a nonlinear least squares formulation.

Step 2: K-S test

For each droplet diameter, the Kolmogorov-Smirnov test compares the cumulative frequency, $P_{i,}$ (the proportion of values less than x_i), with $F(x_i)$, the expected cumulative frequency predicted by the proposed distribution (i.e., Normal, Lognormal, etc.) evaluated at x_i. The K-S test uses the maximum difference over all x_i values as its test statistic. Mathematically, this can be written as

$$\mathrm{H} = 0:\ P = F(x), \tag{5.20}$$

where the data do not reject the proposed hypothesis distribution

$$\mathrm{H} = 1:\ P \neq F(x), \tag{5.21}$$

where the data reject the proposed hypothesis distribution

The Kolmogorov-Smirnov test statistic is defined as

$$D_n = \max_{1 \le i \le N} \left| F(x_i) - P_i \right| \tag{5.22}$$

The proposed hypothesis distribution is rejected if the test is significant at the α level. The significant level of a test is the probability of a type I error (rejection a true hypothesis). That is, the probability of rejecting the hypothesis when it is true called the significant level of the test. We use 5% as the significance level.

Step 3: Evaluating goodness of fit

If more than one proposed CDF passes the K-S test, then goodness of fit must be evaluated. The goodness of fit measures that were considered included: (1) residuals; (2) goodness of fit statistics. Residual is a graphical measure, while goodness of fit statistics are numerical measures.

(1) The residual of a fitted CDF is defined as the difference between the data and the fit to the response data at each predictor value of x_i:

$$r_i = P_i - F(x_i) \tag{5.23}$$

Assuming the fit to the data is correct, the residuals should approximate random errors. Therefore, if the calculated residuals appear to behave randomly, then the curve fit to the data is good. If, however, the calculated residuals display a systematic pattern, then it is a sign of a poor fit.

(2) The two goodness of fit statistics considered in the current study were Degree of Freedom Adjusted R-Square, *adjrsquare*, and Root Mean Square Error, *rmse*.

The adjusted R-square statistic, *adjrsquare*, is generally the best indicator of the fit quality when additional coefficients are added to the model.

$$adjrsquare = 1 - \left(\frac{n-1}{n-m}\right)\frac{SSE}{SST} \tag{5.24}$$

where n is the number of data points included in the fit; m is the number of fitted coefficients; $n-m$ is the residual degrees of freedom. *SSE* is the summed square of residuals and is defined as:

$$SSE = \sum_{i=1}^{n} r_i^2 \tag{5.25}$$

SST is the sum of squares about the mean and is defined as

$$SST = \sum_{i=1}^{n} \left(P_i - \overline{P}\right)^2 \tag{5.26}$$

The adjusted R-square statistic can take on any value ≤ 1, with a value closer to 1 indicating a better fit.

Root Mean Square Error is frequently used to evaluate goodness of fit. This statistic is also known as the fit standard error and the standard error of the regression

$$rmse = \sqrt{\frac{\sum_{i=1}^{n} \left(P_i - F\left(x_i\right)\right)^2}{n-m}} = \sqrt{\frac{SSE}{n-m}} \tag{5.27}$$

A *rmse* value closer to 0 implies a better fit.

5.3.3 Multimodal Distributions

Standard probability density and cumulative distribution functions identified in section 5.3.1 presented problems when fit to droplet size data corresponding to breakup regimes 3 and 4. In these regimes, none of the curvefits passed the K-S test. In the atomization breakup regime 5, only a portion of the data could be fit by a lognormal distribution. Moreover, some curvefits to data at breakup regimes 1 and 2 that passed the K-S tests, yielded residuals that displayed a systematic pattern, implying a poor fit. Figure 5.22

illustrates this problem. Curvefits the Normal, Weibull, Type I Extreme Value and Gamma functions to data from run CDC05WTP52R10 in regime 1 passed the K-S tests. The plots of the residuals, however, display systematic patterns that indicate better fits may be possible.

5.3.3.1 Introduction to Weighted Multimodal Distribution

To resolve the above problems, new mathematical distribution functions were devised which we refer to as weighted multimodal distributions. Descriptions of these functions follow.

Weighted bimodal distribution:

The PDF and CDF of the weighted bimodal distribution are

$$f_{1,2}\left(x\middle| a_1,a_2,a_3,a_4,a_5\right)=a_1 f_1\left(x\middle| a_2,a_3\right)+\left(1-a_1\right)f_2\left(x\middle| a_4,a_5\right) \tag{5.28}$$

$$F_{1,2}\left(x\middle| a_1,a_2,a_3,a_4,a_5\right)=a_1 F_1\left(x\middle| a_2,a_3\right)+\left(1-a_1\right)F_2\left(x\middle| a_4,a_5\right) \tag{5.29}$$

where $0\le a_1\le 1$,

f_1 and f_2 are any two of the PDFs identified in section 5.3.1. F_1 and F_2 are any two of the CDFs identified in section 5.3.1. There are a total of five free parameters, a_1,a_2,a_3,a_4, and a_5, which must be evaluated by curvefit using the method of non-linear least squares. By definition, $F_{1,2}$ is monotone increasing and must satisfy the conditions

$$F_{1,2}\left(0\middle| a_1,a_2,a_3,a_4,a_5\right)=a_1F_1\left(0\middle| a_2,a_3\right)+\left(1-a_1\right)F_2\left(0\middle| a_4,a_5\right)=0$$

$$F_{1,2}\left(+\infty\middle| a_1,a_2,a_3,a_4,a_5\right)=a_1F_1\left(1\middle| a_2,a_3\right)+\left(1-a_1\right)F_2\left(0\middle| a_4,a_5\right)=a_1+\left(1-a_1\right)=1$$

Weighted trimodal distribution:

The PDF and CDF of the weighted trimodal distribution are

$$f_{1,2,3}\left(x\middle| a_1,a_2,a_3,a_4,a_5,a_6,a_7,a_8\right)$$

$$=a_1 f_1\left(x\middle| a_3,a_4\right)+\left(1-a_1\right)\left[a_2 f_2\left(x\middle| a_5,a_6\right)+\left(1-a_2\right)f_3\left(x\middle| a_7,a_8\right)\right]$$

$$=a_1 f_1\left(x\middle| a_3,a_4\right)+\left(1-a_1\right)a_2 f_2\left(x\middle| a_5,a_6\right)+\left(1-a_1\right)\left(1-a_2\right)f_3\left(x\middle| a_7,a_8\right) \qquad (5.30)$$

$$F_{1,2,3}\left(x\middle| a_1,a_2,a_3,a_4,a_5,a_6,a_7,a_8\right)$$

$$=a_1 F_1\left(x\middle| a_3,a_4\right)+\left(1-a_1\right)\left[a_2 F_2\left(x\middle| a_5,a_6\right)+\left(1-a_2\right)F_3\left(x\middle| a_7,a_8\right)\right]$$

$$=a_1 F_1\left(x\middle| a_3,a_4\right)+\left(1-a_1\right)a_2 F_2\left(x\middle| a_5,a_6\right)+\left(1-a_1\right)\left(1-a_2\right)F_3\left(x\middle| a_7,a_8\right) \qquad (5.31)$$

where $0\le a_1,a_2\le 1,$

we have $F_{1,2,3}\left(x=0\right)=0;\qquad F_{1,2,3}\left(x=+\infty\right)=1$

f_1, f_2 and f_3 are any three of the PDFs identified in section 5.3.1. F_1 , F_2 and F_3 are any three of the CDFs identified in section 5.3.1. There are 8 free parameters ($a_1,a_2,a_3,a_4,a_5,a_6,a_7,a_8$) for the trimodal distribution.

Weighted *n*-modal distributions

A weighted *n*-modal distribution uses *n* weighted PDFs or CDFs distributions. The PDF and CDF of a weighted *n*-modal distribution are

$$f_{1,2,\ldots,n}\left(x\middle| a_1,a_2,\cdots,a_{3n-1}\right)$$

$$=a_1 f_1\left(x\middle| a_n,a_{n+1}\right)+\left(1-a_1\right)a_2 f_2\left(x\middle| a_{n+2},a_{n+3}\right)$$

$$+\cdots$$

$$+\left(1-a_1\right)\left(1-a_2\right)\cdots\left(1-a_{i-1}\right)a_i f_i\left(x\middle| a_{3i-2},a_{3i-1}\right)$$

$$+\cdots$$

$$+(1-a_1)(1-a_2)\cdots(1-a_{n-1})f_n(x|\,a_{3n-2},a_{3n-1}) \tag{5.32}$$

$$F_{1,2,\ldots,n}(x|\,a_1,a_2,\cdots,a_{3n-1})$$

$$=a_1F_1(x|\,a_n,a_{n+1})+(1-a_1)a_2F_2(x|\,a_{n+2},a_{n+3})$$

$$+\cdots$$

$$+(1-a_1)(1-a_2)\cdots(1-a_{i-1})a_iF_i(x|\,a_{3i-2},a_{3i-1})$$

$$+\cdots$$

$$+(1-a_1)(1-a_2)\cdots(1-a_{n-1})F_n(x|\,a_{3n-2},a_{3n-1}) \tag{5.33}$$

where $i=1,\cdots,n$

$$0\le a_{1,\cdots,n-1}\le 1$$

we have $F_{1,2,\cdots,i,\cdots,n}(x=0)=0$; $F_{1,2,\cdots,i,\cdots,n}(x=+\infty)=1$

The *n*-modal function has 3*n*-1 coefficients which may be optimized to fit the data. The first *n*-1 coefficients are weighted factors with values between 0 and 1. As mentioned in section 5.3.1, five separate single mode distributions were defined for this study. The data suggest that the droplet size spectra typically exhibit no more than 3 peaks (usually 1 or 2). The number of combinations of the five single mode distributions (where order doesn't matter) for *n* =1 (single mode), *n* = 2 (bimodal) and *n* = 3 (trimodal) is 5, 15 and 35 respectively. The weighted multimodal probability density and cumulative distribution functions at *n* =1, 2, and 3 used in the current study are listed in Tables A.1, A.2 and A.3, in Appendix A, respectively. A few cases used 4 mode functions (*n* = 4). For *n* = 4, there are 70 possible combinations of the five single mode distributions in Table A.4.

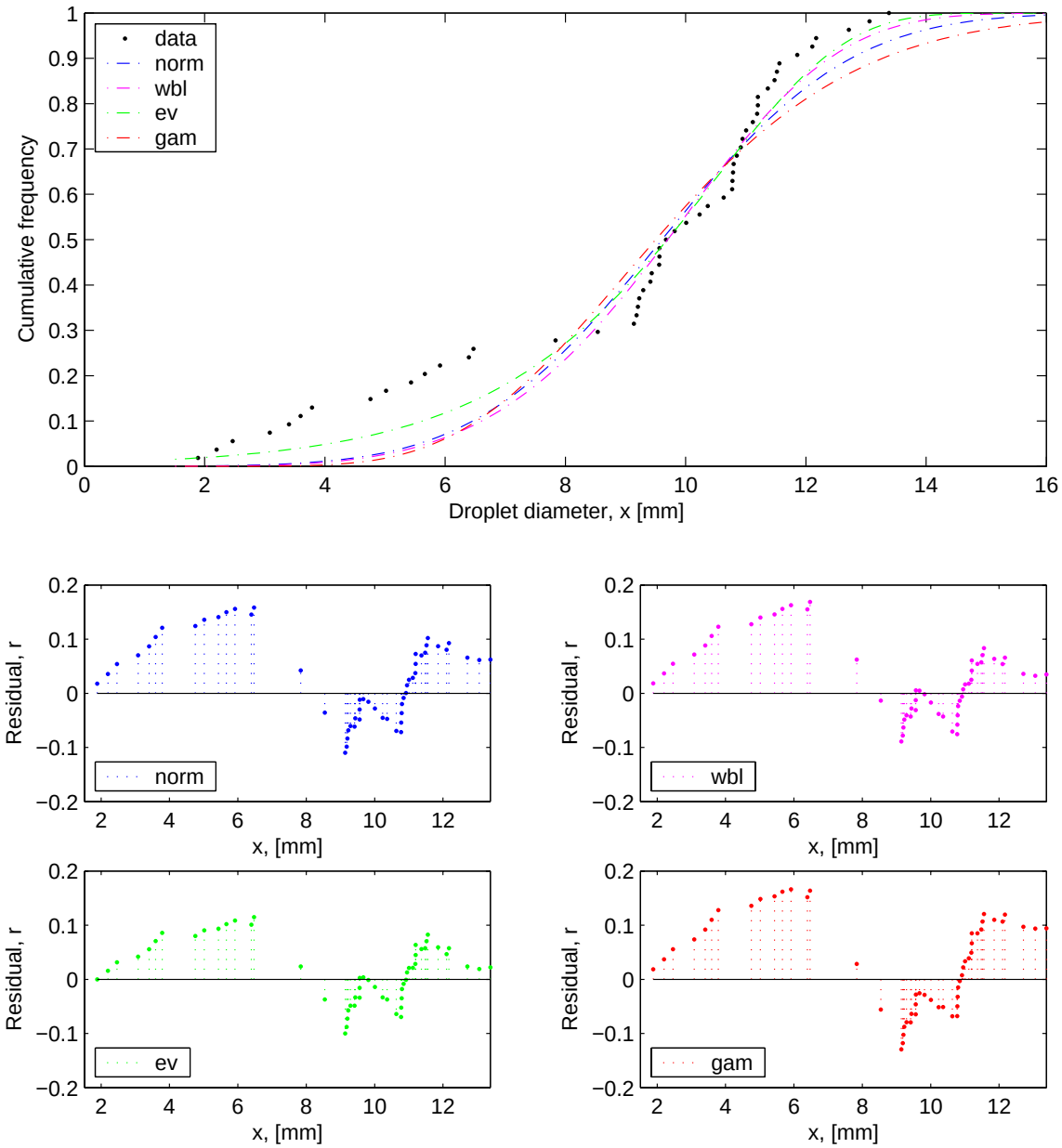

Figure 5.22 Curve fits of 4 CDFs to the data from test run CDC10WTP52R10 in breakup regime 1. The top diagram shows the curve fits and data. All 4 fits passed the K-S tests. The corresponding residual plots display systematic behavior which indicates that the fits are rather poor.

5.3.3.2 Sample Applications of the Weighted Multimodal Distributions for CO_2 Droplet Size Distribution Studies

The application of weighted multimodal distributions to fit the droplet size data over the five instability regimes was evaluated. Spectra were obtained by combining PDPA and digital video analysis data according to the method described in Chapter 2. In instability regime 1, the primary monodispersed droplet size is usually well represented by a single mode distribution; however, as shown previously in Figure 5.22, there are instances, especially as the transition to regime 2 is approached or where satellite drops form, when a multimodal distribution would provide a better fit.

Test CDC10WTP52R10 was employed to compare the fit of single mode and bimodal functions. This regime 1 test corresponds to liquid CO_2 injection into tap water at a pressure of 52 bars. The PDF, CDF and residual for the different tested distributions are shown in Figures 5.23, 5.24 and 5.25. The bimodal distributions clearly better represent the data.

Test CDT02WTP52R12 is representative of instability regime 2. Bimodal characteristics were evident in the data from instability regime 2. In this test, liquid CO_2 was injected from a 2 mm tube nozzle at a pressure of 52 bar. The PDF, CDF and residual for distributions are shown in Figures 5.26, 5.27 and 5.28.

An example of single mode and bimodal fits to data from instability regime 5 is provided in Figures 5.29, 5.30 and 5.31. The data are for liquid CO_2 injection from a 2 mm tube orifice at a pressure of 52 bar. The test is CDT02WTP52R7. Here again, a bimodal distribution provides a superior representation of the polydispersion.

The polydispersed droplet ensemble generated in instability regimes 1, 2 and 5 appear to be well described by weighted bimodal distributions. In instability regimes 3 and 4, however, where multiple instabilities appear to operate in parallel to generate two or three modes of droplets, higher order distributions may be needed.

Comparison of 5 single, 15 bimodal, 35 tri-modal and 70 four-modal functions used to describe experimental spectra from regime 3 are shown in Figures 5.32, 5.33, 5.34, and 5.35. The data are for test CDC02WTP52R20 in which liquid CO_2 was injected into tap water at 52 bar from a 2 mm sharp edge orifice. A similar example of multimodal curvefits to spectra from instability regime 3 is shown in Figures 5.36 and 5.37. In this test (CDT02WTP52R3), liquid CO_2 was injected into tap water at 52 bar from a 2 mm tube orifice. These two examples from regime 3 demonstrate that multimodal functions are needed to describe the complex spectra representative of transitional breakup where multiple instabilities give rise to multiple classes (modes) of droplets.

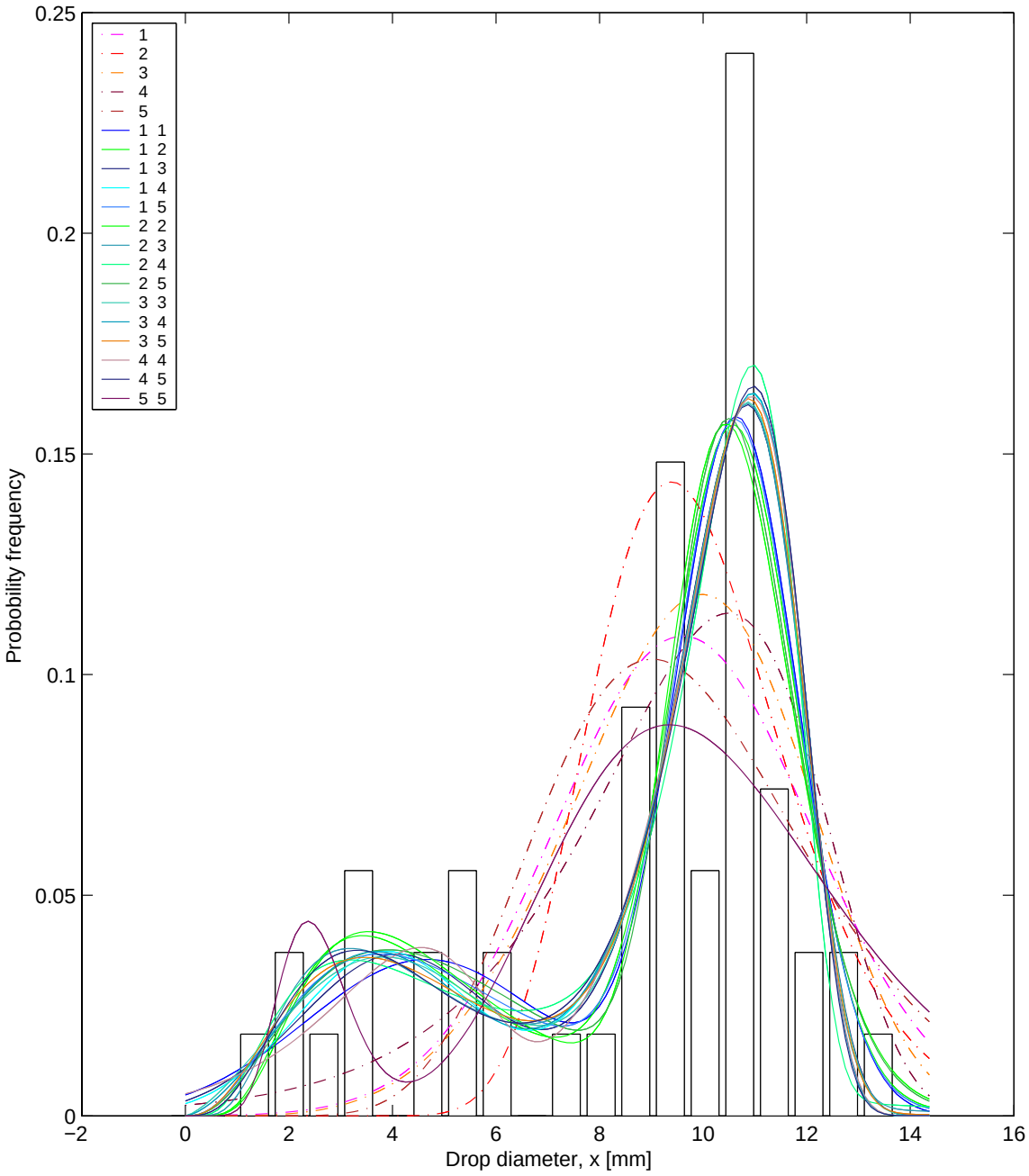

Figure 5.23 Comparison of single mode and bimodal PDFs with the data for CO_2 injection from a 10 mm orifice in instability regime 1. The corresponding CDF and residual plots are provided in Figures 5.24 and 5.25.

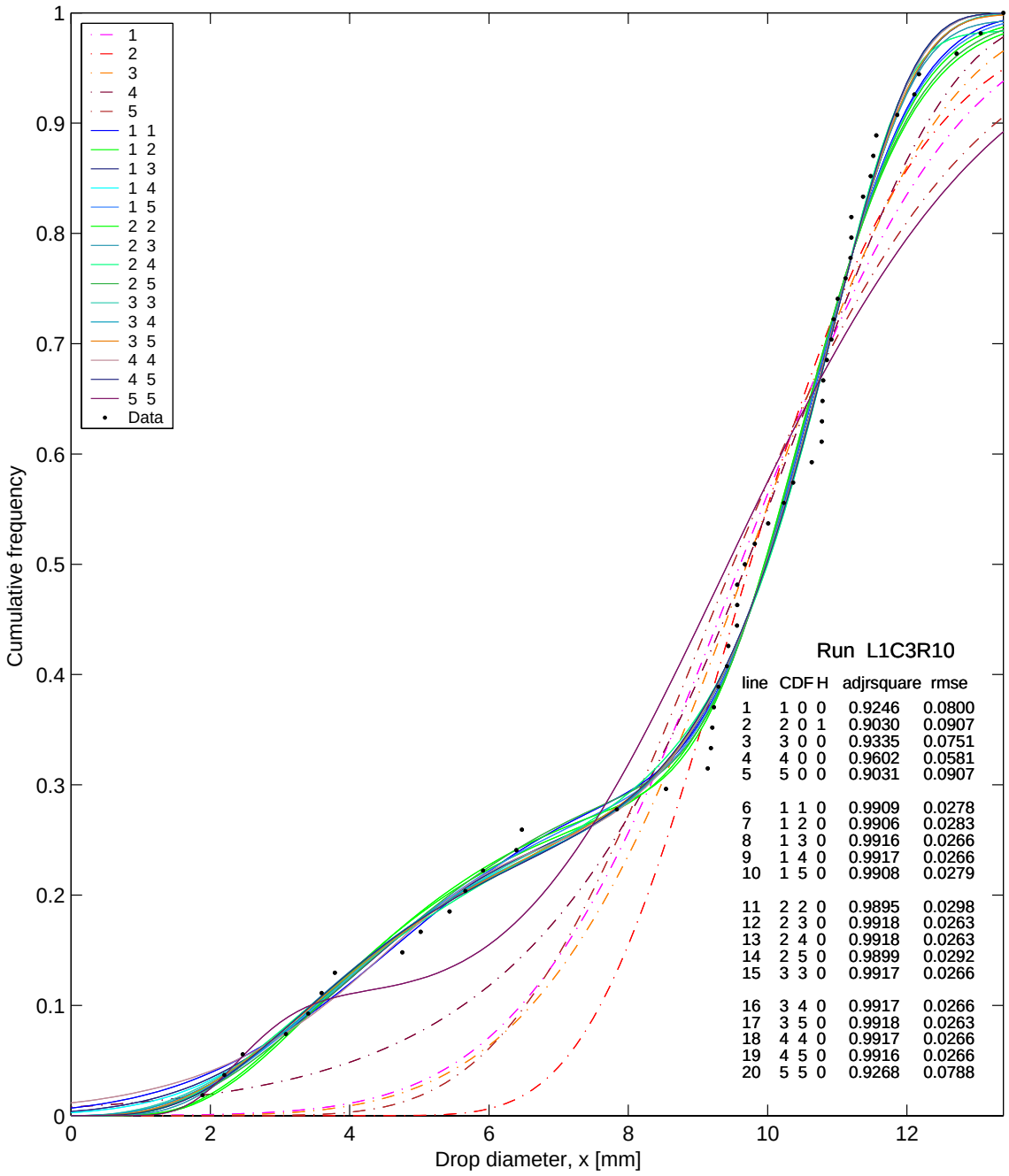

Figure 5.24 Comparison of single mode and weighted bimodal CDFs with the data from CO_2 injection from a 10 mm orifice in instability regime 1. The corresponding PDF and residual plots are in Figures 5.23 and 5.25. Test ID (e.g. L1C3R1) key given in Table 5.1.

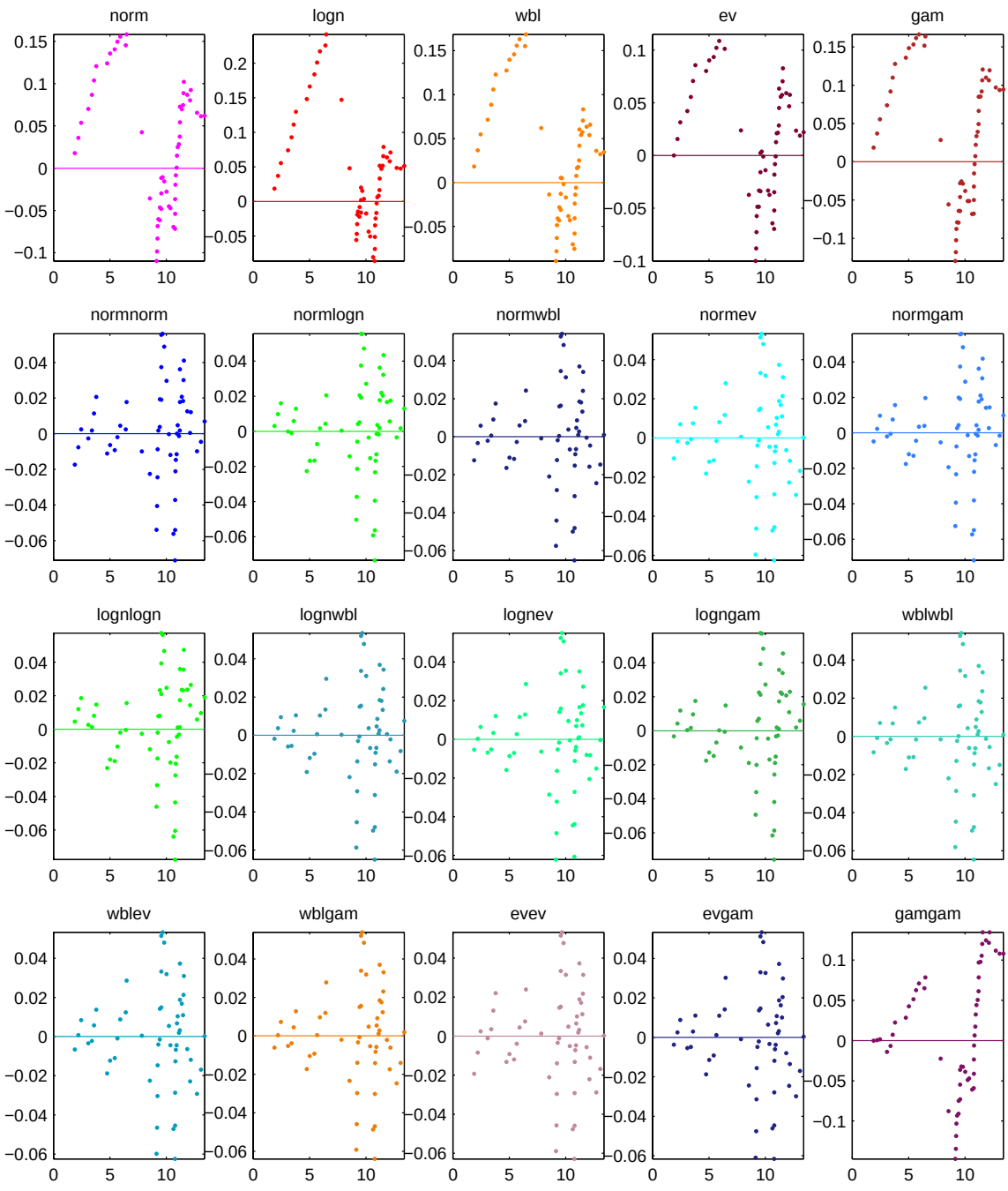

Figure 5.25 Calculated residuals for single mode and weighted bimodal CDFs. Data are for CO_2 injection from a 10 mm orifice in breakup regime 1. The corresponding PDF and CDF plots are provide in Figures 5.23 and 5.24.

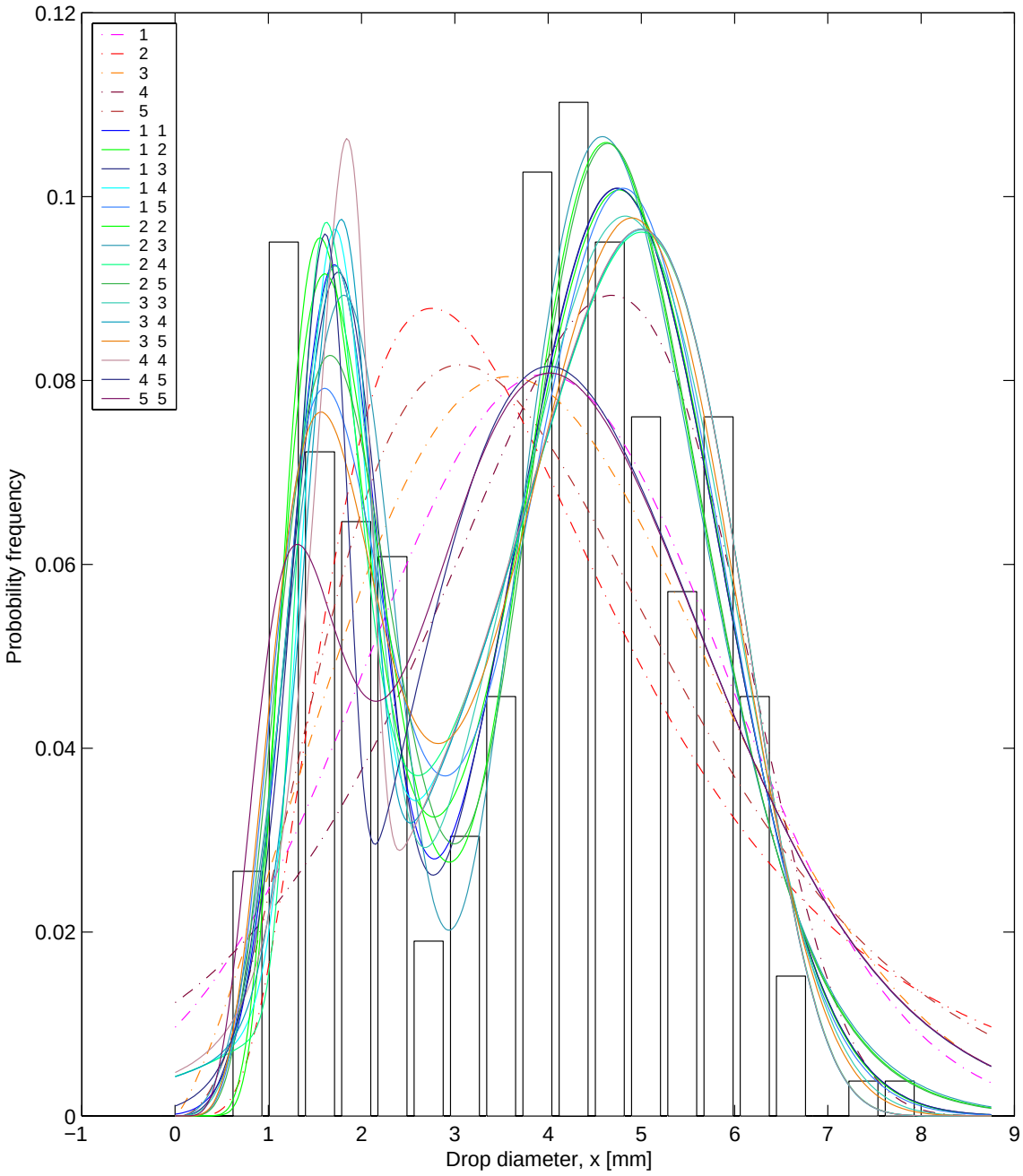

Figure 5.26 Comparison of single mode and bimodal PDFs with the data for CO_2 injection from a 2 mm tube nozzle in instability regime 2. The corresponding CDF and residual plots are provided in Figures 5.27 and 5.28.

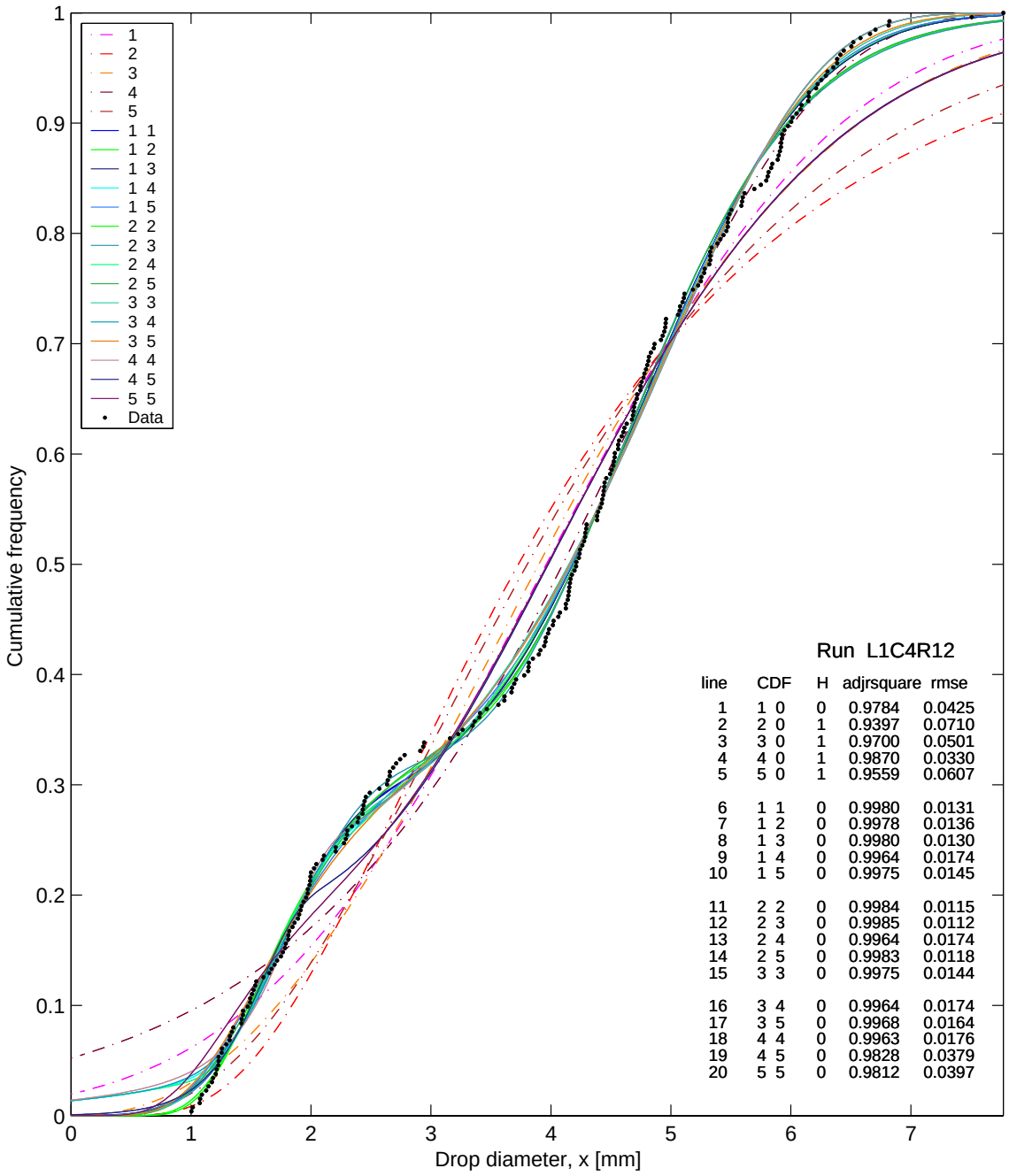

Figure 5.27 Comparison of single mode and bimodal CDFs fittings with the data for CO_2 injection from a 2 mm tube nozzle in instability regime 2. The corresponding PDF and residual plots are provided in Figures 5.26 and 5.28.

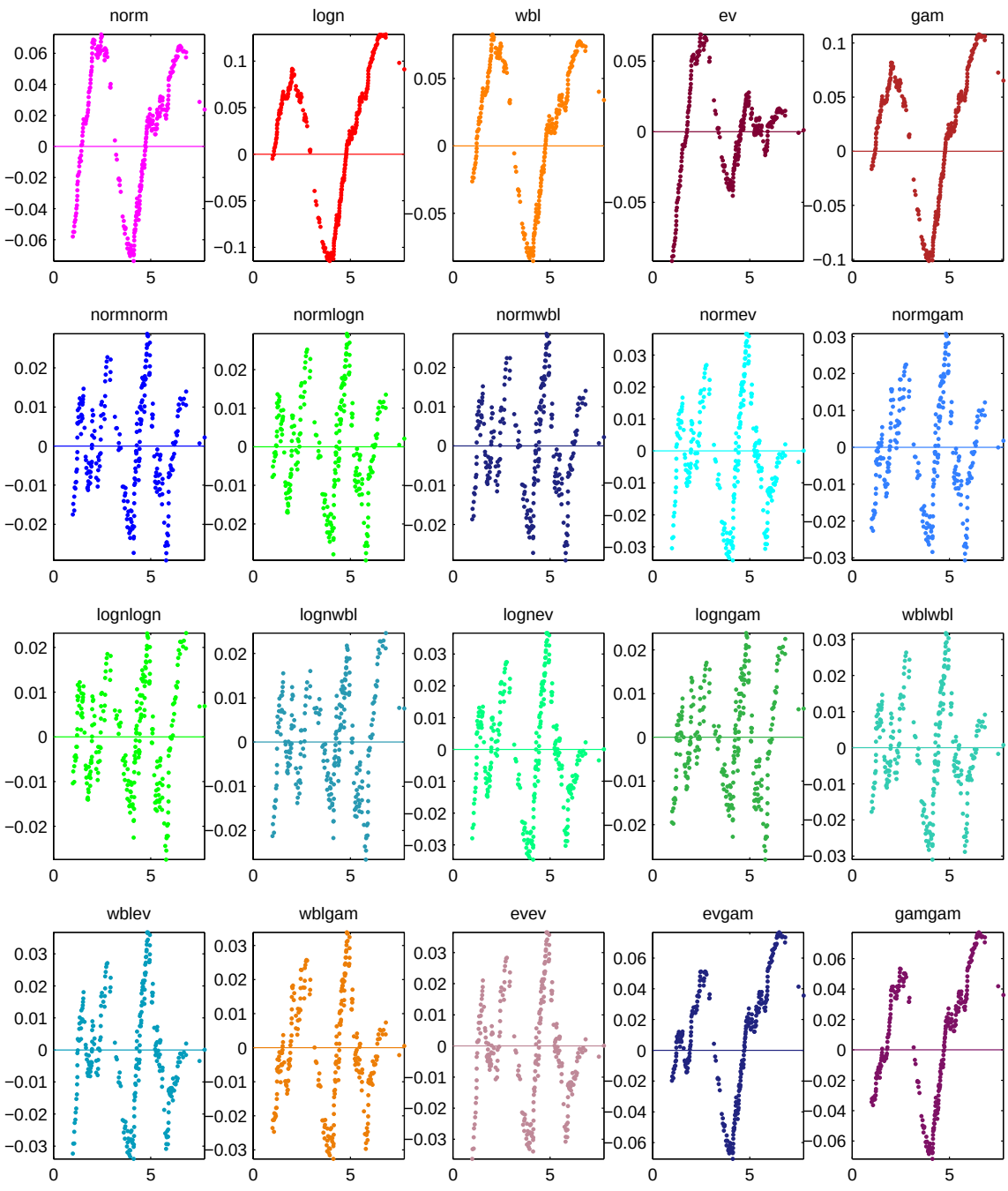

Figure 5.28 Calculated residuals of the data with single mode and bimodal CDFs. Data are for CO_2 injection from a 2 mm tube nozzle in instability regime 2. The corresponding CDF and PDF plots are provided in Figures 5.26 and 5.27.

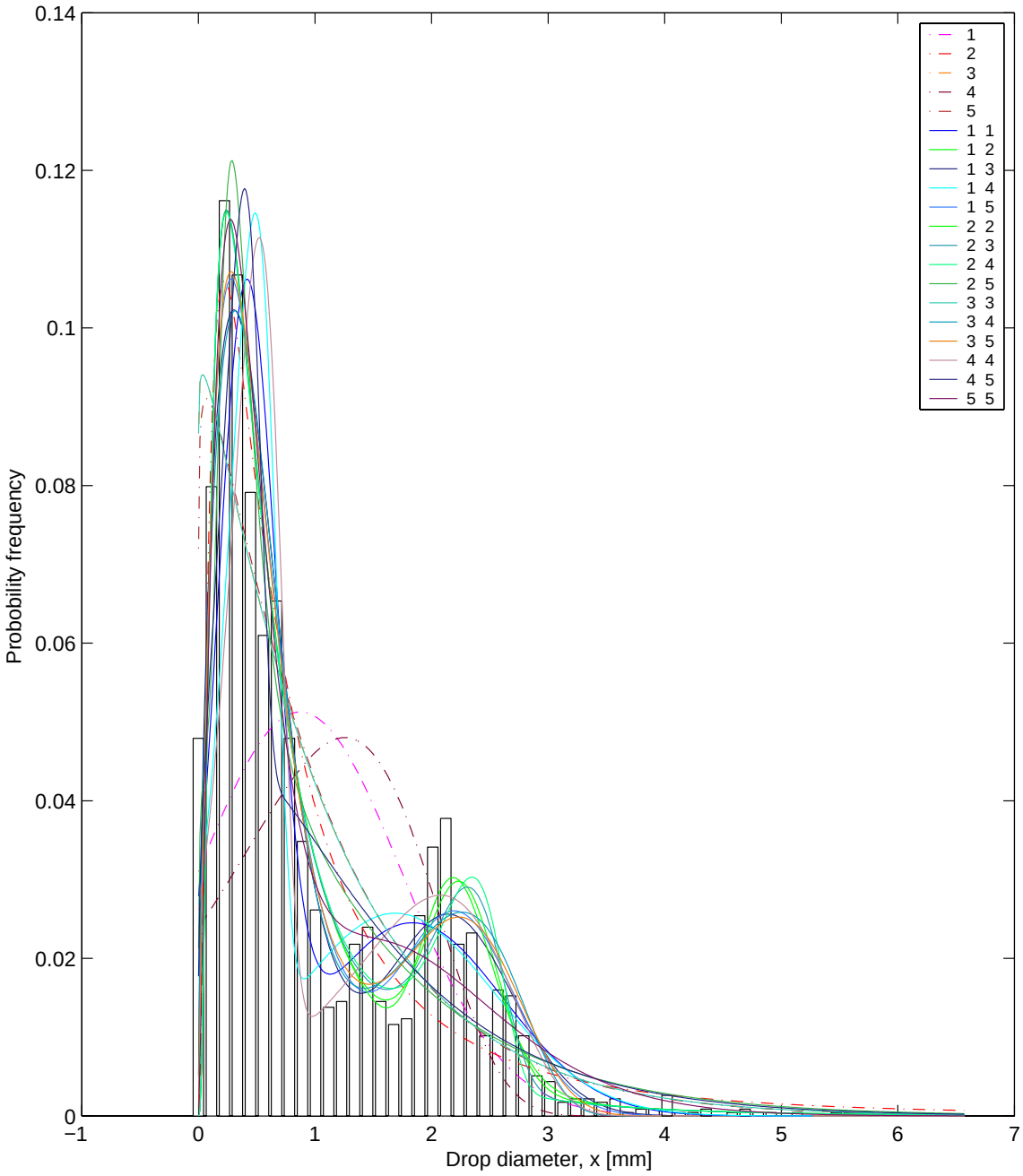

Figure 5.29 Comparison of single mode and bimodal PDFs with the data for CO_2 injection from a 2 mm tube nozzle in instability regime 5. The corresponding CDF and residual plots are in Figures 5.30 and 5.31.

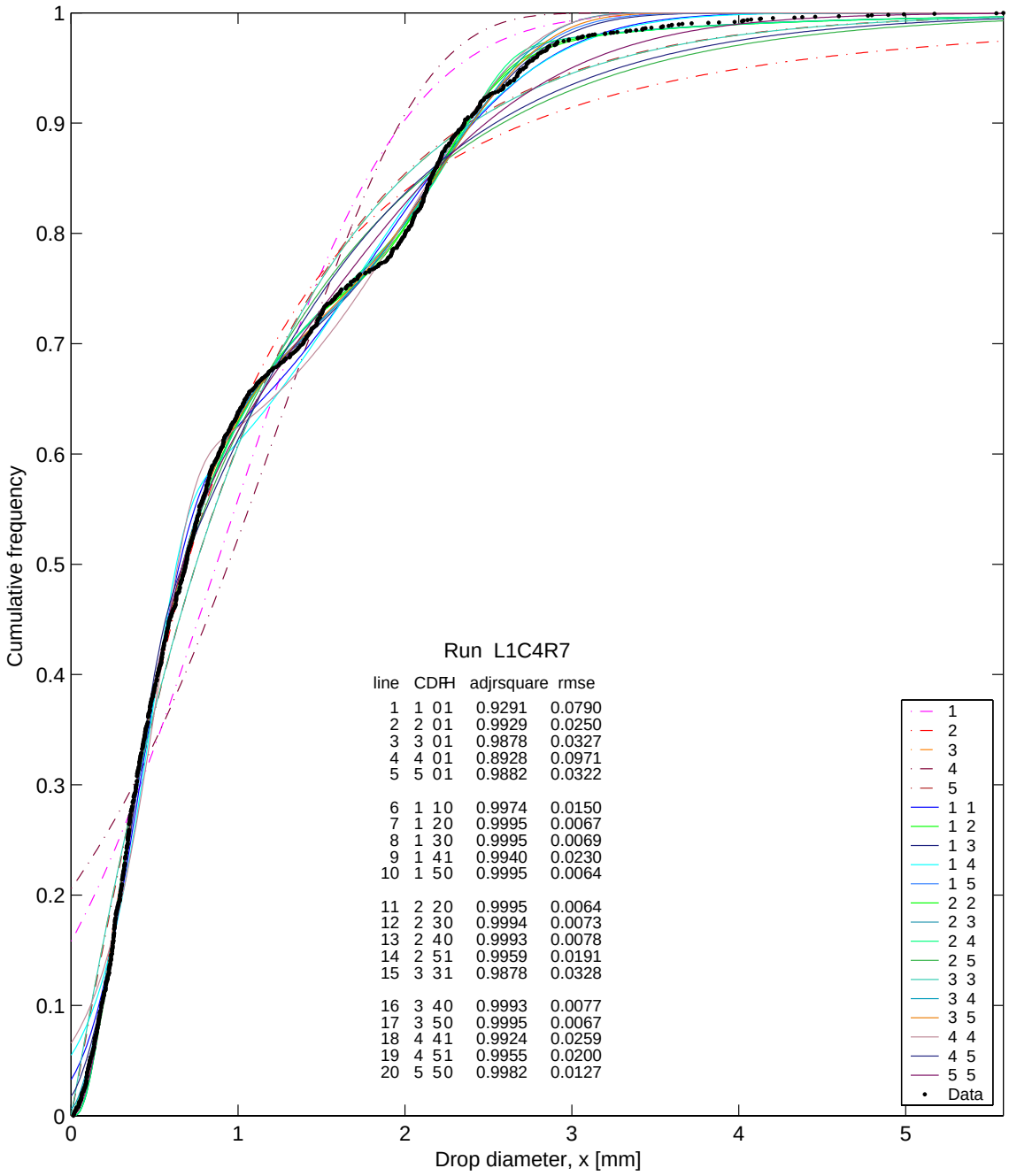

Figure 5.30 Comparison of single mode and bimodal CDFs fittings with the data for CO_2 injection from a 2 mm tube nozzle in instability regime 5. The corresponding PDF and residual plots are provided in Figures 5.29 and 5.31.

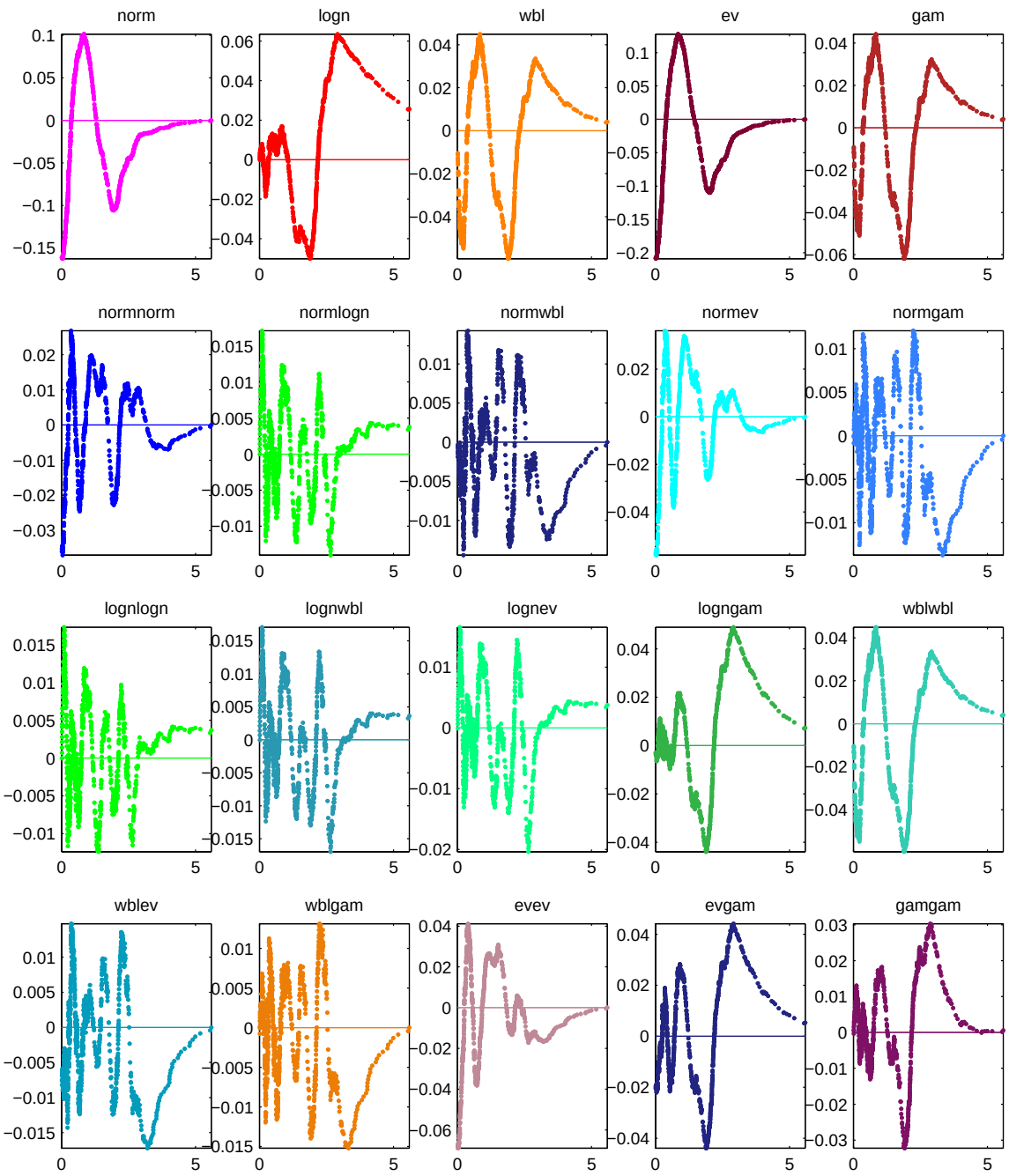

Figure 5.31 Calculated residuals of the data with single mode and bimodal CDFs. Data are for CO_2 injection from a 2 mm tube nozzle in instability regime 5. The corresponding CDF and PDF plots are provided in Figures 5.29 and 5.30.

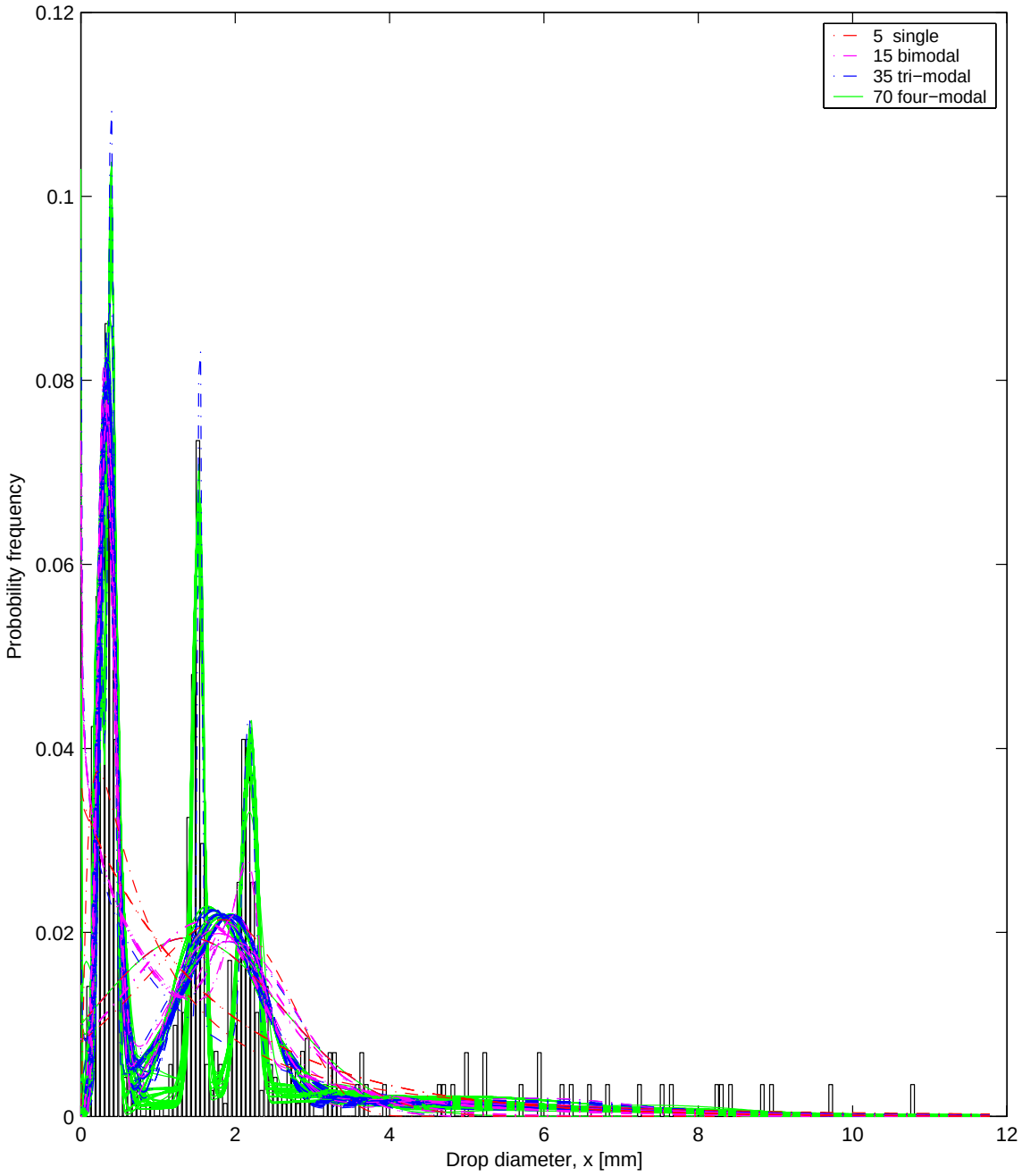

Figure 5.32 Comparison of the single mode, bimodal, tri-modal and four-modal PDFs with data from CO_2 injection from a 2 mm sharp edge office in instability regime 3. The corresponding CDF and residual plots are provided in Figures 5.33, 5.34 and 5.35.

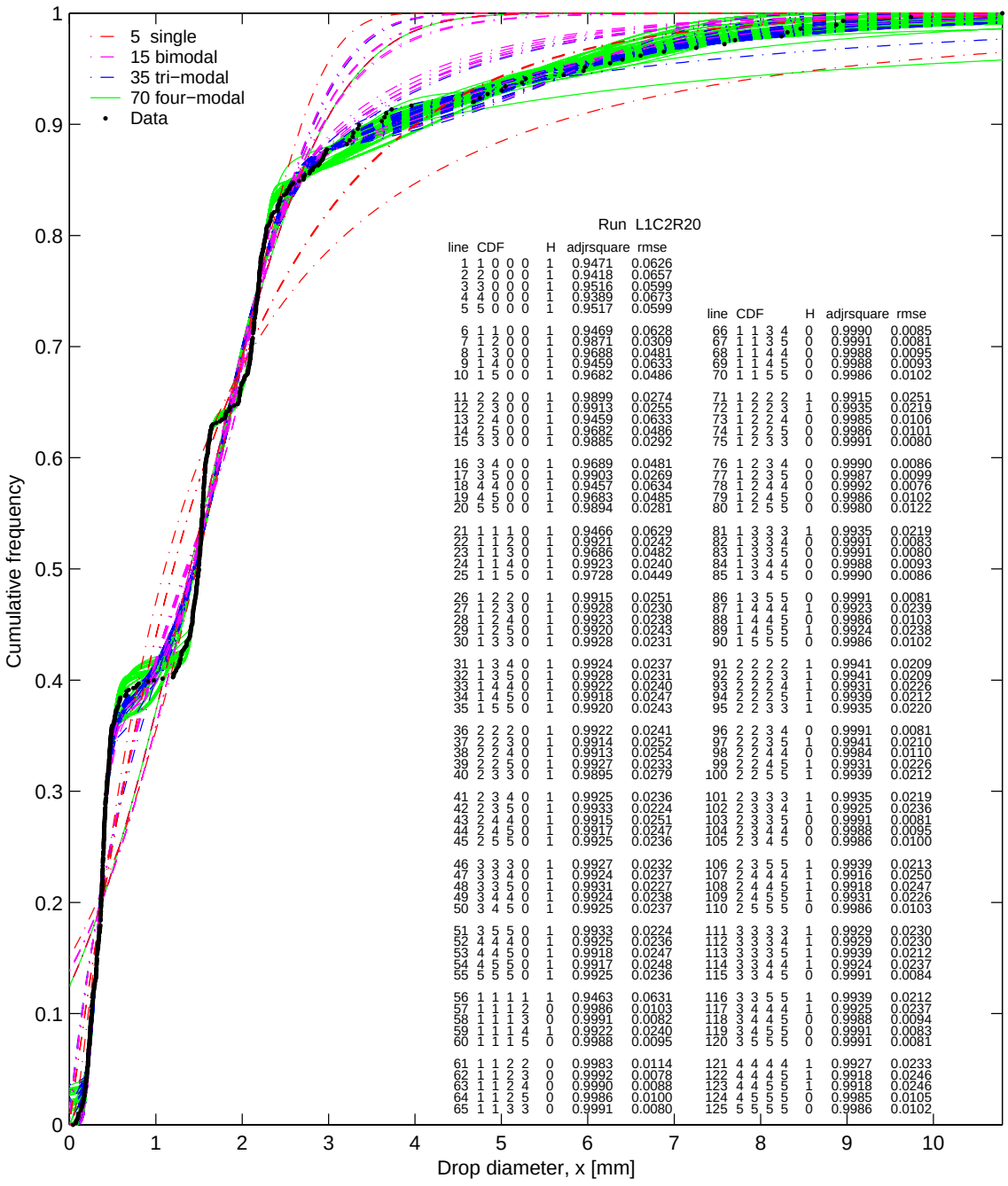

Run L1C2R20

line	CDF				H	adjrsquare	rmse
1	1	0	0	0	1	0.9471	0.0626
2	2	0	0	0	1	0.9418	0.0657
3	3	0	0	0	1	0.9516	0.0599
4	4	0	0	0	1	0.9389	0.0673
5	5	0	0	0	1	0.9517	0.0599
6	1	1	0	0	1	0.9469	0.0628
7	1	2	0	0	1	0.9871	0.0309
8	1	3	0	0	1	0.9688	0.0481
9	1	4	0	0	1	0.9459	0.0633
10	1	5	0	0	1	0.9682	0.0486
11	2	2	0	0	1	0.9899	0.0274
12	2	3	0	0	1	0.9913	0.0255
13	2	4	0	0	1	0.9459	0.0633
14	2	5	0	0	1	0.9682	0.0486
15	3	3	0	0	1	0.9885	0.0292
16	3	4	0	0	1	0.9689	0.0481
17	3	5	0	0	1	0.9903	0.0269
18	4	4	0	0	1	0.9457	0.0634
19	4	5	0	0	1	0.9683	0.0485
20	5	5	0	0	1	0.9894	0.0281
21	1	1	1	0	1	0.9466	0.0629
22	1	1	2	0	1	0.9921	0.0242
23	1	1	3	0	1	0.9686	0.0482
24	1	1	4	0	1	0.9923	0.0240
25	1	1	5	0	1	0.9728	0.0449
26	1	2	2	0	1	0.9915	0.0251
27	1	2	3	0	1	0.9928	0.0230
28	1	2	4	0	1	0.9923	0.0238
29	1	2	5	0	1	0.9920	0.0243
30	1	3	3	0	1	0.9928	0.0231
31	1	3	4	0	1	0.9924	0.0237
32	1	3	5	0	1	0.9928	0.0231
33	1	4	4	0	1	0.9922	0.0240
34	1	4	5	0	1	0.9918	0.0247
35	1	5	5	0	1	0.9920	0.0243
36	2	2	2	0	1	0.9922	0.0241
37	2	2	3	0	1	0.9914	0.0252
38	2	2	4	0	1	0.9913	0.0254
39	2	2	5	0	1	0.9927	0.0233
40	2	3	3	0	1	0.9895	0.0279
41	2	3	4	0	1	0.9925	0.0236
42	2	3	5	0	1	0.9933	0.0224
43	2	4	4	0	1	0.9915	0.0251
44	2	4	5	0	1	0.9917	0.0247
45	2	5	5	0	1	0.9925	0.0236
46	3	3	3	0	1	0.9927	0.0232
47	3	3	4	0	1	0.9924	0.0237
48	3	3	5	0	1	0.9931	0.0227
49	3	4	4	0	1	0.9924	0.0238
50	3	4	5	0	1	0.9925	0.0237
51	3	5	5	0	1	0.9933	0.0224
52	4	4	4	0	1	0.9925	0.0236
53	4	4	5	0	1	0.9918	0.0247
54	4	5	5	0	1	0.9917	0.0248
55	5	5	5	0	1	0.9925	0.0236
56	1	1	1	1	1	0.9463	0.0631
57	1	1	1	2	0	0.9986	0.0103
58	1	1	1	3	0	0.9991	0.0082
59	1	1	1	4	1	0.9922	0.0240
60	1	1	1	5	0	0.9988	0.0095
61	1	1	2	2	0	0.9983	0.0114
62	1	1	2	3	0	0.9992	0.0078
63	1	1	2	4	0	0.9990	0.0088
64	1	1	2	5	0	0.9986	0.0100
65	1	1	3	3	0	0.9991	0.0080
66	1	1	3	4	0	0.9990	0.0085
67	1	1	3	5	0	0.9991	0.0081
68	1	1	4	4	0	0.9988	0.0095
69	1	1	4	5	0	0.9988	0.0093
70	1	1	5	5	0	0.9986	0.0102
71	1	2	2	2	1	0.9915	0.0251
72	1	2	2	3	1	0.9935	0.0219
73	1	2	2	4	0	0.9985	0.0106
74	1	2	2	5	0	0.9986	0.0101
75	1	2	3	3	0	0.9991	0.0080
76	1	2	3	4	0	0.9990	0.0086
77	1	2	3	5	0	0.9987	0.0099
78	1	2	4	4	0	0.9992	0.0076
79	1	2	4	5	0	0.9986	0.0102
80	1	2	5	5	0	0.9980	0.0122
81	1	3	3	3	1	0.9935	0.0219
82	1	3	3	4	0	0.9991	0.0083
83	1	3	3	5	0	0.9991	0.0080
84	1	3	4	4	0	0.9988	0.0093
85	1	3	4	5	0	0.9990	0.0086
86	1	3	5	5	0	0.9991	0.0081
87	1	4	4	4	1	0.9923	0.0239
88	1	4	4	5	0	0.9986	0.0103
89	1	4	5	5	1	0.9924	0.0238
90	1	5	5	5	0	0.9986	0.0102
91	2	2	2	2	1	0.9941	0.0209
92	2	2	2	3	1	0.9941	0.0209
93	2	2	2	4	1	0.9931	0.0226
94	2	2	2	5	1	0.9939	0.0212
95	2	2	3	3	1	0.9935	0.0220
96	2	2	3	4	0	0.9991	0.0081
97	2	2	3	5	1	0.9941	0.0210
98	2	2	4	4	0	0.9984	0.0110
99	2	2	4	5	1	0.9931	0.0226
100	2	2	5	5	1	0.9939	0.0212
101	2	3	3	3	1	0.9935	0.0219
102	2	3	3	4	1	0.9925	0.0236
103	2	3	3	5	0	0.9991	0.0081
104	2	3	4	4	0	0.9988	0.0095
105	2	3	4	5	0	0.9986	0.0100
106	2	3	5	5	1	0.9939	0.0213
107	2	4	4	4	1	0.9916	0.0250
108	2	4	4	5	1	0.9918	0.0247
109	2	4	5	5	1	0.9931	0.0226
110	2	5	5	5	0	0.9986	0.0103
111	3	3	3	3	1	0.9929	0.0230
112	3	3	3	4	1	0.9929	0.0230
113	3	3	3	5	1	0.9939	0.0212
114	3	3	4	4	1	0.9924	0.0237
115	3	3	4	5	0	0.9991	0.0084
116	3	3	5	5	1	0.9939	0.0212
117	3	4	4	4	1	0.9925	0.0237
118	3	4	4	5	0	0.9988	0.0094
119	3	4	5	5	0	0.9991	0.0083
120	3	5	5	5	0	0.9991	0.0081
121	4	4	4	4	1	0.9927	0.0233
122	4	4	4	5	1	0.9918	0.0246
123	4	4	5	5	1	0.9918	0.0246
124	4	5	5	5	0	0.9985	0.0105
125	5	5	5	5	0	0.9986	0.0102

Figure 5.33 Comparison of the single mode, bimodal, tri-modal and four-modal CDFs with data from CO_2 injection from a 2 mm sharp edge office in instability regime 3. The corresponding PDF and residual plots are provided in Figures 5.32, 5.34 and 5.35.

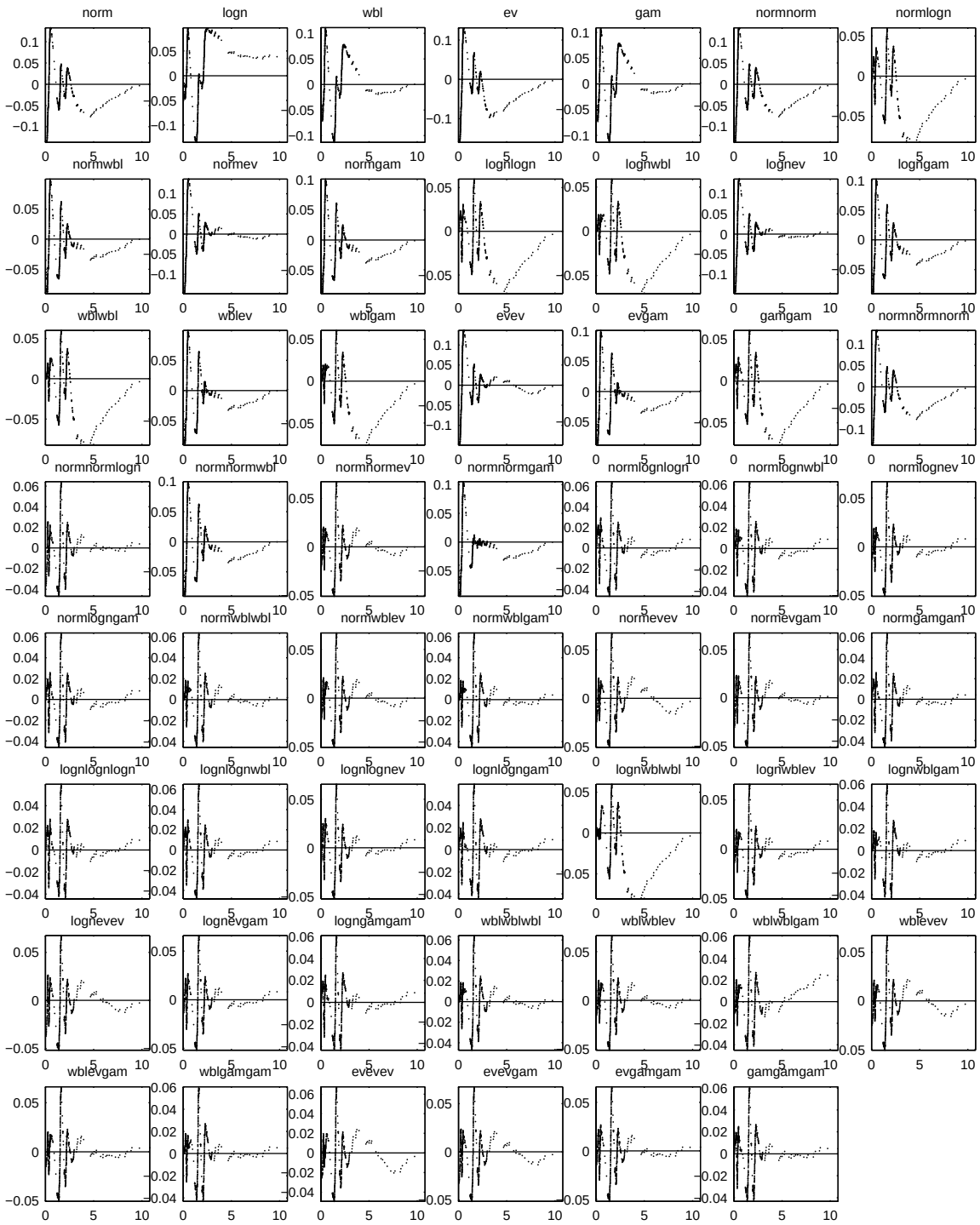

Figure 5.34 Calculated residuals of the 5 single, 15 bimodal, and 35 tri-modal CDFs. Data are for liquid CO_2 injection from a 2 mm sharp edge orifice in instability regime 3.

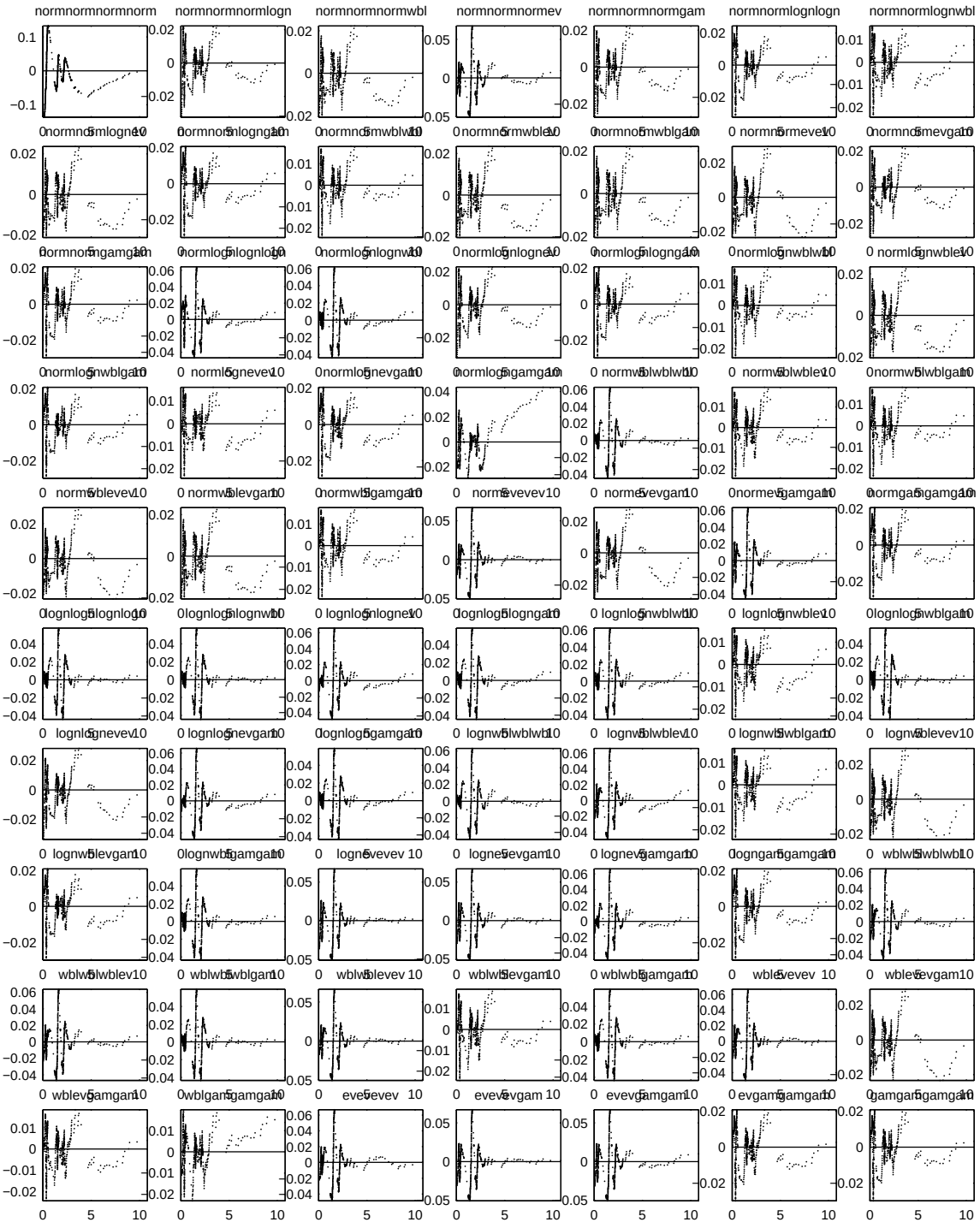

Figure 5.35 Calculated residuals of the 70 four-modal CDFs. Data are for liquid CO_2 injection from a 2 mm sharp edge orifice in instability regime 3.

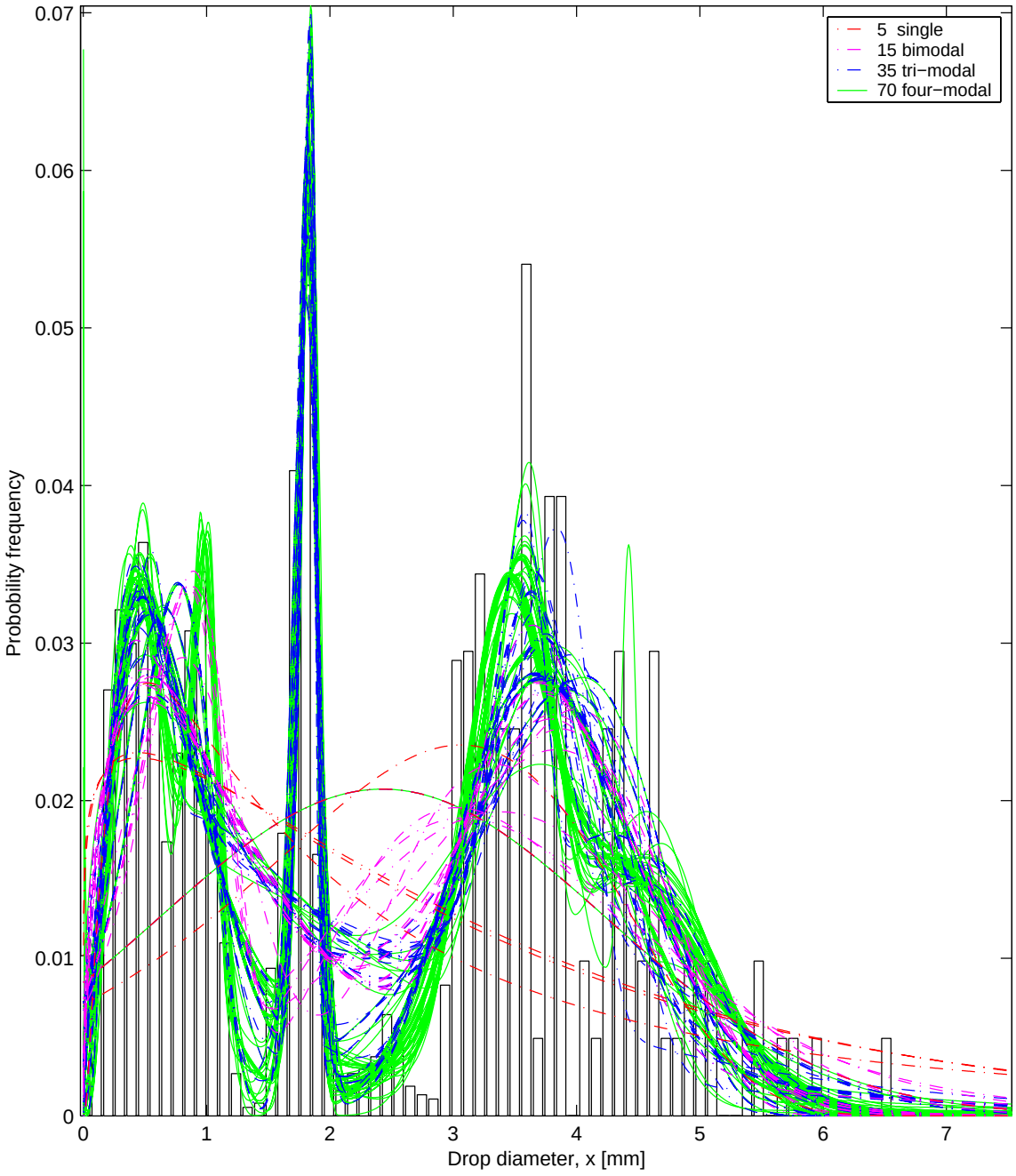

Figure 5.36 Comparison of the single mode, bimodal, tri-modal and four-modal PDFs with data for CO_2 injection from a 2 mm tube nozzle in instability regime 3. The corresponding CDF plot is provided in Figure 5.37.

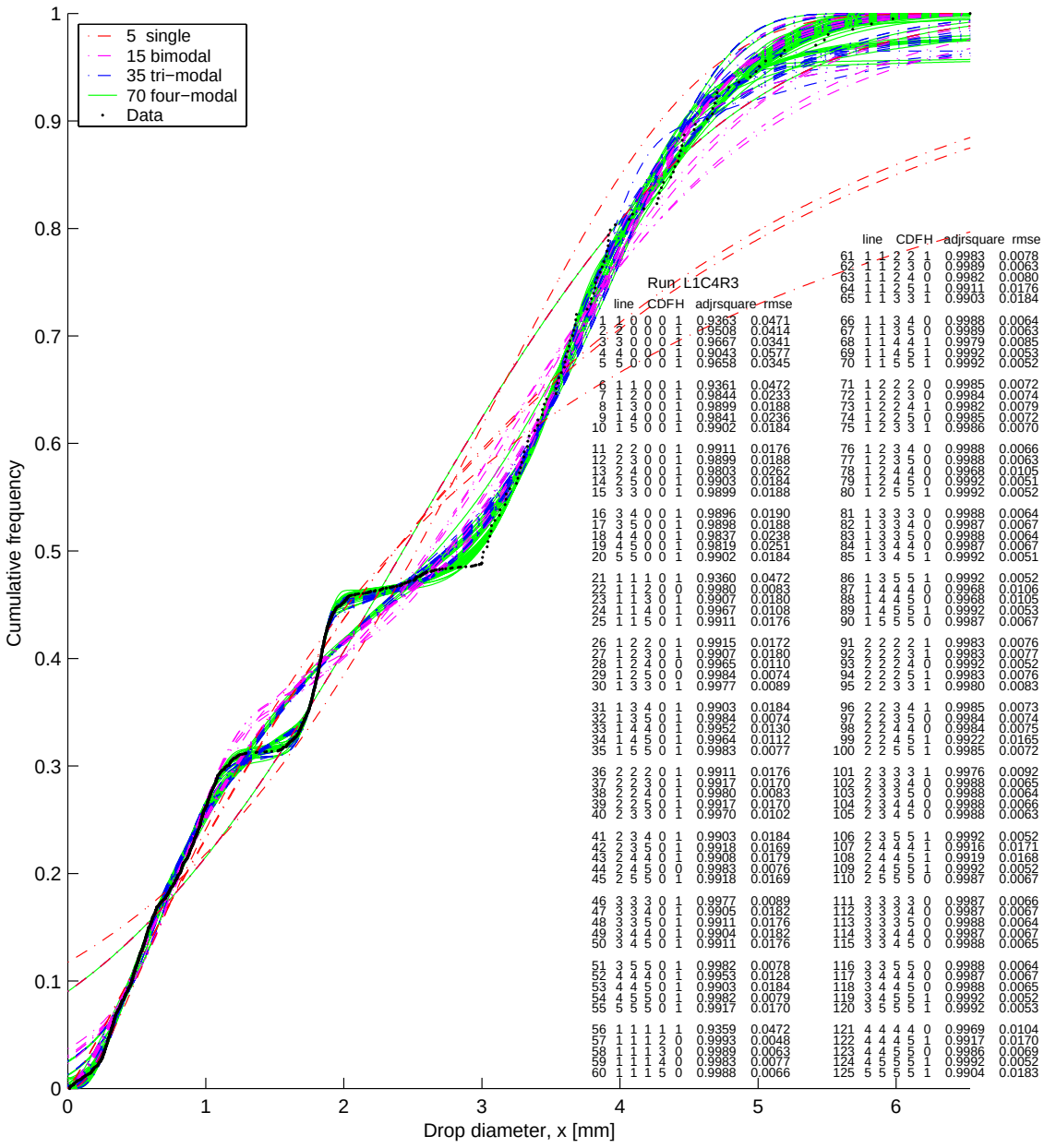

Figure 5.37 Comparison of the single mode, bimodal, tri-modal and four-modal CDFs with data for CO_2 injection from a 2 mm tube nozzle in instability regime 3. The corresponding PDF plot is provided in Figure 5.36.

5.3.4 CO_2 Droplet Size Distributions

Based on the evaluation summarized in section 5.3.3.2, weighted multimodal functions were fit to the composite experimental size spectra from 72 CO_2 tests that spanned the five instability regimes. These functional representations demonstrate the evolution of instability mechanisms which manifest themselves in complex droplet size distributions. Curvefit coefficients and other information are provided in Table B.1 of Appendix B.

5.3.4.1 Varicose Breakup at Instability Regime 1

Fourteen of liquid CO_2 injection tests were classified as instability regime 1. Twenty functions (5 single mode and 15 weighted bimodal distributions) were fitted to data for each of these 14 tests. Of the twenty functions, fourteen bimodal distributions passed the K-S tests. Next we need to choose one from the 14 bimodal distributions for this regime. Following procedures used to evaluate goodness of fit described in section 5.3.2, the evev bimodal function (see Table A.2) was an acceptable choice to approximate size spectra in regime 1. Figure 5.38 presents the calculated Root Mean Square Error, *rmse*, and adjusted R-square statistics, *adjrsquare*, for all curvefits to the size data from the 14 tests. Values of *rmse* close to zero and *adjrsquare* close to 1 indicate a good fit. Note that the bimodal distributions consistently outperform the single mode functions. The evev PDF curvefits are shown in Figure 5.39 along with the data. The CDFs and corresponding residuals are plotted in Figures 5.40 and 5.41, respectively. Table B.1 provides the key for the test run labels used in those and subsequent figures.

Figure 5.42 presents the evev PDF that were fitted to the data for six tests in case CDC05WTP52. In these tests, liquid CO_2 was injected from a 5 mm sharp edge orifice

into tap water at 52 bar. The primary parameter that was varied between runs is jet velocity. All runs are classified as instability regime 1. The five coefficients of the evev function, a1 a2, a3, a4 and a5 are plotted versus U_{jet} in Figure 5.43. Another example for regime 1 is provided in Figure 5.44 where the evev PDFs are fitted to data for four test runs for case CDC10WTP52. The difference between this case and case CDC05WTP52 shown in Figure 5.42 is orifice diameter. Here, a larger 10 mm sharp edge orifice was used to discharge liquid CO_2 into 52 bar tap water. The coefficients a1 a2, a3, a4 and a5 are plotted versus U_{jet} in Figure 5.45.

When $x = a$ for the single mode Type I Extreme Value PDF, we have

$$F(x=a|a,b) = 1 - \exp\left[-\exp\left(\frac{x-a}{b}\right)\right]\Bigg|_{x=a} = 1 - \exp[-\exp(0)] = 1 - e^{-1} = 0.6321$$

This means that 63.21% of the total number of liquid droplets have diameter < a. For the weighted evev bimodal distribution, a2 and a4 are the values of a for in the two single mode ev distributions from which the bimodal distribution is constructed. As seen in Figures 5.43 and 5.45, a2 and a4 appear to evolve as reflections of each other.

The results suggest that, except at very low velocities, a bimodal distribution of droplets is generated in regime 1. As velocity increases, the two peaks move apart then shift toward each other.

5.3.4.2 Sinuous Wave Breakup at Instability Regime 2

Twenty liquid CO_2 injection tests fall in instability regime 2. In this regime, single mode and bimodal functions were again used to fit the composite experimental size data. All 15 bimodal distributions passed the K-S tests. While bimodal distributions appeared to better

describe the data, no particular bimodal distribution was clearly better than the others. Based on *rmse* and *adjsquare* statistics shown in Figure 5.46, the normwbl bimodal distribution was selected to represent size spectra in regime 2.

Figure 5.50 and 5.51 present the weighted normwbl PDFs that were fitted to the data from 5 runs and 4 runs from case CDC05WTP52 and CDT02WTP52, respectively. The coefficients a1 through a5 for these curvefits are plotted as functions of U_{jet} below the PDFs in these figures. The tests correspond to CO_2 injection into tap water at 52 bar. For Figure 5.50, a 5 mm sharp edge orifice was employed; Figure 5.51 used a 2 mm tube orifice.

At instability regime 2, the size distribution broadens as velocity rises, primary as a result of production of increasingly smaller droplets.

5.3.4.3 Filament Core Breakup at Instability Regime 3

Sixteen liquid CO_2 injection tests were categorized as instability regime 3. In regime 3 and 4, multiple instabilities become actuated and operate in parallel. Qualitative evidence of this was presented in the video data in Chapter 3. The multiple instabilities appear each to have a preferred size of droplets and therefore manifest themselves in complex, multimodal size spectra. Because of this, single and bimodal distributions failed the K-S tests. For several cases, even tri-modal distributions were unable to pass the K-S tests. Therefore, a total of 125 different multimodal functions, including 5 single mode, 15 bimodal, 35 tri-modal and 70 four-modal distributions were fitted to the data for each of the 16 tests. Only the four-modal weighted wblevevgam passed the K-S test for all 16 data sets. It was selected to represent size spectra in instability regime 3.

Figure 5.52 presents the calculated *rmse* and *adjrsquare* statistics for the 125 functions fitted to the 16 data sets. The weighted wblevevgam PDF curvefits and the test data are provided in Figure 5.53. The corresponding CDFs and calculated residuals are shown in Figures 5.54 and 5.55, respectively.

The evolution of the complex spectra in regime 3 can be seen in Figure 5.56 which plots the wblevevgam PDF curvefits as a function of jet velocity for case CDC02WTP52. Here, liquid CO_2 was injected into 52 bar tap water through a 2 mm sharp edge orifice. The corresponding coefficients of the weighted multimodal functions are given in Figure 5.57.

5.3.4.4 Wave Atomization at Instability Regime 4

The complex, multimodal behavior that appears in regime 3 continues in regime 4 but began to relax as atomization is approached. Nonetheless, single mode and even bimodal distributions are often not sufficient to capture the characteristics of the droplet spectra.

Ten of liquid CO_2 tests fell within the wave atomization instability regime 4. A total of 55 different functions, including 5 single mode, 15 bimodal and 35 trimodal distributions were fitted to the data from the 10 tests. The weighted tri-modal normwblgam passed the K-S tests for all 10 data sets and it was selected to represent droplet size spectra in instability regime 4.

Figure 5.58 presents the calculated *rmse* and *adjrsquare* statistics for the 55 functions fitted to the 10 data sets. The weighted normwblgam PDF curvefits and test data are provided in Figure 5.59. The corresponding CDFs and calculated residuals are shown in Figures 5.60 and 5.61, respectively.

The evolution of the droplet size distribution with jet velocity (i.e., increasing *Re* or *We*) in regime 4 can be seen in Figure 5.62, which plots the trimodal normwblgam PDF curvefits for case CDC05WTP52. Here, liquid CO_2 was injected in 52 bar tap water through a 5 mm sharp edge orifice. The corresponding coefficients of the normwblgam distribution functions are given in Figure 5.63.

As expected, the size distribution narrows as breakup moves toward atomization. Large droplets that are postulated to form by the breakup of a persistent filament core disappear as the instability that generates small droplets begins to dominate and consume most of the jet material.

5.3.4.5 Full Atomization at Instability Regime 5

In the atomization regime 5, single mode or bimodal functions again became viable candidates to describe the droplet size distribution. Twelve liquid CO_2 injection tests fell within this instability regime. Only two bimodal functions passed the K-S tests for all 12 data sets. Based on the *rmse* and *adjrsquare* statistics, the weighted wblwbl distribution function was selected to represent size spectra in the atomization regime.

Figure 5.64 presents the calculated *rmse* and *adjrsquare* statistics for the 15 functions fitted to the 12 data sets. The weighted wblwbl PDF curvefits and the test data are provided in Figure 5.65. The corresponding CDFs and calculated residuals are shown in Figures 5.66 and 5.67, respectively.

PDFs in the atomization regime 5 can be seen in Figure 5.68. This figure plots the wblwbl curvefits as a function of jet velocity for case CDT02WTP52 where liquid CO_2 was injected into 52 bar tap water through a 2 mm tube nozzle. The corresponding

curvefit coefficients are presented below the PDFs. The multimodal nature of the size spectra that is a distinguishing feature in regime 1 to 4 essentially disappear when atomization is attained. The dispersed phase consists almost entirely of fine droplets with a small fraction of large droplets.

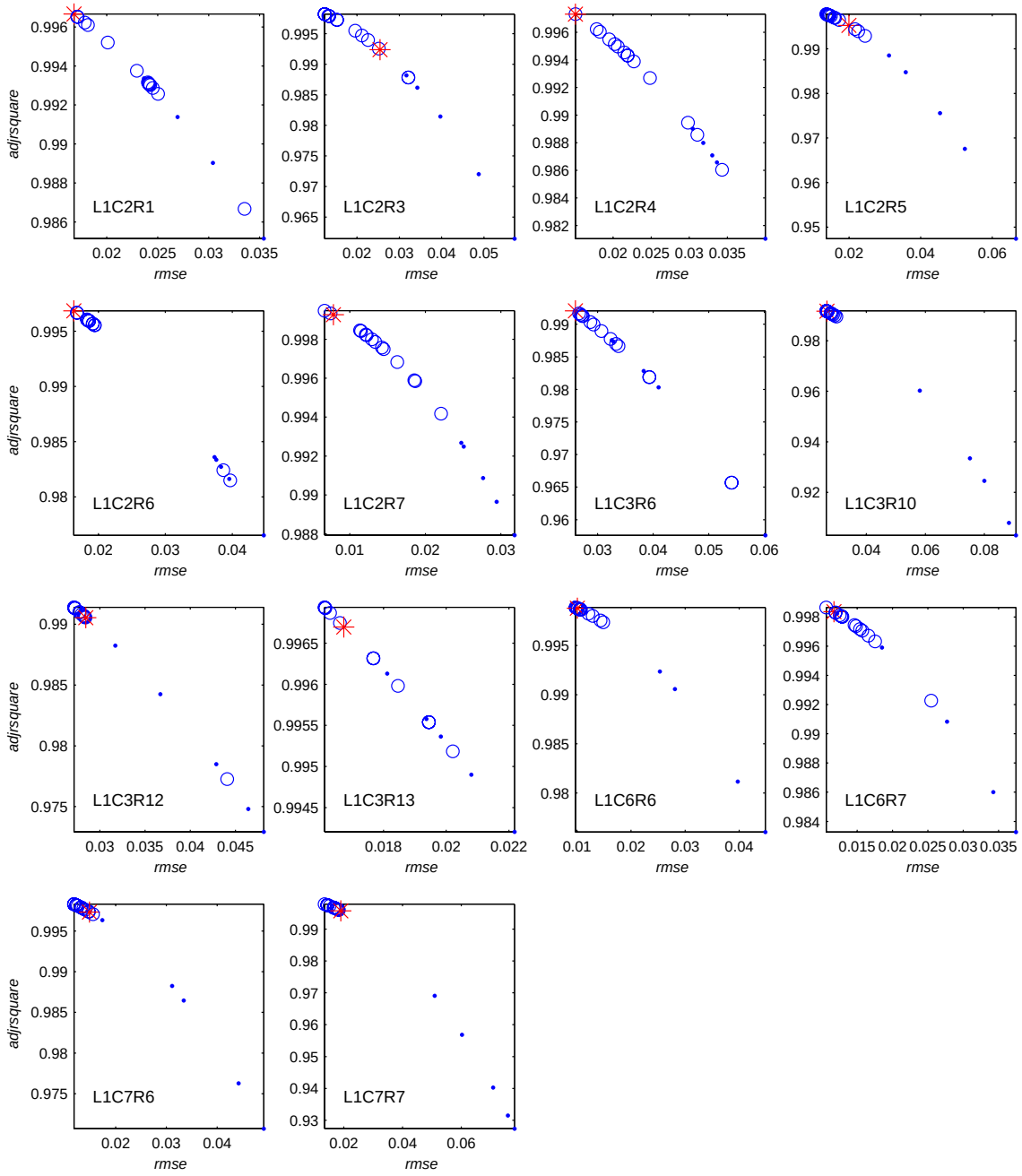

Figure 5.38 Root Mean Square Errors (*rmse*) and Degrees of Freedom Adjusted R-Square (*adjsquare*) for curve fits to 14 liquid CO_2 tests in instability regime 1. *, weighted evev bimodal distribution; • , single distributions; ○, bimodal distributions. Test ID. (e.g. L1C2R1) key given in Table B.1.

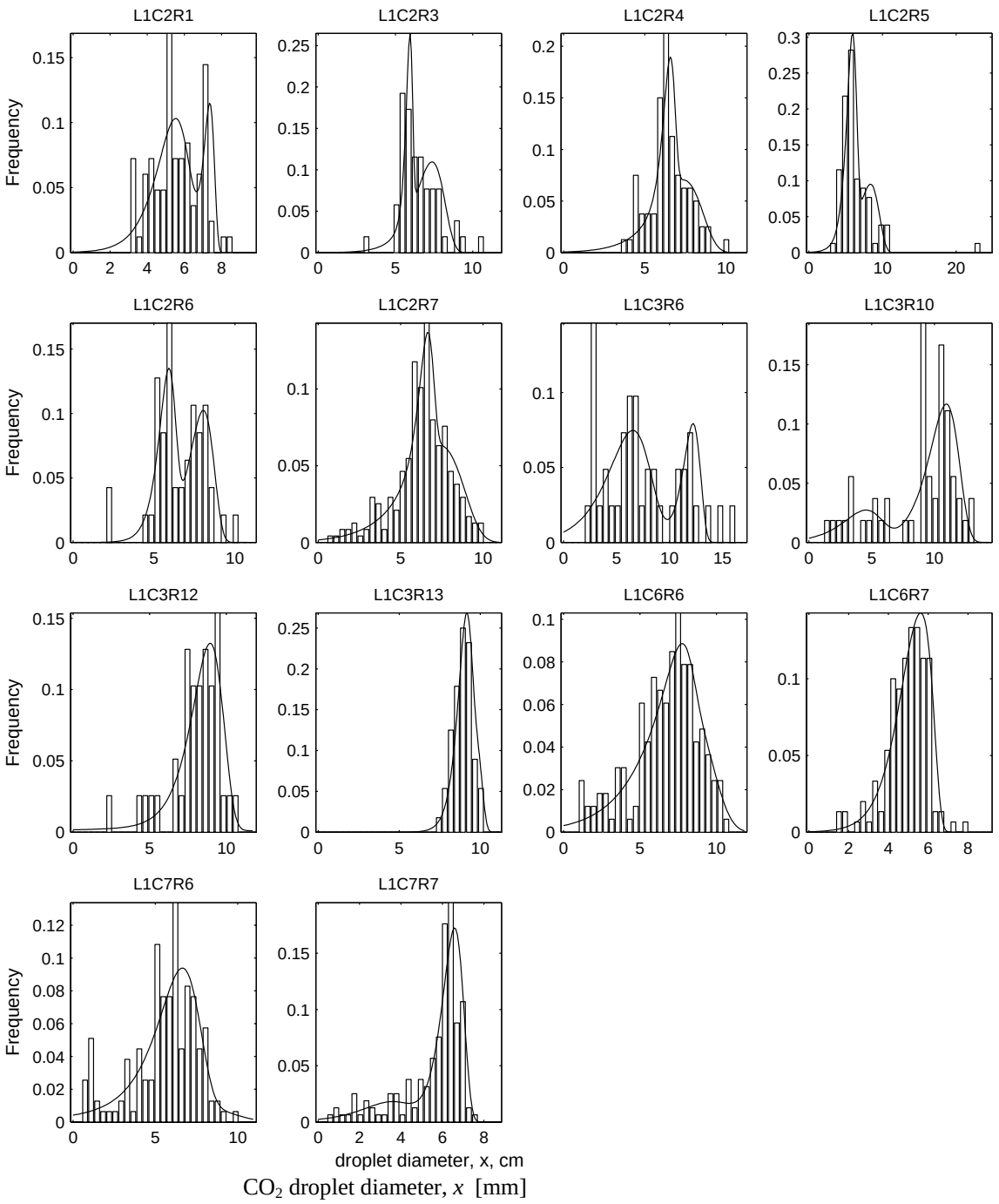

Figure 5.39 Frequency histograms of CO_2 droplet size distribution for instability regime 1 and evev bimodal PDFs. Test ID (e.g. L1C2R1) key given in Table B.1.

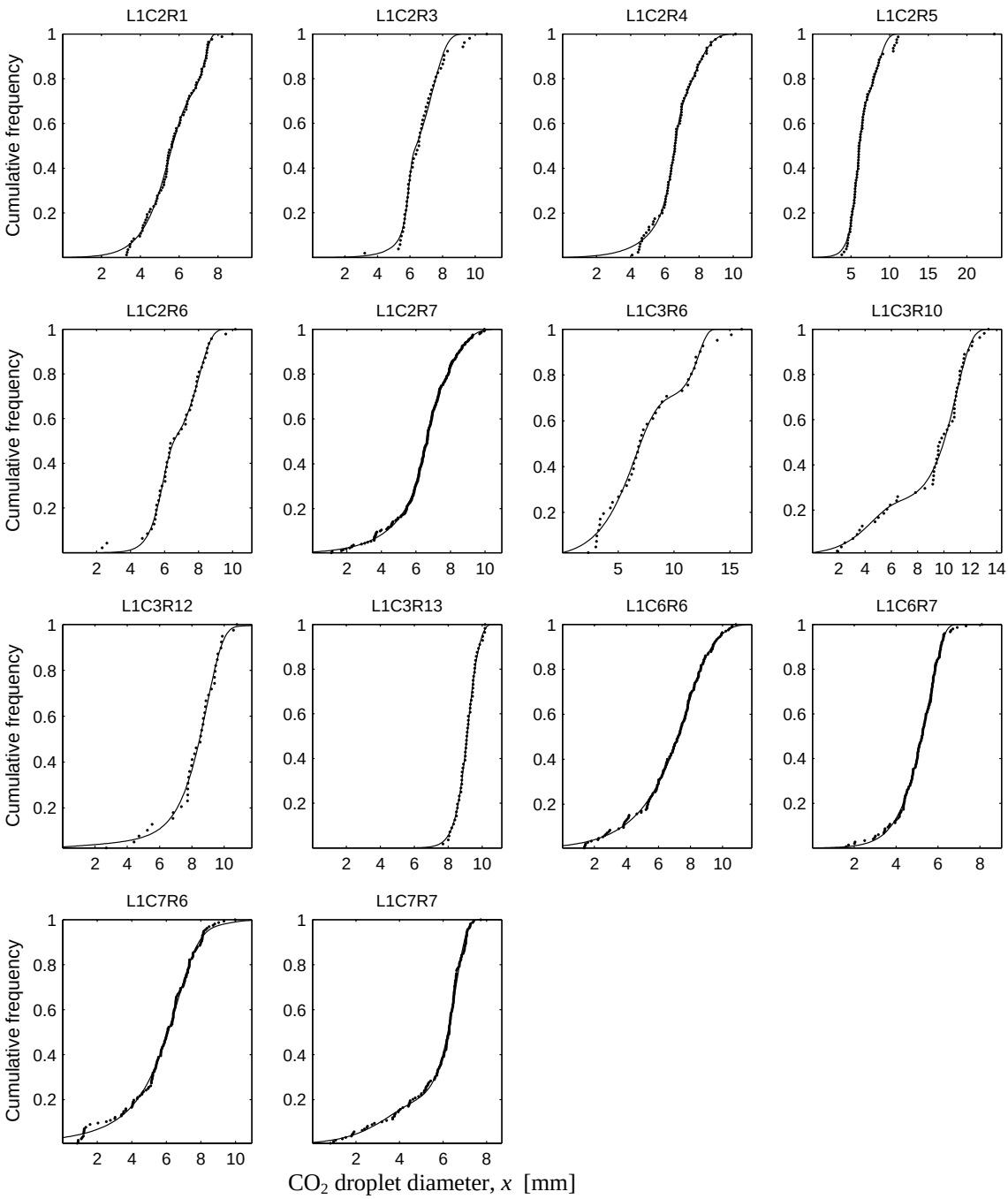

Figure 5.40 Weighted evev bimodal CDFs and data from liquid CO_2 injection tests in regime 1. Test ID (e.g. L1C1R2) key given in Table B.1.

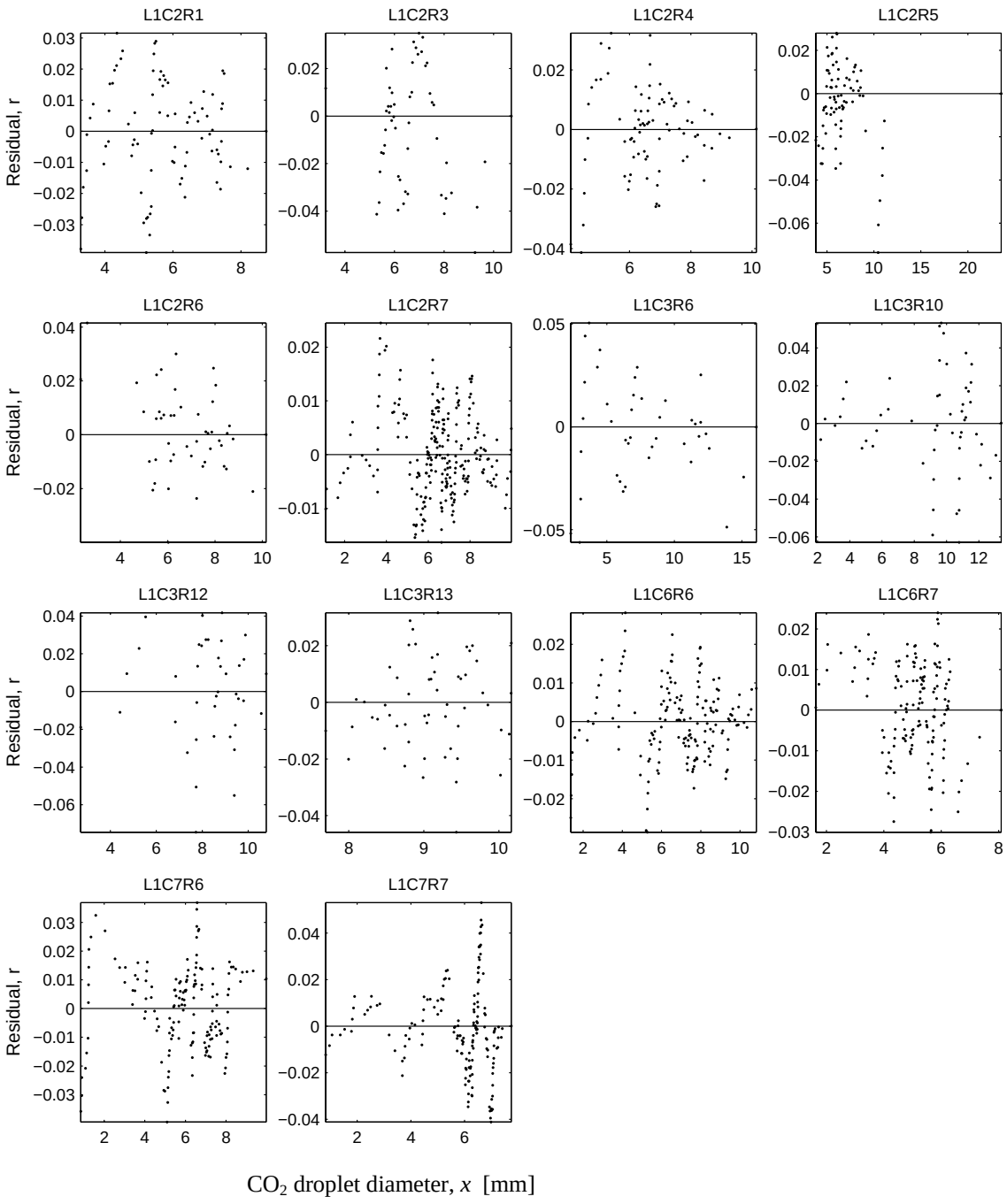

Figure 5.41 Calculated residuals of weighted evev bimodal CDFs presented in Figure 5.40.

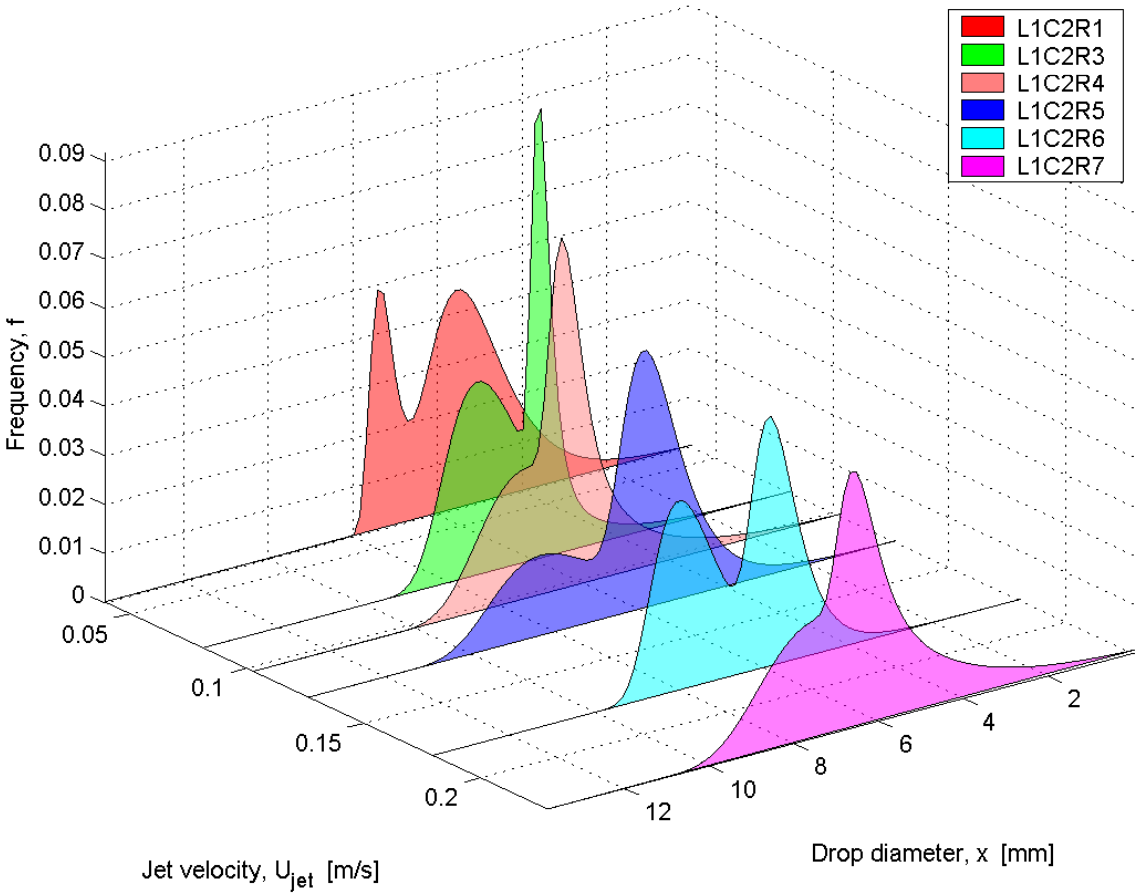

Figure 5.42 Weighted evev bimodal PDFs of CO_2 droplet size vs. jet velocity for liquid CO_2 injection into 52 bar tap water through a 5 mm sharp edge orifice. Case CDC05WTP52. Breakup was classified as instability regime 1.

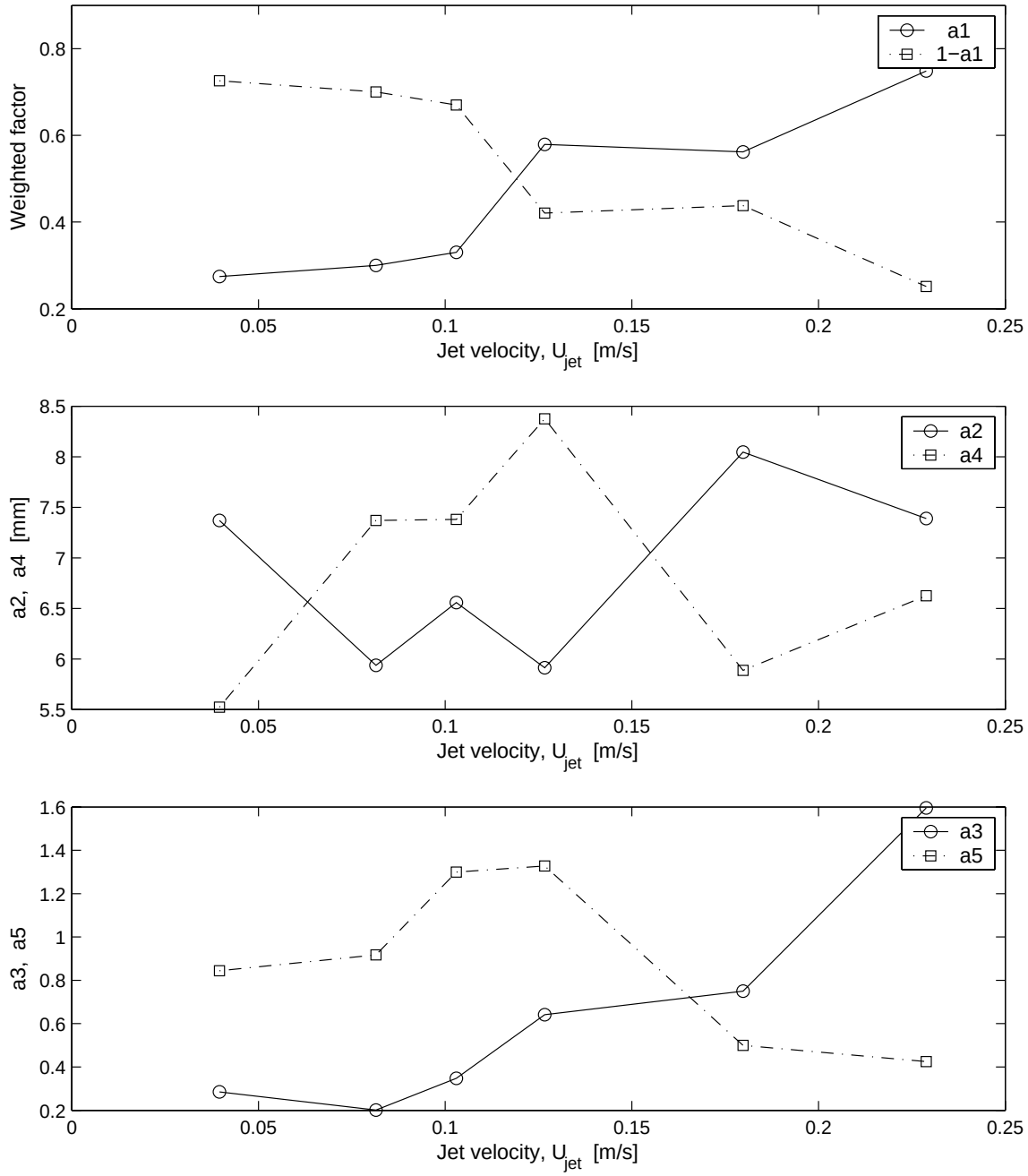

Figure 5.43 Five coefficients of the weighted evev bimodal PDFs shown in Figure 5.42 vs. jet velocity. Case CDC05WTP52.

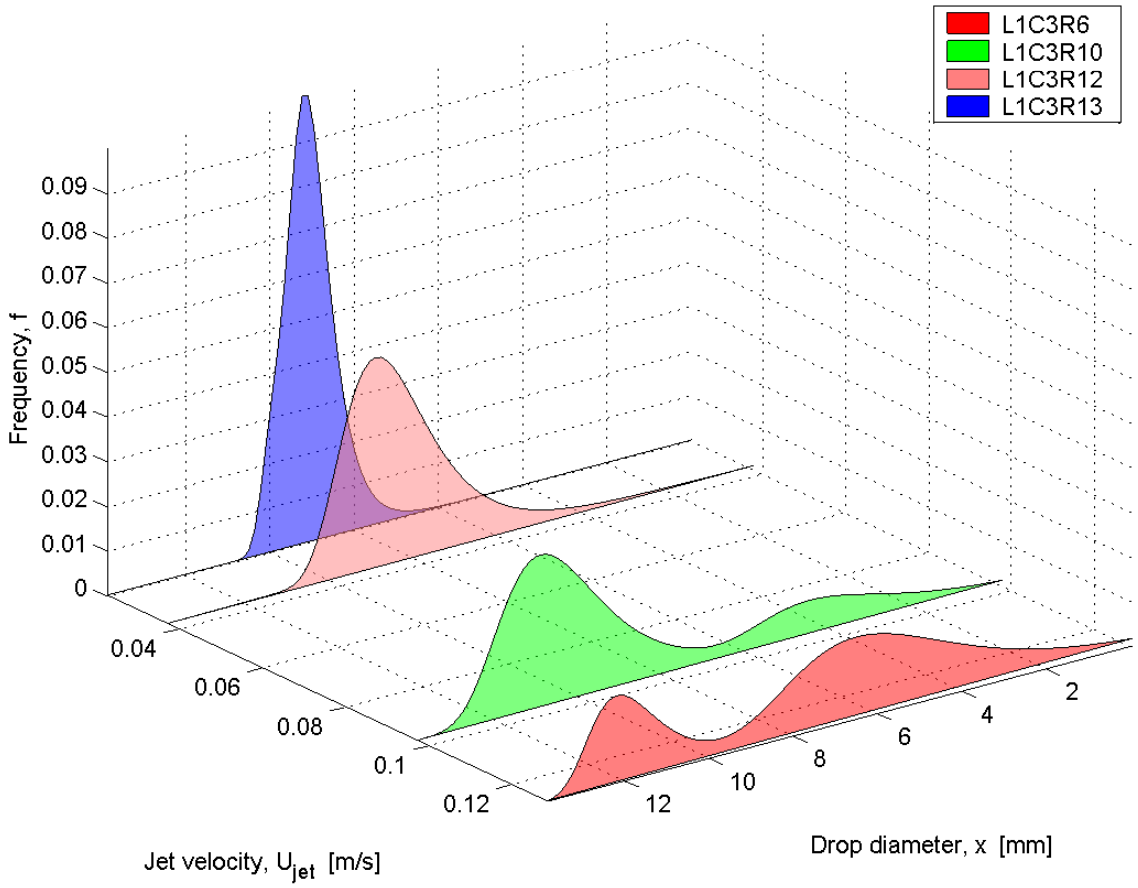

Figure 5.44 Weighted evev bimodal PDFs of CO_2 droplet size vs. jet velocity for liquid CO_2 injection into 52 bar tap water through a 10 mm sharp edge orifice. Case CDC10WTP52. Breakup was classified as instability regime 1.

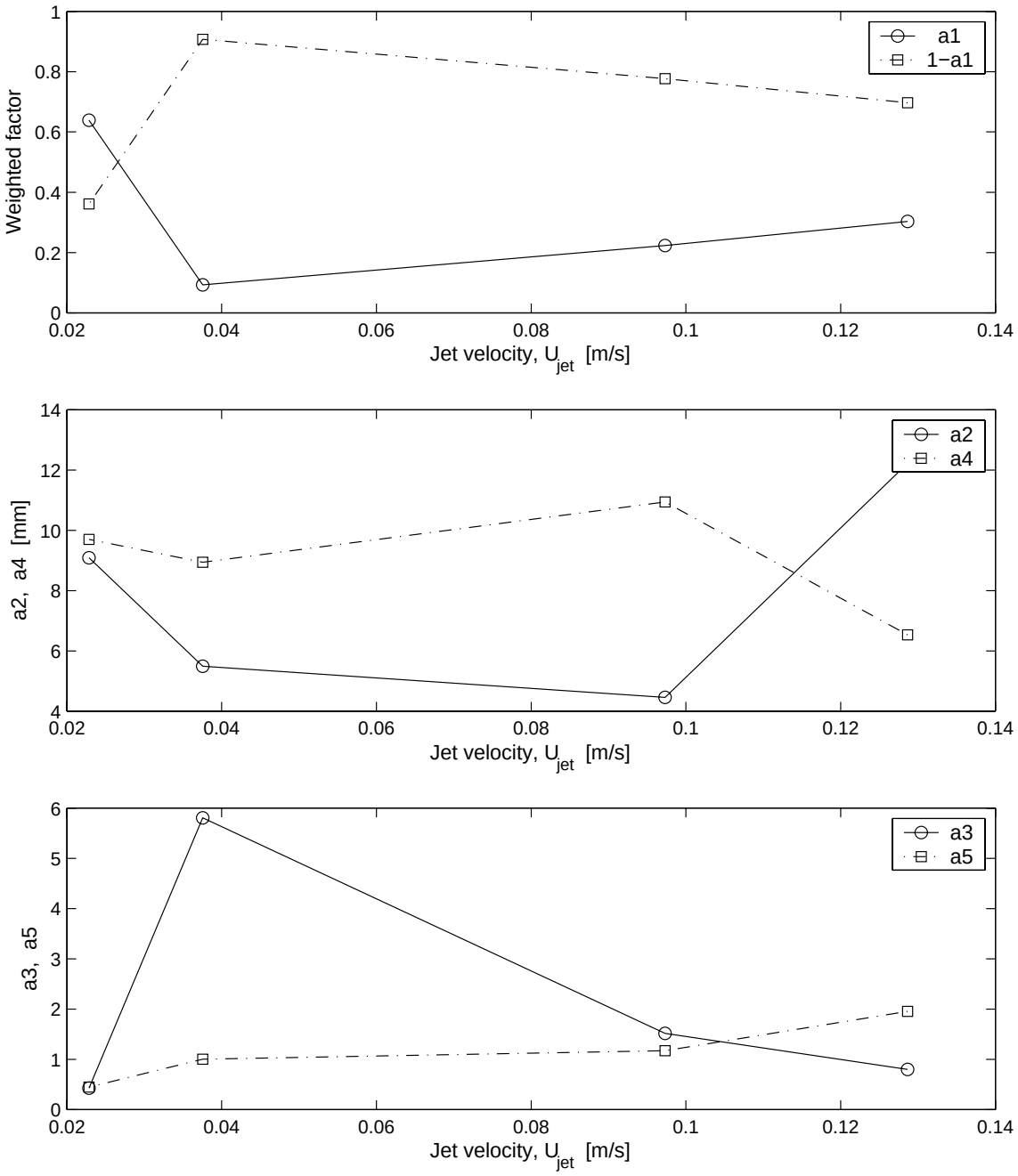

Figure 5.45 Five coefficients of the weighted evev bimodal PDFs shown in Figure 5.44 vs. jet velocity. Case CDC10WTP52.

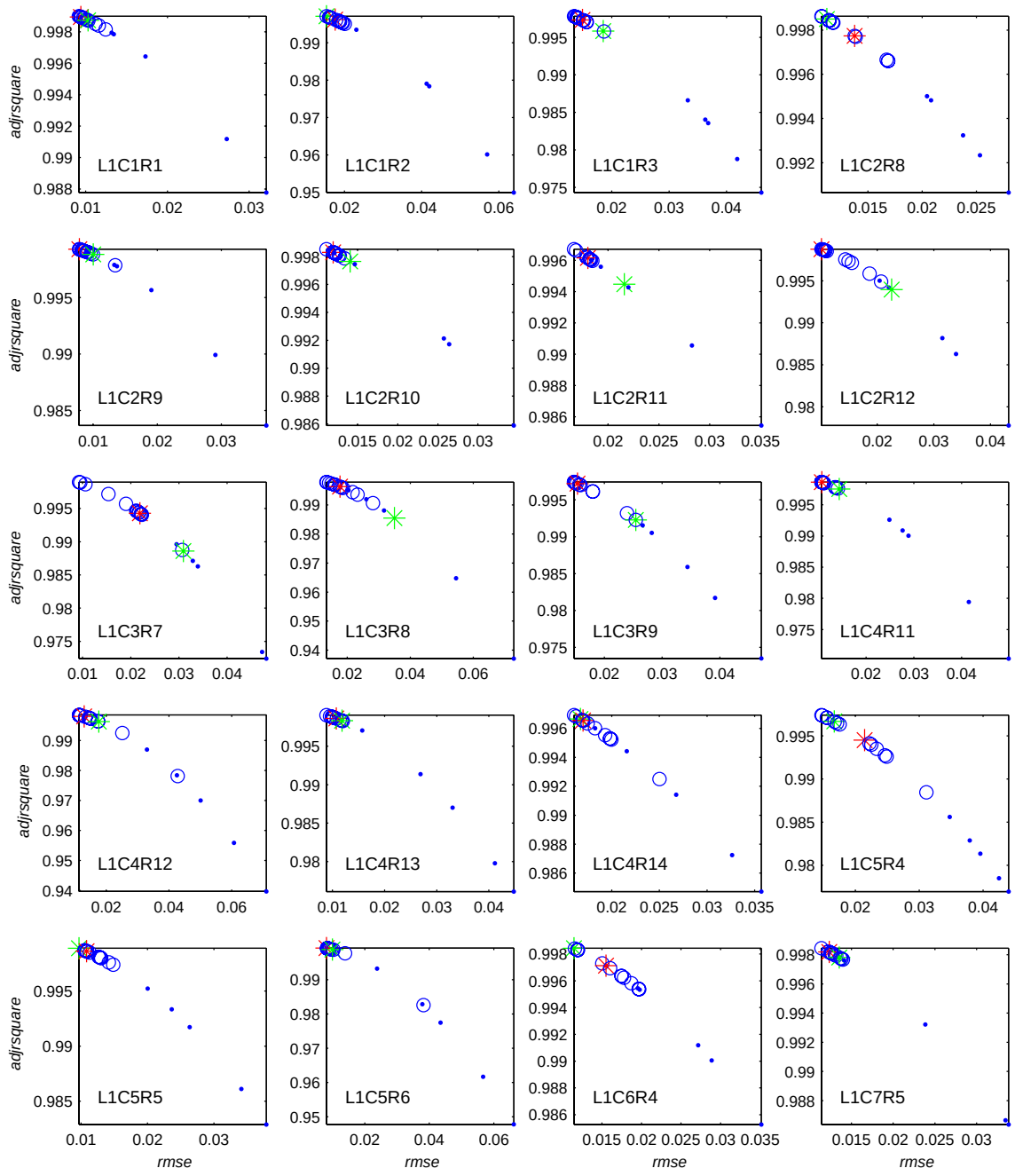

Figure 5.46 Root Mean Square Errors (*rmse*) and Degrees of Freedom Adjusted R-Square (*adjsquare*) for curve fits to 20 liquid CO_2 tests in instability regime 2. • , single distributions. ○, bimodal distributions. *, normwbl distribution; * , evev distribution.

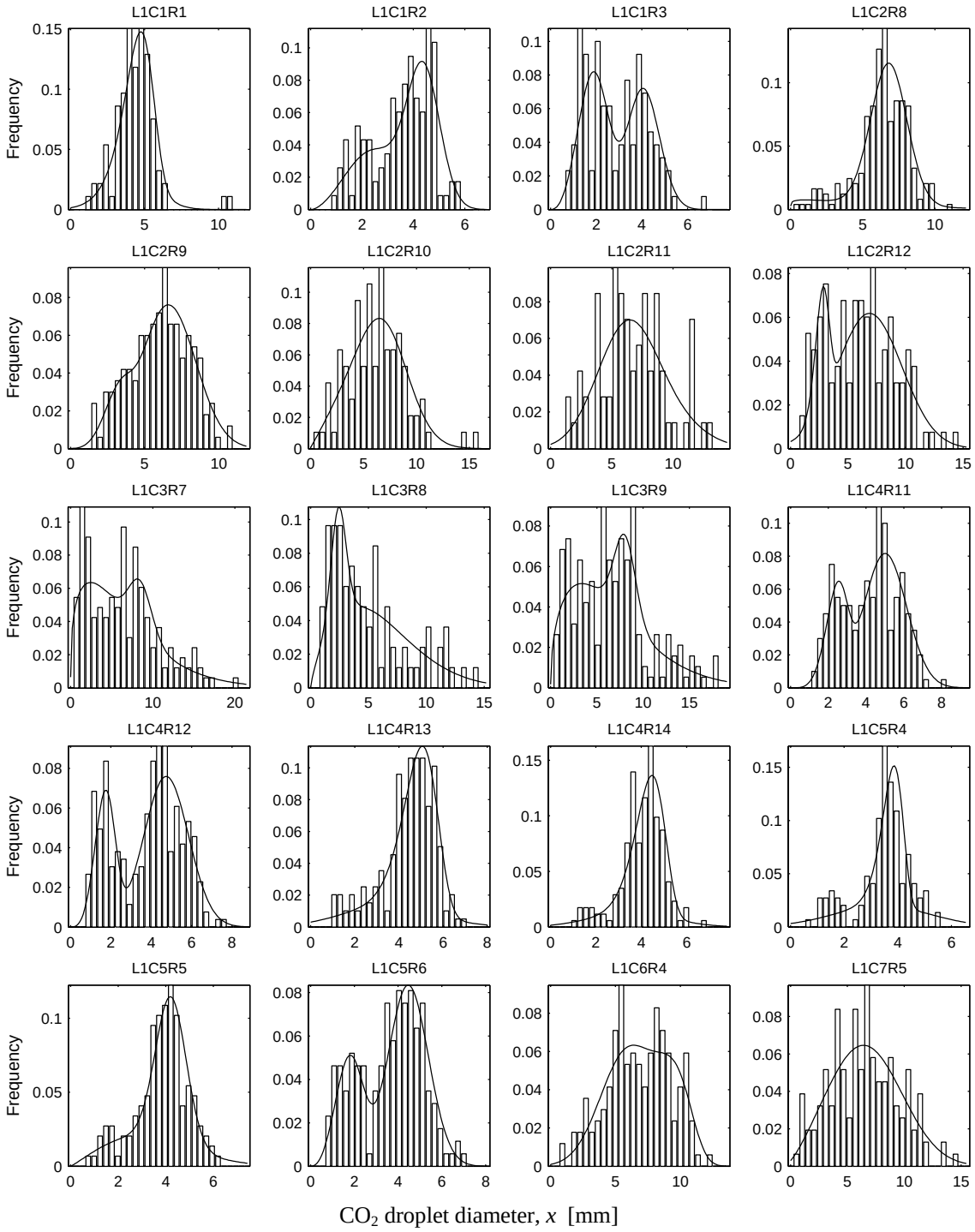

Figure 5.47 Frequency histograms of CO_2 droplet size for instability regime 2 and weighted normwbl bimodal PDFs. Test ID (e.g., L1C1R1) key given in Table B.1.

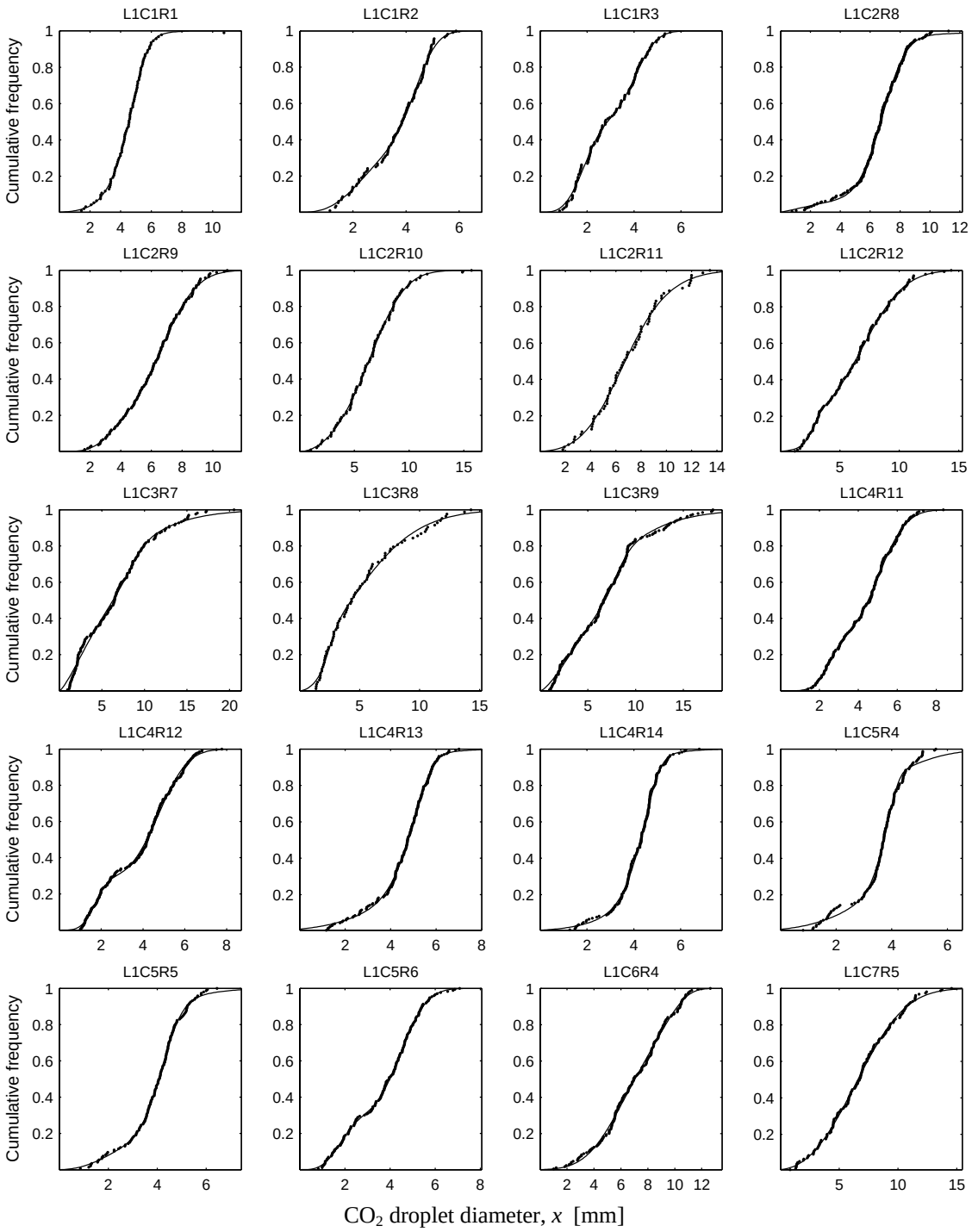

Figure 5.48 Weighted normwbl bimodal CDFs and data from liquid CO_2 tests in instability regime 2. Test ID (e.g., L1C1R1) key given in Table B.1.

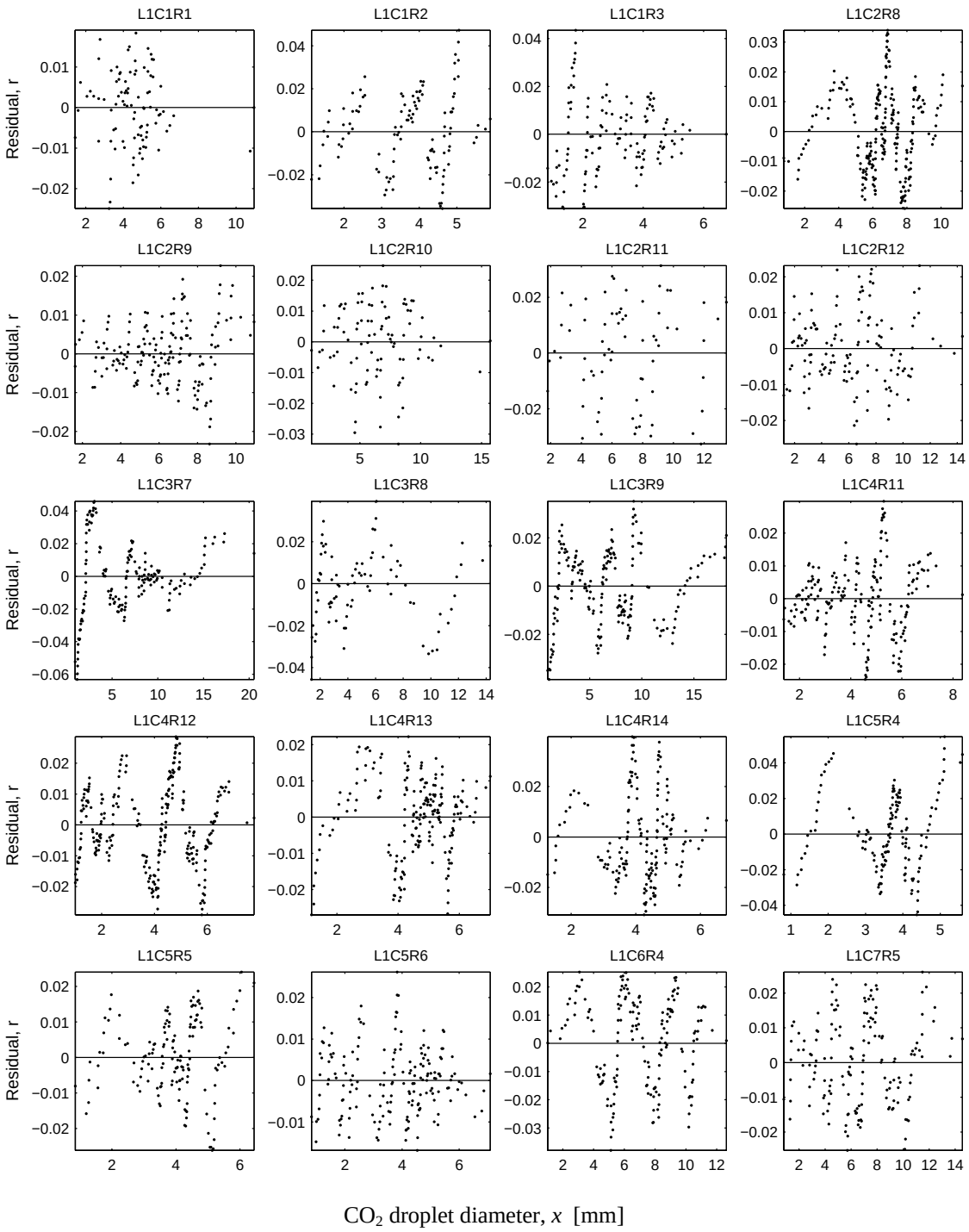

Figure 5.49 Calculated residuals of the weighted normwbl bimodal CDFs presented in Figure 5.48.

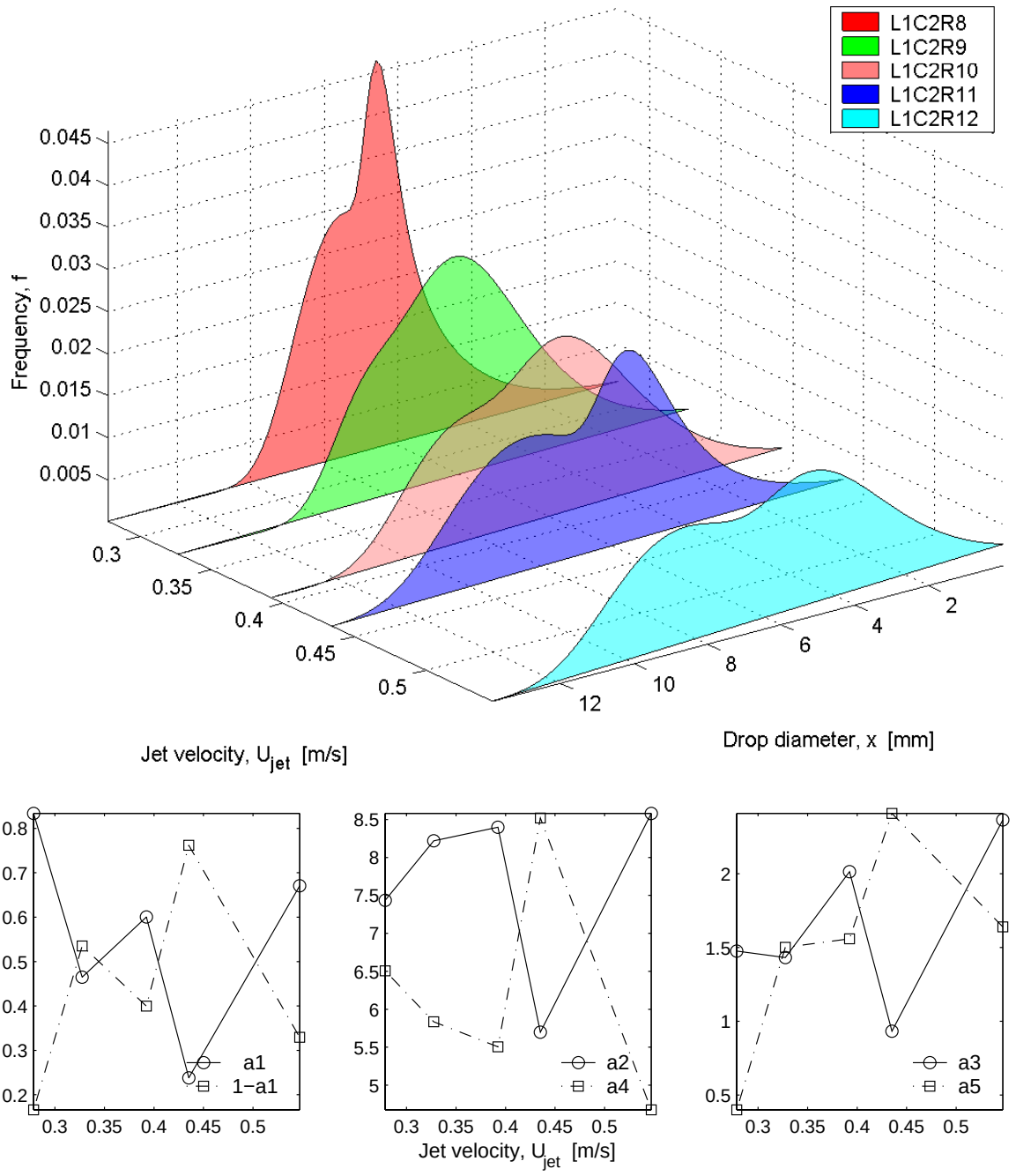

Figure 5.50 Weighted normwbl bimodal PDFs of CO_2 droplet size vs. jet velocity for liquid CO_2 injection into 52 bar tap water through a 5 mm i.d. sharp edge orifice Case CDC05WTP52. Breakup was classified as instability regime 2. Coefficients of the weighted distributions are given in the plots below the PDFs.

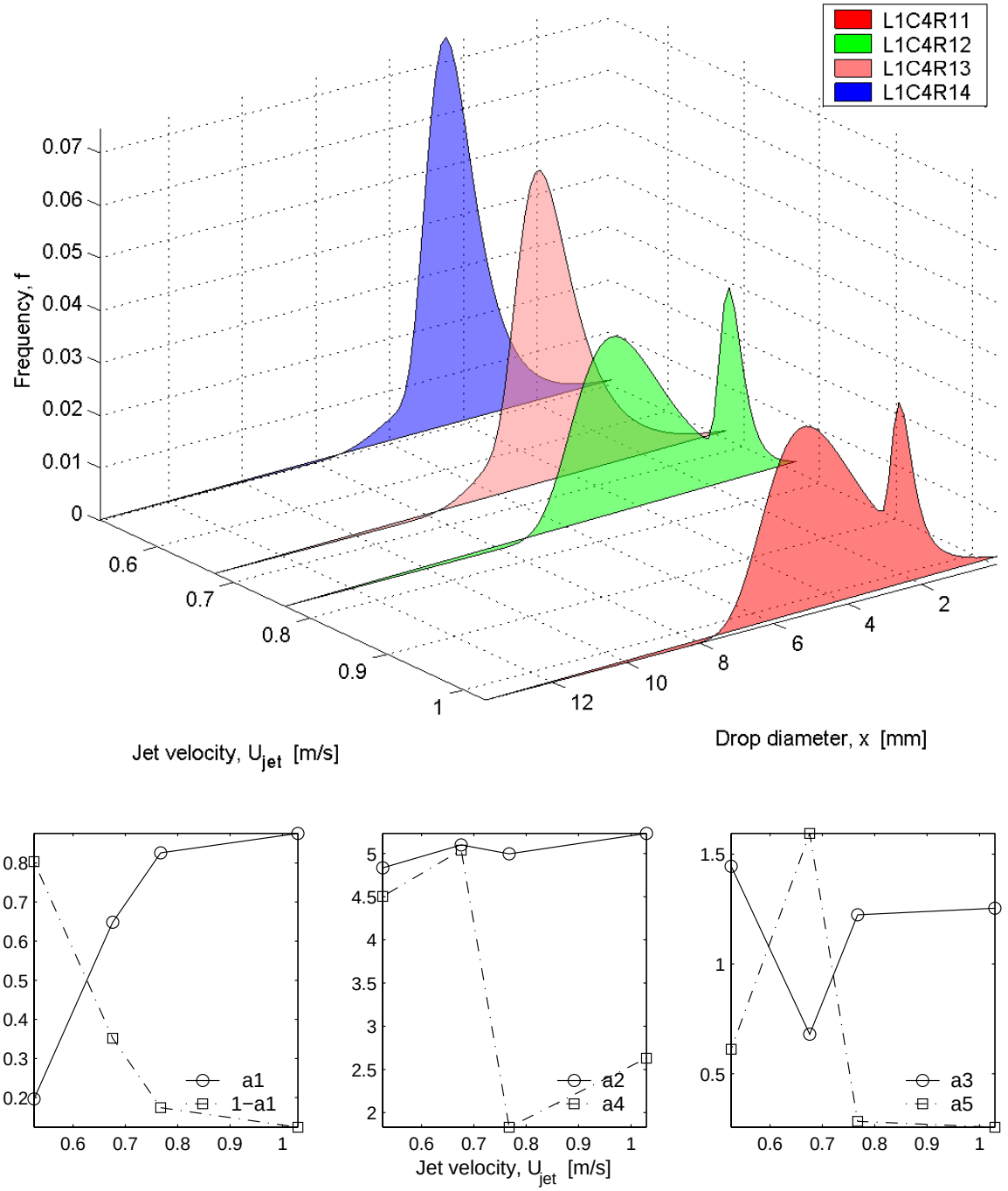

Figure 5.51 Weighted normwbl bimodal PDFs of CO_2 droplet size vs. jet velocity for liquid CO_2 injection into 52 bar tap water through a 2 mm tube edge orifice. Case CDT02WTP52. Breakup was classified as instability regime 2. Coefficients of the weighted distributions are given in the plots below the PDFs.

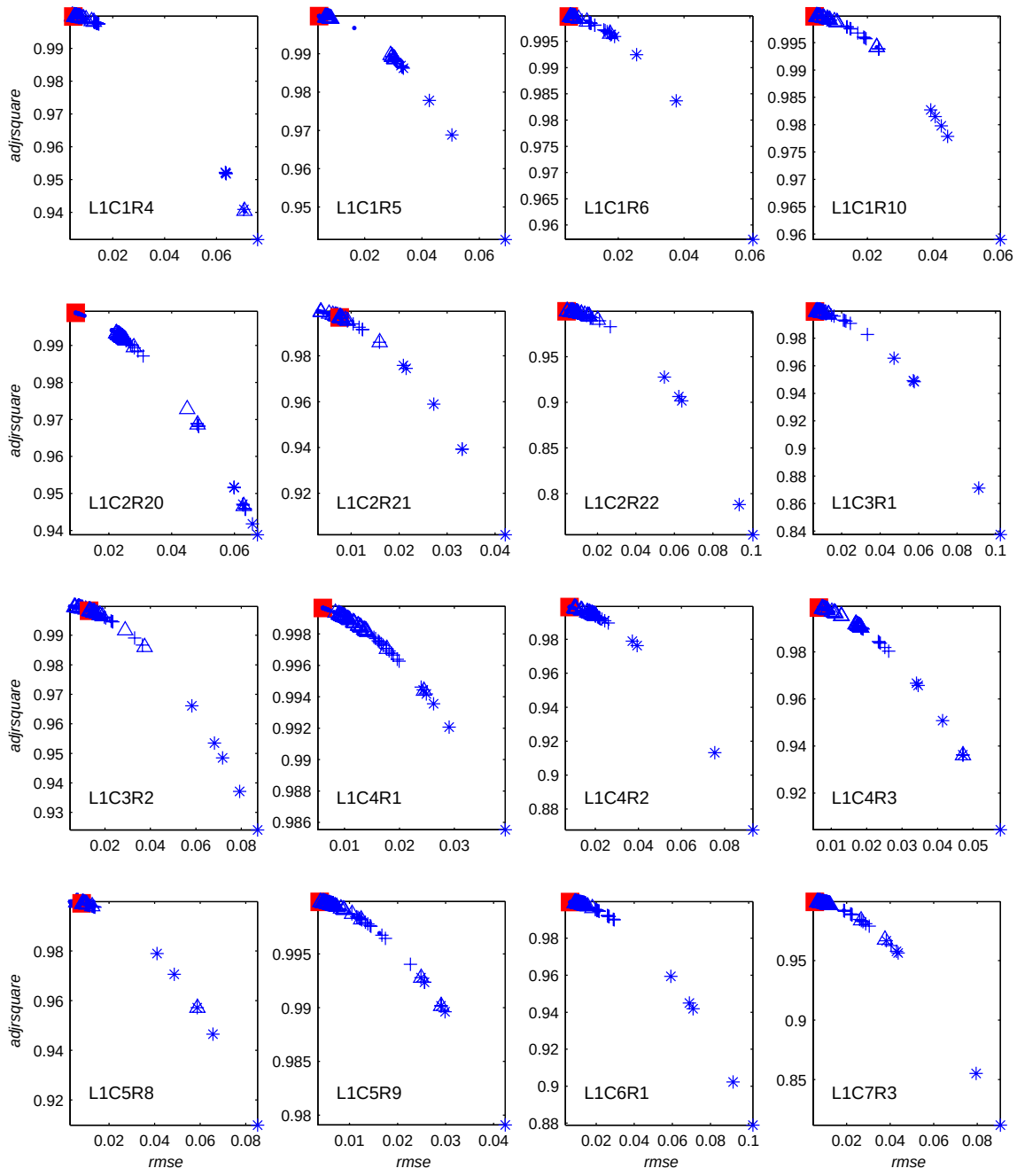

Figure 5.52 Root Mean Square Errors (*rmse*) and Degrees of Freedom Adjusted R-Square (*adjsquare*) for curve fits to 16 liquid CO_2 tests in instability regime 3. * , single mode distribution. +, bimodal distribution. Δ, tri-modal distribution; ■ , wblevevgam distribution.

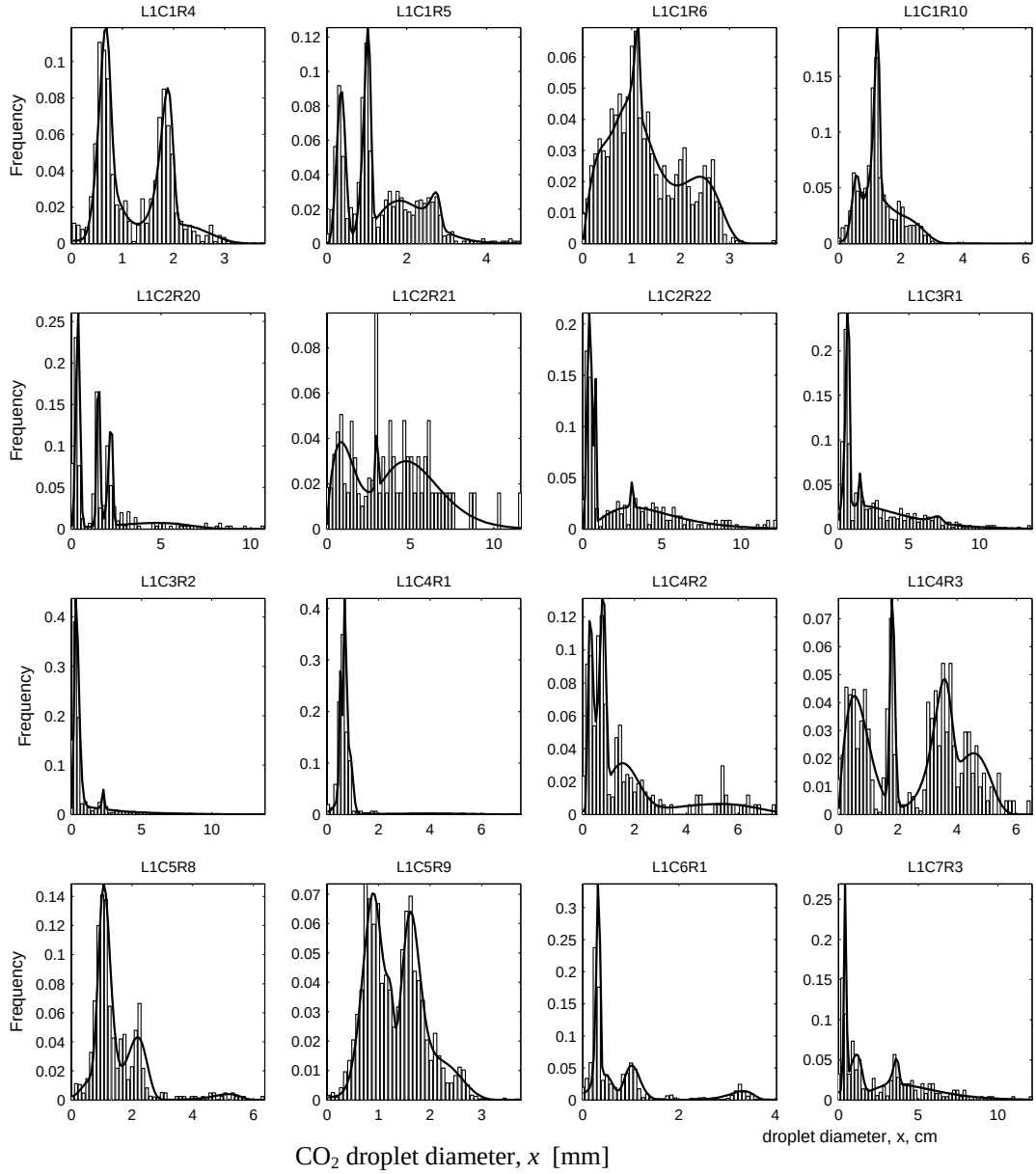

Figure 5.53 Frequency histograms of CO_2 droplet size forinstability regime 3 and weighted wblevevgam bimodal PDFs. Test ID (e.g., L1C1R4) key given in Table B.1.

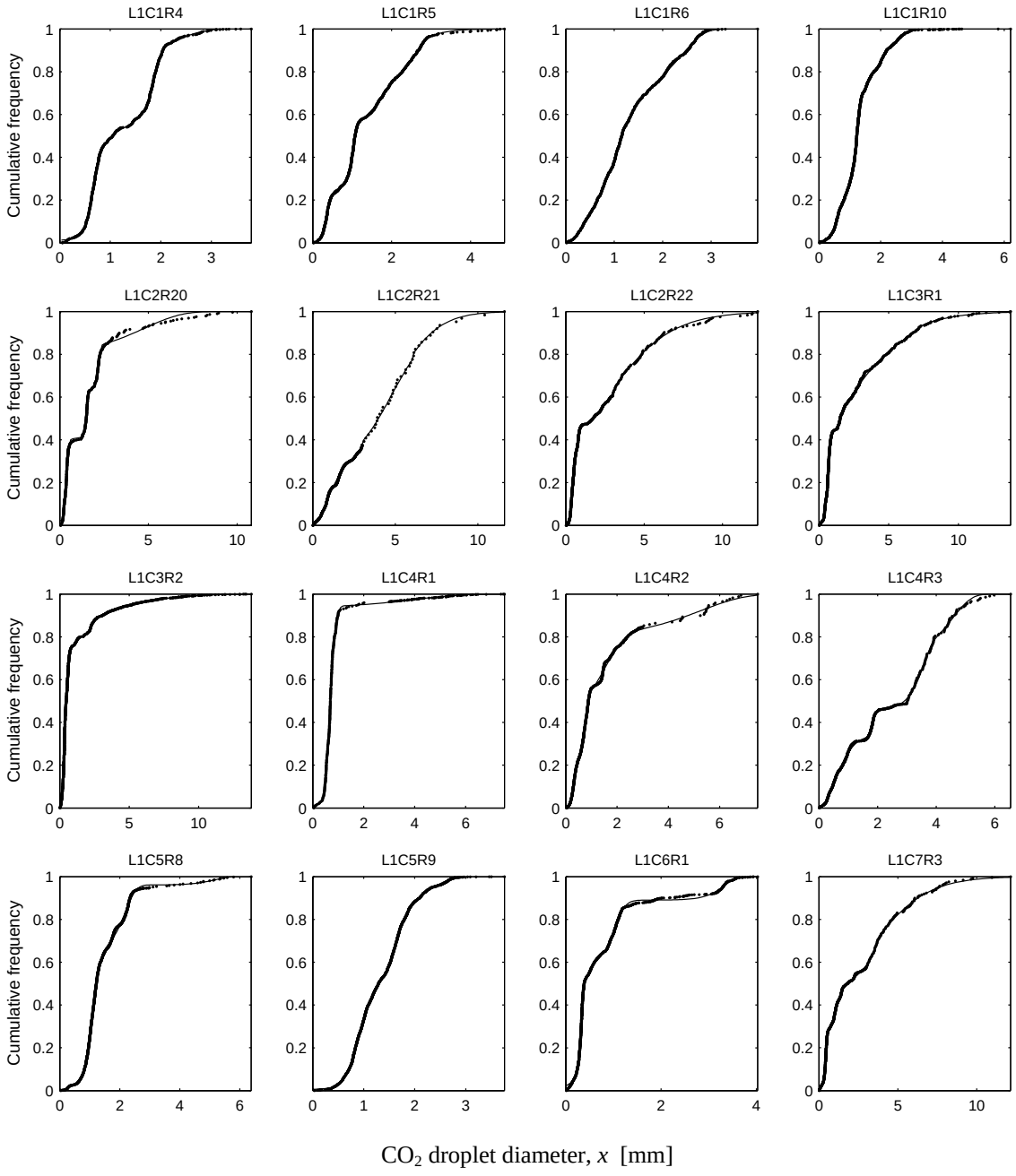

Figure 5.54 Weighted wblevevgam bimodal CDFs and data from liquid CO_2 tests in instability regime 3. Test ID (e.g., L1C1R4) key given in Table B.1.

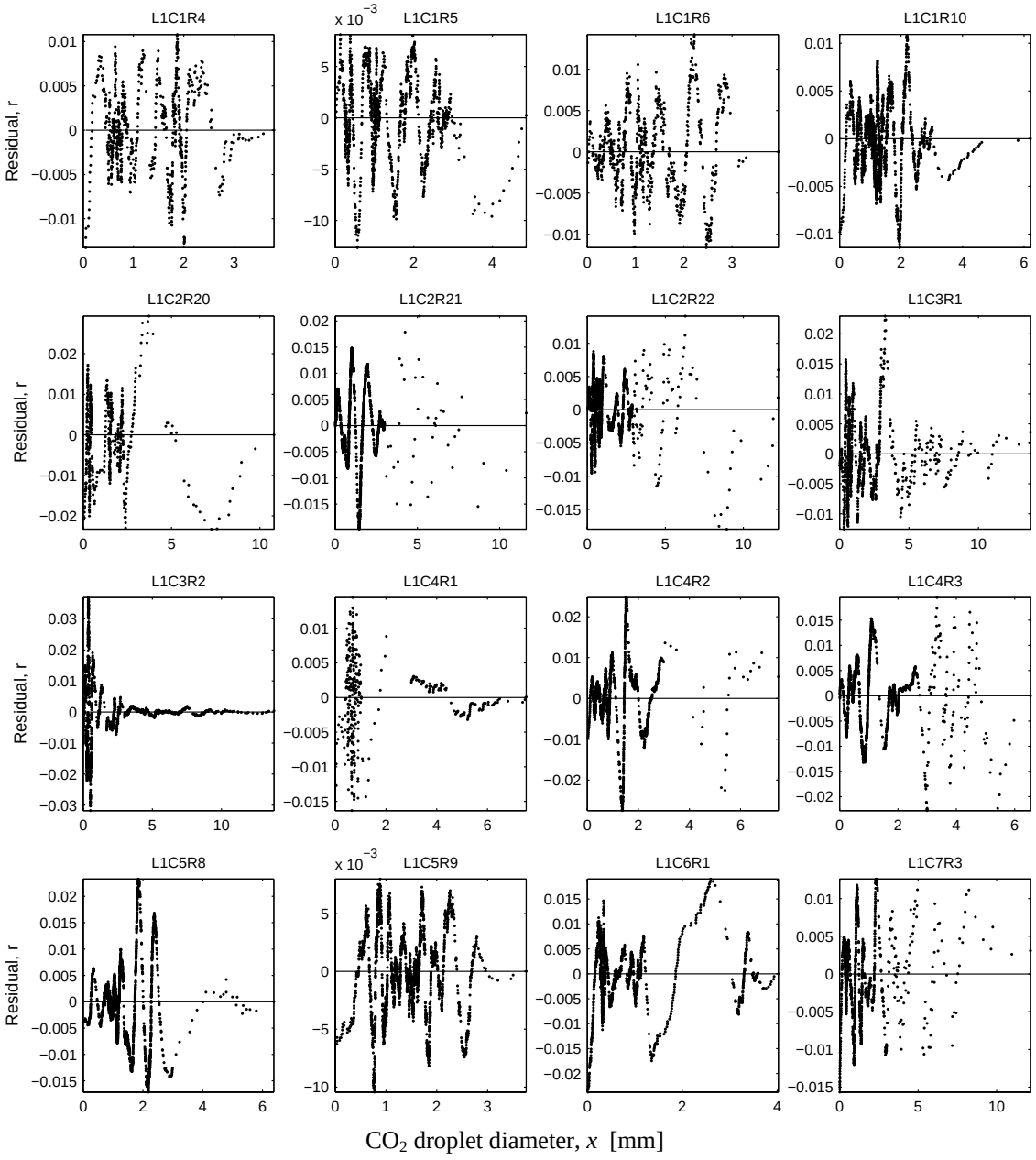

Figure 5.55 Calculated residuals of the weighted wblevevgam four-modal CDFs presented in Figure 5.54.

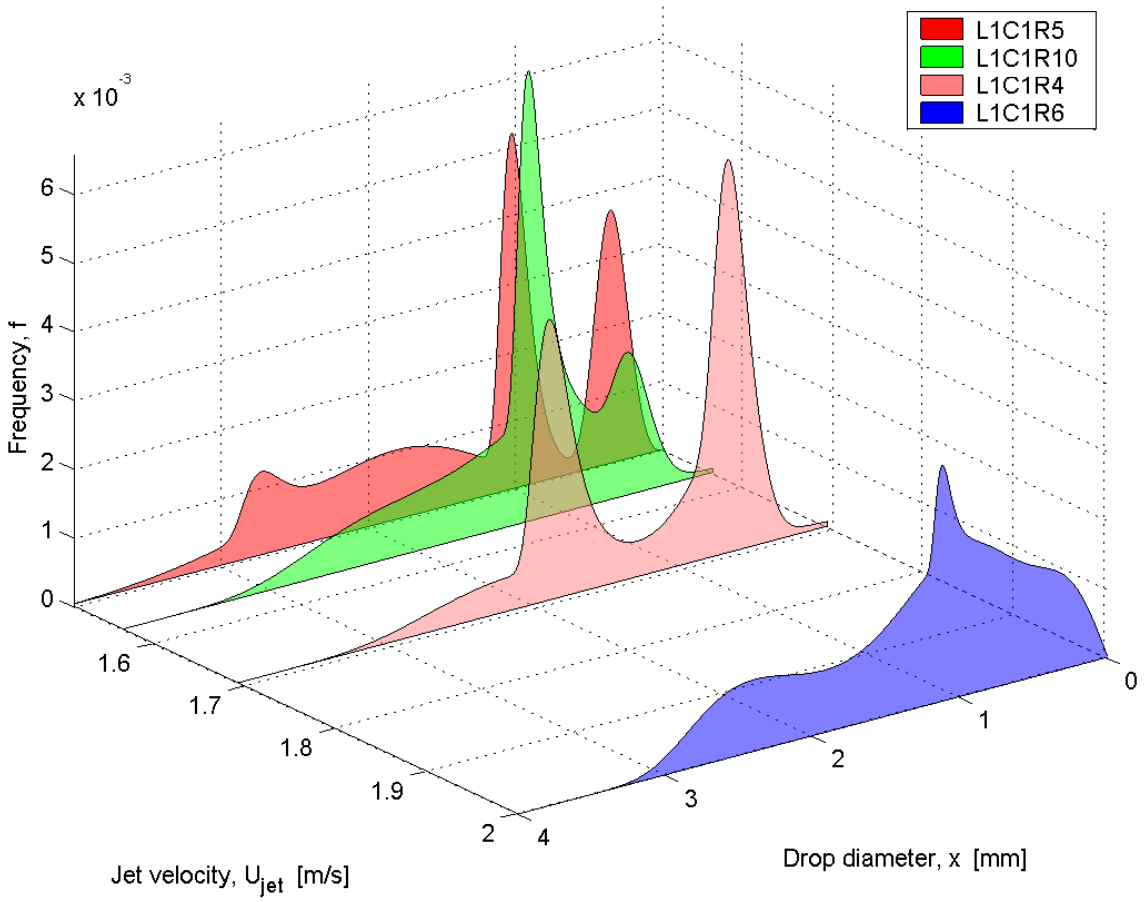

Figure 5.56 Weighted wblevevgam four-modal PDFs of CO_2 droplet size vs. jet velocity for liquid CO_2 injection into 52 bar tap water through a 2 mm sharp edge orifice. Case CDC02WTP52. Breakup was classified as instability regime 3.

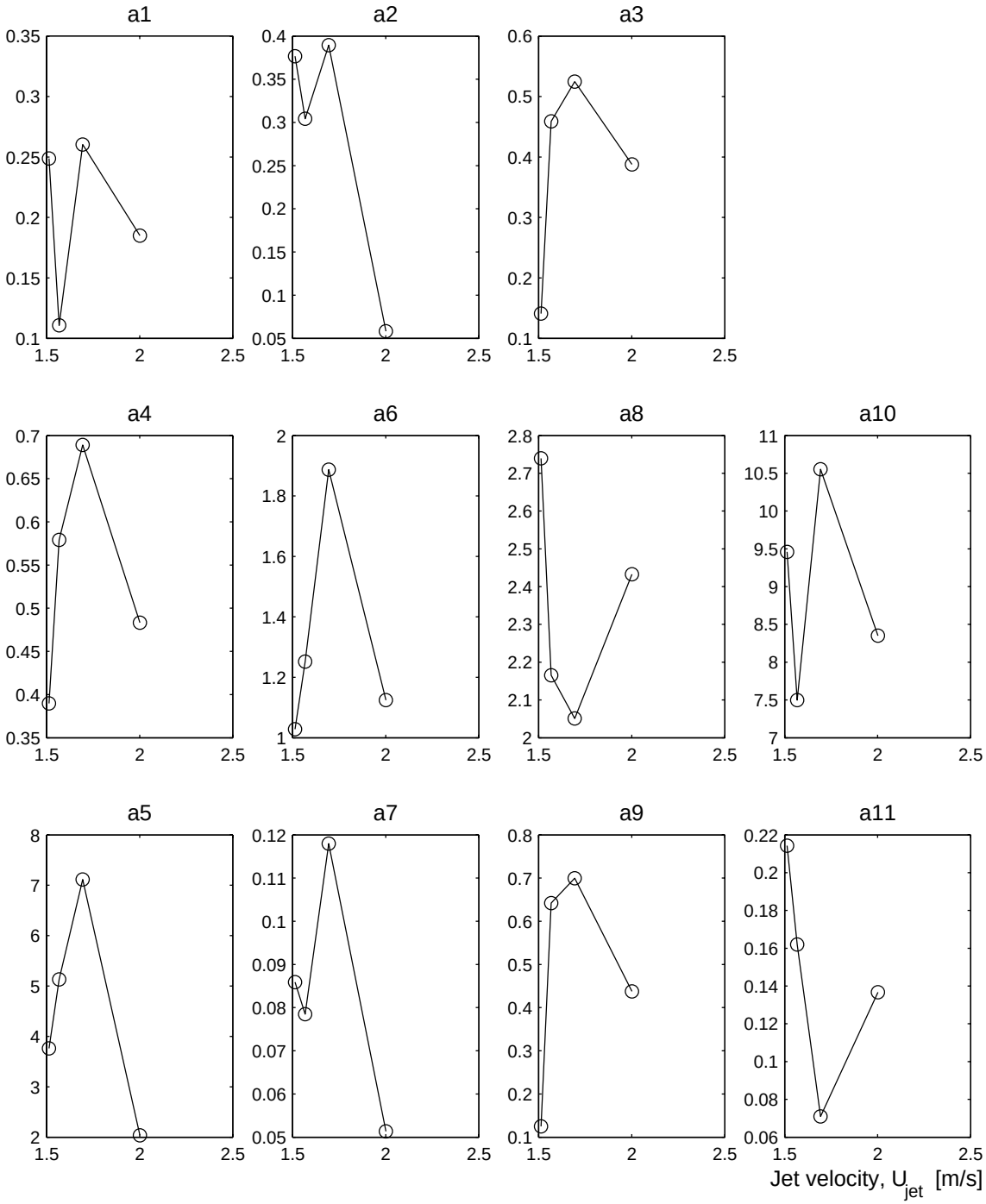

Figure 5.57 Eleven coefficients for PDFs shown in Figure 5.56.

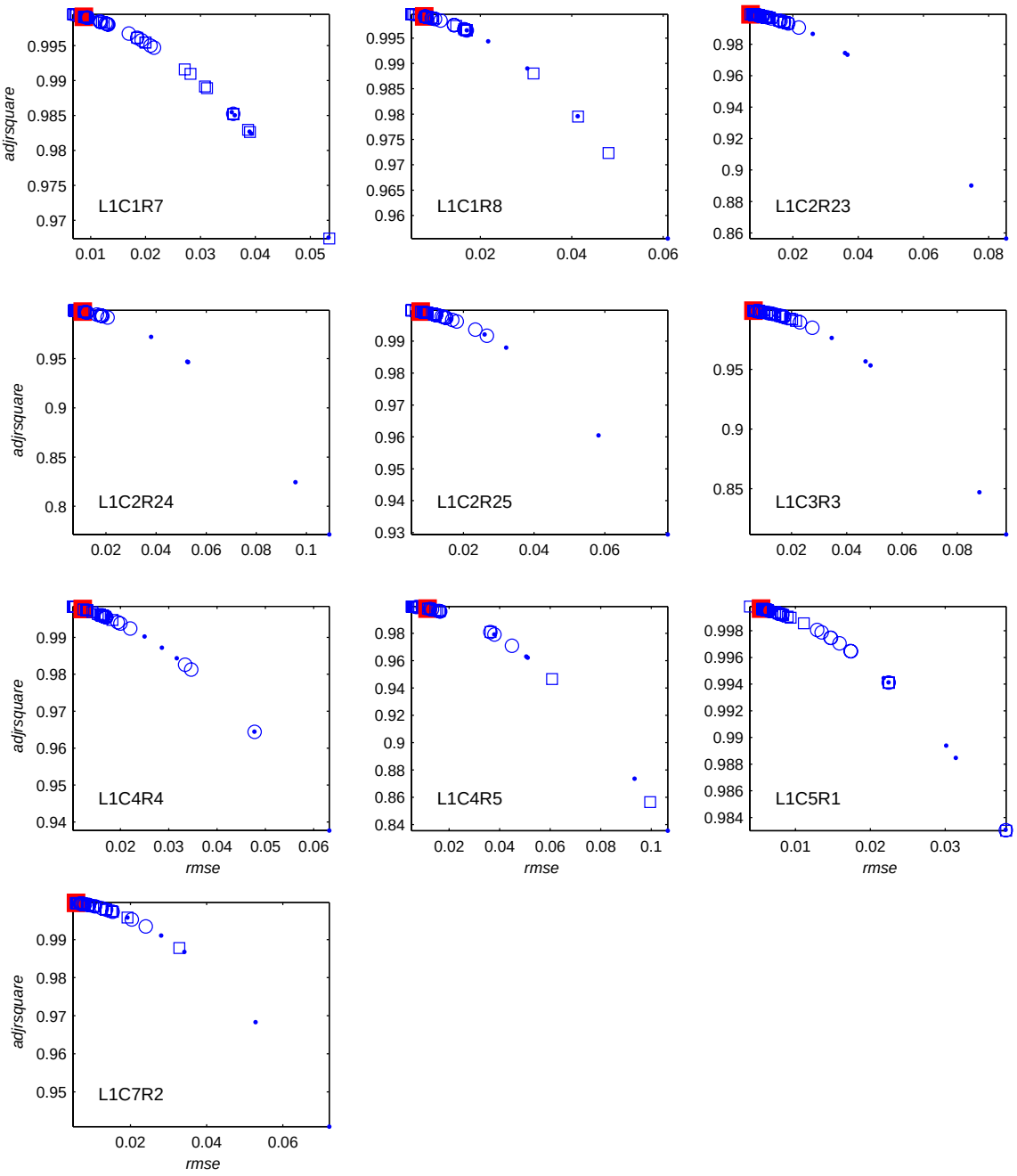

Figure 5.58 Root Mean Square Errors (*rmse*) and Degrees of Freedom Adjusted R-Square (*adjsquare*) for curve fits to 10 liquid CO_2 tests in instability regime 4. ● , single mode distribution. ○, bimodal distribution. .; □, tri-modal distribution ; ■, normwblgam distribution.

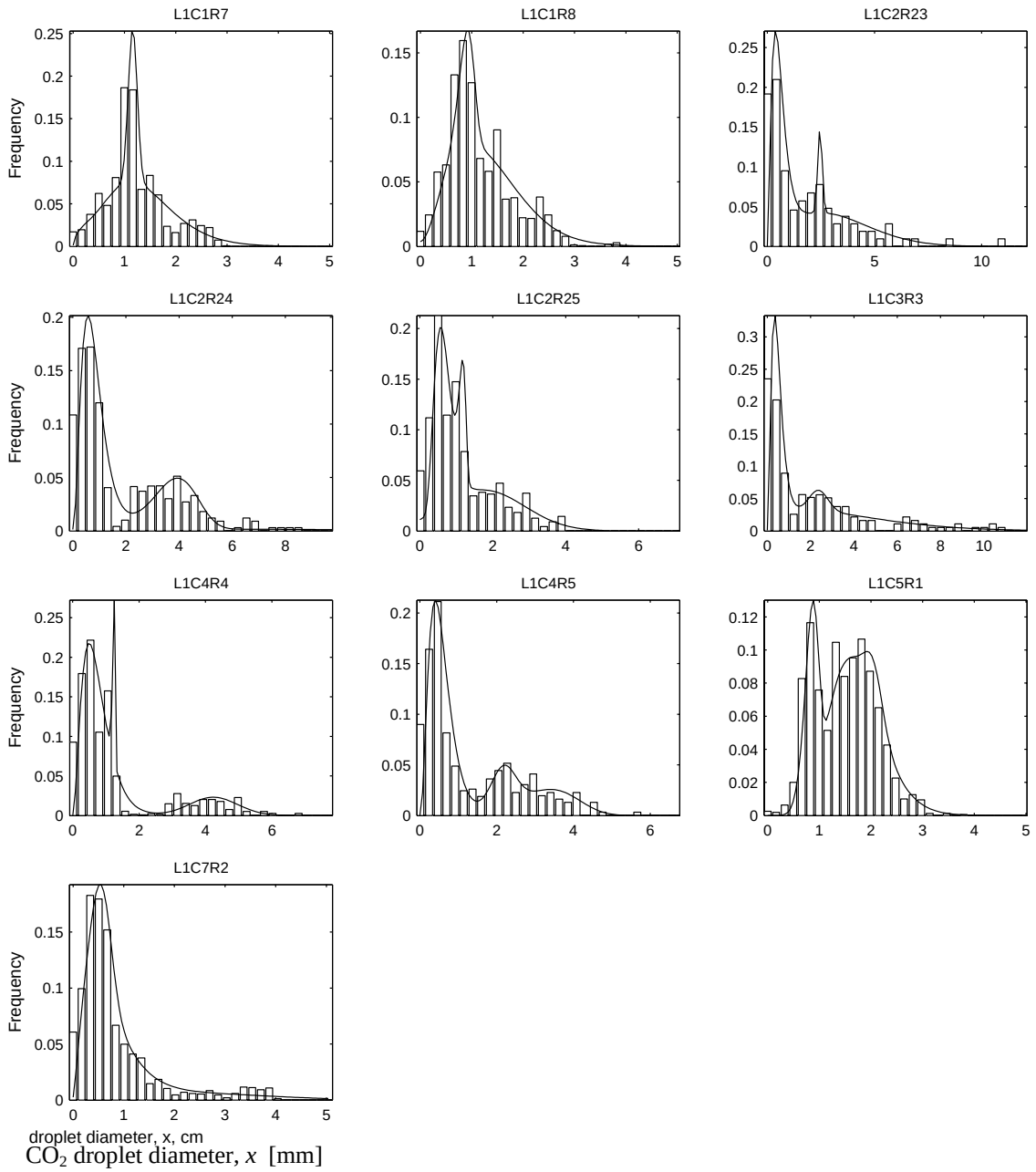

Figure 5.59 Frequency histograms of CO_2 droplet size for instability regime 4 and weighted normwblgam tri-modal PDFs. Test ID (e.g., L1C1R7) key given in Table B.1.

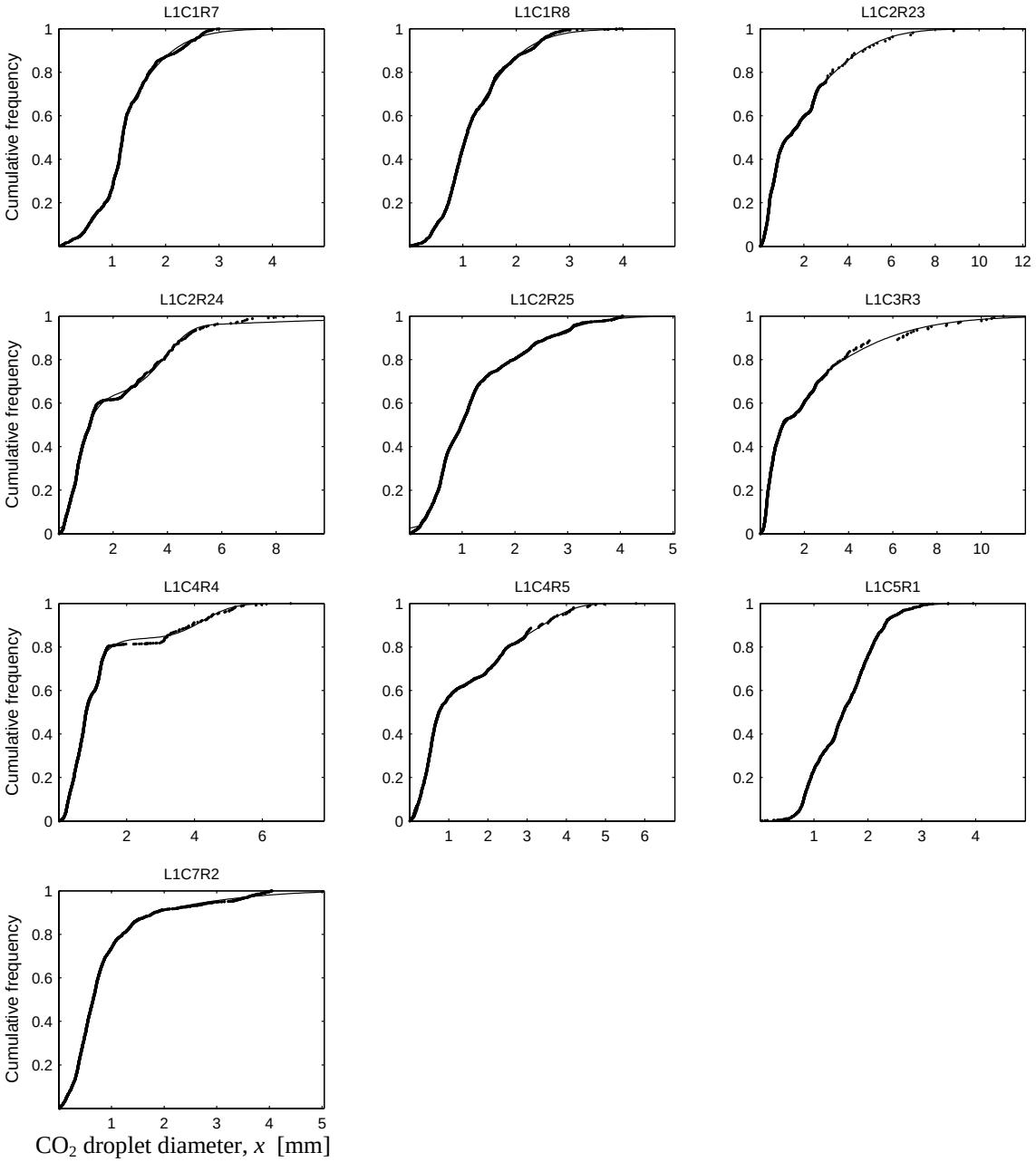

Figure 5.60 Weighted normwblgam tri-modal CDFs and data from liquid CO_2 tests in instability regime 4. Test ID (e.g., L1C1R7) key given in Table B.1.

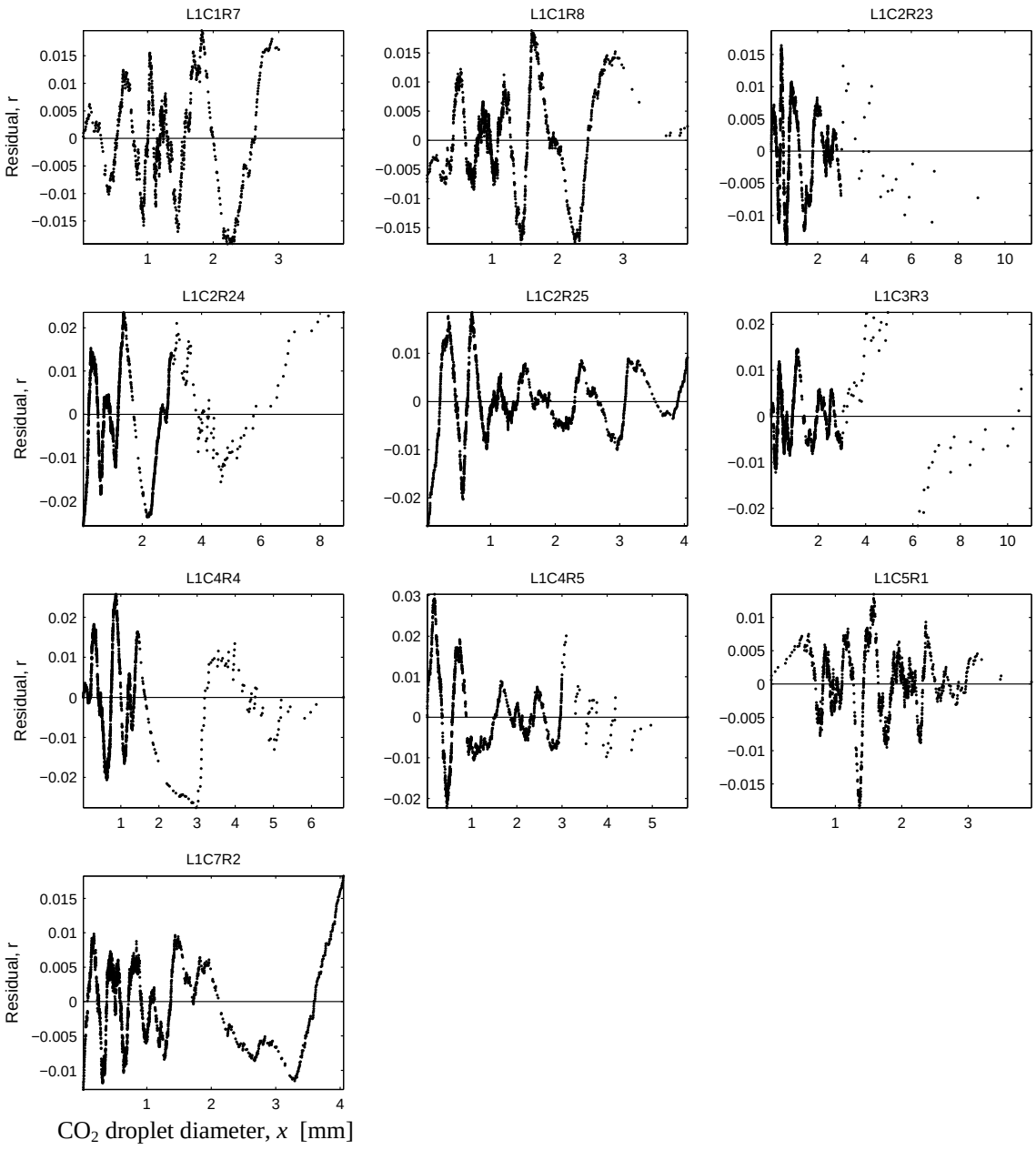

Figure 5.61 Calculated residuals of the weighted normwblgam tri-modal CDFs presented in Figure 5.60.

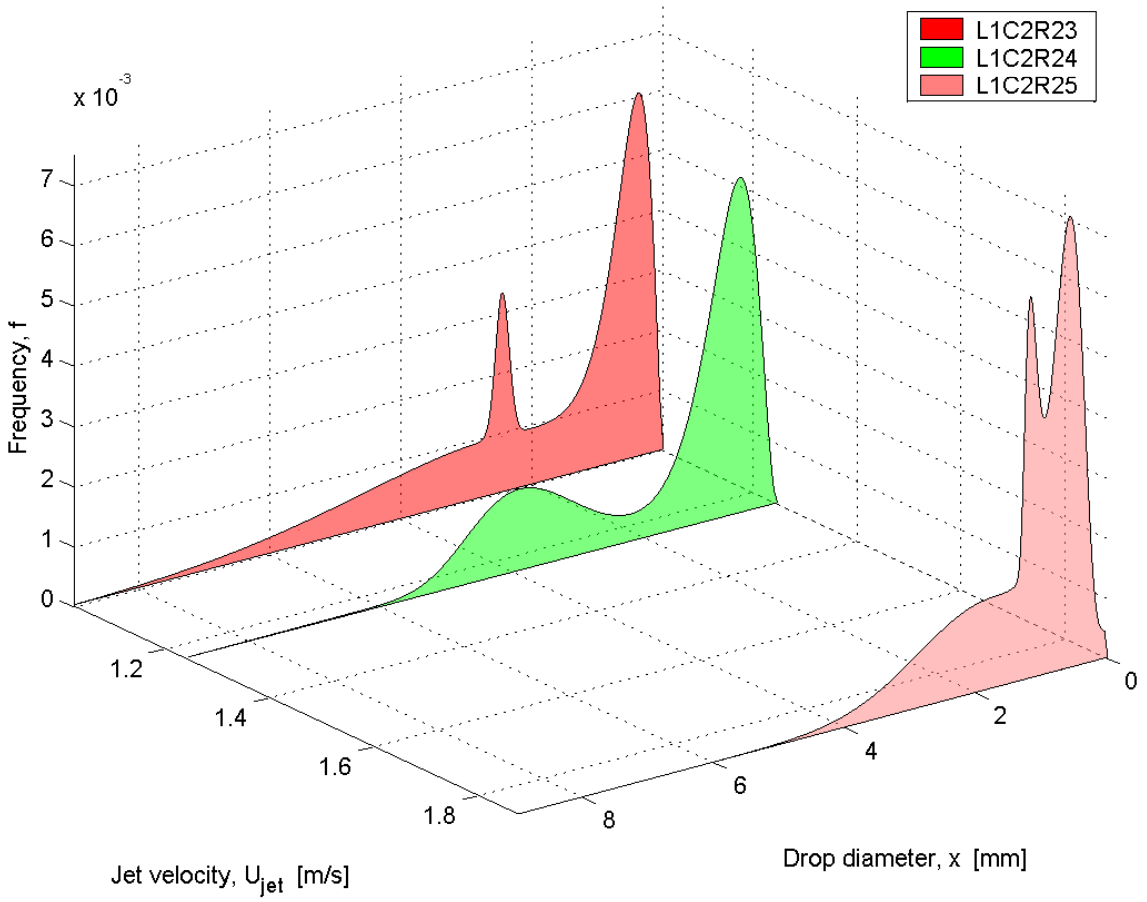

Figure 5.62 Weighted normwblgam tri-modal PDFs of CO_2 droplet size vs. jet velocity for liquid CO_2 injection into 52 bar tap water through a 5 mm sharp edge orifice. Case CDC05WTP52. Breakup was classified as instability regime 4.

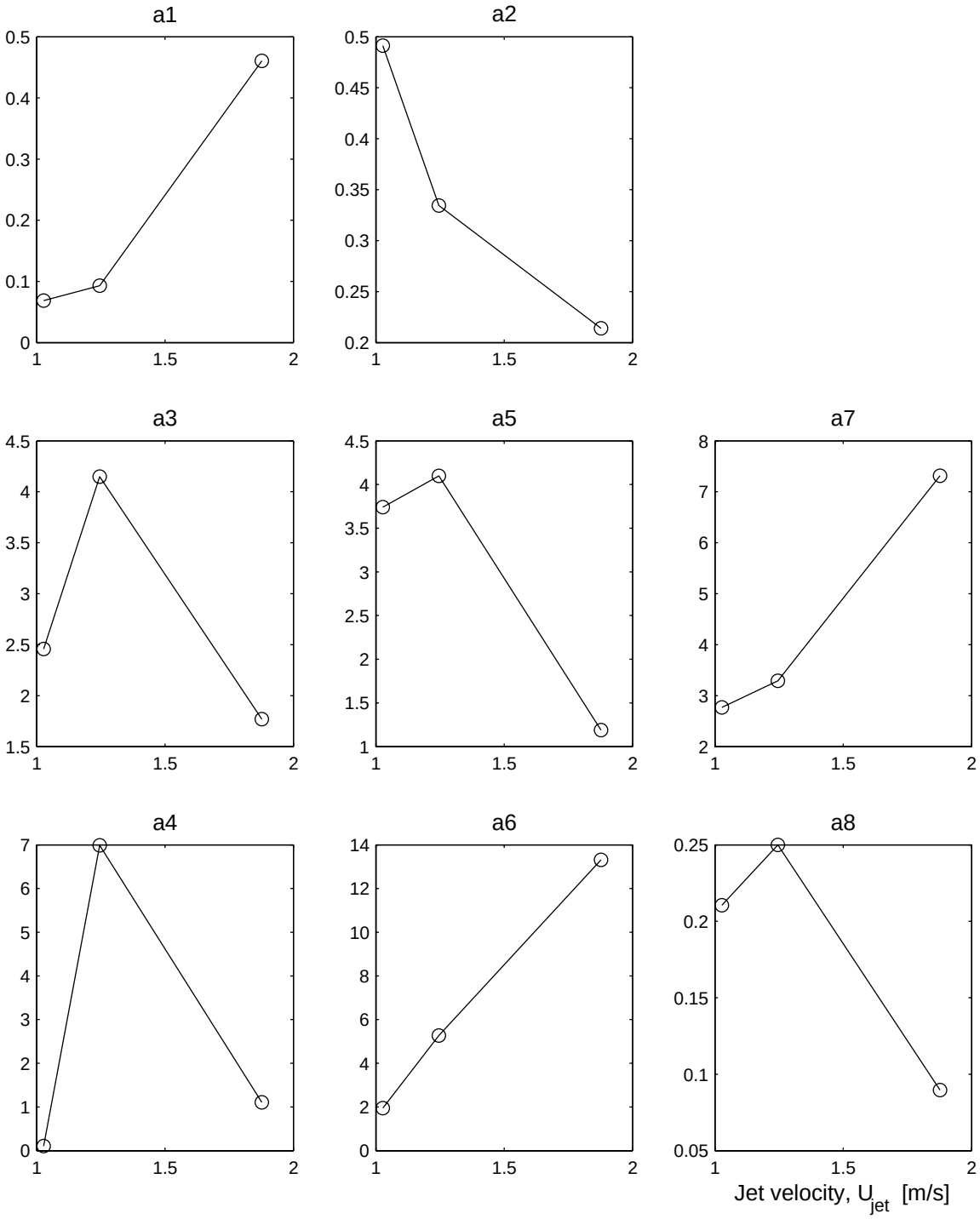

Figure 5.63 Eight coefficients of the PDFs shown in Figure 5.62.

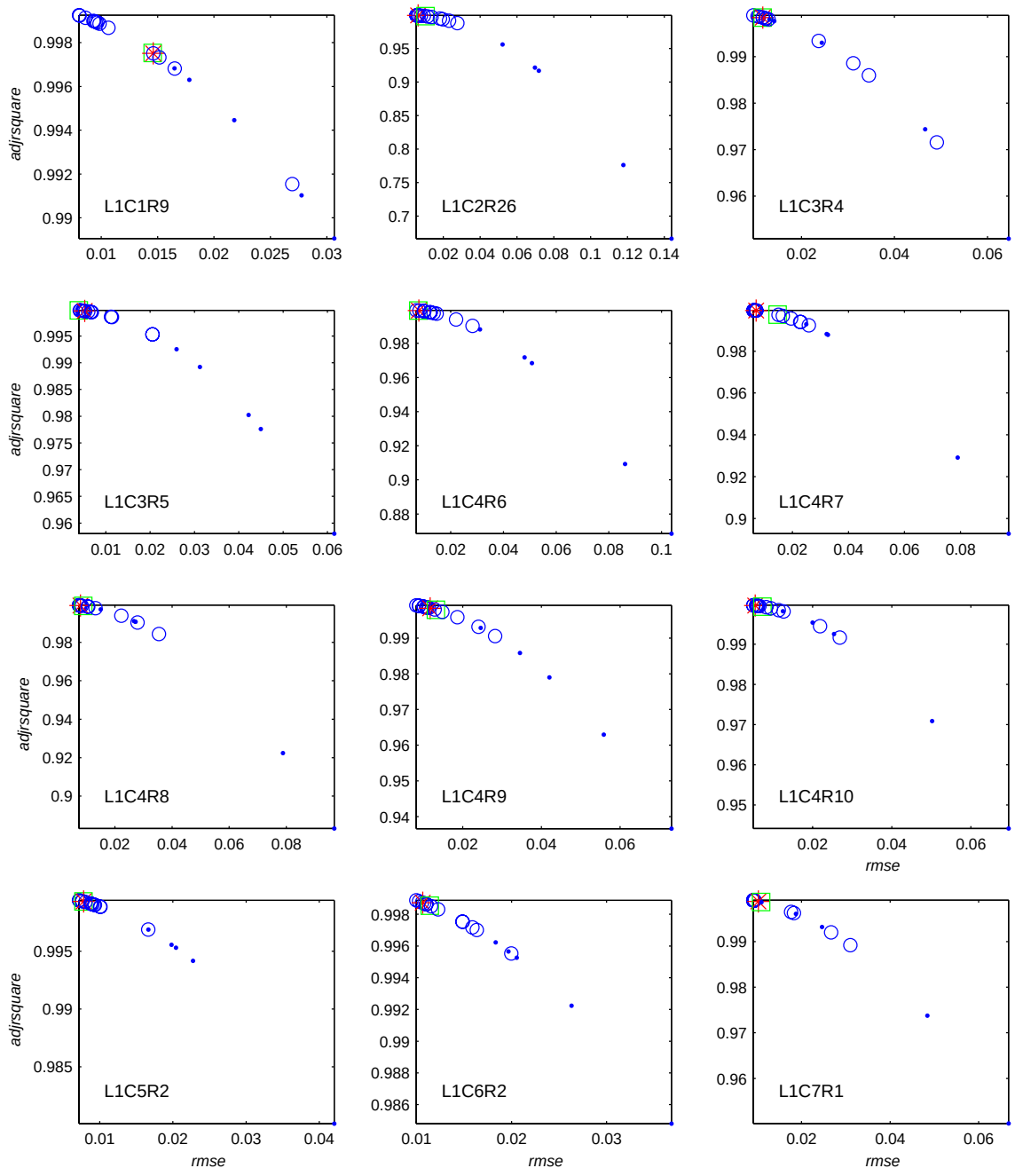

Figure 5.64 Root Mean Square Errors (*rmse*) and Degrees of Freedom Adjusted R-Square (*adjsquare*) for curve fits to 12 liquid CO_2 tests in instability regime 5. • , single mode distribution. ○, other bimodal distribution. *, wblwbl distribution, □, normwbl distribution with $H = 0$.

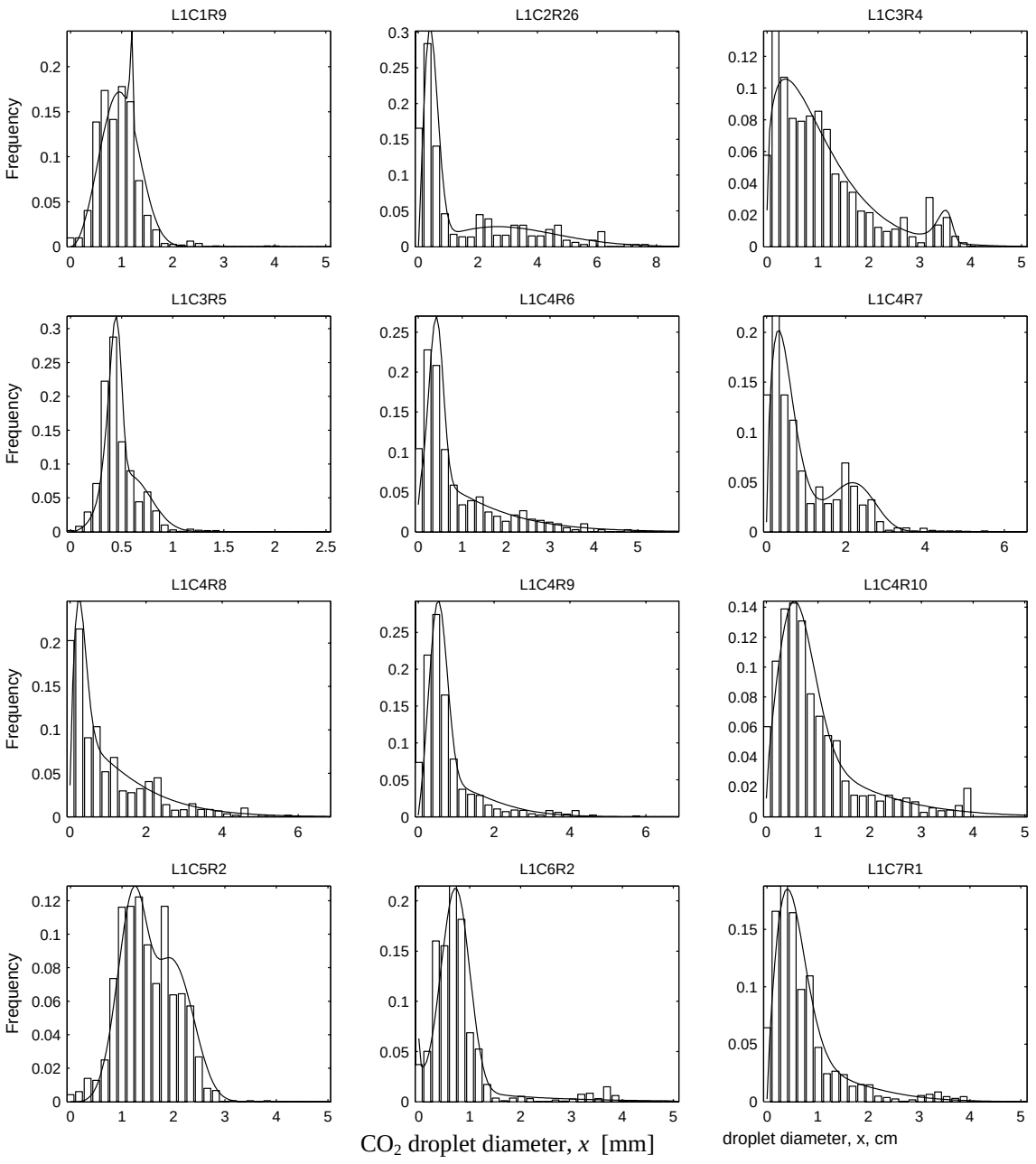

Figure 5.65 Frequency histograms of CO_2 droplet size for instability regime 5 and weighted wblwbl bimodal PDFs. Test ID (e.g., L1C1R9) key given in Table B.1.

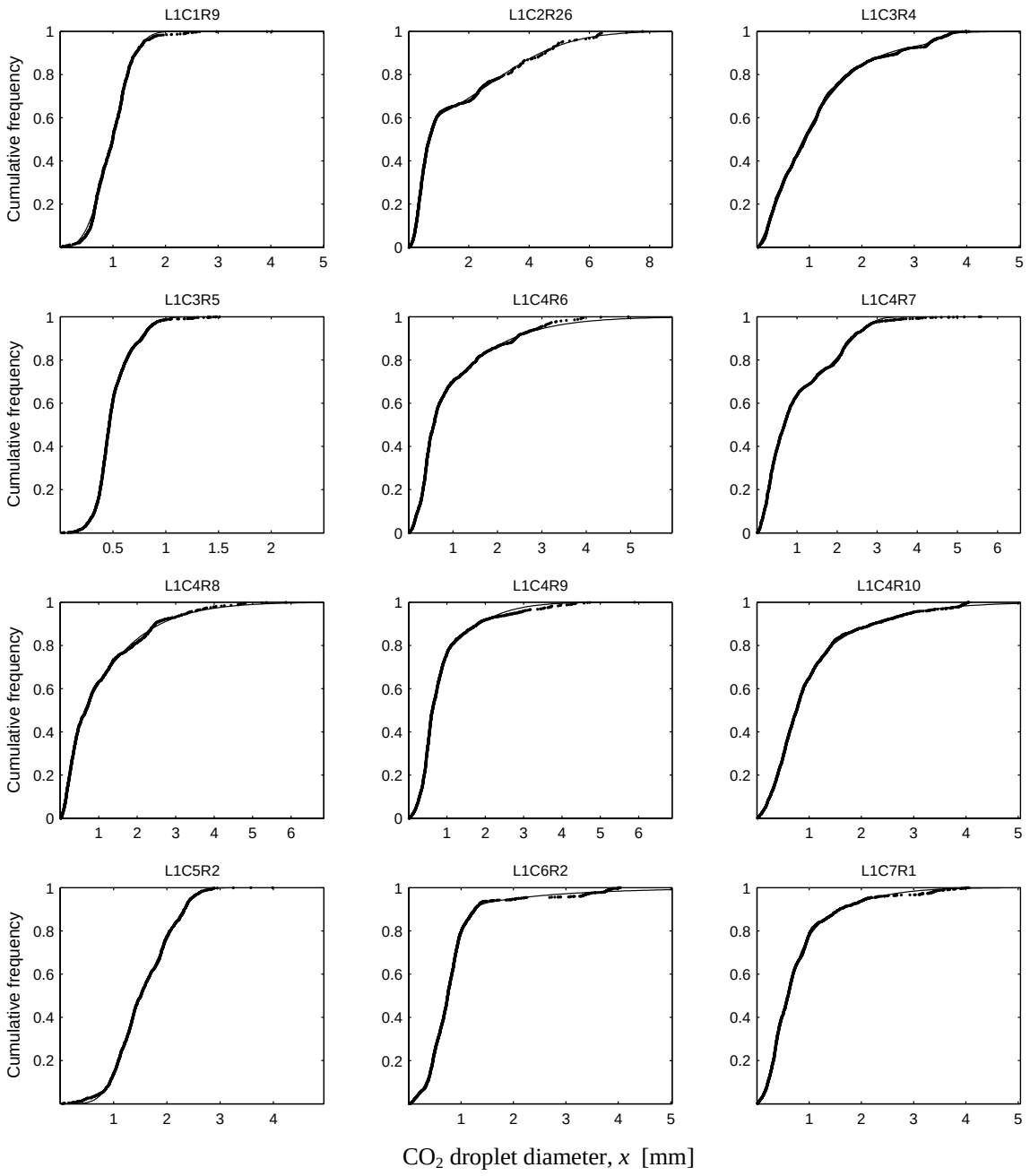

Figure 5.66 Weighted wblwbl bimodal CDFs and data from liquid CO_2 tests in instability regime 5. Test ID (e.g., L1C1R7) key given in Table B.1.

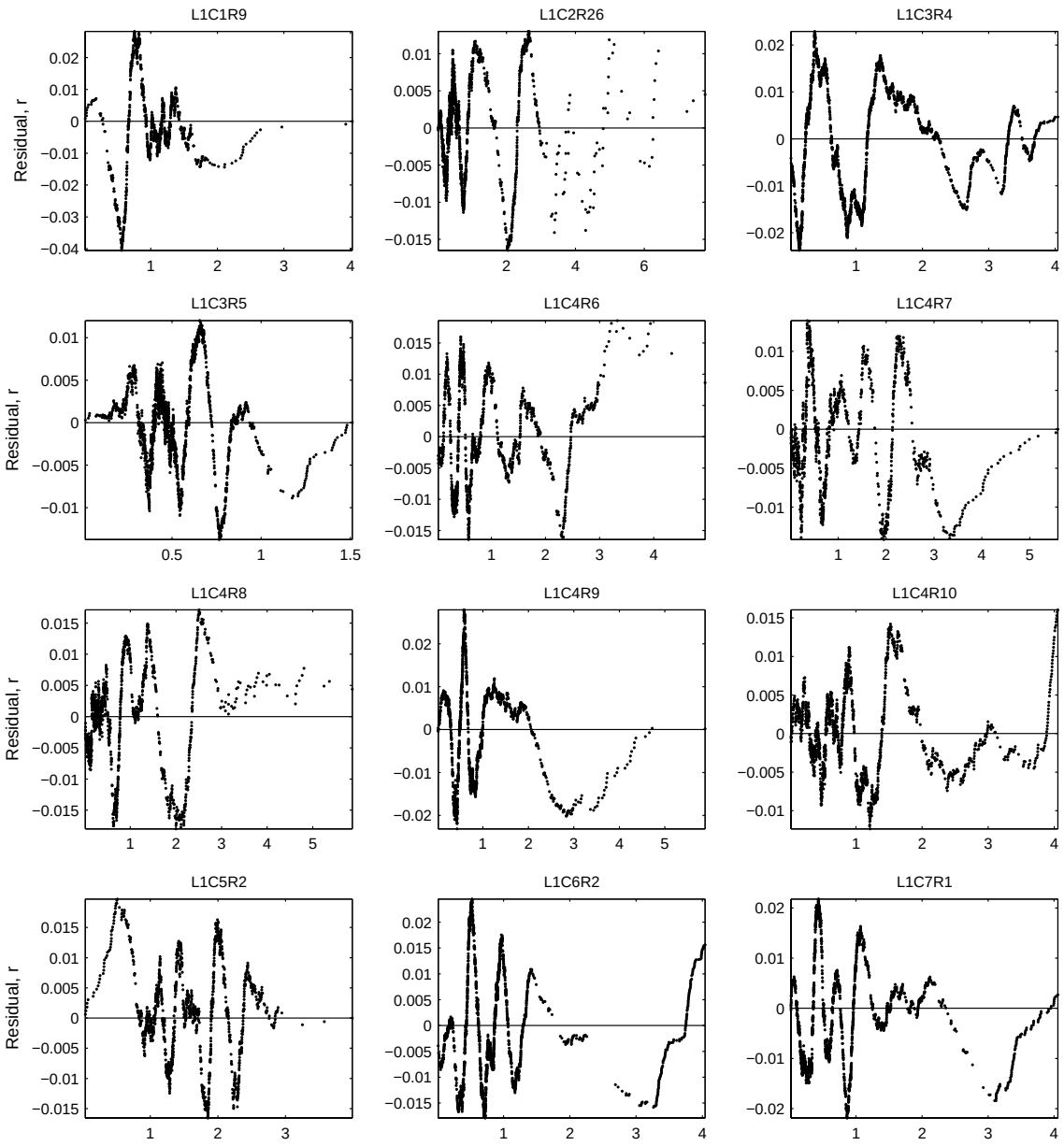

Figure 5.67 Calculated residuals of the weighted wblwbl CDFs presented in Figure 5.66.

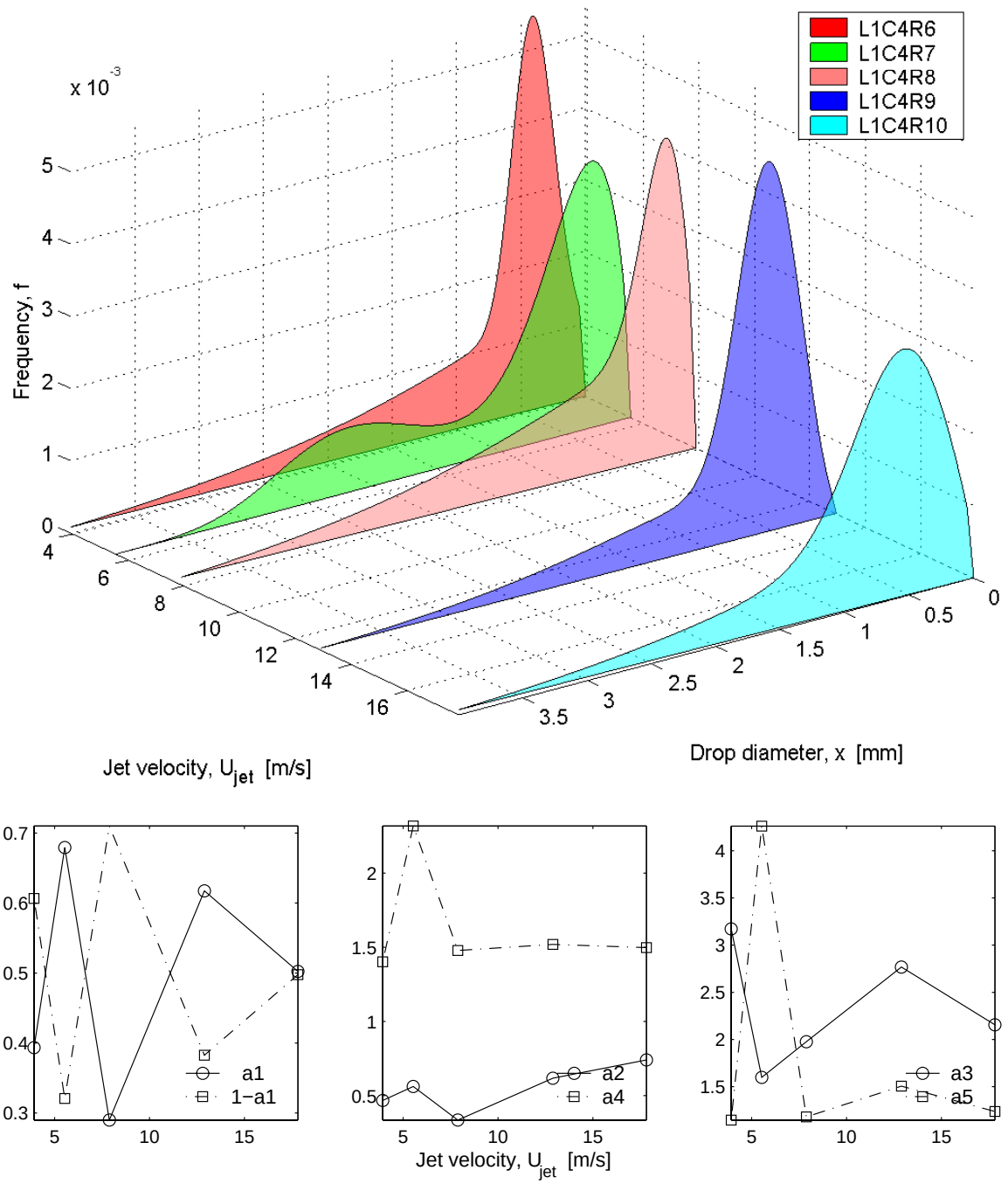

Figure 5.68 Weighted wblwbl bimodal PDFs of CO_2 droplet size vs. jet velocity for liquid CO_2 injection into 52 bar tap water through a 2 mm i.d. tube edge orifice. Case CDT02WTP52. Breakup was classified as instability regime 5. Coefficients of the weighted distributions are given in the plots below the PDFs.

5.4 Experimental Uncertainties

Experimental uncertainties affect the results presented in Chapters 3, 4, and 5. Uncertainties associated with identification of instability regimes and measurements of jet breakup length are believed to be modest. Identification of the instability regime from video images of the jet is subjective and uncertainties therefore are difficult to quantify. Assuming that a frame-by-frame analysis of the digital video records allows accurate identification of the instant that jet breakup occurs, then the uncertainty of the measurement is determined by the optical resolution of that image, given in mm/pixel, which typically is very small. Averaging will further reduce this uncertainty. On the other hand, significant uncertainties may exist in the calculated values of the dimensionless parameters, *Re*, *We*, and *Oh* due to uncertainty in the measured flow rates and fluid properties such as temperature. Droplet size is also subject to error due to PDPA bias and non-spherical droplets; and digital image analysis uncertainties.

The primary source of uncertainty in the values of Weber, Reynolds, and Ohnesorge numbers were different for the three types of jet fluid. The crude oils were vulnerable to devolatilization which could significantly alter their composition and properties (Masutani & Adams 2000). The temperature and flow rates of the pressurized liquid CO_2 were difficult to control. In contrast, the silicone fluids were stable and flow rate and other test conditions were well controlled and accurately measured; the silicone fluid experiments enjoyed the lowest experimental uncertainties in *Re*, *We*, and *Oh*.

An analysis to quantify the uncertainties of the calculated values of *Re*, *We*, and *Oh* was conducted and is described in Appendix C. Results are summarized in Table 5.3.

Table 5.3 Estimated uncertainties of *Re*, *Oh* and *We*

			Uncertainty		
		Units	Crude Oils	CO_2	Silicone Fluids
Orifice Diameter	*D*	%	3	3	3
Jet Flow Rate *Q*	Accuracy	%	1	0.5	1.2
	Fluctuation	%	1	7	3
	Total	%	2	7.5	4.2
Jet Fluid Temperature *T*		°C	3	10	0.4
Jet Velocity *U*		%	8	13.5	10.2
Kinematic Viscosity, ν		%	14	10	0.6
Density ρ		%	4	1	1
Surface Tension σ		%	17	26	1
Re		%	19	20.5	7.8
Oh		%	26	25	3.1
We		%	28	45	13.4

PDPA bias and other problems made it impossible to secure accurate crude oil size data by this technique (Masutani & Adams, 2000). For silicone fluid and liquid CO_2, the primary source of error in the PDPA measurements was believed to be non-spherical droplets. As discussed in Appendix C, image analysis of liquid CO_2 video data was used to estimate the extent of deviations from sphericity (circularity). It was determined that, as anticipated, these deviations increase with droplet size. The deviations are modest within the PDPA measurement range. The estimated maximum error in any single measurement due to non-spherical droplet shape at the upper measurement limit of 4.06 mm is approximately ±30% (±1.2 mm). This error decreases for smaller droplets.

The uncertainty of the image analysis size data was evaluated by conducting multiple measurements of a reference bead of known diameter. 160 different video frames of the same bead were analyzed and a histogram of these results was assembled. Based on this method, droplet diameters determined by image analysis are estimated to have an uncertainty of approximately ±6%. Details are provided in Appendix C.

CHAPTER 6 EXPERIMENTAL RESULTS: CO_2 HYDRATE

6.1 Chapter Overview

During the injection of liquid CO_2 into fresh water or seawater, CO_2 hydrate may form(Aya *et a*l., 1992, 1997; Hirai, *et al*., 1997): (1) prior to the jet breakup on injector internal passages and on the jet surface; and (2) after jet breakup on the surfaces of liquid CO_2 droplets. A number of studies (Teng & Yamasaki, 1999; Uchida *et al*., 2000) have examined hydrate formation on the surface of CO_2 droplets; however little work has been done to understand CO_2 hydrate formation prior to jet break up. In this chapter, results from liquid CO_2 injection experiments are reviewed and analyzed. Of particular interest are the implications of hydrate formation on jet instability as well as potential practical operational problems due to fouling of orifices and internal flow passages.

6.2 Introduction

When CO_2 is injected under conditions resembling the deep ocean (i.e., high pressure and low temperature), a solid hydrate phase will form at the CO_2-water interface. The hydrate stability regime is presented in the CO_2-H_2O phase equilibrium diagram shown in Figure 6.1.

The solid hydrate comprises a crystalline lattice of hydrogen-bonded water molecules. The interstitial spaces are occupied by “guest” molecules, in this case, CO_2. Hydrate formation is described by

$$CO_2 + n\,H_2O \Leftrightarrow CO_2 \cdot nH_2O + \Delta H \qquad (6.1)$$

where ΔH = 60.4 kJ/mole (at 277 K). *n* is the hydration number with a value of 5.75 at stoichiometric conditions (Teng *et al.*, 1996). A value of 7.3 has been experimentally determined by Chen (1972), who suggested that the hydration number is probably sensitive to ambient conditions (Wong & Hirai, 1997). The density of the hydrate is about 1.13 g/cm^3. This value was determined from X-ray crystallography (Wadesley, 1995), while Bozzeo *et al.* (1975) have reported a density of 1.1 g/cm^3.

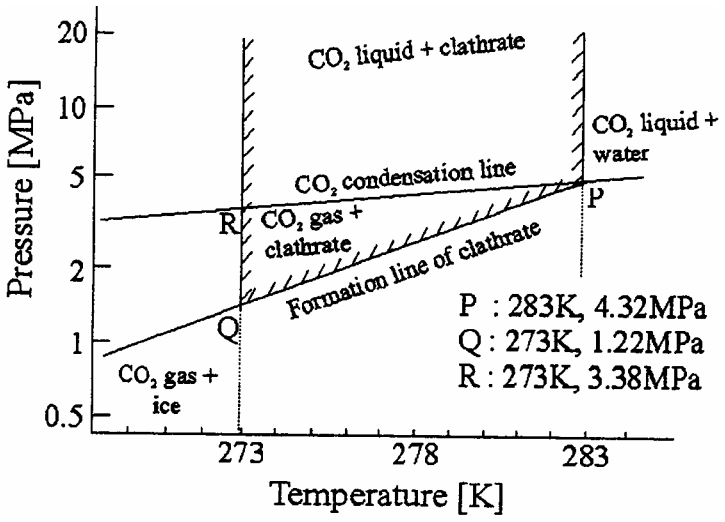

Figure 6.1 CO_2-H_2O equilibria (from Wong & Hirai, 1997)

CO_2 hydrate that forms on CO_2 droplet surfaces in the deep ocean following jet breakup restricts the dissolution of the injected CO_2 (Aya *et al.*, 1992; Nishikawa *et al.*, 1995; Wong & Hirai, 1997; Hirai *et al.*, 1997). This impacts the level and extent of acidification of seawater near the discharge location and, potentially, the effectiveness of this CO_2 sequestration technique.

Hydrate formation that occurs prior to breakup may affect the jet instability mechanism and alter the size of droplets or result in flow blockage in submerged conduits, valves and injectors used to transport and inject liquid CO_2 into the deep ocean. Pre-breakup hydrate formation has not been studied extensively. Hence, the present CO_2 injection experimental results were reviewed: (1) to investigate the influence of hydrate formation on the breakup of jets of liquid CO_2 injected into water; and (2) to investigate CO_2 hydrate formation phenomena in flow in internal passages.

Jet break-up is a consequence of the growth of instabilities at the interface between the jet and ambient fluid. Hydrate formation is also a surface phenomenon. If the formation of a solid hydrate film on the surface of the CO_2 jet occurs faster than the growth of the surface fluid instability, then the instability may be damped and break-up of the jet into droplets may be affected (Teng *et al*., 1996). Since the size of the droplets is an important parameter in the subsequent dissolution and dispersion of the CO_2 into the ocean water column, it is important to understand how and under what circumstances hydrate formation will impact break-up. The analysis of Teng *et al*. (1996) suggested that the time scale of hydrate formation depends primarily on CO_2 and water temperatures and water chemistry (e.g., solubility of CO_2 in water). The characteristic time for instability growth depends on the flow regime (i.e., the dominant mode of instability, such as Rayleigh, asymmetric,etc.). For example, if Rayleigh's maximum-instability theory applies, it can be shown that the characteristic time for jet breakup depends primarily on jet velocity, jet orifice diameter, and interfacial tension (Teng, 1994).

The present CO_2 injection experiments were conducted over a range of jet injection velocities at different CO_2 and water temperatures using a variety of injection

orifices. As a consequence, the data represent flow scenarios corresponding to different characteristic times for hydrate formation and jet instability.

6.3 Hydrate Formation on the Surface of the Jet

Digital video results from the CO_2 injection experiments were reviewed and analyzed to identify conditions that promote pre-breakup hydrate formation and to gain insight into this phenomenon.

6.3.1 Hydrate Tubes

In a number of experiments, hydrate or hydrate and ice tubes were observed to form around the perimeter of the CO_2 jet adjacent to the injector. Figure 6.2 presents images of CO_2 hydrate and ice tubes that formed in the wave breakup and full atomization flow regimes during 3 different runs using the 10mm sharp edge orifice (C10) and tap water. The corresponding flow conditions are described in Table 6.1. The liquid CO_2 jet continued to flow through upon the hydrate tube and droplets formed above the tube.

The formation process of hydrate tube 3 is demonstrated in Figure 6.3. The dissolved CO_2 concentration in the water increases rapidly at high CO_2 injection rates. When the temperature and pressure at the jet-water interface are within the hydrate stability regime, hydrate starts to form at the jet surface on the injector (Figure 6.3a). Since the temperature of CO_2 is lower than the freezing point of water at the experimental pressure level, the solid phase may also include ice crystals mixed with the hydrate. The hydrate ring advances upward along the jet, forming a solid tube around it while the liquid CO_2 continues flowing through the center of the tube (Figures 6.3 b to i). The

thickness of the hydrate tube is increased by the extrusion of liquid CO_2 from small holes on the tube surface or from weak portions of the tube. Smaller hydrate branches grow around the liquid CO_2 extrusions. Eventually, a hydrate web may connect all the branches and the primary hydrate tube (Figure 6.3 j). Note that the slow flow of CO_2 through the branches can generate large droplets that are not anticipated at the total jet flow rate that corresponds to atomization. This is another means by which pre-breakup hydrate formation can alter the size spectra of the droplet phase.

The digital video data were analyzed to estimate the rate that the hydrate tube advanced upward along the jet. In Figure 6.4, tube height is plotted as a function of time for tubes 2 and 3. The data suggests a constant growth rate. A linear regression yields a growth rate of 0.71 mm/s for tube 1 and 0.52 mm/s for tube 2. For these two cases, growth rate appears to scale directly with CO_2 flow rate.

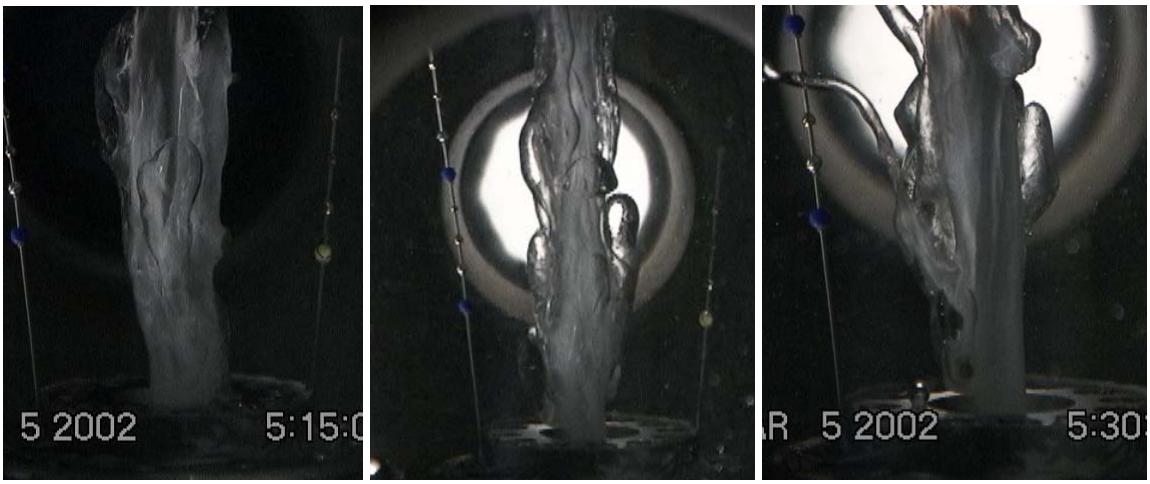

(a) Hydrate tube 1 (b) Hydrate tube 2 (c) Hydrate tube 3

Figure 6.2 CO_2 hydrate tubes with 10 mm sharp edge orifice (C10) in tap water at pressure of 52 bars with different CO_2 flow rates.

Table 6.1 Flow conditions for hydrate tube formation shown in Figure 6.2 in tap water at pressure of 52 bars.

CO_2 hydrate tube No.	Conditions at start of formation			Hydrate growth rate [mm/s]
	CO_2 Temperature [°C]	Ave. Jet velocity [m/s]	Ave. water Temp. [°C]	
1	-9.44[2]	0.89	11.9	N/A[1]
2	-9.15	1.17	12.2	0.52
3	-9.08	1.47	12.5	0.71

1: Data not available since the camcorders weren't recording.

2: CO_2 temperature when the camcorder was turned on after the hydrate tube 1 had already formed (Figure 6.2 a).

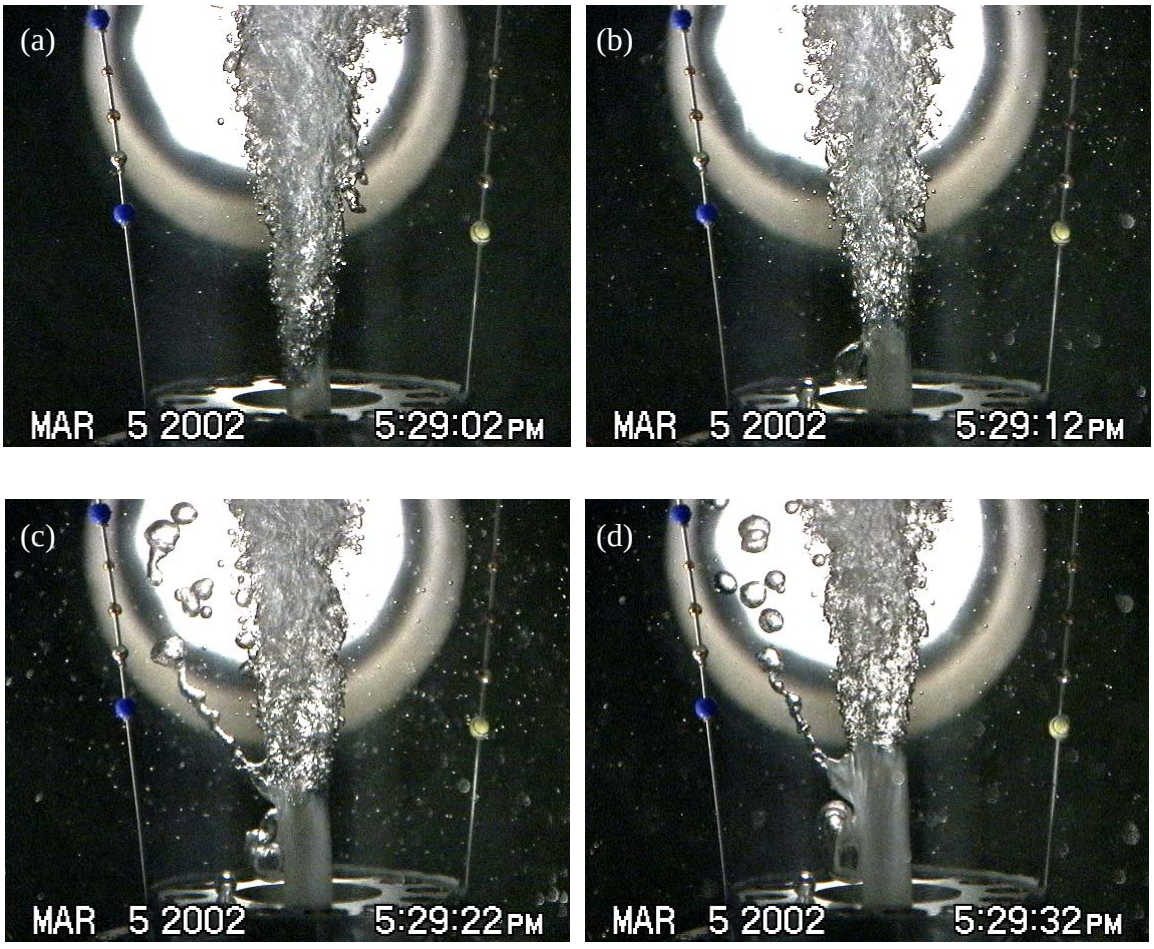

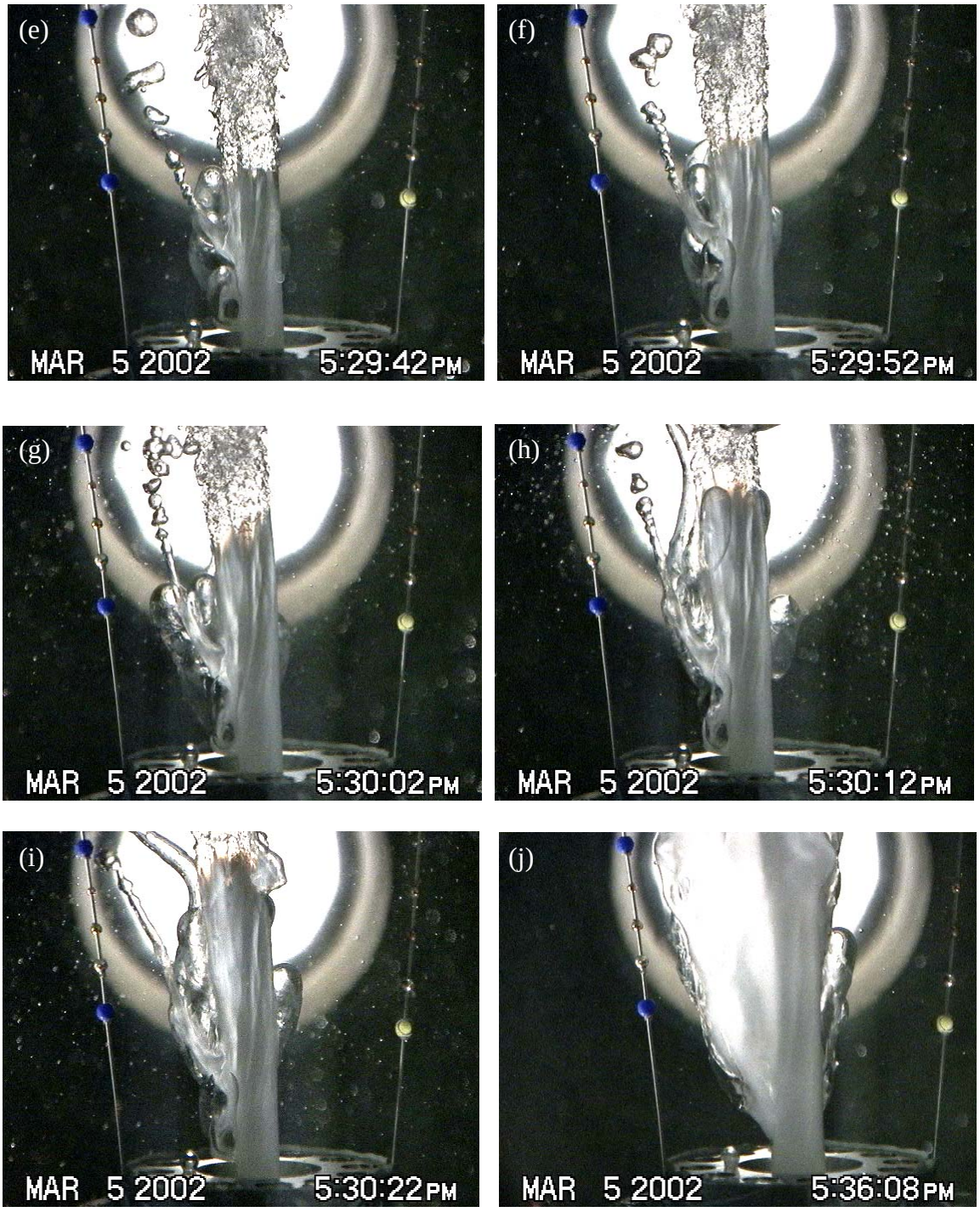

Figure 6.3 Formation process of hydrate tube 3.

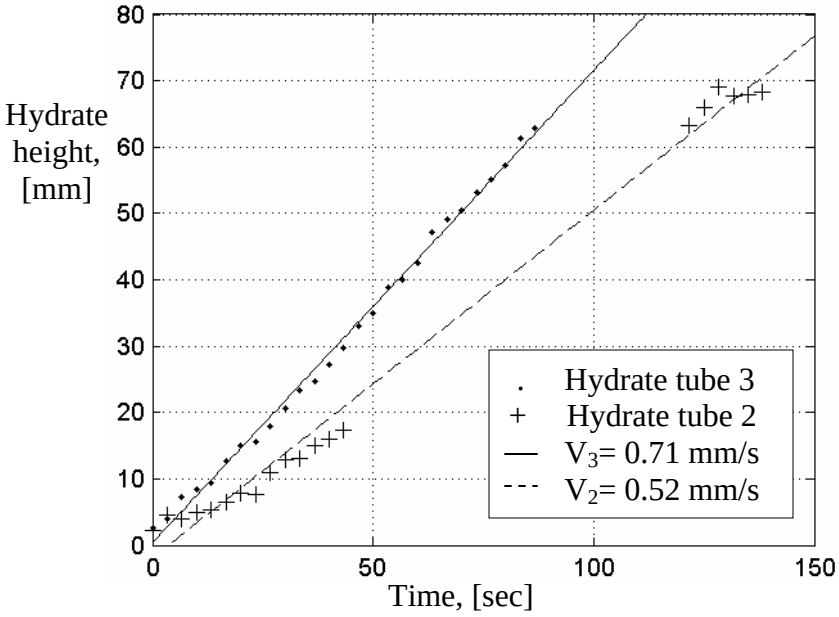

Figure 6.4 Hydrate tube height as a function of time. Solid and dashed lines are linear curve fits to the data.

6.3.2 Thin Film Hydrate Tubes

Thin film hydrate tubes were observed in tests conducted in the varicose breakup regime with low CO_2 flow rates. Examples are shown in Figure 6.5 for different injector orifices. The corresponding test conditions are given in Table 6.2. The thin film tubes appeared to be unstable. As shown in Figures 6.6 and 6.7, the thin film tubes typically persisted for about 10 to 20 seconds before detaching from the orifice. A new tube forms immediately after the old one detaches. This process repeats itself as the flow conditions, such as CO_2 flow rate, temperature and pressure, etc., remain the same.

The thin film tube appeared to be moderately ductile and would deform slightly; they were not perfectly rigid. In many of these tests, CO_2 temperatures were only slightly below or above the freezing point of water. Moreover, the CO_2 flow rates were very low and the ambient water temperature were relatively high, suggesting that the cooling effect of the CO_2 jet would probably not be sufficient to produce much or any ice. The thin film tubes were believed to comprise primarily or entirely hydrates and no ice.

The video records indicate that CO_2 droplet form by breakup of the jet issuing from the end of the thin film hydrate tube. The opening at the end of these tubes may be different in size and shape from the injector orifice and geometry. Since orifice diameter affects droplet size, hydrate formation can alter the spectra of the droplet phase through changes in effective jet diameter and shape.

(a) 5 mm sharp edge orifice (C05)

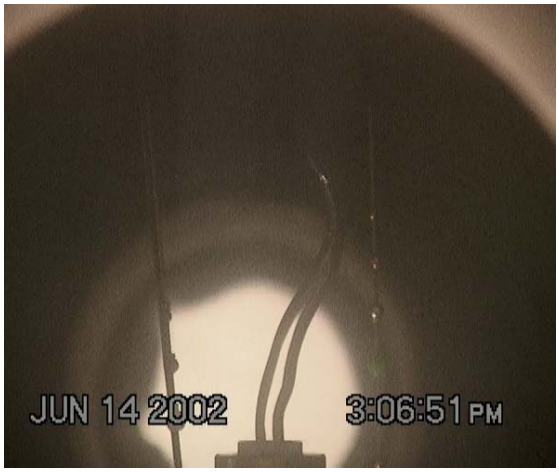

(b) 5 mm tube orifice (T05)

(c) 10 mm sharp edge orifice (C10)

(d) 2 mm tube orifice (T02)

Figure 6.5 Thin film CO_2 hydrate tubes observed in the varicose breakup regime with different orifice diameters and shapes. All photos correspond to liquid CO_2 injection tests into tap water.

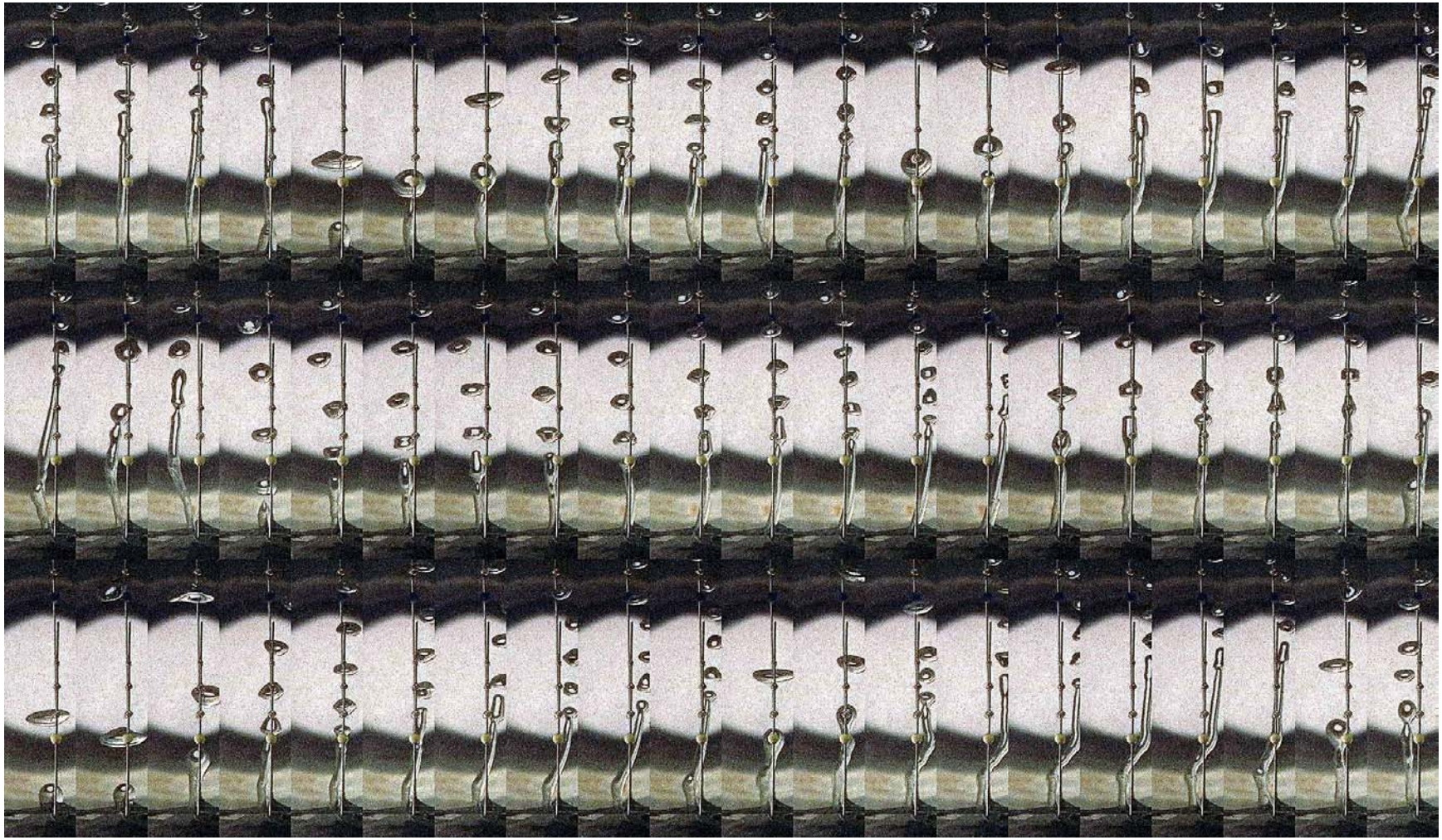

Figure 6.6 Repeating formation of CO_2 thin film hydrate tube for injection from a 5 mm sharp edge orifice. This is the same test run, CDC05WTP52R3, as shown in Figure 6.5 a. Time interval between any two adjacent frames is 1.033 sec.

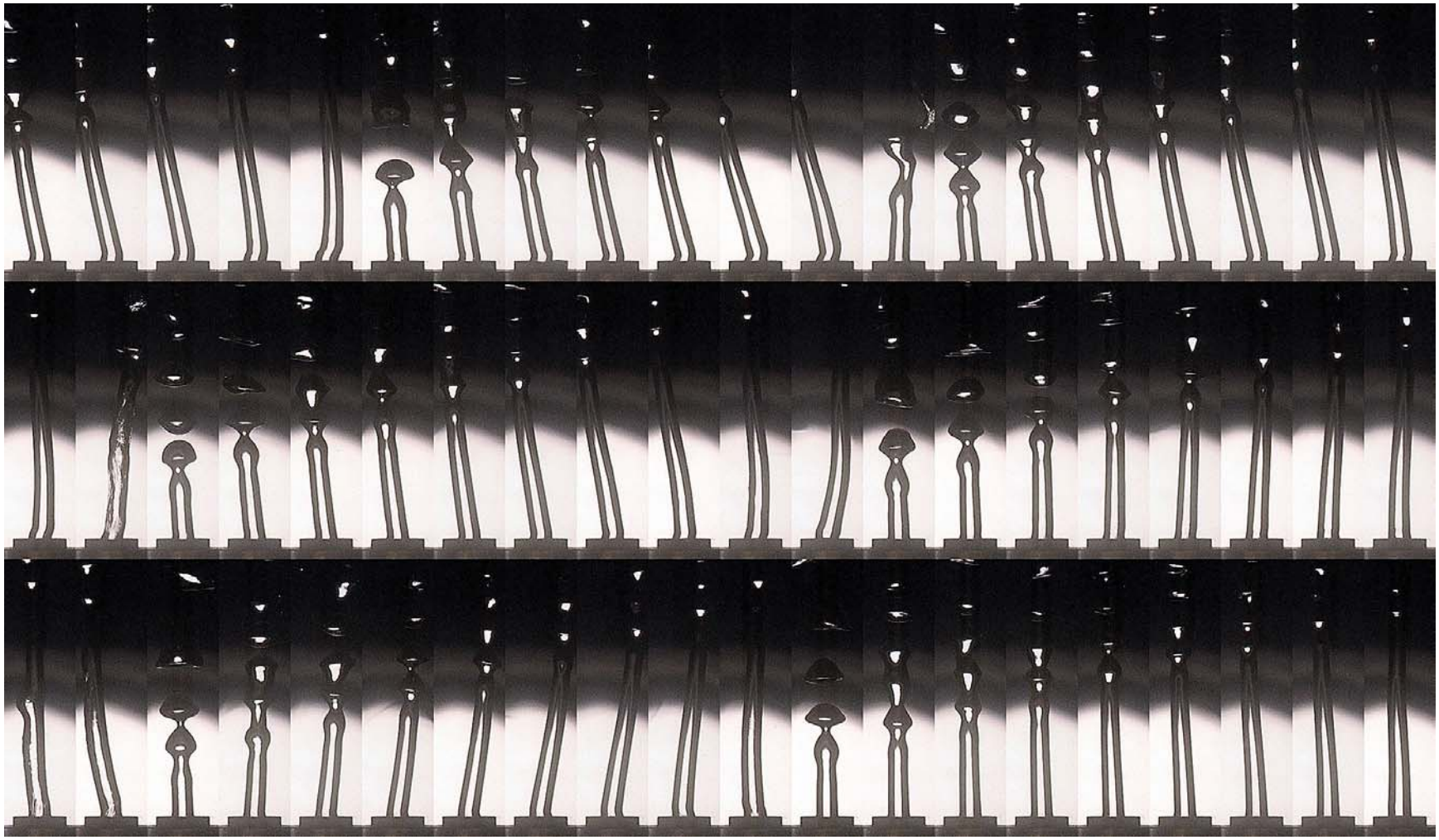

Figure 6.7 Repeating formation of CO_2 thin film hydrate tube for injection from a 5 mm tune orifice. Test run CDT05WTP61R6. Time interval between any two adjacent frames is 2 seconds.

Table 6.2 Injection conditions for the CO_2 thin film hydrate tubes in Figure 6.5.

Thin film hydrate tube in Fig. 5.7	Orifice inside diameter [mm]	Orifice shape	Ave. CO_2 Temp [°C]	Ave. CO_2 mass flowrate [kg/min]	Ave. jet velocity [m/s]	Ave. water temp. [°C]	Pressure [bar]
a	5	Sharp	-0.26	0.09	0.087	6.07	52
b	10	Sharp	-2.00	0.30	0.067	13.2	52
c	5	Tube	2.11	0.10	0.094	9.26	61
d	2	Tube	-2.60	<0.10	<0.55	10.74	52

6.4 Hydrate Blockages

For CO_2 ocean sequestration, liquid CO_2 will be transported to the deep ocean via a submerged conduit. It is generally assumed that by the time the CO_2 reaches the injection depth, it will be in thermal equilibrium with the surrounding seawater, typically less than about 5^oC. The seawater-CO_2 system will then be in the hydrate stability regime. Hydrate formation at the injector orifices or upstream in the conduit, should there be ingress of water, could potentially block the flow system. Based on experience in undersea oil and gas operations where methane hydrate blockage can pose major problems, it is anticipated that clearing CO_2 hydrate blockages may be extremely difficult or impossible. During the present CO_2 injection experiments, a few tests were conducted to investigate hydrate blockage phenomena. Also, unplanned blockages occurred spontaneously in several tests. These results have been analyzed and some anecdotal observations are provided in this section.

Figure 6.6 presents video frames from a test where an unexpected severe hydrate blockage of the injector assembly occurred at start-up. The test, conducted at 5.4 MPa, began with low flow rates through a 10 mm sharp edge orifice (C10) in the varicose breakup regime. About two minutes after initiating the flow of CO_2, hydrates formed inside the injector. At that point, the CO_2 temperature was 11.0°C and ambient water temperature was 5.76°C. Hydrate continued to grow on the top of the orifice (Figure 6.8 a). When CO_2 flow rate was increased to expel the blockage, liquid CO_2 initially jetted from fissures in the hydrate mass (Figure 6.8 b). Total blockage then occurred. Depressurizing the DOS from 5.4 MPa to about 2.7 MPa failed to expel the hydrate blockage inside the orifice. Figures 6.8 c and d show pieces of hydrate debris that were slowly ejected from the nozzle during depressurizing.

In a subsequent test using the stainless steel 10 mm sharp edge orifice (C10) a week later, hydrate blockage occurred again. The CO_2 flow rate, 1.18 kg/min, was higher, corresponding to a jet velocity of about 0.27 m/s. Water temperature was 8.89°C and CO_2 temperature was 3.5°C. Pressure was 5.2 MPa. These conditions fall within the hydrate stability regime. A hydrate blockage of the orifice formed about one minute after flow was initiated. This time, instead of depressurizing, the water inside the DOS was warmed using a heat exchanger. It took about 90 minutes to heat the water to 10.5 °C and expel all the hydrate.

In tests conducted using the same 10mm sharp edge orifice where pressure and temperatures were even slightly outside the hydrate stability regime, no blockage occurred.

A small number of experiments were conducted with the objective of examining hydrate fouling of internal passages. Figure 6.9 shows some sample video images of CO_2 flow though a transparent tube nozzle. The clear acrylic tube had an inside diameter of 0.95 cm (3/8 inch). Water at 3^oC and 5.6 MPa. was allowed to fill the tube, then cold liquid CO_2 was slowly injected. Conditions fell within the hydrate stability regime. Solid hydrates that formed were easily fractured and expelled when the flow rate was increased. This may be due to the adhesion of the hydrate to the plastic surface. Hirai *et al.* suggest that metal surfaces are more prone to hydrate blockages than plastic and other similar materials.

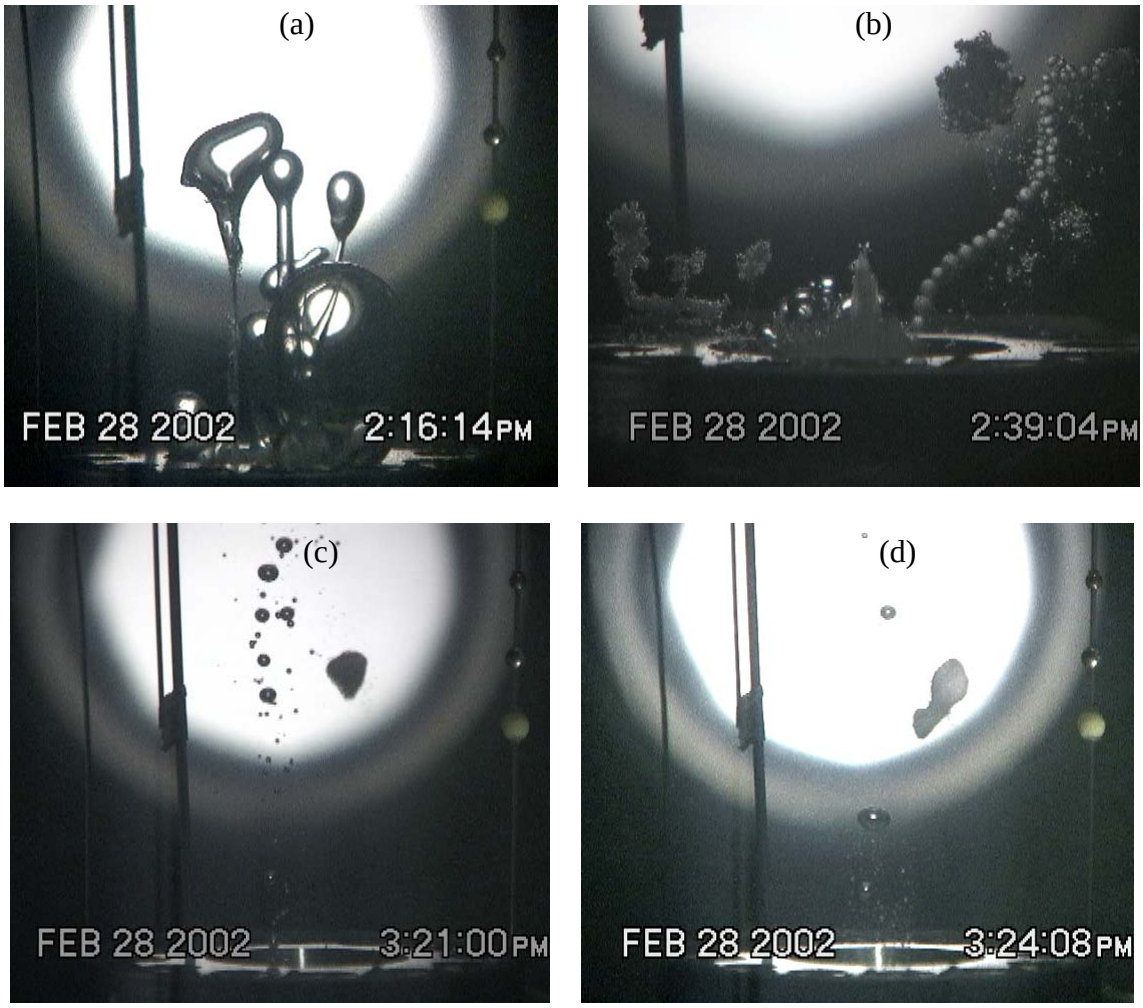

Figure 6.8 Hydrate blockage in the 10 mm sharp edge orifice (C10) for low flow rate CO_2 injection into tap water. (a) Hydrate blockage inside and on the top of the orifice. (b) Restarting at higher flow rate to expel hydrate. (c & d) Pieces of hydrate debris ejected from the inside of the nozzle assembly during depressurization.

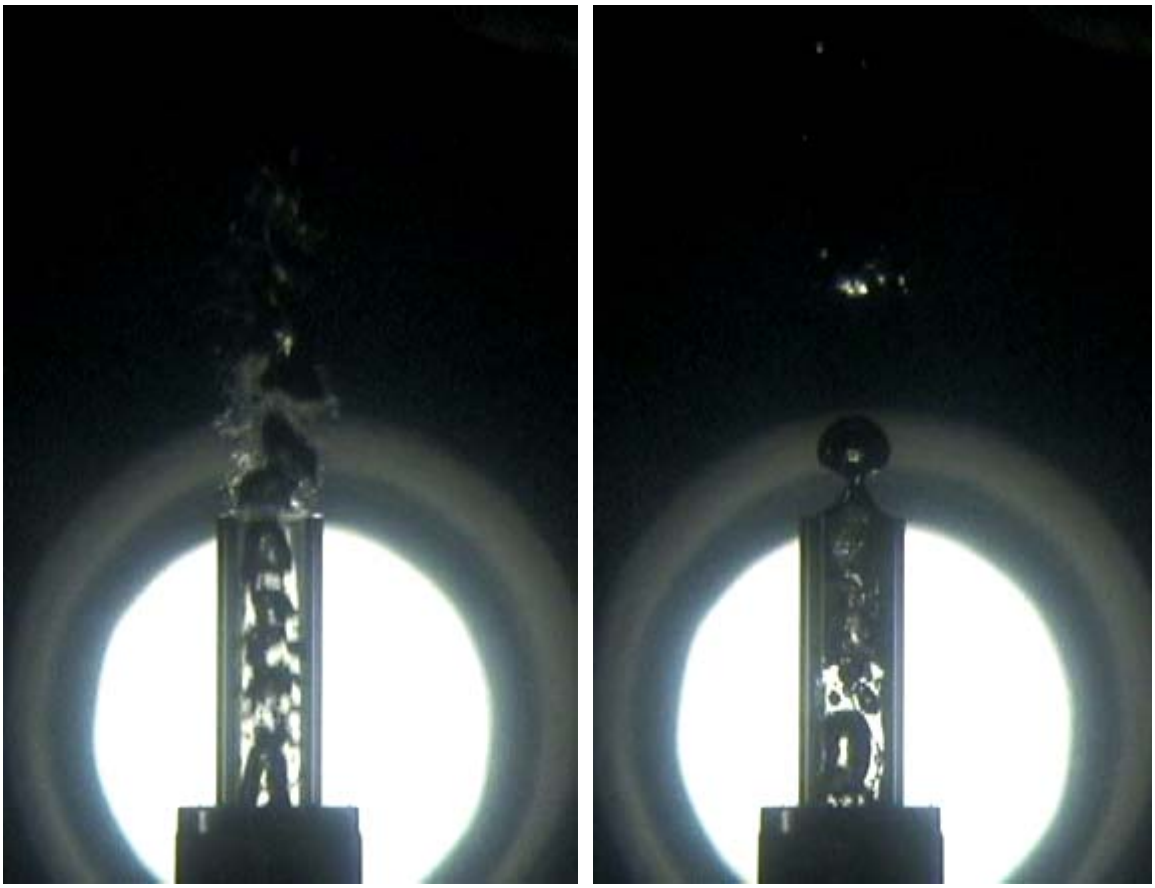

Figure 6.9 Liquid CO_2 and tap water flow through a clear nozzle used to investigate hydrate blockage; pressure = 56 bar; water temperature = 3°C.

6.5 CO_2 Droplet Aggregation

CO_2 droplets covered with hydrate films tend to aggregate (but do not coalesce) once they contact each other following breakup. The video data suggested that aggregated droplets appear to have an enhanced capacity to attract additional droplets than single droplets. To a certain extent, this may simply reflect the larger surface area for contact and "collection" of additional droplets. Eventually, hundreds of droplets may attach to form a large aggregated cluster ball. Figure 6.10 show an example of CO_2 droplet aggregation observed for tests performed under hydrate forming conditions. CO_2 flow rate corresponds to filament breakup regime 3. Here, the droplet density is low. The probability of aggregation of two moving droplets is, therefore, also low. Aggregation in this test occurred when a droplet attached to the steel line of size reference beads near the orifice (Figure 6.10 a). This provided a stationary target that subsequent droplets could contact. As time went by, more and more droplets became attached (Figure 6.10 b and c). As flow rate was increased, the droplet cluster became unstable due to the dynamic reaction with the jet. Finally it took off from the steel line (Figure 6.10 d). Figure 6.11 shows huge droplet clusters observed from the 2nd level of DOS viewports located about 70 cm above the orifice. Again, the clusters from when droplets attached to the wires and form stationary collection points.

At higher CO_2 jet velocities in breakup regimes 4 and 5, droplet number density (i.e., droplets per unit volume) is increased significantly. This increases the probability of droplet-droplet contact, especially near the injection orifice where droplet velocities and

number densities are of the highest. Numerous droplet aggregation clusters were observed with the tube orifice (Figure 6.12 a and b) at 61 and 52 bar.

CO_2 droplet agglomeration has also been observed in the deep ocean *in situ* by Brewer *et al.* (2000) and in other laboratory studies, (Yamane *et al.,* 2001). Agglomerated droplet cluster may have unusual hydrodynamics and will dissolve more slowly that single droplets. This will influence the effectiveness and environmental impacts of the dissolution method of CO_2 sequestration. The critical factor to avoid droplet agglomeration appears to by reducing droplet concentrations, possibly by careful selection of the jet break up regime and be providing adequate separation between CO_2 injectors if a multiple nozzle array is employed.

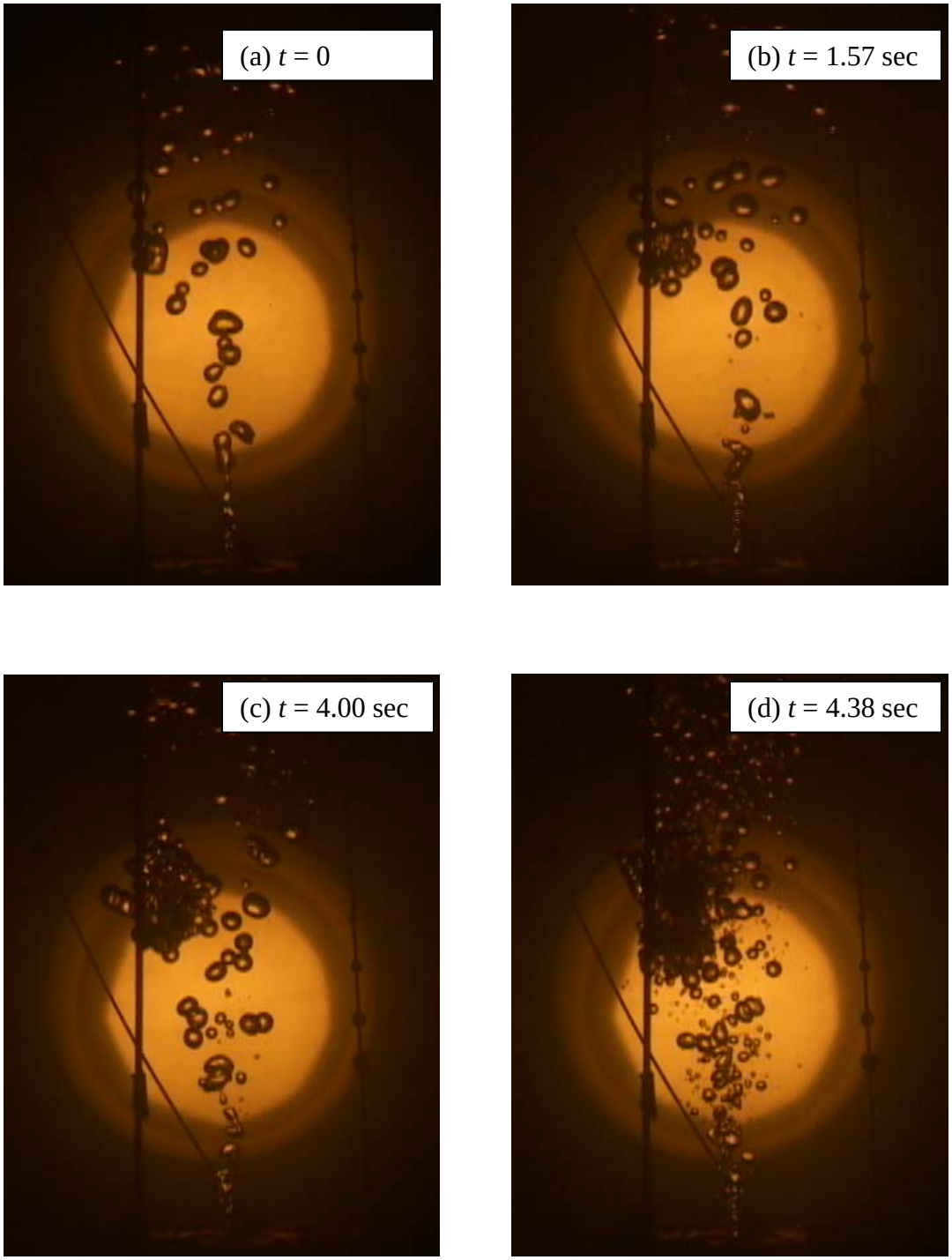

Figure 6.10 CO_2 droplet aggregation. Liquid CO_2 flow rate increases from (a) 0.113 kg/min to (b) and (c) 0.136 kg/min. Flowrate in (d) is 0 .191 kg/min (d). The CO_2 droplet cluster separated from the wire 1 second after frame (d).

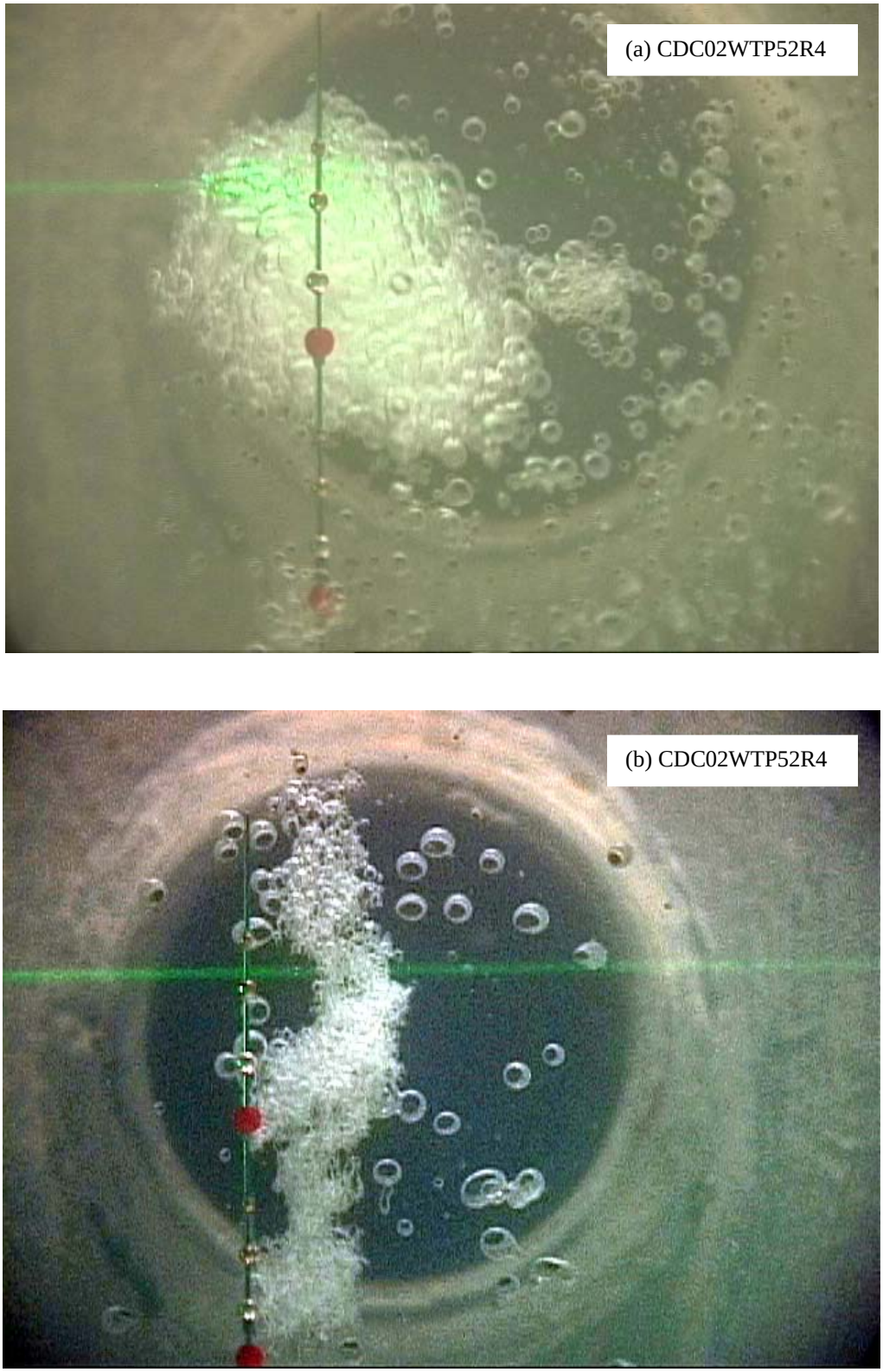

Figure 6.11 Single droplet clusters observed 70 cm above 2mm sharp edge orifice (C02).

Figure 6.12 CO_2 droplet aggregation observed at (a) Q =2.67 kg/min; Tco_2=-3.25°C; T_w=8.13°C, P=61 bar and (b) Q=2.65 kg/min; Tco_2=-2.18°C; T_w=9.45°C, P=52 bar.

6.6 Some Hydrate Photos

During the CO_2 injection experiments, we observed many interesting hydrate geometries. This section provides some photos of those hydrates.

In Figure 6.13 a CO_2 droplet covered with hydrate film formed on the tip of the 2 mm tube orifice when the flow was shut off and CO_2 left in the orifice slowly oozed out. When the flow was suddenly restarted, the jet burst though the top of the CO_2 hydrate film.

CO_2 hydrate with grape-like shapes formed at low flow rates as shown in Figures 6.14 and 6.15. The hydrate film was very thin and elastic. Figure 6.16 is a photo of a tube hydrate. The grape and tube types of hydrates were also observed by Aya & Yamane (1992).

CO_2 hydrates that appeared almost fibrous, like a wad of cotton candy, formed when liquid CO_2 flowed around a solid surface placed above the orifice (Figure 6.17). CO_2 temperature = -6.74 °C; water temperature = 10.10°C; CO_2 flow rate = 5.45 kg/min.

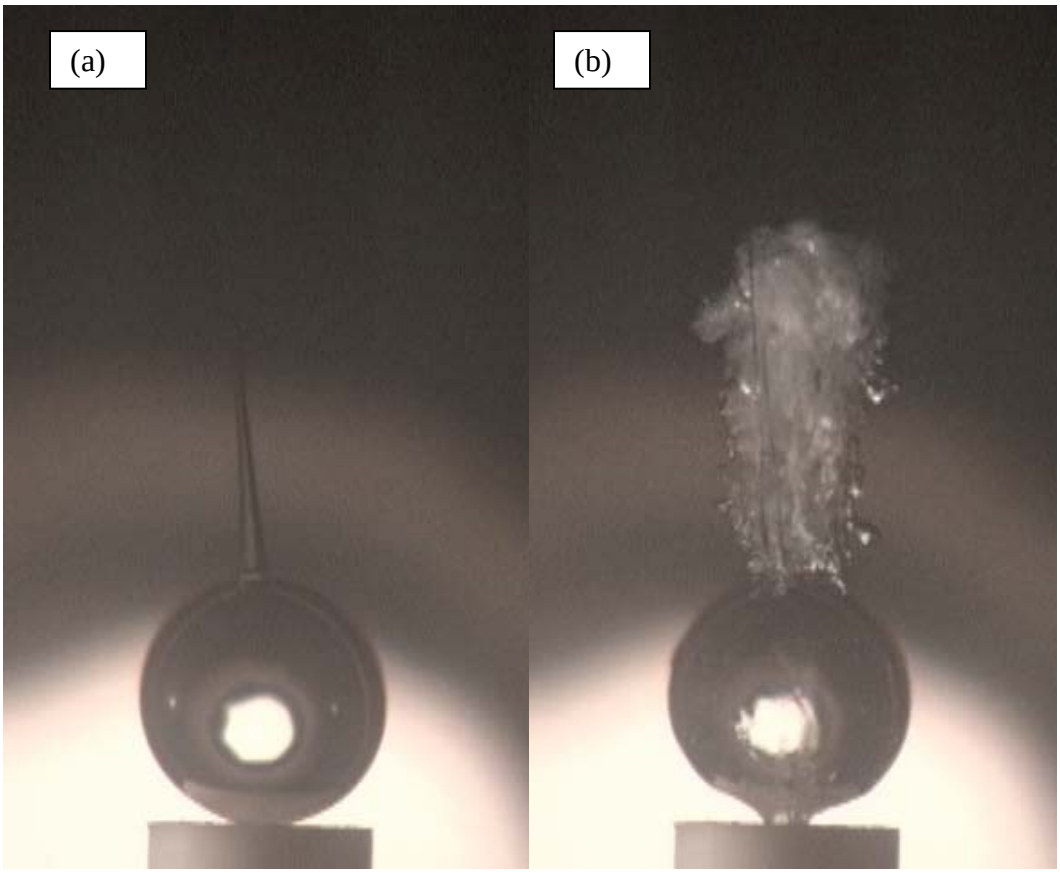

Figure 6.13 (a) CO_2 droplet covered with hydrate film on the tip of the 2 mm tube orifice. (b) When CO_2 flow was restarted, the jet penetrated the top of the CO_2 hydrate film.

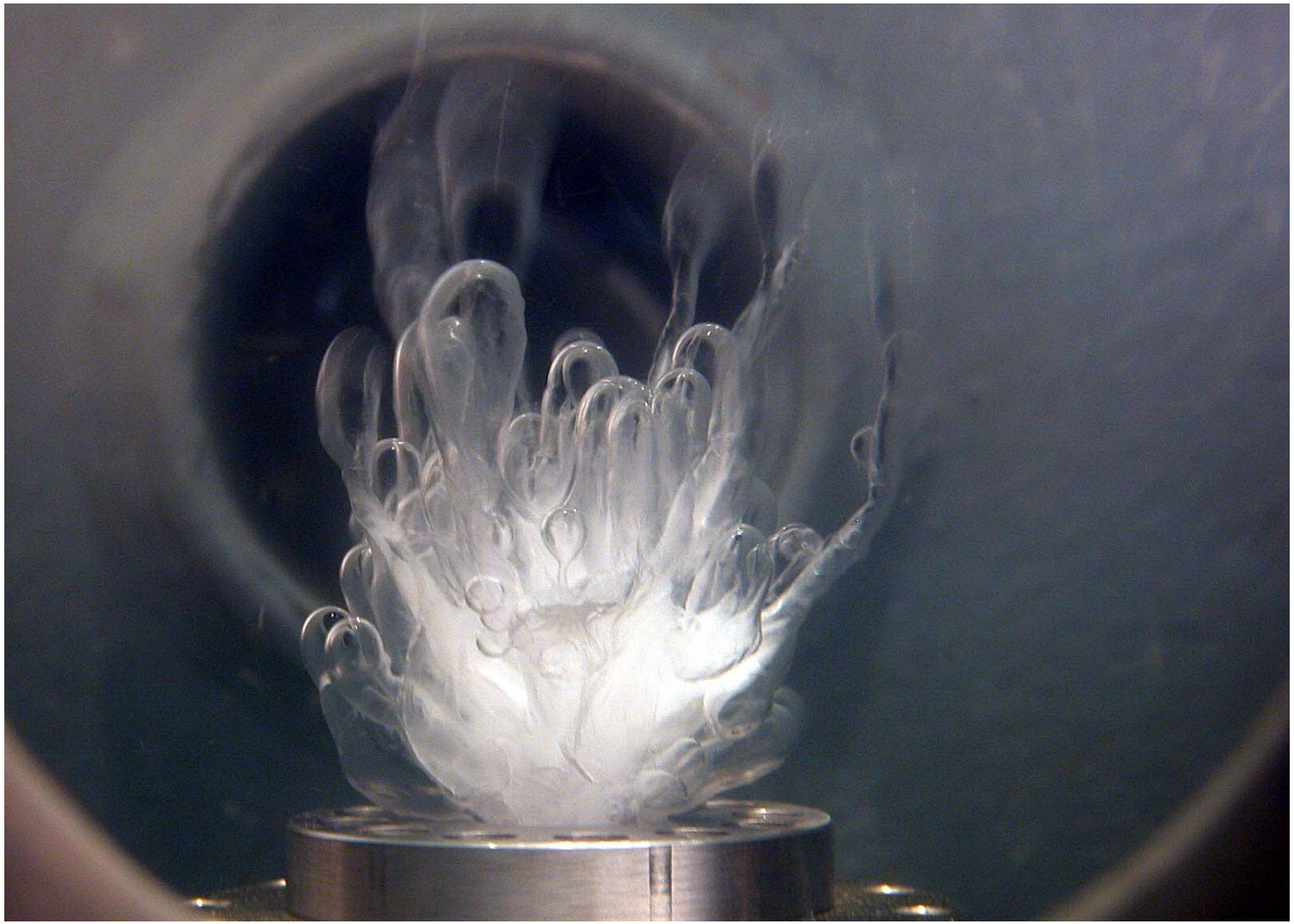

Figure 6.14 Grape type hydrate on the top of the 2 mm sharp edge orifice (C02).

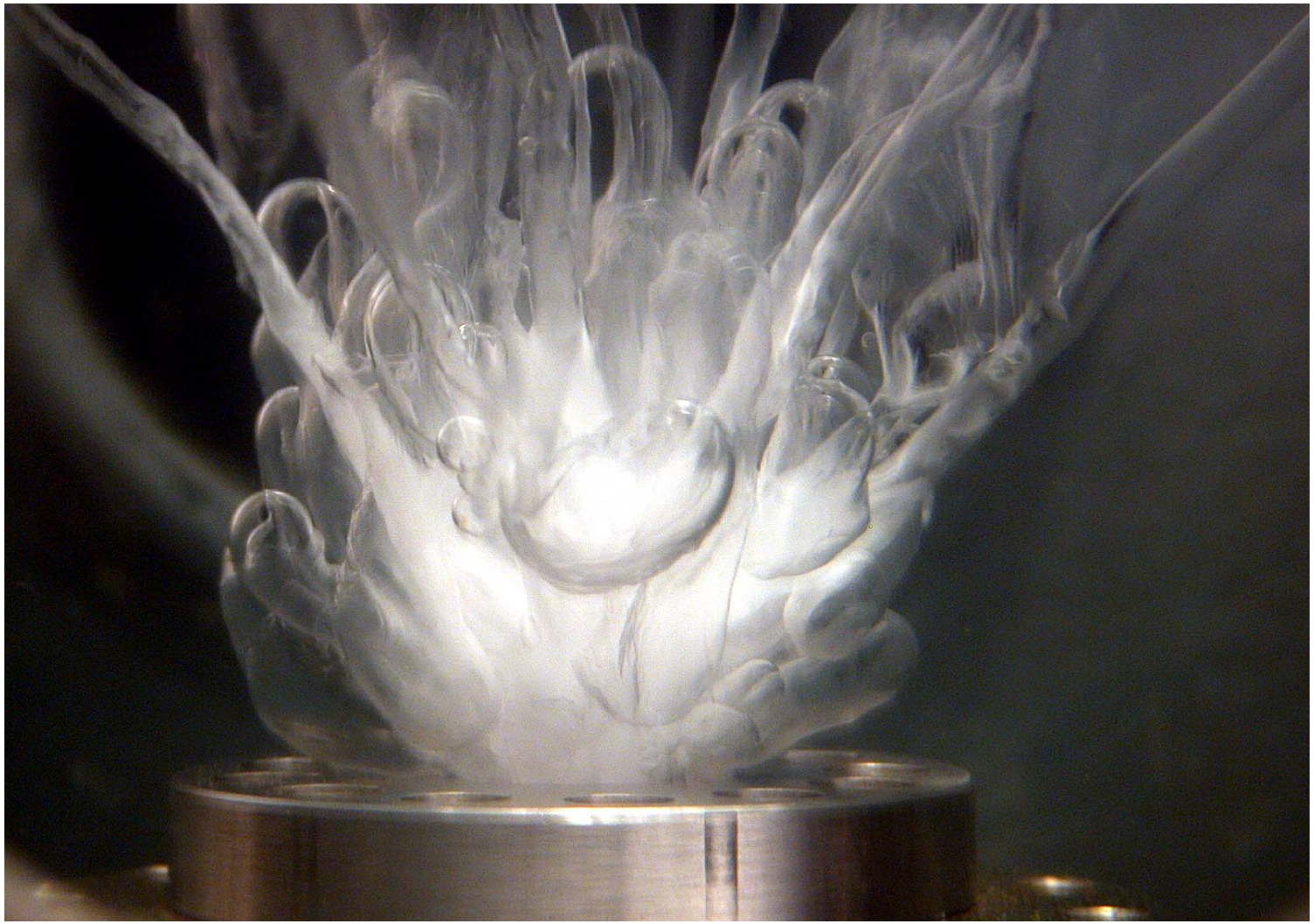

Figure 6.15 Close-up of Grape type hydrate on the top of the 2 mm sharp edge orifice (C02).

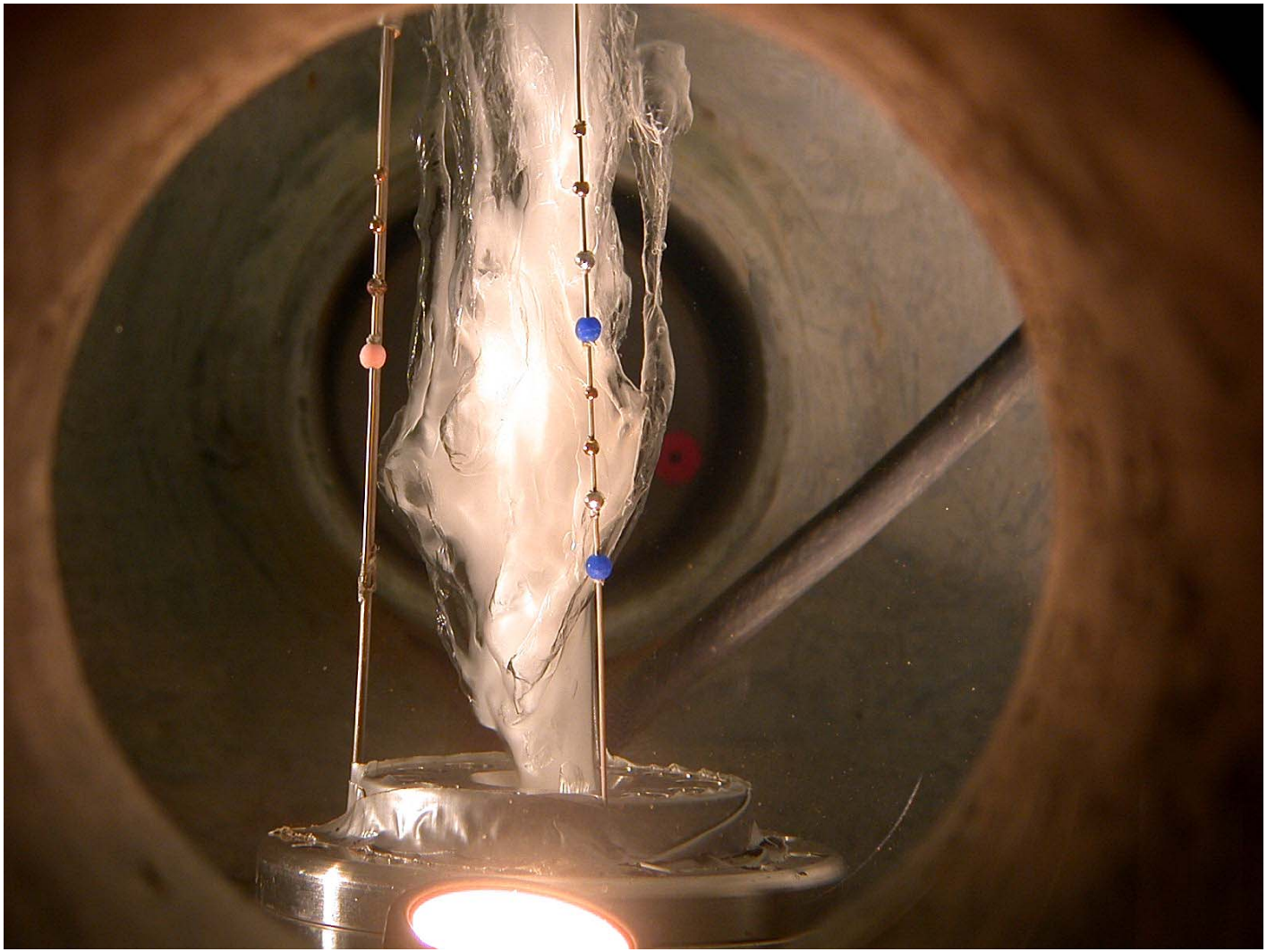

Figure 6.16 Hydrate tube on the top of the 10 mm sharp edge orifice (C10).

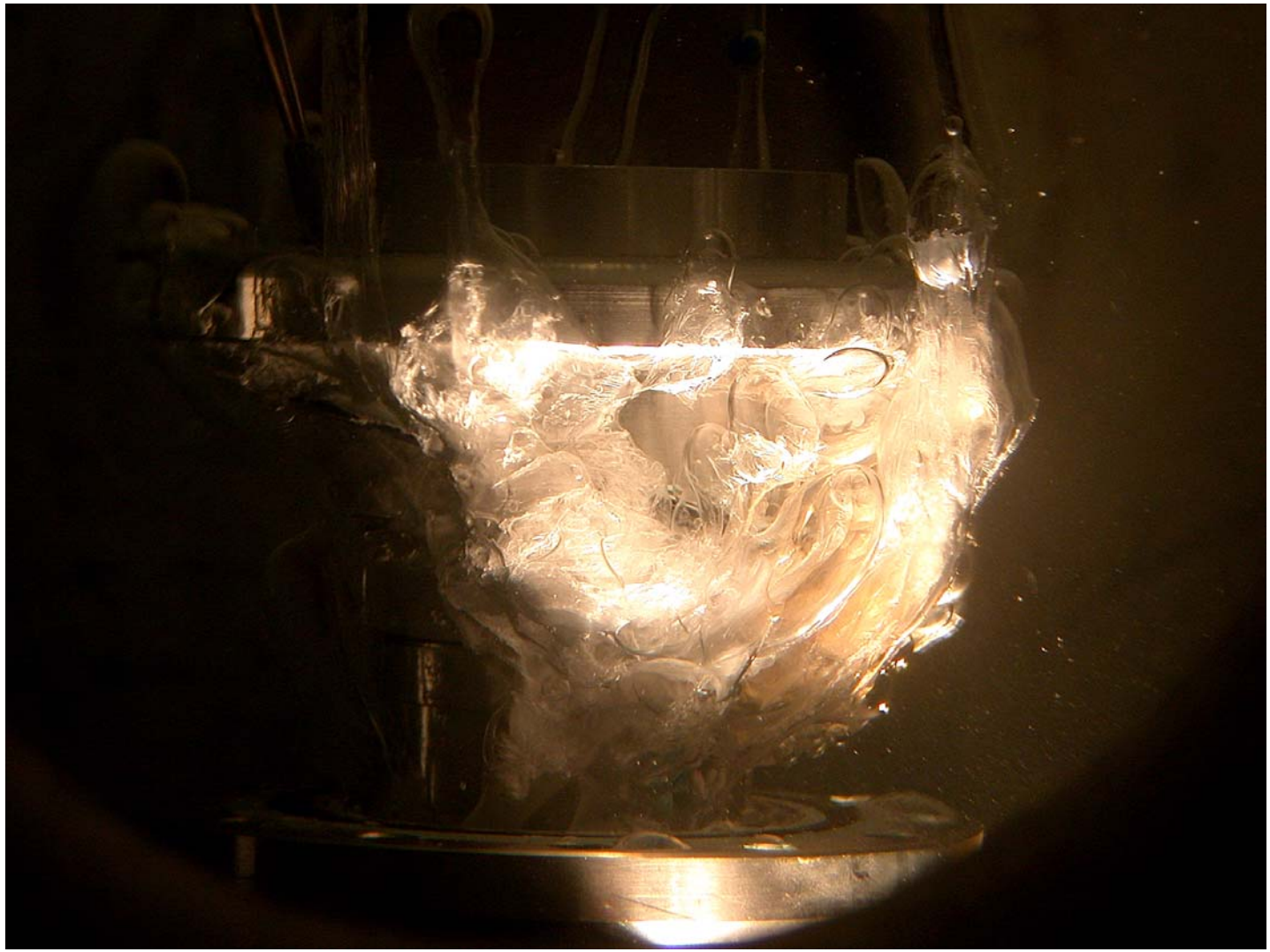

Figure 6.17 Cotton type of CO_2 hydrate observed when liquid CO_2 flows around a solid surface.

6.7 Summary

Figure 6.18 summarizes the types of CO_2 hydrates observed during liquid CO_2 injection tests corresponding to the different instability regimes. The tests employed a variety of orifice diameters, orifice shapes, water temperatures, liquid CO_2 temperatures, and pressures. The orifice diameter and shape, as well as the pressure are indicated by the alphanumeric code on the right-hand axis as explained in section 3.3.2.

Thin film hydrate tubes are likely to form on the jet surface at low flow rates for most test configurations (i.e., orifice sizes and shapes, and fluid temperatures and pressures) in the varicose break up regime. The characteristic time for instability growth is expected to be long relative to the hydrate formation time in this regime. Surprisingly hydrate tubes were not clearly evident in the transitional breakup regimes, but thick hydrate tubes did form for some cases (with sub-zero CO_2 temperatures) in the atomization regime. The vertical growth rate of the thick hydrate tube appears to scale with the CO_2 flow rate.

Pre-breakup hydrate formation appears to affect the size distribution of the droplet phase primarily by changing the effective geometry of the jet. When a hydrate tube forms, the interface between the CO_2 and water begins at the end of the tube, which may have a different size and shape opening than the original orifice. Furthermore, flow through the tube will alter the jet inlet velocity distribution, producing more time for boundary layer growth. In the case of thick tubes, hydrate branches will divert some of the CO_2 out of the main jet flow and could produce larger droplets.

As expected, the experimental results suggest that CO_2 droplet concentration is a critical factor that influences agglomeration. High flow rates corresponding to transitional or atomization breakup generate large numbers of droplet in close proximity near the orifice. This enhances the probability of contact and agglomeration. Aggregate droplet clusters were not observed frequently in the varicose or transitional breakup regimes where droplet concentration is relatively low. Droplets aggregated readily on contact, but the hydrate films on their surfaces prevented coalescence.

Severe hydrate blockage occurred in some tests. There was some evidence that support the proposal that certain materials (e.g., steels) are more prone to blockage since hydrate adheres well to them. Tests performed with plastic nozzles resulted in hydrate blockages that were relatively easy to expel.

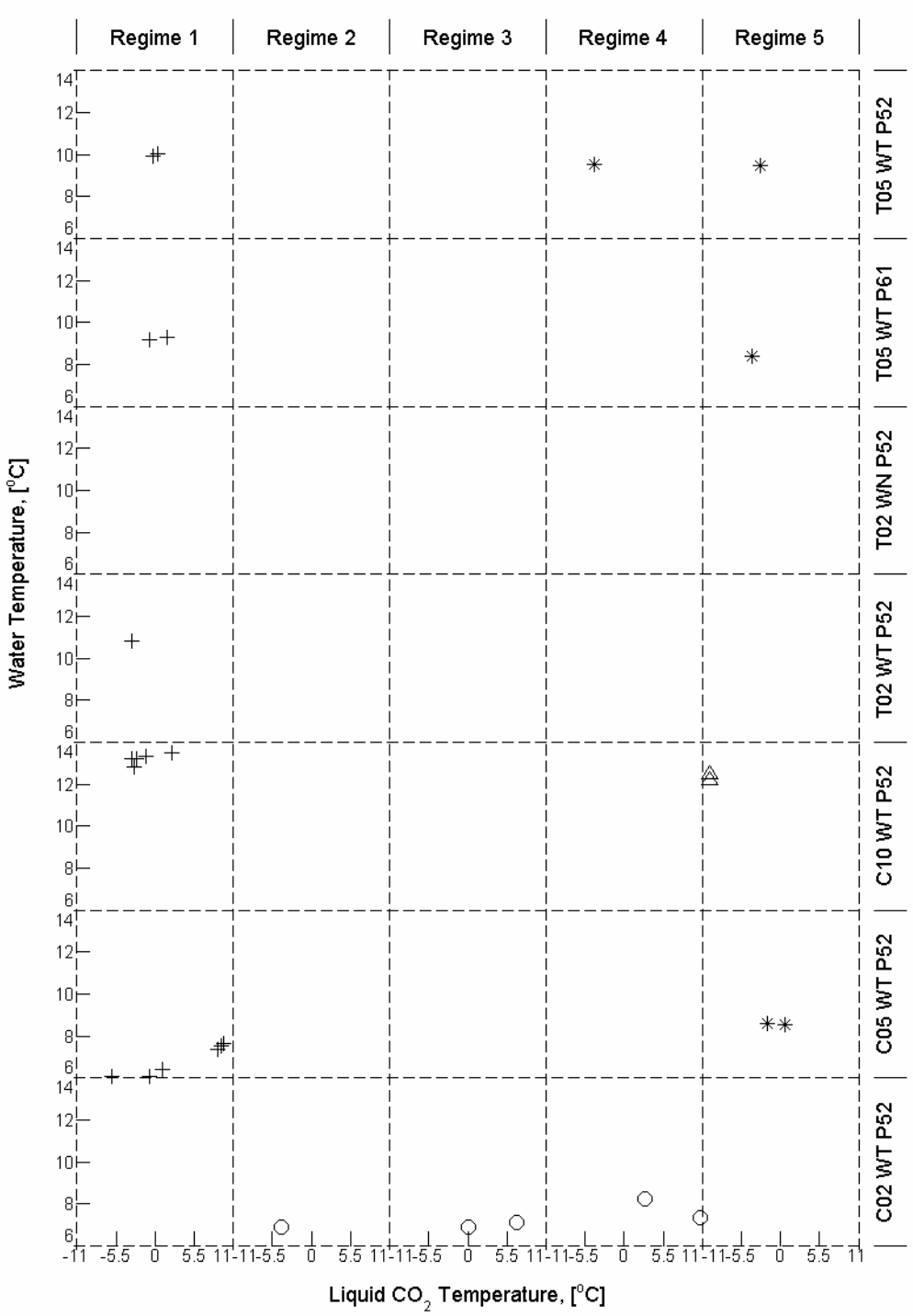

Figure 6.18 Summary of CO_2 hydrates observed in the different breakup regimes. +, thin film hydrate tube. Δ, thick hydrate tube. o, single or several droplet aggregations. *, massive CO_2 droplet aggregations.

CHAPTER 7 SUMMARY AND CONCLUSIONS

Experiments were conducted to investigate the breakup of liquid jets discharging into another liquid over the full range of instabilities extending from disintegration of laminar jets to turbulent atomization. Liquid-liquid jet instability and breakup into a dispersed phase are important phenomena that have direct relevance to a host of ocean resource engineering and other scientific and practical applications. The specific practical applications of interest for this investigation were liquid CO_2 sequestration in the deep ocean and deep ocean oil spills. The present study focused upon elucidating the fundamental mechanisms and parameters that control jet breakup; identifying liquid-liquid jet instability regimes and determining the boundaries of these regimes; and securing quantitative data on droplet size spectra that could provide insight into the breakup phenomena and which could be applied to the development and testing of models. A secondary objective was to explore the effects of solid hydrate formation on CO_2 jets in the deep ocean environment. This topic is relevant to CO_2 ocean sequestration.

The experiments were conducted in several facilities. Jet fluids including four deepwater crude oils, two silicone fluids, and liquid CO_2 with very different properties were injected into tap water, natural seawater or synthetic seawater over a range of flow rates, temperatures, and pressures from a variety of injection nozzles. The independent parameters of the tests were: (1) jet velocity; (2) jet and ambient fluid properties; and (3) injector diameter and geometry. Flow visualization and Phase Doppler particle analysis were the primary measurement techniques.

The major results and conclusions of this study are summarized below:

1. Five instability regimes were identified by a comprehensive review of the digital video records of the 294 test runs. The five regimes which occur in sequence as liquid-liquid jet disintegration progresses from laminar instability to turbulent atomization are: (1) varicose breakup, where Rayleigh instability dominates and a symmetric surface wave forms and grows, eventually pinching off the jet; (2) sinuous wave breakup, where an asymmetric instability emerges that causes the jet to wave sinuously and generate a polydispersion of droplets; (3) filament core breakup, where the surface of the jet becomes unstable to short wavelength disturbances and disintegrates close to the orifice into fine droplets, while the core of the jet persists as a continuum fluid filament that breaks up further downstream into large droplets; (4) wave atomization, where the breakup location of the jet core filament moves closer to the orifice and the fraction of fine droplets increases; and (5) full atomization.
2. A linear regression to the data yielded relationships for the boundaries between the five instability regimes in dimensionless Ohnesorge Number, *Oh*, and jet Reynolds Number, *Re*, space. The relationships are:

   Boundary 1 between instability regions **1** and **2**:

   $$Oh = 4.9196\ Re^{-1.0459}$$

   Boundary 2 between instability regions **2** and **3**:

   $$Oh = 9.5979\ Re^{-1.0255}$$

   Boundary 3 between instability regions **3** and **4**:

   $$Oh = 15.4108\ Re^{-0.9989}$$

Boundary 4 between instability regions **4** and **5**:

$$Oh = 24.9548 \quad Re^{-1.0027}$$

3. The exponent for *Re* in the relationships for the instability regime boundaries are all very close to –1. Referring to the definitions of *Re* and *Oh*, this means that the transition between regimes is independent of jet viscosity, and the relationships for the boundaries can be rewritten as *We* ~ constant, where *We* is the Weber number. The critical transitional Weber numbers are the square of the coefficient of *Re* in the relationships for the boundaries, i.e.,

   Boundary 1 between instability regions **1** and **2**:

   $We \sim 24$

   Boundary 2 between instability regions **2** and **3**:

   $We \sim 92$

   Boundary 3 between instability regions **3** and **4**:

   $We \sim 237$

   Boundary 4 between instability regions **4** and **5**:

   $We \sim 623$

4. Although the present results suggest that the transition between instability regimes may be independent of jet viscosity, the average jet breakup length in instability regime 1 appears to be affected significantly by jet viscosity. Jet breakup length was greater for high viscosity fluids. The effect of viscosity on breakup length diminished in regime 2 as velocity increases and essentially disappears as the

transition to regime 3 is approached. The results also suggest that the properties of the ambient fluid can impact breakup length, probably through surface tension.

5. Tube nozzles produced longer breakup lengths than sharp edge orifices of the same inside diameter at instability regime 2. This indicates the influence of jet velocity profiles at separation on the development of the instability. As in the case of jet viscosity, the difference in breakup length decreased in regime 2 as velocity increases and essentially disappears as the transition to regime 3 is approached.
6. While breakup length appears to scale roughly with orifice diameter, *D*, the results suggest that may not be the appropriate length scale to non-dimensionalize breakup length data.
7. A method was developed to obtain a complete, composite droplet size spectra by combining size data from the PDPA and image analysis. The PDPA was not able to measure droplets larger than about 4 mm. The digital video image analysis could not measure droplets smaller than about 3 mm. The method exploits the overlap between the two incomplete size spectra and can be applied to similar situations involving different particle size diagnostics.
8. Droplet size spectra was measured for liquid-liquid jet breakup over the full range of instabilities from regime 1 through regime 5. Characteristic average diameters and other statistics were calculated from these spectra. Over the range of conditions examined in this study, jet velocity, orifice size and geometry, and jet fluid viscosity affected droplet size. There appeared to be limited or no difference

in spectra obtained for injection into tap water and sea water or for liquid CO_2 tests conducted at 52 and 62 bar.

9. Characteristic diameters decrease steadily with increasing jet velocity (and increasing *We*) in instability regimes 1 through 4, attaining an asymptotic value in regime 5. Orifice diameter appears to influence average droplet size at low *We* in regimes 1 and 2. This effect diminishes as regime 3 is approached and essentially disappears in regimes 4 and 5; the characteristic droplet diameters appeared to be the same for 2 mm, 5 mm, and 10 mm orifices, at the same value of *We*, in these regimes. This may reflect the lack of sensitivity to the transverse length scale (i.e., jet or orifice diameter) of higher order surface instabilities that have been postulated to generate small droplets. Orifice geometry (sharp edge or tube) did not seem to have a significant effect for the very low viscosity liquid CO_2, but did impact droplet size for higher viscosity jet fluids. Larger droplets and a more uniform distribution were produced when silicone fluid was injected from the tube nozzle. Finally, at low *We* in regime 1, jet viscosity seemed to have little effect on mean droplet size. In the transitional breakup regimes, droplet diameters appeared to increase slightly with viscosity.
10. A novel weighted multimodal distribution concept was developed to obtain functional representations of the experimental size distributions (both PDFs and CDFs) that can be applied for model development and testing. The appropriate multimodal distributions for the different instability regimes were selected based on K-S tests and goodness of fit statistics and these functions were fitted to the data.

11. Weighted bimodal functions were found best to describe the droplet size spectra in instability regimes 1, 2, and 5. In instability regimes 3 and 4, both the video records and the size distribution data indicate that multiple instabilities can operate in parallel and manifest themselves in complex, multimodal spectra. In these regimes, trimodal or four-modal functions may be necessary to adequately represent the data.
12. For liquid CO_2 injection under deep ocean conditions, a variety of solid hydrates were observed to form, depending mainly on jet velocity, provided that temperatures and pressures were within the hydrate stability regime. At low CO_2 flow rates, in instability regime 1, thin film hydrate tubes are likely to form on the jet surface. Hydrate tubes were not evident in the transitional breakup regimes 3 and 4, but thick hydrate tubes did form for some cases (with sub-zero CO_2 temperatures) in the atomization regime 5. The streamwise growth rate of the thick hydrate tube appears to scale with CO_2 flow rate.
13. Pre-breakup hydrate formation appears to affect the size distribution of the droplet phase primary by changing the effective geometry of the jet. When a hydrate tube forms, the interface between the CO_2 and water begins at the end of the tube, which may have a different size and shape opening than the original orifice. Furthermore, flow through the tube will alter the jet inlet velocity distribution, producing more time for boundary layer growth. In the case of thick tubes, hydrate branches will divert some of the CO_2 out of the main jet flow and could produce larger droplets.

14. CO_2 droplet concentration was determined to be a critical factor which influences agglomeration. High flow rates corresponding to transitional or atomization breakup generate large numbers of droplet in close proximity near the orifice. This enhances the probability of contact and agglomeration. Aggregate droplet clusters were not observed frequently in the varicose or transitional breakup regimes where droplet concentration is relatively low. Droplets aggregated readily on contact, but the hydrate films on their surfaces prevented coalescence.
15. Severe hydrate blockage occurred in some tests. There was some evidence that support the proposal by other researchers that certain materials (e.g., steels) are more prone to blockage since hydrates adhere well to them. Tests performed with plastic nozzles resulted in hydrate blockages that were relatively easy to expel.

APPEDIX A SINGLE AND WEIGHTED MULTIMODEL CDFS FOR DROPLET SIZE STUDIES

Table A. 1 CDFs of the 5 single mode distributions

No.	*F*	
1	normcdf	(x,a1,a2)
2	logncdf	(x,a1,a2)
3	wblcdf	(x,a1,a2)
4	evcdf	(x,a1,a2)
5	gamcdf	(x,a1,a2)

Table A. 2 15 CDFs of the weighted bimodal distributions

No.	F_1	F_2					Weighted bimodal distribution
1	1	1	normnorm	cdf	(x,a1,a2,a3,a4,a5)	=	a1 *normcdf (x,a2 ,a3)+(1-a1)*normcdf(x,a4 ,a5)
2	1	2	normlogn	cdf	(x,a1,a2,a3,a4,a5)	=	a1 *normcdf(x,a2 ,a3)+(1-a1)*logncdf(x,a4 ,a5)
3	1	3	normwbl	cdf	(x,a1,a2,a3,a4,a5)	=	a1 *normcdf(x,a2 ,a3)+(1-a1)*wblcdf(x,a4 ,a5)
4	1	4	normev	cdf	(x,a1,a2,a3,a4,a5)	=	a1 *normcdf(x,a2 ,a3)+(1-a1)*evcdf(x,a4 ,a5)
5	1	5	normgam	cdf	(x,a1,a2,a3,a4,a5)	=	a1 *normcdf (x,a2 ,a3)+(1-a1)*gamcdf(x,a4 ,a5)
6	2	2	lognlogn	cdf	(x,a1,a2,a3,a4,a5)	=	a1 *logncdf(x,a2 ,a3)+(1-a1)*logncdf(x,a4 ,a5)
7	2	3	lognwbl	cdf	(x,a1,a2,a3,a4,a5)	=	a1 *logncdf(x,a2 ,a3)+(1-a1)*wblcdf(x,a4 ,a5)
8	2	4	lognev	cdf	(x,a1,a2,a3,a4,a5)	=	a1 *logncdf(x,a2 ,a3)+(1-a1)*evcdf(x,a4 ,a5)
9	2	5	logngam	cdf	(x,a1,a2,a3,a4,a5)	=	a1 *logncdf(x,a2 ,a3)+(1-a1)*gamcdf(x,a4 ,a5)
10	3	3	wblwbl	cdf	(x,a1,a2,a3,a4,a5)	=	a1 *wblcdf(x,a2 ,a3)+(1-a1)*wblcdf(x,a4 ,a5)
11	3	4	wblev	cdf	(x,a1,a2,a3,a4,a5)	=	a1 *wblcdf(x,a2 ,a3)+(1-a1)*evcdf(x,a4 ,a5)
12	3	5	wblgam	cdf	(x,a1,a2,a3,a4,a5)	=	a1 *wblcdf(x,a2 ,a3)+(1-a1)*gamcdf(x,a4 ,a5)
13	4	4	evev	cdf	(x,a1,a2,a3,a4,a5)	=	a1 *evcdf(x,a2 ,a3)+(1-a1)*evcdf(x,a4 ,a5)
14	4	5	evgam	cdf	(x,a1,a2,a3,a4,a5)	=	a1 *evcdf(x,a2 ,a3)+(1-a1)*gamcdf(x,a4 ,a5)
15	5	5	gamgam	cdf	(x,a1,a2,a3,a4,a5)	=	a1 *gamcdf(x,a2 ,a3)+(1-a1)*gamcdf(x,a4 ,a5)

Table A. 3 35 CDFs of the weighted trimodal distributions

No.	F_1	F_2	F_3		Cumulative distribution functions of the weighted trimodal distribution		
1	1	1	1	normnormnorm	(x,a1,a2,a3,a4,a5,a6,a7,a8)	=	a1*normcdf(x,a3 ,a4)+a2*(1-a1)*normcdf(x,a5,a6)+(1-a2)*(1-a1)*normcdf(x,a7 ,a8)
2	1	1	2	normnormlogn	(x,a1,a2,a3,a4,a5,a6,a7,a8)	=	a1 *normcdf(x,a3 ,a4)+a2 *(1-a1)*normcdf(x,a5 ,a6)+(1-a2)*(1-a1)*logncdf(x,a7 ,a8)
3	1	1	3	normnormwbl	(x,a1,a2,a3,a4,a5,a6,a7,a8)	=	a1 *normcdf(x,a3 ,a4)+a2 *(1-a1)*normcdf(x,a5 ,a6)+(1-a2)*(1-a1)*wblcdf(x,a7 ,a8)
4	1	1	4	normnormev	(x,a1,a2,a3,a4,a5,a6,a7,a8)	=	a1 *normcdf(x,a3 ,a4)+a2 *(1-a1)*normcdf(x,a5 ,a6)+(1-a2)*(1-a1)*evcdf(x,a7 ,a8)
5	1	1	5	normnormgam	(x,a1,a2,a3,a4,a5,a6,a7,a8)	=	a1 *normcdf(x,a3 ,a4)+a2 *(1-a1)*normcdf(x,a5 ,a6)+(1-a2)*(1-a1)*gamcdf(x,a7 ,a8)
6	1	2	2	normlognlogn	(x,a1,a2,a3,a4,a5,a6,a7,a8)	=	a1 *normcdf(x,a3 ,a4)+a2 *(1-a1)*logncdf(x,a5 ,a6)+(1-a2)*(1-a1)*logncdf(x,a7 ,a8)
7	1	2	3	normlognwbl	(x,a1,a2,a3,a4,a5,a6,a7,a8)	=	a1 *normcdf(x,a3 ,a4)+a2 *(1-a1)*logncdf(x,a5 ,a6)+(1-a2)*(1-a1)*wblcdf(x,a7 ,a8)
8	1	2	4	normlognev	(x,a1,a2,a3,a4,a5,a6,a7,a8)	=	a1 *normcdf(x,a3 ,a4)+a2 *(1-a1)*logncdf(x,a5 ,a6)+(1-a2)*(1-a1)*evcdf(x,a7 ,a8)
9	1	2	5	normlogngam	(x,a1,a2,a3,a4,a5,a6,a7,a8)	=	a1 *normcdf(x,a3 ,a4)+a2 *(1-a1)*logncdf(x,a5 ,a6)+(1-a2)*(1-a1)*gamcdf(x,a7 ,a8)
10	1	3	3	normwblwbl	(x,a1,a2,a3,a4,a5,a6,a7,a8)	=	a1 *normcdf(x,a3 ,a4)+a2 *(1-a1)*wblcdf(x,a5 ,a6)+(1-a2)*(1-a1)*wblcdf(x,a7 ,a8)
11	1	3	4	normwblev	(x,a1,a2,a3,a4,a5,a6,a7,a8)	=	a1 *normcdf(x,a3 ,a4)+a2 *(1-a1)*wblcdf(x,a5 ,a6)+(1-a2)*(1-a1)*evcdf(x,a7 ,a8)
12	1	3	5	normwblgam	(x,a1,a2,a3,a4,a5,a6,a7,a8)	=	a1 *normcdf(x,a3 ,a4)+a2 *(1-a1)*wblcdf(x,a5 ,a6)+(1-a2)*(1-a1)*gamcdf(x,a7 ,a8)
13	1	4	4	normevev	(x,a1,a2,a3,a4,a5,a6,a7,a8)	=	a1 *normcdf(x,a3 ,a4)+a2 *(1-a1)*evcdf(x,a5 ,a6)+(1-a2)*(1-a1)*evcdf(x,a7 ,a8)
14	1	4	5	normevgam	(x,a1,a2,a3,a4,a5,a6,a7,a8)	=	a1 *normcdf(x,a3 ,a4)+a2 *(1-a1)*evcdf(x,a5 ,a6)+(1-a2)*(1-a1)*gamcdf(x,a7 ,a8)
15	1	5	5	normgamgam	(x,a1,a2,a3,a4,a5,a6,a7,a8)	=	a1 *normcdf(x,a3 ,a4)+a2 *(1-a1)*gamcdf(x,a5 ,a6)+(1-a2)*(1-a1)*gamcdf(x,a7 ,a8)
16	2	2	2	lognlognlogn	(x,a1,a2,a3,a4,a5,a6,a7,a8)	=	a1 *logncdf(x,a3 ,a4)+a2 *(1-a1)*logncdf(x,a5 ,a6)+(1-a2)*(1-a1)*logncdf(x,a7 ,a8)
17	2	2	3	lognlognwbl	(x,a1,a2,a3,a4,a5,a6,a7,a8)	=	a1 *logncdf(x,a3 ,a4)+a2 *(1-a1)*logncdf(x,a5 ,a6)+(1-a2)*(1-a1)*wblcdf(x,a7 ,a8)
18	2	2	4	lognlognev	(x,a1,a2,a3,a4,a5,a6,a7,a8)	=	a1 *logncdf(x,a3 ,a4)+a2 *(1-a1)*logncdf(x,a5 ,a6)+(1-a2)*(1-a1)*evcdf(x,a7 ,a8)
19	2	2	5	lognlogngam	(x,a1,a2,a3,a4,a5,a6,a7,a8)	=	a1 *logncdf(x,a3 ,a4)+a2 *(1-a1)*logncdf(x,a5 ,a6)+(1-a2)*(1-a1)*gamcdf(x,a7 ,a8)
20	2	3	3	lognwblwbl	(x,a1,a2,a3,a4,a5,a6,a7,a8)	=	a1 *logncdf(x,a3 ,a4)+a2 *(1-a1)*wblcdf(x,a5 ,a6)+(1-a2)*(1-a1)*wblcdf(x,a7 ,a8)
21	2	3	4	lognwblev	(x,a1,a2,a3,a4,a5,a6,a7,a8)	=	a1 *logncdf(x,a3 ,a4)+a2 *(1-a1)*wblcdf(x,a5 ,a6)+(1-a2)*(1-a1)*evcdf(x,a7 ,a8)
22	2	3	5	lognwblgam	(x,a1,a2,a3,a4,a5,a6,a7,a8)	=	a1 *logncdf(x,a3 ,a4)+a2 *(1-a1)*wblcdf(x,a5 ,a6)+(1-a2)*(1-a1)*gamcdf(x,a7 ,a8)
23	2	4	4	lognevev	(x,a1,a2,a3,a4,a5,a6,a7,a8)	=	a1 *logncdf(x,a3 ,a4)+a2 *(1-a1)*evcdf(x,a5 ,a6)+(1-a2)*(1-a1)*evcdf(x,a7 ,a8)
24	2	4	5	lognevgam	(x,a1,a2,a3,a4,a5,a6,a7,a8)	=	a1 *logncdf(x,a3 ,a4)+a2 *(1-a1)*evcdf(x,a5 ,a6)+(1-a2)*(1-a1)*gamcdf(x,a7 ,a8)
25	2	5	5	lognngamgam	(x,a1,a2,a3,a4,a5,a6,a7,a8)	=	a1 *logncdf(x,a3 ,a4)+a2 *(1-a1)*gamcdf(x,a5 ,a6)+(1-a2)*(1-a1)*gamcdf(x,a7 ,a8)
26	3	3	3	wblwblwbl	(x,a1,a2,a3,a4,a5,a6,a7,a8)	=	a1 *wblcdf(x,a3 ,a4)+a2 *(1-a1)*wblcdf(x,a5 ,a6)+(1-a2)*(1-a1)*wblcdf(x,a7 ,a8)
27	3	3	4	wblwblev	(x,a1,a2,a3,a4,a5,a6,a7,a8)	=	a1 *wblcdf(x,a3 ,a4)+a2 *(1-a1)*wblcdf(x,a5 ,a6)+(1-a2)*(1-a1)*evcdf(x,a7 ,a8)

Table A. 3 (Continued)

No.	F_1	F_2	F_3	Cumulative distribution functions of the weighted trimodal distribution			
28	3	3	5	wblwblgam	(x,a1,a2,a3,a4,a5,a6,a7,a8)	=	a1 *wblcdf(x,a3 ,a4)+a2 *(1-a1)*wblcdf(x,a5 ,a6)+(1-a2)*(1-a1)*gamcdf(x,a7 ,a8)
29	3	4	4	wblevev	(x,a1,a2,a3,a4,a5,a6,a7,a8)	=	a1 *wblcdf(x,a3 ,a4)+a2 *(1-a1)*evcdf(x,a5 ,a6)+(1-a2)*(1-a1)*evcdf(x,a7 ,a8)
30	3	4	5	wblevgam	(x,a1,a2,a3,a4,a5,a6,a7,a8)	=	a1 *wblcdf(x,a3 ,a4)+a2 *(1-a1)*evcdf(x,a5 ,a6)+(1-a2)*(1-a1)*gamcdf(x,a7 ,a8)
31	3	5	5	wblgamgam	(x,a1,a2,a3,a4,a5,a6,a7,a8)	=	a1 *wblcdf(x,a3 ,a4)+a2 *(1-a1)*gamcdf(x,a5 ,a6)+(1-a2)*(1-a1)*gamcdf(x,a7 ,a8)
32	4	4	4	evevev	(x,a1,a2,a3,a4,a5,a6,a7,a8)	=	a1 *evcdf(x,a3 ,a4)+a2 *(1-a1)*evcdf(x,a5 ,a6)+(1-a2)*(1-a1)*evcdf(x,a7 ,a8)
33	4	4	5	evevgam	(x,a1,a2,a3,a4,a5,a6,a7,a8)	=	a1 *evcdf(x,a3 ,a4)+a2 *(1-a1)*evcdf(x,a5 ,a6)+(1-a2)*(1-a1)*gamcdf(x,a7 ,a8)
34	4	5	5	evgamgam	(x,a1,a2,a3,a4,a5,a6,a7,a8)	=	a1 *evcdf(x,a3 ,a4)+a2 *(1-a1)*gamcdf(x,a5 ,a6)+(1-a2)*(1-a1)*gamcdf(x,a7 ,a8)
35	5	5	5	gamgamgam	(x,a1,a2,a3,a4,a5,a6,a7,a8)	=	a1 *gamcdf(x,a3 ,a4)+a2 *(1-a1)*gamcdf(x,a5 ,a6)+(1-a2)*(1-a1)*gamcdf(x,a7 ,a8)

Table A. 4 70 CDFs of the weighted four modal distributions

No.	F_1	F_2	F_3	F_4	Cumulative distribution functions of the weighted four modal distribution		
1	1	1	1	1	normnormnormnorm	(x,a1,a2,a3,a4,a5,a6,a7,a8,a9,a10,a11)=	a1 *normcdf(x,a4 ,a5)+a2 *(1-a1)*normcdf(x,a6 ,a7) +a3 *(1-a2)*(1-a1)*normcdf(x,a8 ,a9)+(1-a3)*(1-a2)*(1-a1)*normcdf(x,a10,a11)
2	1	1	1	2	normnormnormlogn	(x,a1,a2,a3,a4,a5,a6,a7,a8,a9,a10,a11)=	a1 *normcdf(x,a4 ,a5)+a2 *(1-a1)*normcdf(x,a6 ,a7) +a3 *(1-a2)*(1-a1)*normcdf(x,a8 ,a9)+(1-a3)*(1-a2)*(1-a1)*logncdf(x,a10,a11)
3	1	1	1	3	normnormnormwbl	(x,a1,a2,a3,a4,a5,a6,a7,a8,a9,a10,a11)=	a1 *normcdf(x,a4 ,a5)+a2 *(1-a1)*normcdf(x,a6 ,a7) +a3 *(1-a2)*(1-a1)*normcdf(x,a8 ,a9)+(1-a3)*(1-a2)*(1-a1)*wblcdf(x,a10,a11)
4	1	1	1	4	normnormnormev	(x,a1,a2,a3,a4,a5,a6,a7,a8,a9,a10,a11)=	a1 *normcdf(x,a4 ,a5)+a2 *(1-a1)*normcdf(x,a6 ,a7) +a3 *(1-a2)*(1-a1)*normcdf(x,a8 ,a9)+(1-a3)*(1-a2)*(1-a1)*evcdf(x,a10,a11)
5	1	1	1	5	normnormnormgam	(x,a1,a2,a3,a4,a5,a6,a7,a8,a9,a10,a11)=	a1 *normcdf(x,a4 ,a5)+a2 *(1-a1)*normcdf(x,a6 ,a7) +a3 *(1-a2)*(1-a1)*normcdf(x,a8 ,a9)+(1-a3)*(1-a2)*(1-a1)*gamcdf(x,a10,a11)
6	1	1	2	2	normnormlognlogn	(x,a1,a2,a3,a4,a5,a6,a7,a8,a9,a10,a11)=	a1 *normcdf(x,a4 ,a5)+a2 *(1-a1)*normcdf(x,a6 ,a7) +a3 *(1-a2)*(1-a1)*logncdf(x,a8 ,a9)+(1-a3)*(1-a2)*(1-a1)*logncdf(x,a10,a11)
7	1	1	2	3	normnormlognwbl	(x,a1,a2,a3,a4,a5,a6,a7,a8,a9,a10,a11)=	a1 *normcdf(x,a4 ,a5)+a2 *(1-a1)*normcdf(x,a6 ,a7) +a3 *(1-a2)*(1-a1)*logncdf(x,a8 ,a9)+(1-a3)*(1-a2)*(1-a1)*wblcdf(x,a10,a11)
8	1	1	2	4	normnormlognev	(x,a1,a2,a3,a4,a5,a6,a7,a8,a9,a10,a11)=	a1 *normcdf(x,a4 ,a5)+a2 *(1-a1)*normcdf(x,a6 ,a7) +a3 *(1-a2)*(1-a1)*logncdf(x,a8 ,a9)+(1-a3)*(1-a2)*(1-a1)*evcdf(x,a10,a11)

Table A. 4 (Continued)

No.	F_1	F_2	F_3	F_4		Cumulative distribution functions of the weighted four modal distribution
						a1 *normcdf(x,a4 ,a5)+a2 *(1-a1)*normcdf(x,a6 ,a7)
9	1	1	2	5	normnormlogngam	(x,a1,a2,a3,a4,a5,a6,a7,a8,a9,a10,a11)= +a3 *(1-a2)*(1-a1)*logncdf(x,a8 ,a9)+(1-a3)*(1-a2)*(1-a1)*gamcdf(x,a10,a11)
						a1 *normcdf(x,a4 ,a5)+a2 *(1-a1)*normcdf(x,a6 ,a7)
10	1	1	3	3	normnormwblwbl	(x,a1,a2,a3,a4,a5,a6,a7,a8,a9,a10,a11)= +a3 *(1-a2)*(1-a1)*wblcdf(x,a8 ,a9)+(1-a3)*(1-a2)*(1-a1)*wblcdf(x,a10,a11)
						a1 *normcdf(x,a4 ,a5)+a2 *(1-a1)*normcdf(x,a6 ,a7)
11	1	1	3	4	normnormwblev	(x,a1,a2,a3,a4,a5,a6,a7,a8,a9,a10,a11)= +a3 *(1-a2)*(1-a1)*wblcdf(x,a8 ,a9)+(1-a3)*(1-a2)*(1-a1)*evcdf(x,a10,a11)
						a1 *normcdf(x,a4 ,a5)+a2 *(1-a1)*normcdf(x,a6 ,a7)
12	1	1	3	5	normnormwblgam	(x,a1,a2,a3,a4,a5,a6,a7,a8,a9,a10,a11)= +a3 *(1-a2)*(1-a1)*wblcdf(x,a8 ,a9)+(1-a3)*(1-a2)*(1-a1)*gamcdf(x,a10,a11)
						a1 *normcdf(x,a4 ,a5)+a2 *(1-a1)*normcdf(x,a6 ,a7)
13	1	1	4	4	normnormevev	(x,a1,a2,a3,a4,a5,a6,a7,a8,a9,a10,a11)= +a3 *(1-a2)*(1-a1)*evcdf(x,a8 ,a9)+(1-a3)*(1-a2)*(1-a1)*evcdf(x,a10,a11)
						a1 *normcdf(x,a4 ,a5)+a2 *(1-a1)*normcdf(x,a6 ,a7)
14	1	1	4	5	normnormevgam	(x,a1,a2,a3,a4,a5,a6,a7,a8,a9,a10,a11)= +a3 *(1-a2)*(1-a1)*evcdf(x,a8 ,a9)+(1-a3)*(1-a2)*(1-a1)*gamcdf(x,a10,a11)
						a1 *normcdf(x,a4 ,a5)+a2 *(1-a1)*normcdf(x,a6 ,a7)
15	1	1	5	5	normnormgamgam	(x,a1,a2,a3,a4,a5,a6,a7,a8,a9,a10,a11)= +a3 *(1-a2)*(1-a1)*gamcdf(x,a8 ,a9)+(1-a3)*(1-a2)*(1-a1)*gamcdf(x,a10,a11)
						a1 *normcdf(x,a4 ,a5)+a2 *(1-a1)*logncdf(x,a6 ,a7)
16	1	2	2	2	normlognlognlogn	(x,a1,a2,a3,a4,a5,a6,a7,a8,a9,a10,a11)= +a3 *(1-a2)*(1-a1)*logncdf(x,a8 ,a9)+(1-a3)*(1-a2)*(1-a1)*logncdf(x,a10,a11)
						a1 *normcdf(x,a4 ,a5)+a2 *(1-a1)*logncdf(x,a6 ,a7)
17	1	2	2	3	normlognlognwbl	(x,a1,a2,a3,a4,a5,a6,a7,a8,a9,a10,a11)= +a3 *(1-a2)*(1-a1)*logncdf(x,a8 ,a9)+(1-a3)*(1-a2)*(1-a1)*wblcdf(x,a10,a11)
						a1 *normcdf(x,a4 ,a5)+a2 *(1-a1)*logncdf(x,a6 ,a7)
18	1	2	2	4	normlognlognev	(x,a1,a2,a3,a4,a5,a6,a7,a8,a9,a10,a11)= +a3 *(1-a2)*(1-a1)*logncdf(x,a8 ,a9)+(1-a3)*(1-a2)*(1-a1)*evcdf(x,a10,a11)
						a1 *normcdf(x,a4 ,a5)+a2 *(1-a1)*logncdf(x,a6 ,a7)
19	1	2	2	5	normlognlogngam	(x,a1,a2,a3,a4,a5,a6,a7,a8,a9,a10,a11)= +a3 *(1-a2)*(1-a1)*logncdf(x,a8 ,a9)+(1-a3)*(1-a2)*(1-a1)*gamcdf(x,a10,a11)
						a1 *normcdf(x,a4 ,a5)+a2 *(1-a1)*logncdf(x,a6 ,a7)
20	1	2	3	3	normlognwblwbl	(x,a1,a2,a3,a4,a5,a6,a7,a8,a9,a10,a11)= +a3 *(1-a2)*(1-a1)*wblcdf(x,a8 ,a9)+(1-a3)*(1-a2)*(1-a1)*wblcdf(x,a10,a11)
						a1 *normcdf(x,a4 ,a5)+a2 *(1-a1)*logncdf(x,a6 ,a7)
21	1	2	3	4	normlognwblev	(x,a1,a2,a3,a4,a5,a6,a7,a8,a9,a10,a11)= +a3 *(1-a2)*(1-a1)*wblcdf(x,a8 ,a9)+(1-a3)*(1-a2)*(1-a1)*evcdf(x,a10,a11)
						a1 *normcdf(x,a4 ,a5)+a2 *(1-a1)*logncdf(x,a6 ,a7)
22	1	2	3	5	normlognwblgam	(x,a1,a2,a3,a4,a5,a6,a7,a8,a9,a10,a11)= +a3 *(1-a2)*(1-a1)*wblcdf(x,a8 ,a9)+(1-a3)*(1-a2)*(1-a1)*gamcdf(x,a10,a11)
						a1 *normcdf(x,a4 ,a5)+a2 *(1-a1)*logncdf(x,a6 ,a7)
23	1	2	4	4	normlognevev	(x,a1,a2,a3,a4,a5,a6,a7,a8,a9,a10,a11)= +a3 *(1-a2)*(1-a1)*evcdf(x,a8 ,a9)+(1-a3)*(1-a2)*(1-a1)*evcdf(x,a10,a11)
						a1 *normcdf(x,a4 ,a5)+a2 *(1-a1)*logncdf(x,a6 ,a7)
24	1	2	4	5	normlognevgam	(x,a1,a2,a3,a4,a5,a6,a7,a8,a9,a10,a11)= +a3 *(1-a2)*(1-a1)*evcdf(x,a8 ,a9)+(1-a3)*(1-a2)*(1-a1)*gamcdf(x,a10,a11)
						a1 *normcdf(x,a4 ,a5)+a2 *(1-a1)*logncdf(x,a6 ,a7)
25	1	2	5	5	normlogngamgam	(x,a1,a2,a3,a4,a5,a6,a7,a8,a9,a10,a11)= +a3 *(1-a2)*(1-a1)*gamcdf(x,a8 ,a9)+(1-a3)*(1-a2)*(1-a1)*gamcdf(x,a10,a11)
						a1 *normcdf(x,a4 ,a5)+a2 *(1-a1)*wblcdf(x,a6 ,a7)
26	1	3	3	3	normwblwblwbl	(x,a1,a2,a3,a4,a5,a6,a7,a8,a9,a10,a11)= +a3 *(1-a2)*(1-a1)*wblcdf(x,a8 ,a9)+(1-a3)*(1-a2)*(1-a1)*wblcdf(x,a10,a11)
						a1 *normcdf(x,a4 ,a5)+a2 *(1-a1)*wblcdf(x,a6 ,a7)
27	1	3	3	4	normwblwblev	(x,a1,a2,a3,a4,a5,a6,a7,a8,a9,a10,a11)= +a3 *(1-a2)*(1-a1)*wblcdf(x,a8 ,a9)+(1-a3)*(1-a2)*(1-a1)*evcdf(x,a10,a11)
						a1 *normcdf(x,a4 ,a5)+a2 *(1-a1)*wblcdf(x,a6 ,a7)
28	1	3	3	5	normwblwblgam	(x,a1,a2,a3,a4,a5,a6,a7,a8,a9,a10,a11)= +a3 *(1-a2)*(1-a1)*wblcdf(x,a8 ,a9)+(1-a3)*(1-a2)*(1-a1)*gamcdf(x,a10,a11)
						a1 *normcdf(x,a4 ,a5)+a2 *(1-a1)*wblcdf(x,a6 ,a7)
29	1	3	4	4	normwblevev	(x,a1,a2,a3,a4,a5,a6,a7,a8,a9,a10,a11)= +a3 *(1-a2)*(1-a1)*evcdf(x,a8 ,a9)+(1-a3)*(1-a2)*(1-a1)*evcdf(x,a10,a11)

Table A. 4 (Continued)

No.	F_1	F_2	F_3	F_4		Cumulative distribution functions of the weighted four modal distribution
						a1 *normcdf(x,a4 ,a5)+a2 *(1-a1)*wblcdf(x,a6 ,a7)
30	1	3	4	5	normwblevgam	(x,a1,a2,a3,a4,a5,a6,a7,a8,a9,a10,a11)= +a3 *(1-a2)*(1-a1)*evcdf(x,a8 ,a9)+(1-a3)*(1-a2)*(1-a1)*gamcdf(x,a10,a11)
						a1 *normcdf(x,a4 ,a5)+a2 *(1-a1)*wblcdf(x,a6 ,a7)
31	1	3	5	5	normwblgamgam	(x,a1,a2,a3,a4,a5,a6,a7,a8,a9,a10,a11)= +a3 *(1-a2)*(1-a1)*gamcdf(x,a8 ,a9)+(1-a3)*(1-a2)*(1-a1)*gamcdf(x,a10,a11)
						a1 *normcdf(x,a4 ,a5)+a2 *(1-a1)*evcdf(x,a6 ,a7)
32	1	4	4	4	normevevev	(x,a1,a2,a3,a4,a5,a6,a7,a8,a9,a10,a11)= +a3 *(1-a2)*(1-a1)*evcdf(x,a8 ,a9)+(1-a3)*(1-a2)*(1-a1)*evcdf(x,a10,a11)
						a1 *normcdf(x,a4 ,a5)+a2 *(1-a1)*evcdf(x,a6 ,a7)
33	1	4	4	5	normevevgam	(x,a1,a2,a3,a4,a5,a6,a7,a8,a9,a10,a11)= +a3 *(1-a2)*(1-a1)*evcdf(x,a8 ,a9)+(1-a3)*(1-a2)*(1-a1)*gamcdf(x,a10,a11)
						a1 *normcdf(x,a4 ,a5)+a2 *(1-a1)*evcdf(x,a6 ,a7)
34	1	4	5	5	normevgamgam	(x,a1,a2,a3,a4,a5,a6,a7,a8,a9,a10,a11)= +a3 *(1-a2)*(1-a1)*gamcdf(x,a8 ,a9)+(1-a3)*(1-a2)*(1-a1)*gamcdf(x,a10,a11)
						a1 *normcdf(x,a4 ,a5)+a2 *(1-a1)*gamcdf(x,a6 ,a7)
35	1	5	5	5	normgamgamgam	(x,a1,a2,a3,a4,a5,a6,a7,a8,a9,a10,a11)= +a3 *(1-a2)*(1-a1)*gamcdf(x,a8 ,a9)+(1-a3)*(1-a2)*(1-a1)*gamcdf(x,a10,a11)
						a1 *logncdf(x,a4 ,a5)+a2 *(1-a1)*logncdf(x,a6 ,a7)
36	2	2	2	2	lognlognlognlogn	(x,a1,a2,a3,a4,a5,a6,a7,a8,a9,a10,a11)= +a3 *(1-a2)*(1-a1)*logncdf(x,a8 ,a9)+(1-a3)*(1-a2)*(1-a1)*logncdf(x,a10,a11)
						a1 *logncdf(x,a4 ,a5)+a2 *(1-a1)*logncdf(x,a6 ,a7)
37	2	2	2	3	lognlognlognwbl	(x,a1,a2,a3,a4,a5,a6,a7,a8,a9,a10,a11)= +a3 *(1-a2)*(1-a1)*logncdf(x,a8 ,a9)+(1-a3)*(1-a2)*(1-a1)*wblcdf(x,a10,a11)
						a1 *logncdf(x,a4 ,a5)+a2 *(1-a1)*logncdf(x,a6 ,a7)
38	2	2	2	4	lognlognlognev	(x,a1,a2,a3,a4,a5,a6,a7,a8,a9,a10,a11)= +a3 *(1-a2)*(1-a1)*logncdf(x,a8 ,a9)+(1-a3)*(1-a2)*(1-a1)*evcdf(x,a10,a11)
						a1 *logncdf(x,a4 ,a5)+a2 *(1-a1)*logncdf(x,a6 ,a7)
39	2	2	2	5	lognlognlogngam	(x,a1,a2,a3,a4,a5,a6,a7,a8,a9,a10,a11)= +a3 *(1-a2)*(1-a1)*logncdf(x,a8 ,a9)+(1-a3)*(1-a2)*(1-a1)*gamcdf(x,a10,a11)
						a1 *logncdf(x,a4 ,a5)+a2 *(1-a1)*logncdf(x,a6 ,a7)
40	2	2	3	3	lognlognwblwbl	(x,a1,a2,a3,a4,a5,a6,a7,a8,a9,a10,a11)= +a3 *(1-a2)*(1-a1)*wblcdf(x,a8 ,a9)+(1-a3)*(1-a2)*(1-a1)*wblcdf(x,a10,a11)
						a1 *logncdf(x,a4 ,a5)+a2 *(1-a1)*logncdf(x,a6 ,a7)
41	2	2	3	4	lognlognwblev	(x,a1,a2,a3,a4,a5,a6,a7,a8,a9,a10,a11)= +a3 *(1-a2)*(1-a1)*wblcdf(x,a8 ,a9)+(1-a3)*(1-a2)*(1-a1)*evcdf(x,a10,a11)
						a1 *logncdf(x,a4 ,a5)+a2 *(1-a1)*logncdf(x,a6 ,a7)
42	2	2	3	5	lognlognwblgam	(x,a1,a2,a3,a4,a5,a6,a7,a8,a9,a10,a11)= +a3 *(1-a2)*(1-a1)*wblcdf(x,a8 ,a9)+(1-a3)*(1-a2)*(1-a1)*gamcdf(x,a10,a11)
						a1 *logncdf(x,a4 ,a5)+a2 *(1-a1)*logncdf(x,a6 ,a7)
43	2	2	4	4	lognlognevev	(x,a1,a2,a3,a4,a5,a6,a7,a8,a9,a10,a11)= +a3 *(1-a2)*(1-a1)*evcdf(x,a8 ,a9)+(1-a3)*(1-a2)*(1-a1)*evcdf(x,a10,a11)
						a1 *logncdf(x,a4 ,a5)+a2 *(1-a1)*logncdf(x,a6 ,a7)
44	2	2	4	5	lognlognevgam	(x,a1,a2,a3,a4,a5,a6,a7,a8,a9,a10,a11)= +a3 *(1-a2)*(1-a1)*evcdf(x,a8 ,a9)+(1-a3)*(1-a2)*(1-a1)*gamcdf(x,a10,a11)
						a1 *logncdf(x,a4 ,a5)+a2 *(1-a1)*logncdf(x,a6 ,a7)
45	2	2	5	5	lognlogngamgam	(x,a1,a2,a3,a4,a5,a6,a7,a8,a9,a10,a11)= +a3 *(1-a2)*(1-a1)*gamcdf(x,a8 ,a9)+(1-a3)*(1-a2)*(1-a1)*gamcdf(x,a10,a11)
						a1 *logncdf(x,a4 ,a5)+a2 *(1-a1)*wblcdf(x,a6 ,a7)
46	2	3	3	3	lognwblwblwbl	(x,a1,a2,a3,a4,a5,a6,a7,a8,a9,a10,a11)= +a3 *(1-a2)*(1-a1)*wblcdf(x,a8 ,a9)+(1-a3)*(1-a2)*(1-a1)*wblcdf(x,a10,a11)
						a1 *logncdf(x,a4 ,a5)+a2 *(1-a1)*wblcdf(x,a6 ,a7)
47	2	3	3	4	lognwblwblev	(x,a1,a2,a3,a4,a5,a6,a7,a8,a9,a10,a11)= +a3 *(1-a2)*(1-a1)*wblcdf(x,a8 ,a9)+(1-a3)*(1-a2)*(1-a1)*evcdf(x,a10,a11)
						a1 *logncdf(x,a4 ,a5)+a2 *(1-a1)*wblcdf(x,a6 ,a7)
48	2	3	3	5	lognwblwblgam	(x,a1,a2,a3,a4,a5,a6,a7,a8,a9,a10,a11)= +a3 *(1-a2)*(1-a1)*wblcdf(x,a8 ,a9)+(1-a3)*(1-a2)*(1-a1)*gamcdf(x,a10,a11)
						a1 *logncdf(x,a4 ,a5)+a2 *(1-a1)*wblcdf(x,a6 ,a7)
49	2	3	4	4	lognwblevev	(x,a1,a2,a3,a4,a5,a6,a7,a8,a9,a10,a11)= +a3 *(1-a2)*(1-a1)*evcdf(x,a8 ,a9)+(1-a3)*(1-a2)*(1-a1)*evcdf(x,a10,a11)
						a1 *logncdf(x,a4 ,a5)+a2 *(1-a1)*wblcdf(x,a6 ,a7)
50	2	3	4	5	lognwblevgam	(x,a1,a2,a3,a4,a5,a6,a7,a8,a9,a10,a11)= +a3 *(1-a2)*(1-a1)*evcdf(x,a8 ,a9)+(1-a3)*(1-a2)*(1-a1)*gamcdf(x,a10,a11)

Table A. 4 (Continued)

No.	F_1	F_2	F_3	F_4			Cumulative distribution functions of the weighted four modal distribution
							a1 *logncdf(x,a4 ,a5)+a2 *(1-a1)*wblcdf(x,a6 ,a7)
51	2	3	5	5	lognwblgamgam	(x,a1,a2,a3,a4,a5,a6,a7,a8,a9,a10,a11)=	+a3 *(1-a2)*(1-a1)*gamcdf(x,a8 ,a9)+(1-a3)*(1-a2)*(1-a1)*gamcdf(x,a10,a11)
							a1 *logncdf(x,a4 ,a5)+a2 *(1-a1)*evcdf(x,a6 ,a7)
52	2	4	4	4	lognevevev	(x,a1,a2,a3,a4,a5,a6,a7,a8,a9,a10,a11)=	+a3 *(1-a2)*(1-a1)*evcdf(x,a8 ,a9)+(1-a3)*(1-a2)*(1-a1)*evcdf(x,a10,a11)
							a1 *logncdf(x,a4 ,a5)+a2 *(1-a1)*evcdf(x,a6 ,a7)
53	2	4	4	5	lognevevgam	(x,a1,a2,a3,a4,a5,a6,a7,a8,a9,a10,a11)=	+a3 *(1-a2)*(1-a1)*evcdf(x,a8 ,a9)+(1-a3)*(1-a2)*(1-a1)*gamcdf(x,a10,a11)
							a1 *logncdf(x,a4 ,a5)+a2 *(1-a1)*evcdf(x,a6 ,a7)
54	2	4	5	5	lognevgamgam	(x,a1,a2,a3,a4,a5,a6,a7,a8,a9,a10,a11)=	+a3 *(1-a2)*(1-a1)*gamcdf(x,a8 ,a9)+(1-a3)*(1-a2)*(1-a1)*gamcdf(x,a10,a11)
							a1 *logncdf(x,a4 ,a5)+a2 *(1-a1)*gamcdf(x,a6 ,a7)
55	2	5	5	5	logngamgamgam	(x,a1,a2,a3,a4,a5,a6,a7,a8,a9,a10,a11)=	+a3 *(1-a2)*(1-a1)*gamcdf(x,a8 ,a9)+(1-a3)*(1-a2)*(1-a1)*gamcdf(x,a10,a11)
							a1 *wblcdf(x,a4 ,a5)+a2 *(1-a1)*wblcdf(x,a6 ,a7)
56	3	3	3	3	wblwblwblwbl	(x,a1,a2,a3,a4,a5,a6,a7,a8,a9,a10,a11)=	+a3 *(1-a2)*(1-a1)*wblcdf(x,a8 ,a9)+(1-a3)*(1-a2)*(1-a1)*wblcdf(x,a10,a11)
							a1 *wblcdf(x,a4 ,a5)+a2 *(1-a1)*wblcdf(x,a6 ,a7)
57	3	3	3	4	wblwblwblev	(x,a1,a2,a3,a4,a5,a6,a7,a8,a9,a10,a11)=	+a3 *(1-a2)*(1-a1)*wblcdf(x,a8 ,a9)+(1-a3)*(1-a2)*(1-a1)*evcdf(x,a10,a11)
							a1 *wblcdf(x,a4 ,a5)+a2 *(1-a1)*wblcdf(x,a6 ,a7)
58	3	3	3	5	wblwblwblgam	(x,a1,a2,a3,a4,a5,a6,a7,a8,a9,a10,a11)=	+a3 *(1-a2)*(1-a1)*wblcdf(x,a8 ,a9)+(1-a3)*(1-a2)*(1-a1)*gamcdf(x,a10,a11)
							a1 *wblcdf(x,a4 ,a5)+a2 *(1-a1)*wblcdf(x,a6 ,a7)
59	3	3	4	4	wblwblevev	(x,a1,a2,a3,a4,a5,a6,a7,a8,a9,a10,a11)=	+a3 *(1-a2)*(1-a1)*evcdf(x,a8 ,a9)+(1-a3)*(1-a2)*(1-a1)*evcdf(x,a10,a11)
							a1 *wblcdf(x,a4 ,a5)+a2 *(1-a1)*wblcdf(x,a6 ,a7)
60	3	3	4	5	wblwblevgam	(x,a1,a2,a3,a4,a5,a6,a7,a8,a9,a10,a11)=	a3 *(1-a2)*(1-a1)*evcdf(x,a8 ,a9)+(1-a3)*(1-a2)*(1-a1)*gamcdf(x,a10,a11)
							a1 *wblcdf(x,a4 ,a5)+a2 *(1-a1)*wblcdf(x,a6 ,a7)
61	3	3	5	5	wblwblgamgam	(x,a1,a2,a3,a4,a5,a6,a7,a8,a9,a10,a11)=	+a3 *(1-a2)*(1-a1)*gamcdf(x,a8 ,a9)+(1-a3)*(1-a2)*(1-a1)*gamcdf(x,a10,a11)
							a1 *wblcdf(x,a4 ,a5)+a2 *(1-a1)*evcdf(x,a6 ,a7)
62	3	4	4	4	wblevevev	(x,a1,a2,a3,a4,a5,a6,a7,a8,a9,a10,a11)=	+a3 *(1-a2)*(1-a1)*evcdf(x,a8 ,a9)+(1-a3)*(1-a2)*(1-a1)*evcdf(x,a10,a11)
							a1 *wblcdf(x,a4 ,a5)+a2 *(1-a1)*evcdf(x,a6 ,a7)
63	3	4	4	5	wblevevgam	(x,a1,a2,a3,a4,a5,a6,a7,a8,a9,a10,a11)=	+a3 *(1-a2)*(1-a1)*evcdf(x,a8 ,a9)+(1-a3)*(1-a2)*(1-a1)*gamcdf(x,a10,a11)
							a1 *wblcdf(x,a4 ,a5)+a2 *(1-a1)*evcdf(x,a6 ,a7)
64	3	4	5	5	wblevgamgam	(x,a1,a2,a3,a4,a5,a6,a7,a8,a9,a10,a11)=	+a3 *(1-a2)*(1-a1)*gamcdf(x,a8 ,a9)+(1-a3)*(1-a2)*(1-a1)*gamcdf(x,a10,a11)
							a1 *wblcdf(x,a4 ,a5)+a2 *(1-a1)*gamcdf(x,a6 ,a7)
65	3	5	5	5	wblgamgamgam	(x,a1,a2,a3,a4,a5,a6,a7,a8,a9,a10,a11)=	+a3 *(1-a2)*(1-a1)*gamcdf(x,a8 ,a9)+(1-a3)*(1-a2)*(1-a1)*gamcdf(x,a10,a11)
							a1 *evcdf(x,a4 ,a5)+a2 *(1-a1)*evcdf(x,a6 ,a7)
66	4	4	4	4	evevevev	(x,a1,a2,a3,a4,a5,a6,a7,a8,a9,a10,a11)=	+a3 *(1-a2)*(1-a1)*evcdf(x,a8 ,a9)+(1-a3)*(1-a2)*(1-a1)*evcdf(x,a10,a11)
							a1 *evcdf(x,a4 ,a5)+a2 *(1-a1)*evcdf(x,a6 ,a7)
67	4	4	4	5	evevevgam	(x,a1,a2,a3,a4,a5,a6,a7,a8,a9,a10,a11)=	+a3 *(1-a2)*(1-a1)*evcdf(x,a8 ,a9)+(1-a3)*(1-a2)*(1-a1)*gamcdf(x,a10,a11)
							a1 *evcdf(x,a4 ,a5)+a2 *(1-a1)*evcdf(x,a6 ,a7)
68	4	4	5	5	evevgamgam	(x,a1,a2,a3,a4,a5,a6,a7,a8,a9,a10,a11)=	+a3 *(1-a2)*(1-a1)*gamcdf(x,a8 ,a9)+(1-a3)*(1-a2)*(1-a1)*gamcdf(x,a10,a11)
							a1 *evcdf(x,a4 ,a5)+a2 *(1-a1)*gamcdf(x,a6 ,a7
69	4	5	5	5	evgamgamgam	(x,a1,a2,a3,a4,a5,a6,a7,a8,a9,a10,a11)=	)+a3 *(1-a2)*(1-a1)*gamcdf(x,a8 ,a9)+(1-a3)*(1-a2)*(1-a1)*gamcdf(x,a10,a11)
							a1 *gamcdf(x,a4 ,a5)+a2 *(1-a1)*gamcdf(x,a6 ,a7)
70	5	5	5	5	gamgamgamgam	(x,a1,a2,a3,a4,a5,a6,a7,a8,a9,a10,a11)=	+a3 *(1-a2)*(1-a1)*gamcdf(x,a8 ,a9)+(1-a3)*(1-a2)*(1-a1)*gamcdf(x,a10,a11)

APPENDIX B CO_2 DROPLET SIZE CURVEFITS

Table B. 1 Test labels for CO_2 droplet size spectra and coefficients obtained from curve fittings.

Size Test No.	Short Name	Table 3.1 No.	Test Name	U_{jet} [m/s]	Photo Counts	PDPA Counts	*IR*	a1	a2	a3	a4	a5	a6	a7	a8	a9	a10	a11
1	L1C1R1	1	CDC02WTP52R1	0.67	93	0	2	0.330	4.053	1.620	4.962	5.904						
2	L1C1R2	2	CDC02WTP52R2	0.77	116	0	2	0.581	4.396	0.637	2.883	2.758						
3	L1C1R3	3	CDC02WTP52R3	1.13	130	0	2	0.500	4.050	0.716	2.083	3.389						
4	L1C1R4	4	CDC02WTP52R4	1.69	52	896	3	0.260	0.389	0.525	0.689	7.116	1.887	0.118	2.051	0.700	10.55	0.071
5	L1C1R5	5	CDC02WTP52R5	1.51	87	1561	3	0.249	0.377	0.141	0.390	3.763	1.028	0.086	2.739	0.125	9.459	0.214
6	L1C1R6	6	CDC02WTP52R6	2	51	1039	3	0.185	0.058	0.388	0.483	2.034	1.125	0.051	2.433	0.438	8.350	0.137
7	L1C1R7	7	CDC02WTP52R7	2.58	0	1224	4	0.235	0.245	1.162	0.086	0.828	1.567	5.481	0.281			
8	L1C1R8	8	CDC02WTP52R8	3.21	0	1804	4	0.218	0.254	1.338	0.731	0.940	6.853	3.276	0.397			
9	L1C1R9	9	CDC02WTP52R9	4.01	0	1118	5	0.039	1.199	50.00	1.094	2.985						
10	L1C1R10	10	CDC02WTP52R10	1.57	90	2315	3	0.111	0.304	0.459	0.579	5.131	1.252	0.079	2.165	0.642	7.499	0.162
11	L1C2R1	11	CDC05WTP52R1	0.04	83	0	1	0.274	7.370	0.285	5.523	0.844						
12	L1C2R3	13	CDC05WTP52R3	0.08	52	0	1	0.300	5.936	0.201	7.370	0.917						
13	L1C2R4	14	CDC05WTP52R4	0.1	80	0	1	0.330	6.558	0.347	7.379	1.300						
14	L1C2R5	15	CDC05WTP52R5	0.13	78	0	1	0.579	5.913	0.641	8.374	1.328						
15	L1C2R6	16	CDC05WTP52R6	0.18	47	0	1	0.562	8.045	0.750	5.887	0.500						
16	L1C2R7	17	CDC05WTP52R7	0.23	238	0	1	0.749	7.388	1.596	6.624	0.425						
17	L1C2R8	18	CDC05WTP52R8	0.28	245	0	2	0.862	6.810	1.252	5.682	1.163						
18	L1C2R9	19	CDC05WTP52R9	0.33	167	0	2	0.885	6.597	1.848	3.363	4.034						
19	L1C2R10	20	CDC05WTP52R10	0.39	95	0	2	0.645	6.900	2.311	5.923	2.021						
20	L1C2R11	21	CDC05WTP52R11	0.44	71	0	2	0.736	6.193	2.445	9.835	3.224						
21	L1C2R12	22	CDC05WTP52R12	0.55	133	0	2	0.855	6.864	2.827	2.909	5.393						
22	L1C2R20	30	CDC05WTP52R20	0.59	40	649	3	0.377	0.316	0.498	0.406	3.699	2.217	0.111	4.779	2.084	324.3	0.005
23	L1C2R21	31	CDC05WTP52R21	0.73	63	2554	3	0.318	0.048	0.034	1.376	1.743	3.015	0.040	6.112	0.005	8.442	0.637

Table B.1 (Continued)

Size Test No.	Short Name	Table 3.1 No.	Test Name	U_{jet} [m/s]	Photo Counts	PDPA Counts	IR	a1	a2	a3	a4	a5	a6	a7	a8	a9	a10	a11
24	L1C2R22	32	CDC05WTP52R22	0.86	118	2537	3	0.351	0.146	0.046	0.477	3.338	0.818	0.057	3.161	0.058	3.109	1.451
25	L1C2R23	33	CDC05WTP52R23	1.03	63	2554	4	0.069	0.491	2.457	0.103	3.741	1.949	2.770	0.211			
26	L1C2R24	34	CDC05WTP52R24	1.25	130	3155	4	0.093	0.335	4.149	6.989	4.099	5.267	3.290	0.250			
27	L1C2R25	35	CDC05WTP52R25	1.88	21	2307	4	0.461	0.214	1.769	1.108	1.189	13.32	7.316	0.090			
28	L1C2R26	36	CDC05WTP52R26	2.4	89	2058	5	0.590	0.520	2.161	3.705	2.038						
29	L1C3R1	37	CDC10WTP52R1	0.41	234	1256	3	0.595	0.847	0.474	4.032	1.329	0.680	0.125	7.057	0.367	313.2	0.005
30	L1C3R2	38	CDC10WTP52R2	0.66	561	1146	3	0.228	0.045	0.067	2.580	1.137	2.316	0.073	6.484	4.141	5.717	0.072
31	L1C3R3	39	CDC10WTP52R3	0.88	99	2704	4	0.091	0.492	2.356	0.441	4.386	1.479	3.223	0.150			
32	L1C3R4	40	CDC10WTP52R4	1.18	0	2707	5	0.046	3.517	24.65	1.116	1.298						
33	L1C3R5	41	CDC10WTP52R5	1.45	0	3403	5	0.465	0.451	7.695	0.638	3.065						
34	L1C3R6	42	CDC10WTP52R6	0.13	41	0	1	0.303	12.22	0.799	6.533	1.955						
35	L1C3R7	43	CDC10WTP52R7	0.23	165	0	2	0.148	8.474	1.387	7.071	1.325						
36	L1C3R8	44	CDC10WTP52R8	0.28	83	0	2	0.205	2.425	0.637	6.678	1.750						
37	L1C3R9	45	CDC10WTP52R9	0.31	190	0	2	0.186	8.030	1.147	7.450	1.459						
38	L1C3R10	46	CDC10WTP52R10	0.1	54	0	1	0.224	4.458	1.515	10.94	1.172						
39	L1C3R12	48	CDC10WTP52R12	0.04	39	0	1	0.093	5.493	5.806	8.942	1.003						
40	L1C3R13	49	CDC10WTP52R13	0.02	56	0	1	0.639	9.086	0.427	9.697	0.446						
41	L1C4R1	50	CDT02WTP52R1	1.7	209	300	3	0.335	0.691	0.329	0.710	13.80	0.835	0.181	4.050	1.795	195.2	0.003
42	L1C4R2	51	CDT02WTP52R2	1.79	57	1701	3	0.307	0.422	0.522	1.745	3.031	0.788	0.126	5.291	1.685	10.46	0.030
43	L1C4R3	52	CDT02WTP52R3	2.09	161	3011	3	0.335	0.463	0.676	0.813	1.849	4.560	0.648	3.554	0.292	571.2	0.003
44	L1C4R4	53	CDT02WTP52R4	2.58	158	3041	4	0.160	0.084	4.238	0.723	1.249	38.33	2.991	0.250			
45	L1C4R5	54	CDT02WTP52R5	3.18	101	1726	4	0.145	0.255	2.175	0.324	3.569	4.951	3.385	0.169			
46	L1C4R6	55	CDT02WTP52R6	3.92	42	1895	5	0.393	0.467	3.172	1.402	1.147						
47	L1C4R7	56	CDT02WTP52R7	5.54	100	1369	5	0.679	0.561	1.600	2.317	4.261						
48	L1C4R8	57	CDT02WTP52R8	7.88	55	1554	5	0.290	0.335	1.977	1.478	1.180						
49	L1C4R9	58	CDT02WTP52R9	12.9	59	2178	5	0.618	0.617	2.768	1.519	1.506						

Table B.1 (Continued)

Size Test No.	Short Name	Table 3.1 No.	Test Name	U_{jet} [m/s]	Photo Counts	PDPA Counts	IR	a1	a2	a3	a4	a5	a6	a7	a8	a9	a10	a11
50	L1C4R10	59	CDT02WTP52R10	17.8	0	2010	5	0.502	0.740	2.156	1.497	1.238						
51	L1C4R11	60	CDT02WTP52R11	1.03	200	0	2	0.745	5.011	1.136	2.593	4.993						
52	L1C4R12	61	CDT02WTP52R12	0.77	263	0	2	0.721	4.739	1.108	1.859	4.027						
53	L1C4R13	62	CDT02WTP52R13	0.68	198	0	2	0.258	3.518	2.036	5.184	7.297						
54	L1C4R14	63	CDT02WTP52R14	0.53	172	0	2	0.217	3.542	1.734	4.570	7.568						
55	L1C5R1	64	CDT02WNP52R1	2.56	0	1596	4	0.077	0.239	2.051	0.176	0.884	7.248	11.70	0.149			
56	L1C5R2	65	CDT02WNP52R2	3.89	0	1645	5	0.393	1.244	4.861	2.036	4.585						
57	L1C5R4	66	CDT02WNP52R4	0.51	147	0	2	0.402	3.406	1.789	3.900	10.64						
58	L1C5R5	67	CDT02WNP52R5	0.7	147	0	2	0.643	4.212	0.644	3.900	2.085						
59	L1C5R6	68	CDT02WNP52R6	0.78	173	0	2	0.717	4.461	0.924	1.985	3.355						
60	L1C5R8	70	CDT02WNP52R8	1.49	67	3228	3	0.299	0.078	0.061	2.235	7.067	0.555	0.201	5.187	0.439	29.22	0.038
61	L1C5R9	71	CDT02WNP52R9	1.95	0	3130	3	0.373	0.117	0.472	0.922	5.427	1.218	0.082	2.088	0.560	89.27	0.018
62	L1C6R1	72	CDT05WTP61R1	1.26	0	1837	3	0.383	0.178	0.489	0.333	8.938	3.340	0.244	0.456	0.195	41.54	0.025
63	L1C6R2	73	CDT05WTP61R2	2.34	0	2954	5	0.791	0.820	3.165	1.329	0.858						
64	L1C6R4	75	CDT05WTP61R4	0.37	169	0	2	0.629	5.773	2.022	9.713	6.949						
65	L1C6R6	77	CDT05WTP61R6	0.21	165	0	1	0.149	7.725	0.839	7.837	1.962						
66	L1C6R7	78	CDT05WTP61R7	0.09	150	0	1	0.467	5.909	0.486	5.005	0.753						
67	L1C7R1	79	CDT05WTP52R1	2.35	0	2456	5	0.711	0.594	1.857	1.545	1.598						
68	L1C7R2	80	CDT05WTP52R2	1.8	0	2606	4	0.143	0.296	2.191	1.634	0.623	3.407	2.345	0.316			
69	L1C7R3	81	CDT05WTP52R3	1.23	176	1928	3	0.217	0.335	0.138	0.449	6.952	1.114	0.395	3.646	0.174	4.377	1.087
70	L1C7R5	83	CDT05WTP52R5	0.36	155	0	2	0.666	7.204	3.105	6.377	2.187						
71	L1C7R6	84	CDT05WTP52R6	0.21	157	0	1	0.261	6.501	2.966	6.647	1.212						
72	L1C7R7	85	CDT05WTP52R7	0.09	159	0	1	0.184	3.415	1.155	6.586	0.506						

APPENDIX C EXPERIMENTAL UNCERTAINCIES

This Appendix includes details of analyses performed to estimate uncertainties in the calculated values of Reynolds, Weber, and Ohnesorge numbers and the droplet size measurements.

C.1 Uncertainty of *Re, Oh* and *We*

By definition, $Re = f(U, D, \rho, \mu)$; $We = f(U, D, \rho, \sigma)$; and $Oh = f(D, \rho, \mu, \sigma)$. Uncertainties in *Re, Oh, We* therefore reflect the uncertainty in the values of $U, D, \rho, \mu,$ and σ used to calculate these parameters.

Examination of the orifices with a microscope suggests that D agrees with the nominal values to within about ±3%. Although the PDPA has the ability to measure velocity, this requires scattering droplets rather than the continuous jet column that exists before breakup. U was therefore determined using data from the inline flowmeters and the cross sectional area, A, of the discharge orifices:

$$U = \frac{Q}{A} = \frac{4Q}{\pi D^2}$$

where Q is the measured volumetric flowrate. The uncertainty in U can be determined from the uncertainties in Q and D.

Flowrate uncertainties in the present experiment arise from two sources: (1) the measurement device and (2) variations in the flowrate during a test (e.g., due to pumping fluctuations; changes in back pressure, etc.). The crude oil and silicone fluid experiments used the same jet fluid delivery system. The CO_2 experiments required a different

delivery system to supply the high pressure, liquid CO_2. Flowrate fluctuations during the crude oil and silicone fluid tests were small and the flowmeters employed were frequently calibrated to minimize instrument error. The liquid CO_2 system, however, was subject to larger flowrate fluctuations during individual tests (as a consequence of the single-action, positive displacement pumps that had to be used) and direct calibration of the flowmeters was not possible, although redundant flowmeters were employed in some tests for comparison. Based on a review of the flowmeter characteristics and flowrate data records, it is estimated that the uncertainties in Q for crude oils, liquid CO_2 and silicone fluids are ± 2%, ±7.5% and ± 4.2%, respectively. Taking the uncertainty in D to be ±3%, the corresponding errors in the calculated U are ± 8% (crude oil), ±13.5% (liquid CO_2) and ± 10.2% (silicone fluid).

The magnitude of the uncertainties in the values of the fluid properties, ρ, μ, and σ, used to calculate *Re*, *We*, and *Oh* varied widely for the three types of jet fluid and are discussed separately.

Silicone Fluids. Properties of the two silicone fluids, GE silicone SF96-20 and Dow Corning 200(R) (ν = 0.65 cs) are well documented by the manufacturers. The principal source of uncertainty was the temperature at which these properties were evaluated from the database. Viscosity was much more sensitive to changes in temperature than ρ or μ. In the present experiments, the temperature records indicate that the maximum variation in silicone fluid temperature during a test run was 0.04 °C. This corresponds to only a 0.1% uncertainty in ν.

Crude Oils. An extensive discussion of the uncertainties in estimated crude oil properties for these experiments is provided in Masutani & Adams (2000). Environment

Canada analyzed the four crude oils and determined their densities and viscosities. Interfacial tension, σ, however, was not measured was and had to be estimated from surface tension data for similar oils. A mean value of 25.9 dyne/cm was used to calculate *We* and *Oh* in this study. Based on the range of values reported in the database (21.6 to 30.2 dyne/cm), the uncertainty in σ is believed to be approximately ±17%. This potential error is dwarfed by the uncertainties in dynamic viscosity, μ, related to possible changes in oil composition due to devolatilization. Relationships provided by Environment Canada predict that between 12% (Platform Gail) and 19% (Neptune SPAR) of the oil mass could evaporate in 1 hour at the air temperatures at which the experiments were conducted. Anticipating this problem, oil was pumped from the sealed storage barrels and the oil injection system reservoir was filled and covered to minimize evaporation. In the worst case, evaporation would yield a modest increase in density of around 4%. Dynamic viscosity, however, could change by a factor of 14 for Platform Gail and 4 to7 for the other three oils (Masutani & Adams, 2000).

ρ and μ were estimated by extrapolation from the Environment Canada property data reported at 15°C and 25°C. Differences between temperatures measured with the thermistor in the oil supply line before it enters the water tank and actual temperatures of the oil exiting the orifice also contribute to the experimental uncertainty. A detailed heat transfer analysis was conducted to identify the maximum oil temperature change that could occur between the measurement point and the orifice due to heat transfer to the cooler water in the tank. This analysis predicted a difference of less than 3°C for the worst case of extremely low oil flow rate. The corresponding uncertainties in ρ and μ are

insignificant relative to the uncertainties associated with devolatilization.

Liquid CO_2. There is an extensive and accurate database on the properties of pure CO_2 as functions of pressure and temperature. This database was employed to estimate ρ and μ. The effect of contaminants in the liquid CO_2 on jet fluid properties was neglected, since vendor analysis indicated that the level of impurity was very low. CO_2 temperature variations during a test was the primary source of uncertainty in the values of ρ, μ, and σ. The –20°C liquid CO_2 extracted from the refrigerated storage tank is pressurized and passed through heat exchangers to warm it before being injected. Particularly at low flow rates, it was difficult to maintain a constant CO_2 temperature. In the worst case (2mm orifice, low flow rate, long test duration), the temperature of the liquid CO_2 rose by 10°C. This corresponds to an decrease in density of around 1.5% and a decrease in kinematic viscosity of around 19% (the actual uncertainties are about half these values, since properties are evaluated at the time mean temperature during the entire duration of the run). These numbers represent the upper limit of uncertainty, since temperature variations were typically much smaller in other tests. From Uchida (2002), the interfacial tension of liquid CO_2 and pure water at P = 50 bar is approximately 28 mN/m at T = 5 °C (278K) and 38 mN/m at T = 15 °C (288K). For a 3 wt% NaCl solution, interfacial tension increased by about 10% from these values. A value of 30 mN/m was used to calculate *We* and *Oh* for the present liquid CO_2 injection tests. The uncertainty in σ is estimated to be ± 26 %.

Following conventional methods (e.g., Allisy, 1980), the uncertainties in *We*, *Re*, and *Oh* for the three types of jet fluid were calculated using the estimated uncertainties in properties discussed above. The results have been summarized in Table 5.3.

C.2 Droplet Size Uncertainties

Individual measurements of droplet size by means of the PDPA or video image analysis are subject to error. In this section, the manitude of these errors are estimated.

C.2.1 CO_2 Droplet Circularity Analysis

The theory of operation of the PDPA assumes that the measured particles are spherical. Non-spherical droplets result in errors. In order to quantify these errors, it was necessary to estimate the deviations from sphericity of droplets with sizes that fell within the PDPA measurement range in the present experiments. Toward this end, video data from the CO_2 tests (which generally had good image clarity) were analyzed.

Since the video data provide two dimensional projections of the three dimensional droplets, we assume that there is a direct correlation between sphericity (3-D) and circularity (2D). The circular shape parameter, *C* is defined as

$$C = \frac{a}{b}$$

where *a* and *b* are the longest and shortest segments from the centroid of a droplet to its contour (edge) pixels. The shape parameter of a circle is 1. Departures from circularity (and sphericity) increase with increasing *C*.

In the present work, the spatial resolution of the image analysis technique is about 0.19 mm/pixel. It was decided, therefore, to limit the study of circularity to droplets with diameters larger than 3 mm, which would provide good S/N. The circular shape parameter was determined for 3740 different CO_2 droplets. Figure C.1 plots *C* as a function of droplet diameter. As expected, the shape parameter increases with droplet size. Representative images of CO_2 droplets with different shape parameters are provided in Figure C.2. The number inside the image is the individual droplet identifier (between 1 and 3740). The first number in the paranthesis under each image is the shape parameter *C*; the second number is the calculated droplet diameter in mm. The dots in the droplets are their centroids.

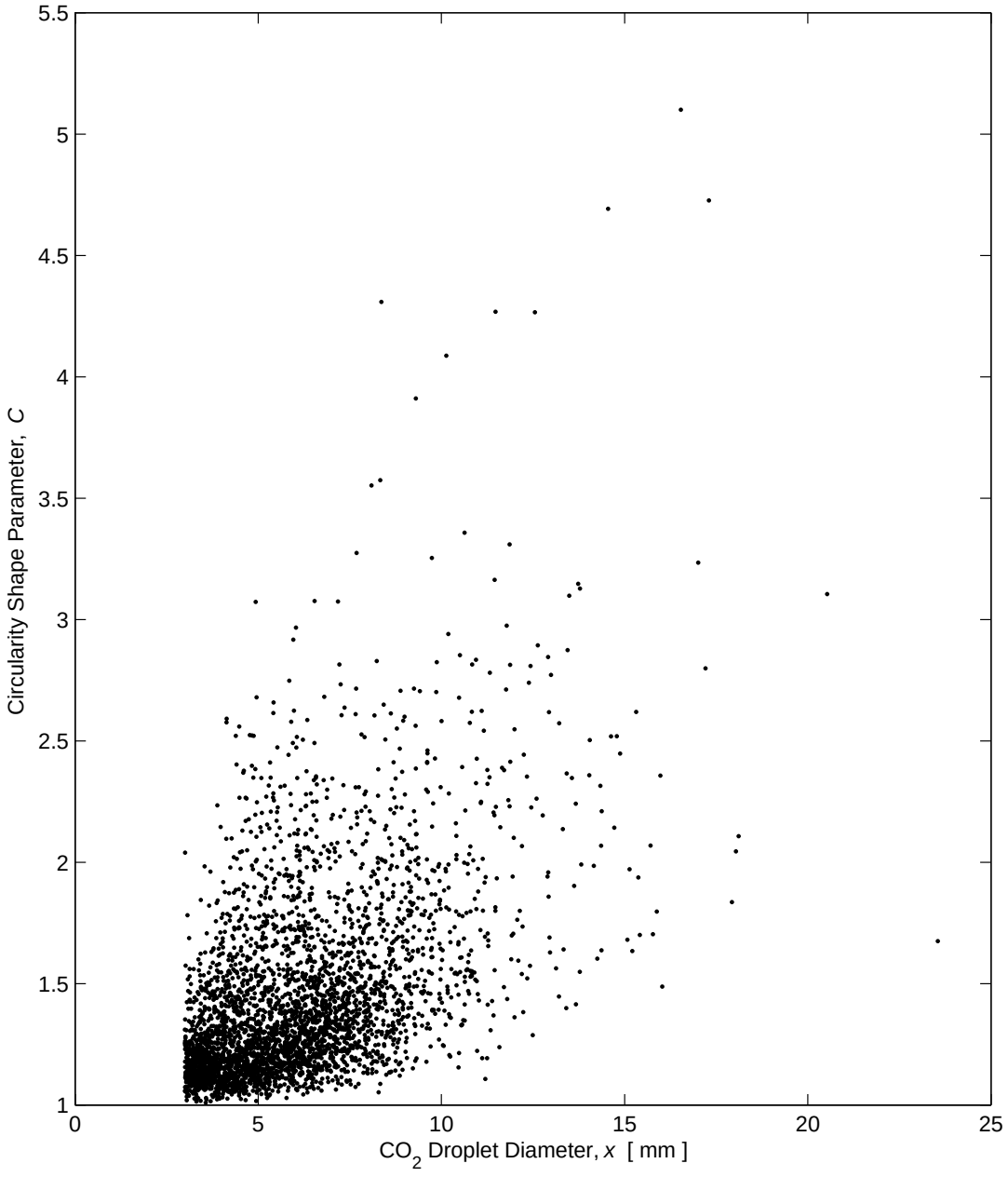

Figure C. 1 Circularity shape parameter versus droplet diameter. Data are for 3740 CO_2 droplets measured by image analysis with $x \geq 3$ mm.

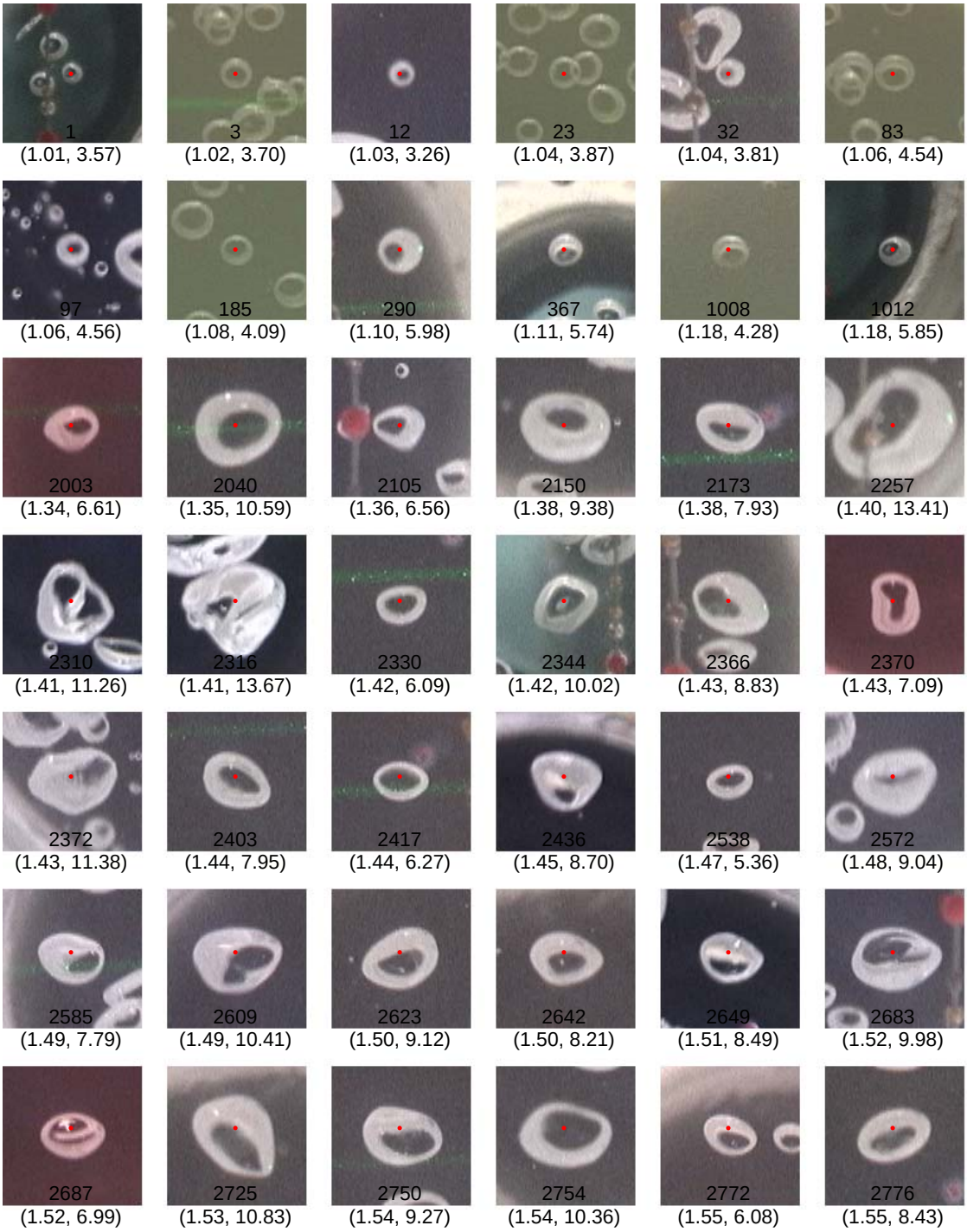
1
(1.01, 3.57)
3
(1.02, 3.70)
12
(1.03, 3.26)
23
(1.04, 3.87)
32
(1.04, 3.81)
83
(1.06, 4.54)
97
(1.06, 4.56)
185
(1.08, 4.09)
290
(1.10, 5.98)
367
(1.11, 5.74)
1008
(1.18, 4.28)
1012
(1.18, 5.85)
2003
(1.34, 6.61)
2040
(1.35, 10.59)
2105
(1.36, 6.56)
2150
(1.38, 9.38)
2173
(1.38, 7.93)
2257
(1.40, 13.41)
2310
(1.41, 11.26)
2316
(1.41, 13.67)
2330
(1.42, 6.09)
2344
(1.42, 10.02)
2366
(1.43, 8.83)
2370
(1.43, 7.09)
2372
(1.43, 11.38)
2403
(1.44, 7.95)
2417
(1.44, 6.27)
2436
(1.45, 8.70)
2538
(1.47, 5.36)
2572
(1.48, 9.04)
2585
(1.49, 7.79)
2609
(1.49, 10.41)
2623
(1.50, 9.12)
2642
(1.50, 8.21)
2649
(1.51, 8.49)
2683
(1.52, 9.98)
2687
(1.52, 6.99)
2725
(1.53, 10.83)
2750
(1.54, 9.27)
2754
(1.54, 10.36)
2772
(1.55, 6.08)
2776
(1.55, 8.43)

(a)

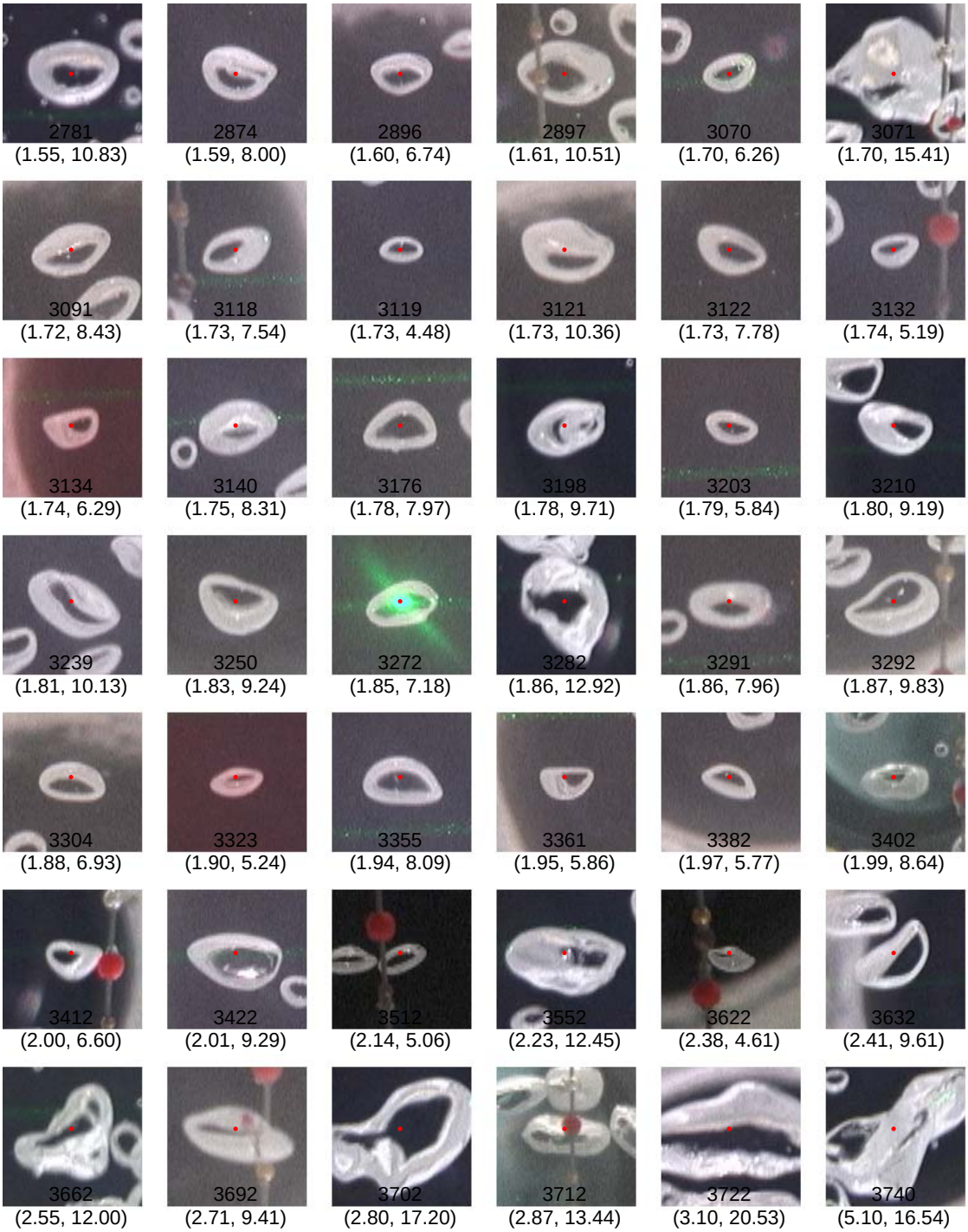

(b)

Figure C. 2 Images of CO_2 droplets with different shape parameters. The numbers inside the images are the droplet identifiers. The first number in the parenthesis is the shape parameter *C*; the second number is the droplet diameter in mm.

C.2.2 PDPA Errors

PDPA bias (i.e., the tendency to detect large droplets of a polydispersion and miss small droplets) precluded application of the instrument to perform measurements of the crude oil. Bias did not appear to be a problem in measurements of the clear silicone fluid and liquid CO_2 (Masutani & Adams, 2000).

The primary source of PDPA error in the present tests is believed to be due to non-spherical droplets. Figure C.3 provides examples of the types of measurement errors that can occur when a non-spherical particle crosses the PDPA optical probe volume.

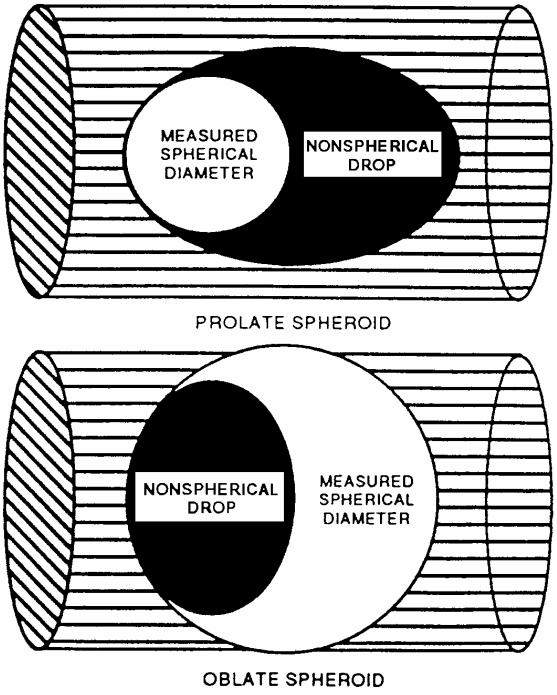

Figure C. 3 Examples of the response of the PDPA to non-spherical droplets (Bachalo, 1994).

As implied in Figure C.3, the Phase Doppler method responds to the radius of curvature of the droplet in the plane of the two incident beams. This idea is depicted further in Figure C.4. The size of an elliptical droplet will be overestimated if its major

axis is perpendicular to the PDPA laser fringes and will be underestimated if it is aligned parallel to the fringes. Hence, the measurement error depends on the orientation of the droplet, as well as its shape. It may be argued that if the non-spherical droplets are randomly orientated or oscillating, then the measured average size will adequately represent the equivalent sphere (Bachalo, 1994).

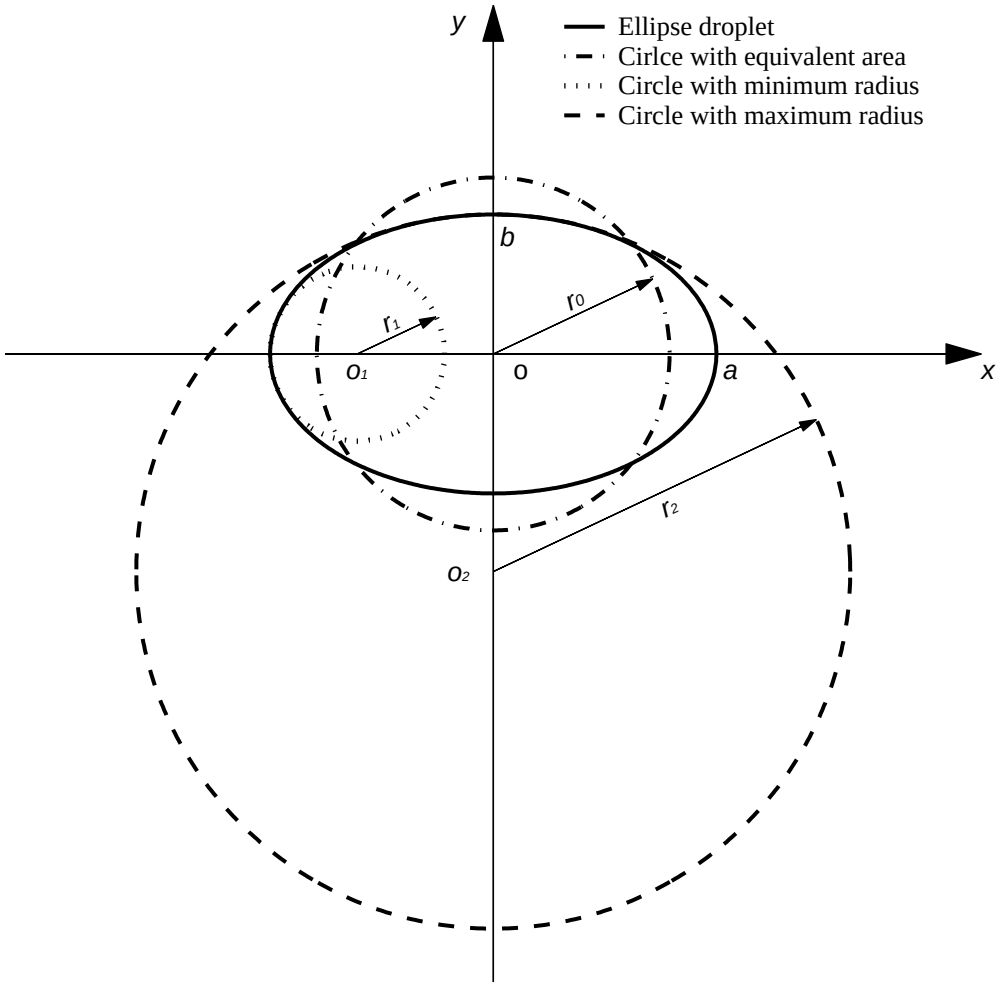

Figure C. 4 PDPA measurement uncertainty of an elliptical droplet with a major axis of 2*a* and a minor axis of 2*b* depending on whether the PDPA fringes align with x or y. r_0 is the equivalent radius of a circle with the same area as the ellipse (desired result); r_1 and r_2 are the minimum and the maximum radius of curvature of the ellipse and the radii of the droplets erroneously detected by the PDPA.

To estimate the magnitude of the uncertainty associated with non-spherical droplets, we assume elliptical (symmetric) droplets. Adopting the terminology from Figure C.4, the droplets have a major axis of length 2*a* and a minor axis of length 2*b*. The projected area of the droplet is πab. A sphere with the same projected area has a radius:

$$r_0 = \sqrt{ab} \tag{C.1}$$

Assuming that the droplet can be oriented at any angle relative to the laser fringes in the PDPA optical measurement volume, the measured value of *r* can be any value between r_1 and r_1, i.e.,

$$r_1 \le r \le r_2$$

where

$$r_1 = b^2 / a\,; \tag{C.2.a}$$

$$r_2 = a^2 / b \tag{C.2.b}$$

Using the circularity shape parameter defined in Section C.2.1:

$$C = a/b, \tag{C.3}$$

we obtain

$$a = r_0 C^{1/2}$$

and

$$b = r_0 C^{-1/2}$$

Equations C.2.a and C.2.b can then be rewritten as

$$r_1 = r_0 C^{-3/2} \tag{C.4a}$$

and

$$r_2 = r_0 C^{3/2} \qquad \text{(C.4b)}$$

The relative error in the measurement as a function of C is then

$$\varepsilon = \frac{r - r_0}{r_0} = C^{\pm 3/2} - 1 \qquad \text{(C.5)}$$

Figure C.5 presents ε as a function of the circularity shape parameter *C*. Also included in this figure is a histogram of measured values of *C* for 821 CO_2 droplets with diameters of 3 mm < *x* < 4.08 mm which fall in the PDPA measurement range. This data set is a subset of the ensemble of 3740 droplets that were analyzed in Section C.2.1. In this size range, the mean value of the circularity parameter is 1.23 and the standard deviation is 0.17. For this value of *C*, ε = +36% and –27%. It should be pointed out, however, that, as seen in the histograms provided in Section 5.3, the fraction of droplets with 3 mm < *x* < 4.08mm measured by the PDPA typically is quite small. Furthermore, since the circularity shape parameter decreases for smaller droplets, the relative error calculated above represents an upper bound. If the droplets are indeed randomly oriented, then deviations from sphericity should have a limited effect on the statistical quantities such as characteristic diameters. In the present experiments, however, hydrodynamic forces exerted on large buoyant droplets would tend to flatten them and favor an orientation where the major axis is aligned with the laser fringes, leading to underestimates of droplet size.

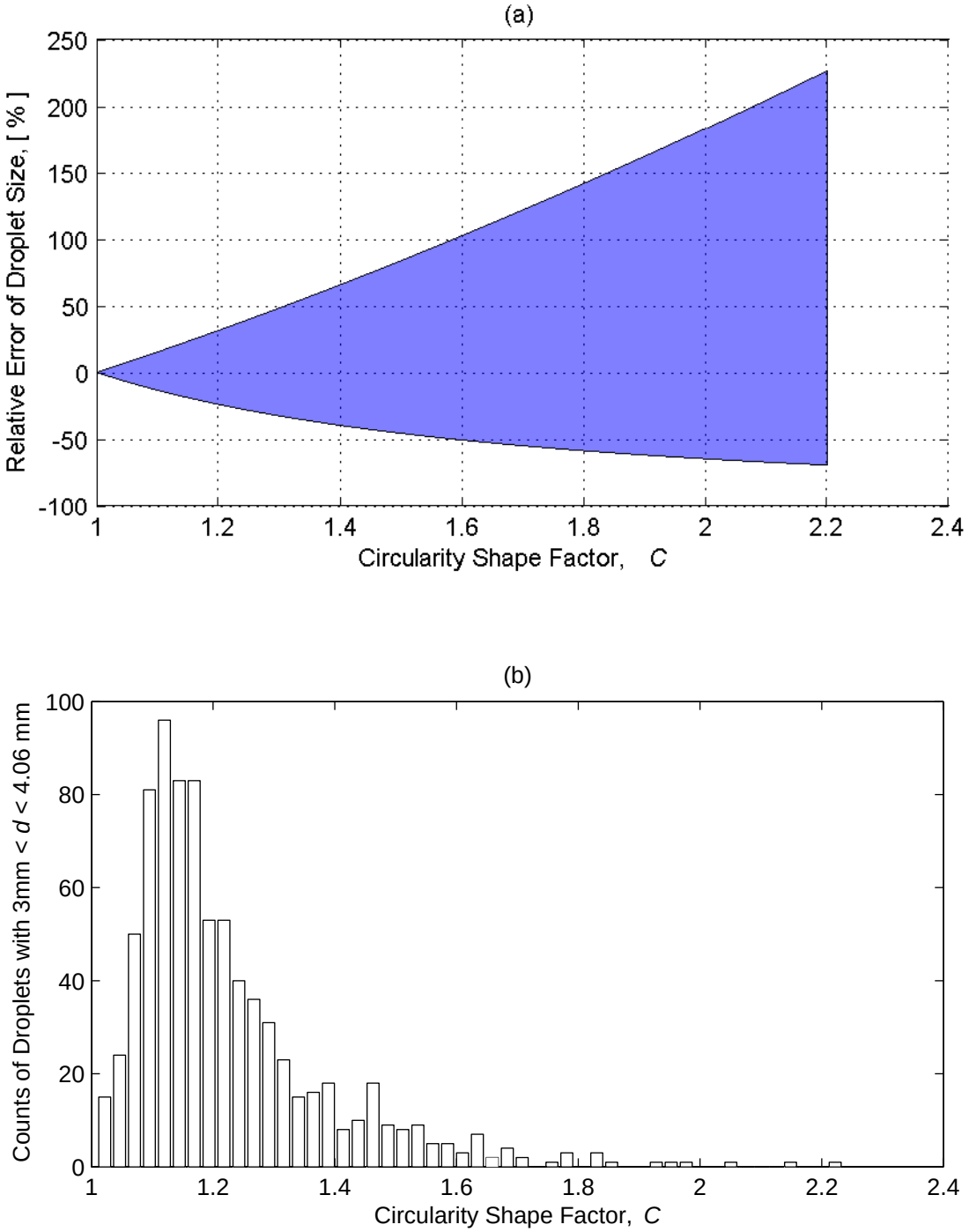

Figure C. 5 PDPA measurement uncertainty. (a) Size relative error versus circularity parameterr *C*. The relative error falls within the darkened band. (b) Histogram of measured shape parameters of 821 CO_2 droplets (3 mm < *x* < 4.06 mm) that fall within the PDPA measurement range.

C.2.3 Image Analysis Errors

To estimate the uncertainty of the image analysis technique, multiple measurements were performed to determine the size of a reference bead of known diameter. The solid spherical reference bead had a diameter of 3.68 mm. 160 different images of the bead were selected from the digital video records of case CDC10WTP52 (liquid CO_2 injection into tap water from a 10 mm sharp edge orifice at a pressure of 52 bar). Figure C.6 present representative images that were analyzed of the bead during different tests. The dimension of each image is 640 × 480 pixels.

The statistics of the 160 video image analysis measurements are provided in Figure C.7. Figure C.7a is the size histogram of the measured reference bead diameter, which is approximated reasonably well by a normal distribution with mean = 19.92 pixels and standard deviation of 0.60. In Figure C.7b, the relative error of these measurements has a normal distribution with mean = 0 and standard deviation of 0.03. Based on this study, the relative uncertainty of the image analysis technique is estimated to be approximately ± 11% of the measured value of diameter.

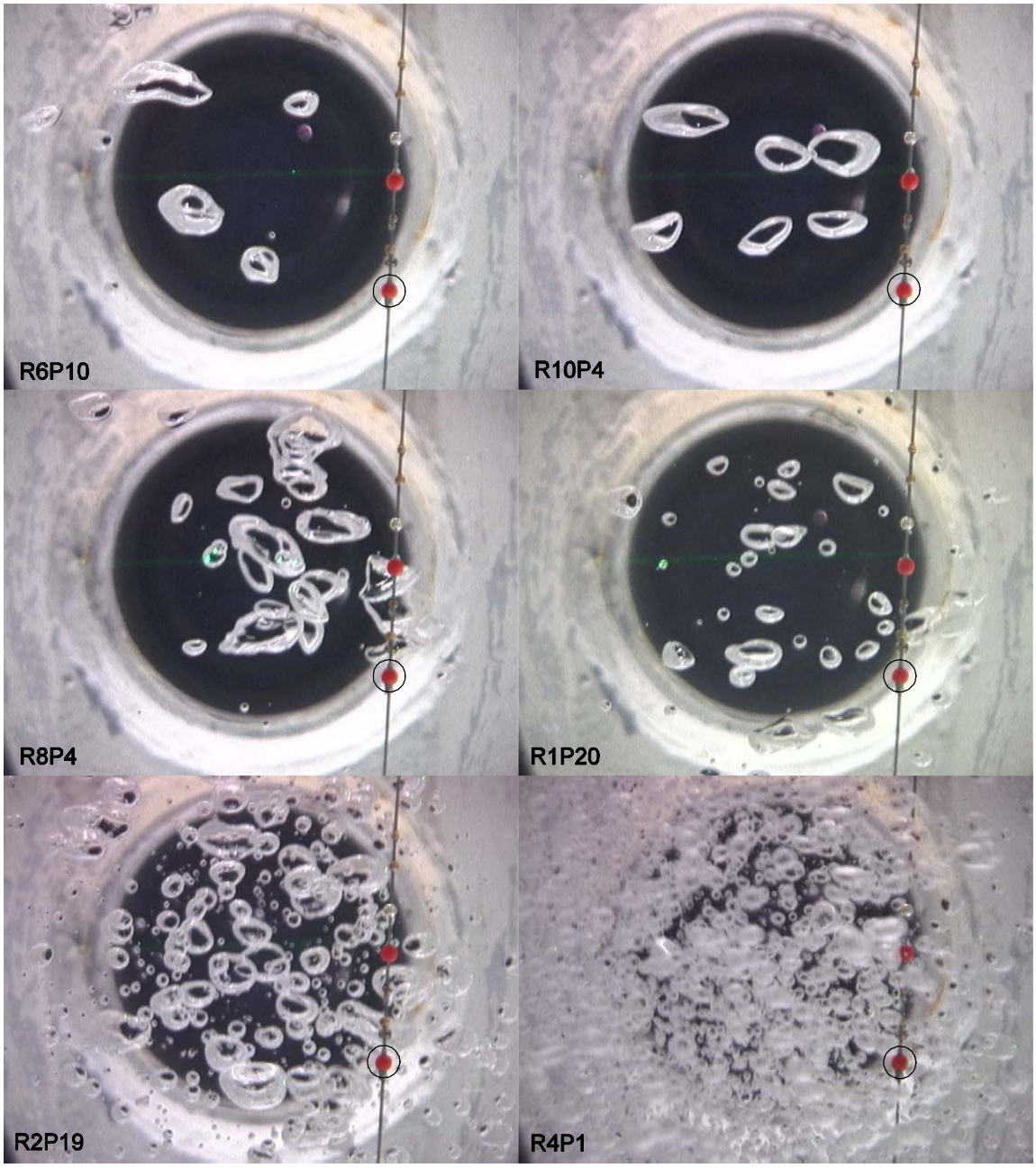

Figure C. 6 Video images of the reference bead (circled). Images are for liquid CO_2 injection into tap water through a 10 mm sharp edge orifice (CDC10WTP52). Dimension of each image is 640 × 480 pixels. ”R”+digit is the run number. “P”+digit is the photo number.

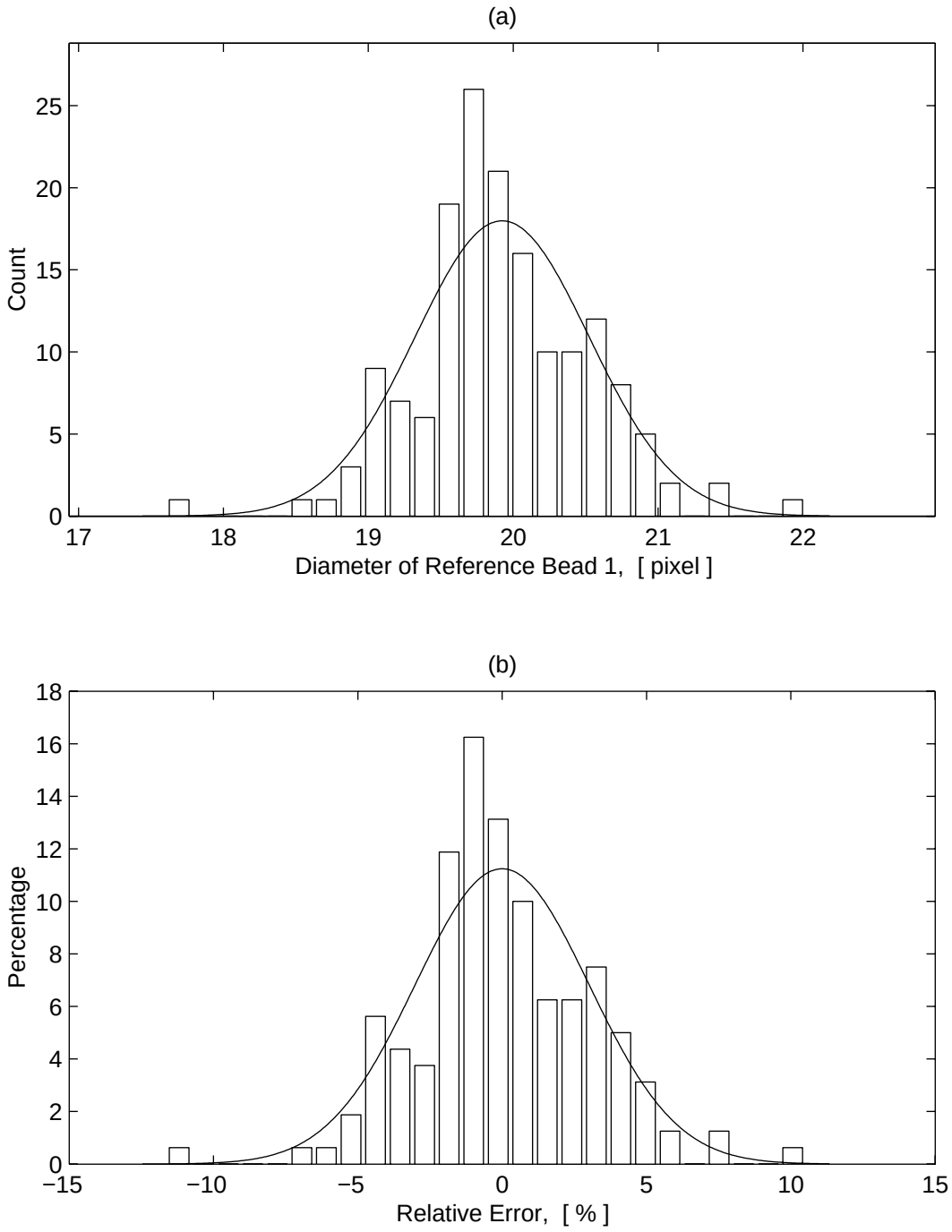

Figure C. 7 (a) Size histogram of multiple image analysis measurements of the same reference bead. Solid line is Normal distribution fitted to the histogram with mean of 19.92 pixels and standard deviation of 0.60. (b) Relative error of (a) has a normal distribution with mean of 0 and standard deviation of 0.03.

REFERENCES

Alendal, G., Drange, H. and Thorkildsen, F. (1998). Two-phase modeling of CO_2 droplet plumes. Technical Report No.153, the Nansen Environmental and Remote Sensing Center, Norway, October 12.

Allisy, A. (1980). Some statistical methods used in Metrology. *Proceedings of the International School of Physics "Enrico Fermi," Course LXVIII*, (Milone, A.F. and Giacomo, P., eds.), North-Holland, Amsterdam.

Arai, M. and Amagai, K. (1999). Surface wave transition before breakup on a laminar liquid jet. *International Journal of Heat and Fluid Flow*, pp. 507-512.

Ashgriz, N. and Mashayekhi, F. (1995). Temporal analysis of capillary jet breakup. *Journal of Fluid Mechanics*, Vol. 291, pp. 163-190.

Auerbach, D. (1996). *Climate change mitigation via ocean disposal of power-plant-generated CO_2: A comprehensive environmental and political analysis*. Master Thesis, Department of Civil and Environmental Engineering, MIT.

Aya I. and Yamane, K. (1992). Stability of Clathrate-hydrate of carbon dioxide in highly pressurized water. *Fundamentals of Phase Change: Freezing, Melting, and Sublimation*, ASME, HTD, Vol. 215, pp. 17-22.

Aya I., Yamane, K. and Nariai, H. (1997). Solubility of CO_2 and density of CO_2 hydrate at 30 Mpa. *Energy*, Vol. 22(23), pp. 263-271.

Bachalo, W. D. (1980). Method for measuring the size and velocity of sphere by dual-beam light scatter interferometry. *Applied Optics*, Vol. 19(3), pp. 363-370.

Bachalo, W. D. and Houster, M. J. (1984). Phase doppler spray analyzer for simultaneous measurements of drop size and velocity distributions. *Optical Engineering*, Vol. 23(5).

Bachalo, W. D. (1994). Experimental methods in multiphase flow. *International Journal of Multiphase Flow*, Vol. 20, supplement, pp. 261-295.

Berger, S. A. (1988). Initial-value stability analysis of a liquid jet. *SIAM Journal of Applied Mathematics*, Vol. 48, pp. 973-991.

Bogy, D. B. (1978). Wave propagation and instability of a circular semi-infinite liquid jet harmonically forced at the nozzle. *J. Appl. Mech., Trans.* ASME 45, 469.

Bozzo, A. Z., Chen, H.-S., Kass, J.R. and Bardhum, A.J. (1975). The properties of the hydrates of chlorine and carbon dioxide. Desalination, 16, pp.461-466.

Brackbill, J. U., Kothe, D. B. and Zemach, C. (1992). A continuum method for modeling surface tension. *J. Comput. Phys.*, Vol. 100, pp 335.

Brewer, P. G., Peltzer, E. T., Friederich, G., Aya, I. and Yamane, K. (2000). Experiments on the ocean sequestration of fossil fuel CO_2: pH measurements and hydrate formation. *Marin Chemistry*, Vol. 72, pp. 83-93.

Chaudhary, K. C. and Maxworthy, T. (1980). The nonlinear capillary instability of a liquid jet. Part 2: Experiments on jet behavior before droplet formation. *Journal of Fluid Mechanics*, Vol. 96, pp. 275-297.

Chen, H.-S. (1972). *Res. Develop. Frog*. Report No. 830. Office of Saline Water, U.S. Dept. of Interior, Washington, D.C.

Chigier, N. and Reitz, R. (1996). Regimes of jet breakup and breakup mechanisms (physical aspects). *Progress in Astronautics and Aeronautics*, Vol. 166, pp. 1.9-135

Clift, R., Grace, J. R. and Weber, M. E. (1978). *Bubbles, drops, and particles*. Academic Press, New York, NY.

Das, T. K. (1997). Prediction of jet breakup length in liquid-liquid system using the Rayleigh-Tomotika analysis. *Atomization and Sprays*, Vol. 7, pp. 549-559.

Donnelly, R. J. and Glaberson, W. (1966). Experiment on capillary instability of a liquid jet. *Proc. Royal Soc. London*, A 290, pp.547-556.

Durst, F., Melling, A. and Whitelaw, J. H. (1976). *Principles and practice of Laser-Doppler anemometry*. Academic Press.

Durrani, T. S. and Greated, C. A. (1977). *Laser systems in flow measurement*. Plenum Press.

Eggers, J. and Dupont, T. F. (1994). Drop formation in a one-dimensional approximation of the Navier-Storkes equations. *Journal of Fluid Mechanics*, Vol. 262, pp.205.

Grant, R. P. and Middleman, S. (1966). Newtonian jet instability. *AIChE. J*., Vol. **12**(4), pp. 669-678.

Green, A. E. (1976). On the non-linear behavior of fluid jets. *Int. J. Eng. Sci*. 14, 49-63.

Goedde, E. F. and Yuen, M. C. (1970). Experiments on liquid jet instability. *J. Fluid Mech.*, Vol. 40, pp. 495-511.

Hayworth, C. B. and Treybal, R. E. (1950). Droplet formation in two-liquid-phase systems. *Industrial and Engineering Chemistry*. Vol. 42(6), pp. 1174-1181.

Haenlein, A. (1931). Disintegration of a liquid jet. Forschung, 2, 139, NACA TN659(1932).

Hewitt, G. F. (1997). From gas-liquid to liquid-liquid flow: a difficult journey? *International Symposium on Liquid-Liquid Two-Phase Flow and Transport Phenomena, International center for Heat and Mass Transfer,* URL: http://ichmt.me.metu.edu.tr/abstracts/llft97-paplist.html

Hirai, S., Okazaki, K., Tabe, Y. Hijikata, K. and Mori, Y. (1997). Dissolution rate of liquid CO_2 in pressurized water flows and the effect of clathrate films. *Energy*, Vol. 22(23), pp. 285-293.

Hirleman, D. E., Bachalo, W. D. and Felton, P. G. (1988). *Liquid particle size measurement techniques*, 2nd volume, ASTM.

Homma, S., Koga, J., Matsumoto, S. and Trggvason, G. (2000). Numerical investigation of a laminar jet breakup into drops in liquid-liquid system. *The 8th International Conference on Liquid Atomization and Spray System*, Pasadena, CA, USA.

Huynh, H., Ashgriz, N. and Mashayek, F. (1996). Instability of a liquid jet subject to disturbances composed of two wave numbers. *Journal of Fluid Mechanics*. Vol. 320, pp. 185.

Lafrance, P. (1975). Non-linear breakup of a laminar liquid jet. *Phys. Fluids*, Vol. 18, pp. 428.

Lefebvre, A. H. (1989). *Atomization and Sprays*. Hemisphere Publishing Corporation.

Lieb, S. J. and Goldstein, M.L. (1986). Convective and absolute instability of a viscous liquid jet. *Phys. Fluids*, 29(4), 952-954.

Lin, S.P. (2003). *Breakup of Liquid Sheets and Jets*. Cambridge University Press.

Longmire, E. K., Norman, T. L. and Gefroh, D. L. (2001). Dynamics of pinch-off in liquid/liquid jets with surface tension. *International Journal of Multiphase Flow*, Vol. 27, pp. 1735-1752.

Keller, J. B., Rubinow, S.I., and Tu, Y. O. (1973). Spatial instability of a jet. *Phys. Fluids*, Vol. 16, pp. 2052-2055.

Kitamura, Y. and Takahashi, T. (1986) Stability of jets in liquid-liquid systems, Chapter 19. *Encyclopedia of Fluid Mechanics*, Vol. 2, (N.P. Cheremisinoff, ed.), Gulf Publishing Company, Houston, TX.

Kowalewski, T. A. (1996). On the separation of droplets from a liquid jet. *Fluid Dynamics Research*, Vol. 19, pp. 121-145.

Kumar, A. and Hartland, S. (1996). Unified correlation for the prediction of drop size in liquid-liquid exaction columns. *Ind. Eng. Chem. Res*., Vol. 35, pp. 2682-2695.

Kumar, A. and Hartland, S. (1984). Correlation for drop size in liquid-liquid spray columns. *Chem. Eng. Commun*. Vol. 31, pp. 193-207.

Kuo, K. K. (1996). *Recent advances in spray combustion: spray atomization and drop burning phenomena*. American Institute of Aeronautics and Astronautics, Inc.

Kuo, K. K. (1996). *Recent advances in spray combustion: spray combustion measurements and model simulation, Volume II*, American Institute of Aeronautics and Astronautics, Inc.

Mansour, N. N and Lundgren, T. S. (1990). Satellite formation in capillary jet breakup. *Phys. Fluids*, Vol. 2 (7), pp. 1141-1144.

Mashayekhi, F. (1994). *Numerical study of capillary and thermocapillary jets and drops*. Ph.D. Dissertation, Department of Mechanical and Aerospace Engineering, State University of New York at Buffalo.

Mashayek, F. and Ashgriz, N. (1995). Advection of axisymmetric interfaces by the volume-of-the-fluid method. *International Journal for Numerical Methods in Fluid*, Vol. 20(12), pp.1337.

Masutani, S. M. and Adams, E. E. (2000). *Experimental study of multi-phase plumes with application to deep ocean oil spills*. Final Report to U.S. Dept. of the Interior, Mineral Management Service, Contract No. 1435-01-98-CT-30946.

Masutani, S. M. (2000). A field experiment to investigate CO_2 ocean sequestration. *OCEANS 2000*, Honolulu, Hawaii.

Masutani,S. M., Nishio, M. and Tang, L.(2000). CO_2 jet break-up under simulated deep ocean conditions. *5th International Conference On Greenhouse Gas Control Technologies*, Cairns, Australia.

Masutani, S. M. and Adams, E. E. (2004). Liquid droplet contaminant plumes in the deep ocean. *Japanese Journal of Multiphase Flow*, in press.

Meister, B. J. and Scheele, G. F. (1969). Drop formation from cylindrical jets in immiscible liquid system. *AIChE J*. Vol. 15, pp. 700-706.

Milosevic, I. N. and Longmire, E. K. (2002). Pinch-off modes and satellite formation in liquid/liquid jet systems. *International Journal of Multiphase Flow* Vol. 28, pp. 1853-1869.

Nihous, G. C., Tang L., and Masutani, S. M. (2002). A sinking plume model for deep CO_2 discharge. *The Sixth International Conference on Greenhouse Gas Control Technologies*. pp.765-770, Pergamon. Japan.

Nishikawa, N., Ishibashi, M., Ohta, H., Akutsu, N., Tajika, M., Sugitani, T. Hiraoka, R., Kimuro, H., and Shiota, T. (1995). Stability of liquid CO_2 spheres covered with clathrate film when exposed to environment simulating the deep sea. *Energy Conv. Mgmt.*, Vol. 36, pp.489-492.

Ohnesorge, W. (1936). Formation of drops by nozzles and the breakup of liquid jets. *Z.A.M.M.*, Vol. 16, pp. 355.

Papageorgiou, D., and Orellana, O. (1998). Study of cylindrical jet breakup using one-dimensional approximations of the Euler equations. *SIAM Journal of Applied Mathematics*, vol. 59(1), pp. 286-317.

Papageorgiou, D.T. (1993). Analytical description of the breakup of liquid jets in air. *ICASE Report*, No. 93-45, NASA Contractor Report 191503.

Pimbley, W.T. and Lee, H.C. (1977). Satellite droplet formation in a liquid jet. *IBM J. Res. Dev*. Vol. 21, pp.21-30.

Ramesh, K. (2000). *Digital Photoelasticity*. Springer.

Rayleigh, L. (1878). Instability of Jets. *Phil. Mag*, Nov, pp. 5-13.

Rayleigh, L. (1879). On the instability of jets. *Proc. London math. Soc.*, 10, pp. 4-13.

Rayleigh, L. (1892). On the instability of a cylinder of viscous liquid under capillary force. *Pil. Mag*. S.5. Vol. 34 (207), pp 145-154.

Reitz, R. D. (1978). *Atomization and other breakup regimes of a liquid jet*. Ph.D. Thesis, Princeton University.

Reitz, R. D. and Bracco, F. V. (1986). Mechanism of breakup of round liquid jets. *Encyclopedia of Fluid Mechanics*, Vol. 3 (N.P. Cheremisinoff, ed.), Gulf Publishing Company, Houston, TX.

Richards, J. R., Neris, A. N., and Lenhoff, A. M. (1993). Steady laminar flow of liquid-liquid jets at high Renolds numbers. *Phys. Fluid A*, Vol. 5(7), pp.1703-1717.

Richards, J. R., Lenhoff, A. M. and Beris, A. N. (1994). Dynamic breakup of liquid-liquid jets. *Phys. Fluid*, Vol. 6(8), pp. 1640-2655.

Richards, J. R., Beris, A. N., and Lenhoff, A. M. (1995). Drop formation in liquid-Liquid system before and after jetting. *Phys. Fluid*, Vol. 7(11), pp. 2617-2630.

Rygg, O. B. and Emilsen, M. H. (1998). *A parameter study of blowout rates for deep water and their effect on oil droplet and gas bubble generation*. Well Flow Dynamics AS.

Schulkes (1993). Dynamics of liquid jet revisited. *Journal of Fluid Mechanics*. Vol. 250, pp. 635-650.

Shokoohi, F. and Elord, H. G. (1987). Numerical investigation of the disintegration of liquid jets. *J. Comput. Phys.*, Vol. 71, pp. 324-342.

Skelland, A. H. P. and Walker, P. G. (1989). The effect of surface active agents on jet breakup in liquid-liquid systems. *The Canadian Journal of Chemical Engineering*, Vol. 67, pp.762-770.

Tang, L., Gorgas, T. J., and Masutani, S. M. (2002). Liquid CO_2 droplet spectra. *Sixth International conference on Green House Gas Control Technologies*, Kyoto, Japan.

Tang, L and Masutani, S. M. (2003). Laminar to turbulent flow liquid-liquid jet instability and breakup. *The Thirteenth International Offshore and Polar Engineering Conference*, Honolulu, Hawaii, USA.

Teng, H. (1994). Laminar instability of cylindrical liquid jets. Ph.D. dissertation, Department of Mechanical Engineering, University of Hawaii.

Teng, H., Kinoshita, C. M. and Masutani, S. M. (1995). Prediction of droplet size from the breakup of cylindrical liquid jets. *International Journal of Multiphase Flow*, Vol. 21(1), pp.129-136.

Teng, H., Masutani, S. M., and Kinoshita, C. M. (1995). Nonlinear analysis of flow in post-dryout. *Heat Transfer*. pp.150-157.

Teng, H., Masutani, S. M., Kinoshita, C. M. and Nihous G. C. (1996). The effect of hydrate formation on CO_2 jet instability. *Prepr. Pap., American Chem. Soc. Div. Fuel Chem.*, 41 (6), pp. 1447-1451.

Teng, H. and Yamasaki, A. (1999). Hydrate formation on surface of buoyant liquid CO_2 drops in a counterflow water tunnel. *Energy and Fuels*, Vol. 13, pp. 624-628.

Tjahjadi, M., Stone, H. A., and Ottino, J. M. (1992). Satellite and subsatellite formation in capillary breakup. *J. Fluid Mech.*, Vol. 243, pp. 297-317.

Tomotika, S. (1935). On the stability of a cylindrical thread of a viscous liquid surrounded by another viscous fluid. *Proc. Roy. Soc*., A150, 322.

Tomotika, S. (1936). Breakup of a drop of viscous liquid immersed in another viscous fluid which is extending at a uniform rate. *Proc. Roy Soc*., A153, 302.

Torpey, P.A. (1989) A non linear theory for describing the propagation of disturbances on a capillary jet. *Phys. Fluids* A (1), pp. 661-671.

Tyler, E. (1933). Instability of liquid jets. *Phil. Mag.*, Vol. 16, pp.504-518.

Uchida, T., Ebinuma, T. and Narita, H. (2000). Laboratory studies on the formation and dissociation processes of CO_2-hydrate crystals-measurements of interfacial tension between CO_2 and water. OCEANS 2000, Honolulu, Hawaii.

Uchida, T., Ohmura, R., Takeya, S., Nagao, J., Minagawa, H., Ebinuma, T. and Narita, H (2002). Estimations of interfacial tension between liquid CO_2 and water from the sessile-drop observations. *Greenhouse Gas Control Technologies*. Ed. Gale, J. and Kaya, Y., Vol. 2, Pergamon.

Unverdi, S.O. and Tryggvason, G. (1992). Computation of multi-fluid flows. *Physica D* Vol. 60, pp. 70-83.

Wadesley, M.W.(1995). Thermodynamics of multi-phase equilibria in the CO2-seawater system. *Direct Ocean Disposal of Carbon Dioxide*. Ed. Hanada, N. and Ohsumi, T., TERRAPUB, Tokyo.

Wong, C. S. and Hirai, S. (1997). *Ocean Storage of Carbon Dioxide: A Review of Oceanic Carbonate and CO_2 Hydrate Chemistry*. IEA Greenhouse Gas R & D Programme Report.

Weber, C. (1931). On the breakup of a liquid jet. *Z.A.M.P*., Vol. 11, pp. 136-141.

Yamane, K., Tang, L., Masutani, S.M., Kojima, R and Aya, I. (2001). Numerical simulation of agglomeration of CO_2 droplets with hydrate film. *The Eleventh International Offshore and Polar Engineering Conference*, Stavanger, Norway.

Yuen, M.C. (1968). Nonlinear capillary instability of a liquid jet. *Journal of Fluid Mechanics*, Vol. 33, pp. 151-163.